Gravity anomalies and segmentation of the Eastern USA passive continental margin

by

Paul Patrick Andrew Wyer



Thesis submitted for the Degree of Doctor of Philosophy, University of Oxford

Department of Earth Sciences &
St. Catherine's College



Michaelmas Term 2003

Gravity anomalies and segmentation of the Eastern USA passive continental margin

Paul Patrick Andrew Wyer
St. Catherine's College and Department of Earth Sciences, University of Oxford
Michaelmas Term 2003

A compilation of high quality post-rift sediment isopach data has been used in conjunction with the observed free-air gravity anomaly to determine segmentation of the long term mechanical properties of the lithosphere at the Eastern USA passive margin. This segmentation is represented by a process-oriented analysis in which the flexural response of the margin to post-rift sediment loading is controlled by spatial variations in effective elastic thickness (T_e) of the underlying lithosphere.

Existing Eastern USA margin T_e estimates range from less than $10km$ to more than $30km$. In this study it is shown that high strengths of $10 - 40km$ T_e are confined to structural arches dividing the broadest marginal basins, while low strengths of less than $10km$ T_e are typically found in structural embayments and beneath the deep basins. The hinge zone, across which the degree of continental thinning increases rapidly, marks the transition between high and low strength. Yield strength envelope models support an argument that regions of low strength were created by lithospheric thinning during rifting, and sustained by thermal insulation and flexural curvature associated with voluminous post-rift sediment deposition. Along-strike T_e variations - reflected in the alternation of basement platforms and embayments - are attributed to inheritance of lithospheric segmentation from earlier tectonic events.

Along-strike segmentation of the margin has previously been observed as a $300 - 500km$ wavelength spectral energy peak in the shelf break Airy isostatic gravity anomaly (IGA) high. That this segmentation is explained by variations in the underlying lithospheric strength is demonstrated by a flexural IGA high in which the equivalent spectral peak is absent. The spectral energy of the along-strike T_e distribution peaks in the same waveband.

Removal of process-oriented components from the observed free-air gravity anomaly reveals other contributions that were not resolved in earlier studies. In particular, the (previously unknown) Carolina Trough Isostatic Gravity Anomaly, has been identified and attributed to an extrusive (syn-rift) volcanic source. Detailed study of this anomaly suggests that the margin is segmented in terms of its volcanic character, and argues against recent estimates of the volume of new igneous material emplaced during rifting.

Extended Abstract

Subsidence of the lithosphere driven by vertically acting loads is often modelled using Airy-type (local) isostasy. However, it has long been recognised that the true lithospheric response is often better represented as that of an elastic plate with finite thickness, T_e. In the oceans this thickness can normally be predicted from the depth of the 450 ± 150^oC isotherm, but diverse continental T_e estimates (varying by as much as two orders of magnitude) show its structure to be more complex. One reason for this is the comparitively long tectonic history experienced by the continents; such that a single area may have inherited the structural contributions of multiple tectonic events.

At passive continental margins the most recent major tectonic event is rifting of the lithosphere. Because this thins the mechanical lithosphere and elevates the geotherm, it is generally thought to reduce T_e. Long-term ($> 10^6 a$) strength recovery is limited by the rate of cooling during and after rifting. Hence, if the newly formed margin is rapidly sediment blanketed blanketed then insulation of the thinned lithosphere will slow the recovery of strength; sustaining margin weakness for longer than would otherwise be expected.

Passive margin T_e has, in the past, been constrained by combined flexural sediment backstripping, rift reconstruction, and gravity modelling. The most robust estimator of T_e is the free-air 'edge effect' gravity anomaly observed across the shelf-break and slope. This anomaly originates at the transition between thick, essentially unrifted, crust and greatly thinned, rift-stage, crust, but is modified by post-rift sedimentation. If this sedimentation is progradational then the edge effect high advances seaward with the shelf-break, and its amplitude and wavelength change as a function of the underlying lithospheric rigidity.

Existing studies of the free-air gravity anomaly at African passive margins have identified along-strike segmentation that is not explained solely by thinning of a uniform initial lithospheric structure. The implication is that the effects of rifting on lithospheric strength are superimposed on earlier structural segmentation.

In this study a process-oriented approach isolates the relative contributions of rifting and flexural sediment loading to the free-air gravity anomaly at the East Coast, USA,

passive continental margin. This allows constraint of T_e because the flexural response contributes directly to the 'sedimentation' gravity anomaly, and the flexural backstrip contributes to the geometry of the total tectonic subsidence from which the crustal structure and 'rifting' gravity anomaly are derived. The 'observed' T_e distribution is that which best describes the free-air gravity anomaly in terms of summed rifting and sedimentation contributions.

The free-air gravity anomaly contains a large component from deposition of large ($> 10km$) thicknesses of post-rift sediment; making it an ideal location for a study of long term structural segmentation. Rifting took place over a $c.40MYr$ period during the Late Triassic to Early Jurassic period, as part of the break-up of Pangea. The result is a passive margin of over $1500km$ in length with close to $200MYr$ of subsidence and a stratigraphic evolution that is focused in four primary offshore basins.

Although the subsidence of this margin has been extensively studied at point locations or along single profiles (mostly in relation to the LASE deep seismic line and deep COST B2 and B3 wells), few estimates of T_e have been made. Those estimates that exist appear, at first, contradictory: across the Baltimore Canyon Trough shelf break a T_e of less than $15km$ has been proposed, yet estimates from the coastal plain and Salisbury Embayment suggest much higher ($T_e > 30km$) values.

Some of this diversity can be explained by differences in the degree of thinning experienced during rifting, but even before rifting a history of major tectonic events had already left a complex tectonically imposed structure. The influence of this pre-existing structure on the rifting process is evident (reflected in the varied geometries of the main sedimentary basins and basement features), but (as at the African margins) inheritance may also be an important contributor to the long term post-rift strength of the lithosphere. If such contributions are evidenced by the flexural response to sediment loading then they can be observed in the form of along-strike segmentation of T_e.

The Eastern USA is thus appropriate for a study that investigates the relative contributions of inherited structure, rifting, and post-rift sedimentation to long term passive margin evolution. This is made possible by availability of high quality sediment isopach and gravity anomaly data, complimented by four deep seismic transects and several deep stratigraphic test wells.

The primary dataset is based on sediment isopach data compiled by the United States Geological Survey (USGS). This data is limited to the deep marginal basins of the shelf, so it has been supplemented by data correlated from other sources. The combined 3-D dataset records the post-rift evolution of the margin as seven (Middle Jurassic through to Quaternary) stratigraphic units extending from the Appalachian fall line to the western

North Atlantic abyssal plain.

The sediment data provide for process-oriented analysis of contributions to the free-air gravity anomaly due to rifting and flexurally compensated sedimentation of the margin. Previous studies of this type have typically relied on a 2-D 'trial and error' method of minimising the difference between observed and calculated gravity anomalies. This study is based on an iterative 3-D method, in which the T_e distribution is efficiently obtained through iterative minimisation of the isostatic gravity anomaly (the remainder of the free-air gravity anomaly after constrained rifting and sedimentation contributions have been removed).

At the simplest level, the results show a direct correspondence between structural arches (observed as basement highs dividing the landward edges of the widest marginal basins) and high T_e estimates of 10 to 40 km. By contrast, structural embayments are associated with low ($< 10km$) T_e estimates. This aspect of observed T_e segmentation has its origins in inherited pre-rift structure; which influenced both the geometry of the hinge zone and the width of the rift-stage crust.

Structural inheritance explains the gross distribution of strength and weakness along-strike, but a magnitude drop in T_e across the hinge zone towards the marginal basins is more easily explained by the combined effects of lithospheric thinning and voluminous sediment deposition on the long term lithospheric strength. In the first case, thinning of the lithosphere causes an initial weakening followed by gradual recovery of strength as the thinned lithosphere cools. However, this strength recovery is not observed in the recovered T_e distribution, suggesting either that the long term T_e is controlled by the earliest sediment deposition, or that the initial weakness has been preserved by sediment driven subsidence and thermal insulation.

Simple yield strength envelope models show that the flexural curvature due to sediment loading also affects the long term lithospheric strength. If the flexural curvature is assumed to cause linear (Hookean) stresses in each mechanical layer then the 'strong' lithosphere is limited to those parts in which yield strength exceeds the bending stress. The mechanical thickness able to support high curvature bending stresses is much less than the total mechanical thickness prior to loading. In the case of the Eastern USA margin, it is shown in this study that for flexural curvatures greater than $10^{-6}m^{-1}$ the dominance of T_e by inheritance and lithospheric thinning gives way to the effects of curvature induced yielding. Between a curvature of $10^{-6}m^{-1}$ and $10^{-5}m^{-1}$ T_e drops from about 50% of its initial value to less than 10%. It should be noted, however, that because high rigidity promotes large radii of curvature, positive feedback tends to confine high curvatures to areas of pre-existing weakness.

Process-oriented analysis has also been used to approximate the location of the ocean to continent transition (or boundary) in two ways. The first approach is novel, and relies on comparison of results from the main analysis sum gravity anomaly with those from an 'oceanic' analysis in which T_e follows the depth of the 450^oC isotherm. Where one method is significantly better at explaining the wavelength and amplitude of the free-air gravity anomaly than the other the lithosphere is attributed as either continental or oceanic accordingly. While this approach works well along some sections, there are parts of the margin along which it is inconclusive. Hence a second approach (based on an earlier study) has been considered. This assumes that the backstripped oceanic basement will be smooth relative to rifted continental and transitional basement, and hence that the oldest oceanic crust will be marked by a flattening of the total tectonic subsidence. Determination of the oldest oceanic crust on this basis provides better spatial coverage than the first method, but offers no indication of the width (if any) of the transition zone.

Spectral analysis reveals that a previously published $300 - 500km$ dominant wavelength in the along-strike Airy isostatic gravity anomaly shelf-break high is effectively explained by a corresponding peak in the recovered T_e distribution. Subtraction of the contributions of rifting and flexurally loaded sediments from the free-air gravity anomaly removes 92.7% of its energy along this profile; an Airy isostatic model removes only 71%.

Among the parts of the observed free-air gravity anomaly that are not explained by the process-oriented analysis is the narrow and linear 'Carolina Trough Isostatic Gravity Anomaly' (CTIGA), which extends some $700km$ along the margin. Despite the great length of this anomaly its presence has previously been concealed by: larger (unrelated) features in the observed free-air gravity anomaly; and unresolved flexural contributions to Airy isostatic gravity anomalies.

The newly identified CTIGA follows a path between the East Coast and Brunswick magnetic anomalies, and lies directly over the landward edge of seaward dipping reflectors resolved by the USGS 32, BA-6, and EDGE-801 deep seismic studies. Both the magnetic anomalies and the seaward dipping reflectors have a proposed volcanic origin, so a volcanic source for the CTIGA is possible. Extrusive volcanism is verified as a likely source by a series of models in which a synthetic margin is loaded (flexurally) by flood volcanism and magmatic underplating, and (through local isostasy) by igneous intrusion. The results argue against the robustness of past estimates of the volume of new igneous material added to the margin during rifting.

The CTIGA is confined to the rift-stage crust of the Carolina Trough (the narrowest marginal basin), which is bounded: to the west by the most extensive of the strong marginal platforms; and to the east by earliest oceanic crust. Its location, together with

the absence of distinct East Coast and Brunswick magnetic anomalies to the north and south, suggests that along-strike segmentation of lithospheric strength is parallelled by the volume of volcanic material extruded during rifting. One possibility is that passive mantle upwelling (a proposed source for Eastern USA syn-rift volcanism) was most active in regions where high strength appears to have narrowly focussed extension during the late stages of rifting.

The methods applied in this study use observable loads and segmentation of effective elastic thickness to reduce the ambiguity associated with gravity modelling of a passive margin. The observed T_e distribution that results is consistent with known features of the margin structure, and is robust against uncertainties in the model parameters and sediment distribution. The accompanying flexural isostatic gravity anomaly provides a basis from which to investigate features of the margin structure and free-air gravity anomaly that had otherwise remained hidden.

In the case of the Eastern USA margin, structural inheritance has been intimately linked to structural segmentation both during and after rifting; and extensive offshore sediment deposition has played a significant role in sustaining long term weaknesses through thermal insulation, load driven subsidence, and curvature induced lithospheric yielding. Similar segmentation of the volume of volcanic material extruded during rifting has been revealed by a characteristic isostatic gravity anomaly that concords with other signifiers of margin volcanism. As is demonstrated in a southeast Greenland case study, the apparent uniformity of this anomaly could make it a useful reference for similar studies at other margins.

Acknowledgements

I would like to thank my supervisors: Tony Watts for supervision of my graduate studies in Oxford; and Roger Scrutton for taking on the same role during my time at Edinburgh, and for valuable advice and other contributions later on. Thanks also to Debbie Hutchinson for providing essential sediment isopach data, and to Western Geophysical for providing seismic data that may form part of a later West African study.

Acadmically, I would like to thank Mark Behn for insights, magnetic data, and willingness to help in any way possible; Gary Karner for inspiring several lines of investigation; and David Haddad and Gareth Armstrong for discussions on (amongst other things) the meaning and relevance of T_e. Thanks also to Steve Usher, for solving innumerable computer problems, and for being both a friend and a sounding board for new ideas and odd mumblings; and to Charlotte Vinnicombe for acting as 'Miss Fixit' with the Oxford system. Most of the figures were made using the GMT software of Wessel & Smith [1995].

Financially, thanks to NERC for funding the project; to the University of Oxford Department of Earth Sciences and University of Edinburgh Department of Geology and Geophysics for working out how to share the consumables part to my best advantage; to the Oxford department for providing last-minute travel funds for the MARGINS meeting in Utah, and to the Burdett Coutts Fund for supporting attendance at Fall 2000 AGU.

Extra special thanks to Jennifer Godwin for patience, dedication, tolerance, and unyielding support (and for lending expert LaTeX skills when needed). General gratitude goes to the many friends and colleagues, particularly to: the Marine Group (both new and old); Conor Snowdon; Lucy Bunce; Richard and Helen Steele (and relatives thereof); Arwen Deus; Catherine Wyer (my cousin); and the graduate communities in both Edinburgh and Oxford. Without their support and interest the past five years would not have been so rewarding.

Finally thanks to my Oxford, Norwich and Guildford relatives. Especially to my parents and brother for trusting my judgement, accepting my occassional unwillingness to travel and providing whatever they could to get me through to the end. This thesis would not have been possible without them.

Contents

1 Introduction 1

1.1 Estimates of lithospheric effective elastic thickness 2

1.1.1 Elastic strength of oceanic lithosphere 3

1.1.2 Elastic strength of continental lithosphere 5

1.2 Elastic strength of passive continental margins 6

1.3 Aims and scope of thesis 8

1.4 Outline of thesis 9

2 The effects of continental rifting on lithospheric rigidity 10

2.1 Yield Strength Envelopes 10

2.1.1 Brittle regime 11

2.1.2 Ductile regime 12

2.1.3 Total strength of the lithosphere 14

2.1.4 Yield strength envelope uncertainties 15

2.2 Mechanical thickness of the lithosphere 18

2.3 Effective elastic thickness of the oceanic lithosphere 20

2.4 Effective elastic thickness of the continental lithosphere 21

2.4.1 Lower crustal weakness 22

2.4.2 Upper mantle weakness 24

2.5 Weakening of the lithosphere by emplaced loads 30

2.5.1 Yielding due to curvature 30

2.5.2 Weakening due to sedimentation 31

2.6 Continental rifting 31

2.6.1 Introduction 31

2.6.2 The McKenzie rift model 33

2.6.3 Lithospheric strength and continental rifting 36

2.6.4 Lithospheric necking 37

2.6.5 Rheology 40

2.6.6 Thermal effects of rifting 42

2.6.7 Post-rift strength 43
2.7 Passive margin strength 43
2.8 Conclusions 45

3 The Eastern USA passive continental margin **48**
3.1 Introduction 48
3.2 Structure and tectonic framework 49
3.2.1 Introduction 49
3.2.2 Rifted sediment basins 51
3.2.3 Crustal structure 55
3.3 Geophysical markers 58
3.3.1 Gravity anomalies 59
3.3.2 Magnetic anomalies 62
3.4 Volcanism 66
3.5 Post-rift evolution 69
3.5.1 Tectonic subsidence 69
3.5.2 Effective elastic thickness 69
3.5.3 Structural segmentation 71
3.6 This study 74
3.6.1 Data 75

4 Process-oriented analysis - Method **84**
4.1 Introduction 84
4.2 The process-oriented method 84
4.2.1 Stage 1: Backstripping 86
4.2.2 Stage 2: Calculation of stretching factor, β 90
4.2.3 Stage 3: Gravity modelling 90
4.2.4 Advantages 92
4.2.5 Application 92
4.3 Backstripping 94
4.3.1 1-D uniform thin elastic plate flexure 94
4.3.2 2-D uniform thin elastic plate flexure 95
4.3.3 Non-uniform thin elastic plate flexure 95
4.3.4 Sediment porosity 104
4.4 Calculation of the stretching factor, β 106
4.4.1 McKenzie-type rift 106
4.4.2 Depth of necking model 106

4.5 Gravity modelling . . . 108
4.5.1 Direct integral method . . . 108
4.5.2 Parker's method . . . 111
4.5.3 Spatial variations in density . . . 113
4.5.4 Efficient application of the process-oriented method . . . 113
4.6 Constraint of effective elastic thickness . . . 115
4.7 Robustness of the method . . . 118

5 Process-oriented analysis - Results 120
5.1 Introduction . . . 120
5.2 Uniform plate models . . . 122
5.2.1 Airy isostasy . . . 122
5.2.2 The role of mechanical strength . . . 125
5.3 Mechanical plate segmentation . . . 129
5.3.1 Initial estimate of effective elastic thickness variations . . . 130
5.3.2 Iterative analysis . . . 131
5.4 Sensitivity of the process-oriented analysis . . . 135
5.4.1 Bias due to the initial effective elastic thickness distribution . . . 135
5.4.2 T_e sensitivity . . . 142
5.4.3 Analysis window size . . . 142
5.4.4 Model parameters . . . 145
5.4.5 Sediment isopach data . . . 145
5.4.6 Strength during rifting . . . 148
5.5 'Oceanic' analysis . . . 150
5.5.1 Backstripping . . . 151
5.5.2 Isostatic gravity anomalies . . . 152
5.6 Summary . . . 153

6 Process-oriented analysis - Discussion 156
6.1 Introduction . . . 156
6.2 Distribution of mechanical strength . . . 157
6.2.1 Effects of rifting on mechanical strength . . . 157
6.2.2 Effects of sedimentation on mechanical strength . . . 160
6.2.3 Inheritance of mechanical strength . . . 165
6.3 Isostatic gravity anomaly . . . 167
6.3.1 The Carolina Trough Isostatic Gravity Anomaly . . . 170
6.3.2 Along strike segmentation . . . 173

6.4 The oceanic to continental transition 177
6.5 Summary 183

7 Igneous contributions to the Eastern USA continental margin 185
7.1 Synthetic models 185
7.1.1 Extrusive volcanism 186
7.1.2 Underplating 186
7.1.3 Intrusive volcanism 189
7.2 A volcanic isostatic gravity anomaly 191
7.3 Volume of igneous crust 192
7.4 Comparison with the Southeast Greenland margin 193
7.5 Summary 197

8 Conclusions 198
8.1 Introduction 198
8.2 Data 198
8.3 Methods 199
8.4 Summary of results 200
8.4.1 Segmentation of mechanical thickness 200
8.4.2 Volcanism 200
8.4.3 Oceanic to continental transition 201
8.5 Primary conclusions 202
8.6 Future work 203

A Finite difference software 205

Bibliography 218

Chapter 1

Introduction

Although the effects of shifting loads on the crust had been considered by Leonardo da Vinci (1452-1519) and others after him, Airy [1855] and Pratt [1859] were the pioneers of isostasy. Airy's hypothesis differed from Pratt's both in geometry, and in the fact that it required 'breakage' of the crust to apply at all. By this measure, Airy inferred that only loads of great scale could generate sufficient stress to result in isostatic compensation of the type he described:

> Again reverting to the condition of breakage of the table-lands, as dominating through the whole of this reasoning, it will be seen that it does not apply in regard to such computations as that of the attraction of Schehallien and the like. It applies only to the computation of the attractions of high tracts of very great horizontal extent, such as those to the north of India. *Airy [1855].*

Implicit in Airy's hypothesis was an assumption that topographic loads would be either wholly supported by the crust, or wholly supported by mantle buoyancy. Gilbert [1874] was probably the first to apply plate flexure as an intermediary between the two mechanisms. In 1874 he considered, and rejected, flexure as an explanation for the overall geometry of the Basin and Range Province of western North America, but his studies of palaeo-shorelines [Gilbert, 1889] suggested that rebound due to unloading of the Late Pleistocene Lake Bonneville water mass had been accommodated through a combination of crustal rigidity, and mantle buoyancy:

> ...assuming that isostatic equilibrium, disturbed by the removal of the water, was restored by viscous flow... the flow was not quantitatively sufficient to satisfy the stresses caused by the unloading. A stress residuum was left to be taken up by rigidity... *Gilbert [1889].*

As with Airy's hypothesis, scale determined the mode of compensation. However, Gilbert's model differed in that it defined a progression in isostatic mechanisms from total rigid support to local isostasy, such that regional isostatic compensation could occur with no requirement for 'breakage' of the crust. This meant that isostasy need not be confined to only the largest topographic features. Further, isostatic compensation could now be viewed as a regional effect, with the potential to extend beyond individual load boundaries.

Gilbert's work provided a reference from which others - most importantly J. Barrell (e.g. Barrell [1914b]), F. A. Vening Meinesz (e.g. Vening Meinesz [1931]), and R. Gunn (e.g. Gunn [1943b]) - developed and refined the concept of flexural isostasy and regional compensation during the first half of the 20th century.

Since then, and partly fuelled by the emergence of plate tectonics, flexural isostasy has found widespread application. By comparing observations of flexure to predictions of elastic plate models it has been possible to determine rigidity in a wide range of tectonic settings. These include, passive continental margins (e.g. Walcott [1972]; Watts & Ryan [1976]; Sawyer [1985a]; Thorne & Watts [1989]), orogenic belts (e.g. Karner & Watts [1983]; Lyon-Caen & Molnar [1983]; Caporali [1995]), volcanic islands (e.g. Watts [1978]), and oceanic trenches (e.g. Caldwell *et al.* [1976]). Because the flexural behaviour of the lithosphere has commonly been characterised as that of a thin elastic plate with an 'effective elastic thickness' (T_e), overlying an invsicid fluid, such studies can be directly compared. The resulting body of work, which continues to expand today, provides a rich source of data from a common approach to characterisation of lithospheric strength.

1.1 Estimates of lithospheric effective elastic thickness

Compilations of continental (e.g. Watts [1992]) and oceanic (e.g. Watts & Zhong [2000]) effective elastic thickness estimates reveal variations of T_e both in time and space, with a range from $0km$ to nearly $130km$ (see Watts [2001]). The result is that the amplitude, geometry, and distribution of the flexural response to a given load will depend both on where it is emplaced, and when.

There are significant spatial rigidity variations at continental scales (e.g. Pinet *et al.* [1991]), and probably more locally. Despite this, many authors have found it adequate to consider T_e as uniform across limited regions (e.g. Watts & Ryan [1976]; Steckler & Watts [1978]). However, models that incorporate spatial changes in T_e may present a more robust means of studying isostatic behaviour in areas where the loading response or lithospheric structure is likely to vary locally (e.g. Audet & Watts [1994]; van Wees &

Cloetingh [1994]). There are many examples of such areas, including: regions in which the lithosphere has undergone thermal (e.g. hotspot) or mechanical (e.g. orogenic) alteration; where the origins of adjacent lithospheric blocks differ; or across structural boundaries such as the oceanic to continental transition (or boundary).

Some authors have considered spatial variations in T_e (particularly in the past decade, e.g. Stewart & Watts [1997]; Watts & Stewart [1998]), but much of the work dating from the early 1970s onwards has focussed on temporal controls (e.g. Walcott [1970]; Watts [1978]). Walcott [1970], for example, suggested that flexural rigidity may depend on load age. He showed that data from young glacial lakes and old oceanic seamounts and islands could be explained by a viscoelastic model in which initial elastic support is modified by increasingly important viscous relaxation over time.

At the time of Walcott's work, differences in evolution and structure of oceanic and continental lithosphere were not commonly accepted or understood. Identification of these differences has allowed the relationship of T_e with lithospheric structure to develop in the context of these two environments.

1.1.1 Elastic strength of oceanic lithosphere

Watts [1978] found that if a Maxwell viscoelastic relaxation model were to explain data from both the Hawaiian Ridge and the Emperor Seamounts then there would have to be an order of magnitude difference in the relaxation time constant between the two regions. Given that both formed on similar age oceanic lithosphere, such a difference is hard to justify. So Watts put forward an alternative explanation in which the flexural response is dependent on the effective elastic thickness at the time of loading. In this case an oceanic load is flexurally compensated over a limited period ($< 10^6 Yr$) following emplacement, and despite subsequent increase in load age, there is little further isostatic adjustment. This preserves the original flexural subsidence and effective elastic thickness from the time of loading, and viscous relaxation is limited only to short times, as the supporting lithosphere thins from its (instantaneous) seismic thickness to its (long-term) elastic thickness.

The Hawaiian Ridge and Emperor Seamount chain T_e estimates of Watts [1978], together with those from other oceanic studies, suggest that the effective elastic thickness of oceanic lithosphere increases as a function of its age. As oceanic lithosphere cools and thicknens away from the spreading center, so the depth at which it can be considered 'ductile' increases. In the simple single layer rheology of oceanic lithosphere, the main control on ductility is temperature. Watts [1978] showed that the Pacific ocean T_e estimates conform to the depth of the $450 \pm 150^o C$ isotherm (Figure 1.1). Later work

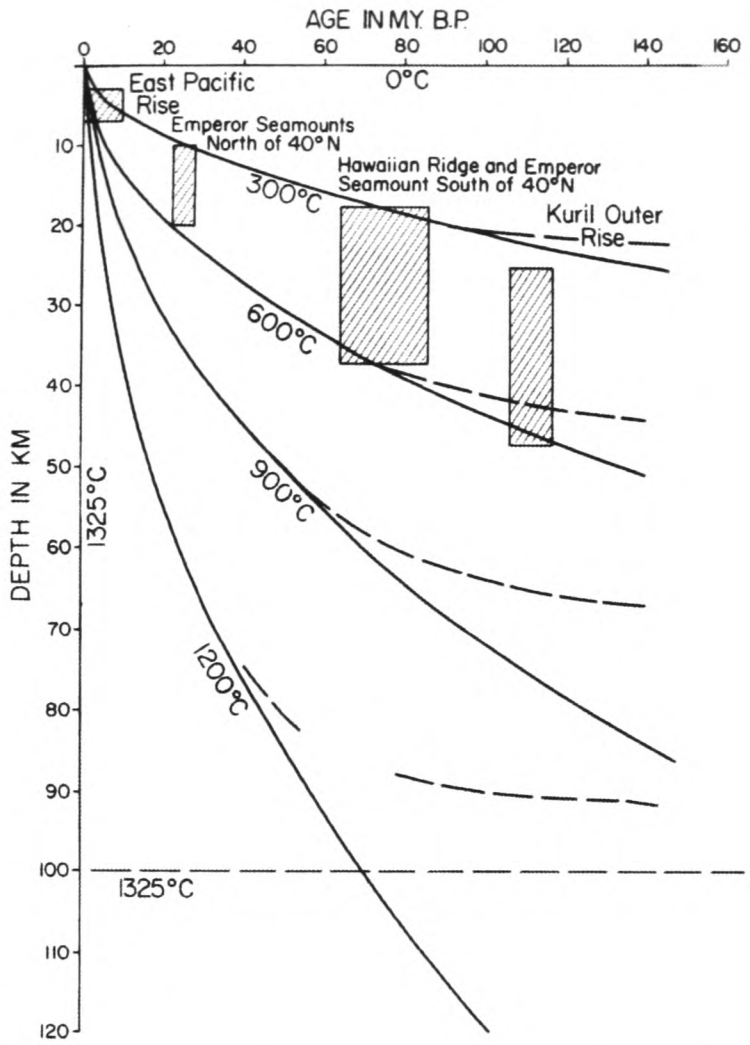


Figure 1.1: Estimates of oceanic effective elastic thickness plotted against the age of the lithosphere at the time of loading. These early estimates (the figure is from Watts [1978]) suggest that T_e is the depth of the $450 \pm 150^o C$ isotherm. A relationship that is supported by later work in most of the World's oceans [Watts, 2001].

involving compilation of many more oceanic T_e estimates [Watts, 2001] suggests that the correspondence between T_e and the depth to the $450 \pm 150^o C$ isotherm applies to most of the World's oceans.

An investigation of oceanic plate flexure at oceanic trenches by McAdoo *et al.* [1985] concluded that undeformed oceanic T_e is controlled by the mechanical base of the lithosphere, at $740 \pm 50^o C$. Although this is considerably deeper than the $450 \pm 150^o C$ isotherm, McAdoo *et al.* [1985] showed that load induced bending stresses reduce the effective T_e such that observed values typically correspond with shallower isotherm depths (see Chapter 2, Section 3).

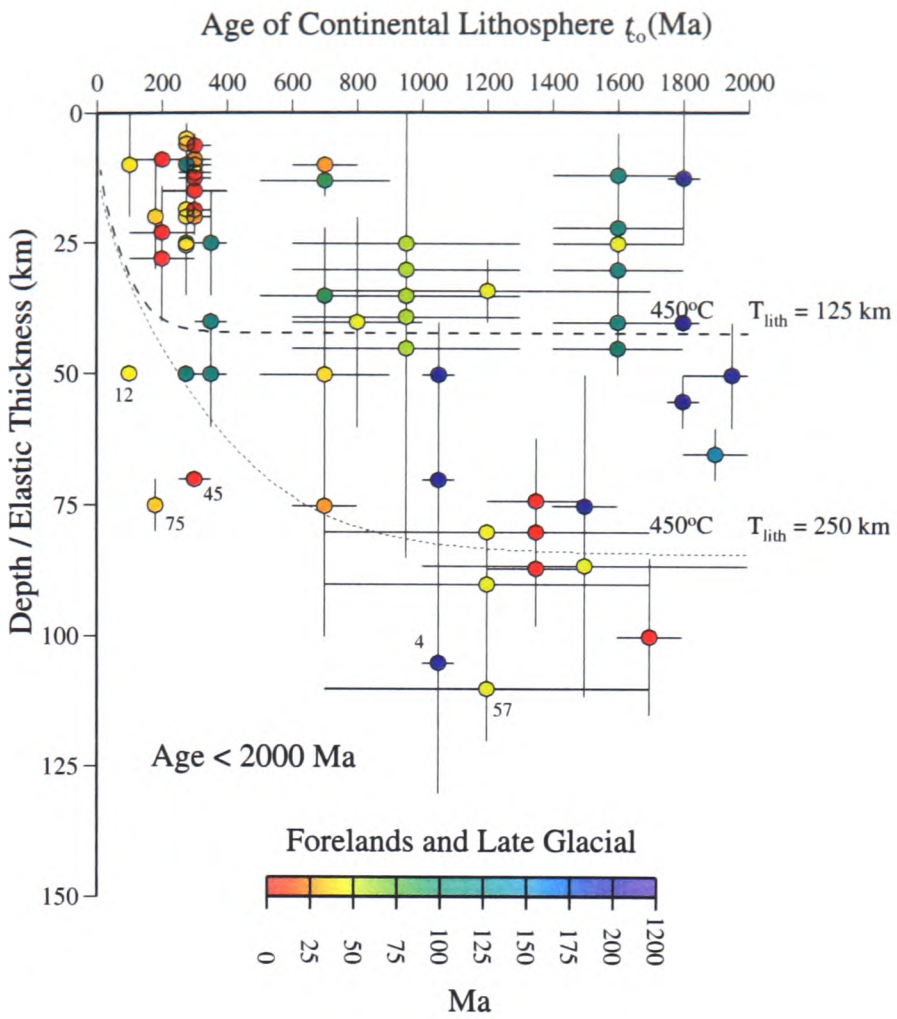


Figure 1.2: Continental effective elastic thickness estimates plotted against the age of the continental lithosphere (t_{co}) at the time of loading. Colours are according to the age of the load. Figure from Watts [2001].

1.1.2 Elastic strength of continental lithosphere

Karner *et al.* [1983] suggested that - as in the oceans - continental T_e depends on the depth to the 450^oC isotherm. There is a basis for this in that rocks become less ductile as temperature decreases, but there are two potential problems. Firstly, continental geothermal gradients are not as well known as those in the oceans, and secondly the origin, evolution and history of continental lithosphere are typically more complex.

The complexity of continental lithosphere limits the reliability with which T_e can be universally tied to a single parameter (such as an isotherm depth). More likely, there will be significant lateral heterogeneity that can be observed as spatial variations in T_e. This alone is enough to make continental elastic modelling more involved than oceanic, but the problem is exacerbated by potential ductility in continental lower crust (see Chapter 2, Section 4), and a generally lesser knowledge of buried structure.

A compilation of (foreland basin and late glacial lake) continental T_e estimates [Watts, 2001] shows no systematic dependency between continental T_e and either the age of the load or the thermal age of the lithosphere at the time that it was emplaced (Figure 1.2)

Many of the larger continental T_e estimates have been determined using spectral coherence of Bouguer gravity anomalies with topography. Recently the validity of the method, and of high continental T_e estimates in general, has been challenged [McKenzie & Fairhead, 1997; Maggi *et al.*, 2000a,b; Jackson, 2002; McKenzie, 2003], leading to fresh debate on the rheological meaning of continental T_e and on the methods by which it is estimated. The key points of this debate are discussed further in Chapter 2, Section 4.2.

1.2 Elastic strength of passive continental margins

Passive continental margins form as the product of continental 'break-up' and consequent formation of new ocean basins; combining continental, oceanic, and rifted continental lithosphere in a single environment. Rifted crust at the landward edge of the margin is typically only lightly thinned and altered by rifting, but across the 'hinge zone' there is a rapid increase in the degree of lithospheric thinning (and therefore basement depth), and in the alteration of both the crustal rheology (e.g. by igneous intrusion) and lithospheric mantle composition (e.g. by upwelling of deeper mantle material). This extends as far as the earliest oceanic crust.

The degree of rift thinning has direct implications for the long term post-rift strength in terms of: how far geotherms have been raised by rifting; the relative thicknesses of rheological units; and how much lithospheric alteration has occurred. Hence abutment of unrifted continental lithosphere, thinned continental lithosphere, and oceanic lithosphere can be expected to lead to large local variations in effective elastic thickness.

In addition, abutment against young, hot oceanic lithosphere drives heat flow that reduces the early post-rift continental strength in the vicinity of the oceanic to continental transition, particularly where transform offsets cause frictional heating and increase the area of contact (e.g. Todd & Keen [1989]). This effect will be mitigated by hydrothermal circulation (perhaps as deep as the base of the crust, Calvert & Potts [1985]), and complicated by variations in the initial thermal structure on the continental side (e.g. as a result of stretching factor variations, Royden & Keen [1980]).

The large basement depth of the thinned continental lithosphere seaward of the hinge zone acts as a depositional trap - in some cases allowing large ($> 10km$) thicknesses of sediment to accumulate after break-up. The effects of this sediment (discussed in Chapter 2, Section 5.2), together with pre-existing variations in lithospheric structure along the margin, could contribute to the complexity of flexural isostasy by adding along-strike segmentation to the structure.

The flexural subsidence due to large thicknesses of post-rift sediment at passive mar-

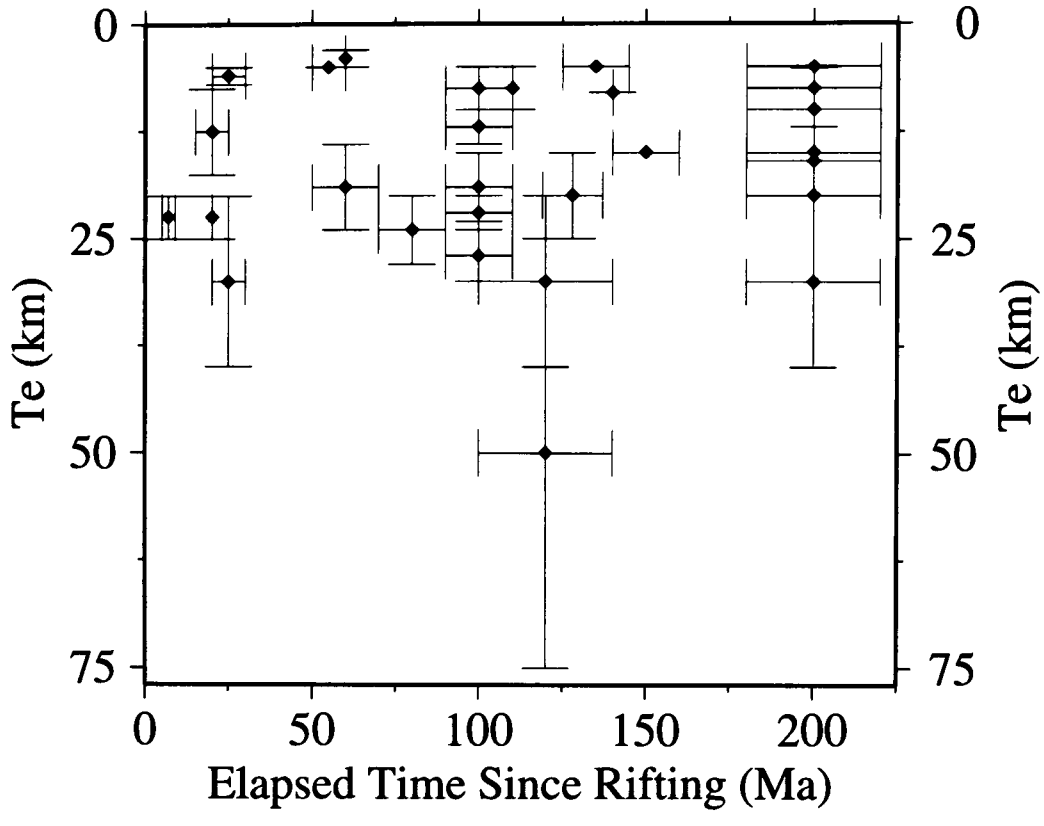


Figure 1.3: Passive continental margin T_e estimates plotted against elapsed time since rifting. For data compilation see Stewart [1998], Table A.3.

gins provides a means of estimating the underlying lithospheric effective elastic thickness. In most cases authors have used sediment data to determine the T_e that either best describes the high-low gravity couple associated with the shelf-break, or that results in flexurally subsidence most closely conforming to the observed stratigraphy.

Despite the apparent complexity of lithospheric structure at passive margins, such studies have generally provided a single T_e estimate that provides the best overall description of the flexural behaviour in a given location. Although all but a few studies place T_e at $30km$ or less, a compilation of these estimates provides little evidence of a single (e.g. thermal) control on T_e at passive continental margins (Figure 1.3).

Where spatial variations in passive margin T_e have been directly investigated (Watts & Marr [1995], Watts & Stewart [1998]), distinct along-strike segmentation has been observed. However, these studies have not resolved the actual variation in T_e between the rifted continental lithosphere of the coastal plain, the deeply thinned and intruded rift-stage lithosphere of the marginal basins, and the oceanic lithosphere beyond.

1.3 Aims and scope of thesis

This thesis presents the first margin-wide study of the controls on effective elastic thickness at a passive continental margin. The aim is to determine the T_e structure, and to use it to identify whether or not the margin is segmented. The segmentation can then be used to investigate the relative contributions of inheritance, rifting, volcanism, and sedimentation to the structure, evolution, and subsidence of the Eastern USA passive continental margin.

Collection of $30,000km$ of seismic reflection data between 1973 and 1978, and deep seismic studies (LASE Study Group [1986]; Trehu *et al.* [1989]; Austin *et al.* [1990]; Oh *et al.* [1991]; Sheridan *et al.* [1993]; Holbrook *et al.* [1994a,b]), have been extensively used in subsidence related studies of the Eastern USA margin (e.g. Steckler & Watts [1978]; Watts & Steckler [1979]; Sawyer [1985b]; Watts [1988]; Pazzaglia & Gardner [1994]; Behn & Lin [2000]). Segmentation of the margin has been discussed, but its study has been limited to interpretation of total tectonic subsidence (Sawyer [1985b]) and isostatic gravity anomalies based on Airy isostatic compensation of the post-rift sediment load (Behn & Lin [2000]). Where T_e has been estimated - by Watts [1988] for the central Baltimore Canyon Trough, and by Pazzaglia & Gardner [1994] for the Salisbury Embayment (Pazzaglia & Gardner [1994]) - markedly different values have been suggested (averaging to $c.9km$ in the former case, and estimated as $40km$ in the latter).

Reprocessing and interpretation of the $1970s$ seismic reflection data in the early $1990s$ allowed the generation of detailed (5 minute) isopach grids that cover most of the volume of the Eastern USA offshore marginal basins (Klitgord & Schneider [1994]; Klitgord *et al.* [1994]; Hutchinson *et al.* [1995, 1996]). These were made available for this thesis with the co-operation of Debbie Hutchinson of the USGS, Woods Hole Oceanographic Institute.

This thesis uses the sediment isopach data (supplemented with correlated data from other sources, see Chapter 3, Section 6.1) to model sediment load driven flexure of the Eastern USA margin. This forms part of a 'process-oriented' analysis in which differences between the free-air gravity anomaly and 'sum' gravity anomalies from successive margin reconstructions are used to constrain spatial variations in T_e.

The resulting T_e distribution is used as a proxy for structural segmentation of the margin. This allows investigation of the role of pre-existing structure in rifting and post-rift evolution, and of the effects of rifting and sediment loading on the mechanical thickness of the lithosphere. The isostatic gravity anomaly is used for study of a possible relationship between pre-existing structure and the volume of igneous material added to the crust during rifting.

1.4 Outline of thesis

The structure of the thesis is as follows:

- Chapter 2 discusses T_e and its rheological significance in the context of lithospheric yield strength envelopes and historical models for continental rifting and post-rift subsidence. This is used to explain the important role of structural segmentation in passive margin evolution.

- Chapter 3 introduces the Eastern USA margin study area. A review of the geology is included, together with commentry on past studies of the post-rift subsidence, and details of how the datasets needed for this study were compiled.

- Chapter 4 is a detailed description of the process-oriented analysis. It covers the origins and benefits of the process-oriented approach, and the methods and modifications that have been made to allow its efficient application to the study.

- Chapter 5 presents the results of process-oriented analysis of the Eastern USA margin evolution.

- Chapter 6 discusses implications of the process-oriented analysis in terms of lithospheric strength and the oceanic to continental transition. It includes comparisons of the analysis results with simple yield strength envelope models, and with past studies of passive margin subsidence and structure.

- Chapter 7 uses a series of synthetic volcanic models to investigate relationships between seismically observed structure and the isostatic gravity anomaly. This leads to new arguments relating to: the volcanic history of the study area; and the use of seismic data, post-rift subsidence, and gravity anomalies, to investigate the volcanic structure of passive continental margins in general.

- Chapter 8 concludes the thesis with a summary of the findings.

Chapter 2

The effects of continental rifting on lithospheric rigidity

This thesis uses constraint of spatial variations of effective elastic thickness (T_e) as a means of investigating structural segmentation at a passive continental margin setting. This chapter explains - through yield strength envelopes [Goetze & Evans, 1979] - how T_e can be placed in a rheological context, and how this relates to historical models of continental rifting and to the long-term flexural properties of rifted continental lithosphere.

2.1 Yield Strength Envelopes

The strength of the lithosphere can be considered as the sum of contributions from depths at which it is able to support differential stresses[1] without undergoing permanent non-linear strain (i.e. yielding) over geological timescales. Goetze & Evans [1979] inferred the depth dependence of rheology, temperature, and pressure in oceanic lithosphere from experimental rock mechanics data. The resulting 'yield strength envelope' (YSE) concept provides a means of defining finite duration yielding limits of the lithosphere.

YSEs allow for the fact that the strength of the lithosphere is limited by brittle failure in the upper part, and ductile failure in the lower part. To define the YSE for a particular rheology it is necessary to specify the constituent mineralogy most likely to fail at any depth by brittle fault slip, or by ductile dislocation creep or dislocation glide (e.g. Brace & Kohlstedt [1980]).

In brittle parts of the lithosphere the yielding limit is the boundary between elastic deformation and brittle slip along existing fault planes. Where deformation is ductile, any differential stress that produces a permanent strain over geological timescales is

[1]Note that elastic plate flexure is controlled by *deviatoric* stress matrices.

considered to exceed the yield strength. Although lower stresses will typically cause some ductile deformation, the strain rate will be so low as to be effectively nil over such periods. In such cases the behaviour is termed quasi-elastic [Burov & Diament, 1995], and a minimum strain rate (typically $10^{-17}s^{-1}$ to $10^{-14}s^{-1}$, e.g. Burov & Diament [1995]) can be defined as the effective yielding threshold.

2.1.1 Brittle regime

In general, seismogenic parts of the crust are considered to dominantly yield by brittle failure. On the assumption that brittle crust is typically already densely fractured, brittle failure will typically be controlled by frictional sliding along existing fault planes (rather than by much higher stress limits for fracture of unbroken rock). Experimental rock mechanics data support a linear relationship between confining pressure and the frictional yield strength that is relatively insensitive to mineralogy and temperature, whereby in the brittle part of the lithosphere (Byerlee's law, Byerlee [1978]):

$$\begin{aligned} \tau_f &= 0.85\sigma_n \quad : \quad \sigma_n \leq 200MPa \\ \tau_f &= 60 + 0.6\sigma_n \quad : \quad 200MPa \leq \sigma_n \leq 1700MPa \end{aligned} \tag{2.1}$$

in which τ_f is the yield shear stress, and σ_n is the stress acting normal to the fault surface. Yielding occurs when shear stress, σ_s, exceeds the frictional yield strength on a given plane at an angle, Θ, between the maximum and minimum principal stresses; σ_1 and σ_3 respectively. The shear stress acting relative to a given plane is:

$$\begin{aligned} \sigma_s &= (\sigma_1 - \sigma_3)(sin\Theta cos\Theta) \\ &= \frac{\sigma_1 - \sigma_3}{2} sin(2\Theta) \end{aligned} \tag{2.2}$$

and the normal stress, σ_n is:

$$\begin{aligned} \sigma_n &= (\sigma_1 cos^2\Theta + \sigma_3 sin^2\Theta) \\ &= \frac{\sigma_1 + \sigma_3}{2} + \frac{\sigma_1 - \sigma_3}{2} cos(2\Theta) \end{aligned} \tag{2.3}$$

If the material contains faults that are optimally oriented then failure will occur when the *maximum* possible shear stress exceeds τ_f. With this assumption, substitution of Equation (2.2) and Equation (2.3) into Equation (2.1) provides failure criteria in terms of differential stress $(\sigma_1 - \sigma_3)$. Using more recently determined constants for Byerlee's

law and an optimal faulting assumption, Burov & Diament [1995] derive the following yielding formulae:

$$\begin{aligned} (\sigma_1 - \sigma_3)_f &= 3.9(\sigma_3 - P_f) \quad : \quad \sigma_3 \leq 120MPa \\ (\sigma_1 - \sigma_3)_f &= 210 + 2.1(\sigma_3 - P_f) \quad : \quad \sigma_3 \geq 120MPa \end{aligned} \tag{2.4}$$

where the least principal stress, σ_3, has been replaced by the *effective* least principal stress, $(\sigma_3 - P_f)$, and P_f is the pore fluid pressure.

Under compression the minimum stress is the lithostatic pressure, and $\sigma_3 = \overline{\rho}gz$ (in which $\overline{\rho}$ is the mean density of overlying rock, g is gravity, and z is the positive down depth.):

$$\begin{aligned} (\sigma_1 - \sigma_3)_f &= 3.9(\overline{\rho}gz - P_f) \quad : \quad \sigma_3 \leq 120MPa \\ (\sigma_1 - \sigma_3)_f &= 210 + 2.1(\overline{\rho}gz - P_f) \quad : \quad \sigma_3 \geq 120MPa \end{aligned} \tag{2.5}$$

which reduces to the failure criterion of Anderson [1951] if $\sigma_3 \leq 120MPa$:

$$(\sigma_1 - \sigma_3)_f = \alpha(\overline{\rho}gz - P_f) \tag{2.6}$$

in which the value of the constant α is determined by the type of faulting.

Under tension it is the *maximum* stress that equals the lithostatic pressure (i.e. $\sigma_1 = \overline{\rho}gz$). Rearranging Equation (2.5) in terms of σ_1 and substituting for lithostatic pressure shows that the brittle strength is considerably lower under tension than under compression.

$$\begin{aligned} (\sigma_1 - \sigma_3)_f &= \frac{3.9(\overline{\rho}gz - P_f)}{4.9} \quad : \quad \sigma_3 \leq 120MPa \\ (\sigma_1 - \sigma_3)_f &= \frac{210 + 2.1(\overline{\rho}gz - P_f)}{3.1} \quad : \quad \sigma_3 \geq 120MPa \end{aligned} \tag{2.7}$$

2.1.2 Ductile regime

Byerlee's law applies up to around half the solidus temperature of the lithospheric rheology. This temperature is typically reached at mid-crustal depths and is associated with a brittle-ductile transition zone in which the lithosphere can deform by a combination of both brittle and plastic processes (e.g. Ranalli [1997]). Moving through this zone, rock failure can be increasingly described by a temperature dependent ductile creep mechanism (e.g. Kirby [1983]):

Mineral/rock	A^* [Pa^{-n} s^{-1}]	H^* [kJ mol^{-1}]	n
quartzite (dry)	5 x 10^{-12}	190	3
diorite (dry)	5.01 x 10^{-15}	212	2.4
diabase (dry)	6.31 x 10^{-20}	276	3.05
DIFFUSION CREEP $(\sigma_1 - \overline{\sigma}) \leq 200$ MPa			
olivine (dry)	7 x 10^{-14}	520	3
DORN'S DISLOCATION GLIDE $(\sigma_1 - \overline{\sigma}) > 200$ MPa			
olivine (dry)	—	535	—

Table 2.1: Material constants for diffusion creep and dislocation glide (see references in Burov & Diament [1995] and Cloetingh & Burov [1996]).

$$\dot{\varepsilon} = A^* d^{-\mathrm{m}} (\sigma_1 - \sigma_3)^n \mathrm{e}^{-\mathrm{H}^*/\mathrm{RT}} \tag{2.8}$$

where $\dot{\varepsilon}$ is the strain rate, A^* is the material constant, d is the average grain size, n and m are empirical constants, H^* is the creep activation enthalpy[2], R is the universal gas constant, and T is the temperature in Kelvin (see references in Burov & Diament [1995]). Table 2.1 gives material constant values for some common minerals and rocks.

However, estimated lithospheric conditions suggest a limited role for grain size dependent diffusion creep (e.g. Kusznir & Park [1987]; Kusznir [1991]), reducing Equation (2.8) to a purely dislocational form ($m = 0, d^{-m} = 1$):

$$\dot{\varepsilon} = A^* (\sigma_1 - \sigma_3)^n \mathrm{e}^{-\mathrm{H}^*/\mathrm{nRT}} \tag{2.9}$$

The dislocation creep that this equation describes occurs by a combination of dislocation glide (in which a dislocation migrates within a plane by replacement of stress broken old bonds with the formation of new), and dislocation climb (in which diffusion around a glide plane allows a dislocation to 'climb' out of that plane to make way for another or to bypass a lattice impurity).

Equation (2.9) dictates that beyond the brittle-ductile transition any shear stress will cause deformation in which the strain rate increases as a function of shear stress and temperature. If the period of stress change is small relative to the strain rate induced by it then the response will remain quasi-elastic. For example, parts of the lithosphere may

[2]Activation enthalpy is $E^* + PV^*$, where E^* is the creep activation energy, P is hydrostatic pressure, and V^* is the activation volume.

act as an elastic solid in response to seismic wave periods, but respond in a fully ductile manner under long term loading stresses.

In terms of rheological significance, only strain rates that allow stress relaxation over geological timescales are important. Hence a yield threshold can be determined by rearrangement of Equation (2.9) to give the threshold differential stress required to drive some minimum strain rate, $\dot{\varepsilon}_{min}$:

$$(\sigma_1 - \sigma_3)_f = \left[\dot{\varepsilon}_{min}(A^*)^{-1}\right]^{\frac{1}{n}} \mathrm{e}^{H^*/nRT} \tag{2.10}$$

Recently, Zoback & Townend [2001] have suggested that sustained critical stress in the upper crust, an average lithospheric strength of $\sim 3 \times 10^{12} Nm^{-1}$, and the ability of the lithosphere to support plate tectonic processes over millions of years, require that the maximum strain rate at which the lithosphere can effectively behave rigidly over geological time is less than $\sim 1 \times 10^{-17} s^{-1}$.

Dislocation glide

Dislocation creep is only a significant mechanism where yielding occurs at low differential stresses and strain rates. In high stress yielding, it is dislocation glide that dominates. Olivine dislocation glide dominated yielding at strain rates greater than $10^{-14} s^{-1}$ is defined by Carter & Tsenn [1987]:

$$(\sigma_1 - \sigma_3)_f = \sigma_0 \left(1 - \left[\frac{RT}{H^*} \ln(\dot{\varepsilon}_0/\dot{\varepsilon}_{min})\right]^{\frac{1}{2}}\right) \quad \sigma_1 - \sigma_3 \geq 200MPa \tag{2.11}$$

where $\dot{\varepsilon}_0 = 5.7 \times 10^{11} s^{-1}$ and $\sigma_0 = 8.5 \times 10^3$ MPa. This equation provides a limit for activation of Dorn's [Dorn, 1954] dislocation glide in geological time.

2.1.3 Total strength of the lithosphere

The yield strength envelope can be stated in a generalised form:

$$(\sigma_1 - \sigma_3)_f = \mathrm{sign}(\varepsilon)\min\left[|(\sigma_1 - \sigma_3)_b(y, T, \mathrm{sign}(\varepsilon))|, |(\sigma_1 - \sigma_3)_d(y, T, \dot{\varepsilon}_{min})|\right] \tag{2.12}$$

in which the yield strength is given by the lesser of brittle and ductile failure thresholds, $(\sigma_1 - \sigma_3)_b$ and $(\sigma_1 - \sigma_3)_d$ respectively, y is depth, T is temperature, and sign(ε) is given the value 1 for extension and the value -1 for compression.

From this the brittle strength of the lithosphere (B) in terms of a finite failure condition can be derived as the integration of finite compressional or tensional yield strength over depth (e.g. Hopper & Buck [1993]):

$$B = \int_0^{\infty} (\sigma_1 - \sigma_3)_f \left[y, T, \dot{\varepsilon}_{min}, \text{sign}(\varepsilon) \right] dy \quad , \quad \text{(y positive down)} \tag{2.13}$$

If lithospheric strength is considered to be insignificant anywhere that differential stresses of $10MPa$ to $20MPa$ (*c.*1% to 5% of the lithostatic pressure at large depths) drive sub-threshold strain rates [Burov & Diament, 1995], then rock mechanics experiments suggest that both oceanic and continental lithosphere retain meaningful brittle strength up to around the 700^oC to 750^oC isotherm [McNutt *et al.*, 1988].

2.1.4 Yield strength envelope uncertainties

Assumptions made in the creation of yield strength envelopes are required either by uncertainties about lithospheric composition and state, or in the translation of laboratory-determined constitutive laws to lithospheric mechanics.

Constitution and state

Figure 2.1 illustrates the effects of pore fluid pressure (one of a number of effects due to fluid inclusion), composition, and thermal age on a simple continental yield strength envelope (in which crustal radiogenic heat production is ignored). Given that, in general, only thermal ages (and sometimes composition) are locally constrained by real data, this has major implications for the application of yield strength envelopes:

1. Fluid inclusion acts to reduce the strength of rocks in both the brittle and ductile regime. In the brittle regime fluids reduce the resistance to frictional sliding by decreasing the effective lithostatic pressure. Throughout the lithosphere the inclusion of fluids can cause weakening by: promoting chemical alterations; increasing dissolution rates; and altering crystalline structure. For example, Chopra & Paterson [1984] determined a significant drop in the strength of dunite for water content as small as $0.01wt\%$.

2. Composition determines the material constants that control ductile deformation. The rheology of oceanic crust is better understood than continental, and the presence of a continental lower crust weak zone is partly dependent on whether a quartz rheology is assumed.

3. Thermal age can be constrained in most oceanic studies. However, problems of unknown composition and radiogenic heat production mean that even if surface heat flow data and/or three-dimensional heat flow models are used, uncertainty in continental thermal structure is generally large.

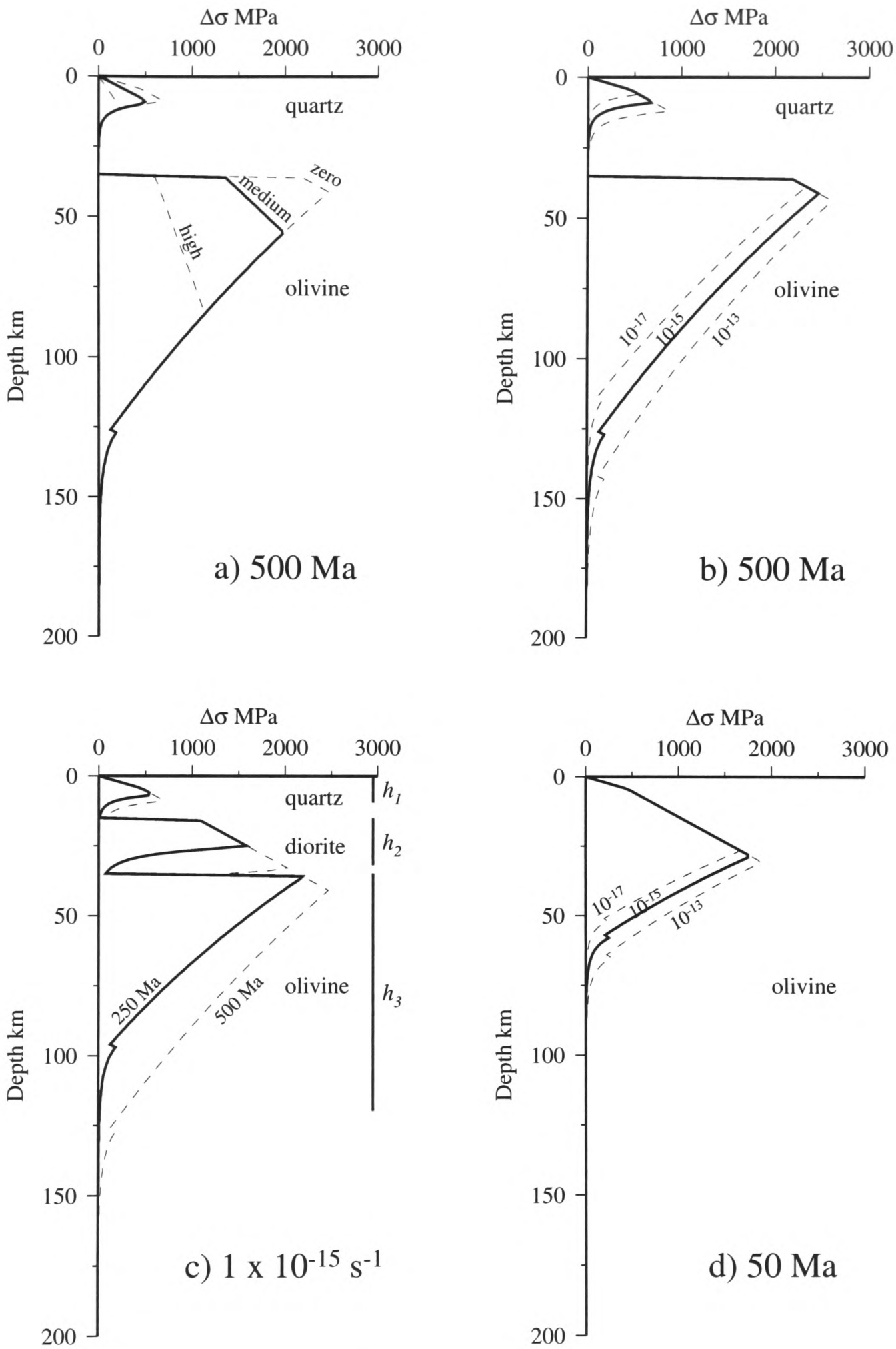


Figure 2.1: Example yield strength envelopes for continental (a-c) and oceanic (d) lithosphere. (a) Effect of pore fluid pressure. (b) Effect of threshold strain rate. (c) Effect of composition and thermal age (which is itself subject to potentially large uncertainties in the continental thermal structure, see text). (d) Oceanic lithosphere (for comparison). Figure from Stewart [1998].

The role of fluids in the crust remains an area of considerable doubt and debate. For example, Pollack [1986] has suggested that extrusion of basalts early in the history of continental lithosphere results in fluid starvation, whereas McKenzie [1989] reaches the conclusion that later addition of metasomatic melt enriches it.

Translation of laboratory-determined constitutive laws

There are profound differences between true lithospheric conditions and laboratory based studies. Deformation of small samples over short timescales and largely under uniaxial applied stresses are not guaranteed to translate well to large scale and potentially long duration deformations in multiaxial lithospheric stress conditions. A number of reviews (e.g. White *et al.* [1980]; Kirby [1983]; Kirby & Kronenberg [1987]; Rutter & Brodie [1991]) discuss the problems in applying laboratory-determined constitutive laws to lithospheric mechanics, and demonstrate the large uncertainties involved.

The application of Byerlee's law is limited by the relatively small (order of $1 \times 10^{-4} m$) displacements produced in rock friction experiments when compared to lithospheric displacements that may be up to 7 orders of magnitude greater. Observations of exposed shear zones reveal offsets and 'drag' features that indicate shear localisation and softening at high strains that are not seen in small displacement experiments (e.g. Kirby & Kronenberg [1987]). High strain processes include:

1. Grain size reduction, which decreases the stresses required for grain boundary sliding, and may make deformation by mechanisms other than frictional sliding more favourable.

2. Preferential alignment of ductile minerals such as quartz due to local rotation of grains under uni-directional shearing.

3. Recrystallisation due to grain boundary migration, which can heal resistant dislocations resulting from earlier shear events.

4. Metamorphic reactions which can produce: weak transformation products; changes in texture; migration of grain boundaries; latent heat release; and volume changes.

At the other end of the scale, geological strain rates as low as $10^{-15} s^{-1}$ to $10^{-19} s^{-1}$ (e.g. Cloetingh & Burov [1996] and Newman & White [1997]) are poorly represented by strain rates achievable at laboratory time scales (i.e. $10^{-4} s^{-1}$ to $10^{-6} s^{-1}$).

It is often taken that failure is controlled by the properties of the weakest constituent mineral (as suggested in Brace & Kohlstedt [1980]), and thus that laboratory tests on

	Young's Modulus E ($\times 10^{11} Pa$)	Poisson's ratio ν
Basalt	0.6-0.8	0.25
Granite	0.4-0.7	0.1-0.25
Diabase	0.8-1.1	0.25
Gabbro	0.6-1.0	0.15-0.2

Table 2.2: Elastic properties of some common crustal rocks (Allen & Allen [1990], and references therein).

monophase minerals can be translated to rock mechanics. However, bonds between minerals may be weaker than the minerals themselves.

Implications

The cumulative effect of uncertainties is a bias towards over-estimation of lithospheric yield strengths. The YSE failure criteria describe a distinct boundary between brittle and ductile rheology, but the reality is probably a broad transition in which failure occurs by a combination of the two.

Despite its limitations, the YSE is a useful concept that describes how the strength of the lithosphere is limited by brittle deformation in its upper part and ductile deformation in its lower part. Its use in studies of effective elastic thickness (some of which are discussed later in this chapter) has helped to explain differences in lithospheric flexure across a range of tectonic settings.

2.2 Mechanical thickness of the lithosphere

Differential stresses in the lithosphere are quasi-elastically supported at depths where strength is significant over a given time scale. A *mechanical thickness* can be defined as the portion of a yield strength envelope that is strong in these terms (Figure 2.2a). Because the yield strength in the ductile domain is strain rate limited, this can only be considered an *effective* mechanical thickness, and will be thicker in the context of short duration stresses than in the context of support of long duration loads.

Although the mechanical thickness delimits a region of combined elastic and quasi-elastic processes, the method of elastic solutions (reported by Burov & Diament [1995], as e.g. Alexandrov & Potapov [1990] [in Russian]) allows its deformation to be characterised

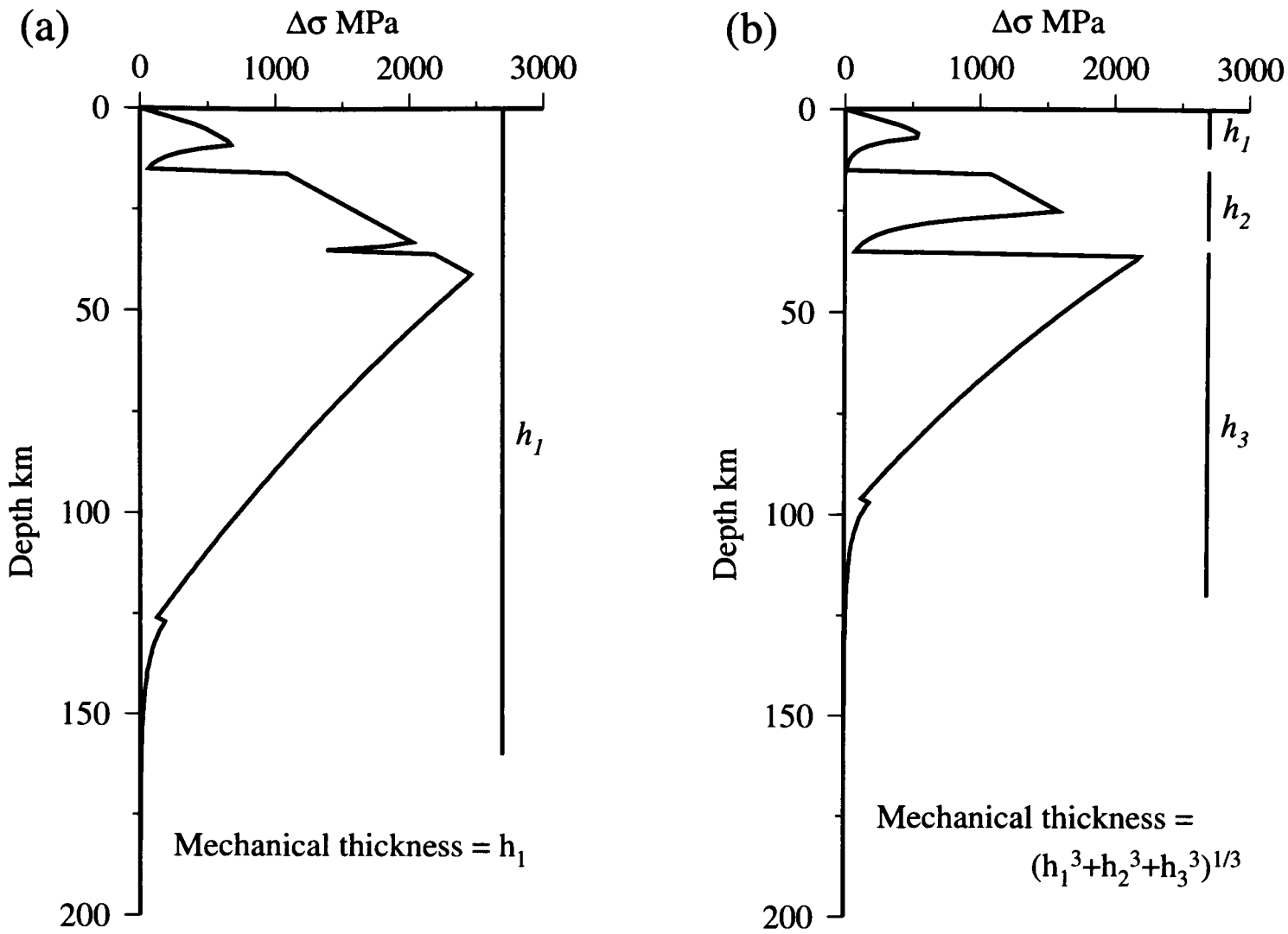


Figure 2.2: Yield strength envelopes and the mechanical thickness of the lithosphere. (a) Coupled lithosphere in which the mechanical thickness is the same as the thickness of lithosphere in which yield strength is significant. (b) Decoupled lithosphere in which the effective mechanical thickness is a 'leaf spring model' summation of distinct mechanical thicknesses (see text).

by flexure of a rigid plate with time-space variable elastic properties.

Appropriate elastic constants for the lithosphere are suggested by rock mechanics data (Table 2.2). Values of 0.25 for Poisson's ratio, and in the range of $0.7 \times 10^{11} Pa$ to $1 \times 10^{11} Pa$ for Young's modulus are typically used for T_e estimation. The effective elastic thickness is only representative of the long term mechanical thickness if these constants are appropriate to actual lithospheric properties. However, if the constants used are known then it is straightforward to convert existing T_e estimates in line with revised estimates of the defining Poisson's ratio and Young's Modulus, and hence to improve the equivalence between effective long term mechanical thickness and T_e.

In parts of the lithosphere where there are multiple detached mechanical layers (Figure 2.2b) the T_e can be approximated by a 'leaf spring' model [Burov & Diament, 1995], that defines the effective thickness of a stack of n uncoupled elastic plates of thickness h_1 to h_n:

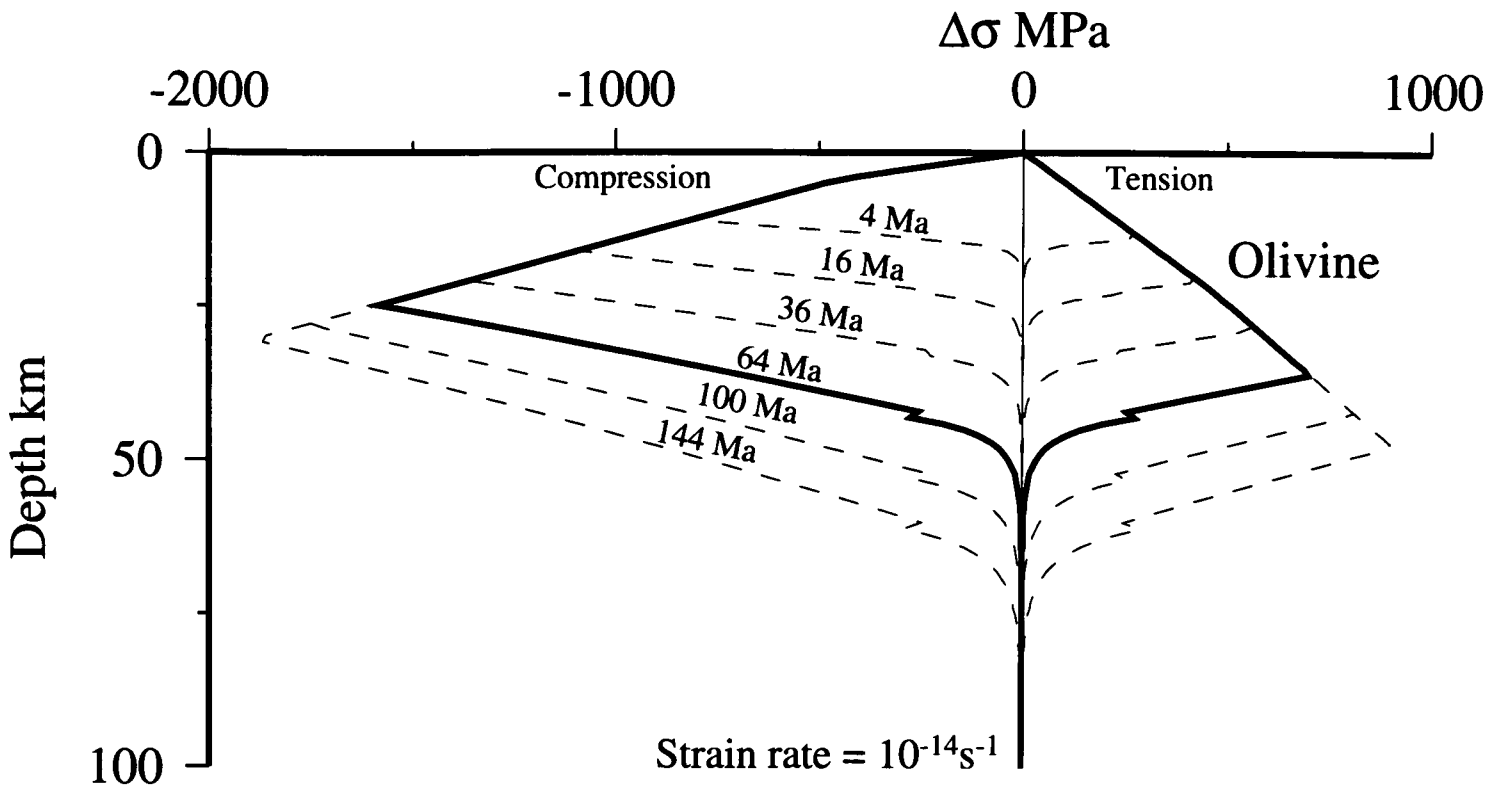


Figure 2.3: Effect of thermal age on an oceanic yield strength envelope.

$$T_e \approx \left(\sum_{i=1}^{n} \Delta h_i^3 \right)^{\frac{1}{3}}, \quad n < 5 \tag{2.14}$$

Because of the cubic terms, T_e will not be much greater than the maximum h_i, and could theoretically be little greater than the total mechanical thickness divided by the number of layers.

2.3 Effective elastic thickness of the oceanic lithosphere

The maximum depth of significant mechanical strength in oceanic lithosphere is strongly age dependent (Figure 2.3). An olivine based model constructed by Caldwell & Turcotte [1979] showed that relaxation of a $100MPa$ differential stress will take an order of 10^3 years at 800^oC, of 10^6 years at 700^oC, and of 10^{10} years at 400^oC. Assuming these values, the effective base of the mechanical lithosphere will decay to the approximate depth of the 700^oC isotherm over a period in the order of a million years. Olivine at significantly lower temperatures can be expected to support such a stress more or less indefinitely.

Bodine *et al.* [1981] similarly suggested that the thickness of oceanic lithosphere that supports a load thins from its short term seismic thickness to a long term mechanical thickness over a period of around a million years (Figure 2.4).

As has already been discussed, compilations of oceanic lithosphere T_e estimates suggest that the mechanical thickness is controlled by the depth of the 450 ± 150^oC isotherm.

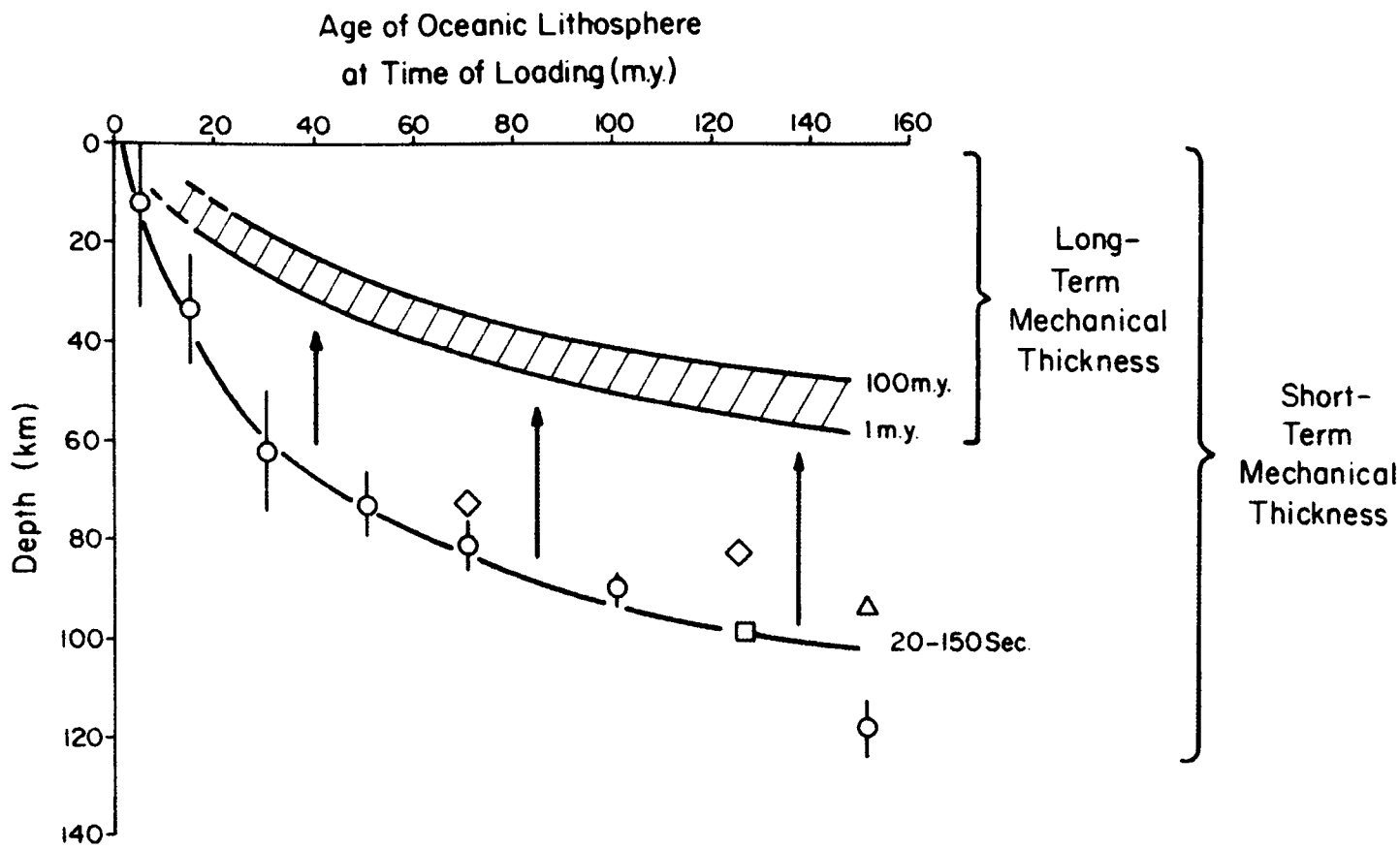


Figure 2.4: Illustration of short-term and long-term mechanical thicknesses of oceanic lithosphere. The short-term mechanical thickness, applying to load durations up to the order of seconds, equates to seismic thicknesses estimated from surface wave data (triangles, Yoshii [1975]; circles, Leeds [1975]; squares, Asada & Shimamura [1975]; diamonds, Forsyth [1977]). Under a long term load the lithosphere responds initially with the short-term mechanical thickness, but over the order of 10^6 years the response relaxes to that of the long-term mechanical thickness. Figure from Bodine *et al.* [1981].

However, as has just been shown, yield strength envelopes suggest that the long term base of the mechanical lithosphere should be close to the 700^oC isotherm (about 1.5 times that depth). The apparent disparity between observation and theory can be reconciled by allowing for inelastic yielding in the upper and lower parts of the mechanical lithosphere caused by flexural stresses (McAdoo *et al.* [1985], Figure 2.5). This allows the mechanical thickness of the lithosphere at ocean trenches and volcanic edifices to thin to levels compatible with the observed T_e.

2.4 Effective elastic thickness of the continental lithosphere

On the basis that the mechanical base of the lithosphere lies at around 700^oC (as in the oceans), Karner *et al.* [1983] suggested that the 450^oC isotherm could apply to estimates of continental T_e. Subsequent work incorporating a growing number of T_e estimates suggests a more complicated relationship (e.g. Watts [2001], see Figure 1.2).

In Section 2.1.4 some of the sensitivities of continental yield strength envelopes to

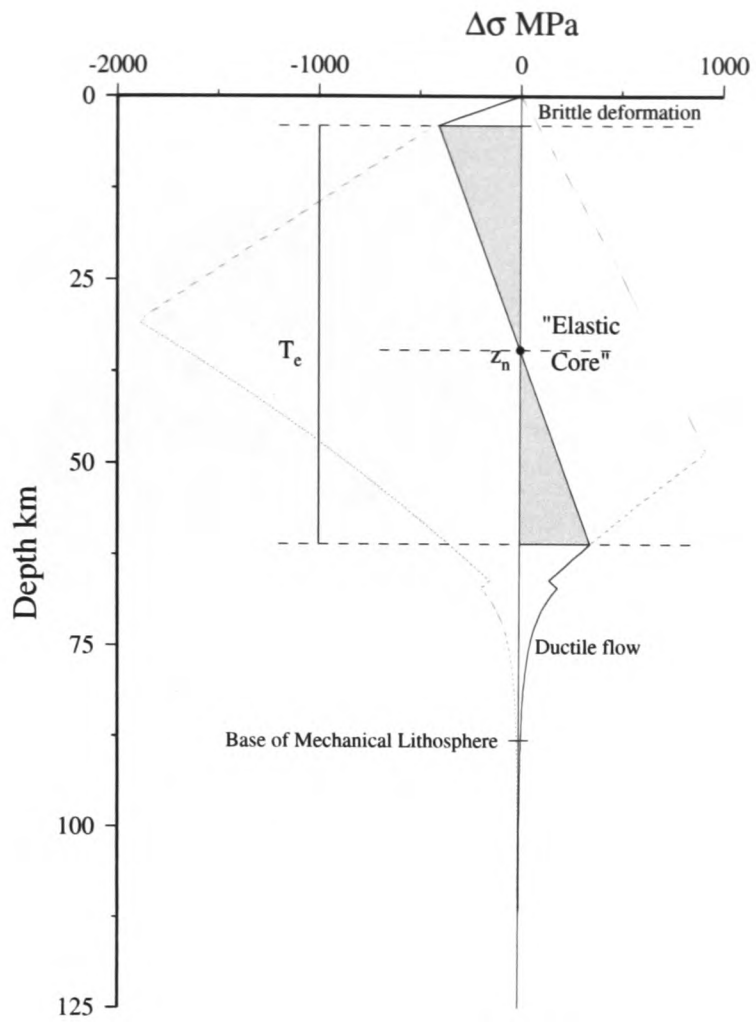


Figure 2.5: Inelastic yielding of an oceanic yield strength envelope due to plate curvature. Bending stresses in the upper and lower part of the mechanical lithosphere result in brittle and ductile yielding respectively. This reduces the effective mechanical thickness, and hence T_e. Note that z_n, the neutral depth at which the bending stress is zero, migrates strongly at high curvatures.

pore fluid, tectonic history, and rheological heterogeneity were discussed. Use of a single parameter (e.g. isotherm depth) as a proxy for effective elastic thickness would only be sustainable if the effects of these contributions to mechanical thickness were small.

While factors such as pore fluid pressure will affect the finite strength in parts of the lithosphere, in many cases they will not significantly alter the mechanical thickness. Critically, however, there are key elements of potential weakness in the lower continental crust and mantle, where the local ability to support sustained loads has a fundamental effect on the integrated strength of the lithosphere as a whole.

2.4.1 Lower crustal weakness

Some rheologies (examples of which are shown in Figure 2.1a and Figure 2.1b) can result in a lower crust that is weak enough that strength decreases to zero above the strong upper mantle. This is most likely with quartz mineralogies, which allow ductile flow at relatively low temperatures because of the low activation enthalpy of quartz (Table 2.1).

If the ductile yield strength is exceeded in the lower part of the crust then the litho-

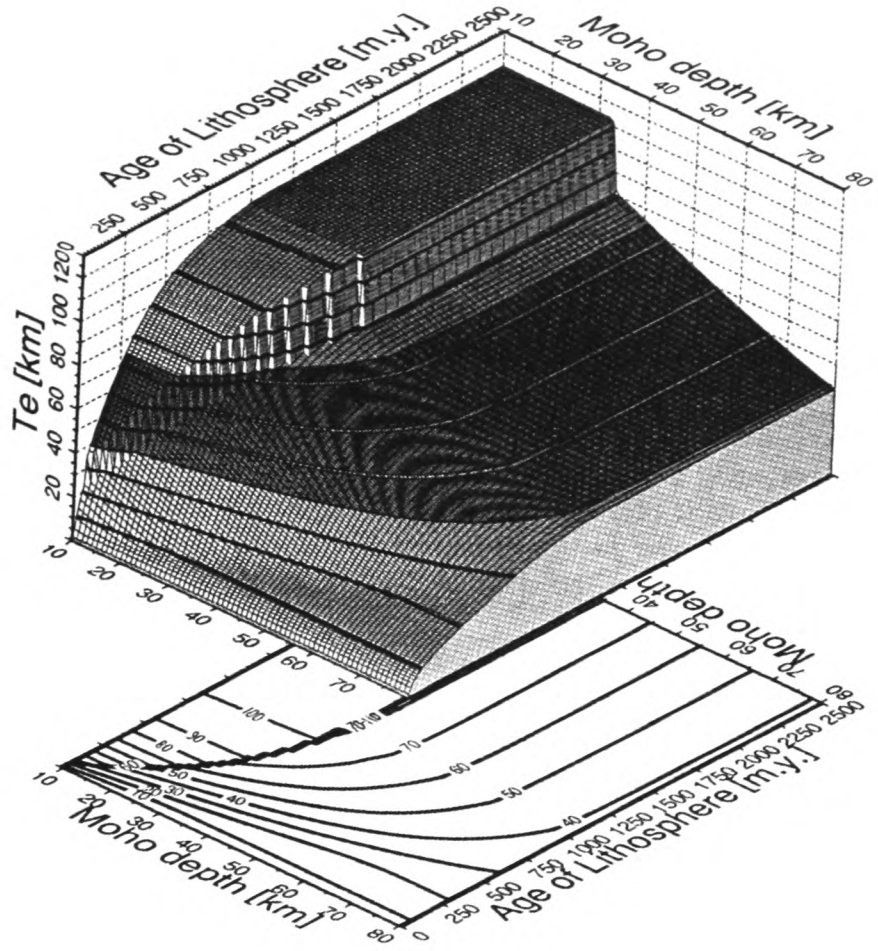


Figure 2.6: Dependence of initial T_e on the age and crustal thickness of continental lithosphere. A sharp transition divides areas of high T_e coupled lithosphere from low T_e decoupled lithosphere (see text). Figure from Burov & Diament [1995].

spheric upper crust and mantle will be decoupled, and the mechanical thickness will be little greater than that of the thickest cohesive unit. Burov & Diament [1995] suggest that for a particular rheology the crustal temperature at the Moho will control whether or not ductile flow (and hence decoupling) can occur under a given differential stress. This makes the potential for decoupling of the crust and lithospheric mantle dependent on: crustal thickness; the thermal age of the lithosphere; and the stress in the lower crust.

Burov & Diament [1995] present dependence between: crustal thickness; lithospheric thermal age; and T_e; for continental lithosphere with a diorite lower crust and no differential stresses. They find that from a young ($< 100MYr$) lithospheric thermal age an enduring bifurcation emerges between coupled and decoupled T_e. By $250Ma$ this bifurcation translates to a distinction between high ($\geq 70km$) T_e values associated with shallow Moho depths (low temperatures at the base of the crust), and low ($\leq 50km$) T_e values associated with deeper Moho depths (high temperatures at the base of the crust). The crustal thickness at which the switch between these two modes occurs increases as the lithosphere cools, eventually settling (in their model) at around $35km$.

If the crust is thinner than $35km$ then cooling will eventually lead to lower crustal

temperatures, at which diorite retains finite strength. However, if the crust is thicker, then even once the geothermal gradient is fully relaxed there will remain a portion of the lower crust that is weak enough to allow decoupling to persist. In this case, however great the lithospheric thermal age, the 'leaf spring' model will apply and the long term T_e will remain in the lower range.

In the rheological model applied by Burov & Diament [1995] permanent coupling with a crust thinner than $40km \pm 5km$ occurs over a period of $50MYr$ to $1000Myr$. Once the crust and mantle are coupled the combined mechanical thickness evolves roughly in line with the 450^oC isotherm depth - as suggested by Karner *et al.* [1983]. However, if the crustal thickness is greater than $40 \pm 5km$ then the lithosphere will remain permanently decoupled and single parameter models of T_e evolution no longer apply.

2.4.2 Upper mantle weakness

The so called 'jelly sandwich' model - in which a 'weak' lower crust is confined between 'strong' upper crust and upper mantle - is the generally accepted view of the typical state of old continental lithosphere. This is supported by high estimates of continental T_e in some cratonic regions (up to $100 - 130km$), which *require* that a large portion of the mechanical lithospheric strength be supplied by a strong upper mantle.

Recently however, McKenzie & Fairhead [1997] and McKenzie [2003] have challenged the validity of continental T_e estimates exceeding the seismogenic thickness of the crust. This has led these authors and others [Maggi *et al.*, 2000a,b; Jackson, 2002] to suggest that the upper mantle of old cratonic regions lacks significant long term strength. Their results and conclusions challenge numerous studies made since the mid-1980s, and are consequently the subject of considerable debate.

To understand the origins of this debate one can first look at the ways in which continental T_e is estimated. The preferred method is forward modelling of known loads to predict observable responses such as bathymetry, Moho geometry, stratigraphy, and gravity anomalies. In the continents the data that would allow such models to be used are frequently too sparsely distributed to be of use in anything more than localised studies (e.g. Karner & Watts [1983], Lyon-Caen & Molnar [1983], and Caporali [1995]). So to obtain more extensive coverage it has been common to use topography and gravity data at provincial to continental scales to invert for T_e in the spectral domain (e.g. Banks *et al.* [1977], Forsyth [1985], Lowry & Smith [1994]).

Spectral methods

Unlike forward models, spectral methods do not directly synthesise the observable responses to individual loads. Instead, they use wavelength dependent relationships between topography and gravity to identify a transition between short wavelengths at which loads are fully supported by the lithosphere, and long wavelengths at which their compensation is essentially Airy isostatic. The waveband of the 'roll-over' between these two states contains wavelengths at which the response is characteristically flexural, and is therefore diagnostic of T_e. In essence, longer transitional wavelengths mean higher T_e.

Early spectral studies used the admittance between topography and free-air gravity anomalies to estimate T_e. Examples produced values of $5 - 10km$ in North America [Banks *et al.*, 1977], and of $\sim 1km$ for the whole of Australia [McNutt & Parker, 1978]. Such estimates were at odds with contemporary knowledge about the depth distribution of continental seismicity (e.g. Chen & Molnar [1983]), and with extrapolation of laboratory rock mechanics data to lithospheric conditions (e.g. Brace & Kohlstedt [1980]). A partial explanation was that spectral weighting proportional to the square of the topographic amplitude biases admittance estimates towards low strength(?) regions of high topographic relief [McNutt & Parker, 1978; Forsyth, 1985].

Early applications of the free-air admittance method assumed topographic loading only. A Bouguer admittance function tested by Forsyth [1985] allowed buried loading to be incorporated as a ratio, f, relative to the topographic load. The results showed that the admittance roll-over is strongly dependent on f, such that admittance based on topography alone will severely underestimate T_e if subsurface loads are present.

Forsyth [1985] therefore introduced a Bouguer coherence method by which T_e could be estimated with a lower sensitivity to the ratio of topography and buried loads coherent with it. This method has become the dominant spectral means of estimating continental T_e. Controversially, it has also produced some of the highest estimates globally (e.g. $\sim 130km$ within the Australian Western Shield, Zuber *et al.* [1989]).

McKenzie & Fairhead [1997] and McKenzie [2003] have been critical of high T_e estimates based on Bouguer coherence studies; citing bias in the method and questioning the credibility of significant mantle strength at temperatures corresponding to depths of $100km$ or more. They argue that as continental lithosphere ages, so the role of erosion and infill greatly reduces the coherence between buried loads and topography on which Bouguer the method relies. Short wavelength incoherent subsurface loads would then cause the method to overestimate T_e. They therefore view Bouguer coherence estimates as upper bounds on T_e in old continental interiors, and advocate a return to methods

that work only with the known loads - i.e. topography. In this context they term the incoherent buried loading as 'noise'. They also argue that Bouguer gravity anomalies remove part of the 'signal' produced by topographic loading processes, and that spectral studies should therefore use the free-air gravity anomaly.

Another reason to question traditional Bouguer coherence T_e estimates is that the mirroring of data prior to Fourier transformation introduces short wavelength artefacts that bias apparent T_e upwards [Lowry & Smith, 1994; McKenzie & Fairhead, 1997; Banks *et al.*, 2001; Ojeda & Whitman, 2002]. McKenzie & Fairhead [1997] suggest that multitapering of the data in the real domain - instead of mirroring - before transformation minimises bias in the spectral analysis. Maximum entropy methods can also be applied to this purpose (e.g. Lowry & Smith [1994].

Using multitapering and a free-air admittance method that includes a component for subsurface crustal loading, McKenzie & Fairhead [1997] and McKenzie [2003] consistently yield $T_e \leq 40km$ in continental interiors. Their results are compatible with a model in which continental T_e is confined to the crust, and is always less than the seismogenic thickness, T_s [McKenzie & Fairhead, 1997; Maggi *et al.*, 2000a,b; Jackson, 2002; McKenzie, 2003].

Elastic thickness and seismic thickness

One of the main contributors to the 'jelly sandwich' model of cratonic rheology was that apparent seismicity was symptomatic of brittle failure within the upper mantle. However, recent investigation of the depth distribution of earthquakes in southern Iran, the Tien Shan, and northern India suggests that seismicity previously thought to be sourced in the upper mantle actually originates within the lower crust [Maggi *et al.*, 2000a,b]. By contrast, oceanic seismicity originates in both the crust and upper mantle - which jointly contribute to oceanic T_e.

An aseismic upper mantle, and a broad correlation between the deepest crustal seismicity and a selection of T_e estimates, have been interpreted by Maggi *et al.* [2000a,b] as evidence that the lithospheric strength contributing to T_e is confined to the crust, and is limited to the seismogenic thickness, T_s, such that $T_e < T_s$ everywhere.

Other arguments have been made to support this view. At the upper end, it is unlikely that mantle rheologies can maintain meaningful strength at the high temperatures ($\sim 1000^oC$) required to support T_e estimates of $> 100km$ [McKenzie & Fairhead, 1997]. From a conceptual point of view, Jackson [2002] perceives combined effects from seismic and aseismic elastic cores as unnecessarily complex when compared to the simplicity of a seismogenic crust and elastic core comprising a single unit. His argument also questions

the viability of a long term effective elastic core that is thicker than the short term brittle thickness implied by crustal seismicity (cf. Figure 2.4).

A likely cause of weakness is accumulation of hydrous phases in the continental mantle [McKenzie, 1989; Harte *et al.*, 1993; Maggi *et al.*, 2000a,b; Jackson, 2002; McKenzie & Jackson, 2002]. Even in proportions as small as a few parts per million, water could reduce the upper mantle strength dramatically [Hirth & Kohlstedt, 1996; Mackwell *et al.*, 1998]. Removal of hydrous phases during melting beneath oceanic ridges would then explain why the oceanic upper mantle is conversely strong.

The ongoing debate

Such has been the prominence of the 'jelly sandwich' model in continental tectonics that, if real, upper mantle weakness would demand extensive re-examination of the principles by which many geodynamic processes have been explained [Jackson, 2002; Lamb, 2002]. However, suggestions of low T_e and a weak upper mantle in the continents have been met by fierce debate, and it is far from accepted that there is new cause to reconsider commonly held views of continental mechanics.

An extensive discussion on the relationship between lithospheric strength, elastic thickness, and seismogenic thickness is presented by Watts & Burov [2003]. They explain that the intuitively obvious argument that instantaneous brittle strength represented by T_s should exceed the effective long term elastic thickness is flawed because of the different mechanics of the two. Because T_e is the long term integrated brittle, elastic and ductile strength of the lithosphere, they see no requirement for it to relate to seismogenic frictional sliding confined to the upper $\sim 40km$ of continental plates[3]. Furthermore, if there are multiple elastic cores (e.g. if the strong mantle and crust are decoupled) then there will be no reason for T_e to consistently correspond to a lithospheric boundary.

A weak mantle also presents problems when considered in relation to known continental features. The height of some orogenic belts would be unsustainable if support were provided by the crust alone [Ellis *et al.*, 1995; Batt & Braun, 1997; Beaumont *et al.*, 1999], as would preservation of crustal roots and dense crustal inhomogeneities in old cratons [Burov *et al.*, 1998]. High integrated strength is also implied by transmission of tectonic stresses over large distances [Watts & Burov, 2003].

The question then returns to which continental T_e estimates can be trusted? Using forward models Burov *et al.* [1998] found that a T_e of at least $50 - 70km$ is required

[3]At typical continental Moho depths ($\sim 35km$) the theoretical brittle rock strength exceeds $0.6GPa$, allowing frictional sliding only under dynamic forces a magnitude greater than any current estimates (Watts & Burov [2003], and see Molnar & Lyon-Caen [1988]).

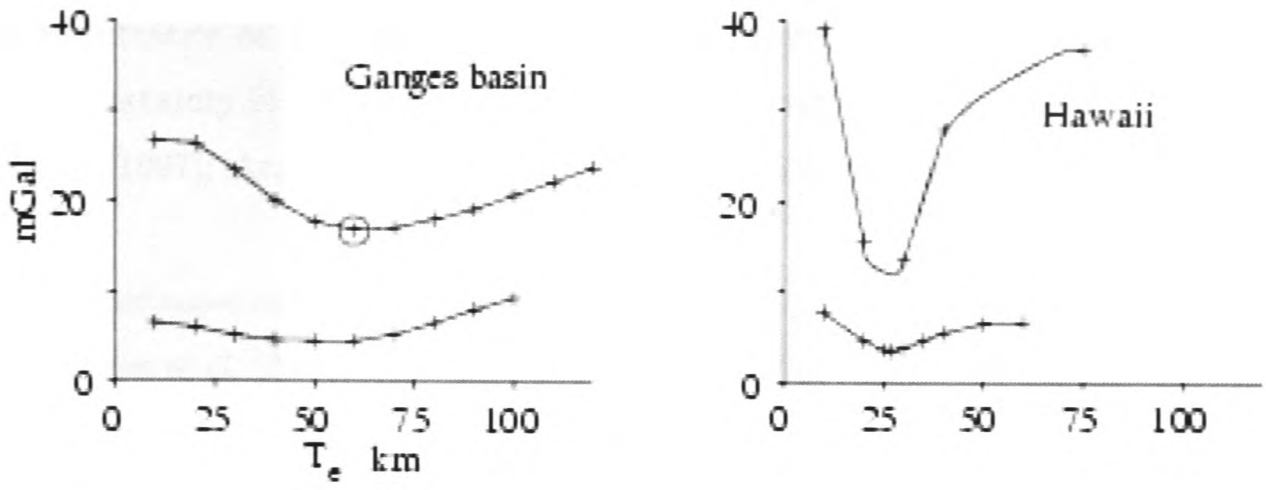


Figure 2.7: Root mean square differences between observed and calculated Bouguer gravity anomalies in the vicinity of the Ganges foreland basin and the Hawaiian Ridge. In each case the upper curve is for forward modelling of known loads and their flexural responses, and the lower curve is for the 'no-load' approach of McKenzie & Fairhead [1997]. Plots from Watts & Burov [2003].

to explain enduring structure (supported for $\sim 2Ga$) of the Kapuskasing uplift in the Superior Province of the Canadian Shield. When spectral methods were used to estimate mean T_e for the region they observed large biases resulting from: localised variations in T_e; crustal density heterogeneities that are incoherent with topography; and the flexural effects of tectonic forces. They therefore concluded that spectral T_e estimates for such regions should be taken with caution.

Forward methods should provide a less controversial means of T_e estimation because they directly relate loads to their observable flexural effects, and - where relevant - are unaffected by whether Bouguer or free-air gravity anomalies are used. Forward models have often yielded $T_e >> T_s$ in the continents (e.g. for the southern Appalachians [Armstrong & Watts, 2001] and the Baikal Rift [Burov *et al.*, 1994; van der Beek, 1997; Petit & Ebinger, 2000]), which are consistent with ranges observed in Bouguer coherence studies. A 'no-load' forward method introduced by McKenzie & Fairhead [1997] yields lower T_e estimates (supporting their low free-air admittance based results), but has been shown by Watts & Burov [2003] to be less sensitive to T_e than a conventional forward model Figure 2.7.

Although the use of forward models in support of spectral continental T_e analyses is becoming more common, issues of data coverage continue to limit their application over large areas. Application of multitapering or maximum entropy methods to data in the real domain produce lesser spurious contributions to the transformed spectra than does conventional mirroring. These methods have been applied using Bouguer coherence and

free-air admittance as a means of attaining higher spatial resolutions, and of reducing bias and uncertainty in spectral T_e estimates (e.g. Lowry & Smith [1994, 1995]; McKenzie & Fairhead [1997]; Armstrong & Watts [2001]; McKenzie [2003]; Perez-Gussinye *et al.* [2003]).

Using multitapering and sliding boxes of varying sizes for spectral T_e estimation, Perez-Gussinye *et al.* [2003] obtained consistent T_e estimates from Bouguer coherence and free-air admittance in Fennoscandia. Resulting T_e estimates range as high as $70-100km$ in central Finland; requiring a coupled strong crust and strong upper mantle. They also found (as did Banks *et al.* [2001]) that unless the theoretical admittance curves are specifically adjusted for bias introduced by multitapering, then apparent T_e will be biased downwards. McKenzie & Fairhead [1997] and McKenzie [2003] did not make this adjustment. In future, wider application of approaches that address such biases may explain disparate spectral T_e estimates in other continental regions. However, even with higher spatial resolution, trade-offs between bias, maximum observable T_e, and box size remain.

Implications for the future

Although McKenzie & Fairhead [1997] and McKenzie [2003] are probably justified in questioning some of the higher continental T_e estimates that have been reported, it appears that their own methods underestimate T_e. Bouguer coherence became the dominant spectral method because early free-air admittance estimates of T_e were too low to be compatible with other observations of lithospheric behaviour. One reason for this was a strong dependence on the role of buried loading. The work of McKenzie & Fairhead [1997] did incorporate buried loading, but their method requires that all loads be compensated within the crust. If this were realistically the case then there should be little or no Moho topography in old cratonic regions [Déverchère *et al.*, 2001; Petit & Ebinger, 2000]. With other biases already discussed, there is little reason to believe that McKenzie & Fairhead [1997] and McKenzie [2003] have solved the problems inherent in the application of spectral methods to T_e estimation in old continental regions.

As things stand now, claims of consistently low T_e in the continents are far from proven, but they have contributed to a wider debate into the biases and assumptions made in estimation of continental T_e in general. As a result, studies increasingly apply combinations of forward modelling and spectral methods to justify their results. Although controversy will no doubt continue, most find no consistent relationship between T_e and T_s (many return $T_e >> T_s$). So unless more evidence to the contrary emerges there seems little reason to abandon established views of continental rheology.

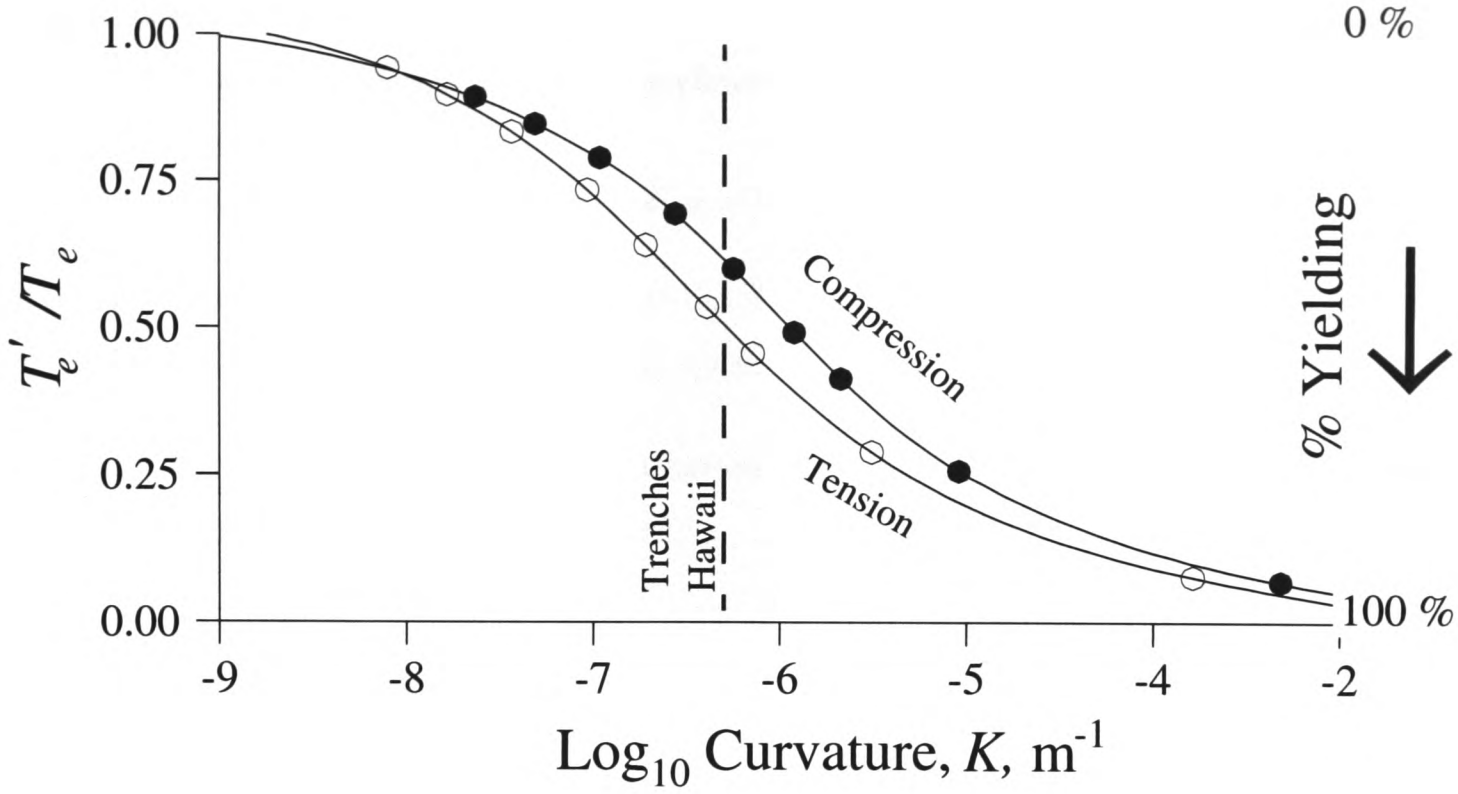


Figure 2.8: Effect of curvature on T_e for an oceanic yield strength envelope. Plot shows ratio of initial to observed effective elastic thickness (T'_e/T_e) against curvature, K. Figure from Watts [2001].

2.5 Weakening of the lithosphere by emplaced loads

Yield strength envelopes can be used to directly assess the mechanical thickness of the lithosphere in the absence of differential stresses. However, emplacement of loads onto the lithosphere can cause failure in parts of the YSE, and may even alter the YSE by modifying the geothermal gradient.

2.5.1 Yielding due to curvature

If bending stresses in a flexed elastic plate exceed the yield strength then yielding will occur. This was mentioned in Section 2.3, in which Figure 2.5 showed an example in which T_e is reduced by bending stresses that exceed the yield strength in the upper and lower parts of an oceanic plate. Greater bending stresses will cause yielding through a larger portion of the YSE, and hence will further reduce T_e.

Brittle strength in the upper part of the yield strength envelope is considerably greater under compression than extension. So the potential for failure due to upwarping - in which bending stresses are tensional in the upper part of the plate - is higher than for downwarping with the same curvature. This means (Figure 2.8) that equivalent curvatures will reduce T_e more if they act upward (e.g. on the ocean plate side of oceanic trenches) rather than downward (e.g. beneath oceanic islands and seamounts).

In the continental lithosphere, curvature may cause sufficient yielding in the lower

crust to effectively decouple the mechanical crust and mantle. In such cases effective elastic thickness will be greatly reduced anywhere that the curvature exceeds this threshold.

2.5.2 Weakening due to sedimentation

Sedimentation loads the lithosphere, causing flexure, and potentially weakening the plate through curvature induced yielding. However, it can also weaken the lithosphere by:

1. Increasing the mean crustal temperature through insulation (Steckler & Ten Brink [1986] and Stephenson *et al.* [1989]).

2. Increasing the depth of the Moho and therefore increasing the temperature at the base of the crust (Stephenson *et al.* [1989] and Lavier & Steckler [1997]).

3. Reducing the lithostatic pressure at brittle depths in the yield strength envelope [Steckler & Ten Brink, 1986].

By applying a 'semi-analytical' model, Lavier & Steckler [1997] demonstrate that sediments may reduce T_e at the Tarim, Kunlun, Zagros, and Andes (Figure 2.9). If the crust is thick and the lithosphere is young and hot (Apenines, Southern Alps) then decoupling occurs in their model even without the inclusion of sedimentation effects. Conversely, coupling of mechanical crust and mantle persists in their model with or without sedimentation if the crust is thin and the lithosphere is old and cold (Himalayas, Ganges). However, in some cases (Andes, Zagros, Tarim, and Kunlun) they find that the effects of sedimentation can promote decoupling that would not otherwise occur. In these cases they find that even sediment thicknesses of as little as $3km$ to $5km$ may cause sufficient thermal adjustment of the yield strength envelope to reduce T_e by as much as $30km$ through decoupling of the crust and lithospheric mantle (Figure 2.10).

2.6 Continental rifting

2.6.1 Introduction

Bullard [1936] was one of the first to consider the state of isostasy at continental rifts, but his model relied on compression to create the basin and flank geometry. Although he and others considered the possibility of extension, it was Vening Meinesz [1950] who presented a model in which extension driven rifting would agree with observations. In his model (Figure 2.11) normal faulting at either end releases a crustal block that is narrower at its base than at the surface, and which therefore sinks isostatically. Similarly, the corresponding unloading of adjacent rift flanks causes them to isostatically upwarp

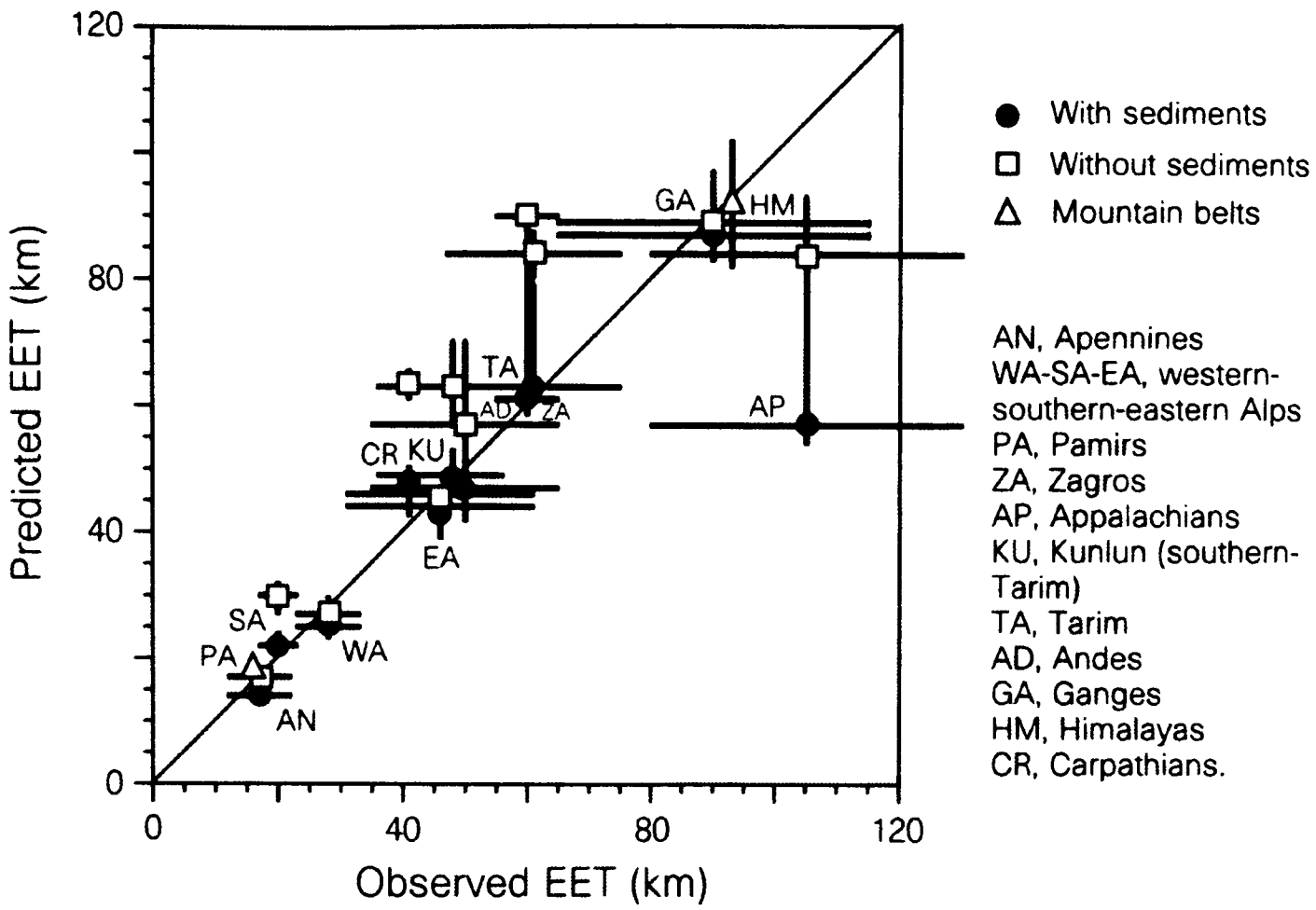


Figure 2.9: Predicted versus estimated T_e values with (filled circles) and without (open squares) inclusion of sedimentation effects in the predicted values. In general the inclusion of sedimentation effects improves the correspondence between predicted and estimated values. Predicted versus estimated values for mountain belts are also shown (open triangles). Figure from Lavier & Steckler [1997].

- a process that Vening-Meinesz modelled using a broken elastic plate solution. The resulting internal structure is essentially a large graben.

Vening-Meinesz's model explained his African rift observations, and accounted for the apparent overcompensation of intra-rift topography when treated using conventional Pratt and Airy isostatic models. However, such is the diversity of rift types and geometries now recognised that no one isostatic model can describe the development of them all, and it is now common to categorise global rift types by characteristic features. In particular, distinctions between 'wide' and 'narrow', and between 'volcanic' and 'non-volcanic' margins are in common use.

As the work of Vening Meinesz [1950] illustrates, lithospheric strength - whether in terms of elastic thickness, or a rheological model - can often play a critical role in explaining topography and gravity data associated with continental rifts. However, as with the loading processes that succeed rifting, direct modelling of the yield strength behaviour is not always practical. So simplified models are widely used to represent the isostatic processes associated with rifting.

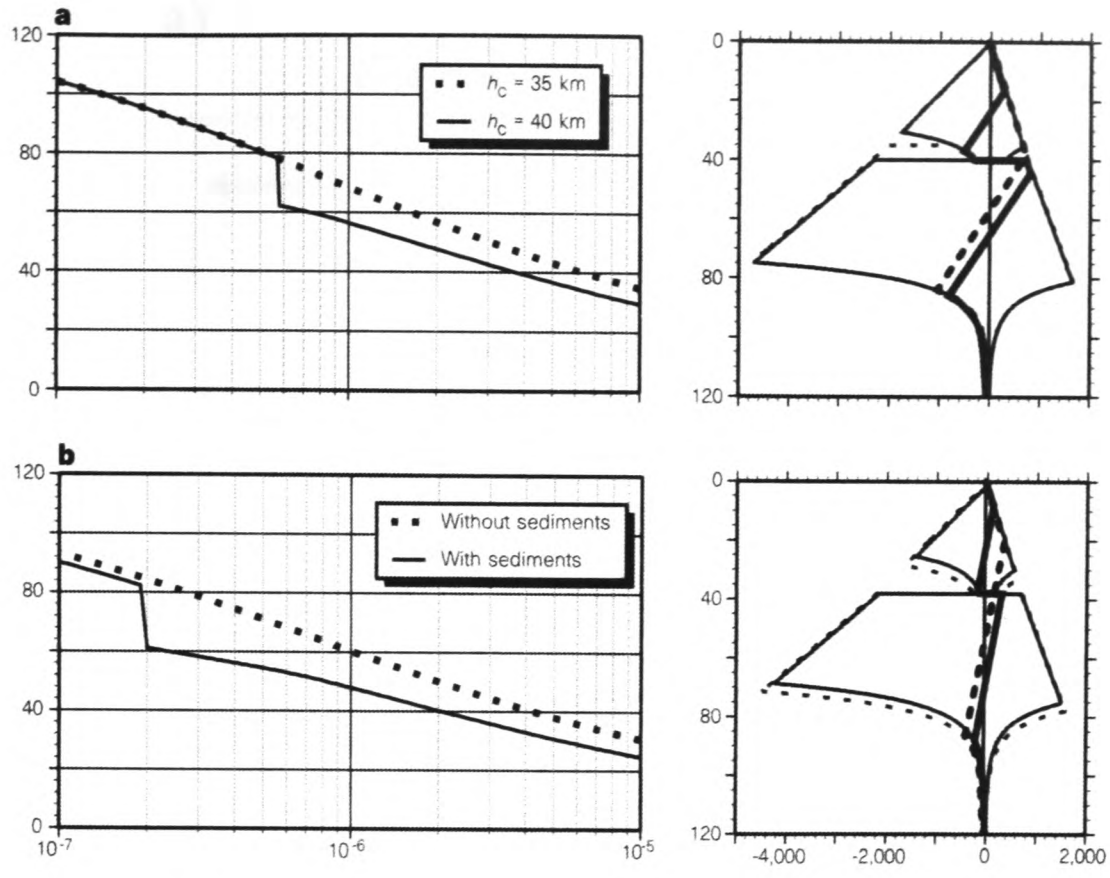


Figure 2.10: Effect of curvature and sedimentation on continental effective elastic thickness. (a) $1000Myr$ old lithosphere without sediments. If the crust is $35km$ thick then the crust and lithospheric mantle remain coupled (dashed line). If the crust is $40km$ then the lower crust is hotter, and hence more ductile. This allows curvature to cause decoupling, and an associated drop in T_e of $\sim 20km$ (solid line). (b) $600Myr$ old lithosphere with sediments. Without sediments the $38km$ thick crust remains coupled with the lithospheric mantle (dashed line). If the thermal effects of a $5km$ thick sediment pile are included then curvature can cause decoupling, again with an associated drop in T_e of $\sim 20km$ (solid line). Note that although the bending stresses in the crust and mantle are often shown as being the same, this is not always required. Figure from Lavier & Steckler [1997].

2.6.2 The McKenzie rift model

The McKenzie rifting model [McKenzie, 1978] is the simplest simulation of continental extension and rifting. A section of uniform thickness lithosphere of length a and thickness L (Figure 2.12a) is instantaneously and uniformly extended by a stretching factor β, such that the new length is βa, and the new thickness is L/β (Figure 2.12b). Crust of initial thickness t_c is similarly thinned, resulting in a water filled depression R_T.

Initially a temperature, T_m, at the base of the lithosphere, and 0^oC at the surface are assumed, with a steady state thermal gradient of T_m/L between the two. If no additional heat generation or loss occurs during rifting then the relocation of material due to extension produces a thermal structure in which the lithospheric geothermal gradient is given by $T_M\beta/L$. With time, the raised isotherms will relax to their original levels, and the depth to the base of the lithospheric mantle will trend towards its original depth.

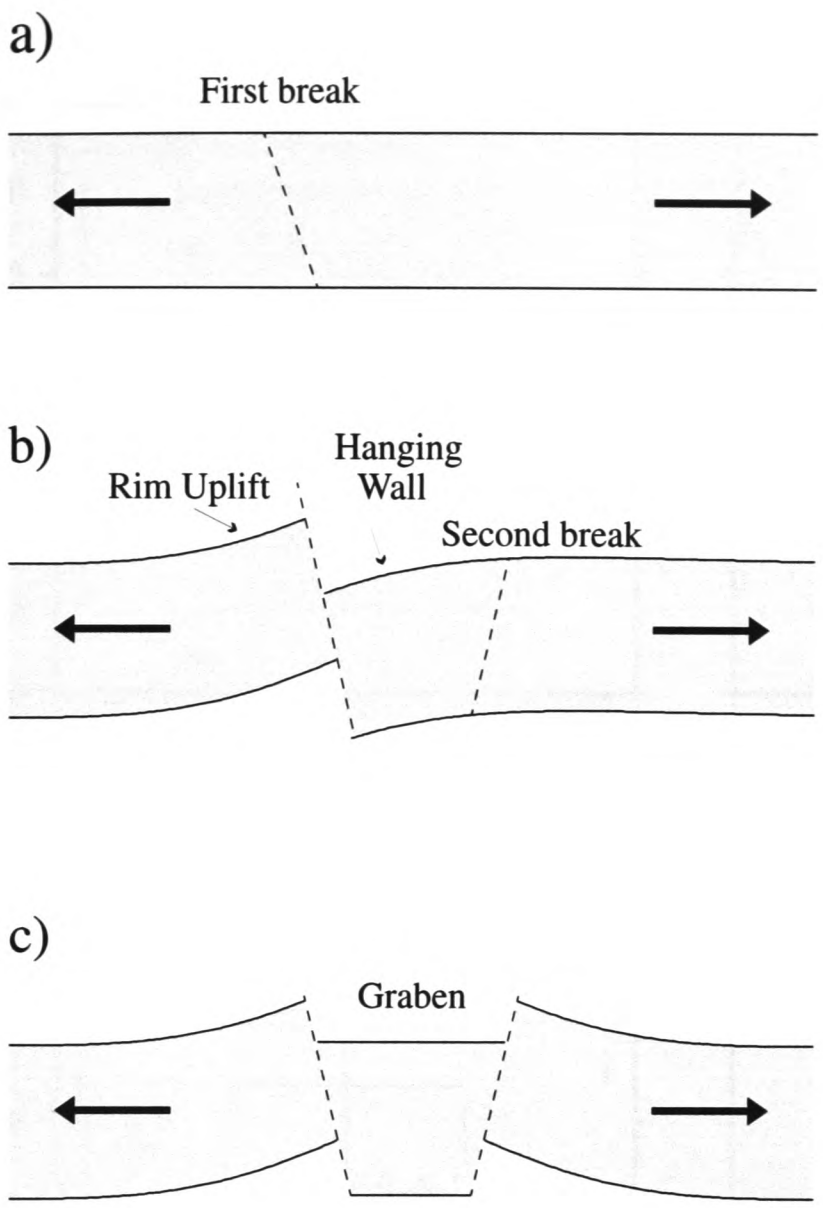


Figure 2.11: Vening-Meinesz's model for graben-type rift development. Figure from Watts [2001] after Heiskanen & Vening Meinesz [1958].

However the rifted crustal thickness will remain unchanged (Figure 2.12c).

If uniform crustal and mantle densities are assumed, then the rift topography, R_T, can be used to infer the amount by which the Moho is raised, M_T, and hence the stretching factor, β (the ratio of original to rifted thickness).

$$M_T = R_T * \frac{\rho_c}{\rho_m - \rho_c} \tag{2.15}$$

$$\beta = \frac{t_c}{t_c - R_T \left(\frac{\rho_m}{\rho_m - \rho_c} \right)} \tag{2.16}$$

The McKenzie rifting model has been successfully applied in a large number of rift evolution models, but it makes a fundamental assumption that the rift topography is in local isostatic balance with the rift Moho. While it is possible that in some cases the rifting T_e may be very low, or that extension may happen to produce an isostatically

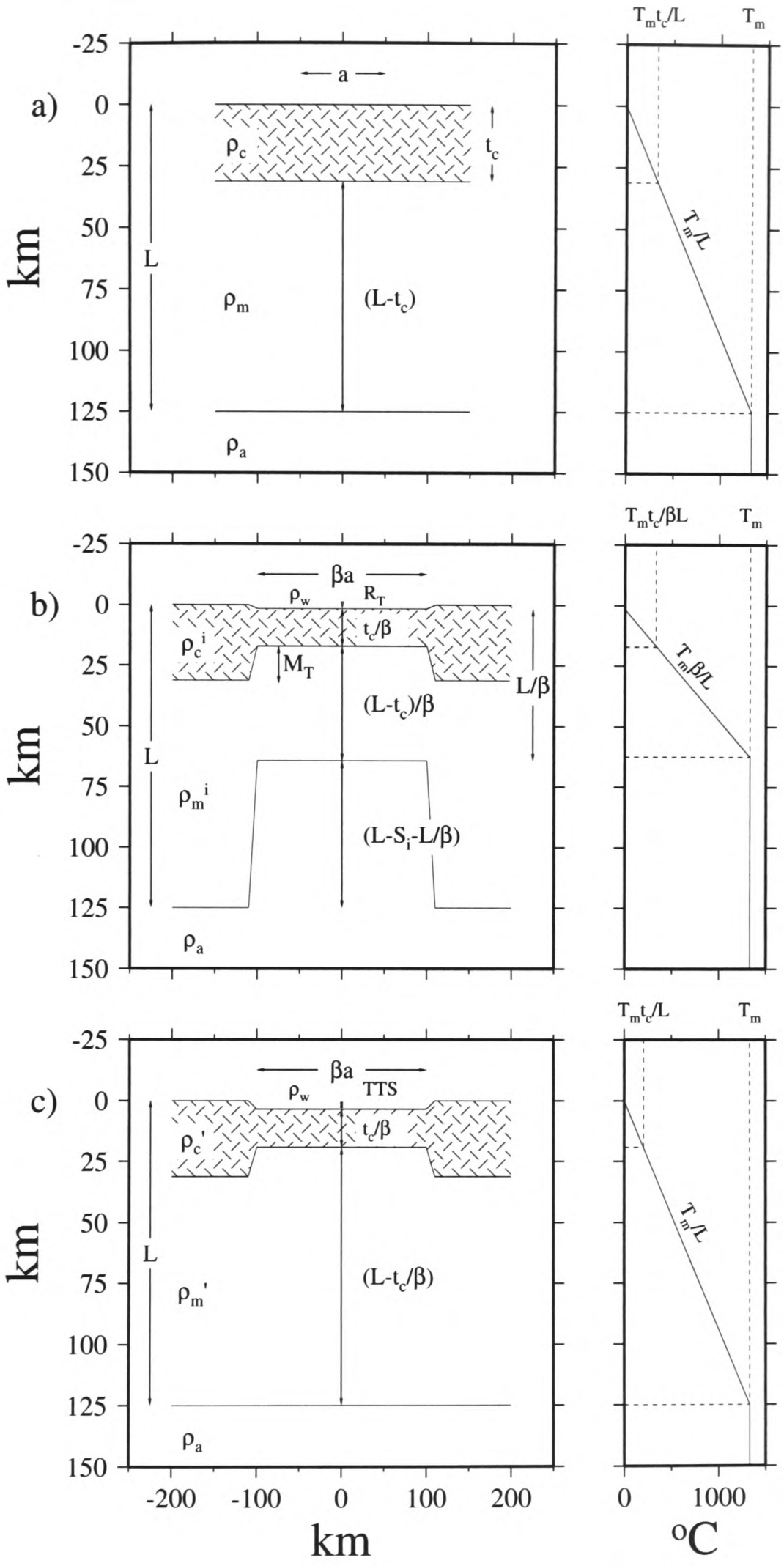


Figure 2.12: The McKenzie rifting model [McKenzie, 1978]. See text for description. Figure from Stewart [1998].

balanced structure, this is by no means required. If lithospheric strength and isostatic compensation do play a significant role in rifting then the result may be quite different from the simple model that the McKenzie rift presents.

2.6.3 Lithospheric strength and continental rifting

As some authors emphasise (e.g. Buck *et al.* [1999]; Dunbar & Sawyer [1989]), it is hard to over-state the diversity of continental rifts and the models that seek to explain them. However, even amongst this diversity there are many common features. Perhaps most significant of these is that (in general) extension preferentially occurs in regions of pre-existing weaknesses such as young orogenic belts and suture zones (see references in Dunbar & Sawyer [1989]). It is the manner in which these weak zones influence, and are influenced by, extensional processes that will control much of a rift's development.

Vening Meinesz [1950] modelled crustal rifting by extension with *regional* isostatic compensation. Once established this approach was widely applied (e.g. Bott [1976]), but more recent works apply regional isostasy to rift models that incorporate extension of the lithospheric mantle as well as of the crust (e.g. Weissel & Karner [1989]; Kusznir & Egan [1990].

One of the models of this type presented by Weissel & Karner [1989] considers continuous elastic plate deformation as a response to isostatic balances generated by a Wernicke-type rift [Wernicke, 1985]. In Wernicke's model (Figure 2.13) a listric fault translates extension from a normal brittle fault geometry at the surface to a horizontal detachment at depth. This detachment divides simple shear in the upper lithosphere from pure shear extension and thinning in the lower lithosphere. Because of the asymmetric geometry there is a lateral displacement between lower lithospheric pure shear thinning and upper lithospheric thinning by slip and fault rotation.

Using such a model Ebinger *et al.* [1991] were able to explain many of the topographic and gravity anomaly features of the Western Rift in East Africa. The fits to observed data that they present (Figure 2.14) rely on rifting asymmetry, and demonstrate one way in which McKenzie-type rifting may fail to represent real processes.

The Wernicke-type models of Weissel & Karner [1989] and Ebinger *et al.* [1991] fall broadly within a category dubbed the *flexural cantilever model* by Kusznir & Egan [1990]. In models of this type the lithosphere implicitly retains a finite rigidity during rifting, and there are long term mechanical isostatic effects that are genetically related to the rifting process [Ollier, 1995].

Evidence of lithospheric strength during rifting has also come from other types of rift study. Some of these have incorporated the effects of finite strength during rifting [Braun

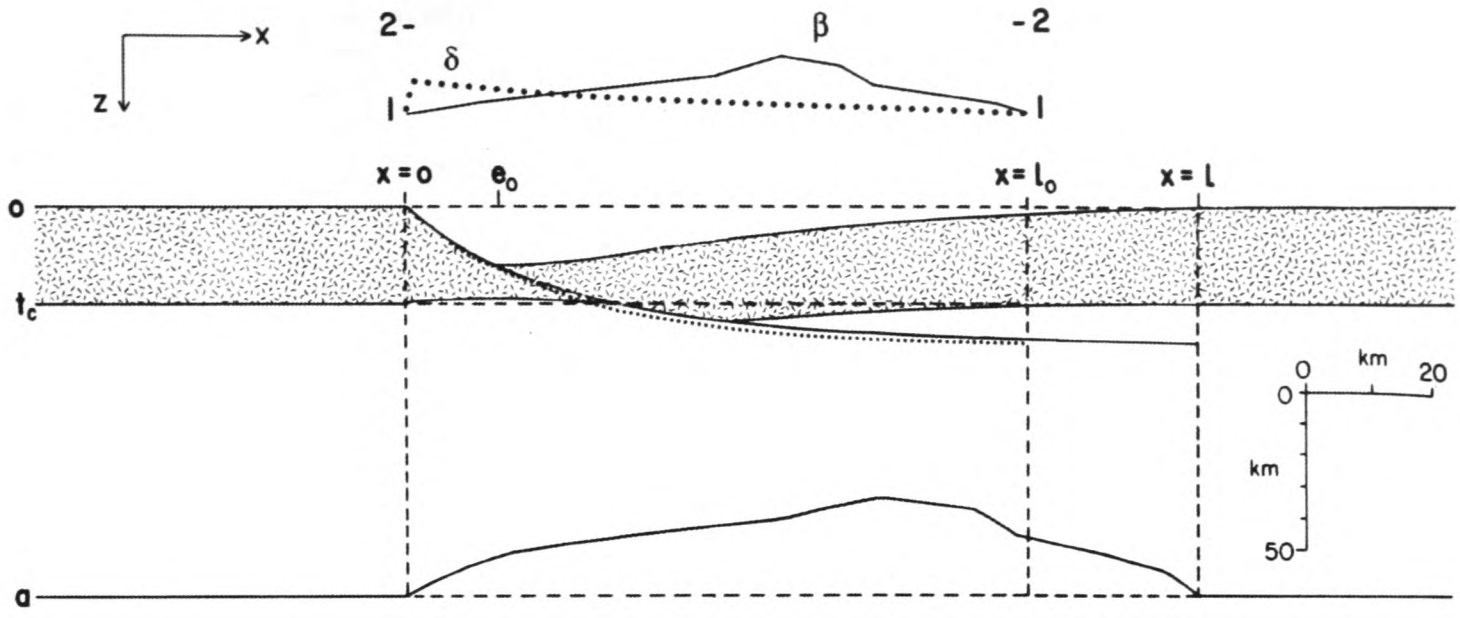


Figure 2.13: Wernicke-type rifting as applied by Weissel & Karner [1989]. Simple instantaneous slip with heave e_0 trending to a horizontal pure shear detachment. Flexural isostasy translates the initial detachment shape (dotted line) to the kinematic shape (solid line). Extension factors δ in the upper plate and β in the lower plate are also shown. Figure from Weissel & Karner [1989].

& Beaumont, 1989; Lynch & Morgan, 1990; Bassi, 1991; Chéry *et al.*, 1992; Govers & Wortel, 1999] and given ways in which necking during extension [Zuber & Parmentier, 1986; Parmentier, 1987] can produce enduring isostatic imbalances that explain observed rift characteristics.

2.6.4 Lithospheric necking

One extensional model that has become popular for simple rift reconstructions has been the 'depth of necking' model of Kooi *et al.* [1992]. This adapts the McKenzie-rifting model by removing the Airy isostatic rifting assumption and allowing the lithosphere to thin around a 'depth of necking', Z_{neck}, defined by the strongest part of the yield strength envelope. The basis for this is numerical work by Braun & Beaumont [1989] that shows preferential centering of extension around the depth of maximum yield strength.

According to the depth at which this necking occurs there will be a resulting isostatic imbalance that can be accommodated either by a weak (~Airy) lithosphere, or by a strong (e.g. elastic plate) lithosphere. The result of the former is a McKenzie-rift equivalent, but the latter provides potential for a long term flexural response to rifting.

Following Weissel & Karner [1989], the thickness of crust above the necking depth will be in proportion with that below for all β. Because the case of $\beta = 1$ (no extension) is already defined by the initial crustal thickness, t_c, the kinematic surface depression, S_T (Figure 2.15), is given by:

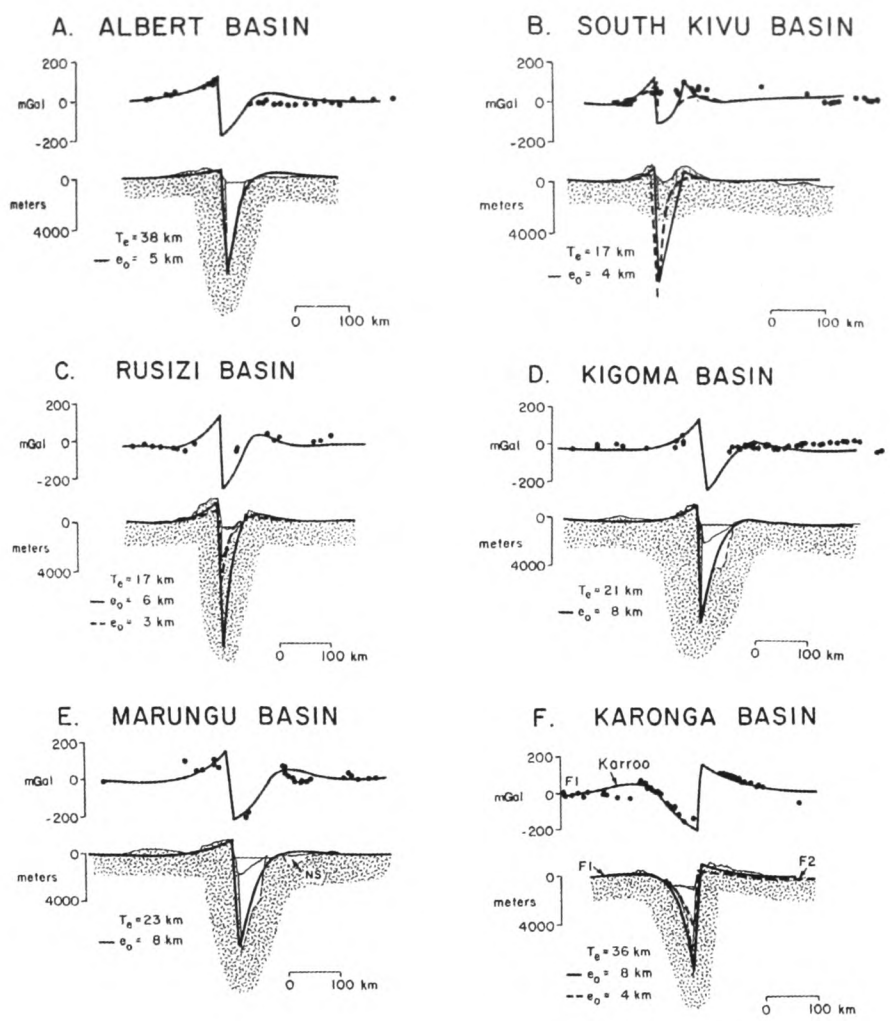


Figure 2.14: Comparison of Wernicke-type extension models (bold solid, dashed lines) of the type applied by Weissel & Karner [1989] and observed Western rift topography (patterned) and free-air gravity anomalies (a-f). The model parameters are T_e and heave (e_0). (b) Incorporates both planar (solid line) and listric (dashed line) faulting modes. Figure from Ebinger *et al.* [1991].

$$S_T = (1 - \frac{1}{\beta}) Z_{neck} \tag{2.17}$$

And the kinematic thickness of upwelled mantle, S_M, is:

$$S_M = (1 - \frac{1}{\beta})(t_c - Z_{neck}) \tag{2.18}$$

The state of isostatic inequilibrium will depend on the balance of forces, q_{net}, between replacement of crust with mantle, and replacement of crust with air or water. Assuming that the rift is water filled:

$$q_{net} = \{S_M(\rho_m - \rho_c) + S_T(\rho_w - \rho_c)\}\, g \tag{2.19}$$

The distribution of q_{net} across the rift is, then, a driving force that can be accommodated flexurally to give a final basin and Moho structure (R_T and R_M respectively).

Depending on the relative densities of crust, mantle, and infill there will also be a unique value of z_{neck} at which $q_{net} = 0$, for which there is no difference between the

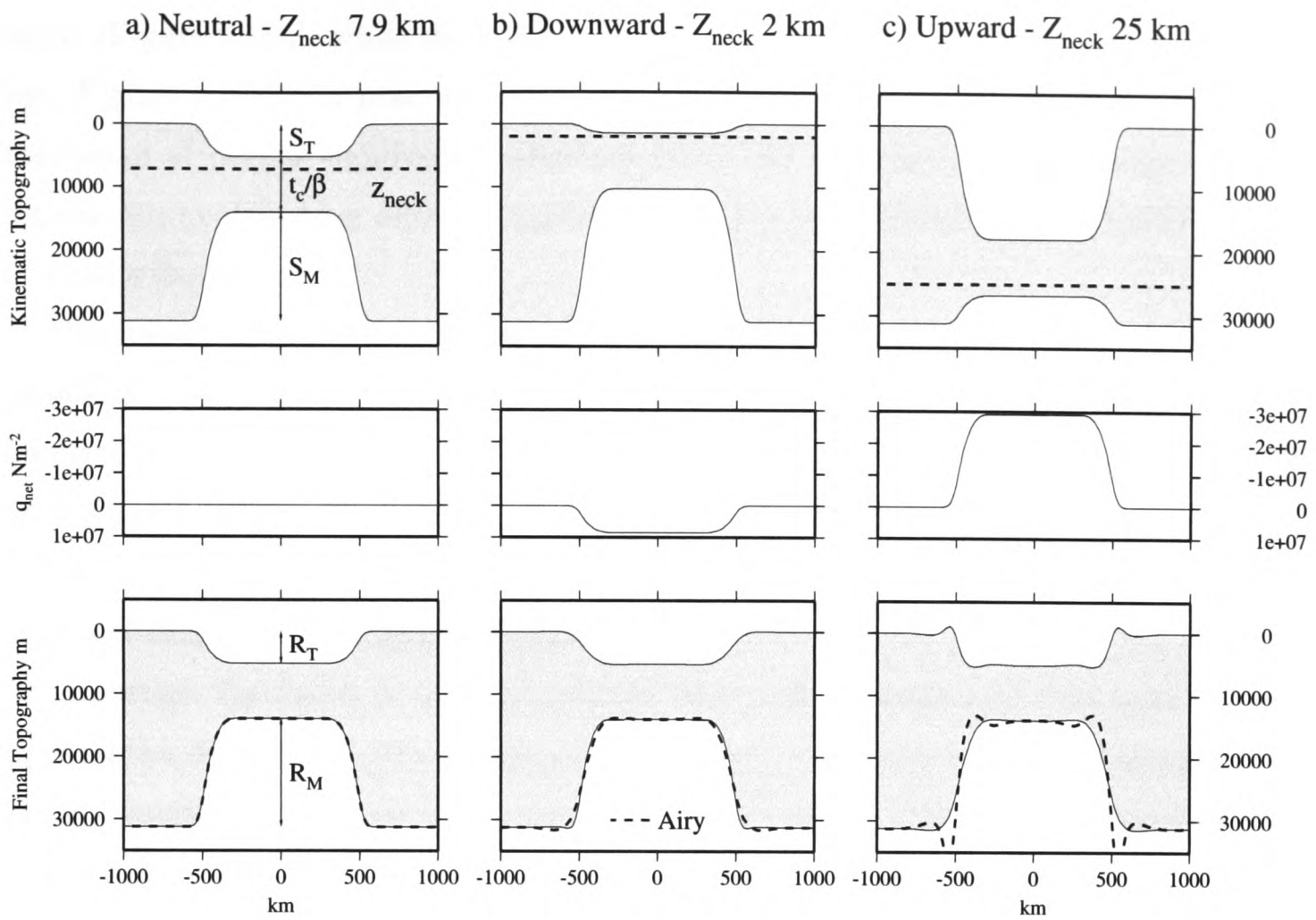


Figure 2.15: Effect of necking depth (Z_{neck}) on continental rifting. (a) A neutral depth of necking results in no net force, and hence no disturbance to the *apparent* local Airy isostatic compensation. (b) A shallow depth of necking results in a net downward force and hence downward flexure. (c) A deep depth of necking results in a net upward force, and hence upward flexure of the central basin and rift flanks. S_T and S_M are the kinematic topography and Moho respectively, while R_T and R_M are their flexurally compensated final states. Figure adapted from Stewart [1998].

kinematic and final states:

$$\begin{aligned} z_{neck_{isostatic}} &= t_c \frac{\rho_m - \rho_c}{\rho_m - \rho_w} \\ \therefore\ q_{net} &= 0 \\ \therefore\ R_T &= S_T \end{aligned}$$

In this case there is no distinction between the McKenzie and depth of necking rifting models, even if the lithosphere retains finite strength during rifting (Figure 2.15a). For the parameters most commonly used in this thesis ($\rho_c = 2850 kgm^{-3}$, $\rho_m = 3330 kgm^{-3}$, $\rho_w = 1030 kgm^{-3}$, $t_c = 38 km$) this is the case if $Z_{neck} \sim 7.9 km$.

This neutral depth of necking marks a transition between downward acting q_{net} if the necking depth is shallower, and upward acting q_{net} if the necking depth is deeper. In the former case flexural subsidence of the basin and downwarping of the flanks will

occur (Figure 2.15b), while the latter case will result in flexural uplift and flank upwarping (Figure 2.15c). In practice, few yield strength envelope models predict a strength maximum at depths significantly shallower than the neutral depth, but deeper necking depths can explain long duration (greater than $50Myr$, Weissel & Karner [1989]) uplift of a rift's flanks.

The depth of necking model avoids some of the complexities that arose from earlier (rheology based) extensional models in which factors such as non-uniform extension with depth were considered (e.g. Royden & Keen [1980]; Rowley & Sahagian [1986]; White & McKenzie [1988]). As well as being used for forward modelling of synthetic rifts, this model can also be simply applied for inverse derivation of the kinematic rift and flank structure from the final basin geometry.

Although the depth of necking concept offers many advantages over more complex approaches, because of strong dependencies on the initial rheology and dynamic extensional processes it may not be applicable in many cases. Using 'fully coupled' models that unify the primary surface and subsurface processes associated with rifting, Burov & Poliakov [2001] find that mechanical and thermal changes during rifting can cause necking to localise simultaneously and/or successively at different levels during extension. They therefore suggest that to remain valid the depth of necking concept will have to be modified to allow for changes in necking depth during the rifting process.

2.6.5 Rheology

The depth of necking model is based on a system in which a uniform rheology is perturbed by a local deformation and then uniformly extended. Other workers have presented similar models in which deformation is controlled by spatial segmentation of the lithospheric yield strength envelope.

One such example is the work of Dunbar & Sawyer [1989] in which localised lithospheric weaknesses are defined by strength perturbations to the strong crust and/or strong mantle. Lithospheric deformation and thermal structure are then allowed to evolve under extension. By altering the relative magnitudes and locations of the perturbations a range of rifting geometries can be synthetically produced that appear broadly analogous to observed rift features (Figure 2.16):

Case 1 (Mantle weakness) - Differential extension of the crust and mantle together with early and voluminous volcanism before graben formation.

Case 2 (Crustal weakness) - Decoupling between the upper and lower crust and between the lower crust and mantle, together with late rifting volcanism after

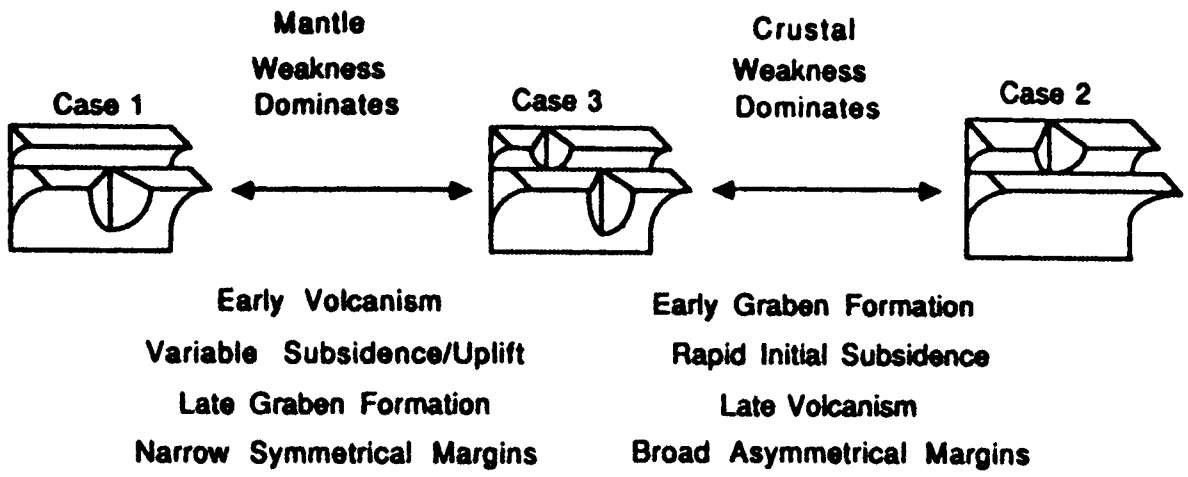


Figure 2.16: Effects of yield strength envelope perturbation on continental rifting. Case 1 - Mantle weak zone. Case 2 - Crustal weak zone. Case 3 - Offset crustal and mantle weak zones. Figure from Dunbar & Sawyer [1989].

graben formation.

Case 3 (Offset crustal and mantle weaknesses) - Develops in a manner comparable to the Wernicke shear model, producing an asymmetric rift. The mantle weakness and crustal weakness ends exhibit features of each of the former models.

The models presented by Dunbar & Sawyer [1989] are only a few of the explanations that have been proffered for rift-associated features. For example, regarding the existence of wide rifts:

1. Some authors (e.g. England [1983]; Kusznir & Park [1987]; Sonder & England [1989]) suggest that slow extension may locally increase the yield strength, causing migration of strong and weak zones, and potentially over-riding the localising effect of necking. This provides a possible explanation for development of wide rifts at slow extension rates, but does not explain why some wide rifts appear to be associated with more rapid extension [Buck, 1991].

2. Buck *et al.* [1999] suggest a mechanism whereby wide rifting can occur at any extension rate if increased regional heat flow causes buoyancy forces that dominate over localising necking effects.

3. Bassi *et al.* [1993] suggest an alternate model in which an initially warm, dry lithosphere cools during rifting; resulting in local increases in strength that cause migration of the locus of thinning.

While most studies have concentrated on either thermomechanical or surficial processes associated with rifting, Burov & Poliakov [2001] suggest that the two could be so

fundamentally linked as to necessitate the use of models in which surface and subsurface processes are fully coupled. Because erosion is a function of tectonic deformation, assumptions of automatic basin infill are not generally sustainable. In turn, the unloading and loading effects of sedimentation may drive flow in the ductile lower crust (Lobkovsky & Kerchman [1992]), and, through corresponding uplift of weaker material, modify the resistance of the lithosphere to extension within and adjacent to the rift. These processes provide a direct feedback to the tectonic deformation. By integrating these processes into a coupled model Burov & Poliakov [2001] show that the complementary effects of erosion, sedimentation, lower crustal flow and upwelling can produce significant non-extensional thinning. Hence apparent crustal β may be as much as $c.2$ times the true extension factor. On the basis of this study, Burov & Poliakov [2001] suggest that the use of 'observed' β (e.g. derived from seismic or gravity data) in reconstruction of thinning, subsidence, and thermal history may be ill-founded.

The relationship between rheology, thermal processes, and rifting is clearly not a simple one. The application of models such as those described here is limited, in that it is not typically straightforward to invert them. However, despite their evident limitations, commonly applied McKenzie and depth of necking rift models generally account well for the first order processes. They can reasonably be applied where post-rift processes overprint second order components of the rifting geometry, and as a means of isolating enduring components of such type. Second order effects that decay over time as a result of thermal relaxation and/or erosion are less easily isolated.

2.6.6 Thermal effects of rifting

As already mentioned in the context of mechanical models, rifting produces anomalies in the thermal structure of the extended lithosphere and its locale. Raising the lithospheric thermal gradient decreases the mechanical thickness, but also has other effects on the rifting geometry.

Lateral heat flow from the rift into flanking regions has been suggested as a mechanism for rift flank uplift [Cochran, 1983]. However, while this is probably a real contributor, it can only explain short-term ($< 60MYr$, Beaumont *et al.* [1982]) uplift. Enduring rift flank uplifts are more easily explained in terms of mechanical causes.

Thermal anomalies also contribute to processes such as rifting volcanism.

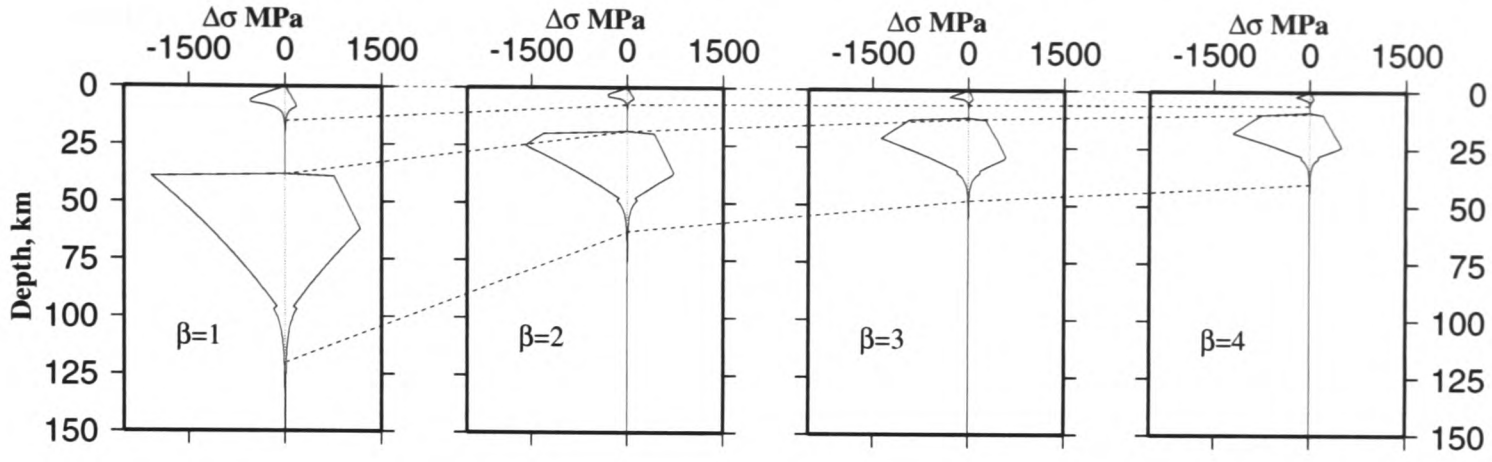


Figure 2.17: Effect of extension factor, β, on T_e for thinning of a continental yield strength envelope (rifting with $5MYr$ cooling).

2.6.7 Post-rift strength

As the raised isotherms subside after rifting it would be expected that the crustal brittle-ductile transition would return to greater depths, and that the depth of the base of the mechanical lithosphere would progressively increase. With time - and in the absence of a later thermal event - it is likely that the mechanical thickness of the lithosphere will increase in a manner comparable to the thermo-mechanical model of Burov & Diament [1995] (Section 2.4). In principle (although observational evidence is so far lacking) there could be cases where eventual coupling of an initially decoupled extended crust and mantle would allow the rift T_e to exceed that of adjacent uncoupled lithosphere.

2.7 Passive margin strength

A passive margin is created when rift-associated thinning leads to 'break-up' and the creation of an oceanic spreading center. A passive margin will therefore have undergone the YSE changes associated with rifting, together with the thermal and igneous effects of break up. These, together with the distinct effective elastic properties of abutting oceanic and rifted continental lithosphere, will modify the flexural isostatic response to post-rift loading.

The yield strength envelope scales with the degree of thinning (Figure 2.17), but cooling during rifting allows recovery of some strength (particularly in the crust) as rifting progresses. Long rifting durations and/or a relatively strong (e.g. Diorite) lower crust may allow the cooling crust to gain enough strength to couple with the mantle at high stretching factors.

If the thinned lithosphere is later flexurally loaded then the yielding caused by bending stresses will also be influenced by the extension factor (Figure 2.18). In practice, however,

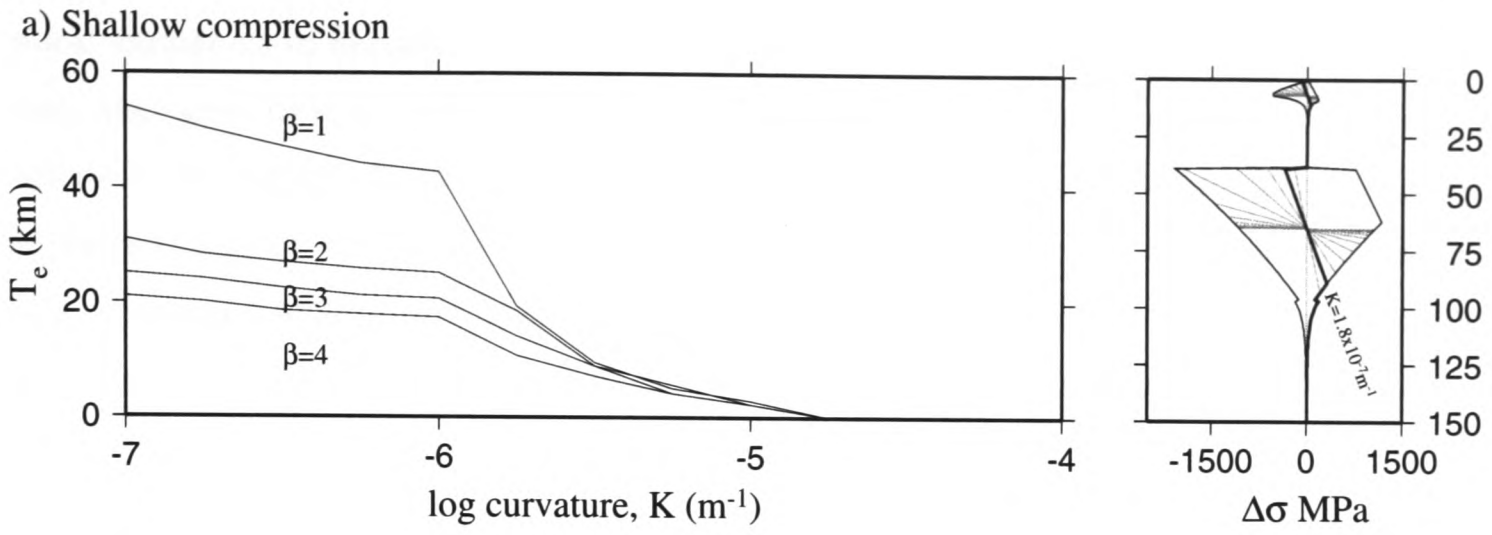


Figure 2.18: Effect of curvature on the effective elastic thickness of rifted continental crust (see also Figure 2.17).

thermal relaxation during and after rifting will modify the yield strength envelopes, and over time the post-rift T_e is likely to be increasingly thicker than this model suggests.

A finite rifting duration, together with modification of the lithospheric rheology by mantle upwelling and igneous intrusion, will ensure that the relationship between rifting and T_e is somewhat more complicated than can be described by a simple thinning of the yield strength envelope. Add the abutment of rifted continental lithosphere against oceanic lithosphere to the structure, and it can be seen that the mechanical thickness of the lithosphere can be expected to vary considerably across a passive continental margin.

Past studies of T_e at passive margins have tended to concentrate on identification of: a uniform defining T_e (e.g. Walcott [1970]; Haxby *et al.* [1976]); a thermally controlled T_e (e.g. Watts *et al.* [1982]; Watts [1988]); or along-strike segmentation of T_e (e.g. Watts & Marr [1995]; Watts & Stewart [1998]).

A compilation of passive margin T_e estimates (see Figure 1.3) shows little correlation between margin age and 'observed' T_e. However, these estimates are based on a 'mean' T_e acting over the period of post-rift deposition, and may therefore be sensitive to tem-

poral variations in deposition rates and to migration of sediment depocenters. Problems may also arise from the use of gravity anomalies over the thinnest rifted lithosphere to constrain the margin T_e in some locations (e.g. Watts [1988]), and the use of depositional surfaces that cross the hinge zone onto lightly rifted lithosphere to constrain T_e in others (e.g. Pazzaglia & Gardner [1994]). This being said, all but two margins (the Labrador Sea and West Greenland margins, Keen & Dehler [1993]) have estimated T_es of $30km$ or less.

Watts [1988] partly addressed across-margin and thermal controls on T_e by invoking an abutment of oceanic ($T_e \equiv 450^oC$ isotherm) and continental ($T_e \equiv 150^oC$ isotherm) lithosphere along a profile through the (Eastern USA margin) Baltimore Canyon Trough. Other studies (e.g. Watts *et al.* [1982]) have shown that increasing T_e as a passive continental margin cools can lead to sediment onlap as the flexural wavelength grows. Within this context the existence of passive margins where offlap dominates (e.g. Michigan Basin, Sleep & Snell [1976]) can be explained either by major erosional events [Sloss & Scherer, 1975] or by slow basin subsidence that is outpaced by falling sea-levels [Pitman, 1978].

Questions of how T_e is controlled at passive margins have been added to by observations of significant along-strike segmentation. A study by Watts & Marr [1995] demonstrated that variations in the geometry and amplitude of the edge-effect gravity anomaly around the African plate could be explained in terms of segmentation of T_e (Figure 2.19). A more local 3-D study of the Gabon margin by Watts & Stewart [1998] reached a similar conclusion.

If along-strike segmentation is a common feature of passive continental margins then the complexities it causes could be just as important as those due to expected across-strike segmentation. However, as yet there has been no comprehensive study of variations both across- *and* along- strike in a passive margin environment. In the absence of such a study their remain uncertainties about how structural segmentation and the rifting process combine to control the distribution of T_e at passive margins.

2.8 Conclusions

The introduction of yield strength envelopes in the late 1970s opened the possibility of directly relating T_e to lithospheric structure. Watts *et al.* [1982] and Karner *et al.* [1983] sought to explain an increasingly diverse range of (respectively) oceanic and continental T_e estimates by thickening of the mechanical lithosphere with increasing thermal age. Only in the oceans has this explanation been borne out by a burgeoning collection of

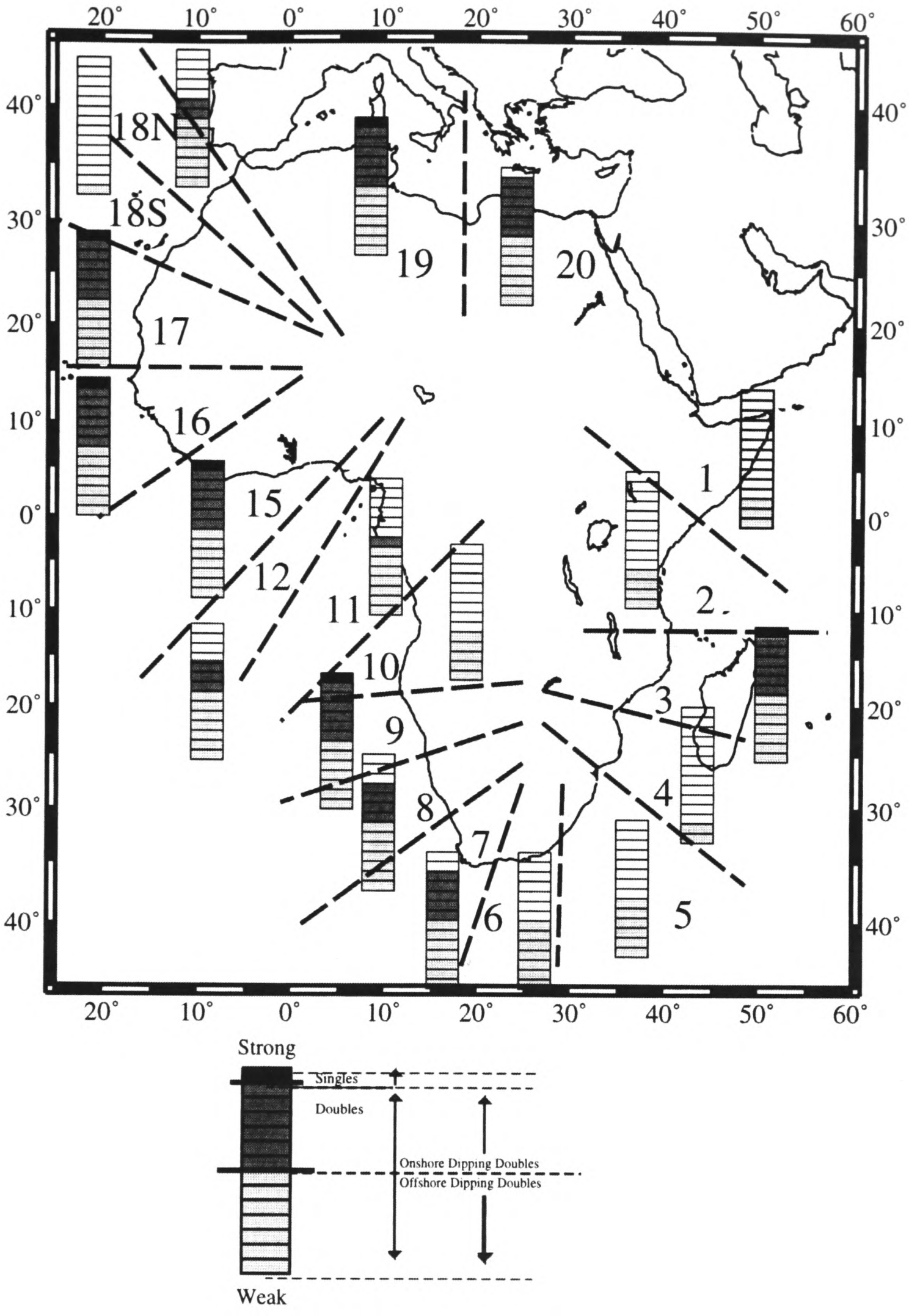


Figure 2.19: Segmentation of African passive margin strength on the basis of amplitude and geometry of the 'edge effect' gravity anomaly associated with rifting and post-rift sediment loading. Figure fron Watts & Marr [1995].

global T_e estimates.

In the continents it is now clear that the thermal history alone is not enough to confine T_e. Reasons for this include a typically more complex (and often longer) tectonic history than the oceans, poorly defined buried structure, and rheological heterogeneity. There is also the possibility of decoupling between the mechanical crust and mantle, whether pre-existing, or caused by the bending stresses arising from flexural loading. Recently, controversial studies have suggested that typical continental mantle offers no significant long term strength at all.

Many of the features of continental rifts and passive margins have been explained by models in which yield strength envelopes (or perturbations thereof) control the rifting process. These, together with studies that have empirically demonstrated significant along-strike segmentation of passive margin T_e, suggest a complex relationship between: yield strength envelopes; structural inheritance; rifting; and the thermal and mechanical effects of post-rift sediment loading. Understanding of rift development is being advanced by the introduction of models in which surface and subsurface processes are fully coupled. The results suggest that the use of existing models to interpret and invert observed rift features is problematic.

It has been shown that passive continental margins should be amongst the most complex of structural environments. Yet the majority of passive margin T_e estimates give either a mean historical value or a single isotherm and thermal age that best describe the gravity anomaly or stratigraphy at a particular location. There remains a need for studies that identify lateral T_e variations and specifically relate them to structural contributions from inheritance, rifting, and post-rift sediment loading.

Chapter 3

The Eastern USA passive continental margin

3.1 Introduction

Atlantic rifting was the most recent of a series of major tectonic events that have impacted on the structure of what is now the Eastern USA passive continental margin. The closure of Iapetus superimposed Variscan-Alleghanian orogeny on previously deformed rocks, to form a complex mixture of ancient plate boundaries and superposed rheologies [Manspiezer & Cousminer, 1988].

A switch from compression to tension in the Late Permian [Ziegler, 1982] extensionally reactivated existing fracture zones, sutures, and transforms, pulling the crust apart along ancient weaknesses. At first this drove the formation of syn-rift basins over a large area between the Pangaean North American and African cratons [Manspiezer & Cousminer, 1988], but as extension continued the rifting localised and deep rifted basins emerged along the modern margin edge. This localised thinning, and led to break-up between North America and Africa sometime after $191Ma$ [Sutter, 1985].

The latest known coastal plain igneous activity provided Sutter [1985] with this earliest date for the transition from rifting to drifting. More recent authors have mostly found dates between $196Ma$ and $202Ma$ (McHone [2000] and references therein), but in any case the date of earliest seafloor spreading is probably somewhat later: the postrift unconformity (or breakup unconformity of Falvey [1974]) marks the base of post-rift sediments that have been dated as latest Lower Jurassic or early Middle Jurassic [Schlee & Fritsch, 1983; Poag & Valentine, 1988; Schlee & Klitgord, 1988]; and plate reconstructions (based on extrapolation of seafloor spreading rates) suggest that rifting may have ended as late as $175Ma$ [Klitgord & Schouten, 1986].

After the rest of the margin had already reached the drift phase, the Blake Spur Fracture Zone allowed rifting in the Blake Plateau Basin to continue alongside seafloor spreading for another $\sim 5Myr$ [Klitgord *et al.*, 1988]. However, by $170Ma$ new seafloor was being created along the entire margin [Klitgord & Schouten, 1986], and sedimentation of the deep Eastern USA marginal basins was well underway.

Subsidence in the post-rift period subsidence - driven mainly by sediment loading and cooling of the rifted lithosphere - has allowed large ($> 10km$) thicknesses of sediment to accumulate in the marginal basins. Up until around 30 years ago these sediments effectively masked the underlying structure of the margin. Since then, improved resolution of the margin structure and potential anomalies, extensive seismic reflection surveying, and deep seismic studies, have made the Eastern USA a major focus of passive margin research.

Together, the studies that have been made of the modern Eastern USA passive continental margin suggest that it is segmented in terms of: extent and degree of thinning prior to break up (e.g. Sawyer [1985a]); volume of volcanic material emplaced during rifting (e.g. Kelemen & Holbrook [1995], and Behn & Lin [2000]); post-rift subsidence rates [Sawyer *et al.*, 1982]; and lithospheric rigidity [Watts, 1988; Pazzaglia & Gardner, 1994]. Segmentation can also be observed as variations in: the width of the coastal plain and continental shelf; marginal basin width and depth; characteristics of the underlying basement; and along-strike potential anomalies.

3.2 Structure and tectonic framework

3.2.1 Introduction

The gross structure of the Eastern USA passive continental margin (Figure 3.1) is dominated by the effects of Late Triassic/Early Jurassic rifting, and the subsequent sediment infill of the subsiding marginal basins.

From the intersection of the Caolinas Fracture Zone to the Georges Bank Basin a narrow shelf ($190 \pm 40km$ wide) and slope cover a series of deep (greater than $10km$ thickness) sedimentary marginal basins. These are backed by a coastal plain that is almost flat from the coastline back to the edge of the Appalachian Orogen. Here a line of waterfalls, known as the fall line, marks the landward limit of rift associated sedimentation.

The coastal plain is a region of low relief underlain by syn-rift grabens, half-grabens, and pull-apart basins, that mostly formed along reactivated basement structures [Manspiezer & Cousminer, 1988]. The sediments within these basins are Middle Triassic and

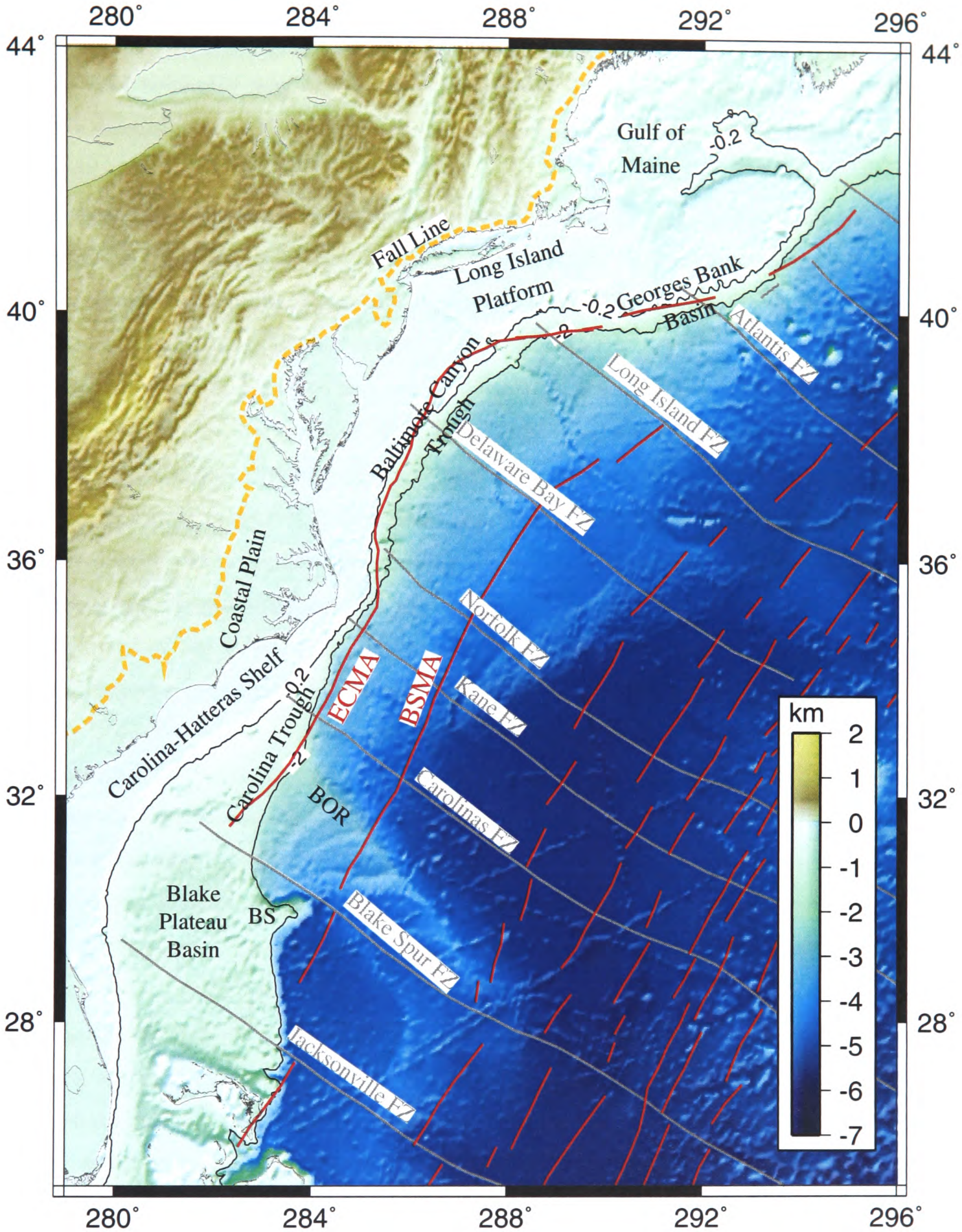


Figure 3.1: Bathymetry and topography of the Eastern USA passive continental margin (data from Smith & Sandwell [1997]). Red lines are magnetic anomalies, grey lines are fracture zones. BOR - Blake Outer Ridge, BS - Blake Spur, ECMA - East Coast Magnetic Anomaly, BSMA - Blake Spur Magnetic Anomaly.

younger [Olsen, 1997], and are interbedded with extensive basalt sills with ages mostly close to $201Ma$ that are associated with numerous Early Jurassic dykes (Ragland [1991]; Olsen [1997]; McHone [2000], see Section 3.4). Up to several kilometers of syn-rift sediments and volcanics may have been eroded after rifting [McHone, 2000], leaving the smooth unconformity onto which coastal plain sediments onlapped from the Cretaceous onwards.

Between the Carolinas Fracture Zone and the Blake Spur Fracture Zone (BSFZ) the rifted margin is widened by a sedimentary platform that has been cut from the slope to around $1 - 1.2km$ depth. This platform reaches its widest south of the BSFZ, forming the broad (greater than $400km$ across) Blake Plateau.

The end of the Palaeocene saw the development of a strong 'Gulf Stream' ocean current that was the most important modulator of the southern margin Tertiary stratigraphy (e.g. Paull & Dillon [1980]). This initially cut across the Florida Straits south of the fall line, but later flowed from the south. As sea-level changes caused its flow to migrate back and forth closer to and further away from the modern Carolinas-Hatteras shelf, so it shaped the Carolina-Hatteras Slope and Blake Plateau.

The end of the Palaeocene also saw the opening of the Norwegian-Greenland Sea, which allowed a strong deep water flow to form a path southward from the Arctic [Mountain & Tucholke, 1985]. Undercutting and erosion from this current caused the Blake Plateau edge to retreat by as much as $15km$; carving the steep Blake Escarpment out of the existing continental slope [Gilbert & Dillon, 1981].

A weaker deep circulation was in place from the middle Miocene onwards. A convergence of deep currents from the north and south deposited sediments as a thick drift (the Blake Outer Ridge) extending across the slope and abyssal plain north of the Blake Spur Fracture Zone [Markl *et al.*, 1970; Markl & Bryan, 1983; Mountain & Tucholke, 1985].

The Blake Spur Fracture Zone, separating the Blake Plateau from the rest of the margin, is a structurally significant member of a series of fracture zones that intersect the margin at $100km$ to $300km$ intervals. The significance of other fracture zones is not always clear. Although their approximate paths have been inferred from plate reconstruction pole rotations (e.g. Klitgord & Schouten [1986]), the earliest traces are masked by the Jurassic Magnetic Quiet Zone, and thick sediment cover that mutes basement magnetic anomalies and conceals basement structure.

3.2.2 Rifted sediment basins

Over most of the $40Myr$ period of extension prior to final break-up rifting was spread across a large area spanning a distance of around $200km$ between the North American

Craton and the African Craton [Schlee *et al.*, 1988]. The syn-rift basins mostly formed along reactivated basement structures [Manspiezer & Cousminer, 1988], and were mostly infilled by lacustrine and evaporitic sediments from transient lakes (references in [Schlee *et al.*, 1988]). However, as rifting proceeded, thinning focused around the eventual line of break-up, allowing as much as $8km$ of continental clastic rocks and evaporites to accumulate in the deepest late syn-rift basins (e.g. Hutchinson *et al.* [1983]).

After break-up a series of platforms and embayments marked the boundary between the coastal plain syn-rift basins, and the post-rift deposition occurring along the newly formed margin. The depocenters defined by this boundary evolved into the four major marginal basins (Figure 3.2) - the Blake Plateau Basin, Carolina Trough, Baltimore Canyon Trough, and Georges Bank Basin - recognised today. Although the shapes of these basins vary considerably, alignment of their tectonic fabric suggests they were formed under a common stress regime [Manspiezer, 1985], and similarities are seen in their depositional histories [Schlee & Jansa, 1981], and some structural features (see Figure 3.3).

In these basins a prominent unconformity separates early Lower Jurassic and Upper Triassic (syn-rift) evaporites, nonmarine clastics, and volcanics, from Lower Jurassic and Middle Jurassic (post-rift) marine carbonate and anhydrite deposits above them [Schlee & Fritsch, 1983; Poag & Valentine, 1988; Schlee & Klitgord, 1988]. Through the remainder of the Jurassic, and into the Early Cretaceous carbonate reefs built upwards and outwards, coalescing into platforms (e.g. Mattick [1982]), and restricting transport of terrigenous sediment across the shelf edge along most of the margin (e.g. Dillon *et al.* [1985]). However, by the late Mesozoic falling temperatures caused the reefs north of the Blake Plateau to be overcome [Jansa, 1981], allowing delta progradation across the shelf edge onto the continental rise (e.g. Dillon *et al.* [1985]).

The Blake Plateau Basin lay in warmer (more southerly) climes than the other basins, and further from major (Appalachian) terrigenous sources [Dillon & Popenoe, 1988]. Its location allowed more extensive Jurassic carbonate deposition to occur, and delayed reef death (possibly due to a marine regression) until the Late Cretaceous [Vail *et al.*, 1977].

Sea-level reached a maximum in the Late Cretaceous, and then fell steadily, keeping the platform submerged at depth (e.g. Watts & Thorne [1984]). During the Tertiary, tectonic subsidence slowed and at first the depocenter shifted gradually seaward until the late Paleocene, when the erosional stages described in Section 3.2 took control of the stratigraphic evolution.

Over the post-rift history sediment infill reached large (greater than $10km$) thicknesses in the marginal basins. The original depths of the marginal basins would not

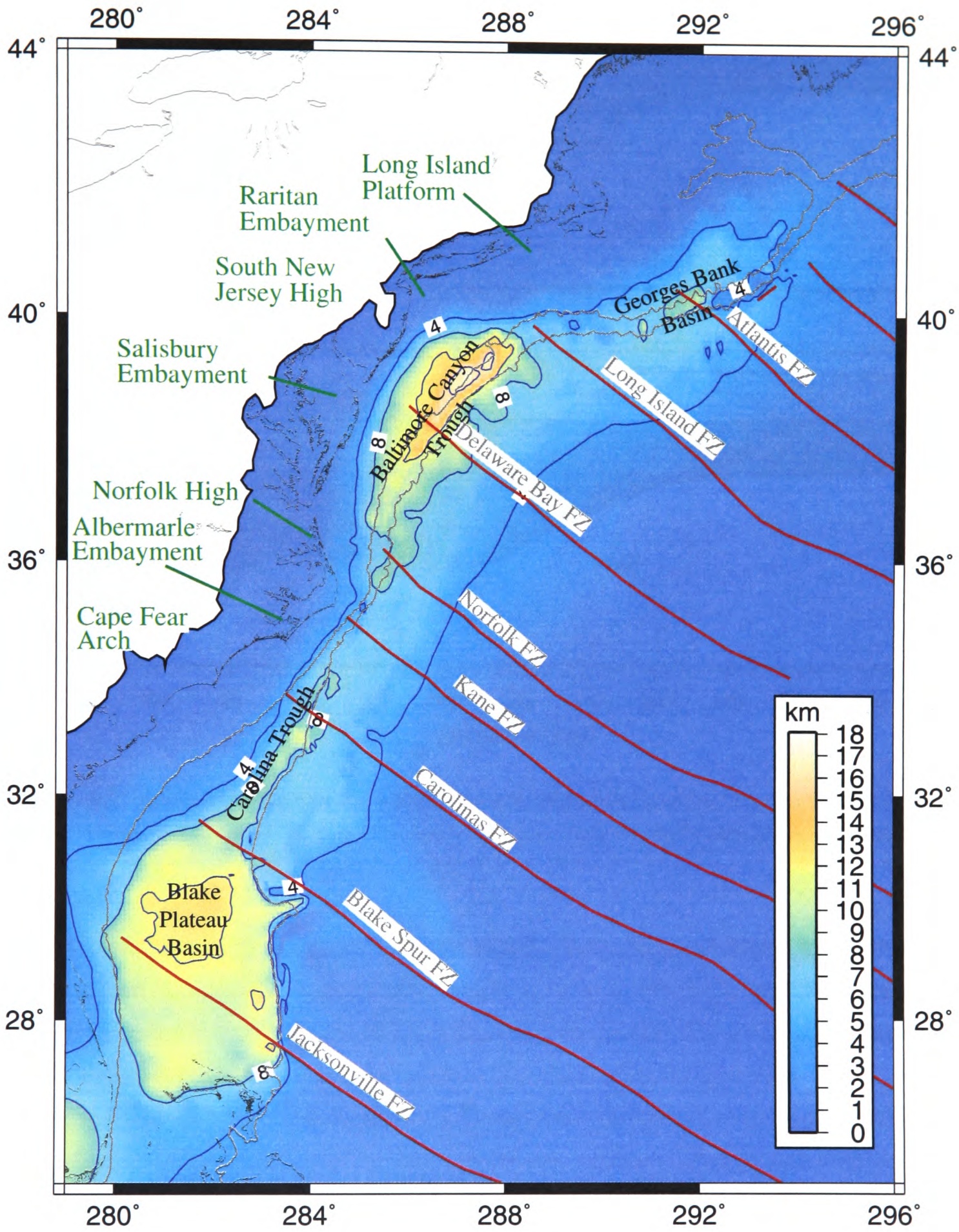


Figure 3.2: Marginal basins of the Eastern USA passive continental margin.

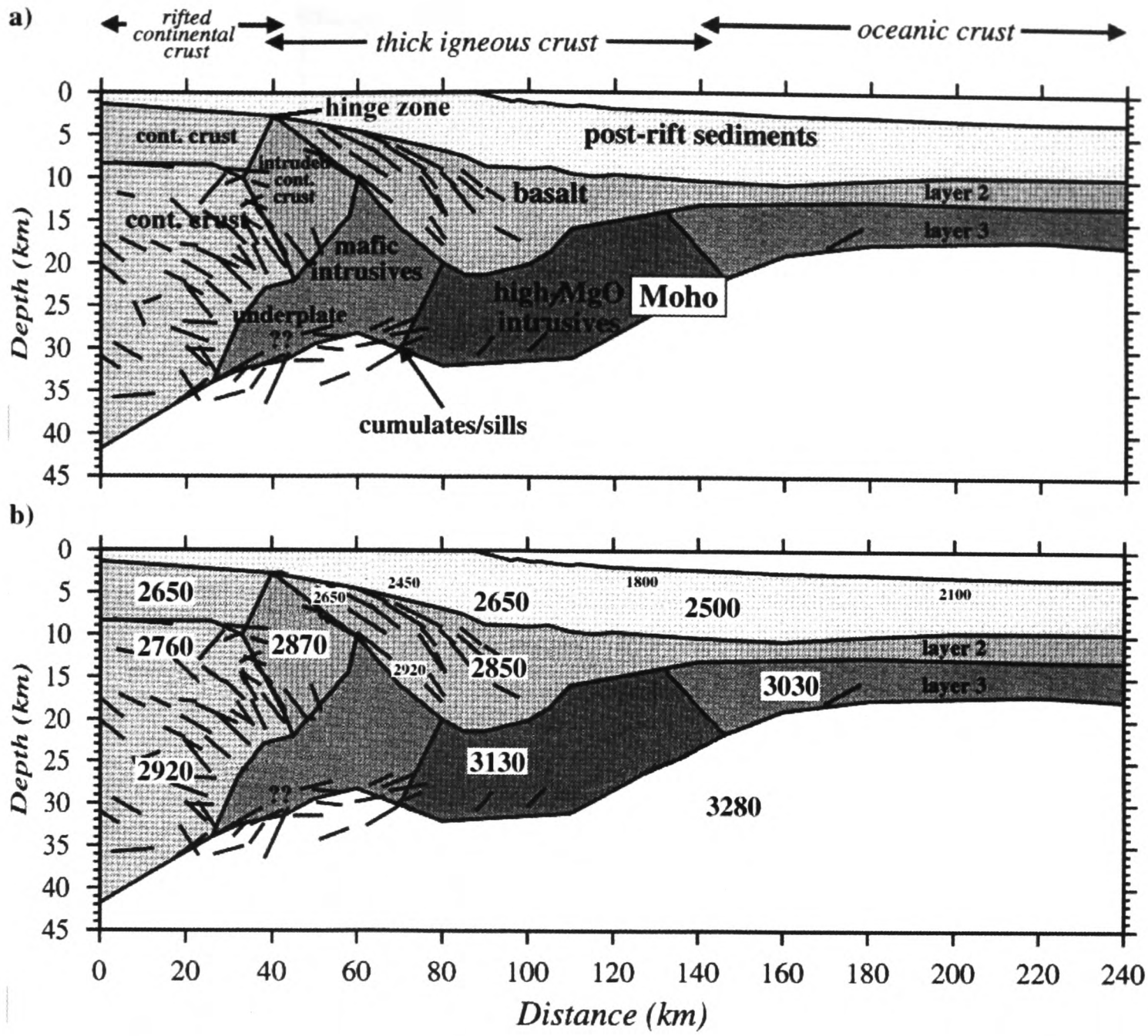


Figure 3.3: Example section through a major Eastern USA marginal basin: The southern Baltimore Canyon Trough (EDGE 801). a) Structure, and b) densities (kgm^{-3}) after Holbrook *et al.* [1994b].

have allowed such large thicknesses to accumulate, but subsidence driven by thermal relaxation and sediment loading provided additional space. The high rate of this offshore subsidence relative to that of the coastal plain transformed the line of marginal platforms and embayments into a 'hinge zone' between the two regions (Figure 3.3).

At first the hinge zone was uplifted, allowing several kilometers of syn-rift sediment and volcanic material to be eroded (Hutchinson *et al.* [1986], and Klitgord *et al.* [1988]), and prevented landward migration of post-rift sediment deposition. However, by the earliest Cretaceous, continued basin infill, subsidence of the eroded hinge zone, and rising sea-level, allowed subsequent deposition to onlap across the erosional surface of the hinge zone and onto the syn-rift basins behind it (e.g. Gohn [1988]). By the Aptian, deltaic sedimentation was occurring as far back as the modern fall line, and a thickness of several kilometers of sediment had accumulated across the hinge zone (e.g. Gohn [1988]). The

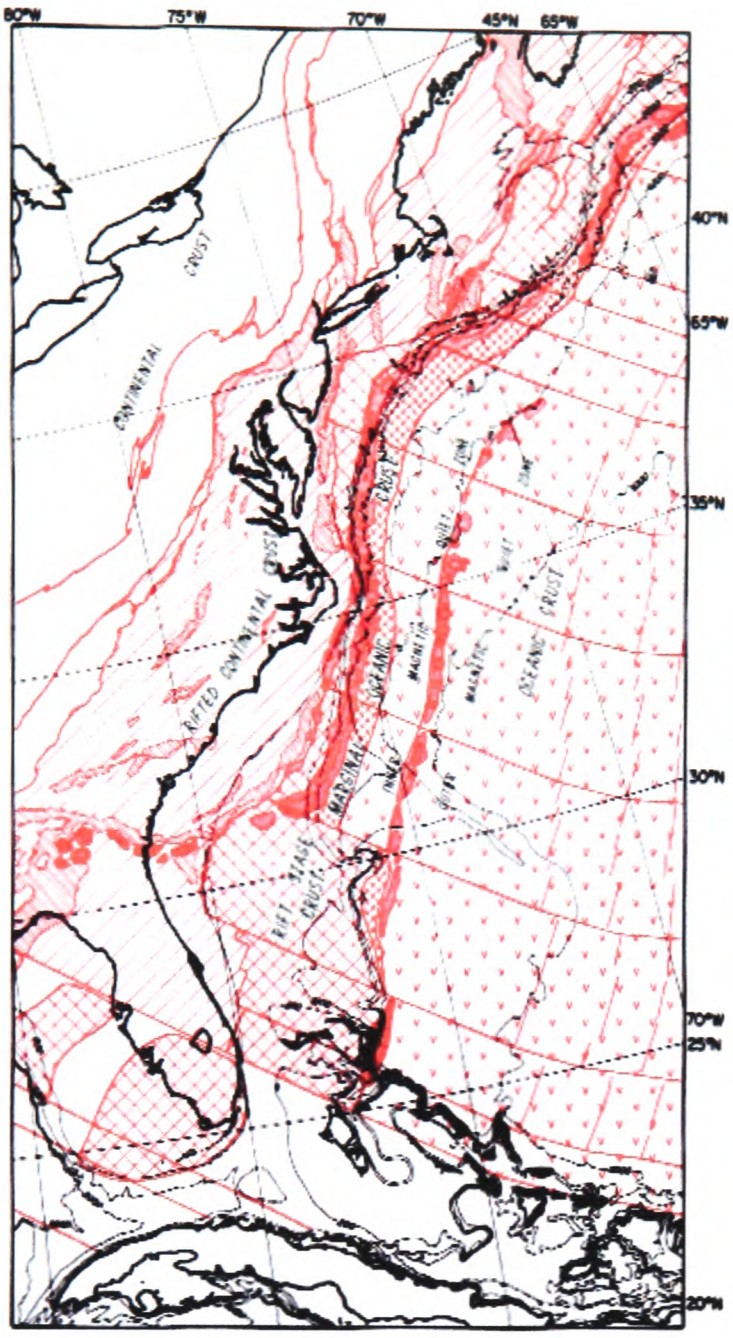


Figure 3.4: Eastern USA passive continental margin crustal types. See text for description. Reproduced from Klitgord *et al.* [1988]

hinge zone is most deeply buried beside the marginal embayments, and is now observed seismically as a steepening of basement at a $2km$ to $4km$ depth. This steepened gradient continues to basement depths greater than $8km$ on the seaward side (Klitgord *et al.* [1988], also see Figure 3.3).

3.2.3 Crustal structure

Klitgord *et al.* [1988] categorised the bulk effects of rifting on the Eastern USA crustal structure by defining zones according to the degree of alteration experienced as the margin formed (Figure 3.4).

'Unrifted crust' is the typically over $30km$ thick crust that existed close to the margin prior to break up, but which was not affected by rifting between the Pangean North American and African Cratons [Klitgord *et al.*, 1988]. Despite its isolation from Atlantic

rifting, this crust retains the segmented nature arising from its complex tectonic history (Williams & Hatcher [1983], and see Section 3.1).

Adjacent to the unrifted continental crust lies 'rifted continental' crust in which some extensional faulting and igneous intrusion occurred during Atlantic rifting, but not enough to significantly alter the bulk composition or crustal thickness [Klitgord *et al.*, 1988]. Its seaward edge is marked by the hinge zone.

The hinge zone is the transition from rifted crust to 'rift stage' crust that has been significantly altered by rifting. This is marked by a rapid increase in basin depth across the hinge zone leading to greater degrees of thinning towards the deepest parts of the marginal basins. This thinning was accompanied by massive alteration of the continental crust as a result of extensive intrusion of igneous material during rifting (e.g. Klitgord *et al.* [1988]).

The platforms that the hinge zone outlines have also been described as 'structural arches' (e.g. Brown *et al.* [1972]), because - even after sediments began to onlap the hinge zone in the Cretaceous - they confined the bulk of post-rift deposition to the subsiding embayments to either side (Figure 3.5).

The rift stage crust contains en echelon relays, some of which form offsets that appear to correlate with oceanic fracture zones. Some of these bound the major basins (e.g. Klitgord *et al.* [1988], also see Figure 3.2), and others have been linked to structural transitions (e.g. a boundary between hinge zone half grabens and tilted blocks in the Georges Bank Basin, Klitgord *et al.* [1988]). However, the structural significance of many of the early offsets is concealed by a thick sediment cover that obscures the syn-rift architecture of the Eastern USA margin (e.g. Klitgord *et al.* [1988]).

Deep seismic studies - using refraction and wide angle reflection techniques - have shown that the degree of alteration in the rift stage crust may be greater than Klitgord *et al.* [1988] suggested. Crustal seismic velocities ($7.1 - 7.5 kms^{-1}$) in this zone are considerably higher than typical $5.9 - 7.0 kms^{-1}$ velocities in the adjacent continental crust (Figure 3.6 - LASE Study Group [1986]; Trehu *et al.* [1989]; Austin *et al.* [1990]; Oh *et al.* [1991]; Sheridan *et al.* [1993]; Holbrook *et al.* [1994a,b]), indicating that little or no original crustal material remains in an unaltered state beneath the deep basins (e.g. Lizarralde & Holbrook [1997]). It has even been proposed that this crustal material is *entirely* new, and is therefore better described as anomalously thick ($15 km$ to $20 km$) 'initial oceanic crust' [Talwani *et al.*, 1995].

The location and characteristics of the continental to oceanic transition are controversial because: the basement is poorly imaged in seismic reflection profile data (especially in the vicinity of carbonate reefs); and there is a lack of an abrupt velocity contrast is

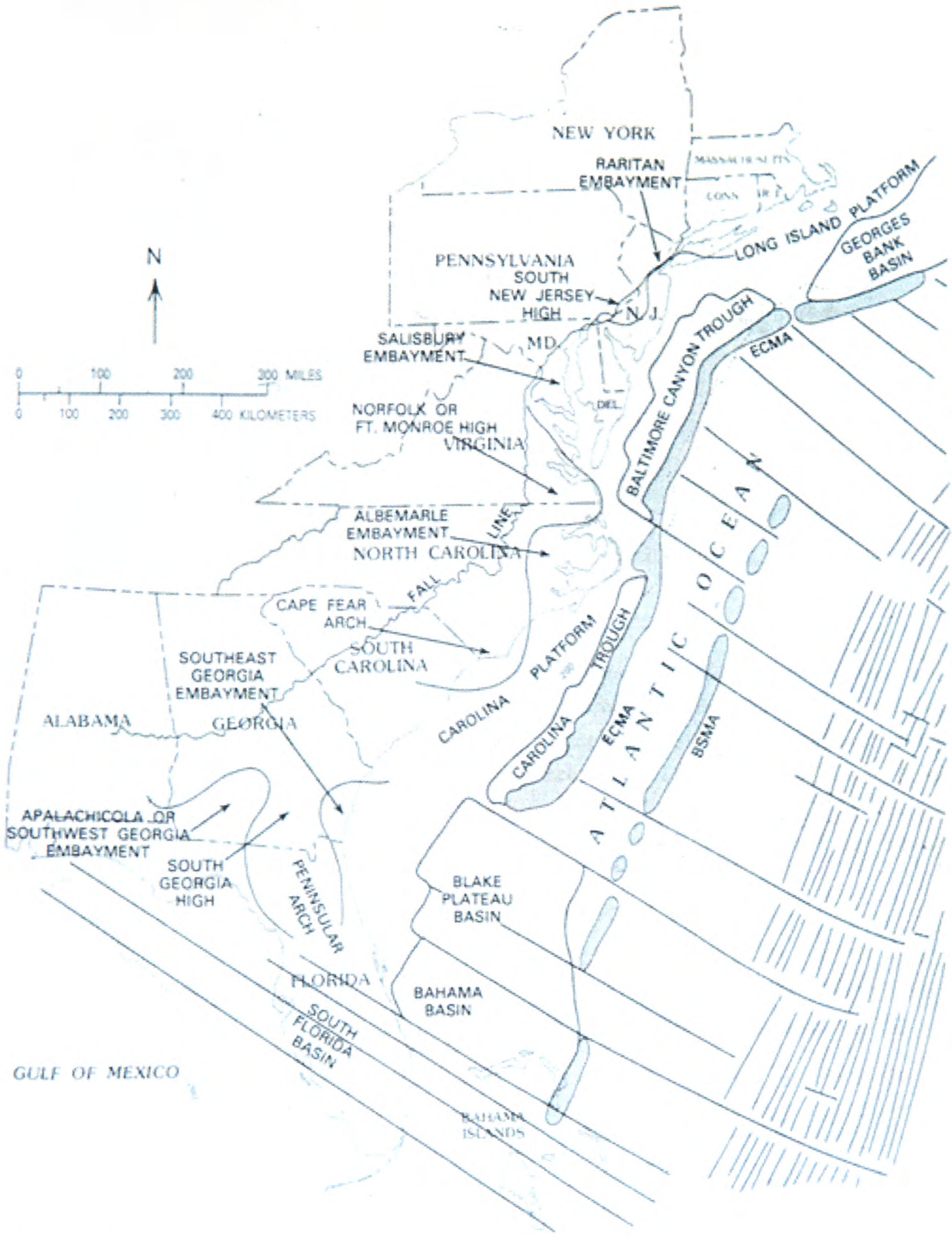


Figure 3.5: Structural arches of the Eastern USA passive continental margin. Figure reproduced from Owens & Gohn [1985]

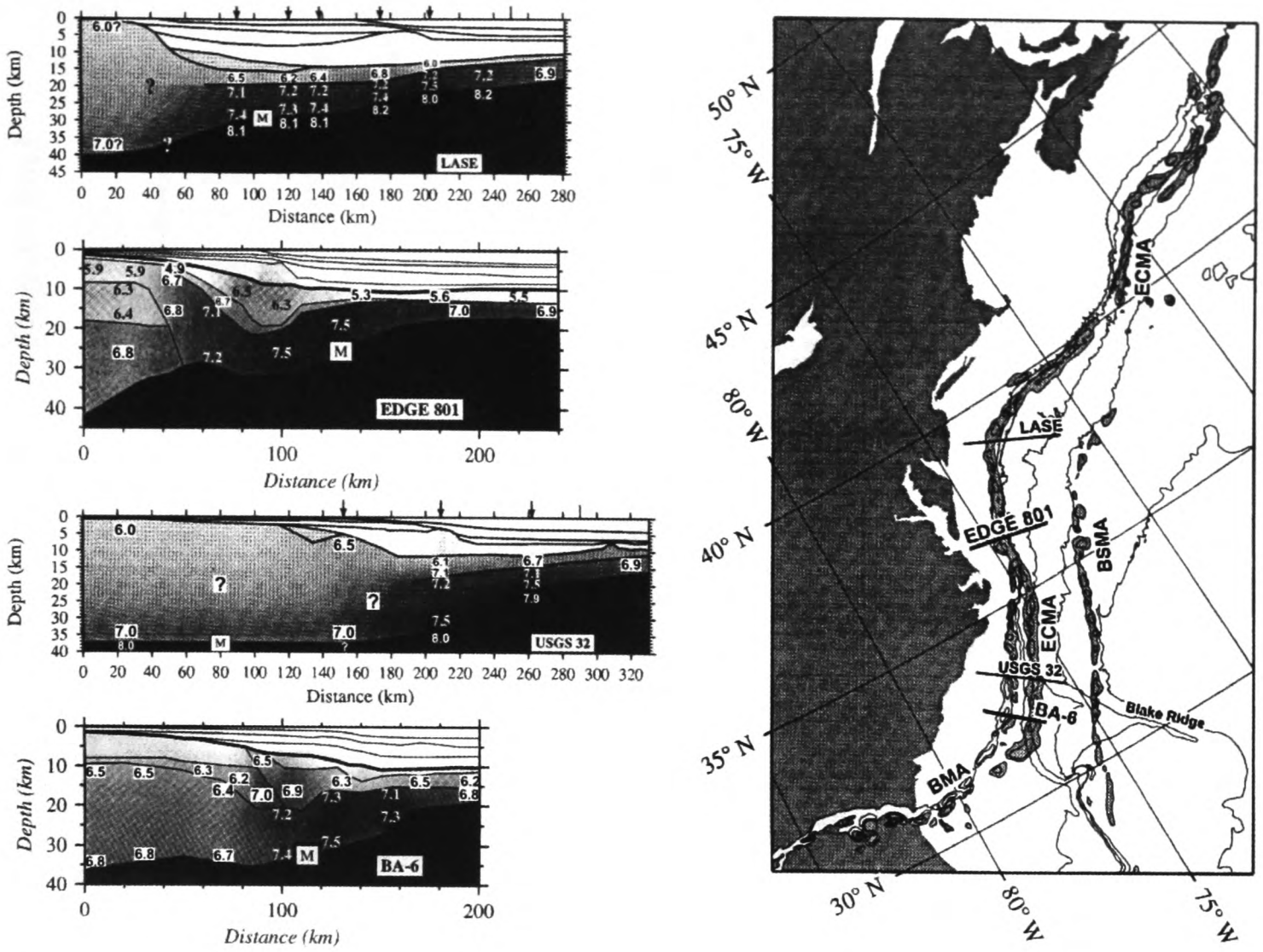


Figure 3.6: Seismic velocities (kms^{-1}) from deep seismic transects of the Eastern USA passive continental margin. LASE - figure from Holbrook & Kelemen [1993] using velocities from LASE Study Group [1986]; EDGE 801 - figure from Kelemen & Holbrook [1995] using velocities from Holbrook *et al.* [1994b]; USGS 32 - figure from Holbrook & Kelemen [1993] using velocities from Trehu *et al.* [1989]; BA 6 - figure from Kelemen & Holbrook [1995] using velocities from Holbrook *et al.* [1994a]. Lines EDGE 801 and BA 6 do not have published mantle velocities. Density models derived from the EDGE 801 and BA 6 seismic velocities are shown in Figure 3.7.

lacking between the magmatically altered rift stage crust and oceanic crust in deep seismic studies (e.g. Holbrook *et al.* [1994b]). Klitgord *et al.* [1988] suggest that the region of uncertain origin could represent a zone of 'marginal oceanic' crust, having a greater thickness ($c.10km$) than normal oceanic crust, and with possible rift stage underplating extending across its base.

3.3 Geophysical markers

Although seismic studies can reveal structural detail that is not directly available from other sources, there are only four deep seismic structure transects across the Eastern USA margin. Potential fields have better areal coverage, and much attention has been

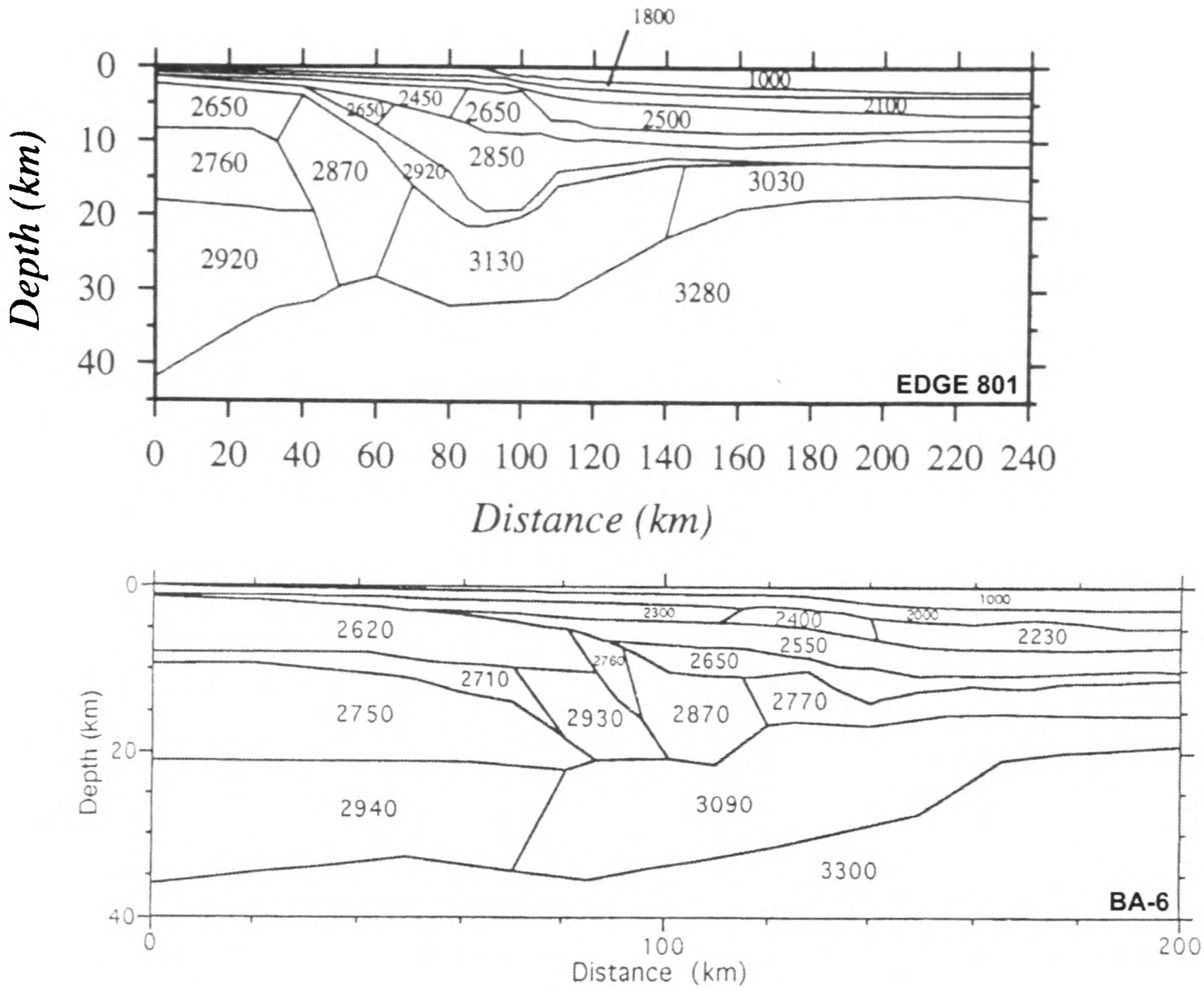


Figure 3.7: Density models corresponding to deep seismic transects of the Eastern USA passive continental margin. EDGE 801 model and figure from Holbrook *et al.* [1994b]; BA 6 model and figure from Holbrook *et al.* [1994a]. Densities are in kgm^{-3}.

paid to identification of geophysical markers that can be directly tied to seismically observed margin features. In principle this allows such features to be extrapolated along the margin.

3.3.1 Gravity anomalies

As is typical of other passive continental margins (e.g. Karner & Watts [1982]), the Eastern USA margin shelf break is marked by a prominent free-air 'edge effect' gravity anomaly consisting of a high and flanking seaward low. The 'high-low couple' is generally attributed to the juxtaposition of thick continental crust against thin oceanic crust (e.g. Worzel [1968]. It is caused by the combined gravity contributions of deepening water and shallowing Moho depth across the continental slope. The edge effect high originates at the original shelf edge and migrates with it as sediments prograde onto the rifted margin (e.g. Walcott [1972]) and its amplitude and wavelength are in part controlled by the

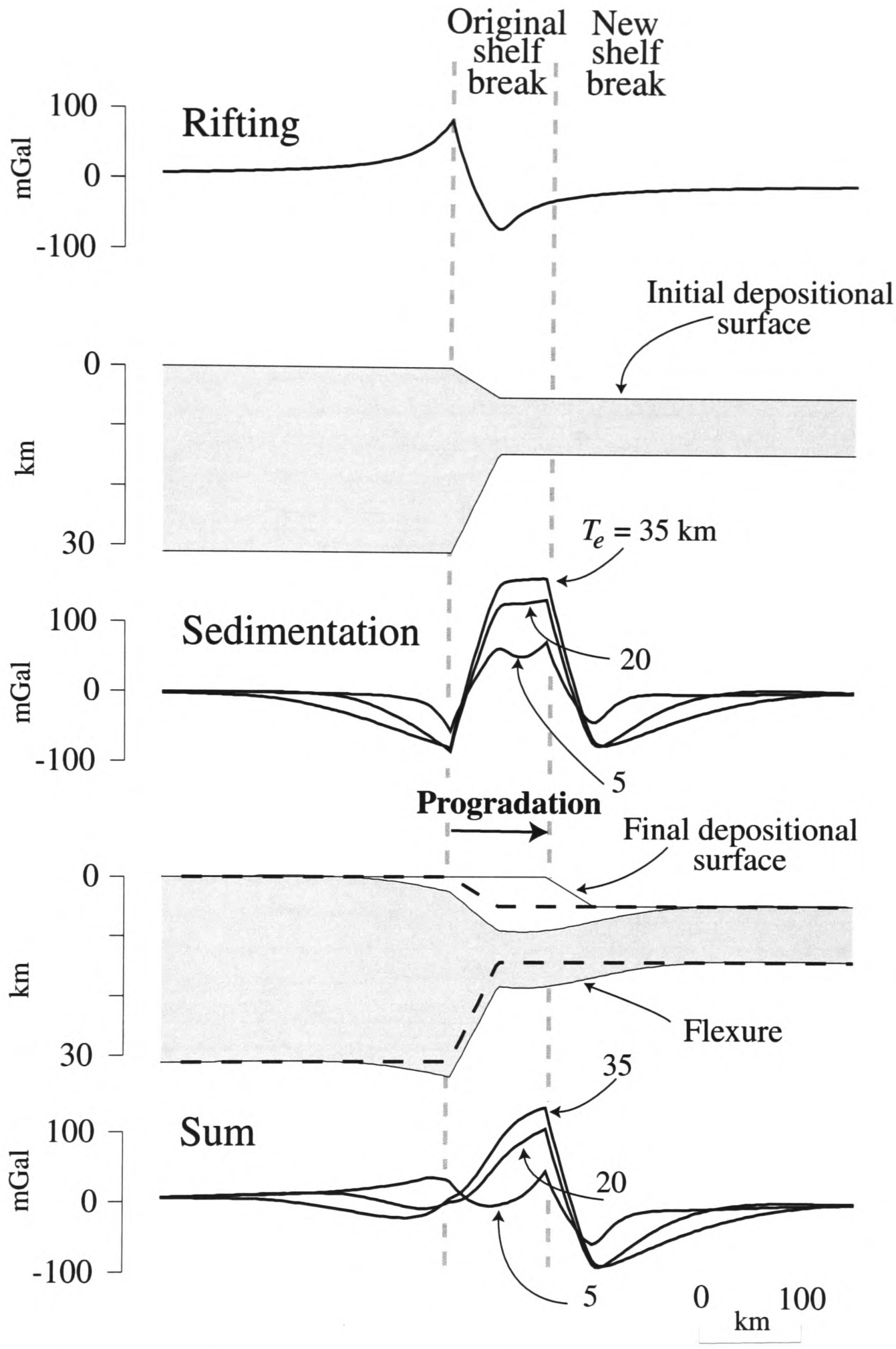


Figure 3.8: Gravity edge effect anomaly migration due to isostatically (flexural) compensated sediment progradation. Anomalies shown are without sedimentation ('rifting'), the contribution of sediment loading to the gravity anomaly ('sedimentation'), and the edge effect anomaly with the sediment in place ('sum'). Figure 4.29 of Watts [2001]

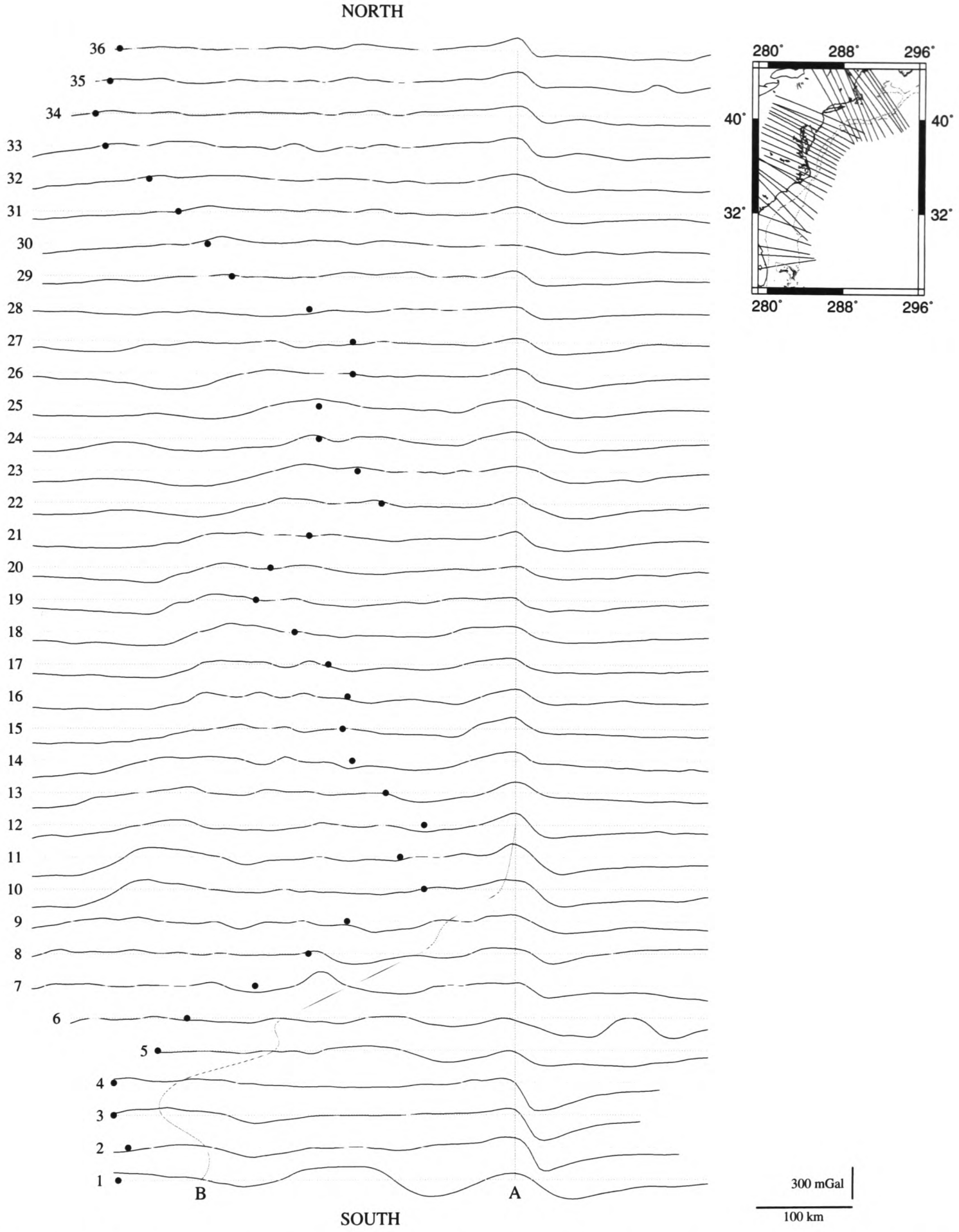


Figure 3.9: Gravity anomaly profiles normal to the USA Atlantic coastline (FA offshore, Bouguer onshore). A - Platform break edge effect anomaly. B - Shelf break edge effect anomaly. A and B are coincident from profile 11 north. Coastline marked by black circles. Source data detailed in Section 3.6.1.

rigidity of the underlying lithosphere (Watts & Marr [1995], Figure 3.8).

The Eastern USA margin edge effect anomaly varies in amplitude along-strike (Figure 3.9A), dividing the margin into distinct zones in which the amplitude is: greater than $125mGal$ (profiles $1-4$, $10-15$), of $90-125mGal$ (profiles $5-6$, $16-26$, $33-36$), and less than $90mGal$ (profiles $7-9$, $27-32$).

South of profile 10 in Figure 3.9 the continental slope is interrupted by the Blake Plateau, causing the edge effect high to increase in width, and eventually separate (between profiles 10 and 9) into a short-wavelength, large amplitude edge effect couple across the Blake Escarpment and a longer wavelength, smaller amplitude edge effect couple across the break of the Carolina-Hatteras Shelf (Figure 3.9, A, B).

On profiles $7-10$, $14-19$, and $24-25$ a second (smaller) gravity high is superposed on the landward flank of the edge effect high. This feature is close to the landward edge of high velocity ($6.2-6.9kms^{-1}$) and high density ($2760-2870kms^{-1}$) volcanic(?) seaward dipping reflectors observed (between profiles 7 and 8) in the BA-6 deep seismic line (see Holbrook *et al.* [1994b]) and (in close proximity to profile 14) in the EDGE-801 deep seismic line located (see Lizarralde & Holbrook [1997]).

3.3.2 Magnetic anomalies

The East Coast Magnetic Anomaly (ECMA - Figure 3.10) typically follows the edge effect anomaly, and, like it, has often been viewed as a marker of the ocean to continent transition (OCT) or boundary (e.g. Keen [1969]; Emery *et al.* [1970]; Grow *et al.* [1979]; Klitgord & Behrendt [1979]; Hutchinson *et al.* [1983]; LASE Study Group [1986]). However, with limited seismic evidence for the OCT as the source, the cause of the ECMA has remained in debate, and igneous sources of intrusive (e.g. Alsop & Talwani [1984]) and/or extrusive (e.g. Austin *et al.* [1990]) type have also been proposed.

The Brunswick Magnetic Anomaly (BMA) lies westward of the ECMA in the southern part of the margin. To the north of the Carolina Fracture Zone (CFZ) it is observed as a large amplitude (typically $> 200nT$) high and lower amplitude (typically $< 200nT$) landward low running parallel to the ECMA. South of the CFZ the BMA high is offset seaward, and the anomaly is dominated by a large amplitude (typically $> 300nT$) low.

The BMA then extends westwards out of the study area, and across the northern Florida peninsular. It has been widely held that this part of the BMA marks a suture zone boundary of pre-Pangaean African material that remained accreted to the North American Plate during Atlantic rifting [Popenoe & Zietz, 1977; Daniels *et al.*, 1983; Klitgord *et al.*, 1983, 1984; Sawyer, 1985a].

Talwani *et al.* [1995] have presented magnetic models that locally explain the Car-

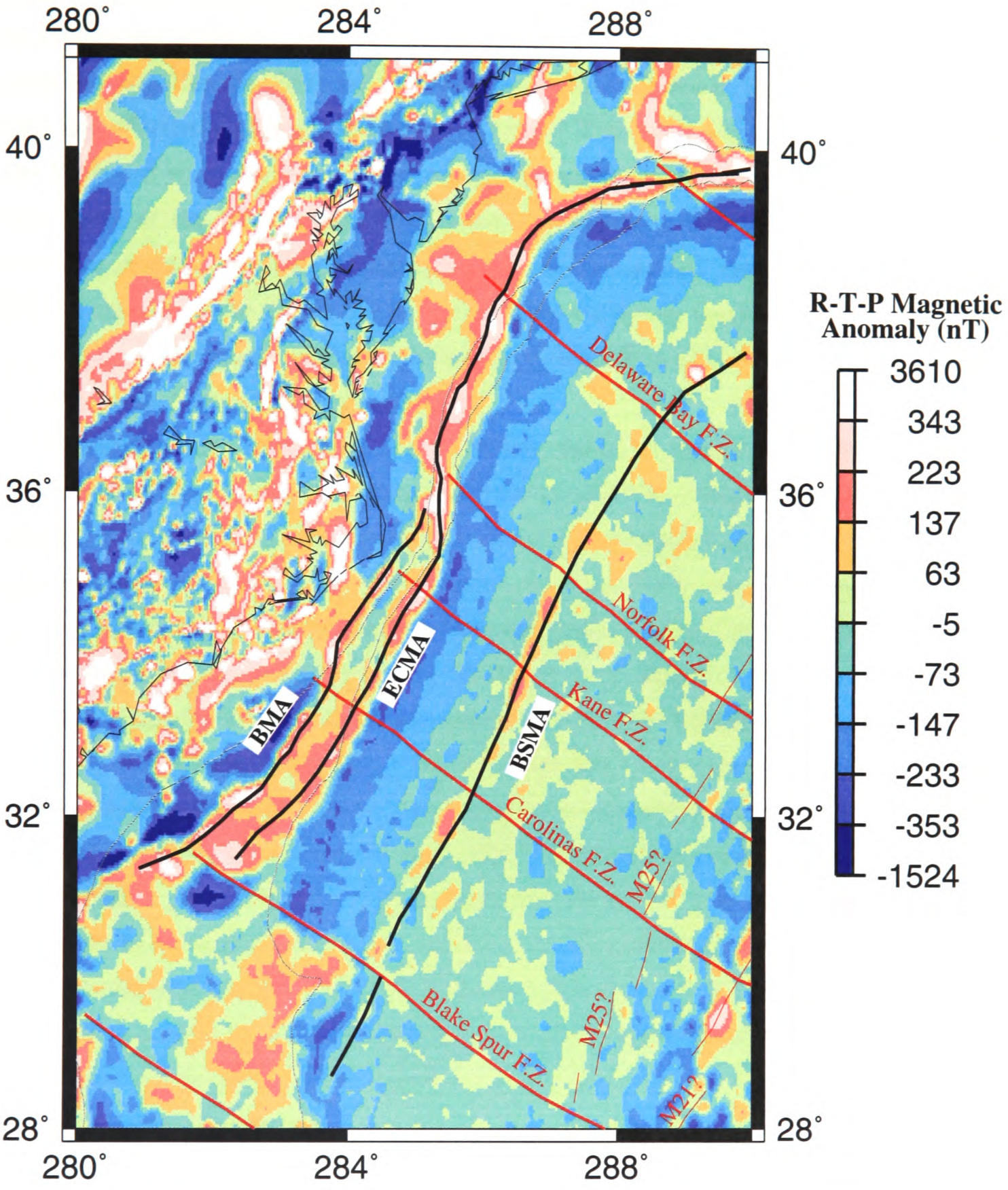


Figure 3.10: Reduced to pole (R-T-P) Eastern USA passive margin magnetic anomaly. Prominent along-strike features are the Brunswick Magnetic Anomaly (BMA), East Coast Magnetic Anomaly (ECMA), and Blake Spur Magnetic Anomaly (BSMA). R-T-P data courtesy of Mark Behn, Massachusetts Institute of Technology, cf. Behn & Lin [2000].

olina Trough ECMA and BMA as signals of a single volcanic body at basement depth (Figure 3.11). Along the USGS32 deep seismic line a voluminous (*c.*120km wide, 12km thick) volcanic wedge extending from the hinge zone across initial oceanic crust is used to explain the magnetic data. In this model the ECMA results from the magnetic contrast between this magnetic volcanic body (intensity 0.005emu, dip 2^o, and inclination 45^o) and effectively unmagnetised oceanic crust[1]. The BMA magnetic low is sourced at the landward end, where the rifted continental crust has a susceptibility of 0.001emu. Just north of the BMA, at the EDGE-801 line (southern Baltimore Canyon Trough), a similar magnetic anomaly is explained by a similar model. However, the part of the ECMA crossed by the LASE line in the northern Baltimore Canyon Trough is narrower and has a smaller amplitude high-low couple. This is explained by a considerably smaller (*c.*70km wide, 7.5km thick) volcanic body.

Holbrook *et al.* [1994a] also use a volcanic model to explain the Carolina Trough BMA and ECMA, in this case along the BA-6 seismic line. They suggest that the most important structural discontinuity at this part of the margin is marked, not by the ECMA high as previously thought, but by the large amplitude BMA low. They argue that from this point seaward crustal seismic velocities and crustal density increase rapidly, and the first seaward dipping reflectors appear [Holbrook *et al.*, 1994a].

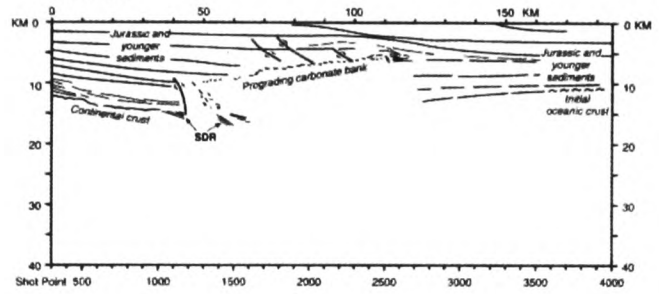
Another major magnetic anomaly associated with development of the margin is the Blake Spur Magnetic Anomaly (BSMA), which lies to the east of the ECMA. This anomaly is thought to lie close to the African edge of seafloor spreading that took place north of the Blake Spur Fracture Zone (BSFZ) while rifting was ongoing in the Blake Plateau Basin [Vogt, 1973]. A ridge jump across the BSMA around 170Ma [Vogt, 1973] is marked by a roughly 1km step in basement, which is flanked by oceanic crust on both sides [Sheridan *et al.*, 1979; Klitgord & Grow, 1980; Trehu *et al.*, 1990]. The ridge jump occurred at around the same time as the rift to drift transition across the Blake Plateau, and hence corresponds with the opening of a permanent seaway between Tethys and the central Atlantic [Jansa, 1986].

[1]Talwani *et al.* [1995] left the oceanic crust effectively unmagnetised in order to reflect the absence of oceanic magnetic anomalies here. They state that a slight magnetisation could be included without dramatically altering their models.

Carolina Trough - USGS 32

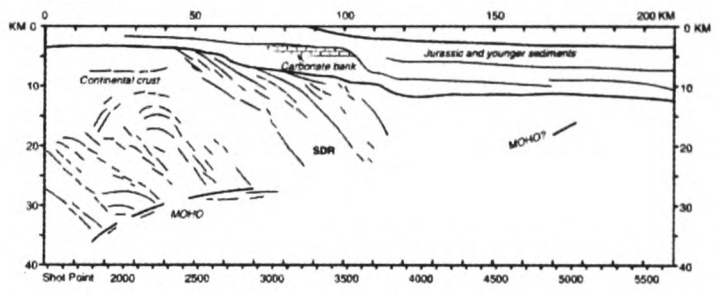
Northern Baltimore Canyon Trough - LASE

Reflection

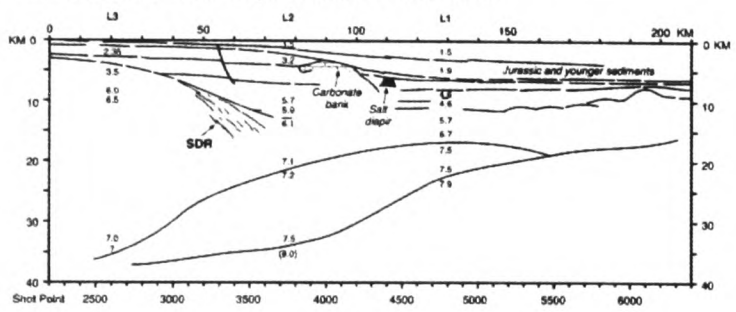


Southern Baltimore Canyon Trough - EDGE 801

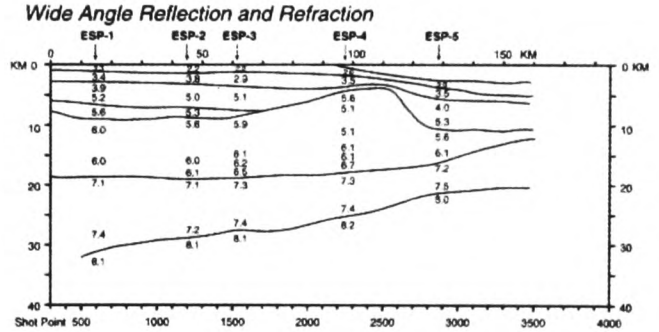
Reflection



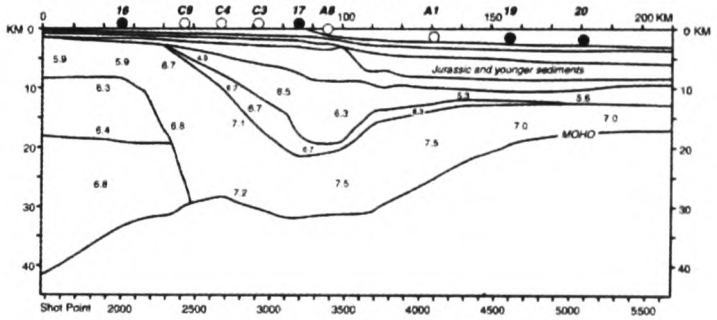
Reflection and Wide Angle Reflection - Refraction



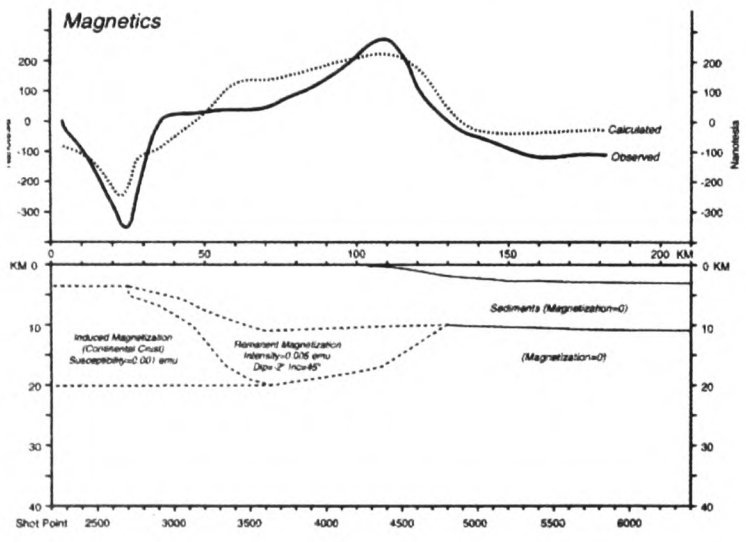
Wide Angle Reflection and Refraction



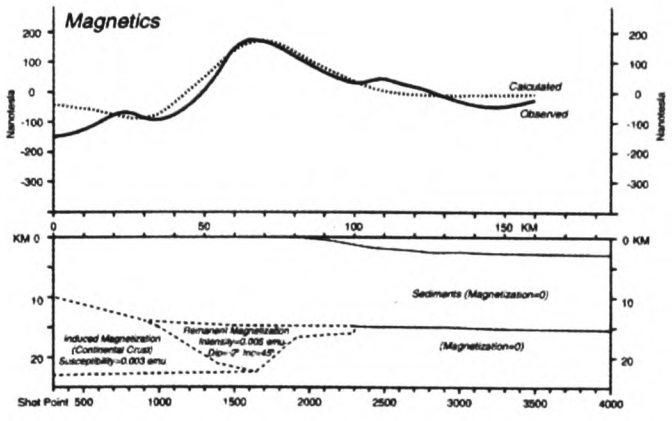
Wide Angle Reflection and Refraction



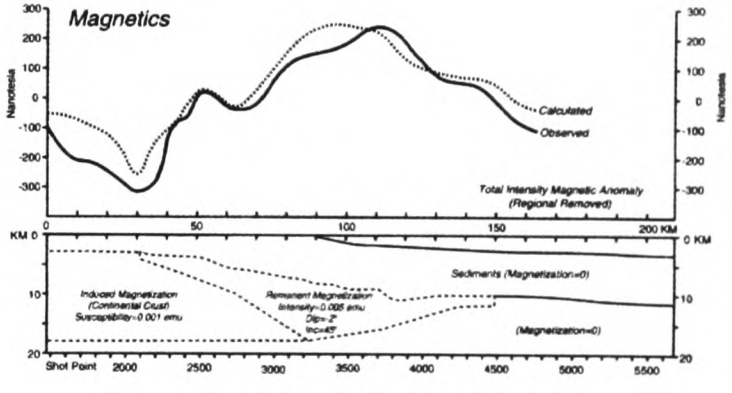
Magnetics



Magnetics



Magnetics



3.4 Volcanism

The Eastern USA passive continental margin is part of what has been termed the central Atlantic magmatic province (CAMP) by Marzoli *et al.* [1999]. This extends at least 5000km by 2000km (e.g. McHone [2000]) and encompasses dyke swarms and flood basalts along eastern North America, northern South America, West Africa, and Iberia (Figure 3.12). The distribution and ages of CAMP volcanism tie the main pulse of magmatism to a common event around $200 \pm 2Ma$ (McHone [2000] and references therein), around $25Myr$ before the apparent onset of seafloor spreading along the Eastern USA margin.

The Eastern USA portion of the CAMP could, by itself, be considered a large igneous province (the East Coast Margin Igneous Province or ECMIP of Kelemen & Holbrook [1995]). Deep seismic lines have consistently resolved high seismic velocities ($7.1 - 7.5kms^{-1}$) in the rift stage crust that have generally been interpreted either as underplate material or intensely intruded extended crust (LASE Study Group [1986]; Trehu *et al.* [1989]; Austin *et al.* [1990]; Oh *et al.* [1991]; Sheridan *et al.* [1993]; Holbrook *et al.* [1994a,b], cf. Figure 3.6). Added to this are rift-related subaerial basalt flows of up to $15km$ thickness which are expressed as seaward dipping reflectors (SDRs) in reflection seismic data along much of the margin (Austin *et al.* [1990]; Holbrook & Kelemen [1993]; Sheridan *et al.* [1993]; Holbrook *et al.* [1994a,b], cf. Figure 3.11).

While it is not clear that volcanism is solely responsible for SDRs along the entire margin (in parts they may be caused by syn-rift sediments and/or sediment wedges with intercalated volcanic sills), it has been shown that a continuous volcanic wedge can provide a possible source for the ECMA (Section 3.3.2). Kelemen & Holbrook [1995] have used this interpretationm, plus the seismic high velocity layer, to estimate the volume of igneous crust along the Eastern USA margin. They suggest that there may be as much as $2.7 \times 10^6 km^3$ of igneous crust along the entire length of the margin, or $1.6 \times 10^6 km^3$ between the BA-6 and LASE deep seismic lines.

Behn & Lin [2000] have questioned the volume estimates of Kelemen & Holbrook [1995] on the basis of an apparent relationship between an Airy isostatic gravity anomaly (from a model in which bathymetry and post-rift sediments are locally compensated by variations in crustal thickness) and the thickness of igneous crust. They argue that there

---

Figure 3.11: Structural models to explain magnetic anomalies along the USGS 32, EDGE 801, and LASE, deep seismic lines [Talwani *et al.*, 1995]. After Talwani *et al.* [1995].

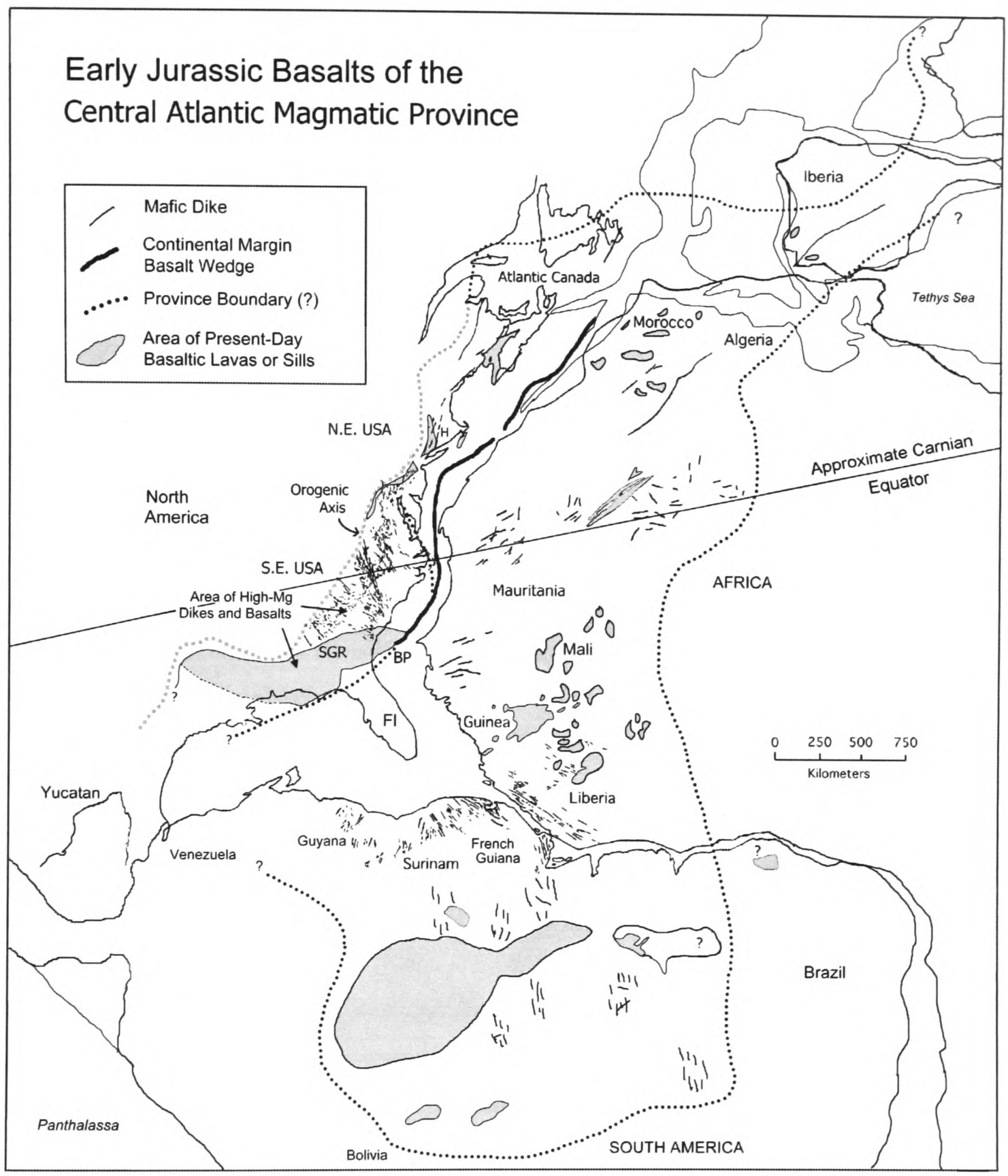


Figure 3.12: Early Jurassic Basalts of the Central Atlantic Magmatic Province. Predrift configuration adapted from Klitgord & Schouten [1986]. Location of North American margin basalt wedge from Kelemen & Holbrook [1995]. Dike locations compiled from various authors (see McHone [2000]. Other features from Olsen [1997]. Abbreviations: BP=Blake Plateau; FL=Florida; SGR=South Georgia Rift. Figure reproduced from McHone [2000].

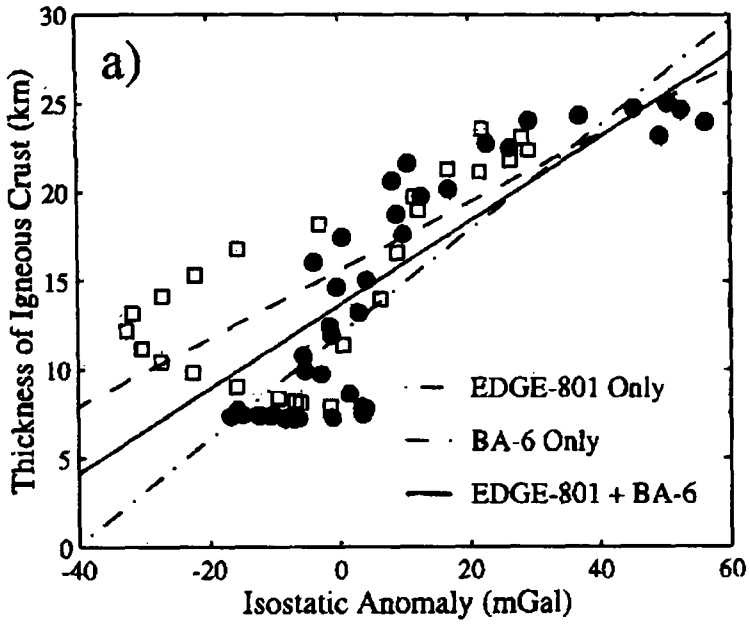


Figure 3.13: Plot of Airy isostatic gravity anomaly against total thickness of igneous crust for two Eastern USA passive margin deep seismic lines, together with best fitting linear trends [Behn & Lin, 2000].

is a linear relationship between these parameters along the BA-6 and EDGE-801 seismic transects (Figure 3.13) that can be used to estimate the volume of igneous material along the margin. On this basis they suggest that Kelemen & Holbrook [1995] may have overestimated the total volume by $\sim 12.5\%$.

However, the method of Behn & Lin [2000] assumes that within a $200km$ band centered on the isostatic gravity anomaly high there is a finite thickness of igneous crust whether the anomaly is positive, negative, or zero. Such a relationship makes no allowance for variations in the width of the volcanic zone, nor for other contributions (such as deviations from an Airy isostatic response to sediment loading) to the Airy isostatic gravity anomaly.

Triassic and Early Jurassic volcanic rocks in the syn-rift basins of the Atlantic coastal plain were not included in the igneous volume estimates of Kelemen & Holbrook [1995] or those of Behn & Lin [2000]. This material is thought to pre-date the rift-stage crust, having been emplaced before rifting focused eastward of the hinge zone in the Early Jurassic, and it is possible that originally much more extensive flood basalts were eroded between break-up and Cretaceous onlapping of coastal sediments [Rampino & Stothers, 1988; McHone, 1996]

3.5 Post-rift evolution

The post-rift evolution of the Eastern USA passive continental margin has been dominated by subsidence and the offshore development of deep (greater than $10km$) sedimentary basins. Although the margin has been extensively surveyed using seismic and potential field data, the large basement depth has limited direct observation of the early margin subsidence. Even the deepest well (the Continental Offshore Stratigraphic Test well COST G-1), which penetrated nearly $7km$ of sediment, was not deep enough to reach the early post-rift sediments. Despite this, the post-rift evolution of the Eastern USA margin has been the focus of many subsidence related studies (Steckler & Watts [1978]; Watts & Steckler [1979]; Sawyer *et al.* [1982,?]; Sawyer [1985a]; Watts [1988]; Pazzaglia & Gardner [1994]).

3.5.1 Tectonic subsidence

Seismic profiling of the US marginal basins in the 1970s, together with deep drilling (COST: B-2, B-3, G-1, and G-2 wells), allowed authors of the time (e.g. Steckler & Watts [1978]; Watts & Steckler [1979]; Sawyer *et al.* [1982,?]) to backstrip the sediments and obtain information on the tectonic subsidence of the margin. They showed that the sediment load contributed only partly to the subsidence. The remaining 'tectonic subsidence' was attributed to thinning during rifting, and relaxation of the steepened geothermal gradient.

3.5.2 Effective elastic thickness

Up until the early 1980s workers seeking to isolate tectonic subsidence had mainly used Airy-type backstripping. However, the acquisition of seismic data along transects of the margin made it possible to flexurally backstrip sediments. By flexurally backstripping and then comparing the observed and calculated free-air gravity anomaly it became possible to estimate effective elastic plate thicknesses (T_e).

Watts [1988] used the gravity anomaly along the LASE transect as a constraint on the effectiveness of a suite of models based on: flexural sediment backstripping; Airy isostatic determination of crustal thickness from the backstrip surface; and calculation of gravity anomalies for the reconstructed geometry. He considered models in which T_e either was uniform through time (Figure 3.14a), or increased as a plate isotherm depth as the margin cooled after rifting (Figure 3.14b).

Calculated free-air gravity anomalies from the uniform T_e models suggest a long term average T_e of $15km$ across the shelf break and continental slope, but fail to match the

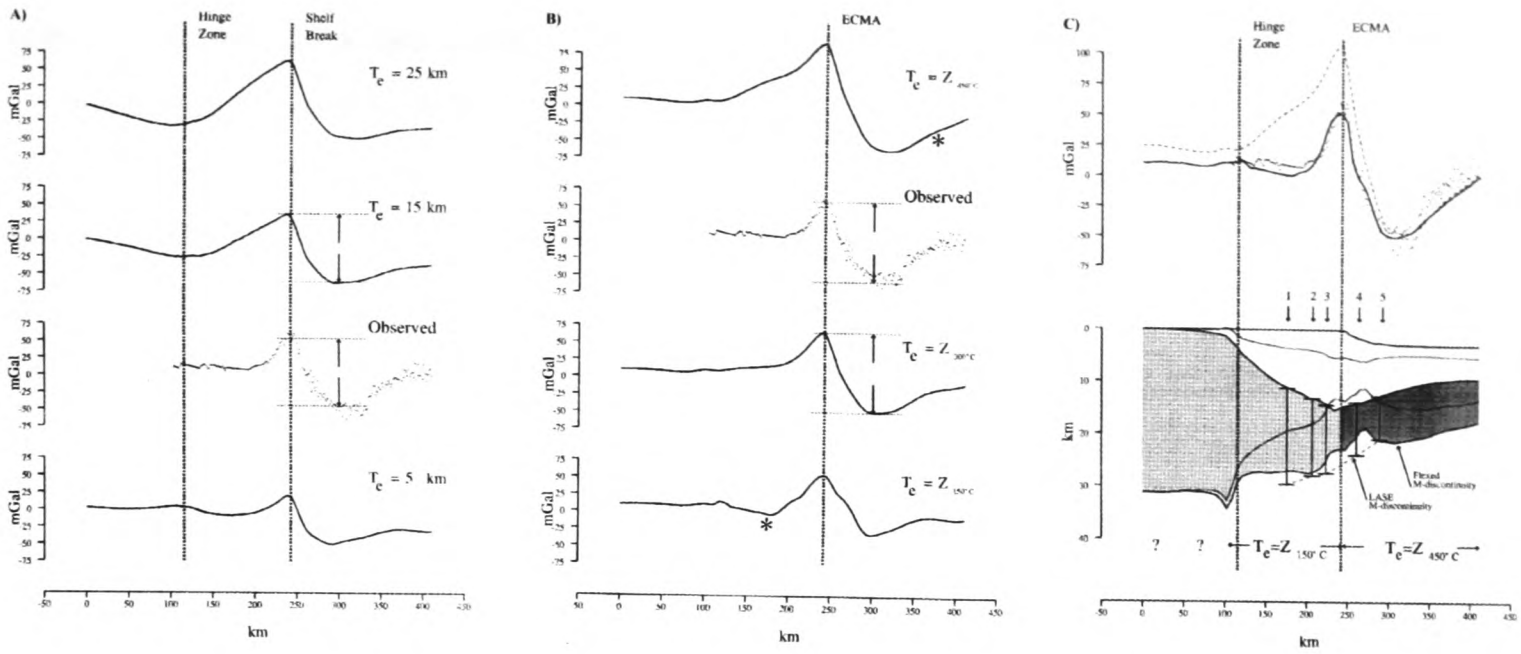


Figure 3.14: Estimation of effective elastic thickness (T_e) along the LASE line [Watts, 1988]. A - Models in which T_e is uniform over time. B - Models in which T_e increases with time as the depth to a geotherm in a cooling lithosphere. C - Model in which T_e seaward of the ECMA follows the $450°C$ isotherm, and T_e landward of the ECMA follows the $150°C$ isotherm. Figures combined from Watts [1988].

observed anomaly seaward of the lower slope and rise (Figure 3.14a).

The observed free-air gravity anomaly is better explained by a model in which T_e is controlled by the depth of specific isotherms in the cooling crust (Figure 3.14b). Some of these models, in which T_e increases over time, match the uniform T_e agreement between the observed and calculated gravity anomaly across the shelf break, while greatly improving agreement to either side. This led Watts [1988] to a final model in which T_e of the continental crust follows the $150°C$ isotherm and T_e of the oceanic crust follows the $450°C$ isotherm. This final model provides a good overall agreement between the observed and calculated gravity anomalies (Figure 3.14c), and is in accord with other estimates of T_e evolution in the oceanic lithosphere (e.g. Bodine *et al.* [1981]), and fits within the lower end of earlier estimates for continental lithosphere (e.g. Karner *et al.* [1983]).

Pazzaglia & Gardner [1994] used stratigraphy of the Susquehanna River, Atlantic Coastal Plain, and Baltimore Canyon trough to investigate Late Cenozoic flexural warping across the central Appalachian Piedmont and Salisbury Embayment. Their method applied eustatic sea-level curves, uniform T_e flexure, variable erosion rates landward of the fall zone, and defined offshore loads to predict isochronous 'time line' surfaces extending from Piedmont fluvial terraces to deposits and unconformities of the Coastal Plain and known offshore loads. From these they demonstrated that stratigraphic relationships along their profile, including zones of erosion and deposition, are well predicted if the

effective elastic thickness averages $40km$ over the $20MYr$ span of the model.

Although the transect of Pazzaglia & Gardner [1994] intersects the same major basin, the estimated T_e is a good deal larger than that of Watts [1988] (a mean T_e of $\sim 9km$ based on the 150^oC isotherm depth). This difference may partly be due to the relatively late subsidence that Pazzaglia & Gardner [1994] modelled, but even $180Ma$ after rifting the 150^oC isotherm would be expected to remain shallower than $15km$. The implication is that the post-rift T_e evolution has not been uniform throughout the margin.

3.5.3 Structural segmentation

Published T_e estimates for the Eastern USA margin fit within a suite of global passive margin estimates ranging from $5km$ to $50km$ (cf. Watts [2001]), but raise questions as to why such a variation should be found within a single margin. If the disparate estimates of Watts [1988] and Pazzaglia & Gardner [1994] accurately represent underlying lithospheric behaviour, then there must exist abrupt and fundamental differences in the rifted crustal and/or lithospheric structure within the margin. Such a conclusion would not be unique; segmentation of passive margin strength has already been observed offshore Gabon (Watts & Stewart [1998]).

Spectral methods of analysing the relationship between gravity anomalies and topography as a function of wavelength have enabled T_e to be estimated over large areas. Regions of North America that have been studied in such ways have subsumed parts of the Eastern USA margin (Bechtel *et al.* [1990] and Armstrong & Watts [2001]). Bechtel *et al.* [1990] used coherence between the Bouguer gravity anomaly and topography to estimate T_e distribution across the North American craton, suggesting a range of $32km$ to $64km$ T_e across the Eastern margin. Coherence analysis by Armstrong & Watts [2001] in the southern Appalachian region, suggests a decrease in T_e from $44km$ to $34km$ across the fall line edge of the coastal plain.

Sawyer [1985a] considered segmentation in terms of lithospheric strength under extension. By using the total tectonic subsidence (TTS) obtained from Airy isostatic and flexural sediment backstripping to investigate along-strike variations in rifting geometry (Figure 3.15), he inferred, in quite broad terms, that the rift-stage crust is widest where the crust was comparitively 'ductile' during rifting, and narrowest where it was comparitively 'brittle'.

On this basis Sawyer [1985a] suggested that the abrupt transition between the narrow Carolina Trough and the broad Blake Plateau Basin (across the Blake Spur Fracture Zone, between profiles 43 and 44 in Figure 3.15) could represent a major structural boundary; perhaps between the 'brittle' craton of Iapetan North America, and a segment of 'ductile'

Iapetan Africa that remained accreted to North America during Atlantic rifting.

Behn & Lin [2000] derived an isostatic gravity anomaly, that could be used to study segmentation of the margin structure, by subtracting the gravity effects of a model in which sediments are locally compensated by Airy isostasy from the observed free-air gravity anomaly. An along strike profile reveals a segmentation in their Airy isostatic gravity anomaly (Figure 3.16) that may relate to the observed anomaly segmentation already discussed (cf. Section 3.3.1).

Power spectra of the ECMA high (Figure 3.16b) and isostatic (Airy) gravity anomaly edge effect high (Figure 3.16d) reveal characteristic wavelengths in the structural segmentation. The ECMA spectrum peaks in a $100 - 120km$ waveband, while the isostatic gravity anomaly spectrum peaks in a $100 - 150km$ waveband. If the source of the ECMA is volcanic in nature (cf. Section 3.4) then this could mean that the depth and/or volume of extrusive material varies along-strike.

The $100 - 150km$ wavelength spectral peaks in the margin anomalies also correspond to spectral peaks in the magnetisation and mantle Bouguer anomaly of the present day Mid-Atlantic Ridge axis [Behn & Lin, 2000]. This could mean that there remains a component of segmentation at the oceanic spreading center that was inherited from that of the margin.

In the South Atlantic, distinct 'tectonic corridors' are marked by along-strike segments of oceanic basement that display distinct characteristics in terms of subsidence rate, zero-age seafloor depth, decrease in geoid height with age, and geochemical properties [Kane & Hayes, 1992]. These segments typically have length scales of $500 - 1000km$, and are often bounded by major oceanic fracture zones extending from the active ridge to the oldest oceanic crust. Behn & Lin [2000] suggest that the $300km$ to $500km$ wavelength peak in the Eastern USA margin isostatic gravity anomaly could mark a comparable North Atlantic tectonic corridor delimited by the Kane and Atlantis fracture zones.

Despite the apparent inheritance of margin segmentation at the mid-Atlantic Ridge, Behn & Lin [2000] were unable to determine whether its origins in the isostatic gravity anomaly were due: to varying igneous volumes emplaced during rifting; to deviations between the Airy isostatic model and a strong lithospheric response to sediment loads; or to some other cause.

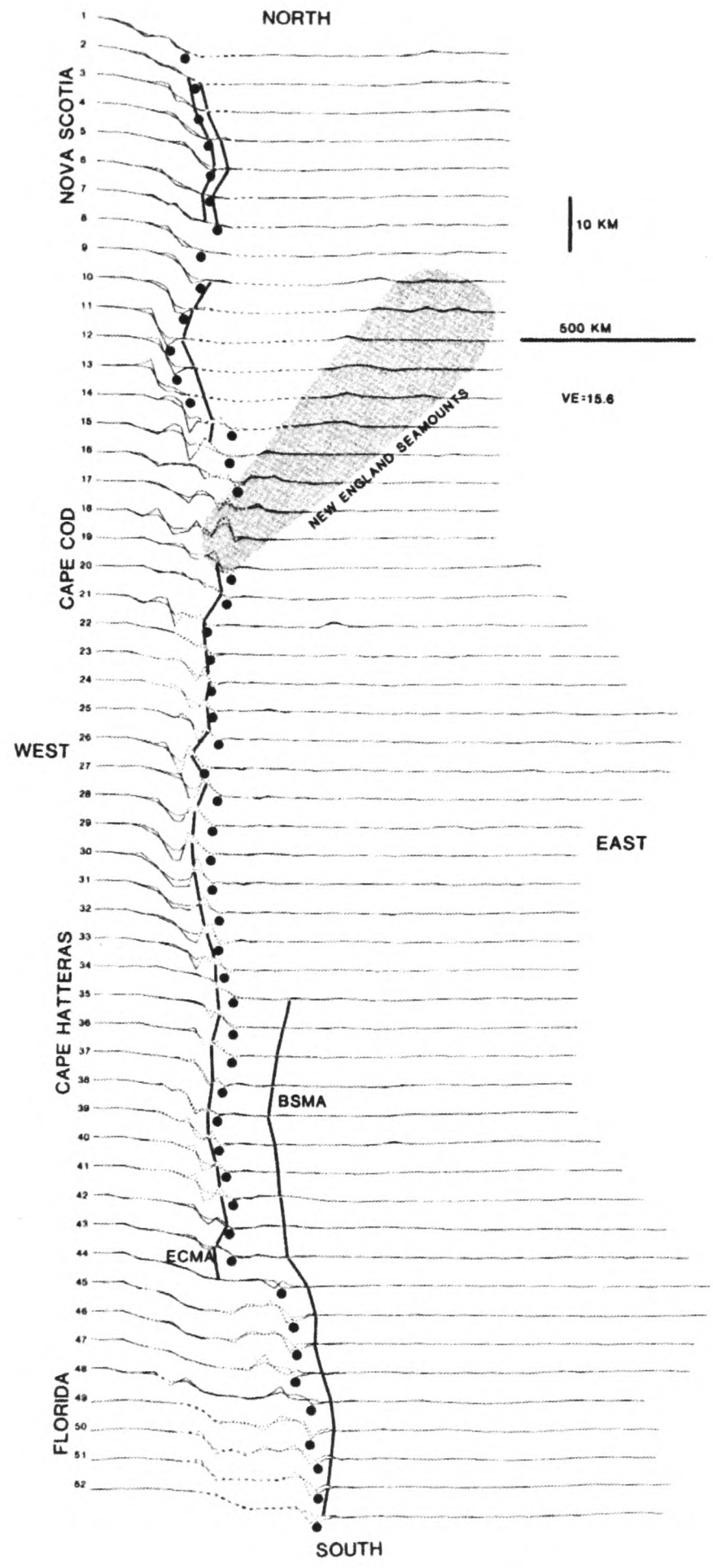


Figure 3.15: Total tectonic subsidence of the Eastern USA passive continental margin. Low relief TTS based on Airy isostatic backstripping and high relief TTS based on flexural isostatic backstripping. Solid circles mark the apparent landward limit of normal oceanic crust. Reproduced from Sawyer [1985a].

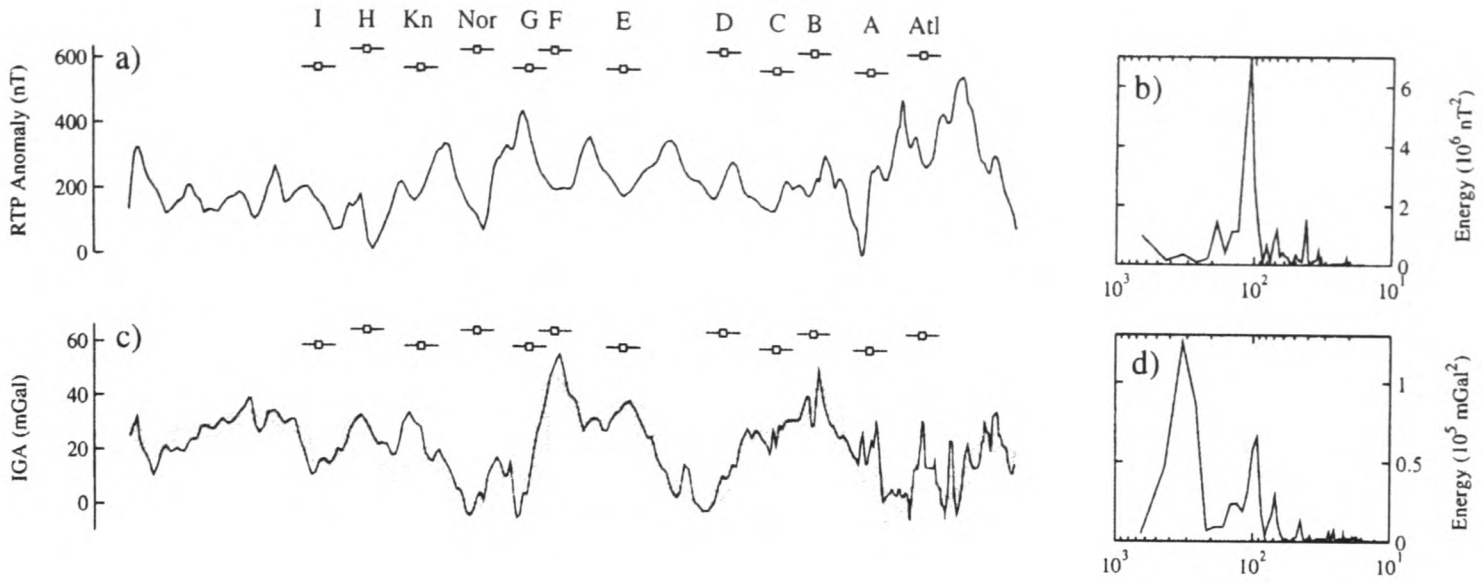


Figure 3.16: Along strike comparison of Eastern USA margin potential anomalies. a) Reduced to pole (RTP) magnetic anomaly ECMA high. b) Normalised power spectrum of the ECMA magnetic anomaly high. c) Isostatic gravity anomaly (IGA) high. d) Normalised power spectrum of the IGA high. Open squares mark where offset zones enter the margin. Plots extracted from figure 11 of Behn & Lin [2000].

3.6 This study

Isostatic models have shown that the Eastern USA passive continental margin is segmented in terms of variations in the width and degree of thinning of the rift-stage crust [Sawyer, 1985a] and in an isostatic gravity anomaly [Behn & Lin, 2000]. In the latter case, Airy isostatic compensation of the post-rift sediments fails to adequately explain the amplitude and wavelength of the free-air edge effect gravity anomaly along much of the margin.

One reason for this may be that lithospheric strength plays a role in the isostatic compensation of sediments deposited on the margin. In other words, that deviations from the local (Airy) isostatic model are indicative of rigidity in the underlying plate. This possibility was explored (in terms of T_e) by Watts [1988] and Pazzaglia & Gardner [1994], but with markedly different estimates of the governing plate rigidity.

Along-strike segmentation of passive margin flexural rigidity is a possibility that has already been explored offshore Gabon [Watts & Stewart, 1998]. Segmentation of the Airy isostatic anomaly, together with differing effective elastic thickness estimates, suggest the need for a similar study at the Eastern USA margin.

In this thesis, a new sediment thickness dataset is used to carry out a 3-D flexural analysis of the entire Eastern USA margin, with the intention of identifying structural segmentation in terms of effective elastic thickness. This will provide new information on the manner in which thinning, plate rigidity, and potential anomalies complement each other as aspects of passive margin segmentation.

3.6.1 Data

Topography and gravity

Topographic and gravity data have been extracted from the Decade of North American Geology (DNAG) dataset, released on CD-ROM in 1989. The gravity data - based on data from the Defense Mapping Agency (DMA) and other academic and commercial sources - is provided on the CD-ROM in digital form on a $4km$ transverse Mercator grid (Bouguer onshore, free-air offshore). This was converted to latitude-longitude positions and averaged to 2.5×2.5 minute bins by Jon Stewart (see Stewart [1998]) and then gridded at a 5 minute interval (Figure 3.17, see also Figure 3.9).

The long-wavelength gravity field, up to degree and order 16, from the OSU91a geopotential model has been subtracted for this thesis in order to remove wavelengths close to and greater than the dimensions of the study area. This will reduce contributions from (typically sub-crustal) structure at larger horizontal scales than the study intends to resolve.

The DNAG topography data is gridded at the same 5 minute interval as the gravity data.

Sediment isopachs

The study relies on flexural backstripping of sediments to control crustal reconstruction and gravity modelling. Hence the quality of available sediment data will have a significant influence on the viability of the method.

On behalf of the United States Naval Oceanographic Office, the United States Geological Survey (USGS) have reprocessed and reinterpreted over $30,000km$ of Eastern USA offshore (mainly continental shelf) reflection seismic data collected between 1973 and 1978 [Klitgord & Schneider, 1994; Klitgord *et al.*, 1994; Hutchinson *et al.*, 1995, 1996]. The resulting dataset (consisting of: seismic and well data; interpretation; and $5' \times 5'$ sediment isopach grids with varying coverage for 19 post-rift units) was kindly made available for the purpose of this thesis by Debbie Hutchinson of the USGS, Woods Hole Oceanographic Institute.

Of primary interest to this study were the sediment isopach grids. However, these grids are limited to the boundaries of the $1973 - 1978$ seismic surveys and, whether through absence or lack of resolution, not all units can be traced across the entire area. As with any dataset based predominantly on seismic data, there are significant potential errors as a result of velocity-depth conversions and uncertainty in interpretation. The effect of such errors is likely to be greatest in the deepest areas, where: the sediments have

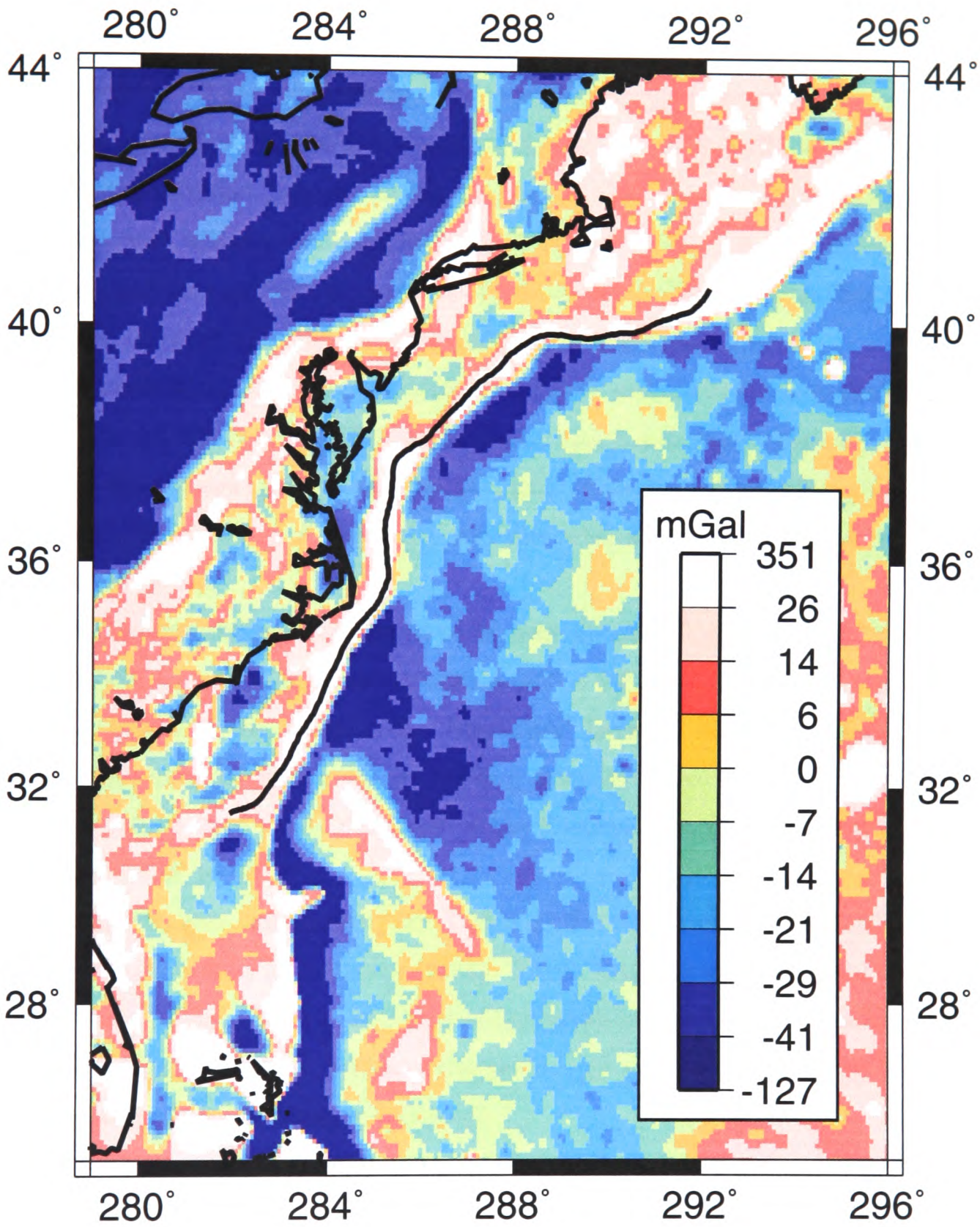


Figure 3.17: Eastern USA passive continental margin gravity anomaly (free air offshore, Bouguer onshore) with long wavelength contributions (up to degree and order 16) removed. Black line marks the tract of the edge effect gravity high profiled in Figure 3.16.

not been sampled by deep drilling; the seismic resolution is lowest; and the cumulative effect of seismic velocity errors is greatest.

Errors in the interpretation and velocity-depth conversion cannot be accurately assessed or remedied here, but the lack of sediment isopach data from the coastal plain and seaward of the shelf break can be addressed using data from other sources. Hence, for this study, the USGS isopach grids have been supplemented using coastal plain well data from the 1993 digital version of the American Association of Petroleum Geologists, 'Correlation of Stratigraphic Units of North America' (COSUNA, Childs & Salvador [1985]) project, and with seismic sediment isopach thicknesses contours that extend from the continental shelf and across the western North Atlantic [Mountain & Tucholke, 1985]. The coverage of these various sources is summarised in Figure 3.18.

Approximate ages for units from each of the data sources have been used to derive a correlated framework of seven offshore isopachs, and five onshore isopachs, that can be traced from the coastal plain to the abyssal plain. The stratigraphic frameworks of each of the studies are shown in Figure 3.19, together with a time line and the framework of the correlated units.

The data were combined (as described in more detail below) by averaging datapoints from the sparse (non-USGS) datasets onto a ($40^o \times 60^o$, $5' \times 5'$ interval) grid extending beyond the limits of the study area. Surfacing[2] between these and the USGS data provided continuous isopach grids (extending from 25^oN to 44^oN and from 81^oW to 66^oW) that can be used for 3-D analysis of the Eastern USA passive margin from 25^oN to 44^oN and 81^oW to 66^oW.

To the north, east, and south, the USGS grids were supplemented using digitised contours from Mountain & Tucholke [1985]. These contours were surfaced in combination with the grid data, and a zero thickness constraint was placed anywhere that the underlying oceanic crust (as dated in the ocean age grid of Müller *et al.* [1997]) was younger than the isopach being constructed.

Isopach thicknesses to the west of the USGS data were constrained using COSUNA well data from the 'AAPG Data-ROM' (1993, ISBN 1-58861-188-4). The provided software did not allow for bulk extraction of data, nor for inconsistencies in the data format. Hence the data were extracted from the ASCII records using custom software and some manual filtering. The extracted data were then surfaced with the offshore grids using the $30m$ ($100ft$) contour of the Appalachian Orogen as the landward limit of rift-associated

[2]Surfacing was performed using 'surface' from the Generic Mapping Tools 3.0 package [Wessel & Smith, 1995]. A tension of 0.1 was used offshore, and minimum curvature (zero tension) was used between the onshore and offshore data

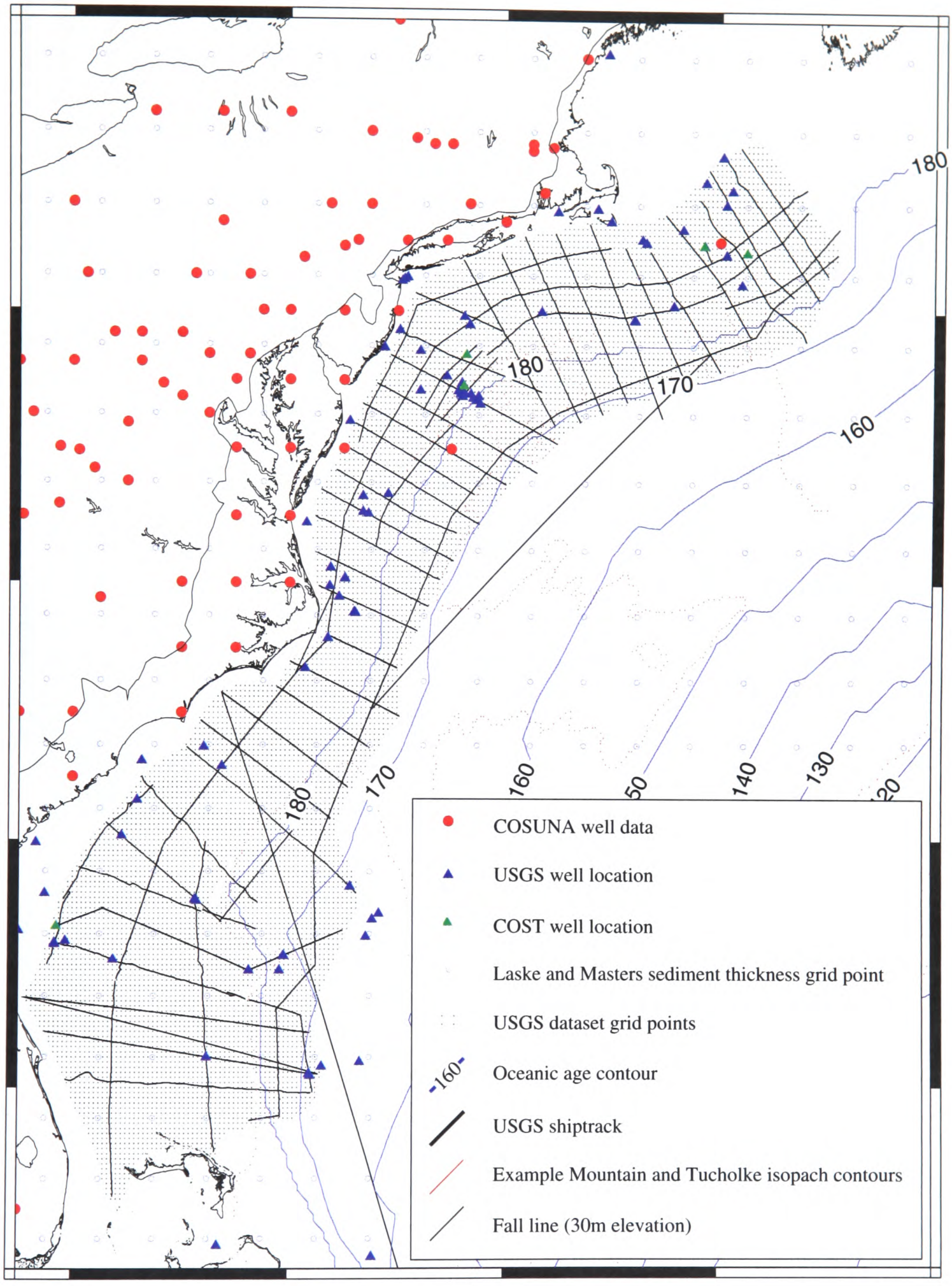
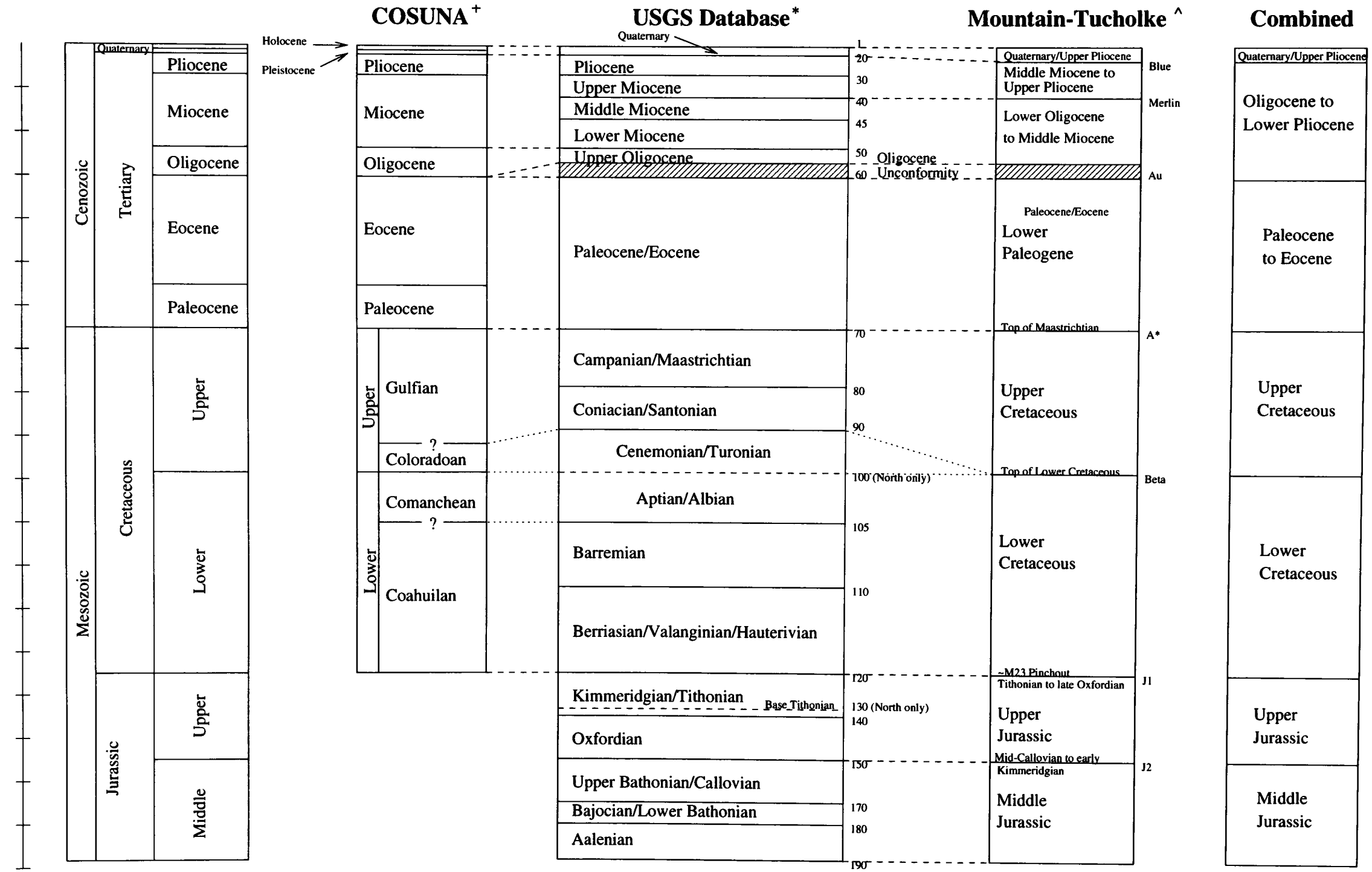


Figure 3.18: Sources of sediment isopach data used in the construction of Eastern USA passive continental margin regional isopach grids.


COSUNA +
USGS Database*
Mountain-Tucholke ^
Combined
Holocene
Pleistocene
Quaternary
Cenozoic
Tertiary
Pliocene
Miocene
Oligocene
Eocene
Paleocene
Mesozoic
Cretaceous
Upper
Lower
Jurassic
Upper
Middle
Gulfian
?
Coloradoan
Comanchean
?
Coahuilan
Lower
Upper Miocene
Middle Miocene
Lower Miocene
Upper Oligocene
Paleocene/Eocene
Campanian/Maastrichtian
Coniacian/Santonian
Cenemonian/Turonian
Aptian/Albian
Barremian
Berriasian/Valanginian/Hauterivian
Kimmeridgian/Tithonian
Base Tithonian
Oxfordian
Upper Bathonian/Callovian
Bajocian/Lower Bathonian
Aalenian
L
20
30
40
45
50
60
70
80
90
100 (North only)
105
110
120
130 (North only)
140
150
170
180
190
Oligocene Unconformity
Quaternary/Upper Pliocene
Middle Miocene to Upper Pliocene
Lower Oligocene to Middle Miocene
Paleocene/Eocene
Lower Paleogene
Top of Maastrichtian
Upper Cretaceous
Top of Lower Cretaceous
Lower Cretaceous
~M23 Pinchout
Tithonian to late Oxfordian
Upper Jurassic
Mid-Callovian to early Kimmeridgian
Middle Jurassic
Blue
Merlin
Au
A*
Beta
J1
J2
Quaternary/Upper Pliocene
Oligocene to Lower Pliocene
Paleocene to Eocene
Upper Cretaceous
Lower Cretaceous
Upper Jurassic
Middle Jurassic
187Ma

sedimentation. This contour approximates the path of the fall line, which links a series of waterfalls along the landward edge of the coastal plain.

In areas where no higher resolution data were available the basement depth was constrained using the $1^o \times 1^o$ Global Digital Map of Sediment Thickness grid of Laske & Masters [1997]. In particular, this prevented uncontrolled extrapolation of basement trends at large distances from the marginal basins.

Finally, the original USGS gridded data were substituted back into the grids[3] and any negative isopach thickness values were clipped to zero.

Figure 3.20 shows sections through both the original USGS dataset and through the final combined grids. These sections illustrate the additional coverage offered by the new grids, and demonstrate that there is no obvious discontinuity between the three datasets. It should be noted, however, that the resolution implied by the 5 minute gridding interval applies only within the boundaries of the original USGS dataset. The comparitively low resolution across the rest of the study area will need to be recognised when interpreting the 3-D analysis presented in this thesis.

[3]Substitution of original data removes any degradation due to interim grid operations

Figure 3.19: Approximate correlation of data used in the construction of Eastern USA passive continental margin isopach grids.

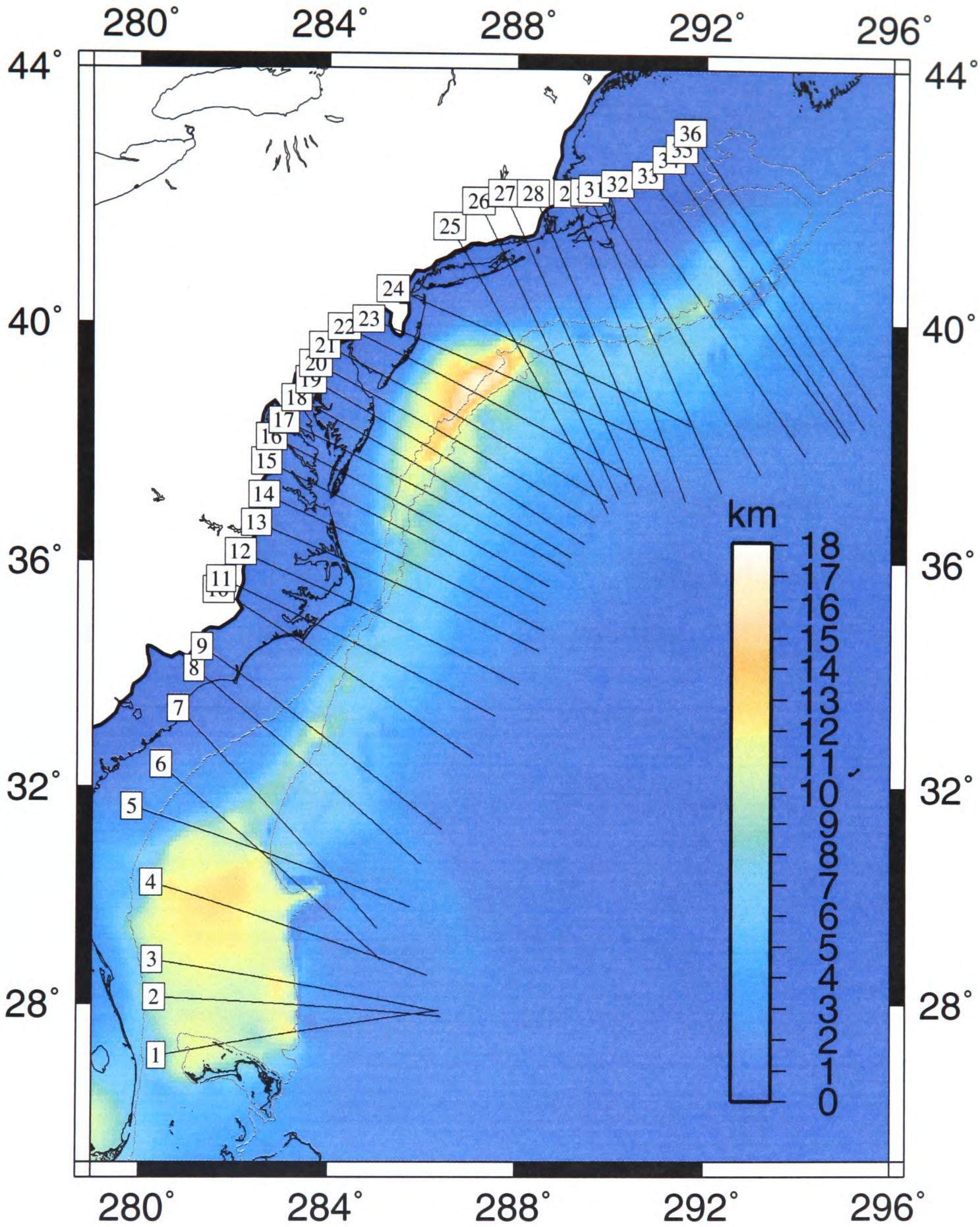
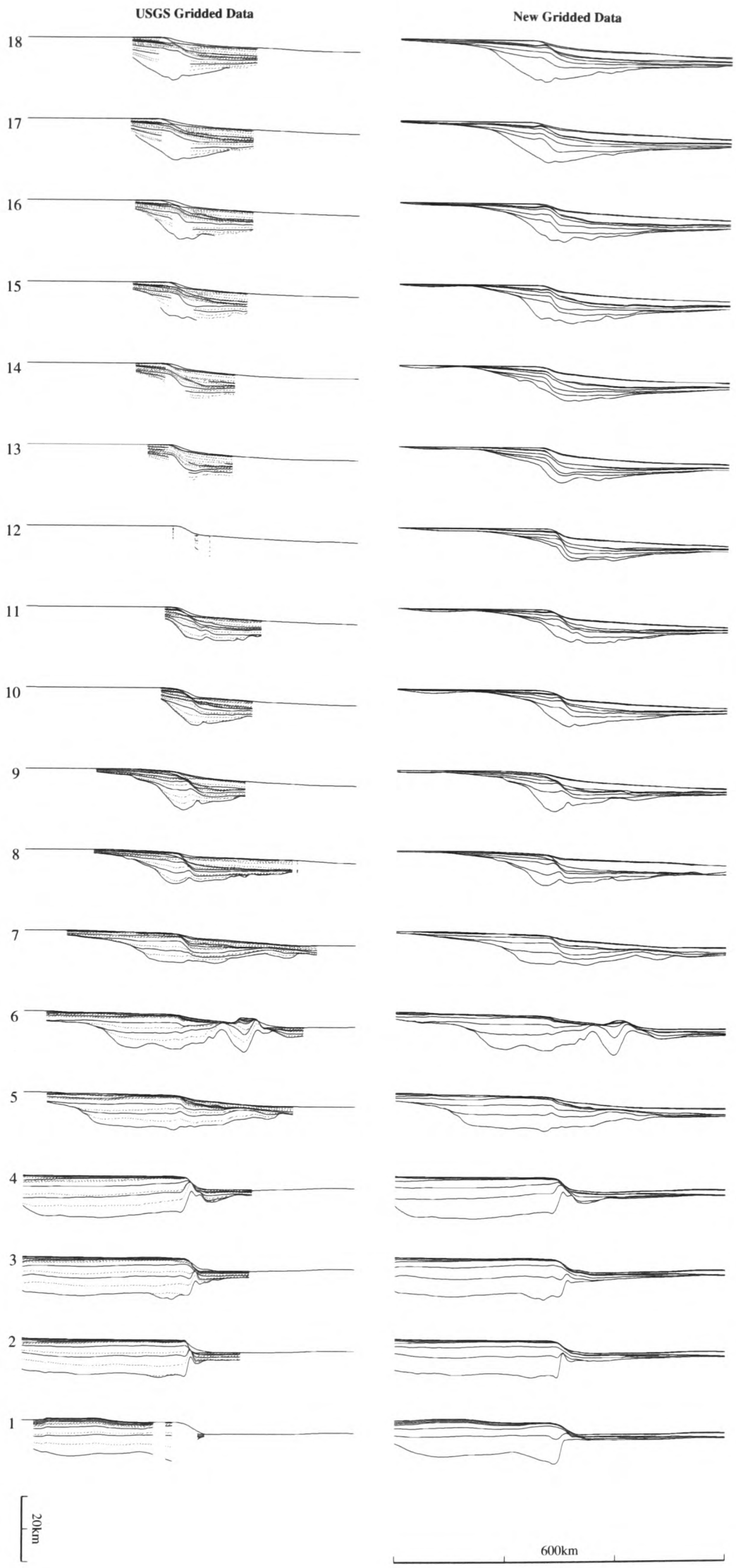
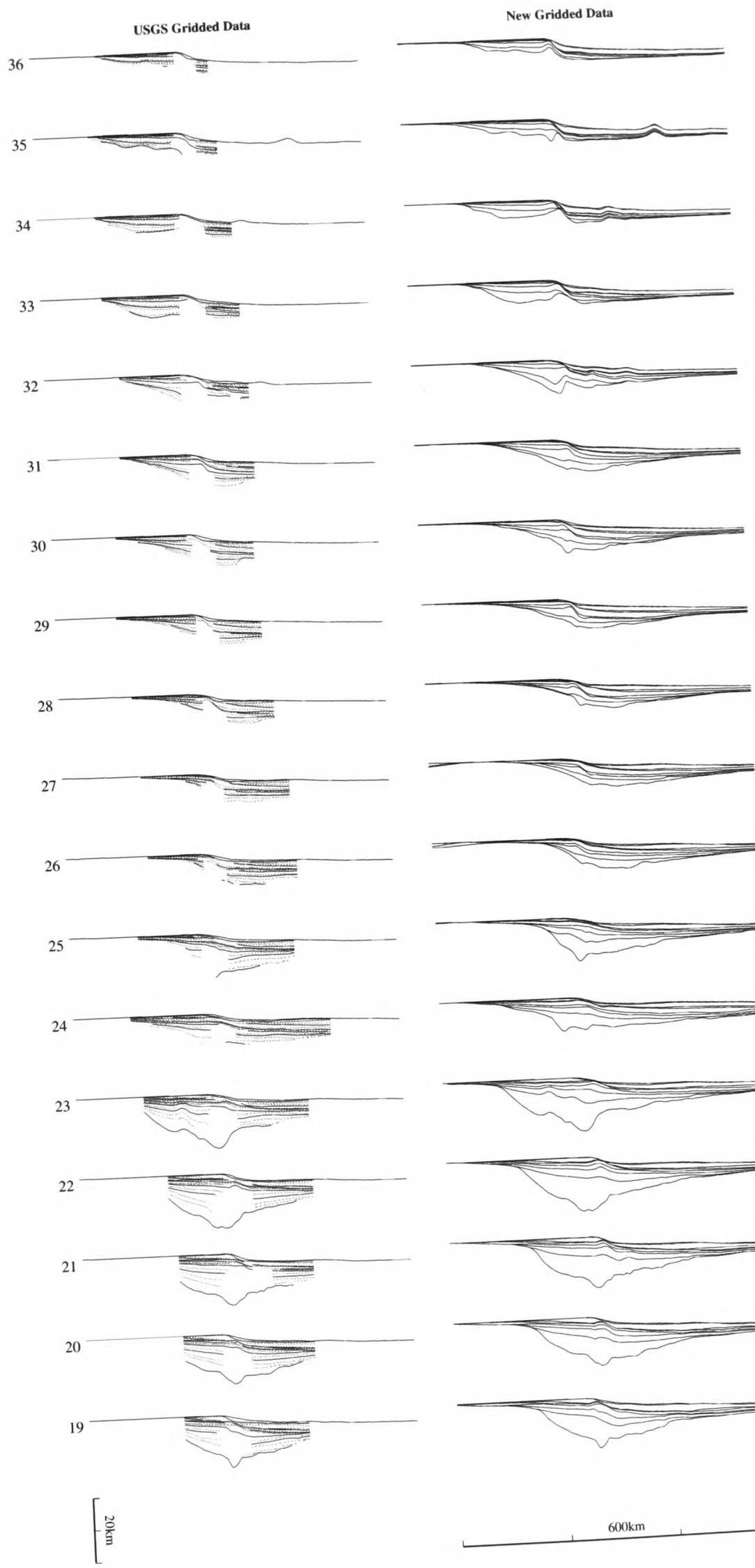


Figure 3.20: Eastern USA passive continental margin sediment isopach grids. Map shows total post-rift sediment thickness and profile locations. Profiles (following pages) allow comparison between post-rift sediment isopachs from the original USGS gridded dataset and correlated isopachs from the new regional dataset.


USGS Gridded Data
New Gridded Data
18
17
16
15
14
13
12
11
10
9
8
7
6
5
4
3
2
1
20km
600km


USGS Gridded Data
New Gridded Data
36
35
34
33
32
31
30
29
28
27
26
25
24
23
22
21
20
19
20km
600km

Chapter 4

Process-oriented analysis - Method

4.1 Introduction

This thesis applies 3-D sediment thickness analysis and gravity modelling methods to passive margin reconstruction and a study of the segmentation of mechanical strength and effective elastic thickness of extended lithosphere. Recently available datasets have made this possible at a margin-wide scale.

The 'process-oriented method' of studying passive margin evolution [Watts, 1988] is used as the basis for a method that involves 'backstripping' [Watts & Ryan, 1976], crustal reconstruction, and gravity modelling. This chapter outlines Watts's method and its components before detailing its application in this study.

4.2 The process-oriented method

The 'process-oriented method' of Watts [1988] aims to explain observed passive margin data in terms of defined evolutionary processes. Application of the method is divided between three stages (Figure 4.1):

1. Backstripping.
2. Determination of stretching factor, β, and margin restoration.
3. Gravity Modelling.

The first stage involves backstripping of post-rift sediment loads to isolate the tectonic subsidence [Watts & Ryan, 1976].

The second stage uses the backstripped 'total tectonic subsidence' to calculate the stretching factor, β, and hence the spatial distribution of crustal thickness. Restoration of

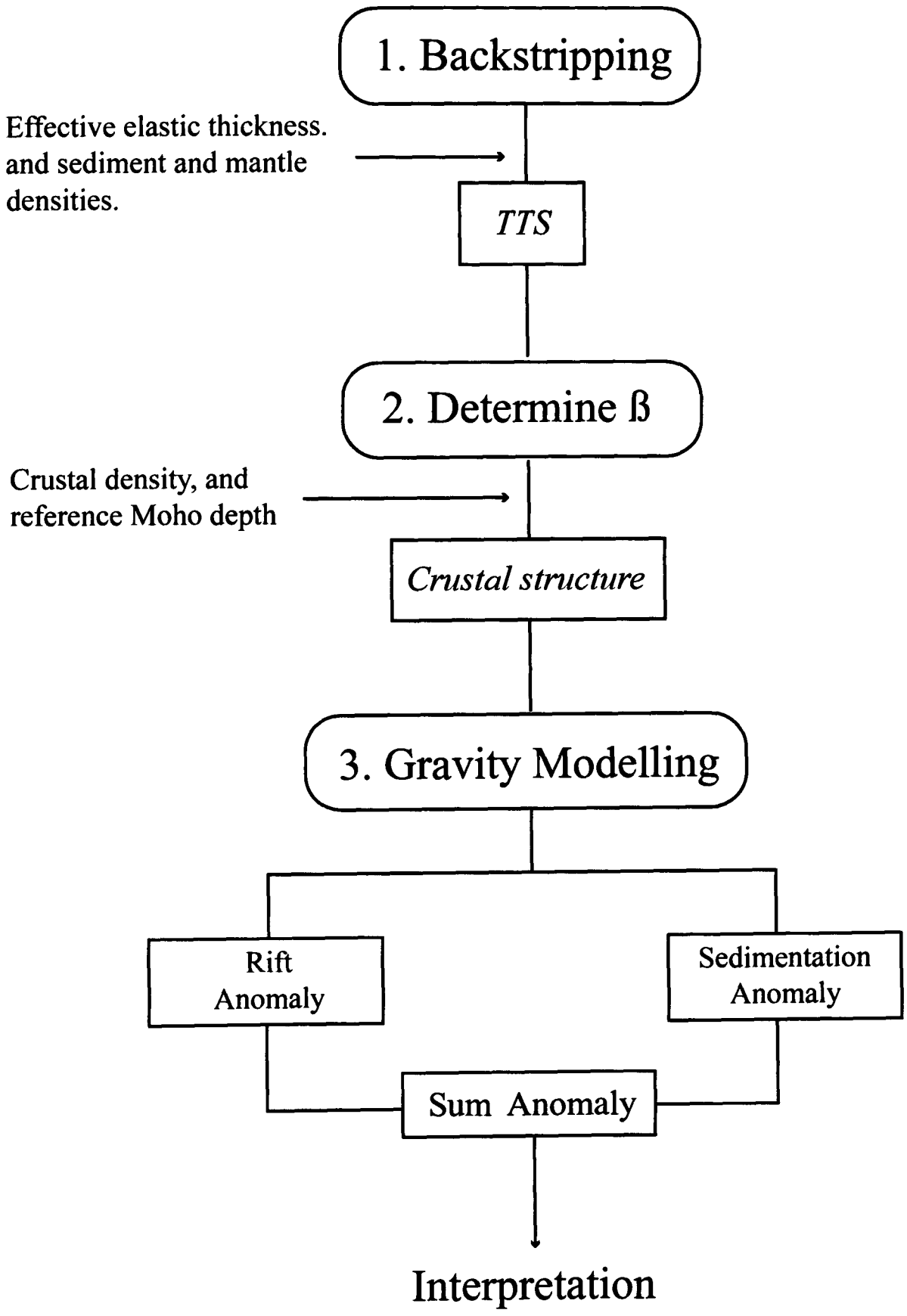


Figure 4.1: The 'process-oriented method' of Watts [1988]. (1) The total tectonic subsidence is determined through backstripping. (2) This provides a basis for determination of the stretching factor, β, and hence the crustal structure. (3) Gravity anomalies due to the rift structure and to the effects of sedimentation are combined to give the sum (calculated free-air) gravity anomaly.

the resulting Moho structure by replacement of the sediment load completes the present-day margin geometry.

The third stage involves calculation of gravity anomalies relating to different components of the margin reconstruction. In the process-oriented method the present-day free-air gravity anomaly is modelled as the sum of gravity anomalies associated with rifting and sedimentation.

The modular format of the process-oriented method allows additional processes to be added at any stage. This means that the influence of distinct processes - such as surface volcanism or volcanic underplating - on the final structure and gravity anomaly can be considered in the context of margin evolution.

4.2.1 Stage 1: Backstripping

'Backstripping' [Watts & Ryan, 1976] describes the process by which the loading effects of post-rift sediments are removed in order to obtain the tectonic subsidence of a rifted basin. It may also be appropriate to backstrip other loads if they post-date the rifting process (e.g. Watts & Fairhead [1997]).

The basement level after backstripping is termed the 'total tectonic subsidence' (TTS, Sawyer [1985a]) because it represents the combined tectonic effects of thinning during rifting and consequent thermal relaxation of the raised geothermal gradient. In effect (ignoring any insulating effects due to sediment cover) the TTS is the level that the present-day basement would have subsided to in the absence of post-rift sediment loading.

The ways in which backstripping can be applied depend on the type of problem, on the data available, and on assumptions made about the behaviour of the lithosphere when gravitationally loaded. In this thesis only the two commonly used forms (Airy and flexural) are considered, but the application of other models (such as loading of a visco-elastic plate) would be similar.

Airy-type backstripping

The simplest form of backstripping assumes Airy-type local isostatic compensation of anomalous loads. This requires that vertically acting loads are balanced by local variations in the Moho depth, and hence makes no allowance for finite lithospheric mechanical strength. Airy backstripping has commonly been used at point locations - mainly wells - as a means of determining the path of the TTS over time, and in conjunction with thermal models to constrain such items as the rift duration or number of rift events.

In general Airy isostasy can be expected to approximate true lithospheric behaviour where the effective plate rigidity is small, or where loads are wide and smoothly varying.

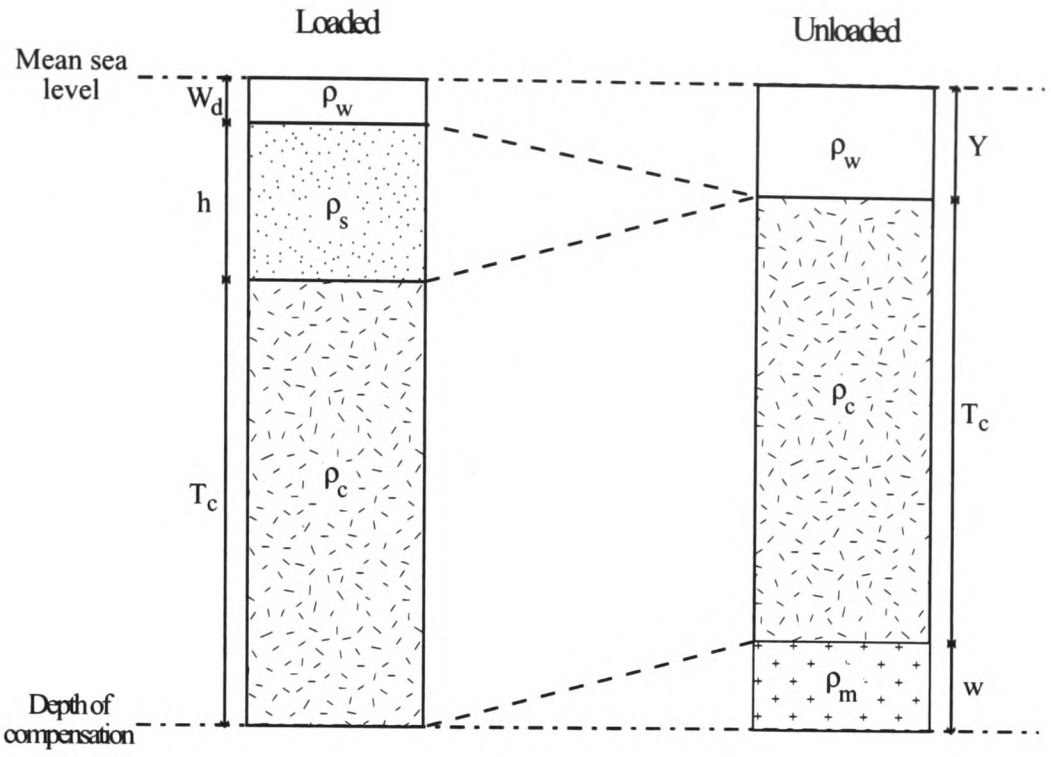


Figure 4.2: Airy backstripping of a sediment load. W_d - present water depth; h - sediment thickness; T_c - crustal thickness; w - vertical displacement; Y - backstripped water depth; ρ_w - water density; ρ_s - sediment density; ρ_c - crustal density; ρ_m - mantle density. $w = h(\rho_s - \rho_w)/(\rho_m - \rho_w)$; $Y = h + W_d - w$.

It may also be appropriate to apply Airy methods where data is sparsely or unevenly distributed, or where only a first-order assessment of the TTS is required. This type of model has been usefully applied as a means of investigating broad scale structural segmentation over regions of large lateral extent (e.g. Sawyer [1985b]; Behn & Lin [2000]).

The method is numerically straightforward. For example, to backstrip a marine sediment load a balance must be established between the displacement of mantle material by the crust and the displacement of water and crust by the sediment (Figure 4.2). Assuming a sub-crustal depth of compensation at which the two mass columns balance:

$$W_d\rho_w + h\rho_s + T_c\rho_c = Y\rho_w + w\rho_m + T_c\rho_c \tag{4.1}$$

in which: W_d is the loaded water depth; h is the sediment thickness; T_c is the crustal thickness; w is the isostatic subsidence; and ρ_s, ρ_w, and ρ_m are mean sediment, water, and mantle densities within the column. Because the crustal thickness is unchanged:

$$Y = h + W_d - w \tag{4.2}$$

Hence (by cancelling terms and rearranging) the mass balance can be reduced to:

$$w = h\left(\frac{\rho_s - \rho_w}{\rho_m - \rho_w}\right) \tag{4.3}$$

Which is the isostatic displacement due to the sediment load. The total tectonic subsidence, Y is given by Equation (4.2) above.

This can also be written in more general terms to apply to any loading effect, such as a change in mean sea level:

$$w = h\left(\frac{\rho_{load} - \rho_{disp}}{\rho_{sub} - \rho_{infill}}\right) \tag{4.4}$$

In which: the load density is ρ_{load}; the infill density is ρ_{infill}; the substrate density is ρ_{sub}; and the density of the material displaced by the load is ρ_{disp}.

Flexural backstripping

Rheological models suggest that extended continental lithosphere is likely to retain significant strength under vertical loading (see discussion in Chapter 2). This strength can be simulated by treating lithospheric deformation as that of a perfectly elastic plate obeying Hooke's law and overlying a fluid substrate.

The general equation for two-dimensional flexural loading of a 'thin'[1] uniform rigidity elastic plate of infinite extent and overlying an inviscid[2] fluid is:

$$D\frac{d^4w}{dx^4} = q(x) - P\frac{d^2w}{dx^2} - q'(x) \tag{4.5}$$

where $w(x)$ is the vertical deflection, P represents horizontal forces, $q(x)$ is the force distribution due to the applied load, and $q'(x)$ is the restoring force that counters it. The flexural rigidity, D, of a beam or plate can be defined by an effective elastic thickness, T_e, such that:

$$D = \frac{ET_e^3}{12(1-\nu^2)} \tag{4.6}$$

in which the elastic properties are characterised by a Young's modulus, E, and a Poisson's ratio, ν.

If deflection due to a load of density ρ_{load} displaces a material of density ρ_{disp} then:

$$q(x) = (\rho_{load} - \rho_{disp})gh(x) \tag{4.7}$$

and if the flexure displaces a substrate of density ρ_{sub} and is infilled by a material of density ρ_{infill} then:

[1] If it is assumed that the thickness of a perfectly elastic plate is very much smaller than the radius of curvature, then the normal stresses due to differential extension/compression between the upper and lower parts of the plate can be ignored and the plate can be considered infinitely thin.

[2] For simplicity, viscosity of the substrate can be neglected so long as the loading duration is long and only the total flexural subsidence is required.

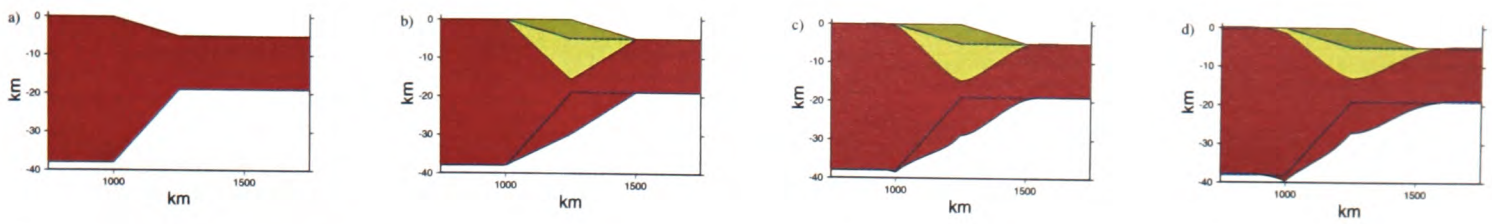


Figure 4.3: Examples of flexural loading of a rifted margin. The 'load' (tan) causes infilled flexure (yellow); the shape, width, and amplitude of which depends on the underlying plate rigidity. (a) TTS without sediments. (b-d) Structure after sediment loading. (b) $T_e = 0km$ (Airy isostatic), (c) $T_e = 10km$, (d) $T_e = 30km$.

$$q'(x) = (\rho_{sub} - \rho_{infill})gw(x) \tag{4.8}$$

If only vertical loading is important then the problem can be simplified by neglecting the small contribution of end loaded pressure, P. Making this assumption and substituting for q(x) and q'(x) gives a 1-D equation for a gravitationally loaded thin elastic plate:

$$D\frac{d^4w}{dx^4} + (\rho_{sub} - \rho_{infill})gw = (\rho_{load} - \rho_{disp})gh \tag{4.9}$$

The minimum value of D is zero, which corresponds to an elastic plate of zero thickness. In this case the flexural equation (Equation (4.9)) reduces to local Airy isostasy (Equation (4.4)). As the plate thickness increases, D grows large, requiring that the gw and d^4w/dx^4 terms tend towards zero. Therefore the load is supported by flexure of diminishing peak amplitude and increasing wavelength.

As Figure 4.3 illustrates (using a post-rift sedimentary basin as an example), the manner in which the effective elastic thickness controls subsidence can significantly affect the final geometry after loading.

Sediment porosity

Newly deposited sediment will tend to have a porosity that depends on the constituent grain sizes and shapes, but as the sediment is buried it will become increasingly compacted by additional over-burden. This reduces the porosity, and hence increases the bulk density of the sediment.

To avoid over-estimation of sediment densities where sediment cover is thin, and under-estimation where cover is thick, it is common to 'decompact' sediments (expanding them to a uniform porosity and density) prior to backstripping (e.g. Watts & Ryan [1976]; Steckler & Watts [1978]; Sawyer [1985b]). Ideally, *in situ* porosity-density-depth data

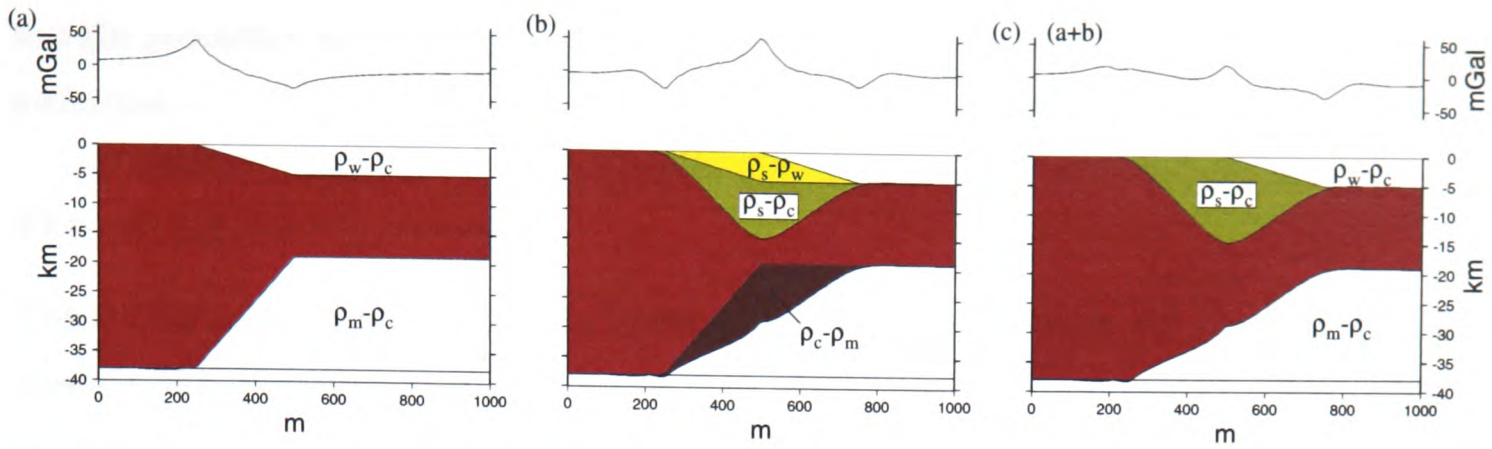


Figure 4.4: Process-oriented gravity anomalies. (a) Rift anomaly. (b) Sedimentation anomaly. (c) Sum anomaly, (a)+(b). The mass substitutions relating to each gravity anomaly are indicated. In the case of (c) the density contrasts result from summation of the contrasts in (a) and (b). ρ_c = crustal density; ρ_w = water density; ρ_m = mantle density; ρ_s = sediment density.

would be used, but this is often not available. In such cases it is usual to apply an empirical porosity-depth distribution as a means of approximating the sediment mass.

4.2.2 Stage 2: Calculation of stretching factor, β

The total tectonic subsidence (TTS) [Sawyer, 1985a] determined by backstripping simulates the position of basement in the absence of post-rift sediment loading. If it is assumed that the TTS is controlled by the degree of crustal (or lithospheric) thinning, then it can be used to determine a stretching factor, β, defined as the ratio between original and extended crustal (or lithospheric) thicknesses. How this is done will depend on the rifting model that is used (see discussion in Chapter 2, Section 6). The methods used in this thesis are described later in this chapter (Section 4.4).

Having determined the extended crustal thickness, and hence the Moho geometry the present-day configuration is derived by adding back in the flexure, w, due to post-rift sediment loading. This is already known from backstripping in Stage 1.

4.2.3 Stage 3: Gravity modelling

In the process-oriented method the present day gravity anomaly is treated as the gravitational product of mass substitutions arising from rifting (the 'rifting anomaly', Figure 4.4a) and sedimentation (the 'sedimentation anomaly', Figure 4.4b), which when summed amount to the calculated free-air gravity anomaly (the 'sum anomaly', Figure 4.4c). The mean of each of these gravity anomalies is always zero because an overall isostatic equilibrium is maintained throughout.

Derivation of the process-oriented components allows elements of the present day

margin geometry and gravity anomaly to be traced to discrete elements of the margin evolution.

The rifting gravity anomaly

The rifting gravity anomaly, G_{rift}, is the anomaly associated with the rifted crust in the absence of backstripped sediment loads. The two bodies that contribute to this anomaly are defined by the TTS and Moho geometry given by backstripping and reconstruction of crustal thickness (Figure 4.4a).

The rifting anomaly generally consists of a gravity high-low couple associated with the shelf break, and slope and rise respectively.

The sedimentation gravity anomaly

The sedimentation gravity anomaly, G_{sed} (Figure 4.4b), is defined as the cumulative gravitational effect of sedimentary loading relative to the TTS structure. The alterations to the rift structure are classified into three parts:

Load: Sediments lying above the TTS surface displace lower density water.

Infill: Sediments lying below the TTS surface displace higher density crust.

Moho flexure: Sediment driven flexure of the rifted crust displaces higher density mantle below.

In each case the associated gravity anomaly is due to the relevant mass substitution. Hence the gravity contribution from the load is positive, while the infill and Moho flexure produce negative anomalies.

The lesser wavelength and depth of the load relative to the flexural changes leads to a sedimentation gravity anomaly that typically consists of a high over the sediment shelf break that is flanked by two lows controlled by the load geometry and flexural rigidity.

The sum gravity anomaly

The sum gravity anomaly, G_{sum}, is the summation of rift and sedimentation anomalies (Figure 4.4c). It may also include the contributions of any other processes that have been modelled.

In general the sum anomaly carries over the seaward high-low couple from the sedimentation anomaly. However, because the landward sedimentation anomaly low is commonly of a smaller amplitude than the corresponding high in the rifting gravity anomaly

then there may remain a gravity high over the hinge zone when the two are summed; particularly if the sedimentation T_e is large, as in the example.

4.2.4 Advantages

Watts's 'process-oriented method' of margin reconstruction [Watts, 1988] contrasts with commonly used object-oriented approaches that aim to statically fit observed data using trial and error construction of physical models.

Although unique features can be identified by treating observed data as a static representation of margin structure, their context within the evolution of the margin as a whole may not be clear. Moreover, the utility of such models may be restricted: by sparsity and limited resolution of deep seismic coverage; by non-uniqueness in the way data is fitted; and by differing acquisition and modelling methods.

The process-oriented modelling method causally links elements of the observed free-air gravity anomaly to margin processes; recovering their context in the evolution of a margin as a whole. Watts [1988] argues that by taking this approach the relative importance and influence of distinct evolutionary processes can be observed.

The direct means by which the process-oriented method generates gravity anomalies using defined formative processes helps to address questions of non-uniqueness that arise in the use of static methods, and offers the opportunity to investigate current data in the context of past evolution.

Where characteristics of the gravity anomaly have been linked to observed structural features (such as a proposed linear relationship between the amplitude of an Airy isostatic anomaly high, and the volume of igneous crust in Behn & Lin [2000]), the process-oriented approach allows them to be reconsidered in terms of their evolutionary context.

4.2.5 Application

The process-oriented method was first applied to 2-D margin reconstructions (e.g. Watts [1988] and Watts & Marr [1995]), but has lately been applied in 3-D (Stewart *et al.* [2000]). This thesis is the first application of a variable thickness elastic plate method of this type to a $> 1500km$ passive continental margin tract.

The method applied (Figure 4.5) is an extension of that described in Section 4.2 (cf. Figure 4.1), with components added for inclusion of sediment porosity (as in Stewart *et al.* [2000]), and for iterative constraint of spatial variations in T_e.

The numerical methods that are applied at each stage are described in the following sections.

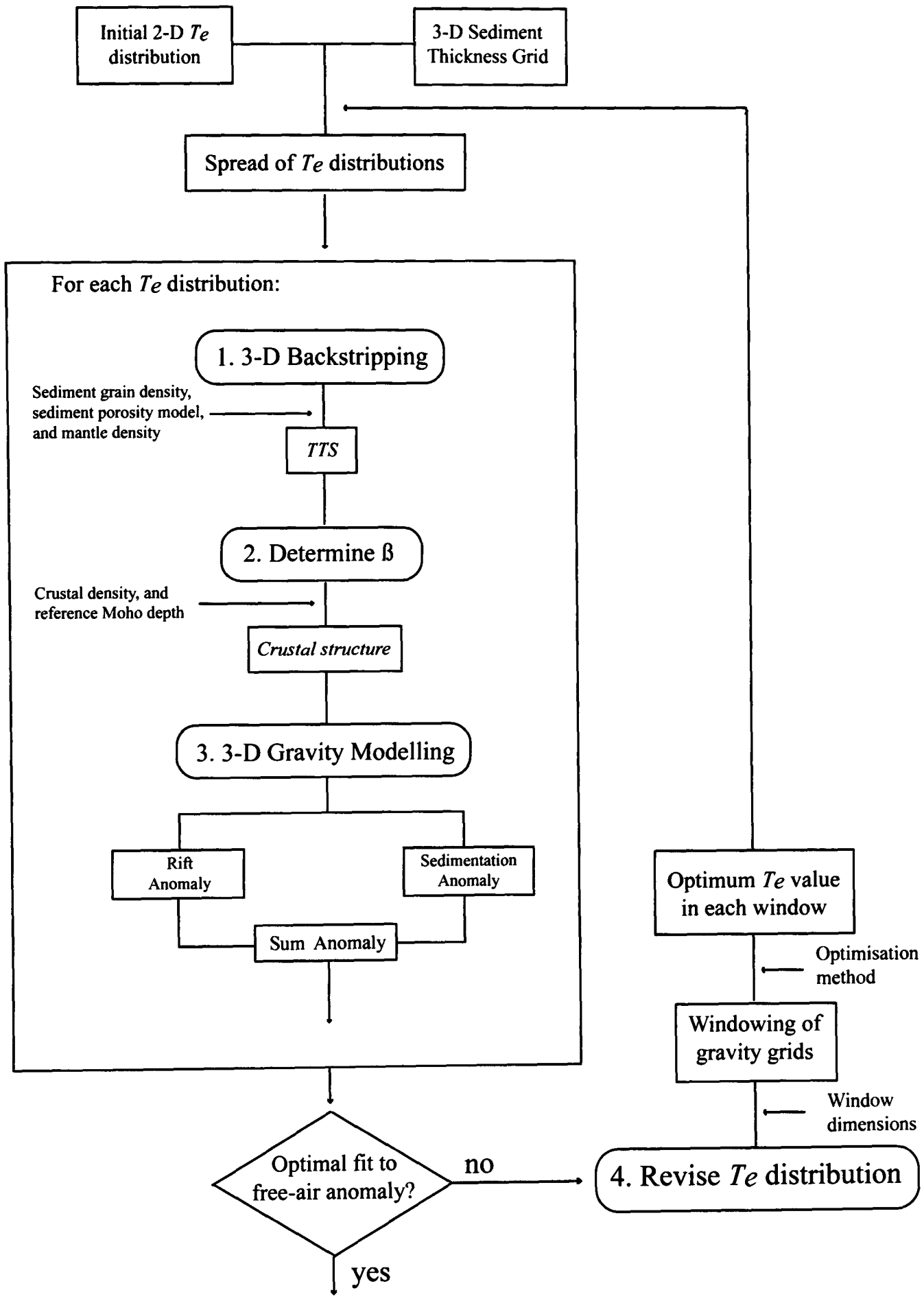


Figure 4.5: The process-oriented method of sediment thickness and gravity anomaly analysis as applied in this thesis. Initial T_e and sediment thickness distributions provide a basis for iterative calculation of rift and present day geometries together with associated effects on the gravity anomaly. The process iterates until an optimal fit between sum and free-air gravity anomalies is reached. See also Figure 4.1

4.3 Backstripping

Backstripping is applied in this thesis in forms using: local Airy isostasy; uniform thin elastic plate flexure due to 2-D and 3-D loads; and non-uniform thin elastic plate flexure due to 3-D loads. Airy load responses can be directly calculated as already described. The methods used for flexural backstripping are detailed in this section.

4.3.1 1-D uniform thin elastic plate flexure

If a two-dimensional uniform density load is sinusoidal and periodic with wavelength λ and amplitude h_0 (such that $h = h_0 sin(2\pi x/\lambda)$) then there is an analytical solution of the equation for 2-D loading of a (1-D) uniform thin elastic plate of infinite extent (Equation (4.9)) such that the flexure, $w(x)$, will also be sinusoidal and of the same wavelength as the load (i.e. $w = w_0 sin[2\pi x/\lambda]$):

$$\left[D(\frac{2\pi}{\lambda})^4 + \Delta\rho_1 g\right] w_0 sin(2\pi x/\lambda) = \Delta\rho_2 g h_0 sin(2\pi x/\lambda) \tag{4.10}$$

in which $\Delta\rho_1$ is the contrast between substrate and infill densities, and $\Delta\rho_2$ is the density contrast between the load and the material it displaces. By rearranging:

$$w_0 = \frac{\Delta\rho_2 h_0}{\frac{D}{g}(\frac{2\pi}{\lambda})^4 + \Delta\rho_1} \tag{4.11}$$

From this it can be seen that for short wavelength loads (small λ) w_0 tends towards zero, but as the wavelength increases the rigidity term diminishes, and at long wavelengths Equation (4.11) tends towards an approximation of local Airy-type compensation (cf. Equation (4.4)). Across the interval between these two states the plate deforms elastically with an amplitude controlled by its rigidity (Figure 4.6).

According to Equation (4.11) the elastic response to a load is confined to the wavelength of that load. For this reason it is possible to solve the elastic plate flexure due to any load by calculating the response to components at all wavelengths. This can be accomplished by applying a Fourier transform to $h(x)$ and determining Equation (4.11) across the spectrum such that:

$$\overline{W} = \frac{\Delta\rho_2 \overline{H}}{\frac{Dk^4}{g} + \Delta\rho_1} \tag{4.12}$$

in which the barred uppercase variable represents the Fourier transform of the lower case variable, k is the wavenumber $(2\pi/\lambda)$, and λ is the wavelength. The flexural response, $w(x)$, is the inverse transform of $\overline{W}$.

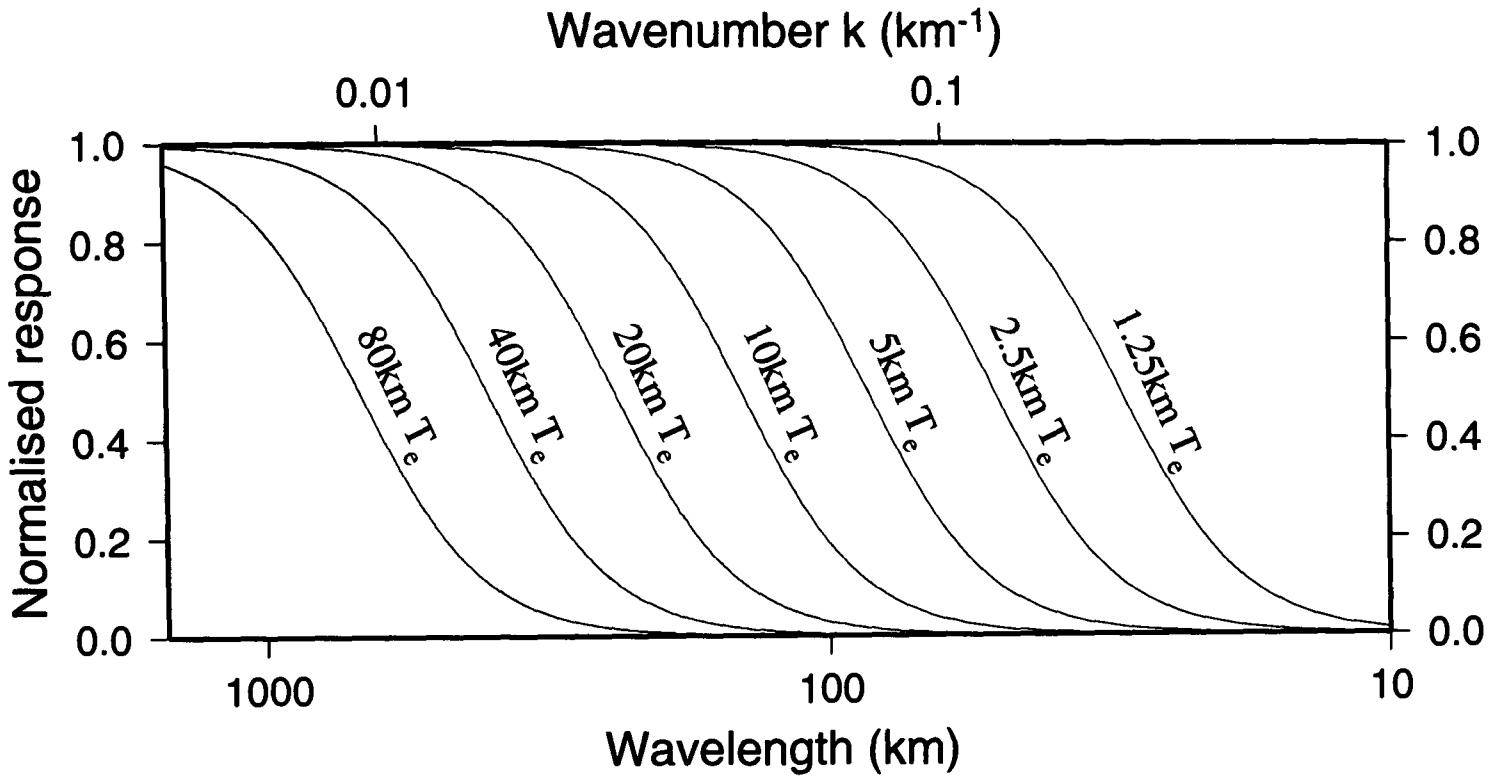


Figure 4.6: Elastic response versus load wavelength for a range of effective elastic thicknesses. The responses have been normalised against Airy isostatic load compensation.

4.3.2 2-D uniform thin elastic plate flexure

The uniform elastic plate solution for flexure due to a 3-D load is similar to that for a 2-D load, except that k is replaced by $\sqrt{(k_1)^2 + (k_2)^2}$ where k_1 and k_2 are the wavenumbers in x and y respectively.

Figure 4.7 shows flexure due to a disc load of $900km$ radius that has been calculated using a fast Fourier transform (FFT) of the load. As can be seen the use of a FFT causes low amplitude resonances (observed as oscillations about zero beyond the flexural bulge) because of discretisation of the infinite Fourier series.

4.3.3 Non-uniform thin elastic plate flexure

The Fourier domain solution for thin plate flexure applies only to problems in which the effective elastic thickness is uniform across the plate. Software has been written for this thesis (see Appendix A) that uses a finite difference approximation to calculate the flexure due to a 3-D load on a *non-uniform* thin elastic plate.

Governing equation

The differential equation for bending of a vertically loaded thin elastic plate of variable thickness and infinite extent is [Timoshenko & Woinowsky-Krieger, 1959]:

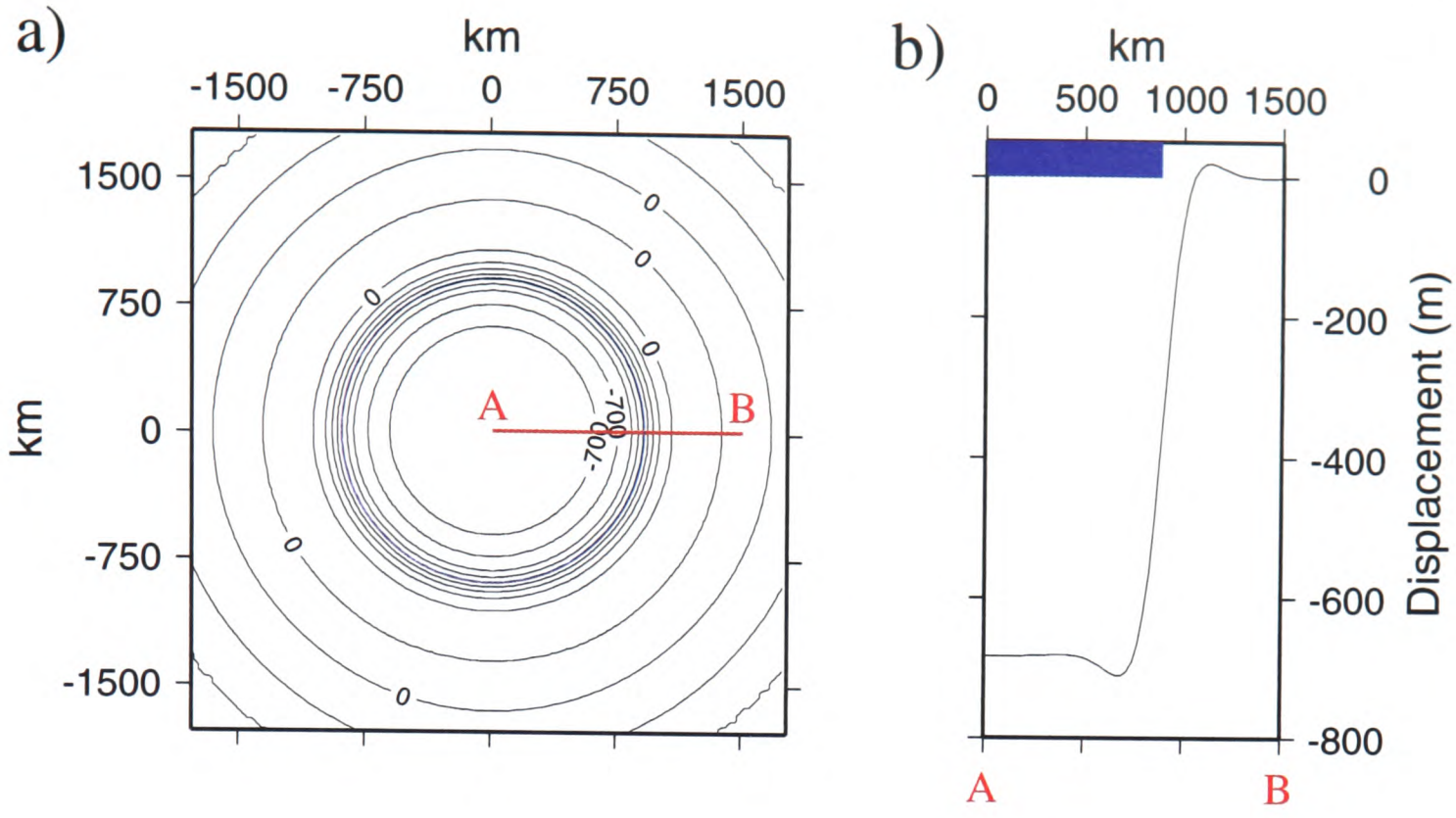


Figure 4.7: Fourier solution of flexure due to a disc load. (a) Plan view. (b) Sectional view. Flexure contours at $100m$, blue markers indicate lateral extent of disc. See Table 4.1 for model parameters.

$$D\nabla\nabla w + 2\frac{\partial D}{\partial x}\frac{\partial}{\partial x}\nabla w + 2\frac{\partial D}{\partial y}\frac{\partial}{\partial y}\nabla w + \nabla D\nabla w$$
$$-(1-\nu)\left[\frac{\partial^2 D}{\partial x^2}\frac{\partial^2 w}{\partial y^2} - 2\frac{\partial^2 D}{\partial x \partial y}\frac{\partial^2 w}{\partial x \partial y} + \frac{\partial^2 D}{\partial y^2}\frac{\partial^2 w}{\partial x^2}\right]$$
$$+\Delta\rho_1 g w = \Delta\rho_2 g h \qquad (4.13)$$

In which $\Delta\rho_1$ is the contrast between substrate and infill densities, $\Delta\rho_2$ is the density contrast between the load and the material it displaces, and:

$$\nabla = \frac{\partial^2}{\partial y^2} + \frac{\partial^2}{\partial x^2}$$

Rigidity distribution and derivatives

The rigidity derivatives in Equation (4.13) are obtained by differentiation of the T_e distribution in the Fourier domain.

These are then converted to derivatives of rigidity using differential terms of:

$$D = \frac{E{T_e}^3}{12(1-\nu^2)} \qquad (4.15)$$

For example:

Parameter	Value
Disc radius	$900km$
Disc height	$1km$
Load density	$2600kgm^{-3}$
Substrate density	$3330kgm^{-3}$
Infill density	$1030kgm^{-3}$
Displaced material density	$1030kgm^{-3}$
Effective elastic thickness	$37km$
Young's Modulus	$8.35 \times 10^{10} Pa$
Poisson's Ratio	0.25

Table 4.1: Disc load model parameters.

$$\begin{aligned} \frac{\partial^2 D}{\partial x \partial y} &= \frac{\partial D}{\partial T_e}\left(\frac{\partial^2 T_e}{\partial x \partial y}\right) \\ &= \frac{E{T_e}^2}{4(1-\nu)}\left(\frac{\partial^2 T_e}{\partial x \partial y}\right) \\ &= \frac{3D}{T_e}\left(\frac{\partial^2 T_e}{\partial x \partial y}\right) \end{aligned} \tag{4.16}$$

Evaluation of the rigidity derivatives is accurately accomplished if the T_e distribution is continuous and smoothly varying (As in Figure 4.8 for example). Plate discontinuities and rapid gradient changes cause resonances in the discrete Fourier transformation that degradade the derivative evaluations. This can be addressed either by bandpass filtering the T_e distribution prior to transformation, or by using a finer grid spacing.

Finite difference expansion

The flexural derivatives in Equation (4.13) can be approximated by direct substitution of centered finite difference terms as in Gahli [1989]. Here the Taylor series expansion up to the first Δx and Δy term is used to approximate first and second order derivatives in x and y of the deflection, $w(x, y)$. For example the first and second order derivatives in x at position i, j are approximated by:

$$\begin{aligned} \left(\frac{\partial w}{\partial x}\right)_{i,j} &\approx \frac{1}{2\Delta x}\left[w_{i+1,j} - w_{i-1,j}\right] \\ \left(\frac{\partial^2 w}{\partial x^2}\right)_{i,j} &\approx \frac{1}{(\Delta x)^2}\left[w_{i+1,j} - 2w_{i,j} + w_{i-1,j}\right] \end{aligned}$$

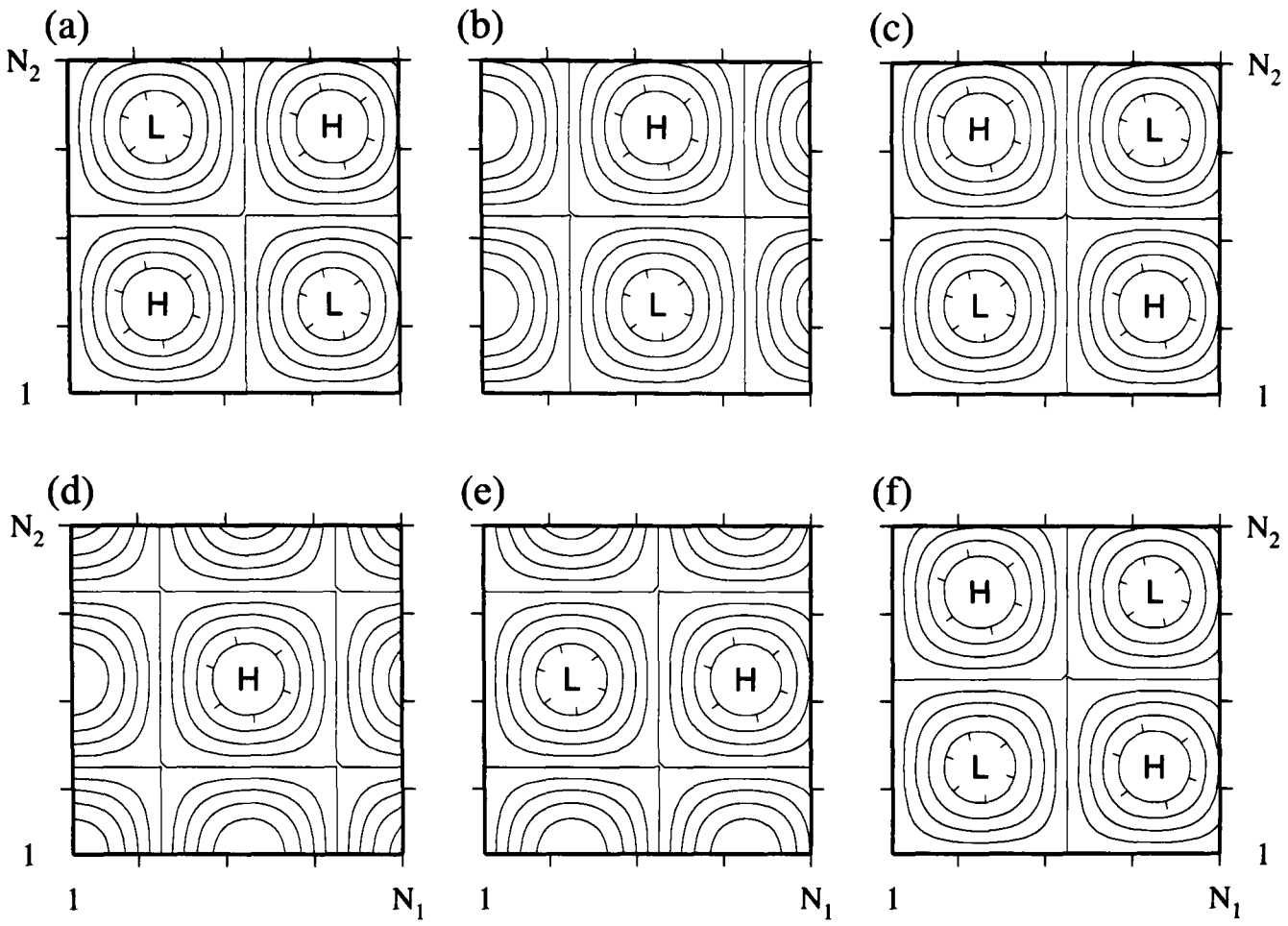


Figure 4.8: T_e distribution (a)($T_e = 1 + sin[2\pi x/N_1]sin[2\pi y/N_2]$), with Fourier derived derivatives; (b) $\partial T_e/\partial x$; (c) $\partial^2 T_e/\partial x^2$; (d) $\partial^2 T_e/\partial x \partial y$; (e) $\partial T_e/\partial y$; (f) $\partial^2 T_e/\partial y^2$.

A centered difference between $w^x_{i,j+1}$ and $w^x_{i,j-1}$ approximates $\partial^2 w/\partial x \partial y$:

$$\left(\frac{\partial^2 w}{\partial x \partial y}\right)_{i,j} \approx \frac{1}{2\Delta y}\left[\left(\frac{\partial w}{\partial x}\right)_{i,j+1} - \left(\frac{\partial w}{\partial x}\right)_{i,j-1}\right]$$

and higher order derivatives are approximated by Taylor series expansions in terms of $\partial^2 w/\partial x^2$ and $\partial^2 w/\partial y^2$ up to the first Δx and Δy terms. For example:

$$\left(\frac{\partial^3 w}{\partial x^2 \partial y}\right)_{i,j} \approx \frac{1}{2\Delta y}\left[\left(\frac{\partial^2 w}{\partial x^2}\right)_{i,j+1} - \left(\frac{\partial^2 w}{\partial x^2}\right)_{i,j-1}\right]$$

$$\left(\frac{\partial^4 w}{\partial x^2 \partial y^2}\right)_{i,j} \approx \frac{1}{(\Delta y)^2}\left[\left(\frac{\partial^2 w}{\partial x^2}\right)_{i,j+1} - 2\left(\frac{\partial^2 w}{\partial x^2}\right)_{i,j} + \left(\frac{\partial^2 w}{\partial x^2}\right)_{i,j-1}\right]$$

Expansion of each of the terms, through cross substitution, allows all of the centered difference terms to be expressed as functions of the plate flexure, w (Table 4.2).

After substitution of the approximations in Table 4.2, the non-uniform thin elastic plate equation (Equation (4.13)) can be rearranged in terms of point deflections relating to the amplitude of the load at each point i, j. Because of the length of the expansion it is expressed here using coefficients Q (see Table 4.3):

Derivative	Finite Difference Approximation
$\frac{\partial w_{i,j}}{\partial x}$	$\frac{w_{i+1,j}-w_{i-1,j}}{2\Delta x}$
$\frac{\partial w_{i,j}}{\partial y}$	$\frac{w_{i,j+1}-w_{i,j-1}}{2\Delta y}$
$\frac{\partial^2 w_{i,j}}{\partial x^2}$	$\frac{w_{i+1,j}-2w_{i,j}+w_{i-1,j}}{\Delta x^2}$
$\frac{\partial^2 w_{i,j}}{\partial y^2}$	$\frac{w_{i,j+1}-2w_{i,j}+w_{i,j-1}}{\Delta y^2}$
$\frac{\partial^3 w_{i,j}}{\partial x^3}$	$\frac{w_{i+2,j}-2w_{i+1,j}+2w_{i-1,j}-w_{i-2,j}}{2\Delta x^3}$
$\frac{\partial^3 w_{i,j}}{\partial y^3}$	$\frac{w_{i,j+2}-2w_{i,j+1}+2w_{i,j-1}-w_{i,j-2}}{2\Delta y^3}$
$\frac{\partial^4 w_{i,j}}{\partial x^4}$	$\frac{w_{i+2,j}-4w_{i+1,j}+6w_{i,j}-4w_{i-1,j}+w_{i-2,j}}{\Delta x^4}$
$\frac{\partial^4 w_{i,j}}{\partial y^4}$	$\frac{w_{i,j+2}-4w_{i,j+1}+6w_{i,j}-4w_{i,j-1}+w_{i,j-2}}{\Delta y^4}$
$\frac{\partial^2 w_{i,j}}{\partial x \partial y}$	$\frac{w_{i+1,j+1}-w_{i+1,j-1}-w_{i-1,j+1}+w_{i-1,j-1}}{4\Delta x \Delta y}$
$\frac{\partial^3 w_{i,j}}{\partial x^2 \partial y}$	$\frac{w_{i+1,j+1}-w_{i+1,j-1}-2(w_{i,j+1}-w_{i,j-1})+w_{i-1,j+1}-w_{i-1,j-1}}{2\Delta x^2 \Delta y}$
$\frac{\partial^3 w_{i,j}}{\partial x \partial y^2}$	$\frac{w_{i+1,j+1}-w_{i-1,j+1}-2(w_{i+1,j}-w_{i-1,j})+w_{i+1,j-1}-w_{i-1,j-1}}{2\Delta x \Delta y^2}$
$\frac{\partial^4 w_{i,j}}{\partial x^2 \partial y^2}$	$\frac{w_{i+1,j+1}-2w_{i+1,j}+w_{i+1,j-1}-2(w_{i,j+1}-2w_{i,j}+w_{i,j-1})+w_{i-1,j+1}-2w_{i-1,j}+w_{i-1,j-1}}{\Delta x^2 \Delta y^2}$

Table 4.2: Terms of the central difference finite difference approximation (Verified from Stewart [1998]).

$$
\begin{aligned}
&(Qw)_{i,j} + (Qw)_{i,j-1} + (Qw)_{i,j+1} + (Qw)_{i-1,j} + (Qw)_{i+1,j} + \\
&(Qw)_{i-1,j-1} + (Qw)_{i+1,j+1} + (Qw)_{i+1,j-1} + (Qw)_{i-1,j+1} + \\
&\qquad (Qw)_{i,j-2} + (Qw)_{i,j+2} + (Qw)_{i-2,j} + (Qw)_{i+2,j} \quad = \quad \Delta\rho_2 g h_{i,j} \qquad (4.18)
\end{aligned}
$$

Calculation of the coefficients in Table 4.3 can be reduced (Table 4.4) using the following repeated functions:

$$
\begin{aligned}
A_x &= \tfrac{1}{\Delta x^3}\tfrac{\partial D}{\partial x} & A_y &= \tfrac{1}{\Delta y^3}\tfrac{\partial D}{\partial y} \\
B_x &= \tfrac{1}{\Delta x^4} D & B_y &= \tfrac{1}{\Delta y^4} D \\
C_{xy} &= \tfrac{1}{2\Delta x \Delta y}(1-\nu)\tfrac{\partial^2 D}{\partial x \partial y} & & \\
D_x &= \tfrac{1}{\Delta x^2 \Delta x}\tfrac{\partial D}{\partial x} & D_y &= \tfrac{1}{\Delta x \Delta y^2}\tfrac{\partial D}{\partial y} \\
E_{xy} &= \tfrac{2}{\Delta x^2 \Delta y^2} D & & \\
F_x &= \tfrac{1}{\Delta x^2}\left[\nabla D - (1-\nu)\tfrac{\partial^2 D}{\partial y^2}\right] & F_y &= \tfrac{1}{\Delta y^2}\left[\nabla D - (1-\nu)\tfrac{\partial^2 D}{\partial x^2}\right]
\end{aligned}
$$

The plate flexure is approximated by solving the series of simultaneous equations resulting from Equation (4.18). Towards the model boundaries cosine tapering reduces the rigidity to zero (Airy isostasy) 6^o outside the study area[3], and a free edge boundary

[3]For the study area in this thesis a larger external tapering distance would raise the Fourier transformed matrix by an additional power of 2

Coefficient	Expansion
$Q_{i,j}$	$-\frac{2}{\Delta x^2}\left[\nabla D-(1-\nu)\frac{\partial^2}{\partial y^2}\right]-\frac{2}{\Delta y^2}\left[\nabla D-(1\nu)\frac{\partial^2}{\partial x^2}\right]+\left[\frac{6}{\Delta x^4}+\frac{6}{\Delta y^4}+\frac{8}{\Delta x^2\Delta y^2}\right]D+\Delta\rho_1 g$
$Q_{i,j-1}$	$\frac{1}{\Delta y^2}\left[\nabla D-(1-\nu)\frac{\partial^2 D}{\partial x^2}\right]+\frac{2}{\Delta y^3}\frac{\partial D}{\partial y}-\frac{4}{\Delta y^4}D+\frac{2}{\Delta x^2\Delta y}\frac{\partial D}{\partial x}-\frac{4}{\Delta x^2\Delta y^2}D$
$Q_{i,j+1}$	$\frac{1}{\Delta y^2}\left[\nabla D-(1-\nu)\frac{\partial^2 D}{\partial x^2}\right]-\frac{2}{\Delta y^3}\frac{\partial D}{\partial y}-\frac{4}{\Delta y^4}D-\frac{2}{\Delta x^2\Delta y}\frac{\partial D}{\partial x}-\frac{4}{\Delta x^2\Delta y^2}D$
$Q_{i-1,j}$	$\frac{1}{\Delta x^2}\left[\nabla D-(1-\nu)\frac{\partial^2 D}{\partial y^2}\right]+\frac{2}{\Delta x^3}\frac{\partial D}{\partial x}-\frac{4}{\Delta x^4}D+\frac{2}{\Delta x\Delta y^2}\frac{\partial D}{\partial y}-\frac{4}{\Delta x^2\Delta y^2}D$
$Q_{i+1,j}$	$\frac{1}{\Delta x^2}\left[\nabla D-(1-\nu)\frac{\partial^2 D}{\partial y^2}\right]-\frac{2}{\Delta x^3}\frac{\partial D}{\partial x}-\frac{4}{\Delta x^4}D-\frac{2}{\Delta x\Delta y^2}\frac{\partial D}{\partial y}-\frac{4}{\Delta x^2\Delta y^2}D$
$Q_{i-1,j-1}$	$\frac{1}{2\Delta x\Delta y}(1-\nu)\frac{\partial^2 D}{\partial x\partial y}-\frac{1}{\Delta x^2\Delta y}\frac{\partial D}{\partial x}-\frac{1}{\Delta x\Delta y^2}\frac{\partial D}{\partial y}+\frac{2}{\Delta x^2\Delta y^2}D$
$Q_{i-1,j+1}$	$-\frac{1}{2\Delta x\Delta y}(1-\nu)\frac{\partial^2 D}{\partial x\partial y}+\frac{1}{\Delta x^2\Delta y}\frac{\partial D}{\partial x}-\frac{1}{\Delta x\Delta y^2}\frac{\partial D}{\partial y}+\frac{2}{\Delta x^2\Delta y^2}D$
$Q_{i+1,j-1}$	$-\frac{1}{2\Delta x\Delta y}(1-\nu)\frac{\partial^2 D}{\partial x\partial y}-\frac{1}{\Delta x^2\Delta y}\frac{\partial D}{\partial x}+\frac{1}{\Delta x\Delta y^2}\frac{\partial D}{\partial y}+\frac{2}{\Delta x^2\Delta y^2}D$
$Q_{i+1,j+1}$	$\frac{1}{2\Delta x\Delta y}(1-\nu)\frac{\partial^2 D}{\partial x\partial y}+\frac{1}{\Delta x^2\Delta y}\frac{\partial D}{\partial x}+\frac{1}{\Delta x\Delta y^2}\frac{\partial D}{\partial y}+\frac{2}{\Delta x^2\Delta y^2}D$
$Q_{i,j-2}$	$-\frac{1}{\Delta y^3}\frac{\partial D}{\partial y}+\frac{1}{\Delta y^4}D$
$Q_{i,j+2}$	$\frac{1}{\Delta y^3}\frac{\partial D}{\partial y}+\frac{1}{\Delta y^4}D$
$Q_{i-2,j}$	$-\frac{1}{\Delta x^3}\frac{\partial D}{\partial x}+\frac{1}{\Delta x^4}D$
$Q_{i+2,j}$	$\frac{1}{\Delta x^3}\frac{\partial D}{\partial x}+\frac{1}{\Delta x^4}D$

Table 4.3: Coefficients Q of w from the finite difference expansion of Equation (4.13).

condition applies. For this condition the boundary bending and twisting moments are zero, such that at $y = 0$:

$$\begin{aligned} -D\left[\frac{\partial^2 w}{\partial y^2}+\nu\frac{\partial^2 w}{\partial x^2}\right] &= 0 \\ -D\left[\frac{\partial^3 w}{\partial y^3}+(2-\nu)\frac{\partial^3 w}{\partial x^2\partial y}\right] &= 0 \end{aligned}$$

Equivalent equations apply at each of the other boundaries.

Combined solution

The complete finite difference approximation for a region of dimensions $N_1 \times N_2$ consists of a series of linear equations defined by an $N_1N_2 \times N_1N_2$ coefficient matrix, Q, and an N_1N_2 matrix, H, containing values of $\Delta\rho_2 gh$. The N_1N_2 matrix of vertical displacements, W, is given by the matrix solution:

$$Q(N_1N_2, N_1N_2)W(N_1N_2) = H(N_1N_2) \tag{4.19}$$

The matrix storage for Q is of the order of N^4 real values, and therefore increases by a factor of 16 if N_1 and N_2 are doubled. Hence as the grid dimensions increase the matrix

Coefficient	Expansion
$Q_{i,j}$	$-2F_x - 2F_y + 6B_x + 6B_y + 4E_{xy} + \Delta\rho_1 g$
$Q_{i,j-1}$	$F_y + 2A_y - 4B_y + 2 - D_x - 2E_{xy}$
$Q_{i,j+1}$	$F_y - 2A_y - 4B_y - 2 - D_x - 2E_{xy}$
$Q_{i-1,j}$	$F_x + 2A_x - 4B_x + 2 - D_y - 2E_{xy}$
$Q_{i+1,j}$	$F_x - 2A_x - 4B_x - 2 - D_y - 2E_{xy}$
$Q_{i-1,j-1}$	$C_{xy} - D_x - D_y + E_{xy}$
$Q_{i-1,j+1}$	$C_{xy} + D_x - D_y + E_{xy}$
$Q_{i+1,j-1}$	$-C_{xy} - D_x + D_y + E_{xy}$
$Q_{i+1,j+1}$	$C_{xy} + D_x + D_y + E_{xy}$
$Q_{i,j-2}$	$-A_y + B_y$
$Q_{i,j+2}$	$A_y + B_y$
$Q_{i-2,j}$	$-A_x + B_x$
$Q_{i+2,j}$	$A_x + B_x$

Table 4.4: Simplified coefficients from Table 4.3 (see text).

storage rapidly becomes less practical. However the series in Q for each $w_{i,j}$ contains only terms relating to points within a radius of $i \pm 2$ and $j \pm 2$ such that most of the matrix data is zero value. By storing and manipulating the non-zero data in a 'banded' matrix (Figure 4.9) it is possible to treat the values outside the radius as *implicitly* zero. Because the implicit values do not need to be stored, this reduces the size of Q from $O(N^4)$ to $O(N^3)$. In this instance the width of the matrix band is $4 * N_1 + 1$, and the width of the packed matrix is $6 * N_1 + 1$ (the first $2 * N_1$ columns of the packed matrix are empty, but are required for temporary storage during lower-upper decomposition). An additional benefit of using a banded matrix is a reduction in lower-upper decomposition operations in the solution of the series of linear equations from $O([N^2]^3)$ operations on the full matrix to $O([N^2])$ on the banded matrix (see Section 2.7 of Press *et al.* [1992]).

The system of linear equations is solved using double precision banded matrix routines from the widely used and freely available Lapack (Linear Algebra PACKage) FORTRAN libraries. These are 'dgbtrf' for lower-upper factorisation and 'dgbtrs' for solution of a system of linear equations after lower-upper factorisation.

The use of band storage improves the software efficiency by minimising memory usage and reducing the number of calculations required to solve the finite difference approximation. Together with other numerical efficiencies this reduces the $N_1 = N_2 = 128$ runtime

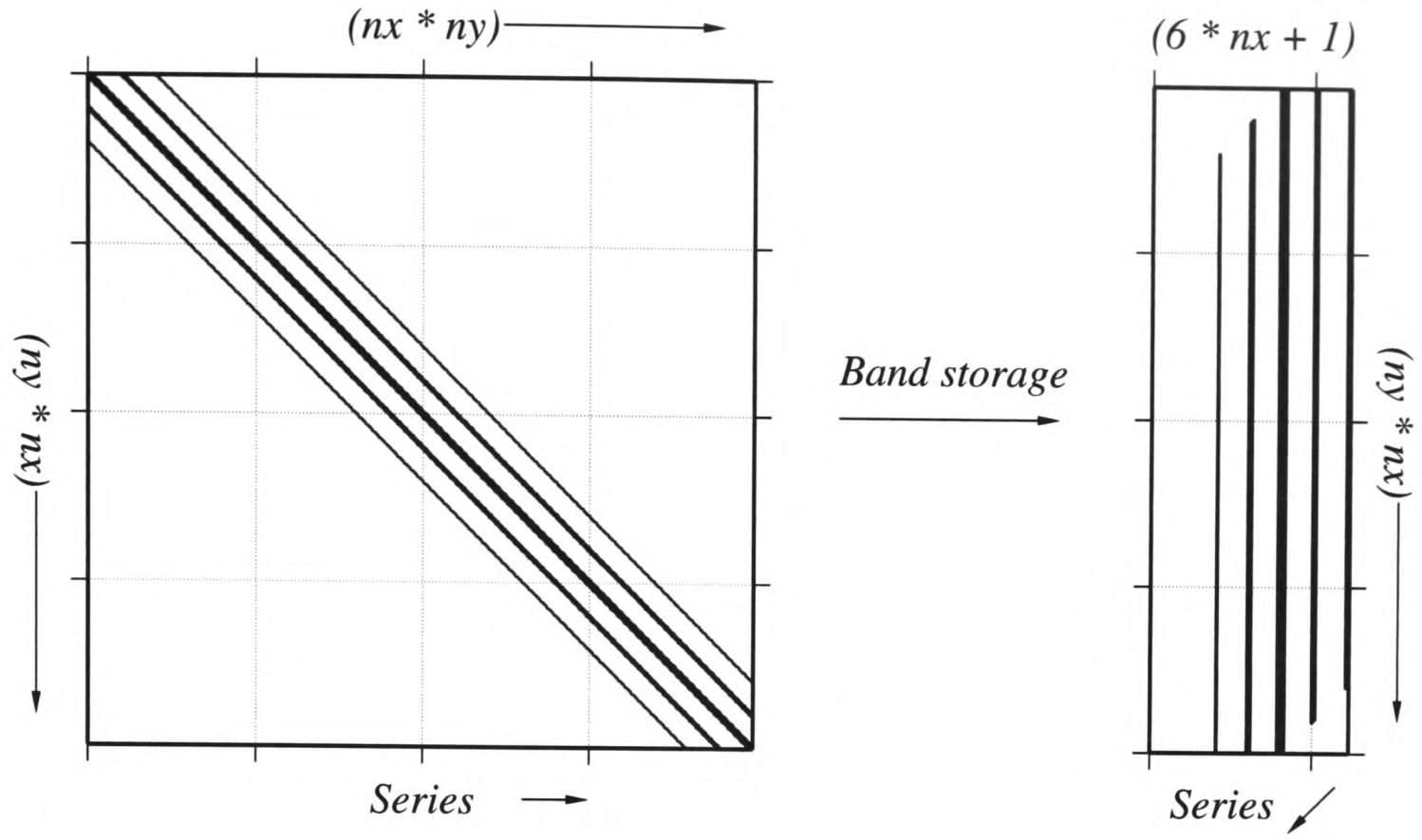


Figure 4.9: Use of band packing to reduce the storage and solution of a series of linear equations in a sparse matrix. Data points are non-zero data before and after band packing. Series arrows represent the direction in which linear equation coefficients relating to a given point are stored within the matrices.

(for example) from c. 9 minutes to less than 10 seconds on the same machine[4]. The final solutions are identical.

In principle, the banded matrix dimensions can be reduced from $O(N^3)$ to $O(N^2)$, with a width of 19 cells, by omitting zero-terms within the matrix band. However this requires a non-standard adaptation of the Lapack routines, limiting portability of the code.

Figure 4.10 shows the flexure due to a uniform disc load approximated using the finite difference approximation. The problem is identical to that in Section 4.3.2 (Figure 4.7), and the solutions are the same to within $\pm 1.8m$ (c. 0.25% of the maximum deflection).

More importantly, the finite difference approximation has been tested against the analytical uniform plate solution of Brotchie & Silvester [1969](Figure 4.12) for loading by a disc of radius, A, and uniform thickness, h. In this solution the deflection, w, at a point, x, is given by:

$$w = \frac{\Delta\rho_2 h}{\rho'}\left[a\ ker'(a)ber(r) - a\ kei'(a)bei(r) + 1\right]\ ,\ x < A \qquad (4.20)$$

$$w = \frac{\Delta\rho_2 h}{\rho'}\left[a\ ber'(a)ker(r) - a\ bei'(a)kei(r)\right]\ ,\ x > A$$

[4]Sun Sparc Ultra 10 330MHz, 640Mb RAM

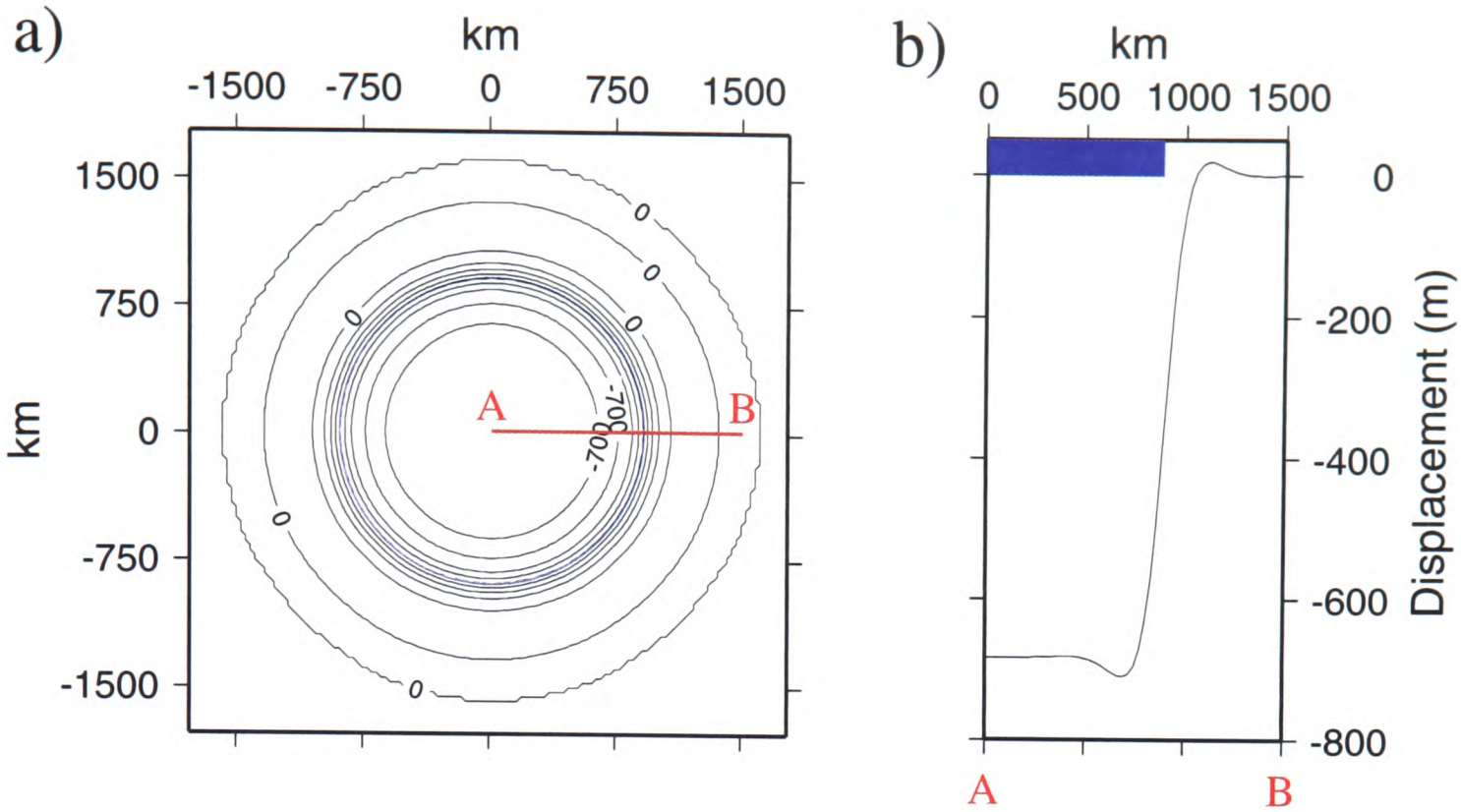


Figure 4.10: Finite difference approximation of flexure due to a 900km radius disc load. Plan and sectional views. See Table 4.1 for model parameters and *cf.* Figure 4.7.

Where, ber and bei are Bessel-Kelvin functions of zero order, and for mean Earth radius R:

$$
\begin{aligned}
l &= \sqrt[4]{\left[\frac{ET}{R^2} + \rho_{sub}\right]} \\
a &= A/l \\
r &= x/l \\
\rho' &= \rho_1 + \frac{ET_e}{R^2}
\end{aligned}
$$

Dimensions (including T_e) are in m, D is in Nm, E is in Nm^{-2}, and densities are in[5] Nm^{-2}. Figure 4.11 shows the effect of disc radius on the flexural response.

Figure 4.12 compares the finite difference approximation against that of Brotchie & Silvester [1969] (calculated using GMT - Wessel & Smith [1995]) for the same disc load as before. The results agree to within $-0.23m$ to $+11.66m$ with an RMS misfit of $3.39m$ (c. 0.5% of the maximum deflection). The Bessel-Kelvin functions have been approximated by an 8 term expansion, so it is possible that a small part of the discrepancy is due to missing terms.

The effect of a 'flat Earth' assumption (in which the Earth's curvature is ignored) in the finite difference approximation has also been considered. If Brotchie and Silvester's

[5] Nm/m^3

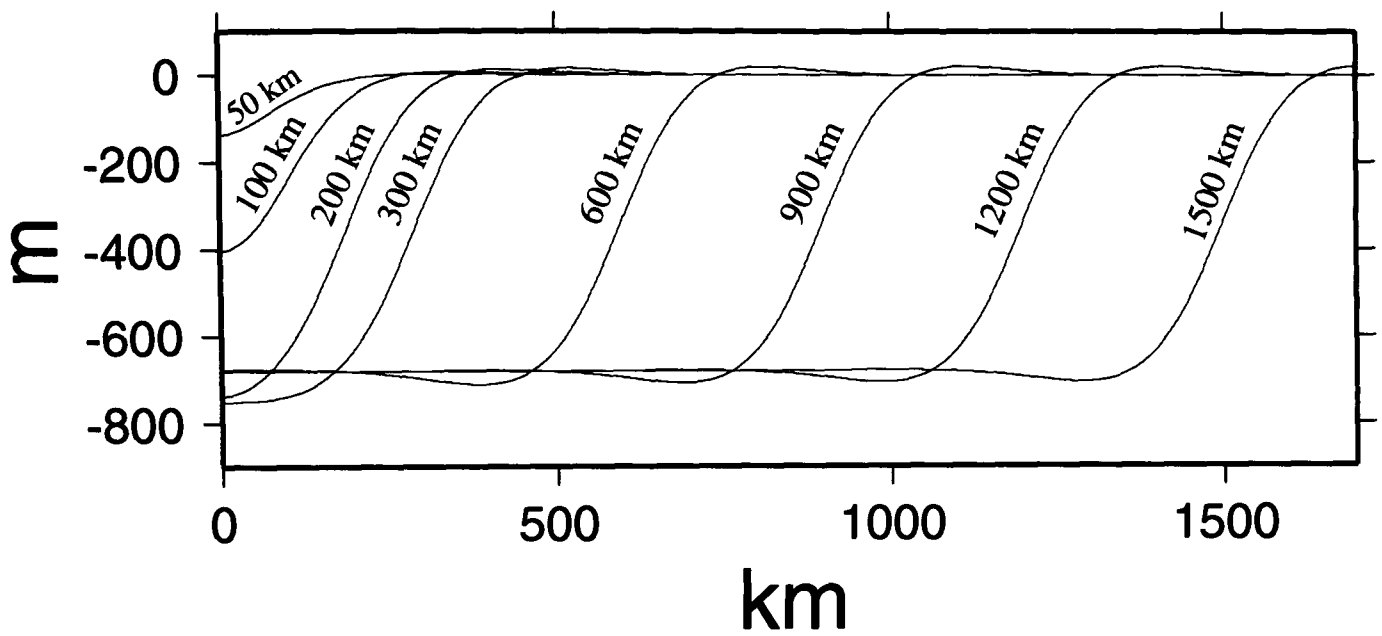


Figure 4.11: Analytical solution [Brotchie & Silvester, 1969] to flexure of a uniform elastic thickness plate due to disc loads of uniform thickness and density (all as defined in Table 4.1), and stated radius.

term for curvature of the Earth[6] (ET_e/R^2) is neglected then the RMS misfit of the finite difference approximation reduces to $2.715m$ (c. 0.4% of the maximum deflection).

4.3.4 Sediment porosity

Backstripping provides the TTS for crustal reconstruction, so it is important to describe the mass of backstripped loads as accurately as possible. The role of sediment porosity in determining the mass of a sediment load of given thickness has already been described in Section 4.2.1. In the finite difference approximation the backstrip load is described in terms of a point-by-point thickness and mean density. For this reason spatial variations in mean porosity can be directly included without prior decompaction. Although not used in this thesis, spatial variations in any of the other model densities can be included in the finite difference approximation.

For the mean density $\overline{\rho_s}$ of a given sediment column:

$$\overline{\rho_s} = \overline{\phi}\rho_w + (1 - \overline{\phi})\rho_{sg} \tag{4.21}$$

in which ρ_{sg} and ρ_w are the sediment grain and water densities, and $\overline{\phi}$ is the mean porosity.

To determine $\overline{\phi}$, an empirical [Athy, 1930] porosity depth relationship can be applied, whereby:

[6] In the example, T_e is $37km$, R is $6.35 \times 10^3 km$, and E is $8.35 \times 10^{10} Nm^{-2}$, such that $(ET_e/R^2) = 76.6 Nm^{-3}$ and is used in summation with ρ_1 which has a magnitude of the order of $10^4 Nm^{-3}$.

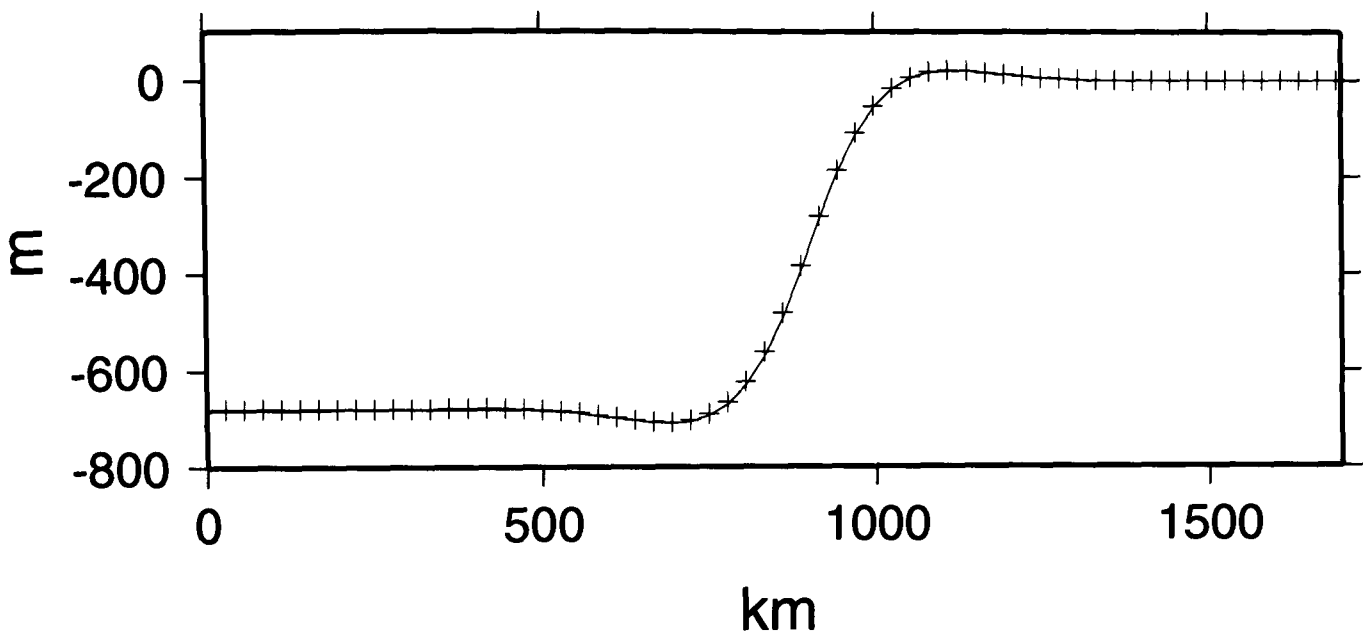


Figure 4.12: Comparison between the finite difference solution (solid line) and the analytical solution of Brotchie & Silvester [1969] (crosses) for flexure of a uniform elastic thickness plate due to a 900km radius uniform disc load. See Table 4.1 for model parameters and *cf.* Figure 4.7, Figure 4.10 and Figure 4.11.

$$\phi(z) = \phi_0 e^{-kz} \tag{4.22}$$

in which the decrease of porosity, ϕ, with thickness of overlying sediment, z, is dependent on the decay constant, k, and on the surface porosity, ϕ_0. ϕ_0 and k can be selected using either: the observed porosity depth distribution from well data or seismic velocities; or empirical porosity-depth curves based on a particular lithology (e.g. Korvin [1984]).

Athy's empirical solution is both well established and simple to implement. The mean porosity, $\overline{\phi}$, can be calculated by integrating ϕ_z from the top of the column to the base:

$$\overline{\phi} = \frac{\int_0^Z \phi(z)dz}{Z} = \frac{\int_0^Z (\phi_0 e^{-kz})dz}{Z} = \frac{\phi_0}{kZ}(1 - e^{-kZ}) \tag{4.23}$$

This can be used to calculate the mean density in Equation (4.21).

The use of $\overline{\rho_s}$ in backstripping depends on the loading environment. In Equation (4.13) the density contrast between the load and the material it displaces, $\Delta\rho_2$, is given by:

$$\begin{aligned} \Delta\rho_2 &= \overline{\rho}_s \quad Subaerial \\ \Delta\rho_2 &= \overline{\rho}_s - \rho_w \quad Marine \end{aligned} \tag{4.24}$$

There is also a special case in which the basement elevation is below sea level, but the sediment surface is above sea level with a topographic elevation, t. In this case there is a sediment thickness, $Z - t$, below sea level:

$$\Delta\rho_2 = \overline{\rho}_s - \frac{Z-t}{Z}\rho_w \tag{4.25}$$

The *in situ* thickness of sediment is already defined when backstripping. Therefore it is assumed that the infill density refers to that part of the flexure that has not been filled by sediment (e.g. peripheral bulges). The substrate density is that of the mantle. Hence:

$$\begin{aligned} \Delta\rho_1 &= \rho_m \quad Subaerial \\ \Delta\rho_1 &= \rho_m - \rho_w \quad Marine \end{aligned} \tag{4.26}$$

4.4 Calculation of the stretching factor, β

4.4.1 McKenzie-type rift

The backstripped total tectonic subsidence, TTS, is used to derive the stretching factor, β. In this thesis a McKenzie-type rift model is used for the 3-D models in which β is the ratio of normal to extended crustal thickness, and is attained by Airy-type local isostatic compensation of the TTS:

$$\begin{aligned} \beta &= \left[1 - \frac{TTS}{t_c}\left(\frac{\rho_m}{\rho_m - \rho_c}\right)\right]^{-1} \quad Subaerial \\ \beta &= \left[1 - \frac{TTS}{t_c}\left(\frac{\rho_m - \rho_w}{\rho_m - \rho_c}\right)\right]^{-1} \quad Marine \end{aligned} \tag{4.27}$$

Although β can be reasonably estimated in this way for post-rift reconstruction, it should be noted that the component of thinning attributable to extension (rather than processes associated with erosion, sedimentation, and lower crustal flow; see Chapter 2, Section 6.5) may be as little as half of the apparent extension factor.

4.4.2 Depth of necking model

The McKenzie-type rift model results in a TTS that is compensated at the Moho through Airy-type local isostasy. Because significant lithospheric rigidity may persist throughout rifting, this thesis also includes 2-D 'depth of necking' reconstructions (see Chapter 2, Section 6.4, for description and limitations) for comparison against sections from the 3-D Airy-type reconstructions.

Repeating Equation (2.19) for the net restoring force corresponding to an initial isostatic imbalance due to crustal necking:

$$q_{net} = [S_M(\rho_m - \rho_c) + S_T(\rho_w - \rho_c)]\, g \tag{4.28}$$

in which S_M and S_T are the kinematic Moho and topography due to rifting:

$$\begin{aligned} S_T &= TTS - w \\ S_M &= \left(1 - \frac{1}{\beta}\right) t_c - S_T \\ &= \left(1 - \frac{1}{\beta}\right) t_c - TTS + w \end{aligned} \tag{4.29}$$

in which w is the flexure driven by q_{net}, and:

$$\begin{aligned} S_T &= \left(1 - \frac{1}{\beta}\right) z_{neck} \\ \therefore \left(1 - \frac{1}{\beta}\right) &= \frac{S_T}{z_{neck}} \\ &= \left(\frac{TTS - w}{z_{neck}}\right) \end{aligned} \tag{4.30}$$

which when substituted into Equation (4.29) gives:

$$S_M = \left(\frac{TTS - w}{z_{neck}}\right) t_c - TTS + w \tag{4.31}$$

Now, using the uniform thin plate flexure equation for 2-D loading (Equation (4.5)), assuming no horizontal forces ($P = 0$), and substituting q_{net} for $q(x) - q'(x)$:

$$\begin{aligned} D\frac{d^4w}{dx^4} &= [S_M(\rho_m - \rho_c) + S_T(\rho_w - \rho_c)]\, g \\ &= \left(\left[\frac{TTS - w}{z_{neck}} t_c - TTS + w\right][\rho_m - \rho_c] + [TTS - w][\rho_w - \rho_c]\right) g \end{aligned} \tag{4.32}$$

Which rearranges to:

$$D\frac{d^4w}{dx^4} + \left(\rho_w - \rho_m + \frac{t_c}{z_{neck}}(\rho_m - \rho_c)\right) gw = TTS\left(\rho_w - \rho_m + \frac{t_c}{z_{neck}}(\rho_m - \rho_c)\right) g \tag{4.33}$$

This can be solved using a Fourier solution as in Section 4.3.1 by substituting:

$$\begin{aligned} \rho_w - \rho_m + \frac{t_c}{z_{neck}}(\rho_m - \rho_c) &\equiv \Delta\rho_1 \\ \left(\rho_w - \rho_m + \frac{t_c}{z_{neck}}(\rho_m - \rho_c)\right) TTS &\equiv \Delta\rho_2 h \end{aligned} \tag{4.34}$$

Finally:

$$\left(1-\frac{1}{\beta}\right) z_{neck} = S_T$$
$$\therefore \beta = \frac{z_{neck}}{S_T + z_{neck}}$$
$$\therefore \beta = \frac{z_{neck}}{TTS - w + z_{neck}} \tag{4.35}$$

4.5 Gravity modelling

In this thesis gravity anomalies are derived using either a 2-D direct line integral method [Talwani *et al.*, 1959] for which the precision is limited only by that of the original data, or a 3-D 'Parker's method' approximation [Parker, 1972], in which the precision is limited by the number of terms in a Taylor series expansion.

4.5.1 Direct integral method

The gravity anomaly due to a buried body is described by a volume integral in which contributions from infinitesimal masses, dm, are summed. In this thesis a line integral method [Talwani *et al.*, 1959] is used to calculate gravity anomalies due to 2-D structure that is infinite in the third dimension.

Beginning with the gravitational potential, U, due to a point mass, dm, of density ρ, at a distance, R:

$$U = -\int_V \frac{G dm}{R} = -G\rho \int_V \frac{1}{R} d^3R \tag{4.36}$$

Which in Cartesian coordinates can be used to derive the potential anomaly ΔU due to an anomalous 3-D body of relative density $\Delta\rho$:

$$\begin{aligned} R &= \sqrt{x^2+y^2+z^2} \\ \therefore \Delta U &= -G\rho \int_V \left(x^2+y^2+z^2\right)^{-\frac{1}{2}} dxdydz \end{aligned} \tag{4.37}$$

If the body is of infinite extent and uniform cross section in y then this can be reduced to 2-D:

$$\begin{aligned} \Delta U &= -G\Delta\rho \int_S \left[\int_{-\infty}^{\infty} \left[x^2+y^2+z^2\right]^{-\frac{1}{2}} dy\right] dxdz \\ &= -G\Delta\rho \int_S ln\left[x^2+z^2\right]^{\frac{1}{2}} dxdz \end{aligned} \tag{4.38}$$

The gravity anomaly, Δg, is the vertical gradient of the potential anomaly:

$$\Delta g = \frac{\partial U}{\partial z} = \frac{\partial U}{\partial r}\frac{\partial r}{\partial z} \tag{4.39}$$

in which:

$$\begin{aligned} r &= \sqrt{x^2 + z^2} \\ \therefore \frac{\partial r}{\partial z} &= \frac{z}{\sqrt{x^2 + z^2}} \end{aligned} \tag{4.40}$$

Such that:

$$\begin{aligned} \Delta g &= -2G\Delta\rho \int_S \frac{1}{\sqrt{x^2 + z^2}} \frac{z}{\sqrt{x^2 + z^2}} dxdz \\ &= -2G\Delta\rho \int_S \frac{z}{x^2 + z^2} dxdz \end{aligned} \tag{4.41}$$

Converting to polar coordinates ($x = rsin\theta, z = rcos\theta, dxdz = rdrd\theta$):

$$\begin{aligned} \Delta g &= -2G\Delta\rho \oint \frac{rcos\theta}{r^2} rdrd\theta \\ &= -2G\Delta\rho \oint cos\theta drd\theta \end{aligned} \tag{4.42}$$

Integration with respect to r gives:

$$\Delta g = -2G\Delta\rho \int_0^{2\pi} rcos\theta d\theta = -2G\Delta\rho \oint z d\theta \tag{4.43}$$

This line integral can be evaluated by approximating the body as an n-sided polygon (Figure 4.13) as described by Talwani *et al.* [1959]. Solving the integral along each side:

$$\oint z d\theta \approx \sum_{i=1}^{n} \int_{P_i}^{P_{i+1}} z d\theta \tag{4.44}$$

At a given point Q:

$$z = (x - a)tan\phi \tag{4.45}$$

where ϕ is the angle from horizontal of the polygon side that Q lies on, and a is the point of intersection between that line and the x-axis (see Figure 4.13).

From similar triangles:

$$x(tan\phi - tan\theta) = atan\phi \tag{4.46}$$

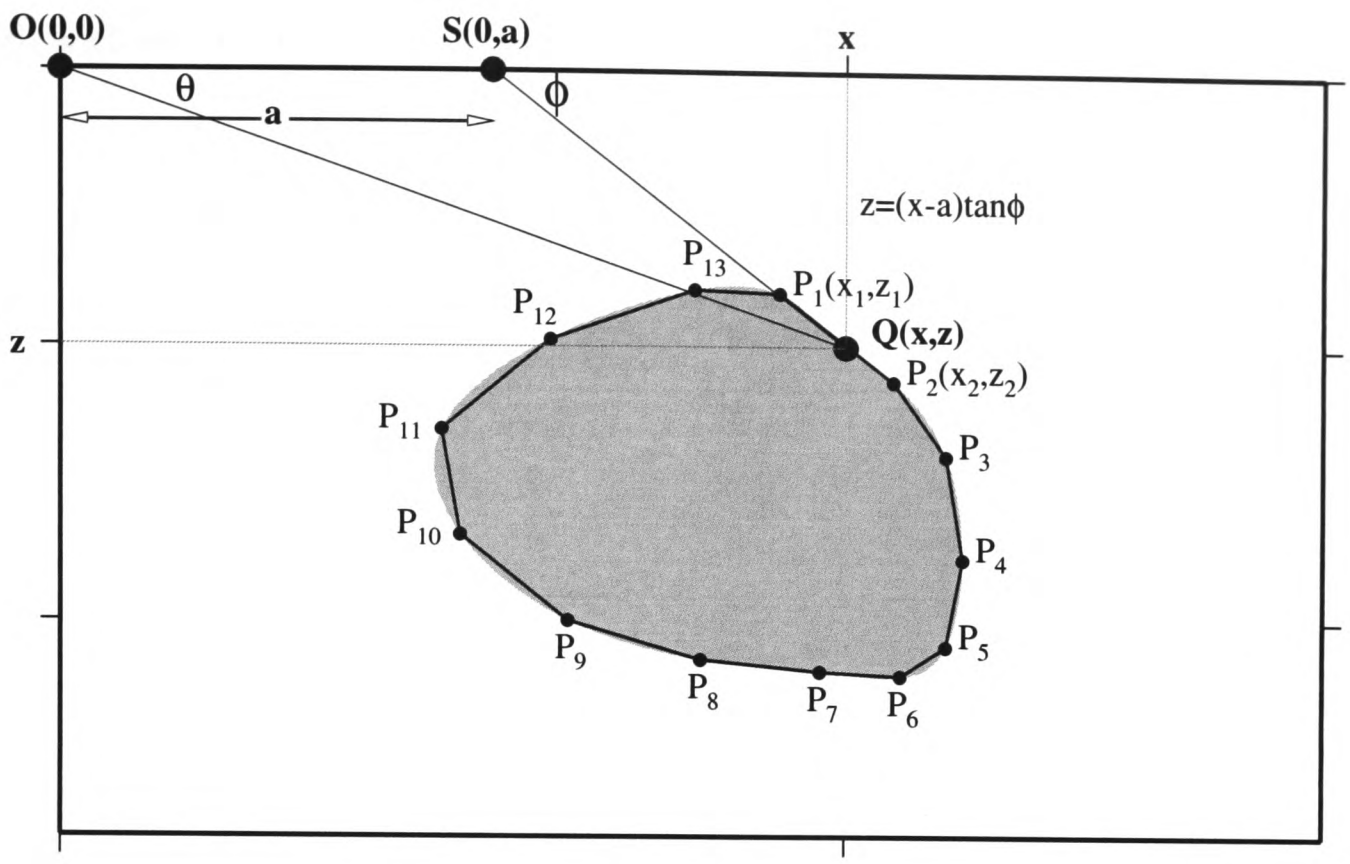


Figure 4.13: Line integral method of calculating the gravity anomaly due to a 2-D body by approximating its geometry as a 2-D polygon. Positions, $P_i(x_i, z_i)$ are relative to the observation point O(0, 0).

where θ is the angle relative to the horizontal of a line from O to Q. Substituted into Equation (4.45):

$$\begin{aligned} z &= \left[\frac{a tan\phi}{tan\phi - tan\theta} - a\right] tan\phi \\ &= a tan\phi \left[\frac{tan\phi}{tan\phi - tan\theta} - 1\right] \\ &= \frac{a tan\phi tan\theta}{tan\phi - tan\theta} \end{aligned} \tag{4.47}$$

and therefore:

$$\begin{aligned} \int_{P_i}^{P_{i+1}} z d\theta &\equiv \int_{\theta_i}^{\theta_{i+1}} \frac{a tan\phi tan\theta}{tan\phi - tan\theta} d\theta \\ &= a sin\phi cos\phi \left[(\theta_i - \theta_{i+1}) + tan\phi ln\left(\frac{cos\theta_i \left[tan\theta_i - tan\phi_i\right]}{cos\theta_{i+1}\left[tan\theta_{i+1} - tan\phi_i\right]}\right)\right] \end{aligned} \tag{4.48}$$

Now,

$$\begin{aligned} cos\phi_i &= \frac{x_{i+1} - x_i}{\sqrt{(x_{i+1} - x_i)^2 + (z_{i+1} - z_i)^2}} \\ sin\phi_i &= \frac{z_{i+1} - z_i}{\sqrt{(x_{i+1} - x_i)^2 + (z_{i+1} - z_i)^2}} \\ tan\phi_i &= \frac{z_{i+1} - z_i}{x_{i+1} - x_i} \end{aligned} \tag{4.49}$$

which with substitution and rearranging gives:

$$\int_{P_i}^{P_{i+1}} z d\theta = \left(\frac{x_i z_{i+1} - z_i x_{i+1}}{[x_{i+1} - x_i]^2 + [z_{i+1} - z_i]^2} \right) \cdot \left([x_{i+1} - x_i] [\theta_i - \theta_{i+1}] + [z_{i+1} - z_i] ln \frac{r_{i+1}}{r_i} \right) \quad (4.50)$$

In which $r_i = (x_i^2 + z_i^2)^{1/2}$.

Hence:

$$\Delta g = -2G\Delta\rho \sum_{i=1}^{n} \left(\frac{x_i z_{i+1} - z_i x_{i+1}}{[x_{i+1} - x_i]^2 + [z_{i+1} - z_i]^2} \right) \cdot \left([x_{i+1} - x_i] [\theta_i - \theta_{i+1}] + [z_{i+1} - z_i] ln \frac{r_{i+1}}{r_i} \right) \quad (4.51)$$

where n is the number of polygon sides.

This solution can be readily evaluated at any observation point using a polygon extracted directly from the body data.

4.5.2 Parker's method

The line integral method described above is in common use for the calculation of 1-D gravity anomalies and similar methods exist for direct calculation of 2-D potential anomalies. However, direct 3-D methods are numerically intensive, and hence time consuming. In order to calculate 2-D gravity anomalies more efficiently, Parker's 'method for the rapid calculation of potential anomalies' [Parker, 1972] can be used. The full derivation of the method is too long to detail here, so only the principles of the method are described.

Parker's method expands from a Fourier domain solution of the volume integral for gravitational potential, U, on a surface, z_0, due to a layer of anomalous material confined by an overlying surface[7], z_1.

The volume integral is explicitly integrated to form a surface integral in terms of z_1 and a mean plane z_2. Solution of the z-integral provides a surface integral for U in x and y.

Finally, using $\Delta g = \partial U / \partial z$ a Fourier expression for the gravity anomaly that can be solved through Taylor expansion is obtained:

$$\mathcal{F}[\Delta g] = -2\pi G \Delta\rho e^{-|k|z_0} \sum_{n=1}^{\infty} \frac{(\mid k \mid)^{n-1}}{n!} \mathcal{F}[(z_1)^n - (z_2)^n] \quad (4.52)$$

[7]Anomalies due to bodies confined by an underlying surface can be calculated in the same way by changing the polarity of z_1

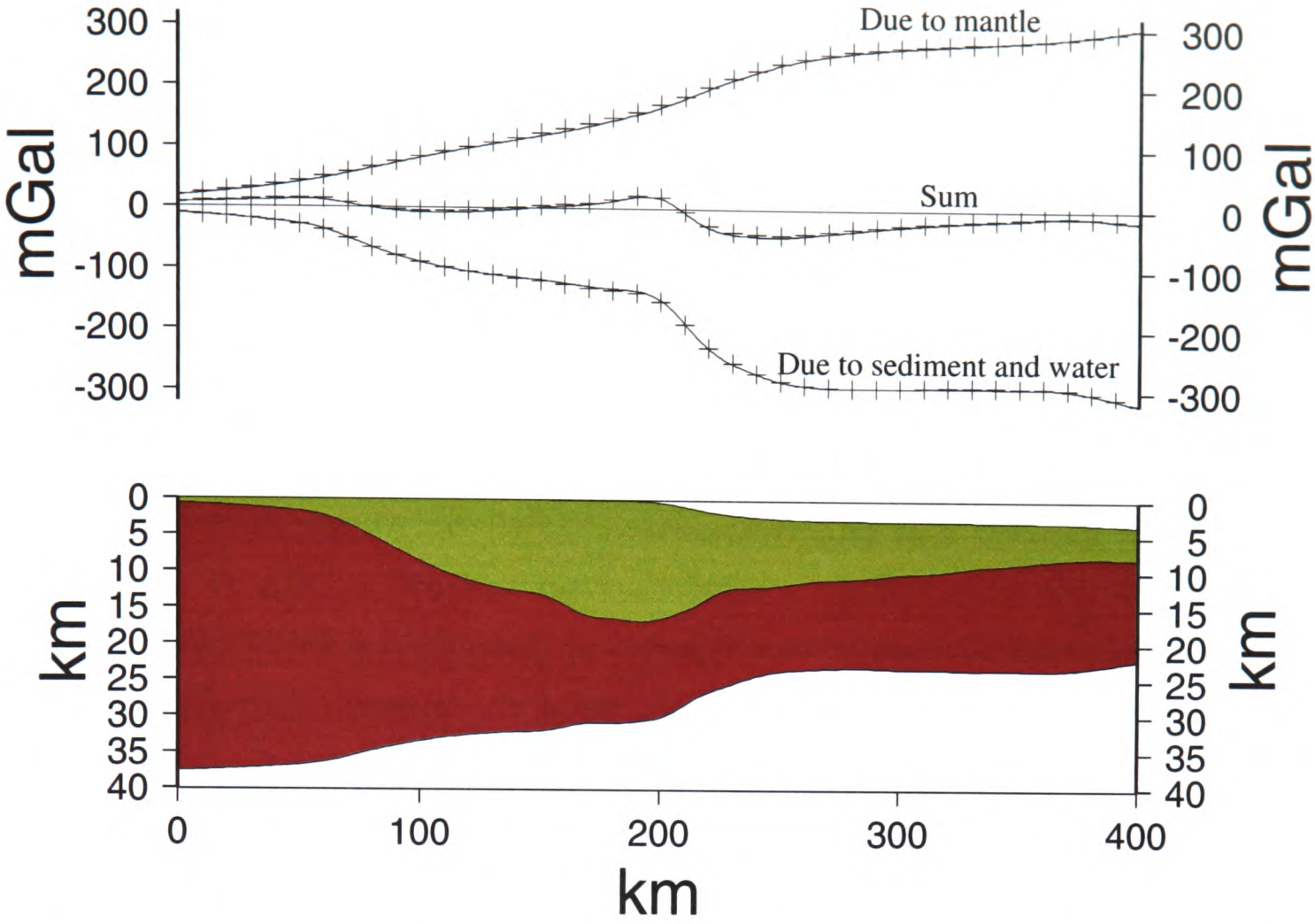


Figure 4.14: Comparison of gravity anomalies approximated using Parker's method (solid lines) with those from an exact line integral method (crosses). The gravity anomaly is the sum of anomalies due to sediment and water (lower line) and due to mantle material (upper line).

where $\mathcal{F}$ represents a Fourier transformed variable. Because $n!$ increases rapidly relative to $(z_i)^n$ the series converges rapidly, and only low order terms ($n \leq 4$) are generally needed.

The expansion given above is for a 2-D body - as in Parker [1972] - but the extension to 3-D is simply a matter of replacing k with $\sqrt{(k_x^2 + k_y^2)}$ where k_x and k_y are the wave numbers in x and y.

Finally, the anomaly is elevated from the mean plane, z_2, to the plane of observation, z_d, using an infinite slab formula:

$$\Delta g \mid_{z_d} = \Delta g \mid_{z_2} -2\pi G(z_2 - z_d)\Delta\rho \tag{4.53}$$

Figure 4.14 shows gravity anomalies approximated using Parker's method ($n \leq 4$) against anomalies calculated using an exact line integral method. In the example shown the RMS error on the sum anomaly is $2.81 mGal$ (c.4.3% of the peak amplitude).

4.5.3 Spatial variations in density

Up to this point only gravity anomalies due to uniform density bodies have been considered. This may be reasonable on a broad scale for the crust and mantle, at least in the absence of confining data. However - in addition to the direct effect on gravity anomalies - spatial variations in the sediment density due to facies changes and compaction have a direct influence on the geometry of the flexure due to the sediment load, and hence on the backstrip and crustal reconstruction geometries.

In this thesis, spatial variations in sediment density due to compaction are allowed for when backstripping by calculating a mean density for each sediment column (Section 4.3.4). In order to conserve the mass balance established by backstripping and crustal reconstruction it is necessary to incorporate those same variations in the gravity anomaly derivations. However, unlike the plate flexure, the gravity anomaly is sensitive to the full 3-D distribution of sediment density.

The problem of 3-D variations in sediment porosity is addressed by treating the sediment mass as a series of stacked thin slivers, each of approximately uniform density (Figure 4.15), and $100m$ thickness. Gravity anomalies corresponding to each sliver are then calculated before summation to give the full anomaly due to the sediment mass.

Although this method robustly approximates the actual mass distribution, it is not particularly efficient. For a basin of greater than $10km$ maximum depth, it requires calculation of more than 100 distinct 2-D gravity anomalies. In the case of the process-oriented method sedimentation anomaly, separate 'load' and 'infill' anomalies must be calculated; doubling the numerical effort.

4.5.4 Efficient application of the process-oriented method

For a region of 512×512 data points, evaluation of Parker's method takes in the order of one minute per body anomaly (Sun Ultra 10, as before). If applied to the iterative process-oriented analysis in this thesis then each sedimentation anomaly would be calculated in around 3 hours for a $10km$ deep basin. As each iteration involves 11 models, this would bring the time per iteration to a minimum of 30 hours, plus the time taken by other stages in the analysis.

In order to improve efficiency a novel means of deriving rift-, sedimentation-, and sum- gravity anomalies is presented. Rearrangement of the traditional process-oriented method reduces the *total* time per iteration (including all the process-oriented stages) to around 1 hour.

In the standard process-oriented method, gravity anomalies are calculated for the rift

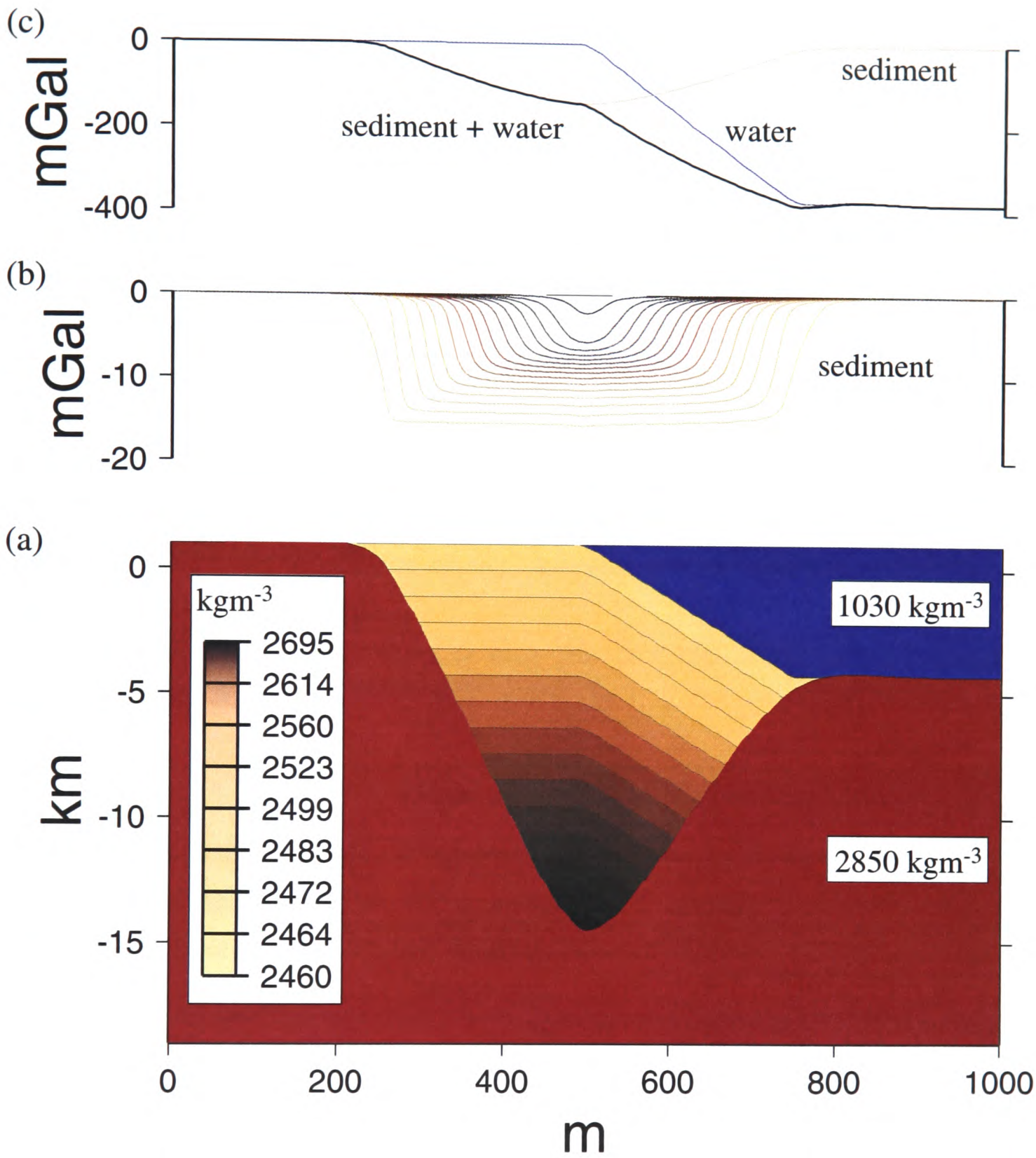


Figure 4.15: Calculation of gravity anomalies due to a sediment wedge of varying density with depth. (a) The sediment is divided into slivers of approximately uniform density. (b) Gravity anomalies due to replacement of crust by each sliver are calculated. (c) Summation of the anomalies gives the total sediment anomaly which can then be combined with other anomalies (in this case the anomaly due to replacement of crust with water).

geometry, and for the effects of sedimentation (cf. Section 4.2). Summation of these two anomalies gives the sum anomaly as in Figure 4.16a:

$$G_{sum} = G_{rift} + G_{sed} \tag{4.54}$$

In which G_{sum}, G_{rift}, and G_{sed} are the sum-, rift-, and sedimentation- gravity anomalies respectively.

However, the sum anomaly contributions of sediment and water are dictated by the known water depth and sediment wedge geometry. The gravity anomaly due to these bodies is here named the 'super-crustal anomaly', or G_{upper} (Figure 4.17a), and is not affected by the crustal reconstruction.

Summation of G_{upper} with gravity anomalies due to the rifted Moho (Figure 4.17b) and flexure of the Moho to its present-day position (Figure 4.17c) gives the process-oriented sum gravity anomaly (Figure 4.17d).

The rifting gravity anomaly, G_{rift} (Figure 4.17e), is then given by summing the gravity anomaly from the rift topography, $G_{rifttopo}$ with the (already calculated) rift Moho gravity anomaly, $G_{riftmoho}$.

Finally, the sedimentation anomaly G_{sed} (Figure 4.17f) is derived by rearranging Equation (4.54), such that:

$$G_{sed} = G_{sum} - G_{rift} \tag{4.55}$$

This identically completes the sequence of anomalies required by the traditional process-oriented method (Figure 4.16b) without direct calculation of distinct load and infill sediment contributions for each iteration. After the initial calculation of G_{upper} (in which sediment porosity can be included), only a small number of gravity anomalies due to uniform density bodies (the rift topography, rift Moho, and Moho flexure) need be calculated during the iterative analysis.

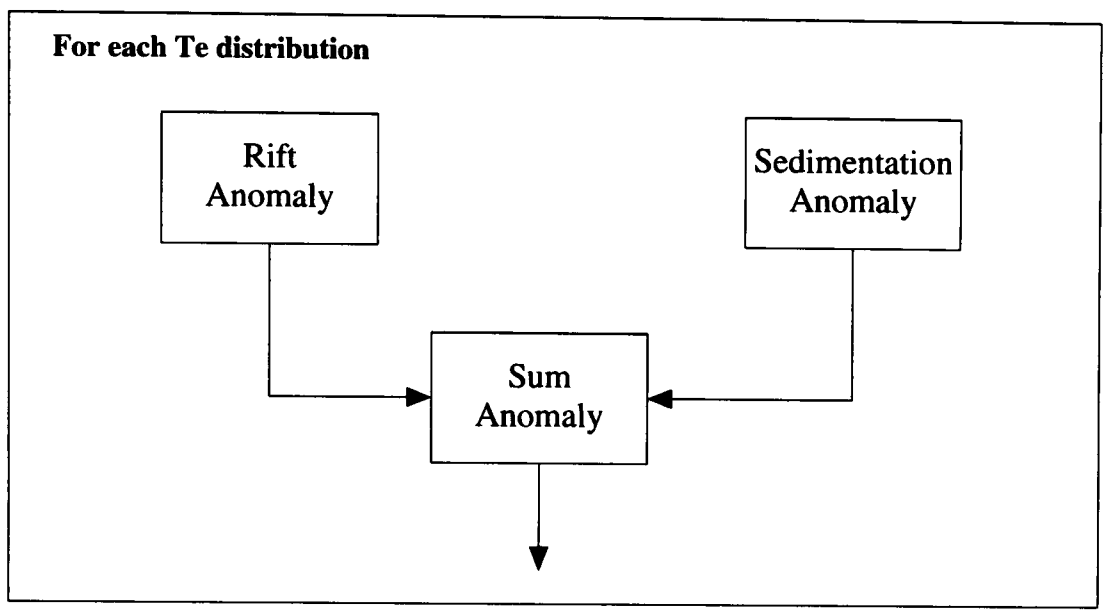
4.6 Constraint of effective elastic thickness

The final iterative step is revision of the effective elastic thickness distribution through minimisation of RMS differences between observed and calculated free-air gravity anomalies ($G_{free\text{-}air}$ and G_{sum} respectively). For this purpose, a 'flexural isostatic gravity anomaly'[8], γ, is defined where:

$$\gamma = G_{free\text{-}air} - G_{sum} \tag{4.56}$$

[8]Comparable to a traditional Airy isostatic isostatic gravity anomaly.

(a) Traditional process-oriented method



(b) Adapted process-oriented method

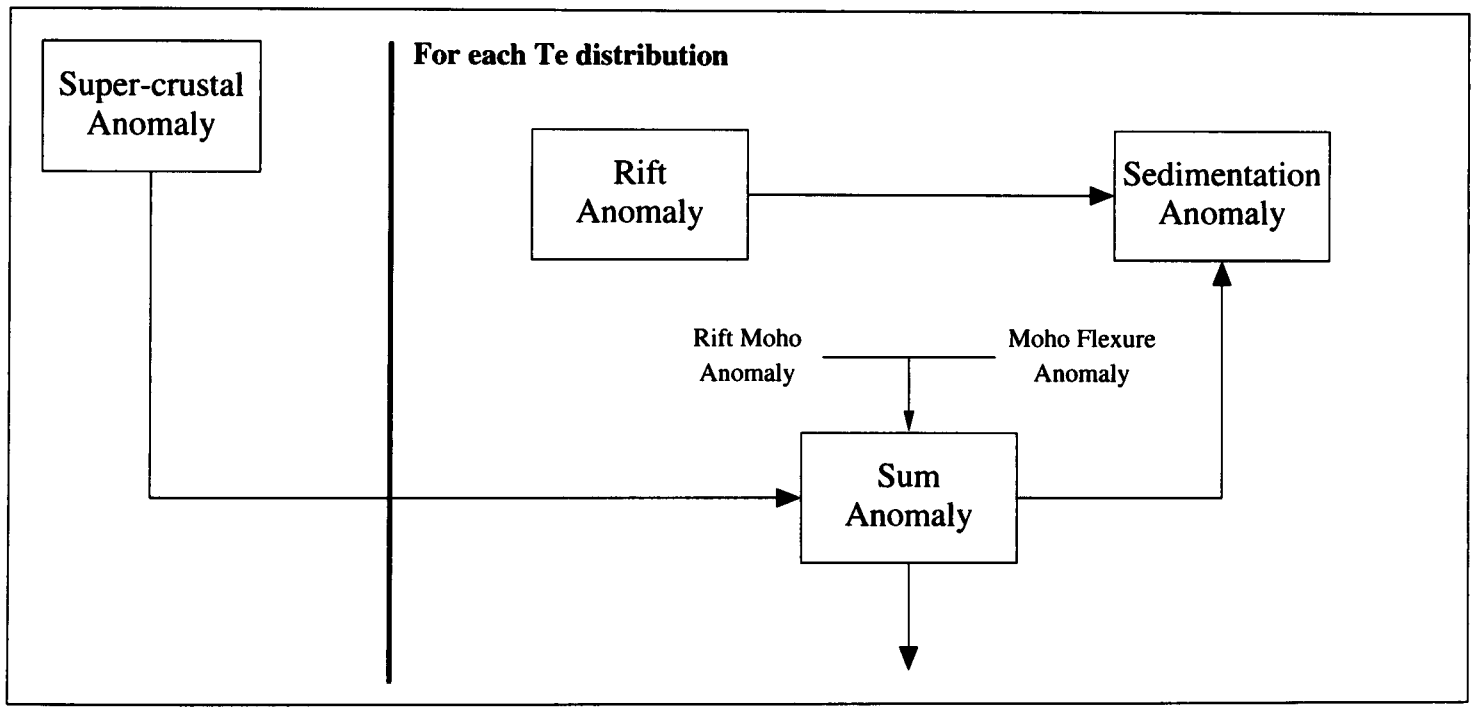


Figure 4.16: An alternative approach to calculation of process-oriented gravity anomalies in an iterative method. The traditional method (a) has been adapted (b) to allow a single calculation of a summed sediment and water ('super-crustal') gravity anomaly to be repeatedly re-used in derivation of sum and sedimentation anomalies.

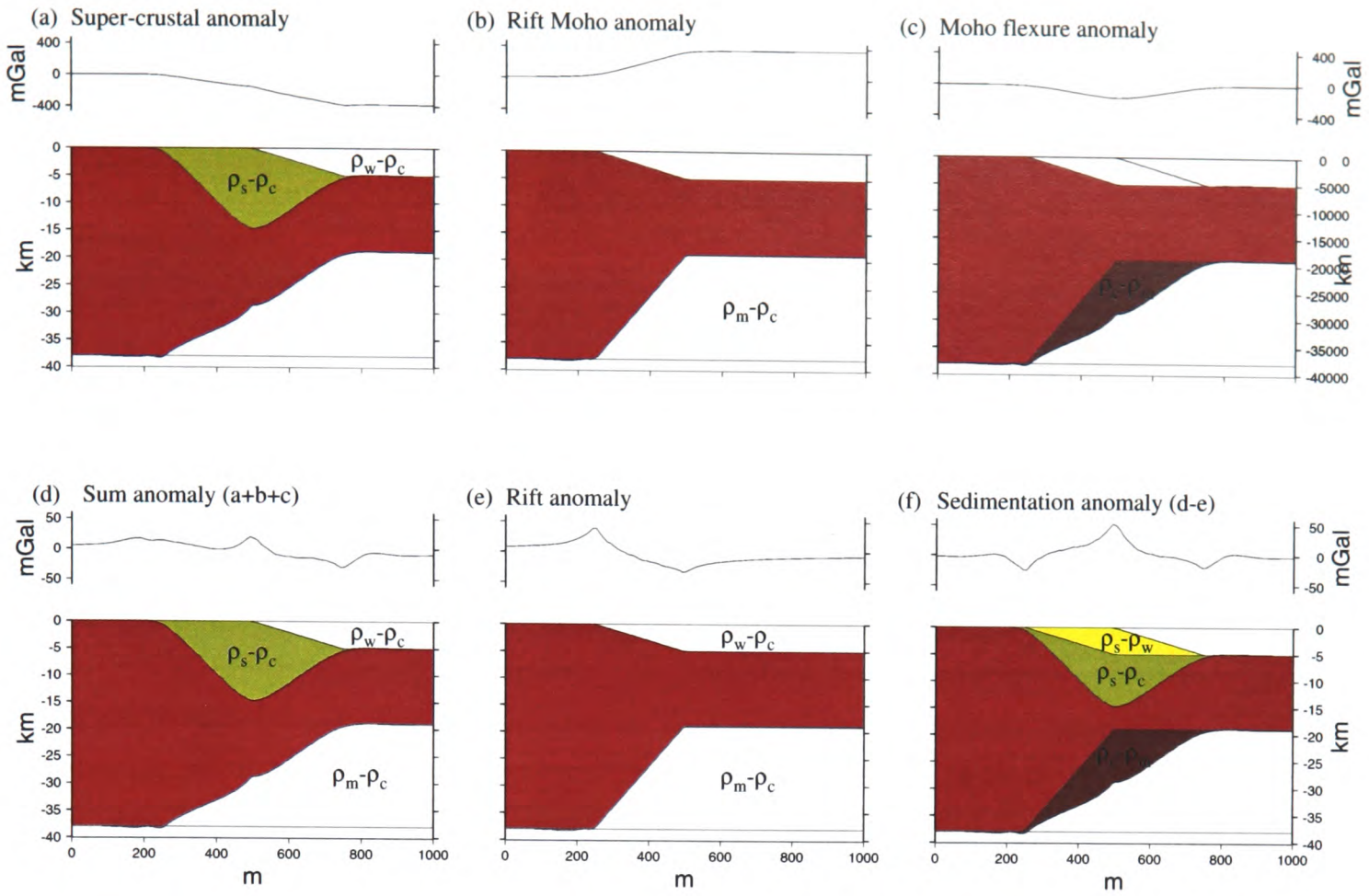


Figure 4.17: Bodies and density contrasts relating to each component of an alternative method of process-oriented gravity modelling. (a) Super-crustal anomaly. (b) Rift Moho anomaly. (c) Moho flexure anomaly. (d) Sum anomaly, (a)+(b)+(c). (e) Rift anomaly. (f) Sedimentation anomaly, (d)-(e). ρ_c = crustal density; ρ_w = water density; ρ_m = mantle density; ρ_s = sediment density.

In grid form this can be used to compare the success of reconstructions based on different T_e distributions. Firstly the grids of γ for each reconstruction are divided into overlapping windows. Within each of these windows the RMS γ value for each T_e distribution is calculated, and the distribution corresponding to the smallest RMS flexural isostatic gravity anomaly determined.

In order to minimise biases due to the locations of window edges, each window overlaps by half its width with those adjacent to it. The window dimensions are selected by trial and error determination of the most rapid RMS minimisation.

This method of selection is applied to 11 models per iteration. The revised T_e values that result are surfaced to the grid interval, and are then bandpass filtered to remove short wavelength features that could cause problems in evaluation of the rigidity derivatives. This T_e distribution is the base for the next iteration in which the next 11 reconstructions are made using variable elastic plates ranging in thickness from $5km$ below ($T_e >= 0km$) to $5km$ above ($T_e <= 100km$) in $1km$ intervals.

An identical approach is applied in selection of the T_e distribution for the first iteration, except that RMS gravity anomaly minimisation is applied to 101 *uniform* plate

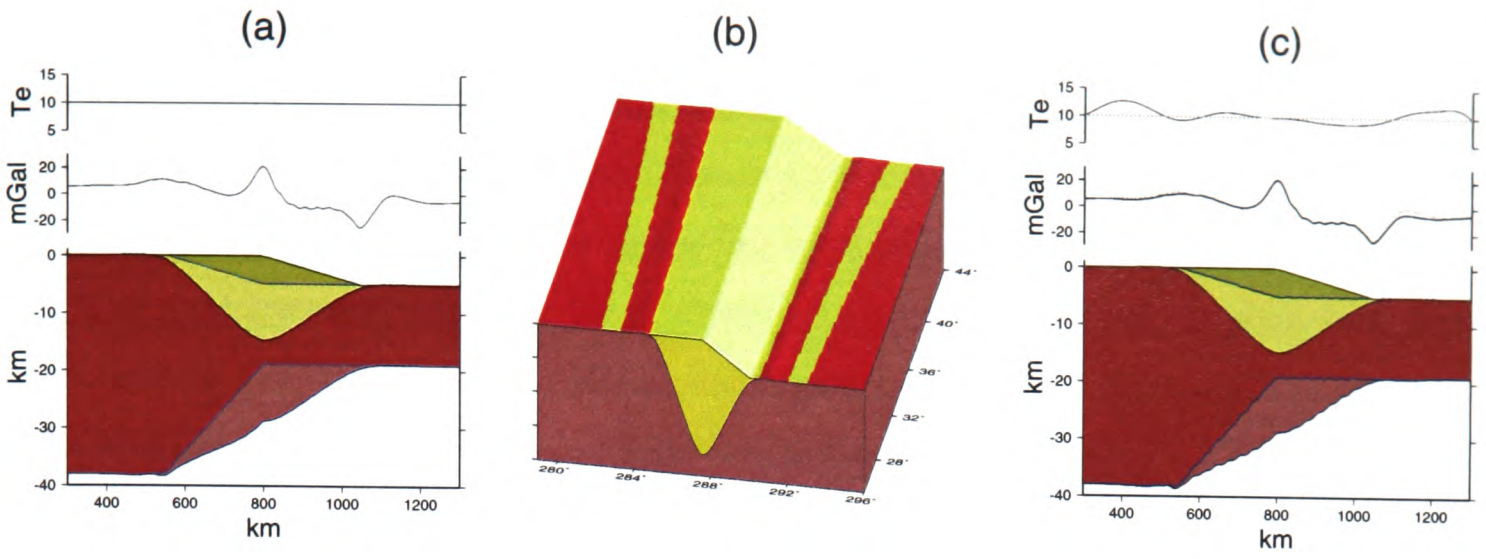


Figure 4.18: Synthetic recovery of effective elastic thickness. (a) A simple rifted margin (blue lines) is loaded by a simple wedge of sediments (dark yellow) with sediment infilled flexure (pale yellow). Flexure ($T_e = 10km$) depresses the Moho (brown). (b) Projection onto a geographic grid gives a synthetic 'observed' sediment distribution and topography (shown), and gravity anomaly (not shown). (c) Transect through the center of the structure recovered through process-oriented analysis, together with the sum (solid line) and 'observed' (feint line) gravity anomalies, and the recovered T_e.

$(T_e = 1km, 2km, 3km, ..., 100km)$ reconstructions.

The iterative process is halted when (in the region of best data) the mod-mean variations in T_e distribution are small from one iteration to the next.

4.7 Robustness of the method

In this thesis backstripping and margin reconstruction techniques are used to assess the relationship between effective elastic thickness and the evolution of a passive continental margin. The adaptations that have been made to the process-oriented method as presented here are previously untested, and it is not obvious whether the assumptions made can be reliably applied to a region of large lateral extent.

For this purpose an independent elastic plate model has been used to generate a synthetic passive margin type sedimentary basin that will act as the reference for process-oriented reconstruction.

To produce the basin an initial rift geometry in local isostatic balance is sediment loaded with a flexural response determined by a fixed effective elastic thickness (Figure 4.18). The rift is defined by a total tectonic subsidence that grades linearly over a $250km$ distance from $0km$ to a constant depth of $5km$ below sea level. The associated Moho geometry is derived assuming local Airy isostasy and water, crust, and mantle densities of $1030kgm^{-3}$, $2850kgm^{-3}$, and $3330kgm^{-3}$ respectively.

To this synthetic margin a triangular 'load' wedge of sediments of $250km$ half-width,

$5km$ peak thickness, and $2600kgm^{-3}$ density is added. The flexure due to this load plus sediment infill of the same density is calculated using a Fourier method (Section 4.3.2) and an effective elastic thickness of $10km$ (Figure 4.18a). The corresponding 'observed' free-air gravity anomaly is calculated using the line integral method described in Section 4.5.1.

Note that because a Fourier based elastic plate solution is used, implicit infill contributions to the flexure apply whether the flexure is upward or downward, resulting in false amplification of any upwarps peripheral to the basin flexure.

If erosion were included in the model then the rift flank upwarp would be greatly eroded, causing additional isostatic flexural uplift, and hence subaerial erosion, across the early basin shelf. According to modelling by van Balen *et al.* [1995] this process could produce offlap of the early postrift basin sequences extending by as far as 20km from the hinge zone. They found that significant onlap would only follow if other processes produced a rise in regional relative sea-level against lesser late-postrift uplift rates.

Projection of the 2-D data onto a geographic grid (Figure 4.18b) provides 3-D data for the process-oriented analysis. Only the sum gravity anomaly, basement shape, and topography are projected because the analysis is required to recover the T_e distribution and Moho structure.

The analysis recovers the effective elastic thickness to within $\pm 1km$ across most of the region (Figure 4.18c). However, there is an increase in apparent T_e across the peripheral bulges, which is accompanied by a small degradation in the agreement between the 'observed' and calculated free-air anomalies.

The problems over the peripheral bulges are a consequence of their over-amplification during construction of the loaded margin. This results in a geometry that cannot be matched using the constructed sediment thickness data. A local increase in T_e across the bulges increases their vertical displacement during backstripping, and hence delocalises the differences between the original and recovered rift geometries. This, in turn, minimises the RMS flexural isostatic gravity anomaly in the area.

This test shows that the method is effective in recovering a simple basin geometry, T_e structure, and associated gravity anomaly. It is also seen that the method behaves in a stable and explicable manner when presented with inconsistent data. Questions of analysis sensitivity and the uniqueness of the RMS minimisation method are dealt with in the context of real data in Chapter 5, Section 3.

Chapter 5

Process-oriented analysis - Results

5.1 Introduction

Structural segmentation is an inferred feature of the Eastern USA passive continental margin (see Chapter 3), but has yet to be quantified in terms of identifiable processes. This, together with data availability, makes it an ideal location to apply a process-oriented analysis (see Chapter 4) that quantifies structural segmentation in the form of spatial variations in effective elastic thickness.

Gridded shipboard gravity data is readily available from the Decade of North American Geology (DNAG) database (see Chapter 3, Section 6.1). High quality sediment isopach grids from the USGS (courtesy of Debbie Hutchinson, USGS, Woods Hole) have been correlated with other sources; allowing the post-rift sequence to be expanded in the form of 7 isopachs extending from the fall line to the abyssal plain (see Chapter 3, Section 6.1).

This chapter presents application of process-oriented analysis methods (see Chapter 4) with compensation of the post-rift sediment load by: Airy isostasy; uniform thickness thin elastic plate flexure; and variable thickness elastic plate flexure. In the latter case, variations in T_e of the rifted lithosphere are constrained by iterative minimisation of the 'isostatic gravity anomaly' (IGA), which is the difference between the observed and modelled free-air gravity anomaly (see Table 5.1.

Finally, a method in which T_e is controlled by an isotherm depth in the cooling oceanic plate forms the core of an analysis in which sediments are accommodated in a manner characteristic of oceanic plates. This adds to discussion of the iterative T_e distribution in Chapter 6.

Gravity Anomaly	Acronym	Definition
Observed		
Free-air	FA	Gridded DNAG shipboard gravity data after processing described in Chapter 3, Section 6.1.
Process-oriented		
Rifting		Calculated gravity effect of the topography at the time of rifting and its isostatic compensation.
Sedimentation		Calculated gravity effect of the sediment load and its isostatic compensation.
Sum		Calculated gravity anomaly for the sediment loaded margin (rifting anomaly + sedimentation anomaly). Can also be termed 'calculated free-air anomaly'.
Isostatic (observed-calculated FA anomaly)		
Airy	Airy IGA	IGA for a model in which local Airy isostasy is assumed for the crustal column, including sediments. This follows the definition of Behn & Lin [2000], rather than that used by Simpson *et al.* [1986] (in which sediment thickness data were unavailable).
Flexural	Flexural IGA	Observed - IGA for a model in which sediment loading is flexurally compensated.
Root mean square	*RMS* IGA	Root mean square of the isostatic gravity anomaly. For the purpose of this thesis this is calculated where the sediment data is most reliable. I.e. a region bounded by the edges of the high quality USGS sediment data.

Table 5.1: Gravity anomaly definitions

Figure 5.1 shows the relief of the margin, together with the locations of the principle basins, fall line, shelf break (0.2km depth), platform break (2km depth), and deep seismic profiles [1].

5.2 Uniform plate models

The primary purpose of the process-oriented analysis is to resolve structural segmentation of the margin in the form of effective elastic thickness (T_e) variations. To do this, it must be shown that such an analysis is justified by Airy isostatic and uniform elastic plate flexural studies.

5.2.1 Airy isostasy

If the lithosphere is treated as infinitely weak ($T_e = 0km$) then the elastic plate model reduces to an Airy isostatic condition (i.e. all loads, including sediment, are locally compensated). This is the simplest form that the analysis can take.

The Airy isostatic gravity anomaly (Airy IGA, analysis constants in Table 5.2) retains many of the features of the free-air gravity anomaly (Figure 5.2), but the amplitudes are generally reduced. Where the sediment load is best defined (within the confines of the high quality USGS sediment isopach data, covering most of the shelf and continental slope), the RMS isostatic gravity anomaly is $18.7mGal$ ($\sim 64\%$ of the $29.3mGal$ RMS free-air anomaly in the same region).

However, there are instances where the amplitude of the Airy IGA is larger than that of the observed free-air anomaly. Prominent examples of this are amplification of the nearshore gravity low along the central part of the margin, and the creation of IGA highs seaward of the Georges Bank shelf break. These are areas where the calculated free-air gravity anomaly has a larger amplitude than the observed free-air anomaly.

Of particular interest to this study is the edge effect free-air gravity anomaly, the amplitude and form of which have been shown by Watts & Marr [1995] to be indicators of effective elastic thickness. Segmentation of the Airy isostatic anomaly along the edge effect high has already been observed at this margin (Behn & Lin [2000], see Chapter 3, Section 5.3), and is similarly observed in the Airy IGA derived in this study (Figure 5.3).

Comparison of the Airy IGA with the free-air gravity anomaly along this transect shows that subtraction of calculated Airy isostatic contributions significantly reduces the edge effect gravity high along most of the margin's length. However, the Airy isostatic

[1] 'Deep seismic' data is defined for this study as refraction and wide-angle reflection data with deep enough penetration to resolve deep crustal structure.

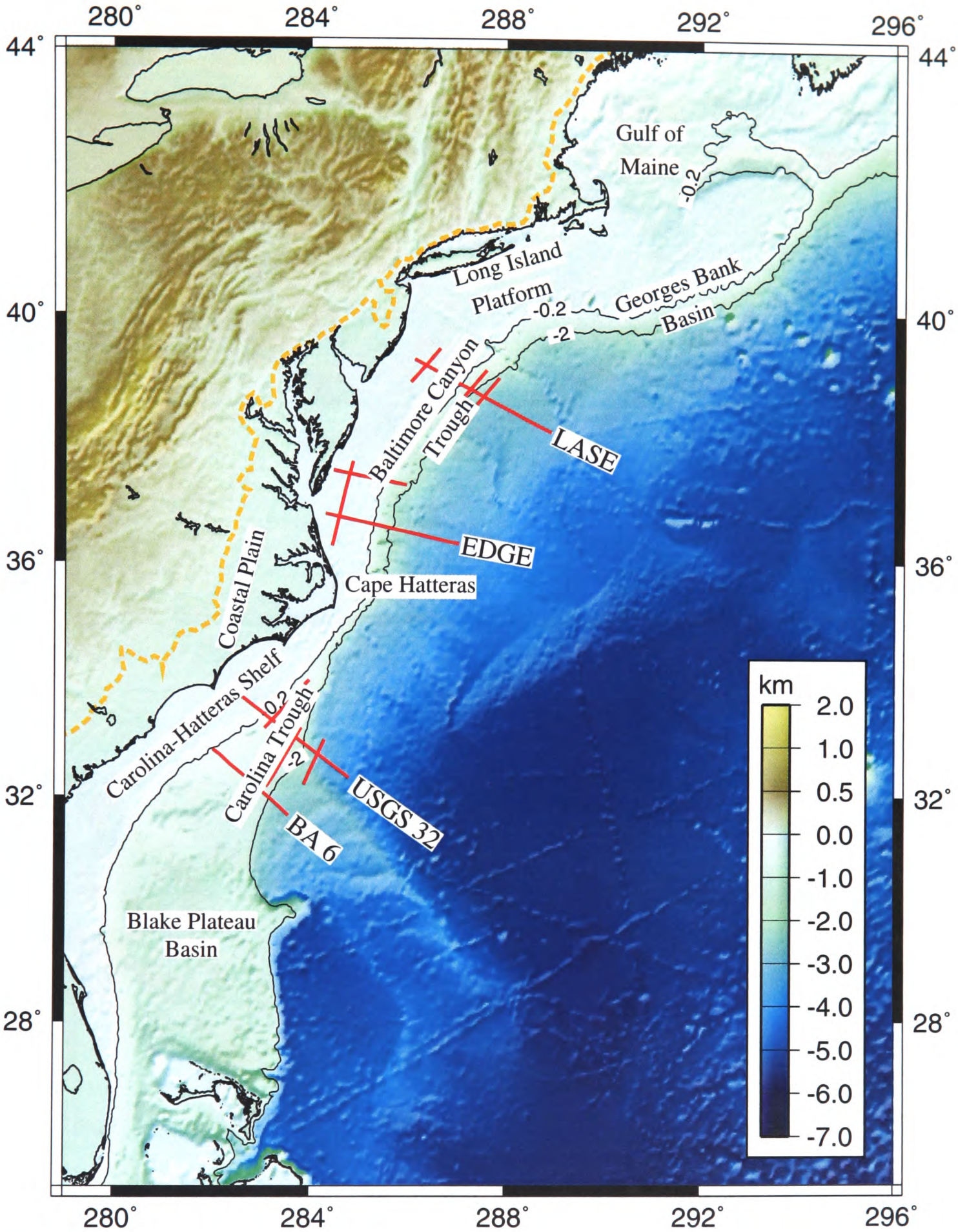
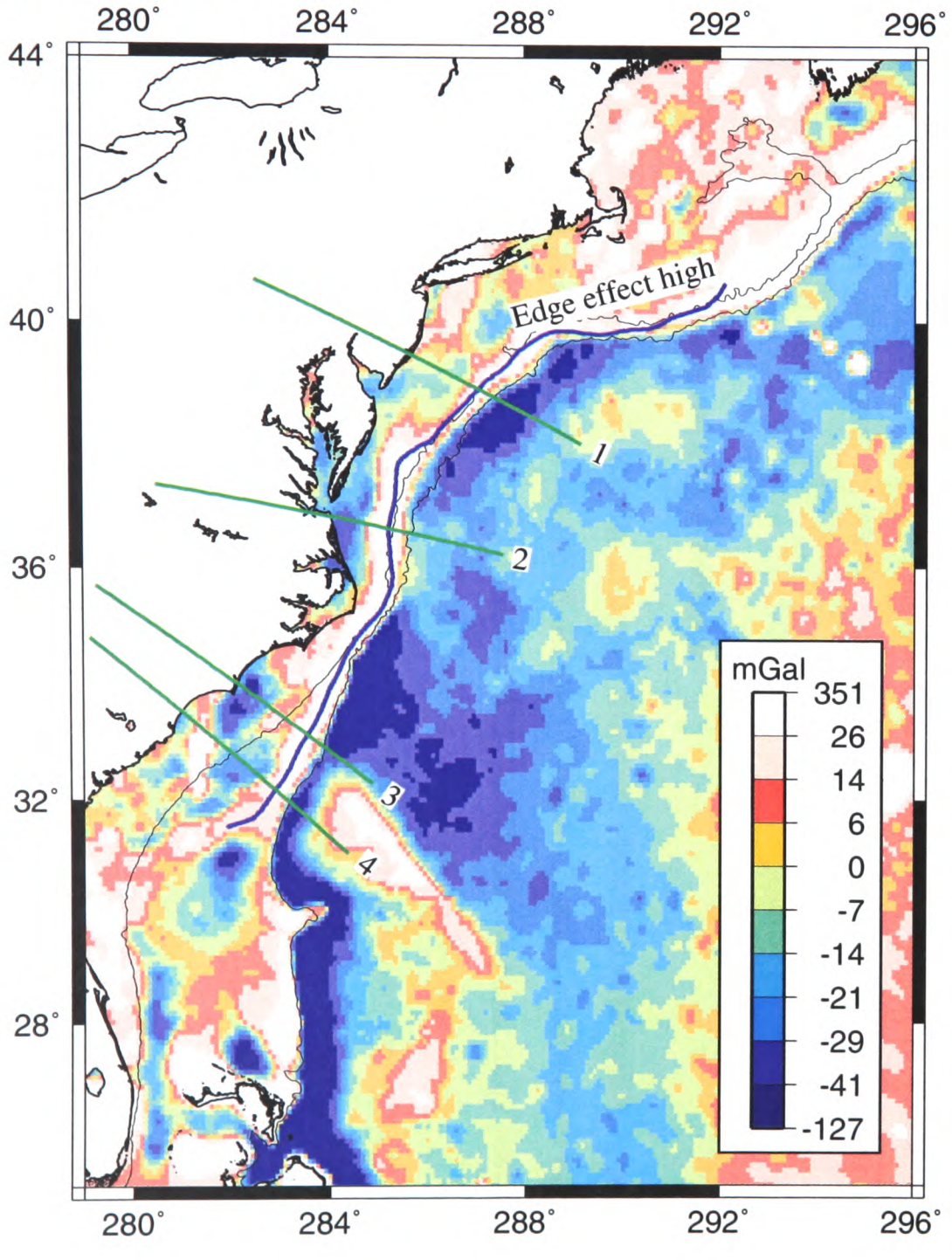
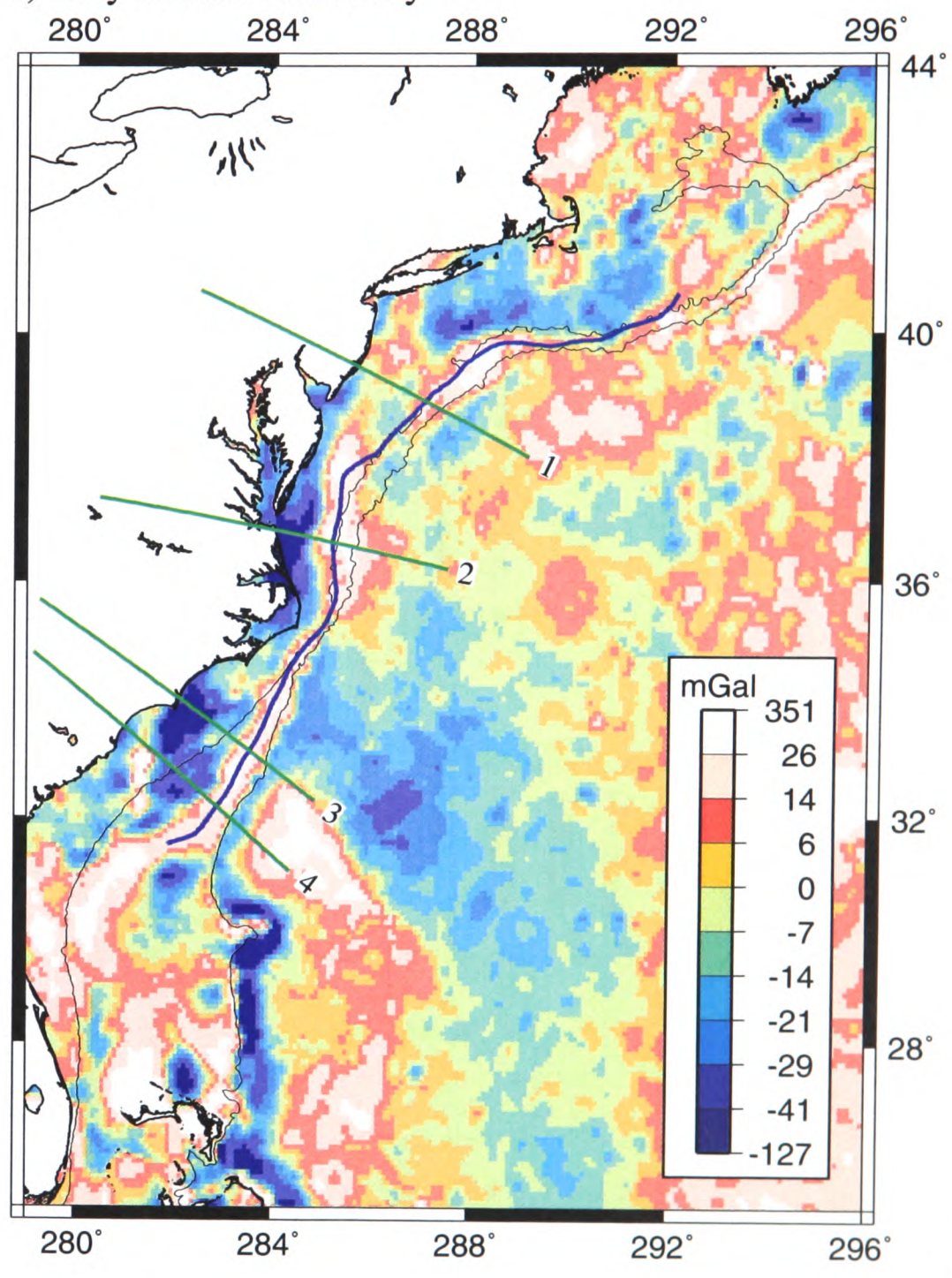


Figure 5.1: Map of the study area. Relief and main features of the Eastern USA passive continental margin are shown together with the shelf break ($-0.2km$ contour) and platform edge ($-2km$ contour). The dashed line is the landward limit of the coastal plain. Also shown are the locations of deep seismic profiles: LASE, EDGE, USGS 32, and BA-6.

a) Free-air anomaly



b) Airy isostatic anomaly



Parameter	Value
T_c (Thickness of unrifted crust)	$38km$
ρ_{water}	$1030kgm^{-3}$
ρ_{sed}	$2720kgm^{-3}$
ρ_{crust}	$2850kgm^{-3}$
ρ_{mantle}	$3330kgm^{-3}$
Athy depth constant, k	0.000216
Athy surface porosity, ϕ_0	0.15

Table 5.2: Analysis constants.

model generally leaves more than $20mGal$ of the free-air anomaly unaccounted for. Exceptions to this are minima that correspond to generally low Airy IGA amplitude in the vicinity of Cape Hatteras, the central Baltimore Canyon Trough, and the Georges Bank Basin (see Figure 5.2).

The reasons for segmentation in the along-strike transect are illustrated by four cross-strike profiles (Figure 5.4). Of these, only Profile 1 demonstrates a general correspondance of form and wavelength between the observed and calculated free-air edge effect gravity anomalies. The result is a smaller Airy IGA edge effect high than is observed in the vicinity of the other profiles, along which there is little similarity between the observed and calculated data.

5.2.2 The role of mechanical strength

Although the Airy model free-air gravity anomaly has been shown to reasonably approximate the observed anomaly in the central Baltimore Canyon Trough, comparison of the observed free-air anomaly with the Airy IGA (cf. Figure 5.2) shows that many features of the observed anomaly are not fully explained by the Airy isostatic model.

A possible reason for disparities between the observed and calculated free-air anomalies is that the underlying lithosphere has an intrinsic strength that prevents it from

---

Figure 5.2: Comparison of the free-air gravity anomaly with the isostatic gravity anomaly from an Airy-type model. a) Free-air gravity anomaly. b) Airy isostatic gravity anomaly. A transect along the edge effect gravity high (blue line) is shown in Figure 5.3, and profiles along lines 1-4 are shown in Figure 5.4.

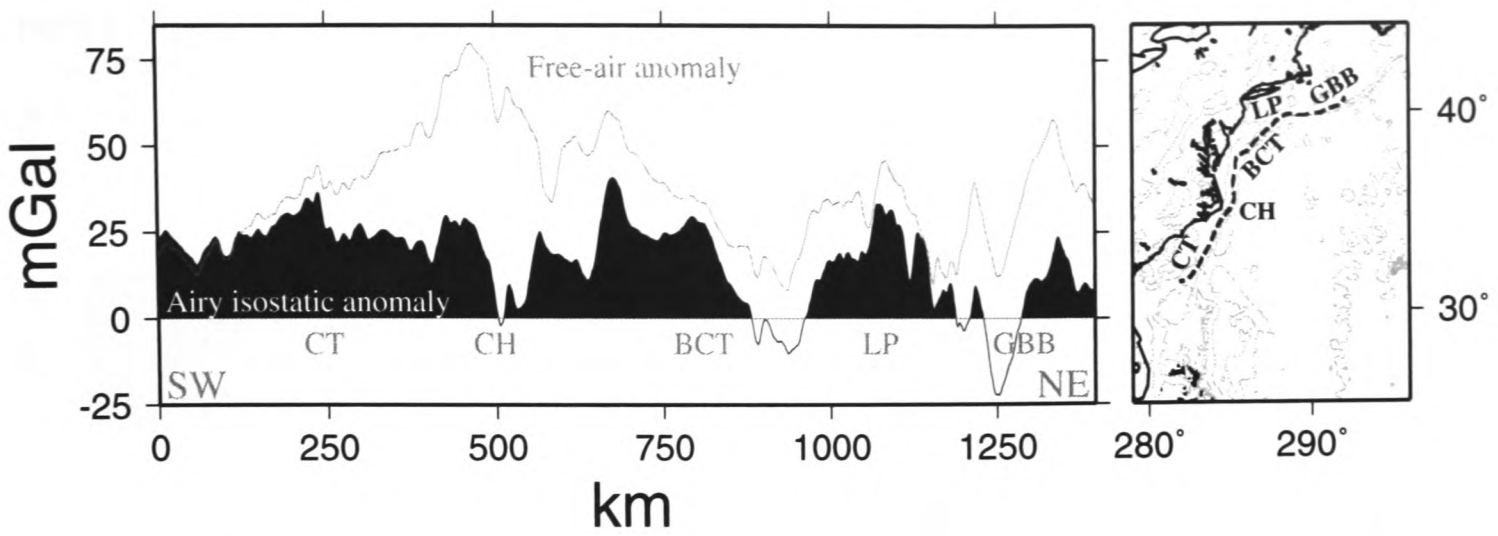


Figure 5.3: Along-strike transect of the free-air edge effect gravity high and corresponding Airy isostatic gravity anomaly. Map shows the transect path (also shown in Figure 5.2). SW - South west; NE - North east; CT - Carolina Trough; CH - Cape Hatteras; BCT - Baltimore Canyon Trough; LP - Long Island Platform; GBB - Georges Bank Basin.

responding to sediment loads in an Airy isostatic (infinitely weak) manner. Whether this is the case can be tested by repeating the process-oriented analysis using uniform effective elastic thickness plate flexure. This will represent the role of finite lithospheric mechanical strength in controlling the isostatic response to sediment loading.

A selection of flexural isostatic gravity anomalies (flexural IGAs, see Table 5.1) resulting from a series of such models (in which uniform elastic plate thicknesses ranges from $1km$ to $100km$ in $1km$ intervals) are shown in Figure 5.5.

In the part of the Baltimore Canyon Trough labelled 'A', and towards the Georges Bank Basin (labelled 'B') low T_e $(5 - 10km)$ flexural models reduce the amplitude of the edge effect gravity high to less than $20mGal$. By contrast, south of the Baltimore Canyon Trough, deep landward IGA lows (labelled 'C') remain unless a higher T_e $(20km)$ is modelled. However, sediment loading with this higher T_e causes large IGA amplitudes along much of the rest of the margin. In particular, the large amplitude of the $20km$ T_e calculated free-air anomaly across the Baltimore Canyon Trough (A) and Georges Bank Basin (B) shelf breaks results in a large amplitude flexural IGA low in both locations.

If T_e is raised beyond $20km$, then the amplitudes of the calculated free-air anomaly edge effect lows and highs increase beyond those in the observed free-air gravity anomaly, resulting in an IGA high-low-high anomaly that becomes more prominent as T_e increases (e.g. at location 'A' compare the $20km$ T_e isostatic anomaly in Figure 5.5c with the $30km$ T_e isostatic anomaly in Figure 5.5d).

Along-strike profiles demonstrate the effectiveness of various T_es at minimising the isostatic gravity anomaly in different parts of the margin (Figure 5.6). While the $10 -$

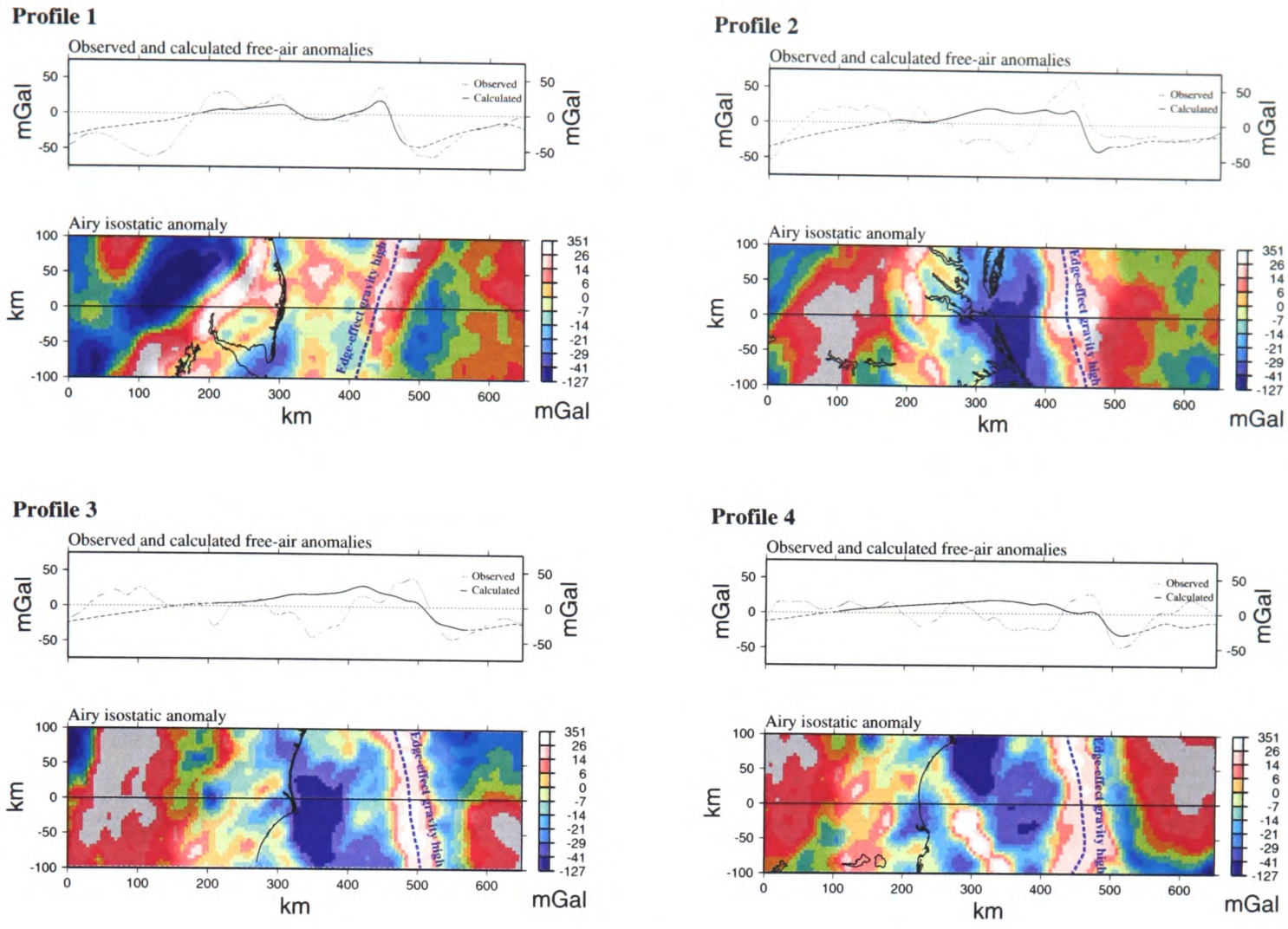


Figure 5.4: Observed and calculated (Airy model) free-air gravity anomalies along strike-normal profiles labelled 1 to 4 in Figure 5.2. Calculated anomaly is dashed in areas landward of the fall line and seaward of the earliest dated oceanic crust (according to Müller *et al.* [1997]). Maps show Airy isostatic gravity anomalies.

$20km$ T_e IGAs generally have the smallest amplitude along the free-air edge effect high from transect kilometers $0 - 450$ and $520 - 770$, they also produce large ($100mGal$) gravity lows centered on transect kilometer 1000 (Baltimore Canyon Trough) and transect kilometer 1300 that are not seen if the T_e is $5km$ or less. These lows appear where the positive process-oriented sum gravity anomaly exceeds the amplitude of the free-air edge effect gravity anomaly high; suggesting that T_e has been over-estimated.

Across-strike profiles showing observed and calculated (uniform plate) free-air anomalies confirm this apparent along-strike variation, and suggest that T_e also varies across-strike (Figure 5.7). The free-air edge effect gravity anomaly along Profile 1 is well represented by a low T_e ($6km$) model. Along each of the other profiles, the edge effect gravity high and seaward low are best reproduced if the T_e is $16km$ or less, but the landward low can only be accounted for if higher T_e values ($T_e > 20km$) are used.

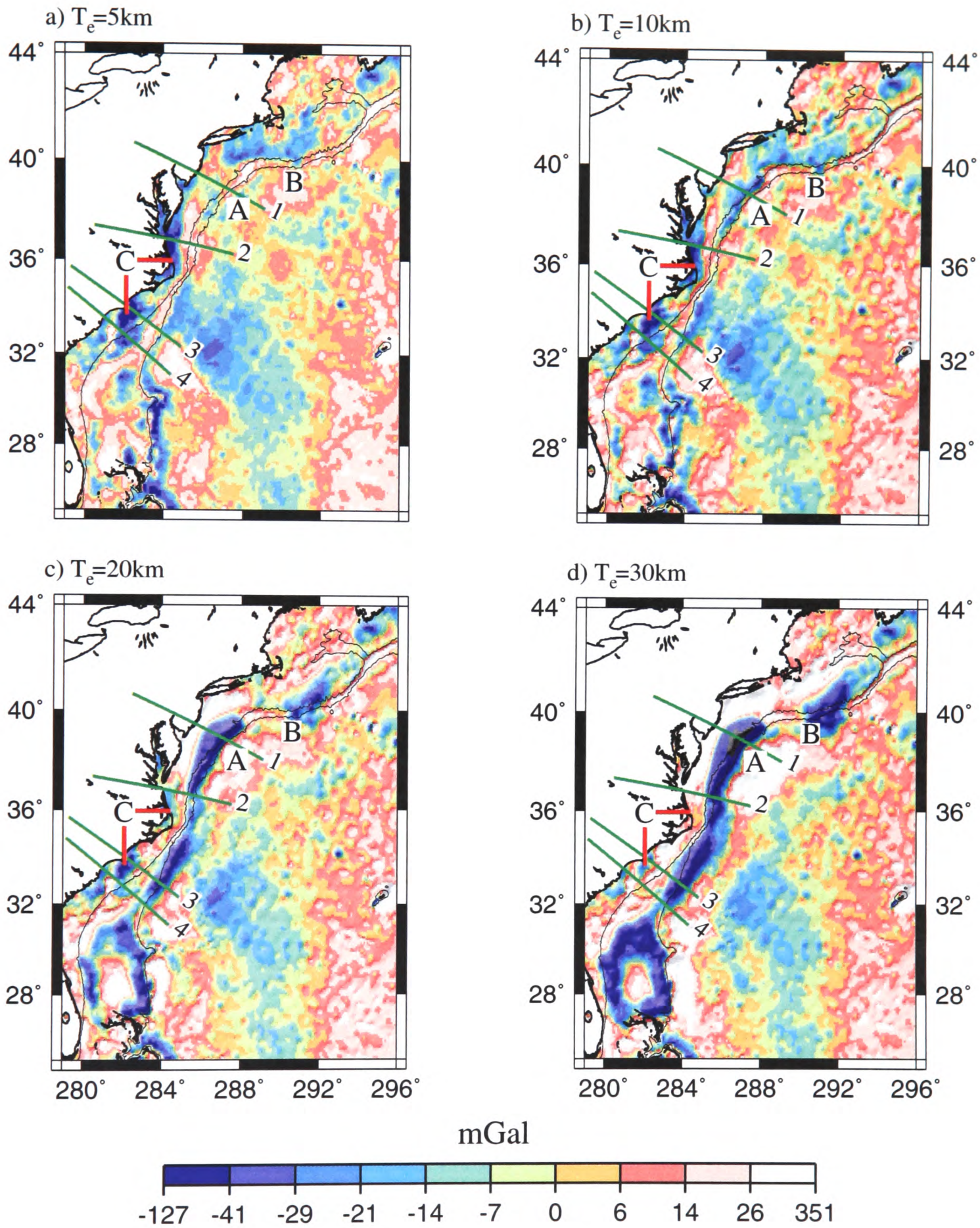


Figure 5.5: Uniform elastic plate model flexural isostatic gravity anomalies. a) $T_e = 5km$, b) $T_e = 10km$, c) $T_e = 20km$, d) $T_e = 30km$. Labels A, B, and C are referred to in text.

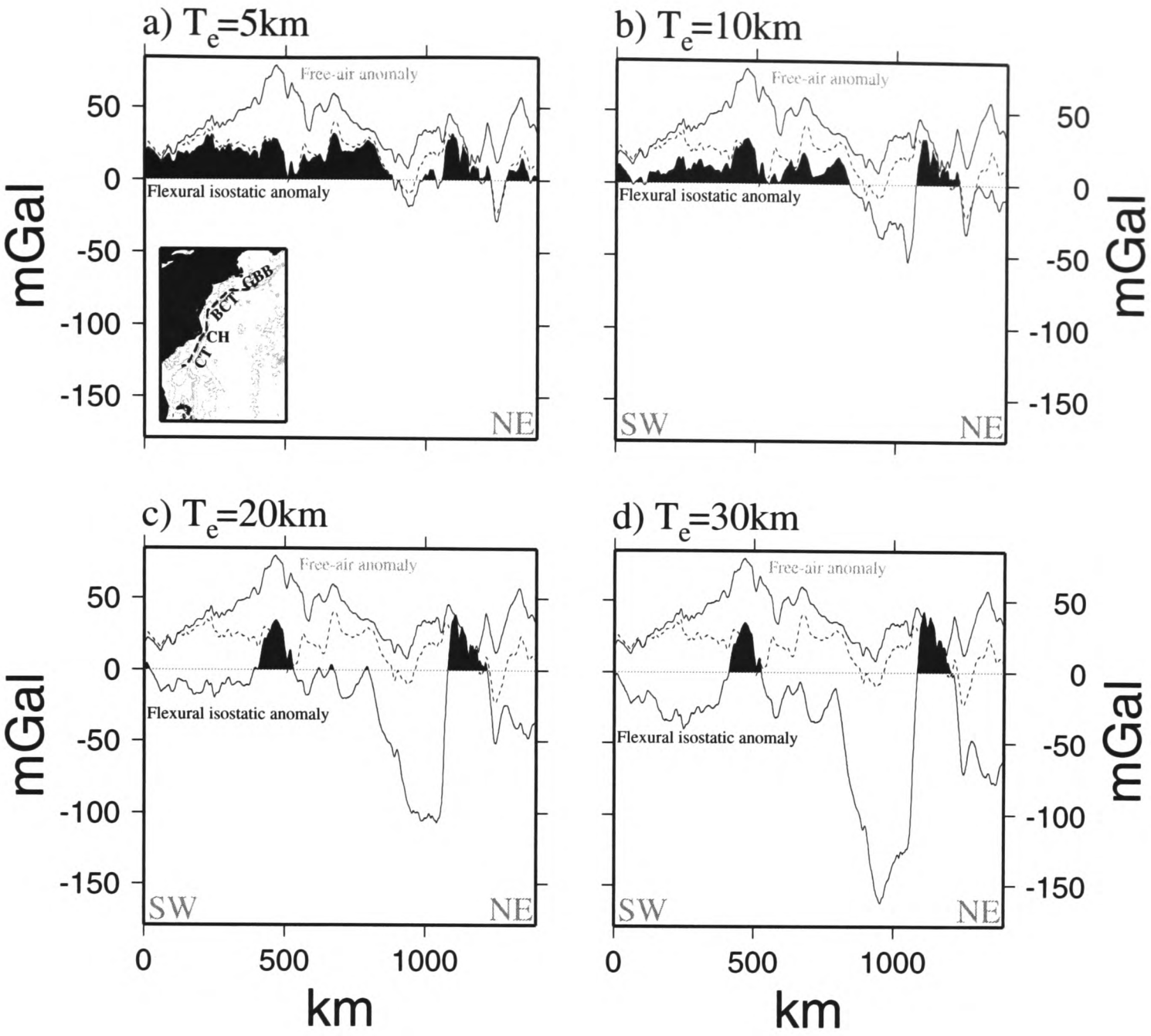


Figure 5.6: Along-strike transect of the free-air edge effect gravity high and corresponding uniform T_e isostatic gravity anomalies. The Airy isostatic gravity anomaly (dashed line) is shown for comparison. Map shows the transect path (also shown in Figure 5.5). SW - South west; NE - North east; CT - Carolina Trough; CH - Cape Hatteras; BCT - Baltimore Canyon Trough; GBB - Georges Bank Basin.

5.3 Mechanical plate segmentation

Analyses presented thus far have been based on an assumption of uniform T_e. These have shown that there is no one T_e that best explains the free-air gravity anomaly along the entire margin. Instead, flexural isostatic gravity anomalies suggest that the margin is segmented in terms of its effective elastic response to sediment loading. This is the basis for a version of the process-oriented analysis that identifies segmentation in the form of spatial changes in effective elastic thickness.

The analysis method (described in the previous chapter) relies on iterative refinement of the T_e distribution through minimisation of the flexural isostatic gravity anomaly. If a uniform T_e initial distribution were used then the main iterative process (allowing T_e to

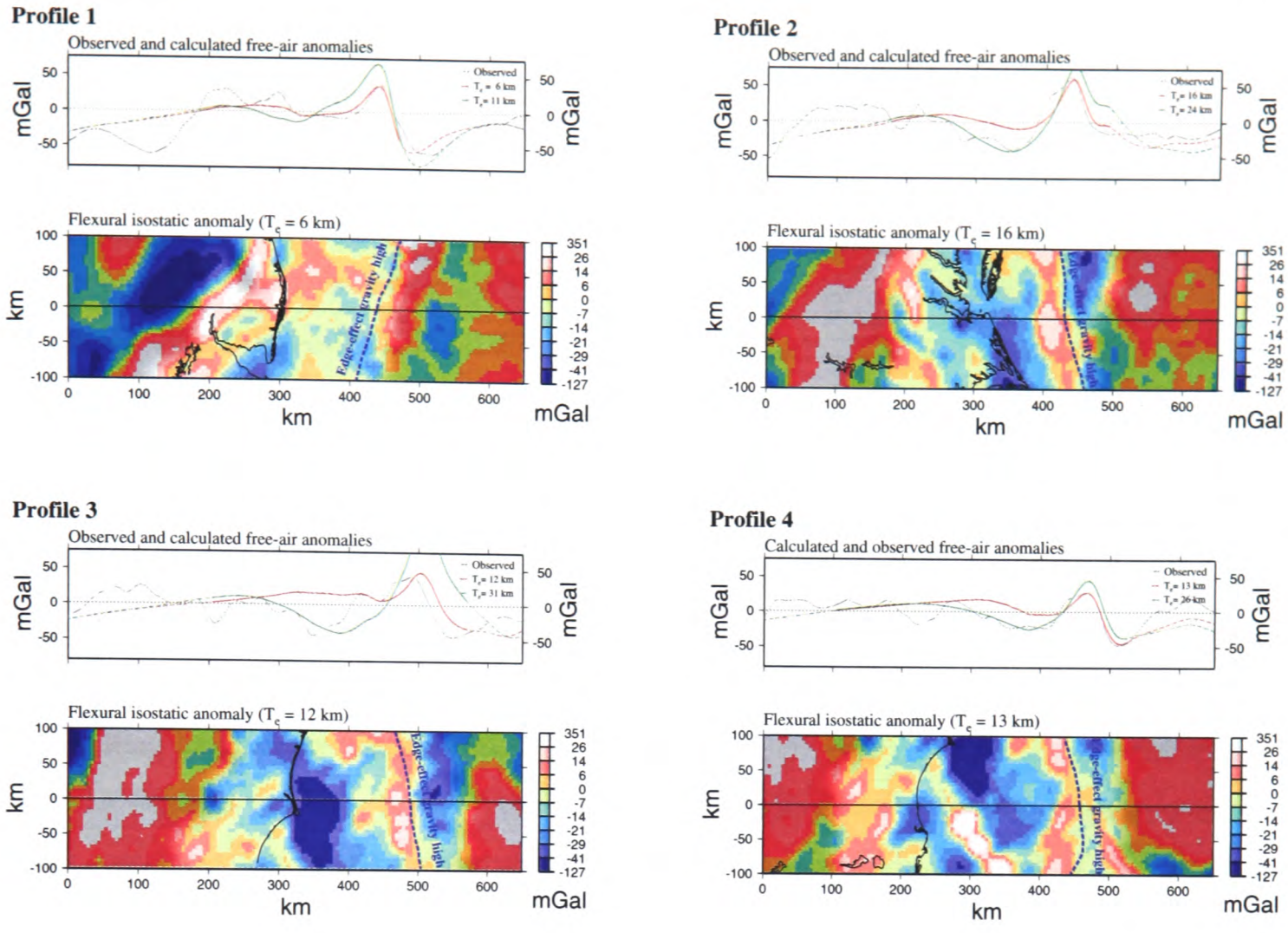


Figure 5.7: Observed and calculated (uniform plate model) free-air gravity anomalies along strike-normal profiles labelled 1 to 4 in Figure 5.5. Example plate thicknesses have been chosen to demonstrate correspondence of differing T_e calculated free-air anomalies with the observed free-air anomaly according to the location on the margin. To place emphasis on the rifted margin basins, the calculated anomalies are dashed in areas landward of the fall line and seaward of the earliest dated oceanic crust (according to Müller *et al.* [1997]). Maps show the uniform T_e isostatic gravity anomaly that is best minimised landward of the shelf break.

change by only $\pm 5km$ per iteration) would be slow to resolve variations in T_e that may be an order of magnitude larger. For this reason an inital estimate of effective elastic thickness variations is made using uniform plate models of the type already discussed.

5.3.1 Initial estimate of effective elastic thickness variations

An initial estimate of the effective elastic thickness distribution is provided by windowed $(0.5^o \times 0.2^o)$ RMS minimisation of the uniform plate model isostatic gravity anomalies (as described in Chapter 4, Section 6). The initial T_e distribution (Figure 5.8) agrees with conclusions drawn from the uniform T_e analyses, with the highest apparent strength lying landward of the shelf break as far north as the southern end of the Baltimore Canyon Trough, and a region of low T_e corresponding to the central Baltimore Canyon Trough.

Effective elastic thickness of the lithosphere seaward of the marginal basins is masked here, but is discussed in Section 5.5.

5.3.2 Iterative analysis

Discrete uniform elastic plate analyses do not provide an accurate representation of how the plate deforms locally if T_e varies across a larger area. This means that the initial T_e distribution derived from uniform T_e isostatic gravity anomalies can only provide a first estimate of what the actual distribution might be.

Iterative analysis (as described in Chapter 4, Section 6) allows the T_e distribution to be refined until an optimal minimisation of the isostatic gravity anomaly is achieved. The final distribution (Figure 5.9) maintains the main features associated with the initial distribution (Figure 5.8), but reveals more subtle variations in effective elastic thickness both along and across the margin.

The flexural isostatic gravity anomaly corresponding to the final T_e distribution retains some features of the free-air gravity anomaly, particularly seaward of the marginal basins where sediment cover is thin. However, across the marginal basins (where sediment loading has made a greater contribution to the free-air anomaly) the isostatic gravity anomaly contains little of the free-air gravity high and landward low, even where it is most prominent: over the northern Baltimore Canyon Trough; southern Baltimore Canyon Trough; and the north-western Blake Plateau. These reductions contribute to a $RMS\ IGA$ of $14.2mGal$; $4.5mGal$ less than for the Airy model.

Where the edge effect gravity high persists in the flexural IGA it is either fragmented, or greatly reduced in amplitude. An along-strike transect (Figure 5.11) shows that although the flexural IGA high exceeds $20mGal$ in places, it consistantly maintains a smaller amplitude than both the free-air gravity anomaly and the Airy IGA. This is reflected in a ($11.3mGal$) RMS flexural IGA along the transect; which is 27.7% of the ($40.7mGal$) RMS observed free-air high and 53.9% of the ($20.9mGal$) RMS Airy IGA high.

Across-strike profiles demonstrate a strong correspondence between the wavelengths and amplitudes of the observed and calculated free-air anomalies (Figure 5.12). Comparison against Figure 5.4 and Figure 5.7 shows that the variable T_e analysis consistently approximates the observed free-air gravity anomaly more successfully than do the Airy and uniform plate models.

Along Profile 1 (central Baltimore Canyon Trough) a low T_e results in a calculated free-air gravity anomaly that is similar to that from the Airy isostatic model (cf. Profile 1, Figure 5.4). However, an increase in T_e across the shelf break increases the amplitude

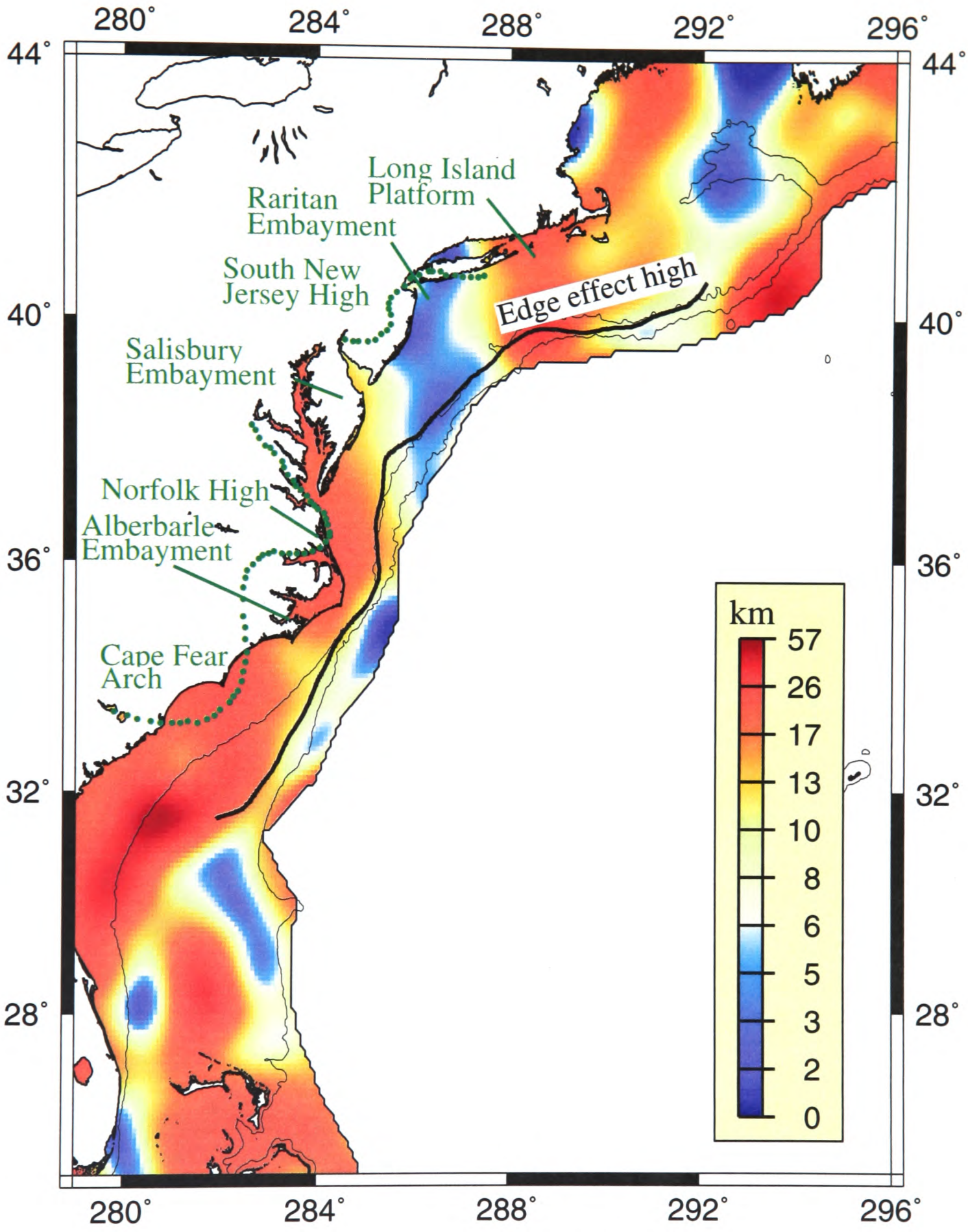


Figure 5.8: Initial approximation of the T_e distribution based on minimisation of RMS isostatic gravity anomalies (see text for details). Named basement features after Owens & Gohn [1985].

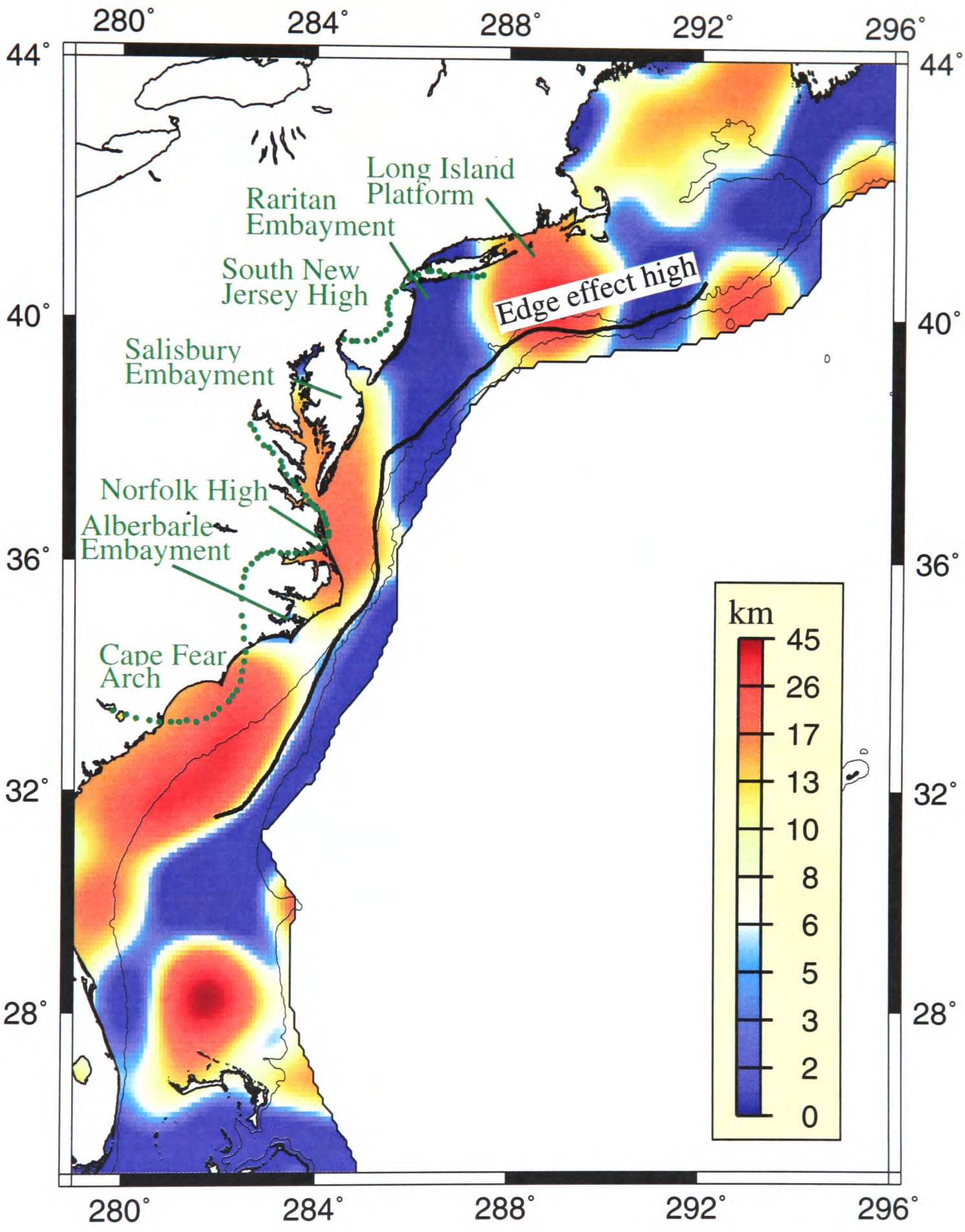
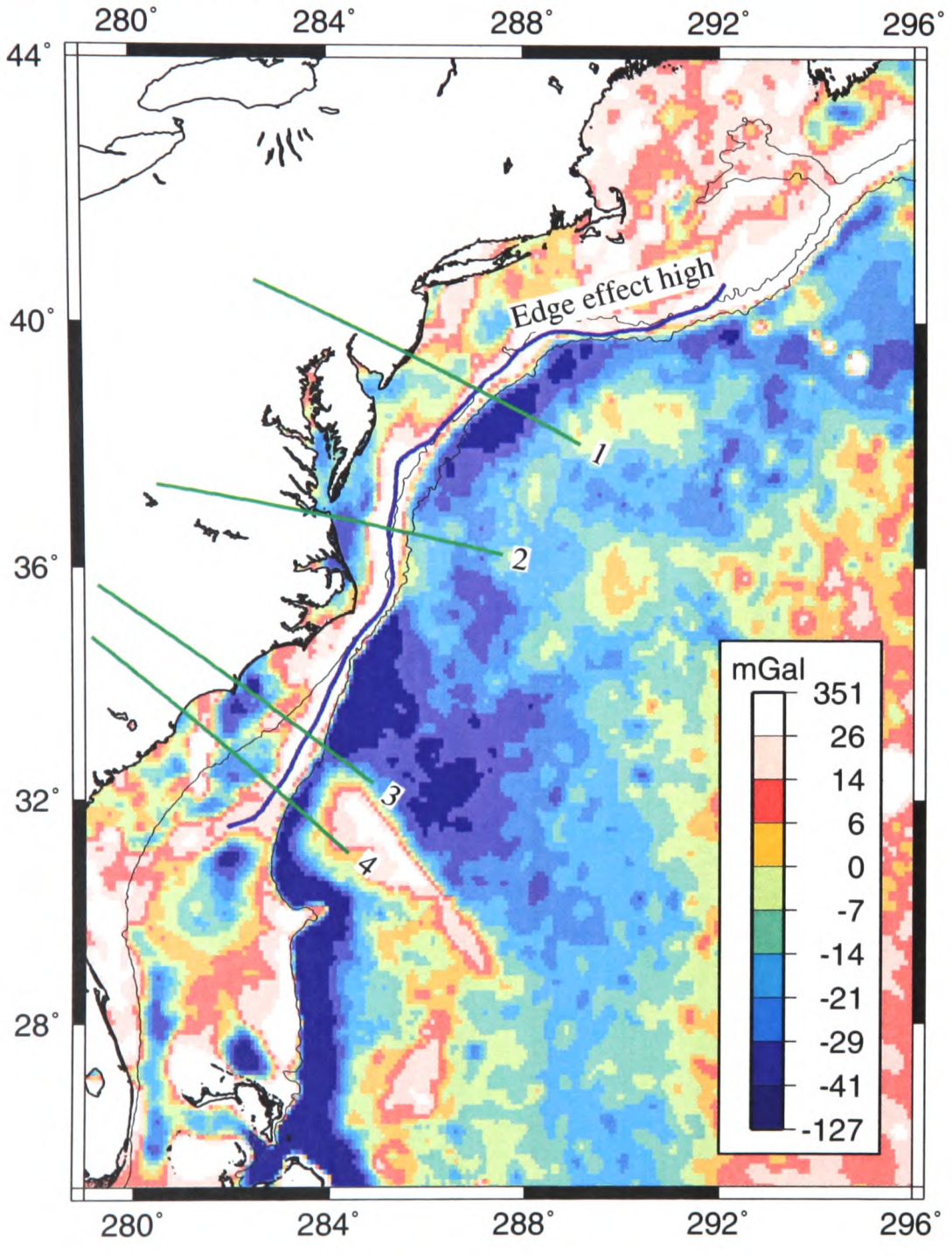
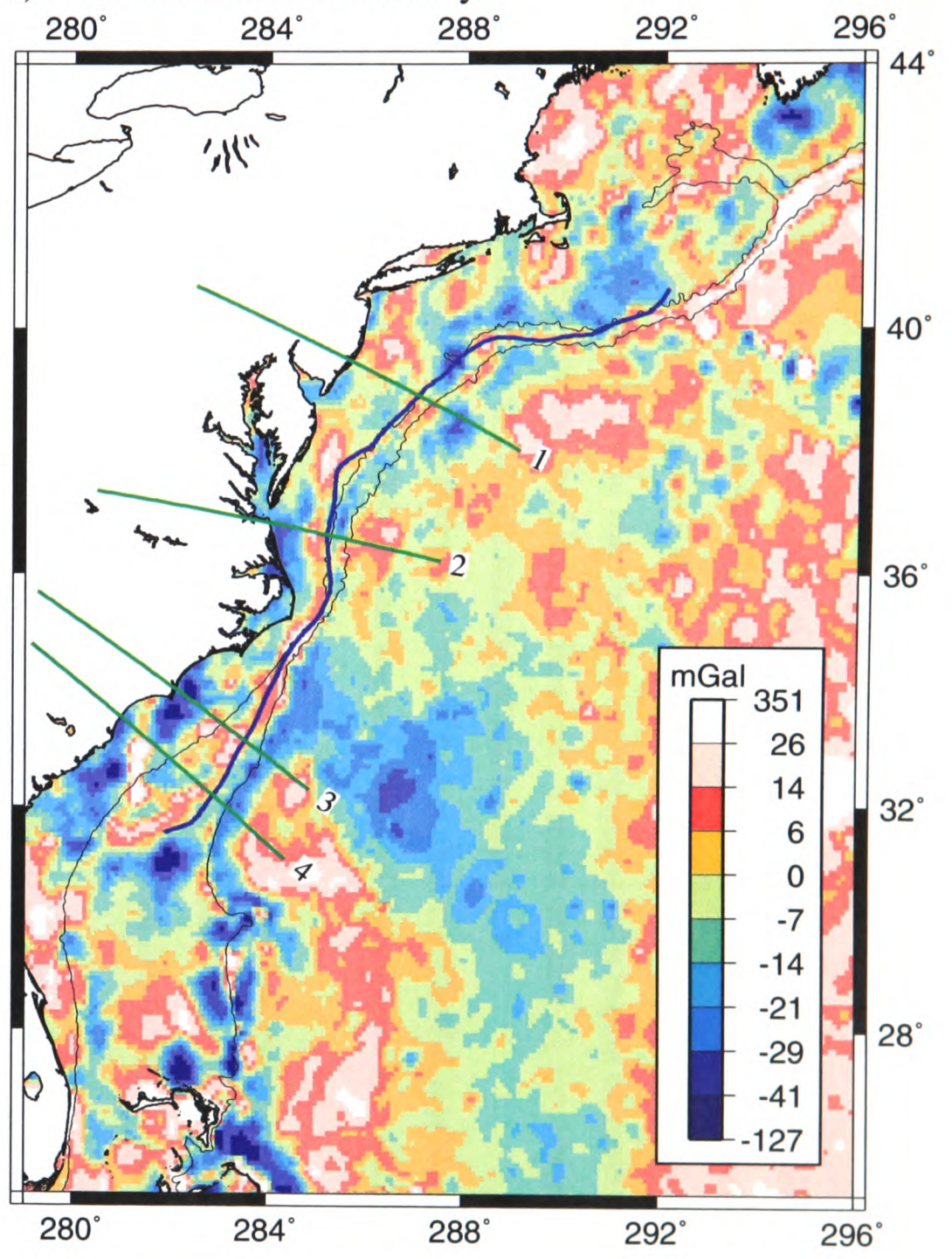


Figure 5.9: Final T_e distribution constrained by iterative process-oriented analysis. Named basement features after Owens & Gohn [1985].

a) Free-air anomaly



b) Flexural isostatic anomaly



of the calculated edge effect gravity high; bringing it closer to the observed free-air edge effect high.

The improvement offered by the iterative analysis is more evident along Profile 2, where the Airy method calculated free-air anomaly has little in common with the observed free-air anomaly (cf. Profile 2, Figure 5.4). The large amplitudes of the free-air anomaly edge effect high and landward low in this location are explained by a region of moderate T_e $(13 - 26km)$ landward of the shelf break. However, a much smaller T_e $(< 10km)$ is required to explain the small amplitude seaward of the seaward low.

A similar relationship is observed along Profile 3, except that landward T_es are higher (increasing southwards towards $> 26km$), and the amplitude of the seaward free-air edge effect gravity low is not reproduced in the calculated anomaly.

On Profile 4 high T_es $(> 26km)$ landward of the shelf break are observed once again, and again the iterative analysis provides a much better approximation of the observed free-air gravity anomaly than does the Airy method. However, the origin of the seaward free-air edge effect gravity anomaly low remains elusive.

The significance of these results, together with implications of the recovered T_e distribution and flexural isostatic gravity anomaly are discussed in the following chapter.

5.4 Sensitivity of the process-oriented analysis

Although an iterative version of the process-oriented analysis that identifies spatial variations in T_e demonstrably minimises the isostatic gravity anomaly (relative to Airy and uniform T_e models), it has yet to be proven that the recovered T_e distribution is unique. It is therefore necessary to test this, and to investigate to what extent data and assumptions can bias the analysis.

5.4.1 Bias due to the initial effective elastic thickness distribution

The T_e distribution derived from iterative analysis retains many of the features of the initial T_e distribution obtained from uniform plate models. The uniqueness of the iterative T_e solution can therefore be tested by using a different initial T_e distribution and determining whether it converges towards the same final model.

The result of applying the iterative method with an initial uniform T_e plate of $5km$

Figure 5.10: Comparison of the free-air gravity anomaly with the iterative analysis flexural isostatic gravity anomaly. a) Free-air gravity anomaly. b) Flexural isostatic gravity anomaly.

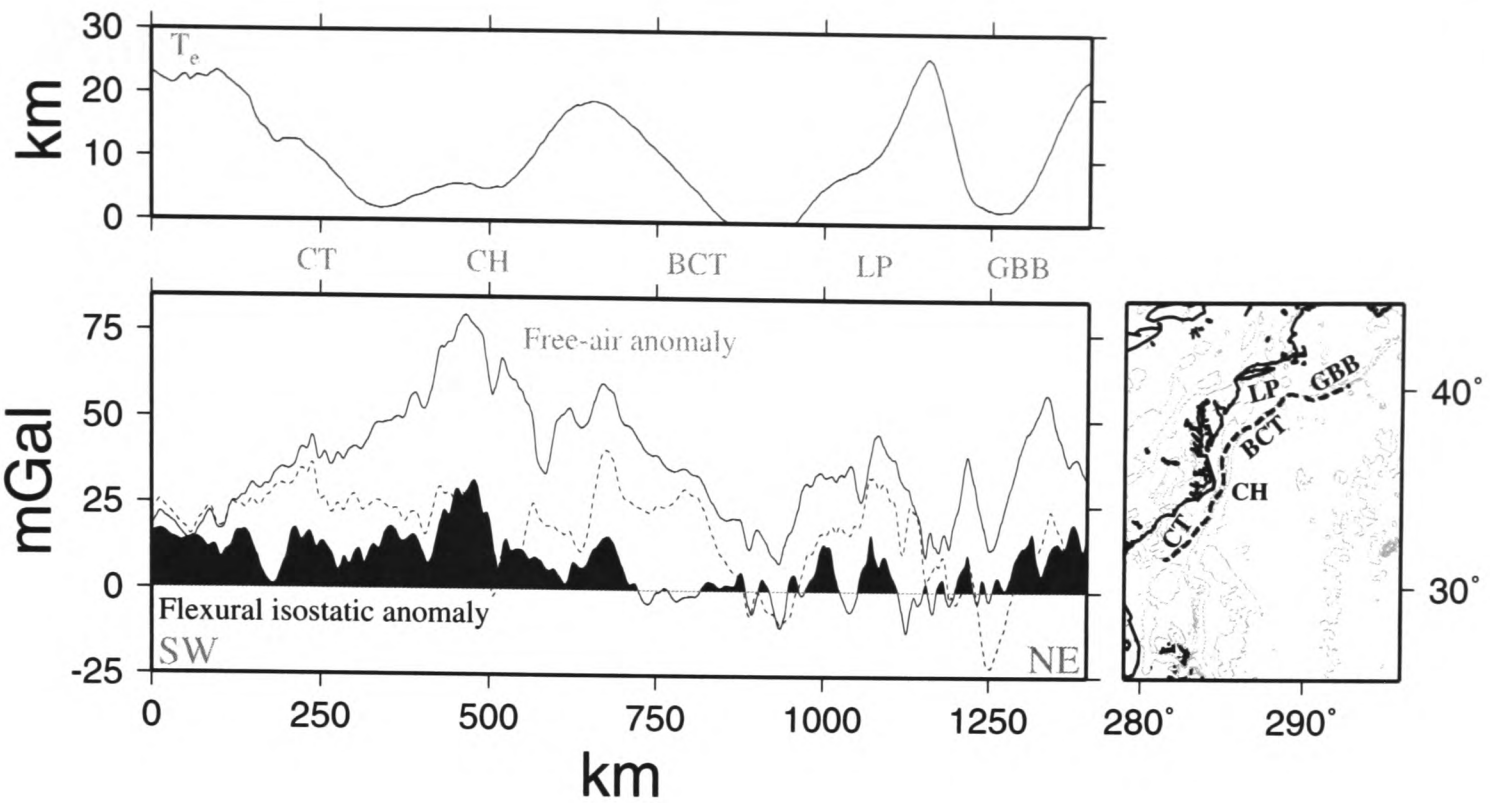


Figure 5.11: Along-strike transect of the free-air edge effect gravity high and corresponding iterative analysis flexural isostatic gravity anomaly. The Airy isostatic gravity anomaly (dashed line) is shown for comparison. Map shows the transect path. SW - South west; NE - North east; CT - Carolina Trough; CH - Cape Hatteras; BCT - Baltimore Canyon Trough; LP - Long Island Platform; GBB - Georges Bank Basin.

thickness is shown in Figure 5.13. Convergence is slower than in the original analysis (which converged after 18 iterations) and was eventually halted, in order to free processing time for other tests of the method robustness, after 36 iterations[2]. By this point the RMS isostatic gravity anomaly was within $0.1mGal$ of the original iterative analysis ($14.16mGal$), and the main features of the T_e distribution were already in place; suggesting that the most T_e sensitive parts of the gravity anomaly had already been addressed. These are the high strength regions behind the shelf break of the central margin and Long Island Platform, and zones of low T_e across the central Baltimore Canyon Trough and seaward of the shelf break. High southern Blake Plateau Basin T_e and seaward of the Long Island Platform observed in the original analysis distribution was not matched when an initially uniform T_e was used.

The main difference between this determination and the original model is that the regions of high T_e are less even and of generally lower amplitude, perhaps reflecting the fact that the distribution was not yet fully formed when the iterative analysis was halted.

[2]Convergence is referred to here in the sense of iterative mod-mean changes in the analysis T_e distribution within the boundaries of the high quality USGS sediment isopach grids

Profile 1

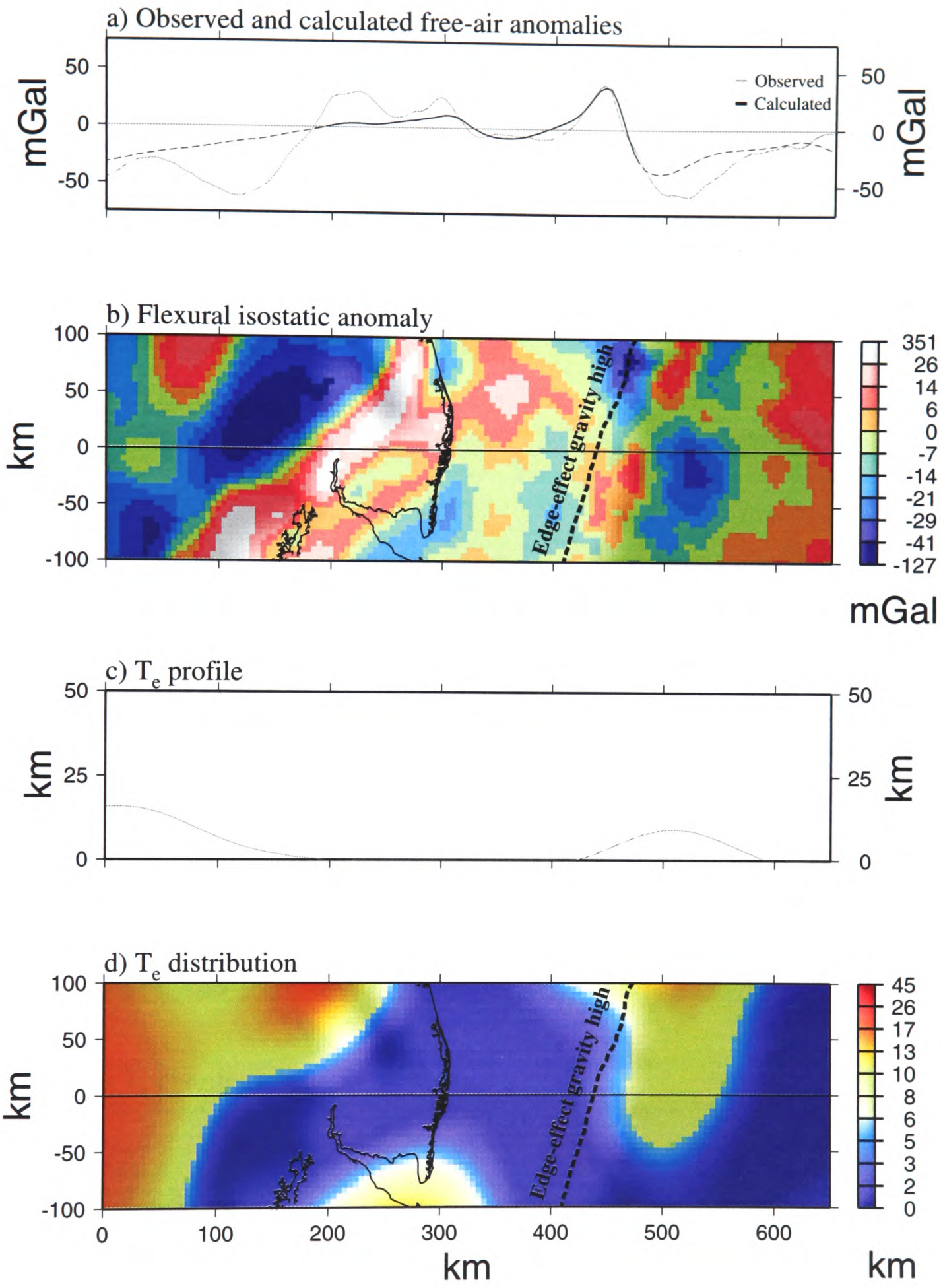
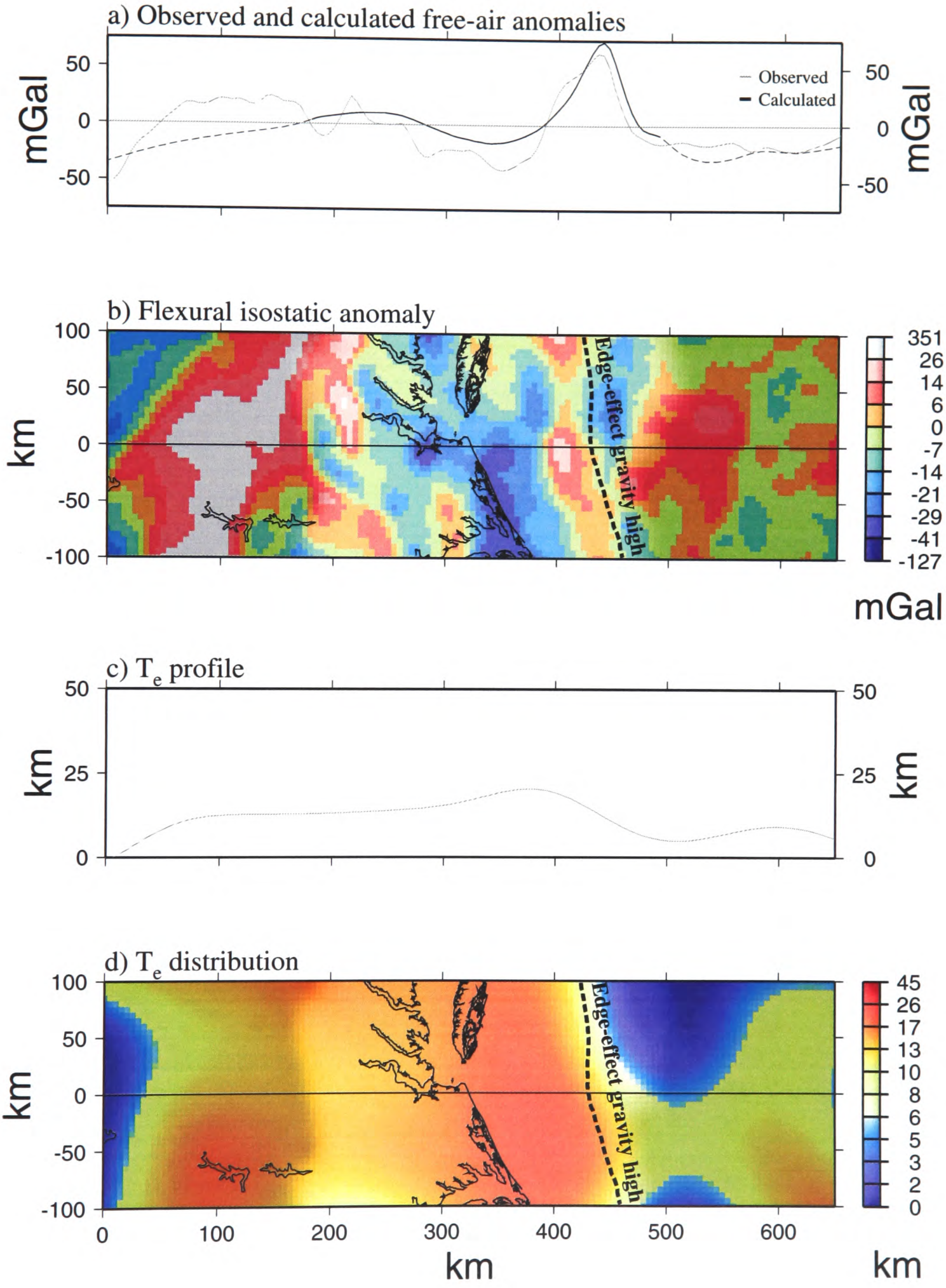
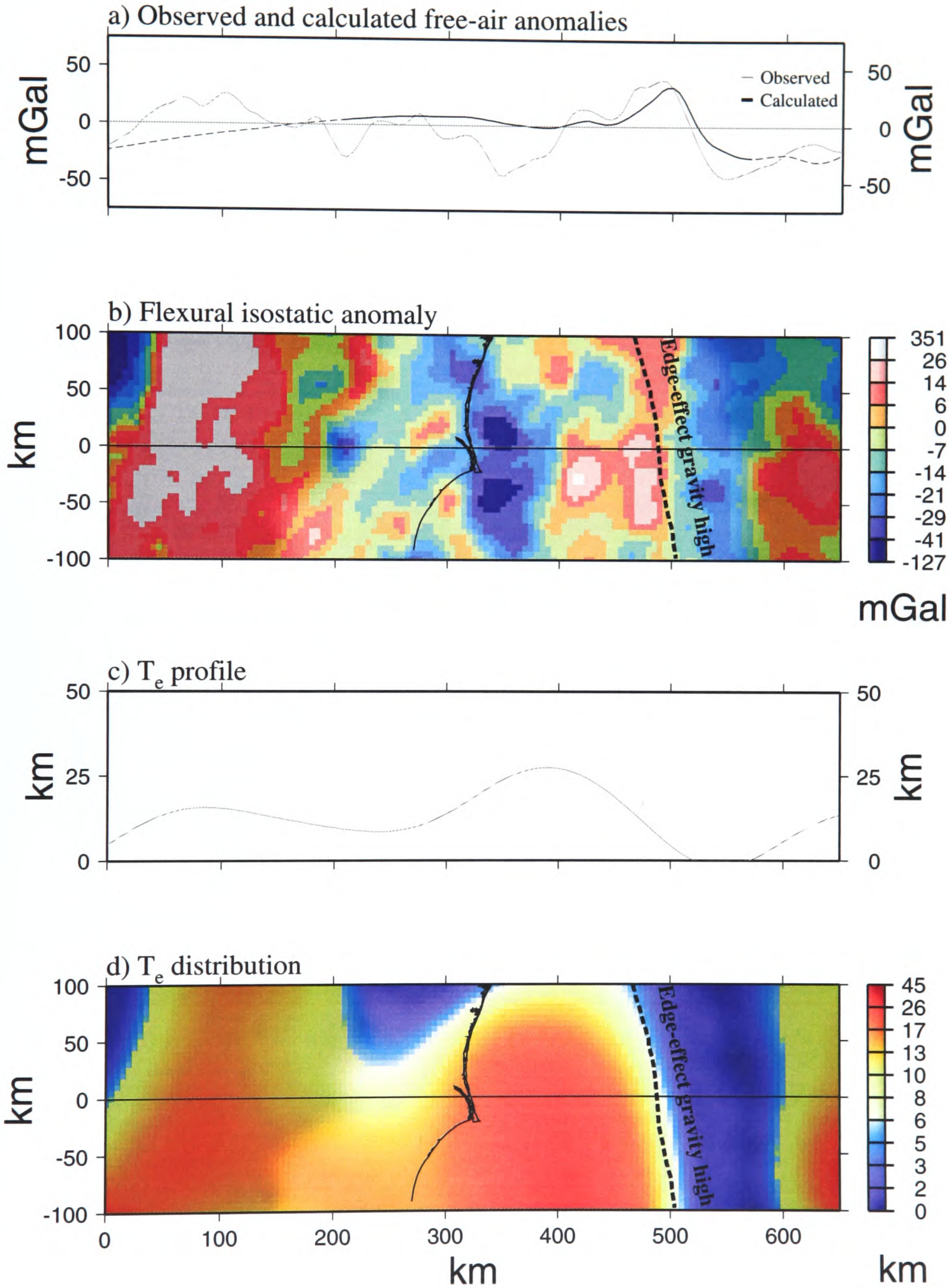


Figure 5.12: Profiles (next four pages) showing results of iterative process-oriented analysis (see Figure 5.10 for locations). a) Observed and calculated free-air gravity anomalies. To place emphasis on the rifted margin basins, the calculated anomaly is dashed in areas landward of the fall line and seaward of the earliest dated oceanic crust (according to Müller *et al.* [1997]). b) Flexural isostatic gravity anomaly. c) & d) T_e distribution.

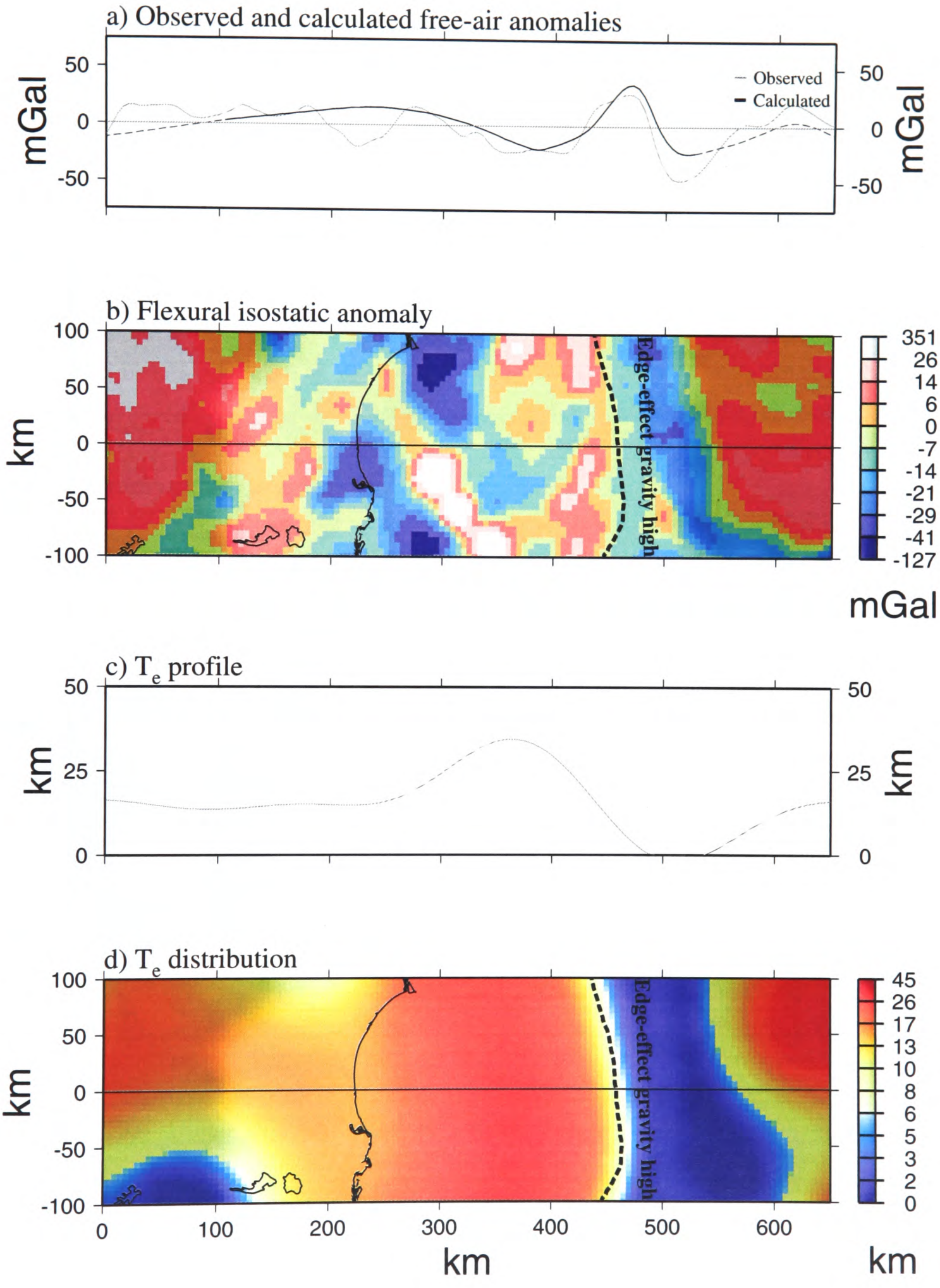
Profile 2


a) Observed and calculated free-air anomalies
mGal
50
0
-50
Observed
Calculated
b) Flexural isostatic anomaly
km
100
50
0
-50
-100
Edge-effect gravity high
351
26
14
6
0
-7
-14
-21
-29
-41
-127
mGal
c) T_e profile
km
50
25
0
d) T_e distribution
km
100
50
0
-50
-100
Edge-effect gravity high
45
26
17
13
10
8
6
5
3
2
0
0
100
200
300
400
500
600
km

Profile 3


a) Observed and calculated free-air anomalies
mGal
50
0
-50
Observed
Calculated
b) Flexural isostatic anomaly
km
100
50
0
-50
-100
Edge-effect gravity high
351
26
14
6
0
-7
-14
-21
-29
-41
-127
mGal
c) T_e profile
km
50
25
0
d) T_e distribution
km
100
50
0
-50
-100
Edge-effect gravity high
45
26
17
13
10
8
6
5
3
2
0
0
100
200
300
400
500
600
km
km

Profile 4


a) Observed and calculated free-air anomalies
mGal
50
0
-50
Observed
Calculated
b) Flexural isostatic anomaly
km
100
50
0
-50
-100
Edge-effect gravity high
351
26
14
6
0
-7
-14
-21
-29
-41
-127
mGal
c) T_e profile
km
50
25
0
d) T_e distribution
km
100
50
0
-50
-100
Edge-effect gravity high
45
26
17
13
10
8
6
5
3
2
0
0
100
200
300
400
500
600
km
km

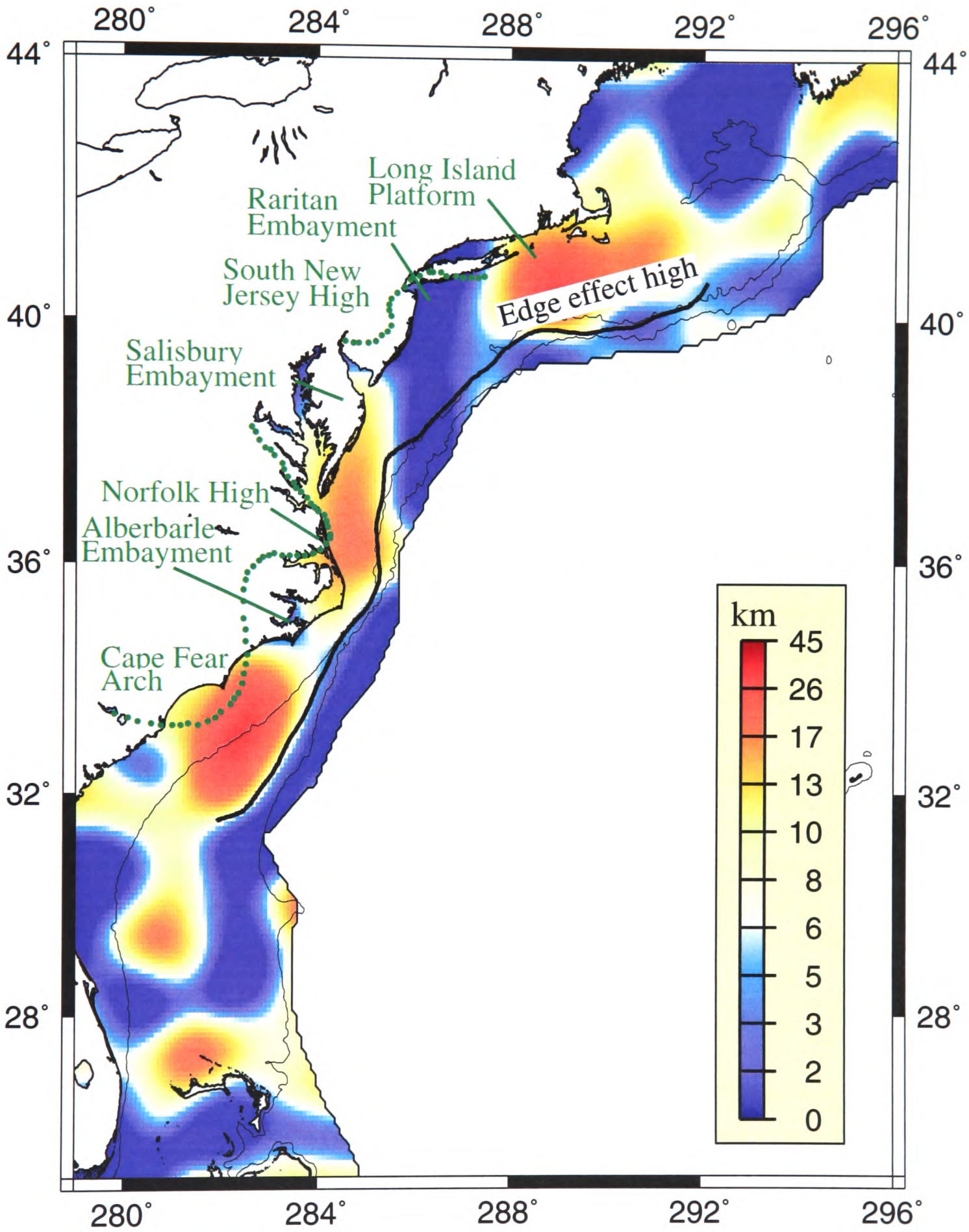


Figure 5.13: T_e distribution resulting from iterative process-oriented analysis based on a uniform T_e distribution of $5km$. Compare with Figure 5.9, for which a spatially varying initial T_e distribution was assumed. Named basement features after Owens & Gohn [1985].

5.4.2 T_e sensitivity

The sensitivity of the flexural isostatic gravity anomaly to the T_e distribution has been investigated by examing the effect of a $5km$ increase or decrease (clipped such that $T_e \geq 0km$) in the iterative T_e distribution. The results are presented as the RMS isostatic gravity anomaly in the same $0.5^o \times 0.2^o$ windows as were used for iterative constraint of T_e (Figure 5.14).

In the vicinity of the marginal basins either increasing or decreasing the T_e results in a dominantly larger RMS isostatic gravity anomaly (greens to reds). A decrease in T_e tends to increase the isostatic gravity anomaly in areas where the T_e is high (Figure 5.14c). By contrast, an increase in T_e results in a *reduced* isostatic gravity anomaly along high T_e regions of the central margin, Long Island Platform, and southern Baltimore Canyon Trough, but at the expense of a large (up to $40mGal$) increase in the windowed RMS isostatic gravity anomaly both seaward of the shelf break and along the landward rim of the Blake Plateau Basin.

It seems that a higher T_e landward of the shelf break from 31^oN to 37^oN (backing the Carolina Trough and southern Baltimore Canyon Trough) cannot co-exist with a low amplitude isostatic gravity anomaly across the edge effect high. This may mean that there is a transition from high to low T_e across the shelf break in this region that is steeper than the analysis can resolve.

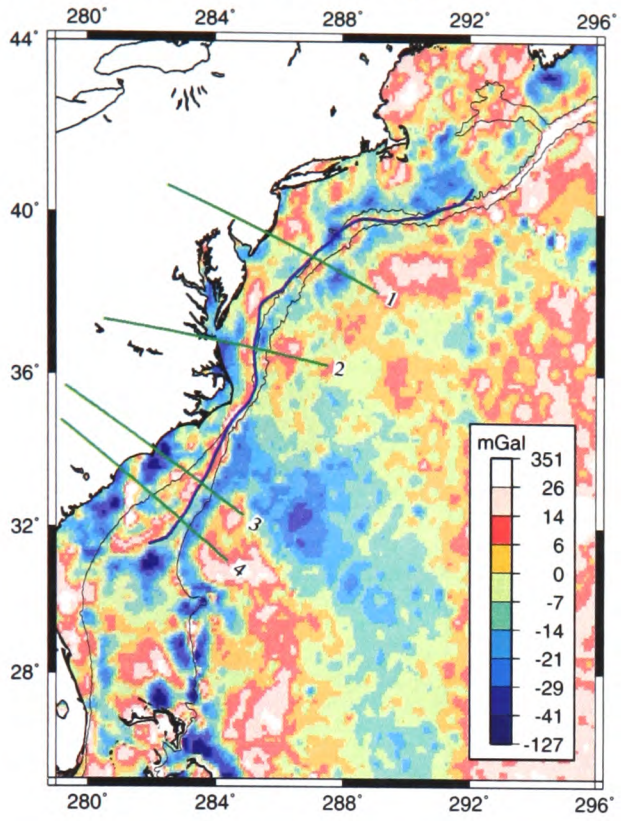
Around the Bahamas in the south ($c.26 - 27^oN$) and the Gulf of Maine in the north ($c.42^o - 44^oN$) the isostatic gravity anomaly is relatively insensitive to small changes in T_e. These are areas where the sediment data lacks the short wavelength features (whether it be through low data resolution, even deposition, or thin sediment cover) from which the iterative analysis derives its sensitivity to T_e.

5.4.3 Analysis window size

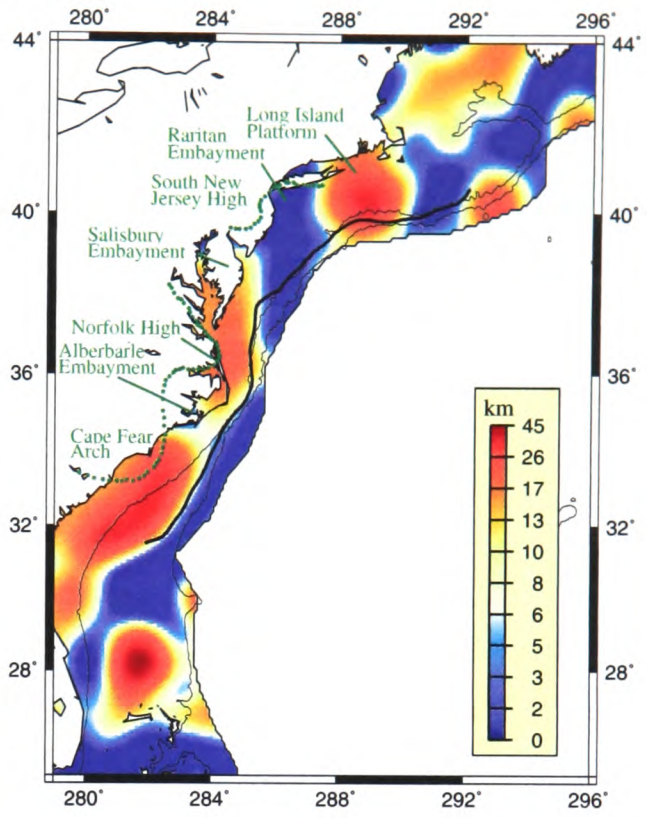
The iterative process-oriented analysis uses minimisation of isostatic gravity anomalies within $0.5^o \times 0.2^o$ windows to constrain the T_e distribution. The window size was selected from a range on the basis of the rate at which the T_e distribution converged, but as Figure 5.15 shows, even if the window size is as large as $1.5^o \times 0.2^o$ the T_e distribution is similarly recovered across the margin. Only if the window size is increased further (to $1.5^o \times 0.4^o$) does the analysis begin to degrade, resulting in a less focussed distribution and over-estimation of T_e in high strength areas.

The three T_e distributions marked 'a' to 'c' produce very similar isostatic gravity anomalies (Figure 5.16a-c) with comparable RMS amplitudes (respectively $14.2mGal$,

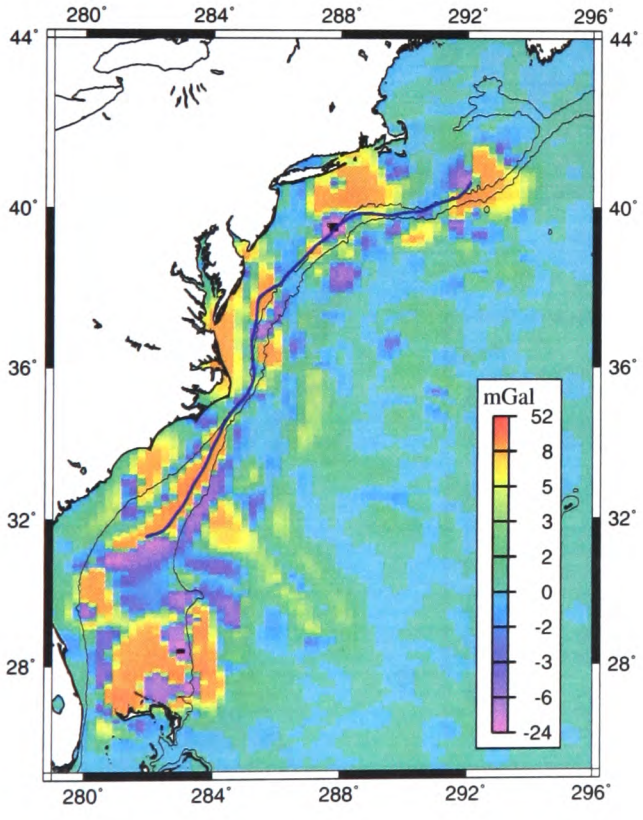
a) Flexural isostatic anomaly (IGA)



b) T_e distribution



c) T_e -5km effect on RMS IGA



d) T_e +5km effect on RMS IGA

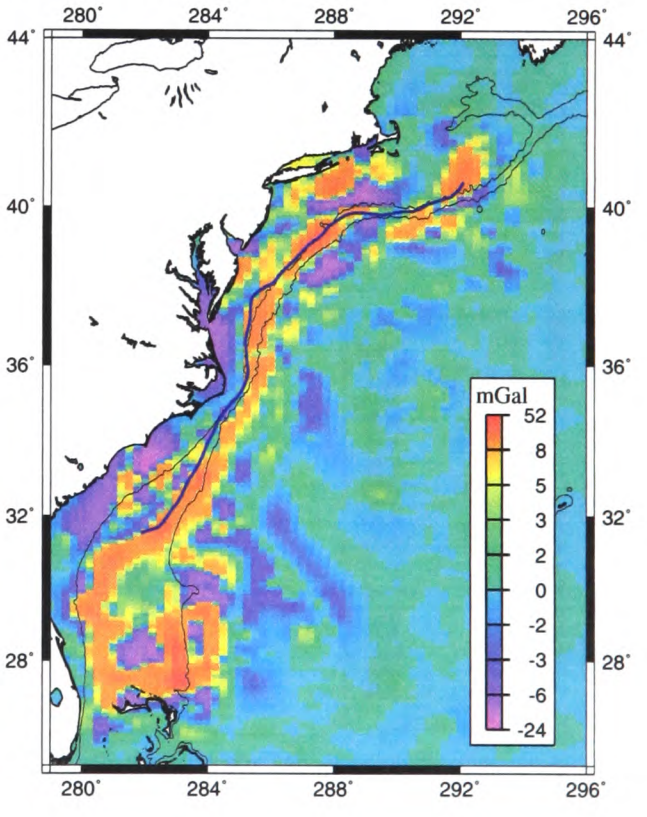
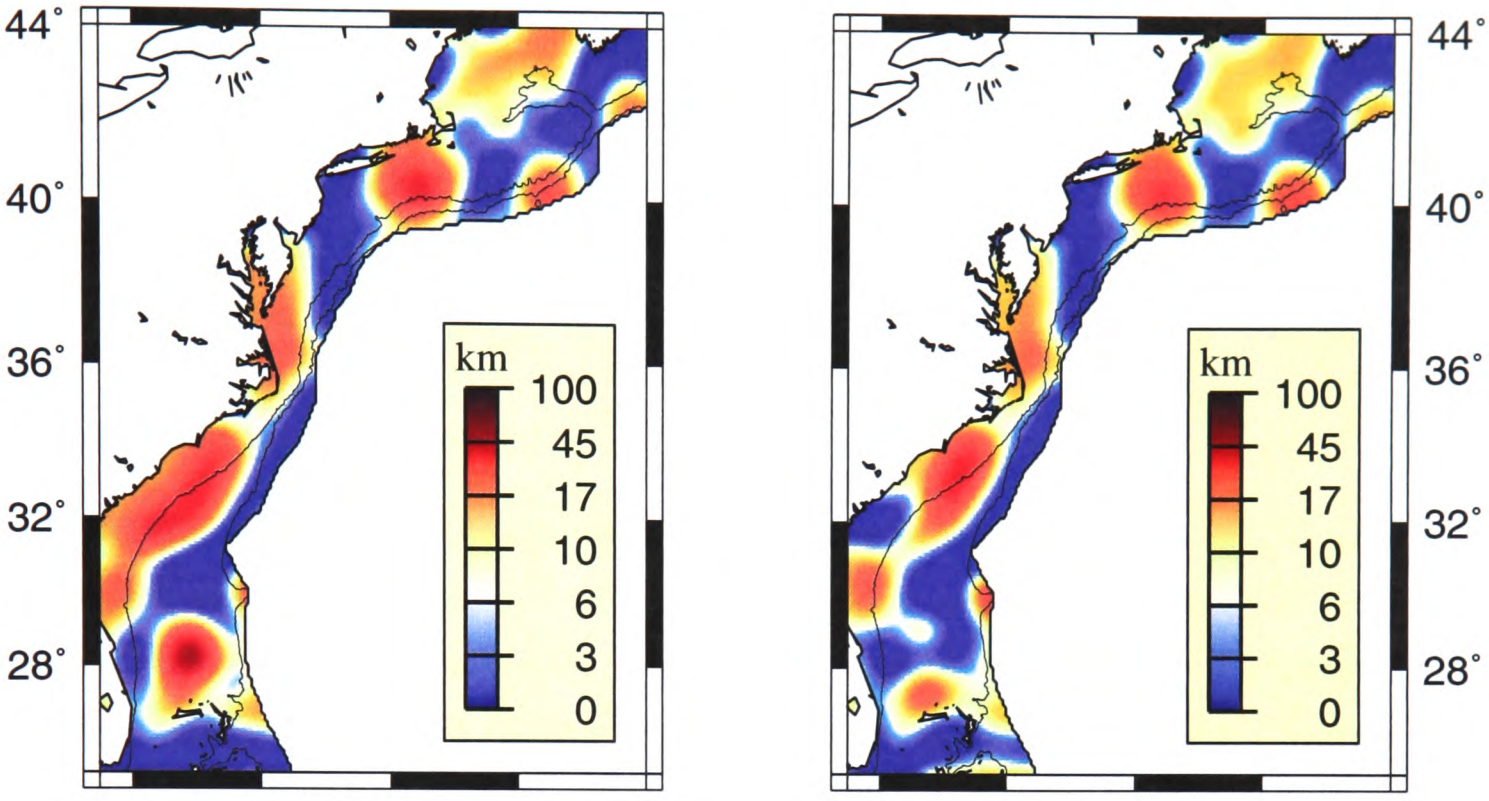


Figure 5.14: Effect of an increase or decrease in T_e of $5km$ on the RMS isostatic gravity anomaly. a) Iterative process-oriented analysis flexural isostatic gravity anomaly. Named basement features after Owens & Gohn [1985]. b) Analysis T_e distribution. c) Change in the windowed RMS isostatic gravity anomaly caused by a $5km$ reduction in the analysis T_e distribution. d) Change in the windowed RMS isostatic gravity anomaly caused by a $5km$ increase in the analysis T_e distribution.

a) Window size 0.5°x0.2°

b) Window size 1.0°x0.2°



c) Window size 1.5°x0.2°

d) Window size 1.5°x0.4°

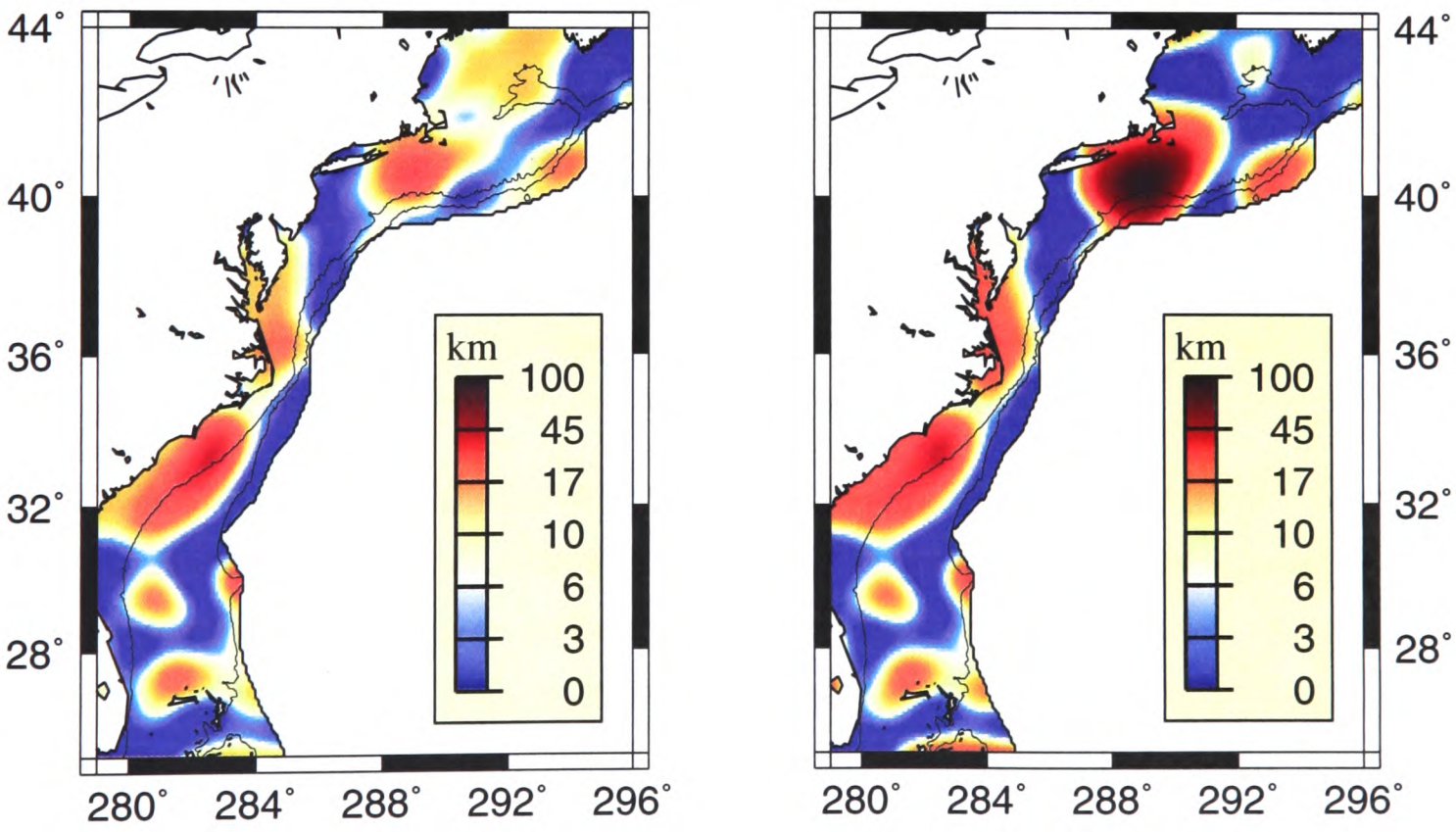


Figure 5.15: Effect of the data window size used to constrain T_e on the recovered T_e distribution. a) Original analysis ($0.5^o \times 0.2^o$ window size). b) Repeat of the analysis with a $1^o \times 0.2^o$ window size. c) Repeat of the analysis with a $1.5^o \times 0.2^o$ window size. b) Repeat of the analysis with a $1.5^o \times 0.4^o$ window size.

$13.9mGal$, and $14.2mGal$). However, despite producing a broadly comparable isostatic gravity anomaly along most of the margin, the degraded fourth distribution results in a large isostatic gravity anomaly low centered on the Long Island Platform, where the recovered T_e is highest, and a correspondingly large RMS amplitude of $23.1mGal$ (considerably larger even than the $18.7mGal$ RMS Airy IGA). Why this happens specifically at this location is unclear, but it may relate to a change in the margin orientation that brings the path of the Long Island Platform shelf break closer to the long axis of the analysis windows.

5.4.4 Model parameters

The sensitivity of the method to model parameters (densities of the crust, mantle, and sediment; surface sediment porosity and Athy depth constant; T_e; and the 'reference' crustal thickness for zero elevation topography) is tested using repeated uniform T_e reconstructions in which two parameters at a time are sequentially adjusted against each other. This allows the relative impact of model assumptions on the isostatic gravity anomaly to be assessed.

The sensitivity analyses have been plotted as the effects of parameter pairs on the RMS isostatic gravity anomaly (Figure 5.17). This figure shows that the main control on the RMS isostatic gravity anomaly is T_e; particularly for $T_e > 10km$.

Other noteworthy features of the sensitivity plots include:

- A gap in the plotted data in Figure 5.17c arises from combinations of reference crustal thickness and mantle density that require a Moho that is locally shallower than the basement depth. I.e. a negative thickness crust.

- The RMS isostatic gravity anomaly increases rapidly if a large surface porosity is combined with a small Athy depth constant (Figure 5.17e). This is because such a combination produces sediment porosities that remain high even at depths of several kilometers. This unrealistic under-estimation of the total sediment mass adversely affects both the calculated backstrip and the direct contribution of the sediment to the process-oriented sum gravity anomaly.

5.4.5 Sediment isopach data

The sediment isopach data used in this thesis have been derived using reflection seismic data. The interpretation was referenced against well data, but the apparent maximum total thickness of post-rift sediments is more than $15km$, and the deepest well penetrates

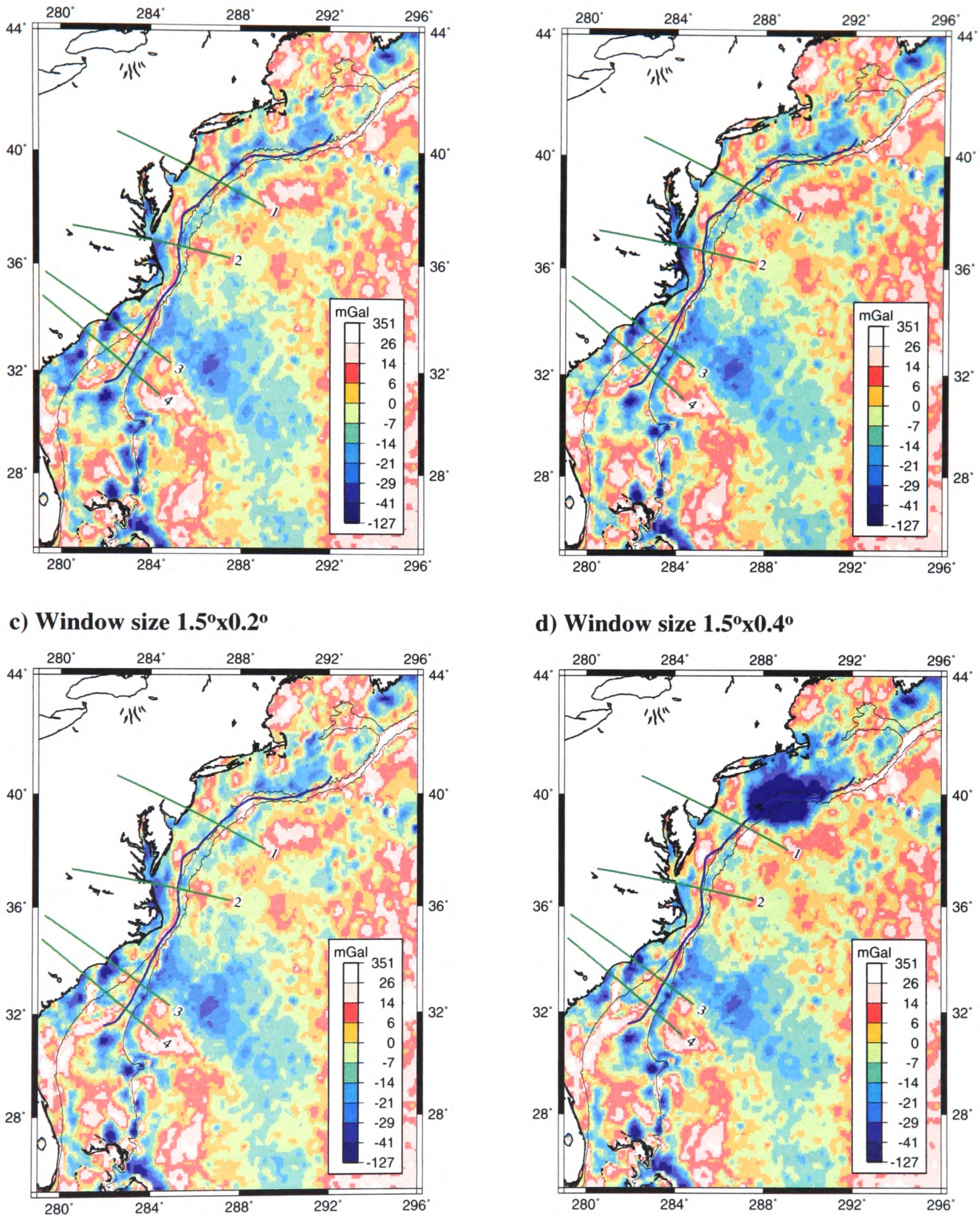


Figure 5.16: Effect on the flexural isostatic gravity anomaly of the data window size used to constrain T_e in the iterative process-oriented analysis. a) Original analysis ($0.5^o \times 0.2^o$ window size). b) Repeat of the analysis with a $1^o \times 0.2^o$ window size. c) Repeat of the analysis with a $1.5^o \times 0.2^o$ window size. b) Repeat of the analysis with a $1.5^o \times 0.4^o$ window size.

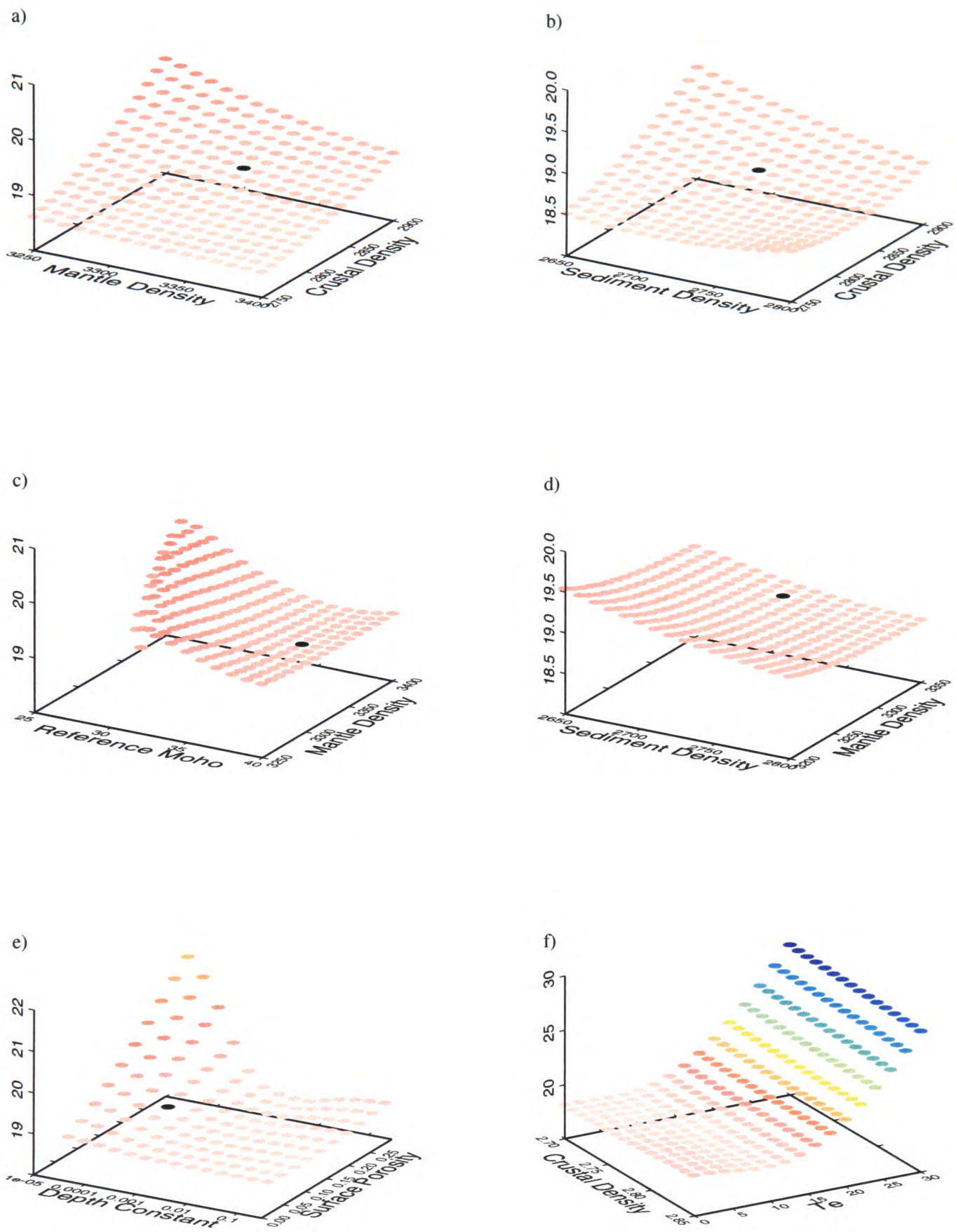


Figure 5.17: Sensitivity of the RMS isostatic gravity anomaly to model parameters (densities, sediment porosity-depth relationship, and 'reference' Moho depth for unrifted crust). (a) Mean crustal density and mantle density (Airy isostasy). (b) Mean crustal density and mean sediment density (Airy isostasy). (c) Reference Moho depth for unrifted crust and mantle density (Airy isostasy). (d) Mean sediment density and mantle density (Airy isostasy). (e) Athy sediment porosity parameters (Airy isostasy). (f) Mean crustal density and effective elastic thickness (Flexural isostasy). Black circles mark parameter values used in the iterative analysis.

less than $7km$. At greater depths, the absence of well data increases the likelihood of significant errors both in the seismic interpretation and in the travel-time to depth conversion. It is therefore uncertain how accurately the thicknesses of the deepest units have been determined.

Repetition of the iterative process-oriented analysis with a 30% thinning of the deepest (Middle Jurassic[?]) sedimentary unit produces a T_e distribution that is similar to that originally determined (Figure 5.18). This unit is generally confined to the deepest parts of the marginal basins, where the depth estimates are most likely to be in error, and is generally as thick as the other 6 post-rift units combined. The fact that the T_e distribution is similarly recovered despite a large decrease in basement depth suggests that the isostatic gravity anomaly (and hence the iterative analysis) is insensitive to the thickness of the deepest unit.

5.4.6 Strength during rifting

The models presented so far have assumed an Airy-isostatic model for the reconstruction of rifting crustal structure from total tectonic subsidence. This assumption implies that the crust (and lithosphere) has no significant strength during rifting. Application of a finite strength 'depth of necking' model (discussed in Chapter 4, Section 4.2) to the total tectonic subsidence from uniform T_e analyses allows the validity of this assumption to be tested.

In Figure 5.19 the sensitivity of the isostatic gravity anomaly to the depth of necking and rifting T_e is plotted for each of the profiles shown in Figure 5.10. The RMS IGA minima give the apparent necking response of the lithosphere to rifting at each location.

As is shown in Chapter 4, Section 4.2, the depth of necking model can produce a rift structure that is identical to the Airy model if either a particular 'neutral' depth of necking ($7.9km$ in this case) or zero lithospheric strength ($T_e = 0km$) is assumed. In profiles 1, 2, and 4 the RMS IGA minima correspond either to a depth of necking that is close to the neutral depth, or to a low lithospheric rigidity.

In one case (Profile 3) the optimum rifting T_e and necking depth are large (c.$25km$ and $19km$ respectively). However, the minimum RMS isostatic gravity anomaly associated with this profile is more than 35% larger than the minima associated with the other three, suggesting that there is some other contribution to the observed free-air anomaly that is skewing the analysis at this location.

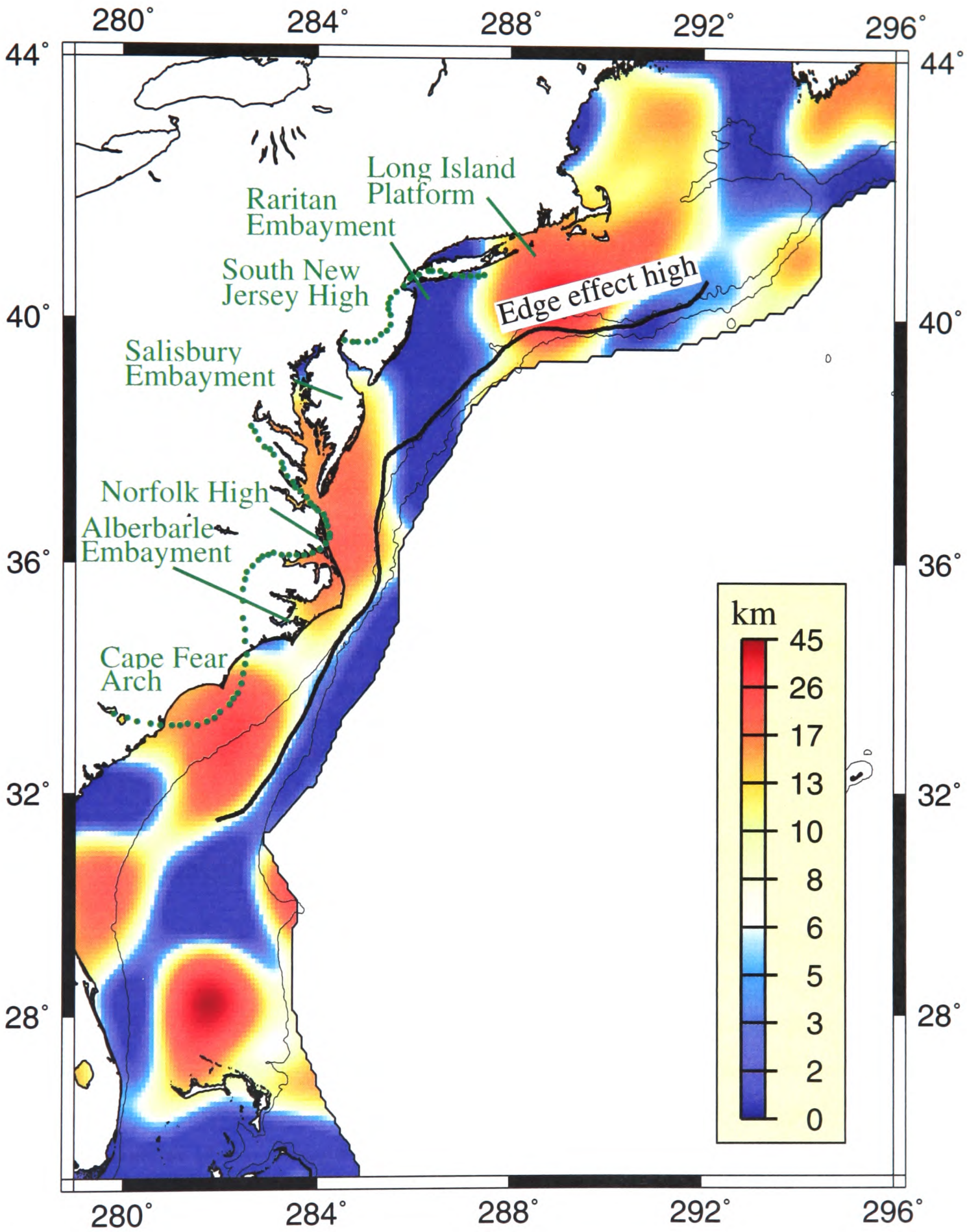


Figure 5.18: Effect of a 30% thinning of the Middle Jurassic(?) isopach on the derived T_e distribution.

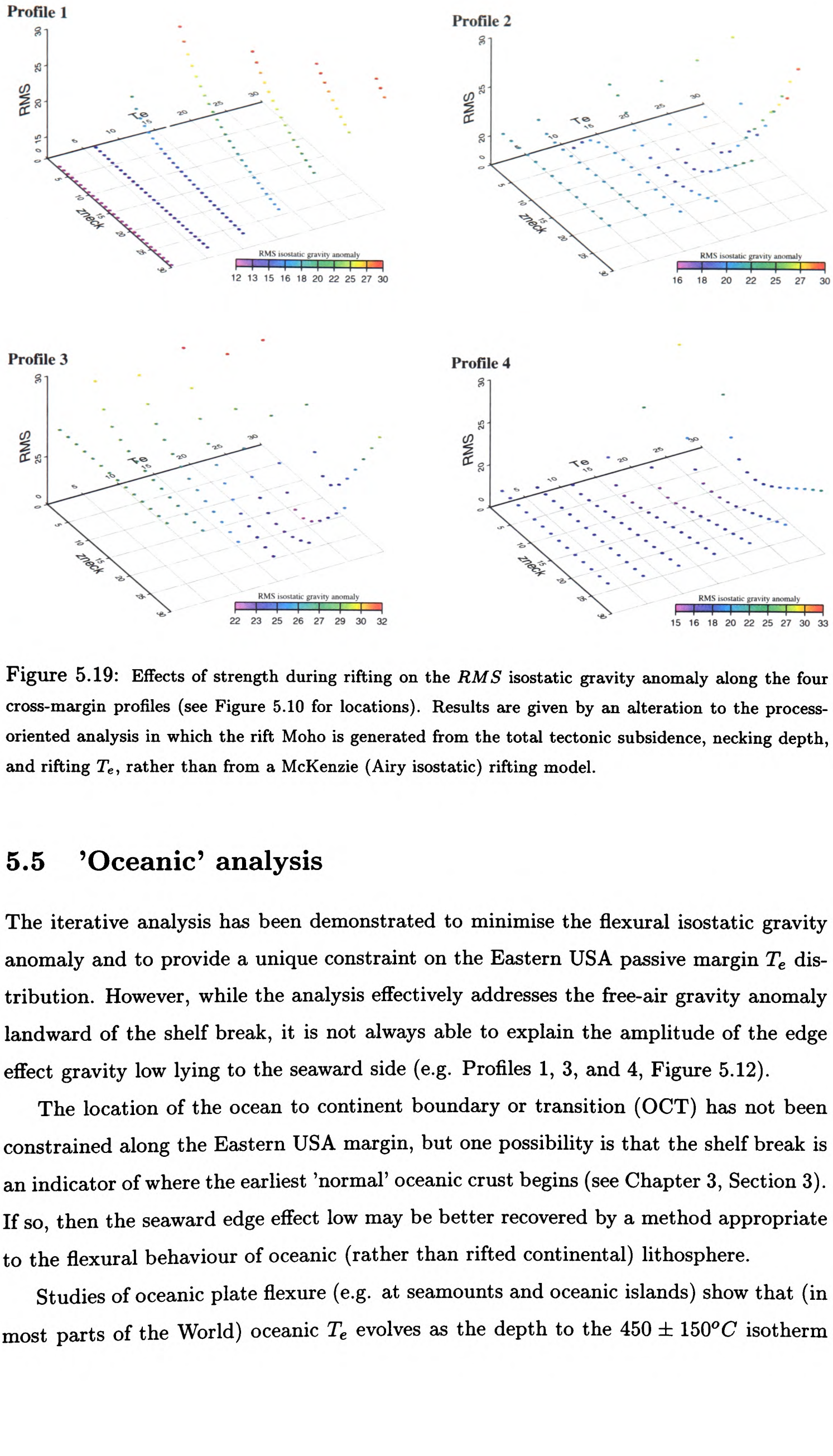


Figure 5.19: Effects of strength during rifting on the RMS isostatic gravity anomaly along the four cross-margin profiles (see Figure 5.10 for locations). Results are given by an alteration to the process-oriented analysis in which the rift Moho is generated from the total tectonic subsidence, necking depth, and rifting T_e, rather than from a McKenzie (Airy isostatic) rifting model.

5.5 'Oceanic' analysis

The iterative analysis has been demonstrated to minimise the flexural isostatic gravity anomaly and to provide a unique constraint on the Eastern USA passive margin T_e distribution. However, while the analysis effectively addresses the free-air gravity anomaly landward of the shelf break, it is not always able to explain the amplitude of the edge effect gravity low lying to the seaward side (e.g. Profiles 1, 3, and 4, Figure 5.12).

The location of the ocean to continent boundary or transition (OCT) has not been constrained along the Eastern USA margin, but one possibility is that the shelf break is an indicator of where the earliest 'normal' oceanic crust begins (see Chapter 3, Section 3). If so, then the seaward edge effect low may be better recovered by a method appropriate to the flexural behaviour of oceanic (rather than rifted continental) lithosphere.

Studies of oceanic plate flexure (e.g. at seamounts and oceanic islands) show that (in most parts of the World) oceanic T_e evolves as the depth to the 450 ± 150^oC isotherm

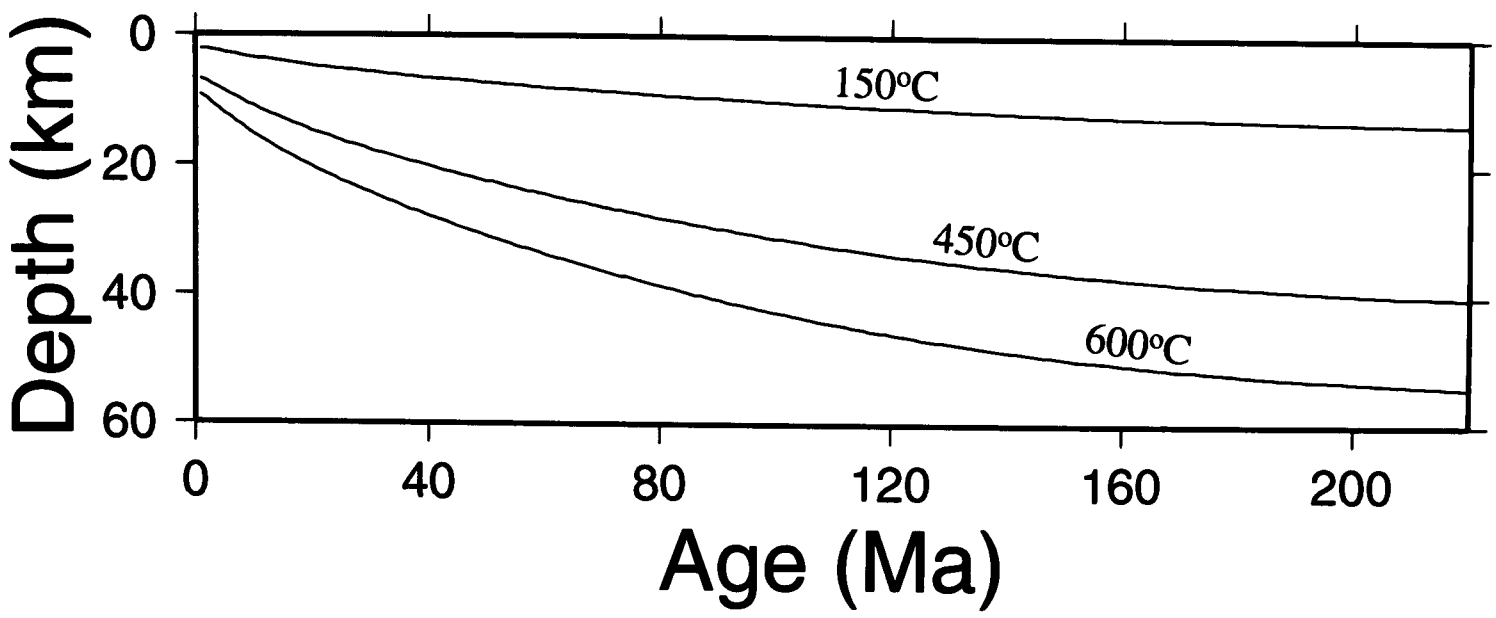


Figure 5.20: Depth to the $150°C$, $450°C$, and $600°C$ oceanic isotherms based on a 1-D cooling plate model [Parsons & Sclater, 1977].

based on a cooling plate model (e.g. Watts [1978], see Chapter 1, Section 1.1). Because the sediment units used in this thesis are tied to approximate depositional ages, it is possible to assign a loading T_e distribution to each unit, and hence to backstrip them with the assumption that they loaded lithosphere of oceanic type.

5.5.1 Backstripping

In order to define the T_e distribution for backstripping of each unit, the ocean age grid of Müller *et al.* [1997] can be used in conjunction with the approximate mean age of each of the 7 isopachs to determine lithospheric ages at the time of loading. This is simply a case of subtracting the mean age of each isopach from the present-day ocean age grid, and converting the ages to T_e using an isotherm depth in a 1-D cooling plate model (Figure 5.20). However, because the location of the ocean-continent transition (OCT) is unknown, the ocean age grid is incomplete. So to avoid prejudicing the apparent location of the ocean-continent transition, all areas of undefined origin and age are treated as lithosphere of earliest oceanic age.

The result is a series of T_e distributions for each of the 7 sedimentary isopachs (an example of which is shown in Figure 5.21). Cumulative backstripping of each of the units with the corresponding T_e distribution provides the total tectonic subsidence and sediment driven flexure from which the process-oriented gravity anomalies can be determined.

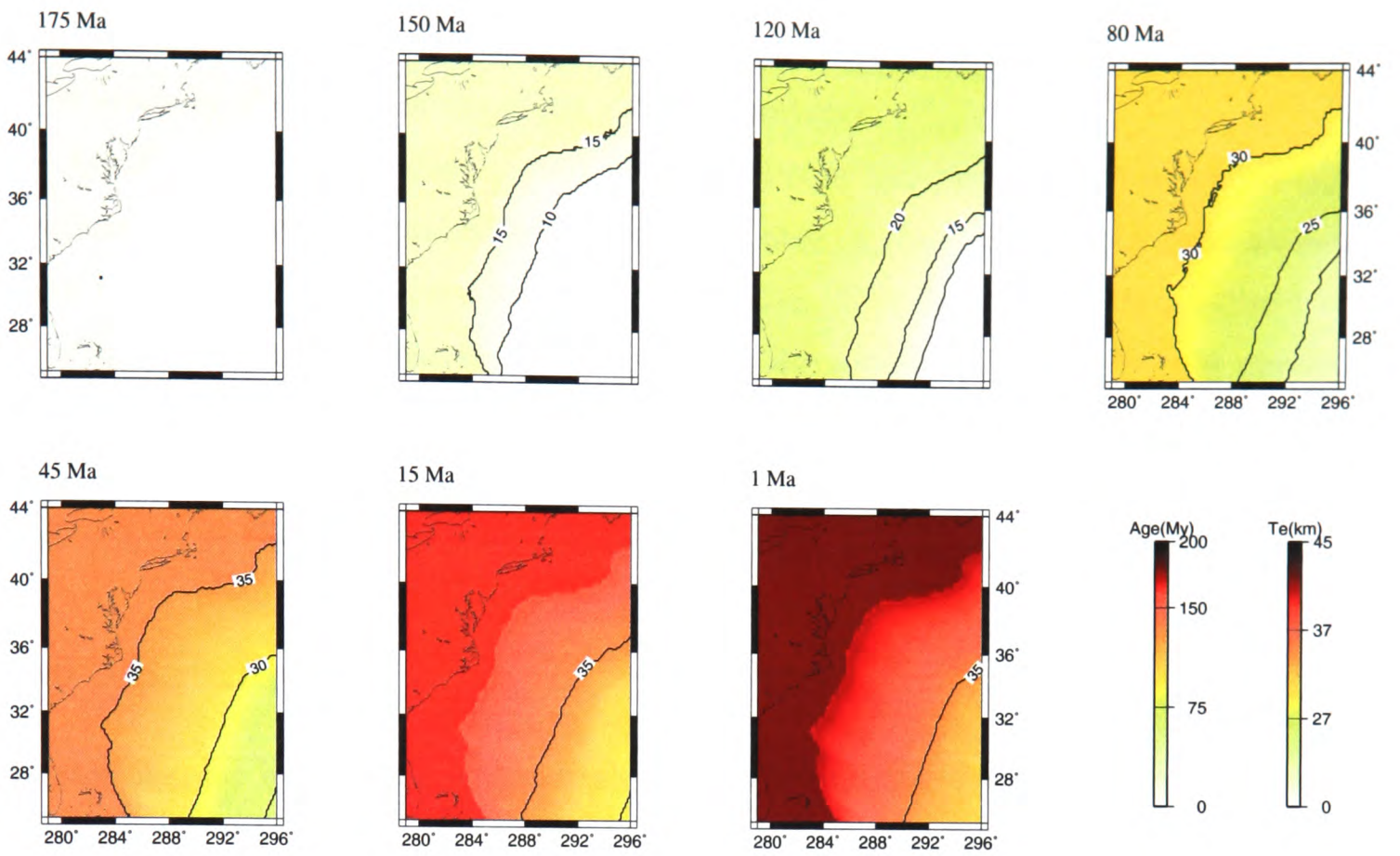


Figure 5.21: Evolution of T_e assuming that T_e is given by the depth of the 450^oC isotherm based on a 1-D cooling plate model. A $180Ma$ age of earliest seafloor spreading has been assumed in this example. Time steps are the mean ages of each of the backstripped isopachs. Contours are T_e in km.

5.5.2 Isostatic gravity anomalies

Figure 5.22 shows the 'oceanic' method flexural isostatic gravity anomalies for assumptions of: $200Ma$, $180Ma$, and $160Ma$, initial seafloor spreading ages; and T_e controlled by oceanic 1-D cooling plate model 300^oC, 450^oC, and 600^oC isotherms (representing 450 ± 150^oC).

Of particular importance is the manner with which the isostatic edge effect gravity low lying seaward of the shelf break is minimised. This is the area in which the iterative analysis often fails to account for the amplitude of the observed free-air gravity anomaly.

As Figure 5.22 shows, 450^oC is the optimum isotherm for depth of T_e estimation. Use of a higher temperature isotherm (which is deeper and therefore results in higher T_e) tends to result in large amplitude along-strike IGA fluctuations landward of the shelf break, while use of a lower temperature (lower T_e) isotherm leaves a large isostatic anomaly edge effect gravity low seaward of the Blake Plateau. Changing the age of earliest seafloor spreading produces similar effects, with an age older than $180Ma$ leading to higher T_e close to the margin, and a younger age leading to lower T_e in the same area.

Although there is some trade-off between the controlling isotherm and the rifting age, the lowest amplitude along-strike fluctuations in the IGA seaward of the shelf break

result from analyses in which the age of earliest seafloor spreading is $160 - 180Ma$ and T_e is given by the depth of the 450^oC oceanic isotherm.

Across-strike profiles demonstrate that in parts of the margin the 'oceanic' analysis produces a calculated seaward edge effect low that is closer to the observed anomaly than that from the iterative analysis (Figure 5.23). This can be seen on profiles 1 and 4, where the iterative analysis did not explain the amplitude of the free-air anomaly. However, on Profile 2 the iterative analysis accounts equally well for the observed free-air gravity anomaly, and on Profile 3 neither the 'oceanic' method nor the iterative analysis successfully recover the observed free-air gravity anomaly seaward of the shelf break.

5.6 Summary

In this chapter it has been demonstrated that the observed free-air gravity anomaly of the Eastern USA passive continental margin can only be partially explained by models in which sediments load a uniform T_e lithosphere. Particular emphasis has been placed on how closely the calculated free-air gravity anomaly corresponding to each uniform plate T_e agrees with the observed edge effect anomaly; the amplitude and wavelength of which is strongly influenced by the flexural response to sediment loading (e.g. Watts & Marr [1995]). Comparative minimisation of specific uniform T_e isostatic gravity anomalies over others in different regions is suggestive of margin wide structural segmentation.

An iterative process-oriented analysis - in which spatial variations in T_e are constrained by minimisation of the flexural isostatic gravity anomaly - provides stronger evidence for segmentation of the margin. The recovered T_e distribution is stable, and the accompanying calculated free-air gravity anomaly is in good agreement with the observed free-air edge effect gravity anomaly high and landward low along most of the margin.

The robustness of this analysis has been demonstrated through a series of tests for: bias arising from the initial T_e distribution; the influence of small T_e variations on the isostatic gravity anomaly; the influence of changes in analysis window size; the effect of model densities and the reference zero elevation crustal thickness on isostatic gravity anomalies; the sensitivity of the method to errors in the deepest sediment isopach data; and the possibility of strength during rifting.

Only the results of the iterative process-oriented analysis have been presented so far. These provide the basis for discussion and further analysis in the following chapters, in which structural segmentation and isostatic gravity anomalies of the margin are interpreted.

An additional 'oceanic' analysis has been applied, in which backstripping is controlled

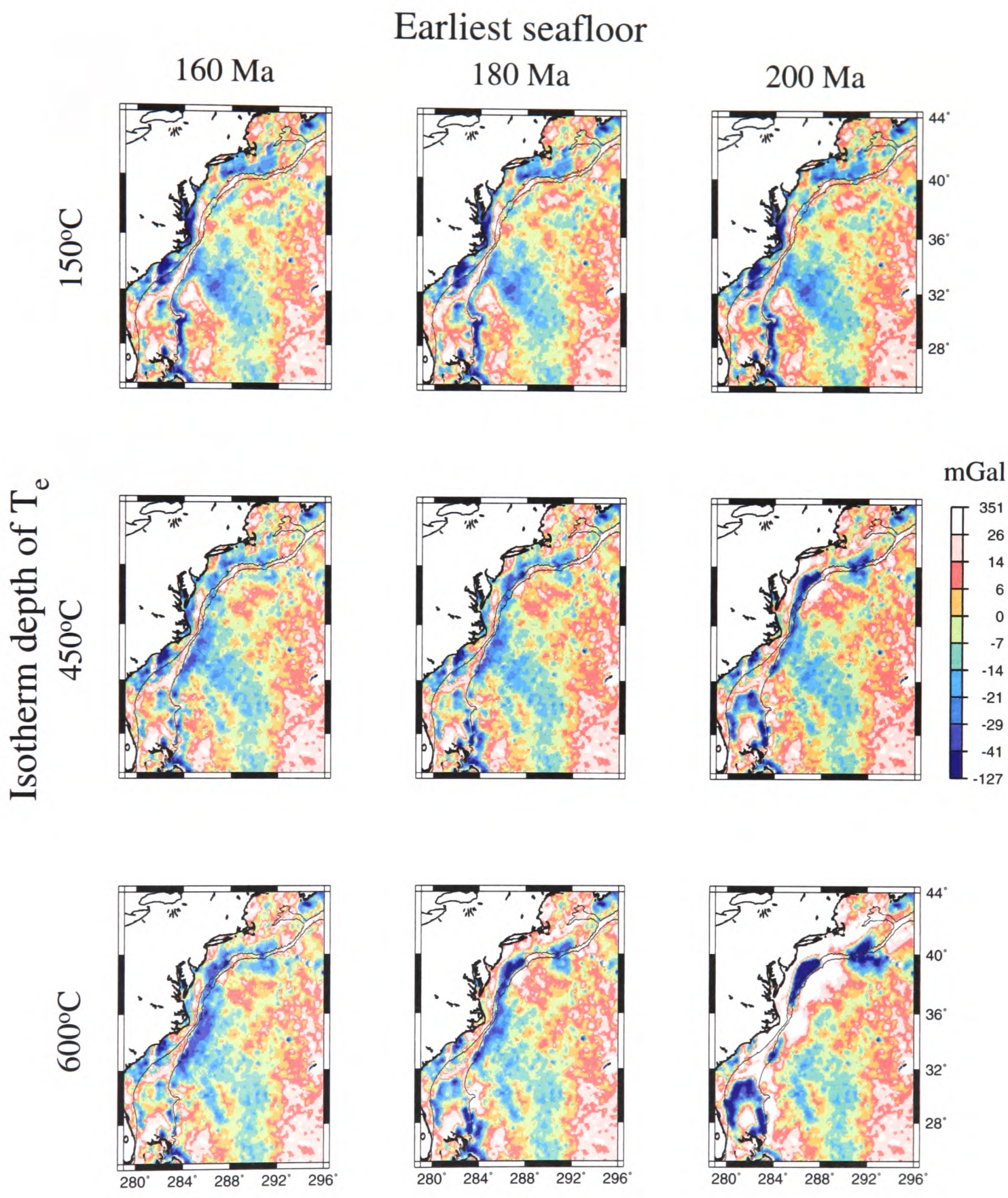


Figure 5.22: Effect of T_e limiting isotherm and assumed age of earliest seafloor spreading on the 'oceanic' analysis isostatic gravity anomaly.

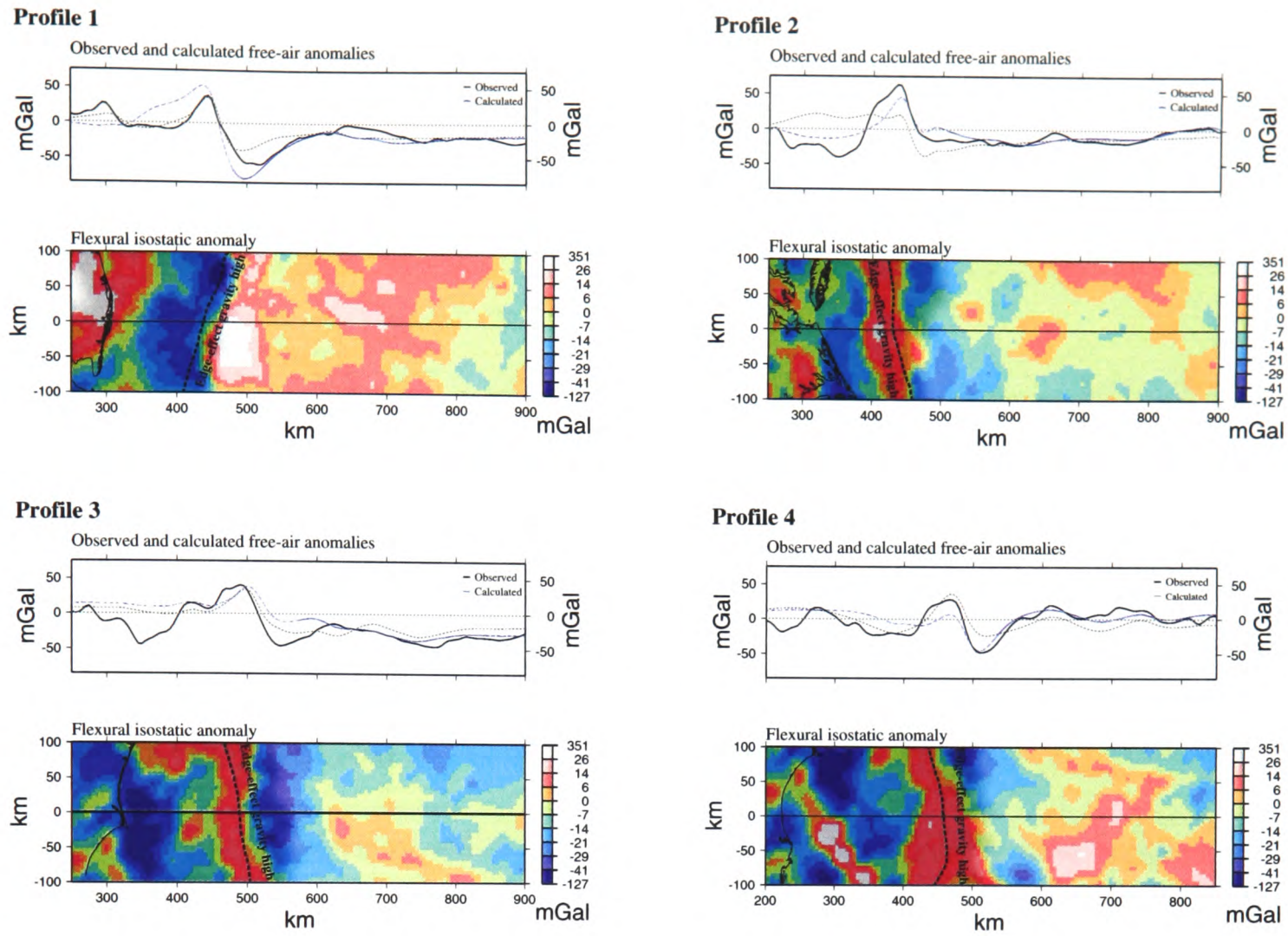


Figure 5.23: Observed and calculated ('oceanic' model with $180Ma$ earliest seafloor spreading and T_e given by depth of the $450°C$ isotherm) free-air gravity anomalies along strike-normal profiles labelled 1 to 4 in Figure 5.10. To place emphasis on the rifted margin basins, calculated anomalies are dashed in areas landward of the earliest dated oceanic crust (according to Müller *et al.* [1997]. Free-air gravity anomalies from the iterative process-oriented analysis are shown for comparison (dashed lines). Maps show the 'oceanic' model flexural isostatic gravity anomaly.

by a T_e that evolves with lithospheric age after initial seafloor spreading. This produces a calculated free-air gravity anomaly that, on two out of four cross-margin profiles, conforms more closely to the observed seaward edge effect low than that of the iterative method. Whether this offers a means of constraining the location of the ocean to continent transition (or boundary) along parts of the margin is a further discussion point in the following chapter.

Chapter 6

Process-oriented analysis - Discussion

6.1 Introduction

Process-oriented analysis of sediment thickness and gravity anomaly data suggests that the Eastern USA margin is segmented in terms of its effective elastic thickness. The most likely origins for this segmentation are: inheritance of pre-rift structure; alteration of the yield strength envelope by thinning during rifting; and post-rift lithospheric yielding caused by load driven curvature. The first of these possibilities is not easily tested, but the effects of thinning and flexural curvature due to sedimentary loading can be assessed from the process-oriented analysis.

Any segmentation that is not directly explained by these effects can be considered as resulting from: structural inheritance; second-order controls such as sedimentary thermal blanketing; and limitations of the analysis methods and assumptions. In particular, there may be fundamental segmentation of lithospheric structure relating to earlier major tectonic events (see Chapter 3, Section 1).

The iterative variable elastic plate thickness analysis significantly reduces the isostatic gravity anomaly relative to Airy and uniform elastic plate methods. In so doing, it exposes secondary contributions to the gravity anomaly. Isolation of these anomalies allows them to be related to structural segmentation and to the location of the ocean to continent boundary or transition.

6.2 Distribution of mechanical strength

In Chapter 5 structural segmentation of the Eastern USA passive continental margin was identified in terms of significant and long term spatial segmentation of effective elastic thickness (an analog for effective mechanical strength of the lithosphere). There are questions regarding to what extent this segmentation is a result of: inheritance of pre-existing structure; the rifting process; and the effects of sedimentation (e.g. curvature induced yielding).

The effects of rifting and sedimentation are considered here first, as these can be assessed using components of the process-oriented analysis. The role of inheritance is then discussed in the context of segmentation that is not explained by these processes alone.

6.2.1 Effects of rifting on mechanical strength

Continental rifting thins the lithospheric crust and mantle, and raises the geothermal gradient in proportion to the stretching factor, β. Hence, if thermal relaxation during rifting is ignored, there is an expectation that early in the margin evolution the mechanical thickness will be reduced as the thinning ratio of the lithosphere.

The recovered T_e distribution does indicate a correlation between crustal thinning and reduction of mechanical strength (Figure 6.1), with notable exceptions in the southern Blake Plateau and towards the seaward side of the Georges Bank Basin. Regions of narrow rift stage crust are bounded by high T_e platforms extending offshore from the Carolinas and east of Long Island. These separate the low T_e embayments fringing the broad rift stage crust of the Blake Plateau Basin and Baltimore Canyon Trough.

A region of high strength within the Blake Plateau Basin centers on an observed gravity anomaly high that does not correspond with features of the basement or topography structure in the analysis datasets. It is likely that the large apparent T_e is due to structure that provides a large contribution to the gravity anomaly, but is not related to flexural sediment loading. A smaller high T_e zone in the seaward part of the Georges Bank Basin is located towards the edge of the USGS seismic surveys, and may reflect an according lack of basement resolution.

A quantitative examination of the relationship between effective elastic thickness, T_e, and lithospheric thinning, β, is shown in Figure 6.2. Beginning with a model in which the lithosphere consists of a stack of n uncoupled elastic plates of initial thickness h_1 to h_n are instantaneously thinned with stretching factors β_1 to β_n respectively, T_e is defined by:

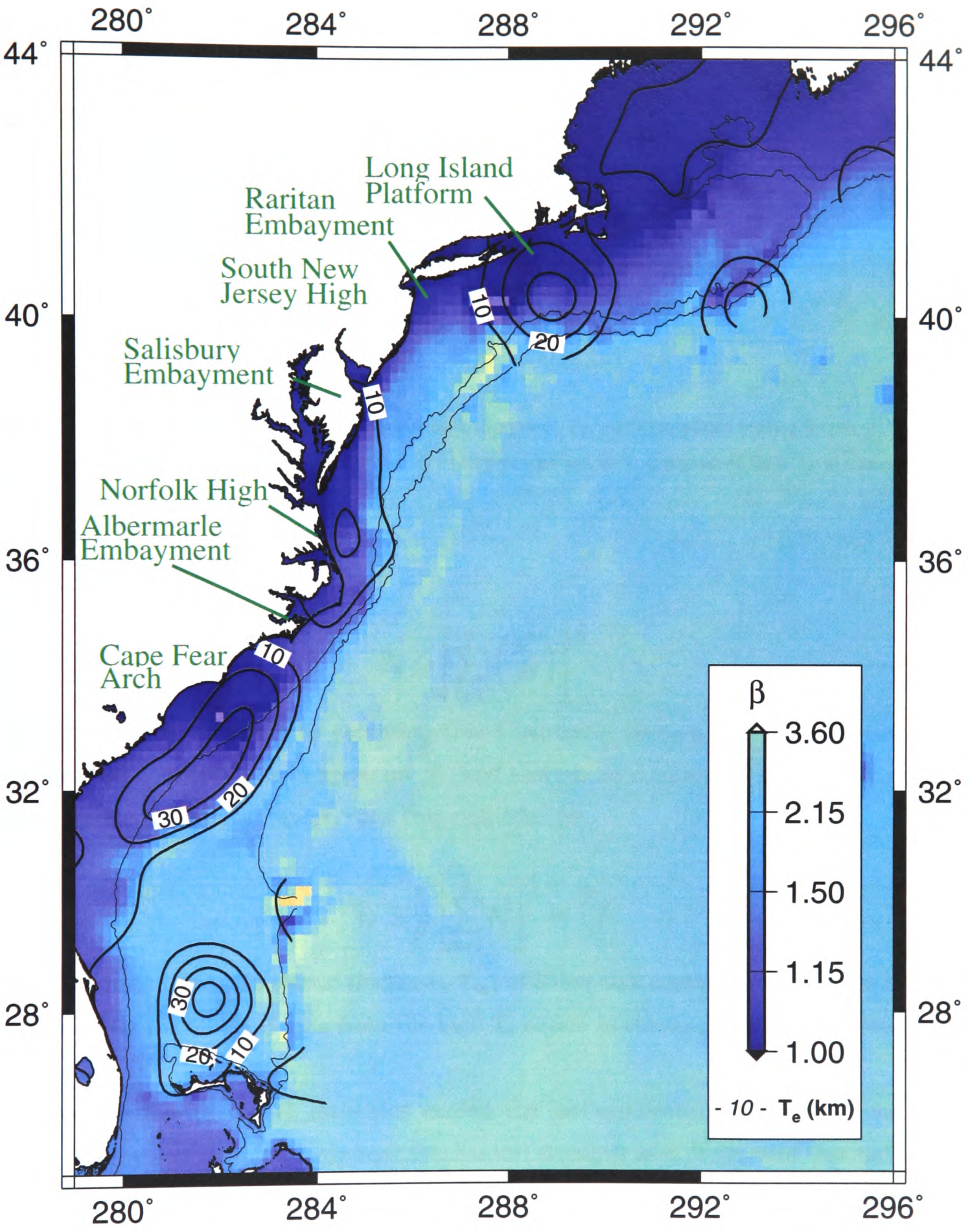


Figure 6.1: Crustal stretching factor, β, and effective elastic thickness ($10km$ contours).

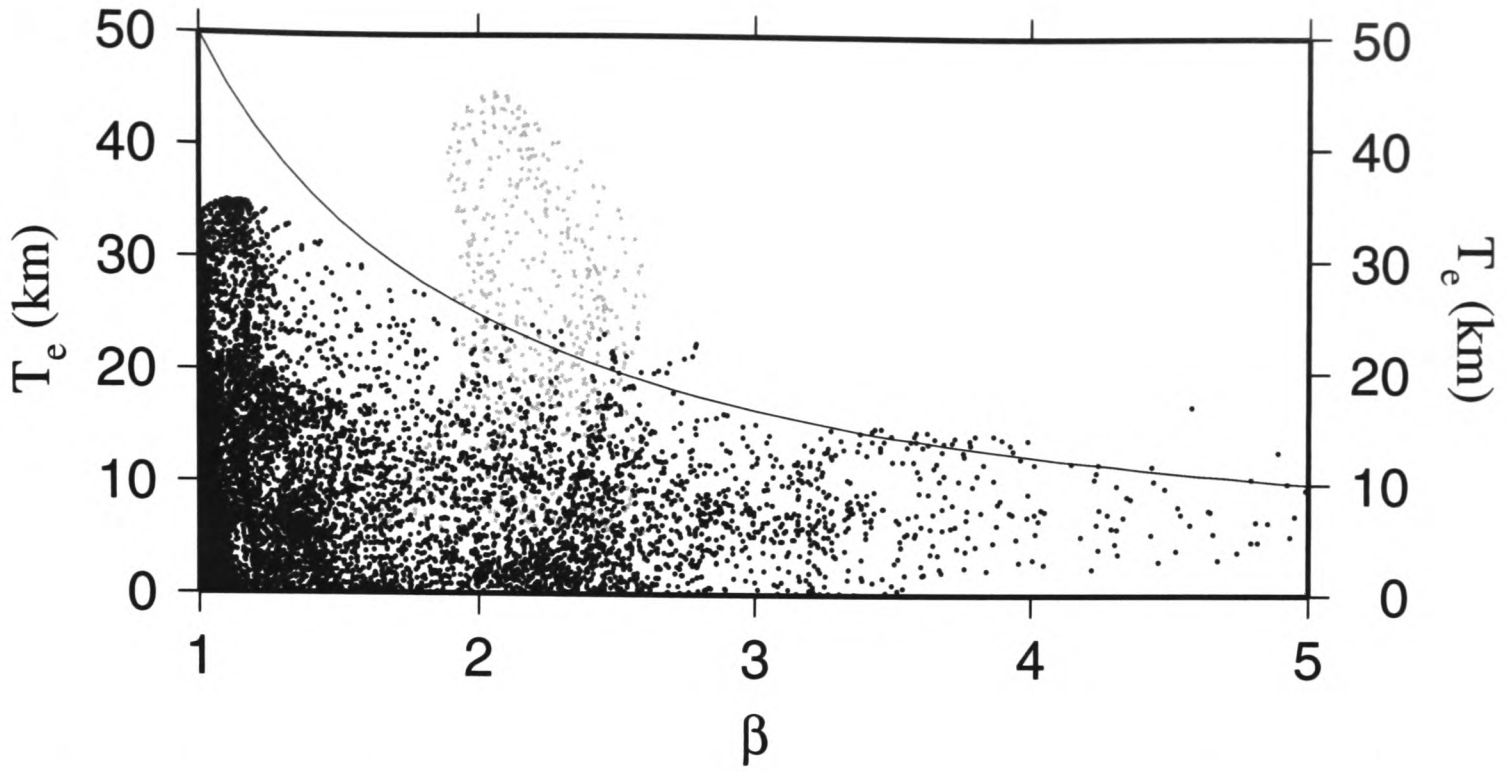


Figure 6.2: Relationship between effective elastic thickness, T_e, and crustal stretching factor, β. Plotted curve is for linear thinning of a $50km$ initial T_e. Grey points are from a region of high T_e in the southern Blake Plateau (see text).

$$T_e \lesssim \left[\sum_{i=1}^{n}\left(\frac{h_i^3}{\beta_i^3}\right)\right]^{\frac{1}{3}} \tag{6.1}$$

If β is uniform, due only to extension (see Chapter 2, Section 6.5, for potential non-extensional contributions to apparent β), and there is no coupling of initially uncoupled lithospheric mechanical layers, then this simplifies to:

$$T_e \lesssim \frac{1}{\beta}\left[\sum_{i=1}^{n} h_i^3\right]^{\frac{1}{3}} = \frac{T_{e_0}}{\beta} \tag{6.2}$$

With an initial effective elastic thickness, T_{e_0}, of $50km$ this confines 97.5% of the margin T_e estimates (or 99.5% if data from the high T_e region in the southern Blake Plateau are excluded).

Because few of the T_e estimates exceed the instantaneously thinned T_e (see Figure 6.2), any recovery of lithospheric mechanical strength as a product of thermal relaxation and possible coupling of the thinned mantle and crust is not evident in the recovered segmentation. It may be that the estimates are biased towards low values because the largest proportion of sediments were deposited early in the margin history.

6.2.2 Effects of sedimentation on mechanical strength

Continental extension is undoubtably a contributor to lithospheric weakening, but has been shown only to confine the *maximum* T_e of the rifted lithosphere. The bulk of estimates are widely scattered beneath the values suggested by thinning alone. The most significant post-rift alteration to the margin has been the accumulation of large sediment thicknesses in the offshore marginal basins. These may have contributed to post-rift weakening of the lithosphere and slowed thermal relaxation in the post-rift phase.

Sediment distribution

Early post-rift deposition along the margin was controlled by the availability of marginal basin space provided by lithospheric thinning. As increasing sediment thicknesses accumulated, the basins continued to subside as an isostatic response both to cooling of the rifted lithosphere and to the sedimentary loading of the margin. This confined the bulk of post-rift deposition to the marginal basins, and explains the similarity between the distribution of lithospheric extension already shown in Figure 6.1 and the distribution of sediment thickness shown in Figure 6.3.

The marginal basins are marked by low T_e, which increases rapidly across the hinge zone of the southern Baltimore Canyon Trough, Carolina Trough, and northwestern Baltimore Canyon Trough. The landward edges of these basins are effectively marked by the $10km$ T_e contour.

The coincidence of thick sediments with high stretching factors limits the degree to which the contributions of rifting and sedimentation to T_e can be distinctly resolved. The association of thick sediments with low T_e may be because sediments preferentially accumulated in what were already the weakest parts of the rifted margin. However, the sediment load will also have acted - through thermal blanketing and load driven subsidence - to maintain higher temperatures, and hence lower lithospheric strength, than would otherwise be expected.

Flexural curvature

In order to evaluate the role of yielding, the flexural curvature, K, due to post-rift sediment loading has been calculated[1] and compared to the resolved T_e distribution (Figure 6.4). The $10km$ T_e contour is seen to delimit areas of high curvature and low strength;

[1]Maximum curvature (including polarity) derived from second derivatives of flexure calculated in the Fourier domain using 'grdfft', from the Generic Mapping Tools 3.0 package [Wessel & Smith, 1995].

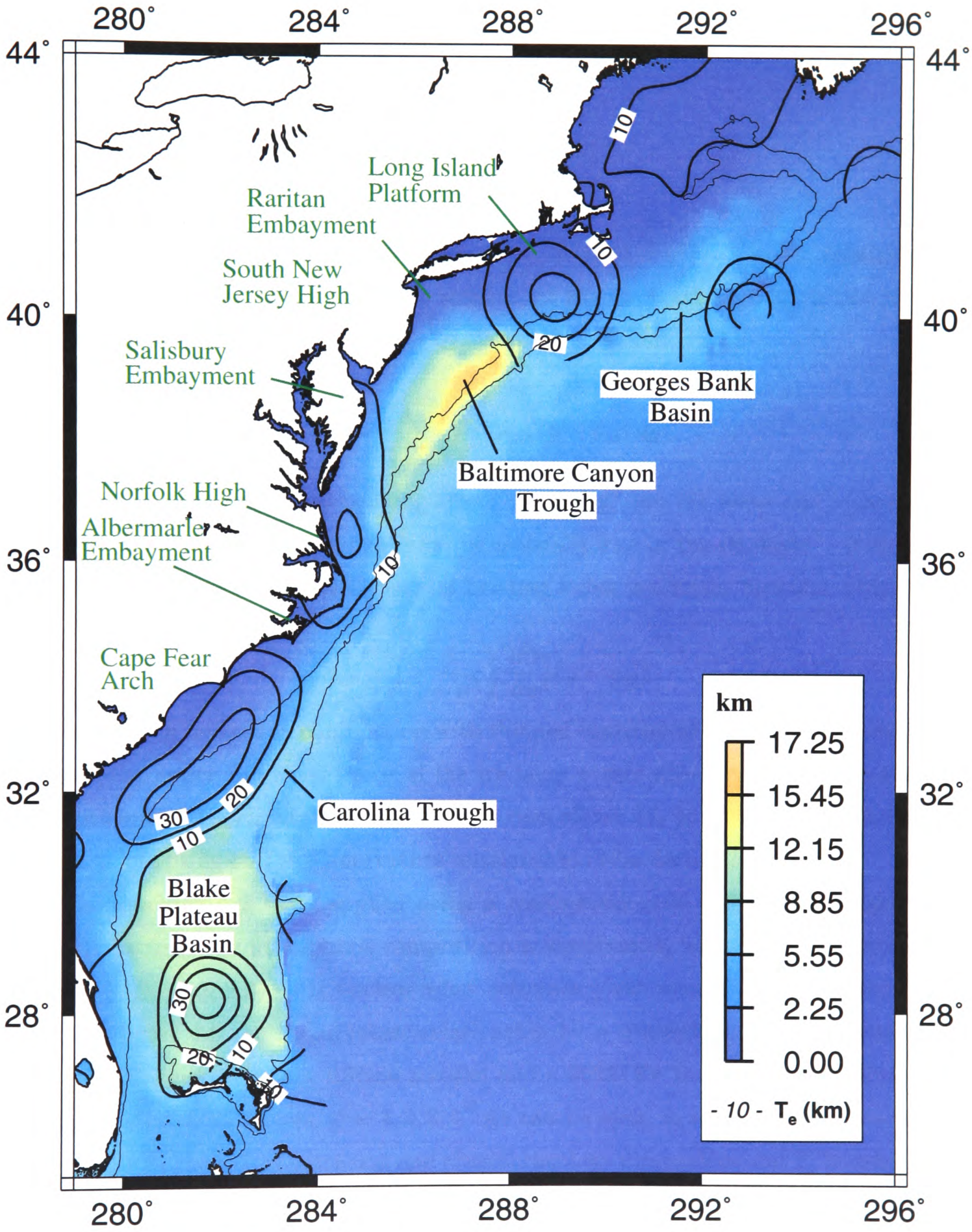


Figure 6.3: Sediment thickness and effective elastic thickness (10km contours).

supporting a link between mechanical thickness and yielding caused by lithospheric curvature.

The stresses induced by flexural curvature cause yielding in parts of the lithospheric yield strength envelope. Burov & Diament [1995] define the dependence of effective elastic thickness on curvature as:

$$T_e = \left[\frac{M_x}{D_0} \left(\frac{\partial^2 w}{\partial x^2} \right)^{-1} \right]^{\frac{1}{3}} \tag{6.3}$$

In which $(\partial^2 w / \partial x^2)$ is the plate curvature, $D_0 = E\left[12\left(1-\nu^2\right)\right]^{-1}$ and is dependent on the Young's modulus, E and Poisson's ratio, ν, of the material, and M_x is the bending moment defined for an n-layered plate by [Burov & Diament, 1995]:

$$M_x = -\sum_{i=1}^{n} \int_{y_i^-}^{y_i^+} \sigma_{xx} \left(y - y_{ni}\right) dy \tag{6.4}$$

In which σ_{xx} is the horizontal bending stress, y_i^- and y_i^+ are the lower and upper limits of the ith layer, and y_{ni} is the depth to the neutral plane of the ith layer[2]. If Hookean behaviour is assumed then the horizontal bending stress is a linear function of depth:

$$\sigma_{xx} = \left(\frac{E}{1-\nu^2} \right) \frac{\partial^2 w}{\partial x^2} (y - y_{ni}) \tag{6.5}$$

Which can then be used in conjunction with thinned continental yield strength envelopes to define the upper and lower limits of the ith layer within which yield strength exceeds curvature induced horizontal stresses. This in turn allows M_x to be calculated and hence the effects of rifting on the T_e-curvature relationship to be derived.

This approach has been applied using a continental yield strength envelope (Figure 6.5). Because the lithospheric composition is significantly altered during rifting (see Chapter 3, Section 2.3), it is unclear what reference yield strength envelope should be used. In Figure 6.5 the T_e-curvature relationship for a lithosphere with: a $38km$ thick quartz rheology crust; a dry olivine mantle; and a $250MYr$ thermal age; is plotted for a range of stretching factors, $\beta = 1, 2, 3, 4$. As can be seen, in regions of high curvature $(K > 1 \times 10^{-6})$ the role of extension and crustal rheology diminishes, and T_e is dominated by the amount of curvature induced yielding. This means that in this range of curvatures the T_e is relatively insensitive to the applicable yield strength envelope.

Comparison of the yield strength envelope model with curvature and T_e from the Eastern USA margin (black dots in Figure 6.5a,b) confirms the role of yielding in controlling the observed decay of maximum T_e in regions of high curvature. At lower curvatures

[2] y_{ni} migrates to maintain the neutral surface in each mechanical layer at a given curvature

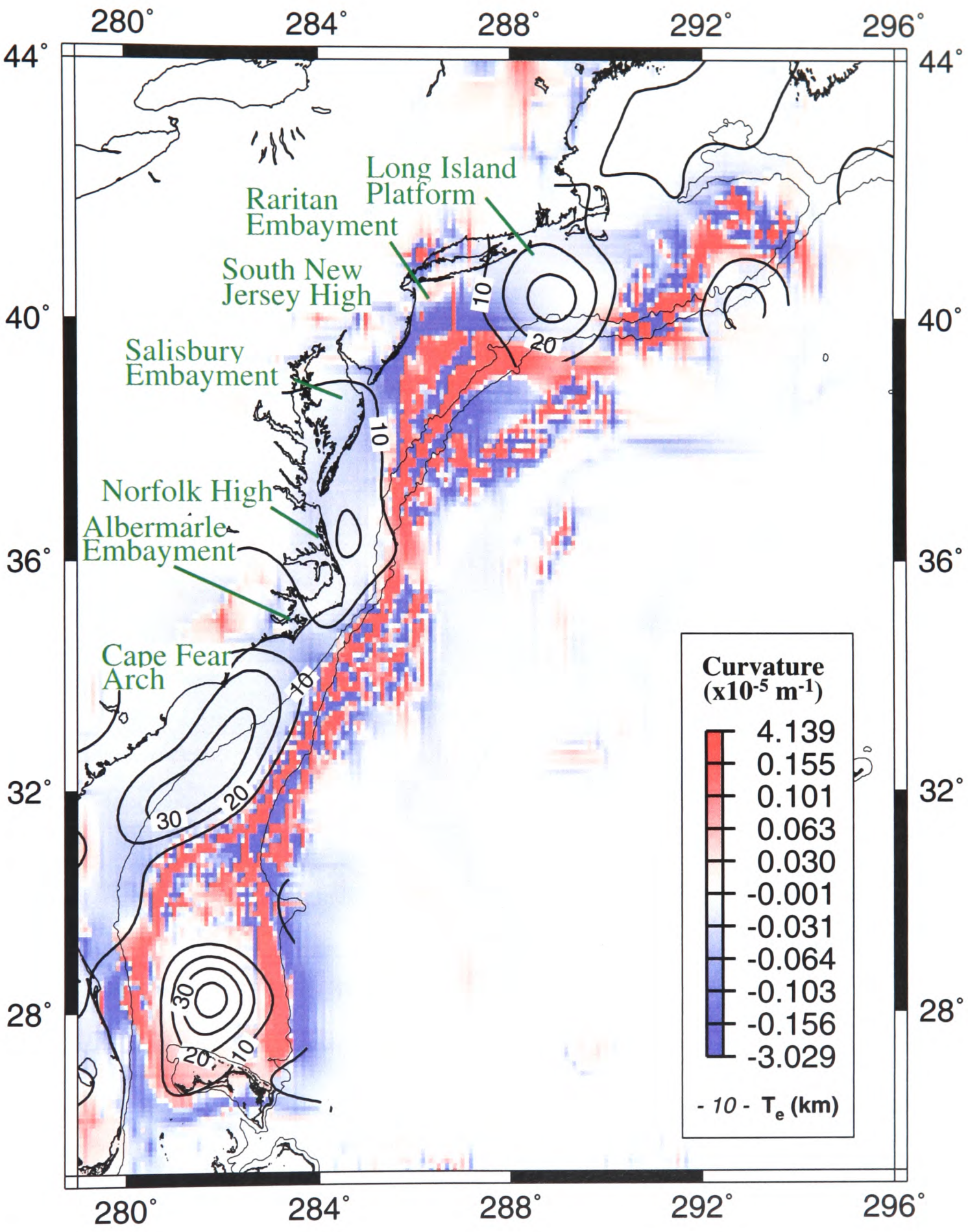


Figure 6.4: Maximum flexural curvature due to sediment loading, and effective elastic thickness ($10km$ contours). Positive curvature involves shallow compression, negative curvature involves shallow tension.

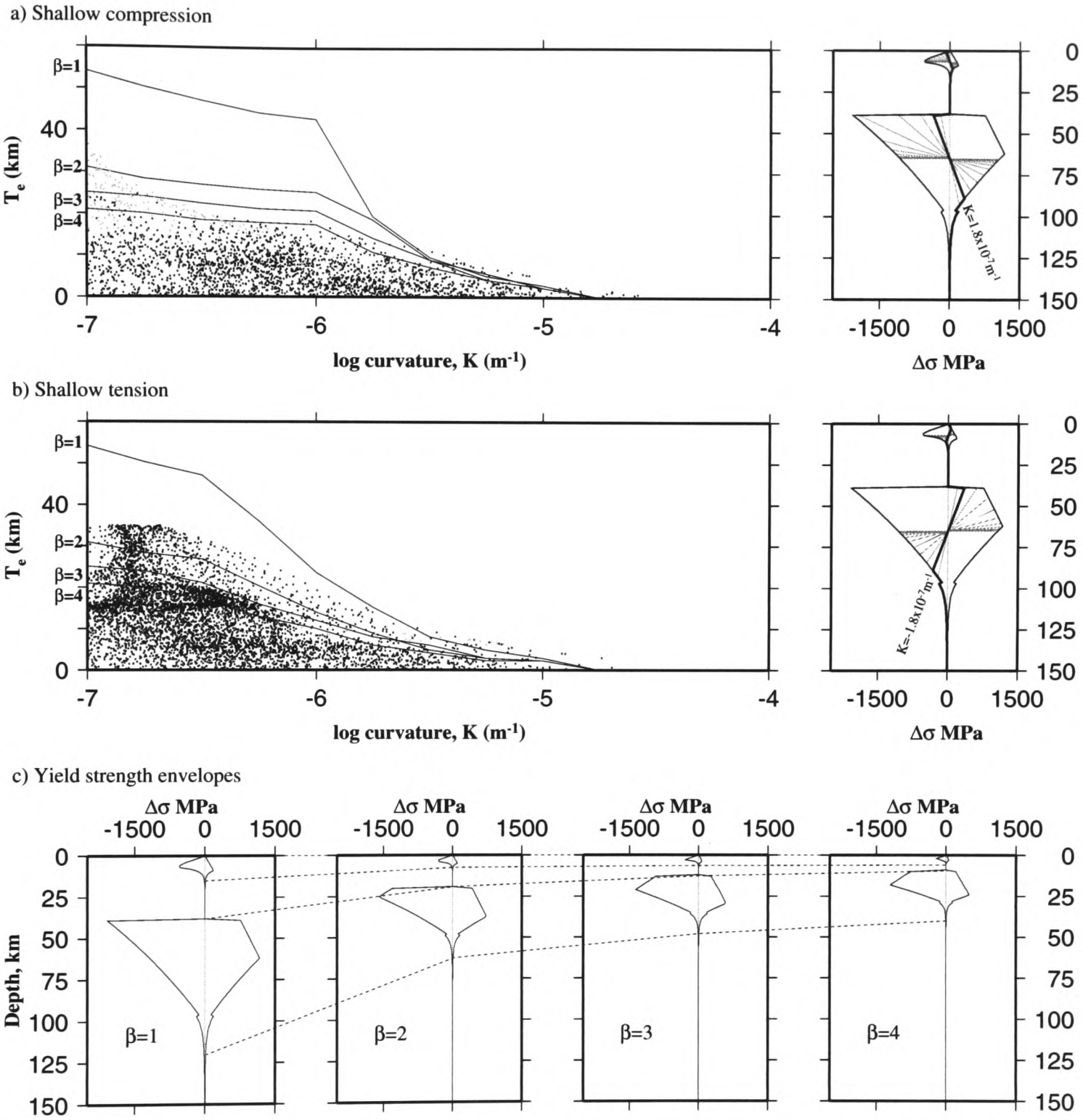


Figure 6.5: Relationship between effective elastic thickness and curvature induced yielding of a continental yield strength envelope. Observed data (black points) are plotted against curves calculated for curvature induced yielding of thinned lithosphere ($\beta = 1, 2, 3, 4$). a) Shallow compression, b) Shallow tension, c) Effect of thinning of the yield strength envelope (rifting with $5MYr$ cooling). See text for description of the models.

($K < 1 \times 10^{-6}$) the relationship is less well confined, and T_e estimates are increasingly widely scattered; suggesting a range of controlling yield strength envelopes.

Returning to the T_e-curvature map (Figure 6.4), it can be seen that high curvatures are generally observed around the edges of the marginal basins. It appears that flexural curvature driven by the accumulating sediments has caused yielding in the hinge zone, and thus has helped to confine load driven subsidence to the marginal basins. This provides a positive feedback between ongoing sediment deposition, weakening of the hinge zone, and the maintenance of existing depocenters. As sedimentation progressed, so the weakening hinge zone will have increasingly limited sediment load driven subsidence to the offshore basins, allowing T_e to remain high in the platforms that define their boundaries.

6.2.3 Inheritance of mechanical strength

Platforms and embayments

Yielding of the hinge zone due to flexural curvature has helped to maintain a sharp contrast between the strong marginal platforms and adjacent weak marginal basins. However, the strong platforms bounding the narrow Carolina Trough separate structural embayments that are marked by broadening of the rift stage lithosphere (forming the Blake Plateau Basin and central Baltimore Canyon Trough), and weakness that persists landward of the hinge zone (see Figure 6.3). Because these along-strike variations in basin geometry and T_e are not explained by lithospheric thinning and flexural yielding, their probable origins are in margin structure that pre-dates Atlantic rifting. It seems that the long history of major tectonic events affecting the region has been inherited both as segmentation of the integrated strength landward of the hinge zone, and as a control on the width of the rift stage lithosphere.

Some of the along-strike alternations between strength and weakness may relate to older accreted terranes, but Chowns & Williams [1983] hypothesized that the Brunswick Magnetic Anomaly (BMA, Figure 6.6) signifies a suture between the Iapetan cratons of Africa and North America. On this basis Sawyer [1985b] suggested that differences in extensional style between the north and south side of the BMA demonstrate differing behaviour of the 'brittle' North American and 'ductile' African craton rheologies during rifting.

Comparison of a reduced-to-pole (R-T-P) magnetic anomaly (data courtesy of Mark Behn at MIT, cf. Behn & Lin [2000]), with the T_e distribution derived from gravity modelling (Figure 6.6) reveals a close correspondence between the BMA and a rapid change in lithospheric rigidity between high strength ($T_e > 30km$) lithosphere to the

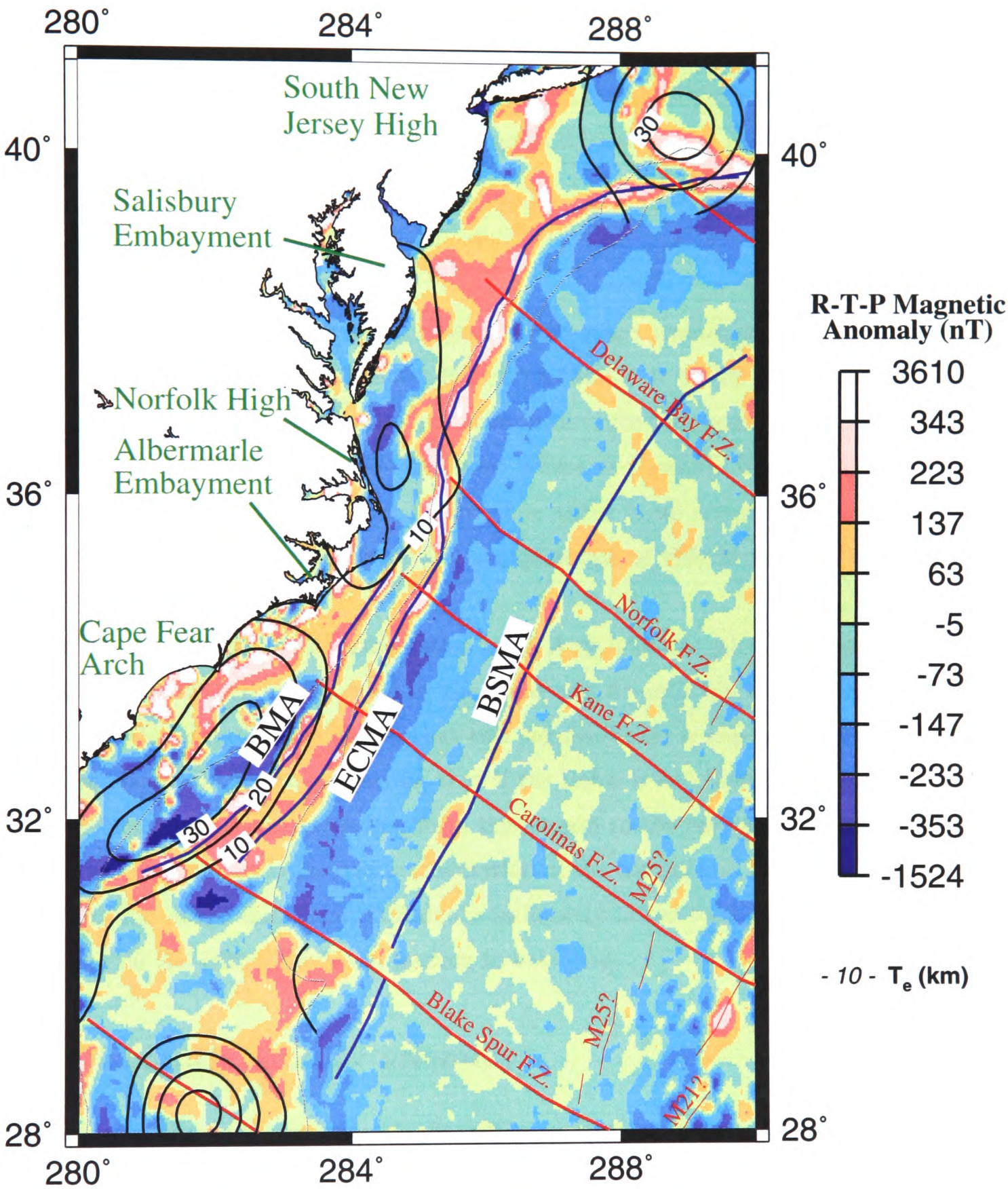


Figure 6.6: Reduced-to-pole magnetic anomaly and effective elastic thickness (10km contours). Magnetic data courtesy of Mark Behn at MIT, see Behn & Lin [2000].

north and west, and weaker ($T_e < 10km$) lithosphere to the south and east. This supports the suggestion of Sawyer [1985b] that the yield strength envelopes on each side have distinct origins and properties.

In Figure 6.7 it can be seen that the BMA traces the northwestern boundary of a narrow region of high extension ($\beta > 3.5$) at the landward edge of the Blake Plateau Basin. It may be that rifting first focussed between the old African and American cratons before diffusely migrating across the more ductile African craton to refocus on the seaward side of the Blake Plateau.

Fracture zones

Atlantic fracture zones have their origins in rift-stage transforms that controlled the initial geometry of the mid-Atlantic Ridge. Although it seems that at least some of these transforms mark structural boundaries in the rifted continental crust (see Chapter 3, Section 2.3), there remain doubts about where the oceanic fracture zones intersect the margin. However, even allowing for this, there is no simple correspondence evident between basement transforms and segmentation of effective elastic thickness (see Figure 6.7).

Behn & Lin [2000] used segmentation of an Airy isostatic gravity anomaly to infer a possible tectonic corridor bounded by the Kane and Atlantis fracture zones. In the next section of this chapter it is shown that this segmentation is explained by variations in effective elastic thickness; suggesting that if (as Behn & Lin [2000] suggest) there is an oceanic tectonic corridor extending from the margin to the mid-Atlantic Ridge, then its origins can be traced to observed segmentation of the continental lithosphere. If so, then segmentation of the mid-Atlantic Ridge is intimately linked to the effects of pre-existing structure on the rifting processes leading to break-up.

6.3 Isostatic gravity anomaly

Leaving observation errors aside, the flexural isostatic gravity anomaly (IGA, Figure 6.8) consists of contributions to the observed free-air anomaly that are due to structure that has not been adequately modelled in the analysis; whether through omission, poorly defined densities and boundaries, or limitations of the analysis method.

That elements of the margin structure have been omitted from the process-oriented analysis is obvious; amongst other features of the margin that have not been included are possible volcanic contributions at all levels (sub-crustal, intrusive, and extrusive), salt-domes, syn-rift sediments, and the ocean-continent transition. Similarly, there will

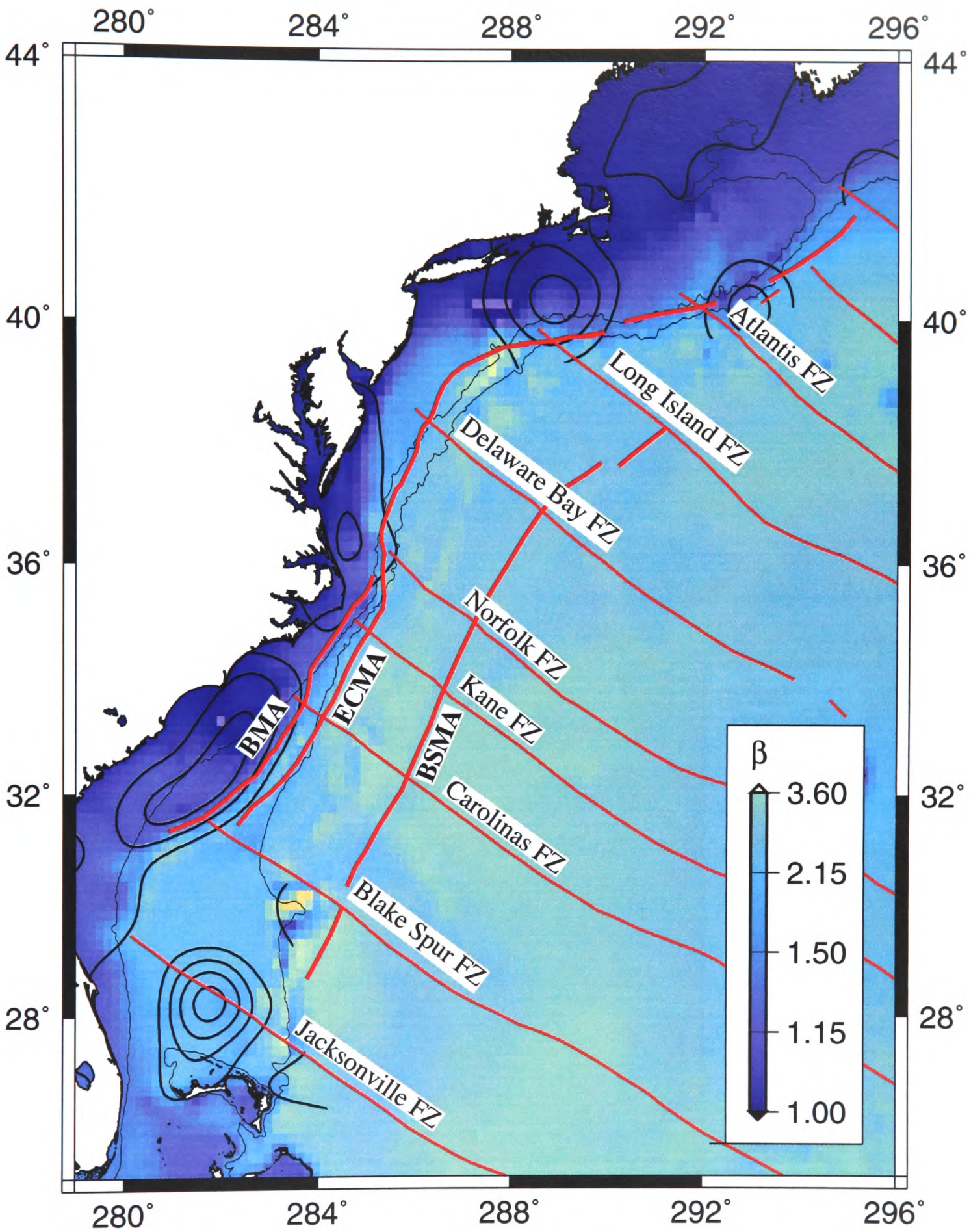


Figure 6.7: Crustal stretching factor, β, fracture zones, and effective elastic thickness ($10km$ contours). BMA - Brunswick Magnetic Anomaly; ECMA - East Coast Magnetic Anomaly; BSMA - Blake Spur Magnetic Anomaly.

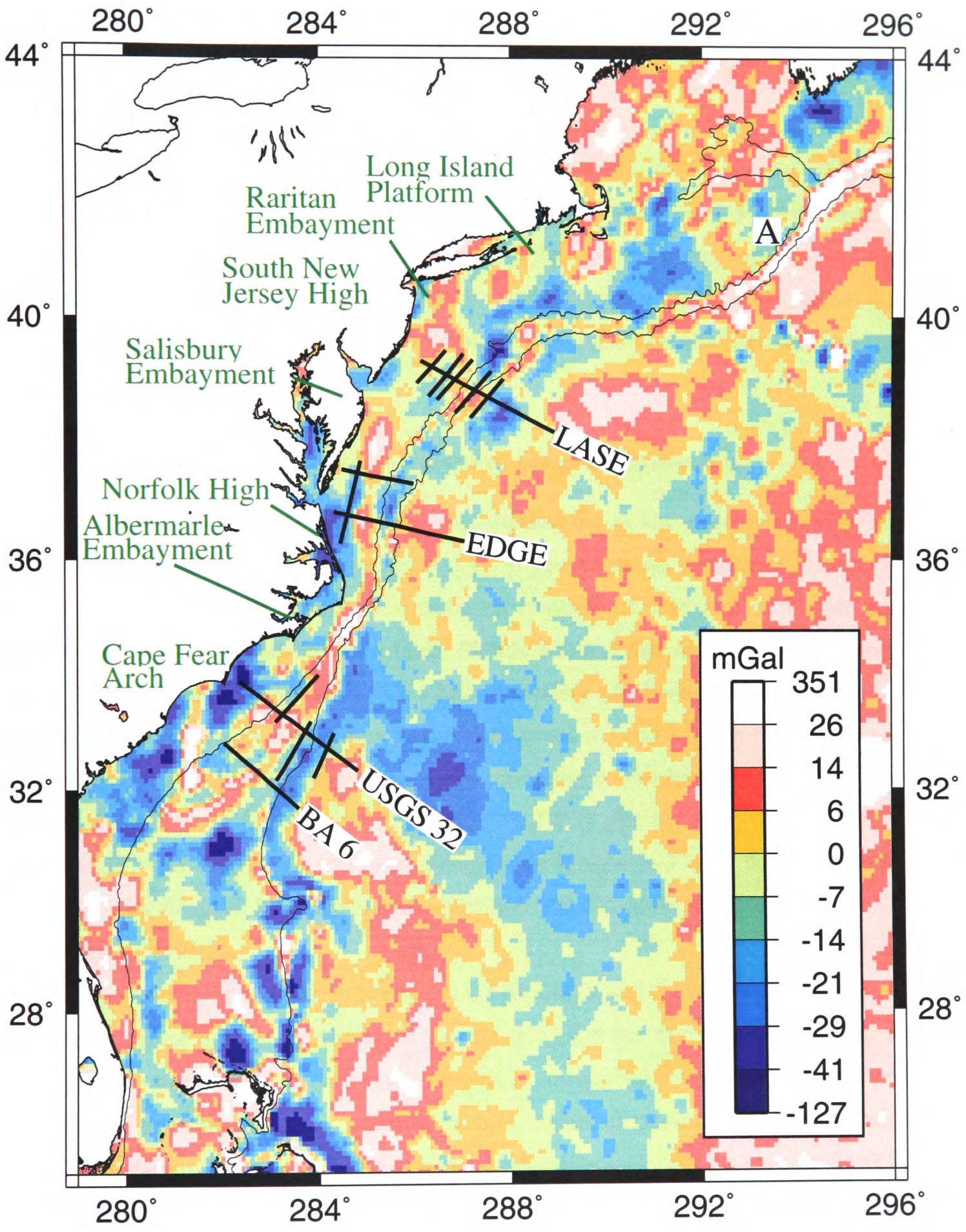


Figure 6.8: Flexural isostatic gravity anomaly with locations of deep seismic surveys.

be density interfaces within the sediment, crust and mantle that contribute to the IGA.

It has already been shown (Chapter 5, Section 3.2) that there may be areas in which T_e varies more rapidly than the analysis can resolve (particularly across the edge effect high between 32^oN and 38^oN). Limitations of the elastic plate assumption may also explain elements of the flexural IGA.

Despite these limitations, the process-oriented analysis, with its implicit structural segmentation, is markedly more successful at minimising the IGA than either Airy or uniform elastic plate models. More effective removal of the contributions arising from rifting and the flexural response to sediment loading, provides an isostatic anomaly that more closely relates to other elements of the margin structure, and hence offers an opportunity to reconsider the relationship between isostatic gravity anomalies and along-strike segmentation.

6.3.1 The Carolina Trough Isostatic Gravity Anomaly

While errors in sediment distribution and limitations of the process oriented analysis may explain some features of the flexural IGA, there remain prominent anomalies that are not explained in this way. One example (marked as line A-B in Figure 6.9) is a gravity high which extends more than $700km$ along-strike of the margin seaward of the Carolina Trough hinge zone. This has previously not been identified because of its proximity to flexural contributions to the shelf-break gravity high in both observed free-air and Airy-isostatic anomalies. Despite its proximity to the free-air edge effect anomaly, swaths following the flexural IGA high show that it is distinct from it in terms of path, wavelength, and amplitude (compare perspective images in Figure 6.9). Because of its location, the flexural IGA high is here termed the Carolina Trough Isostatic Gravity Anomaly, or CTIGA.

There is a correspondence between the CTIGA high and the landward edge of volcanic seaward dipping reflectors (SDRs) on the BA-6, USGS 32, and EDGE 801 deep seismic lines (Figure 6.10). In each case the SDRs are accompanied by a large disparity between the seismic and flexed Moho, which may be a result of massive igneous intrusion and possible underplating marked by high seismic velocities in the rift stage crust (see Chapter 3, Section 2.3).

Importantly, SDRs on the LASE line, which crosses the margin some distance north of the CTIGA, do not correspond to an isostatic gravity anomaly high. However, the extent of these SDRs is controversial (see Chapter 3, Section 4), and differences between the observed and flexed Moho along this line are small. If the CTIGA is volcanic in origin, then this suggests less pervasive igneous activity here than in the vicinity of the

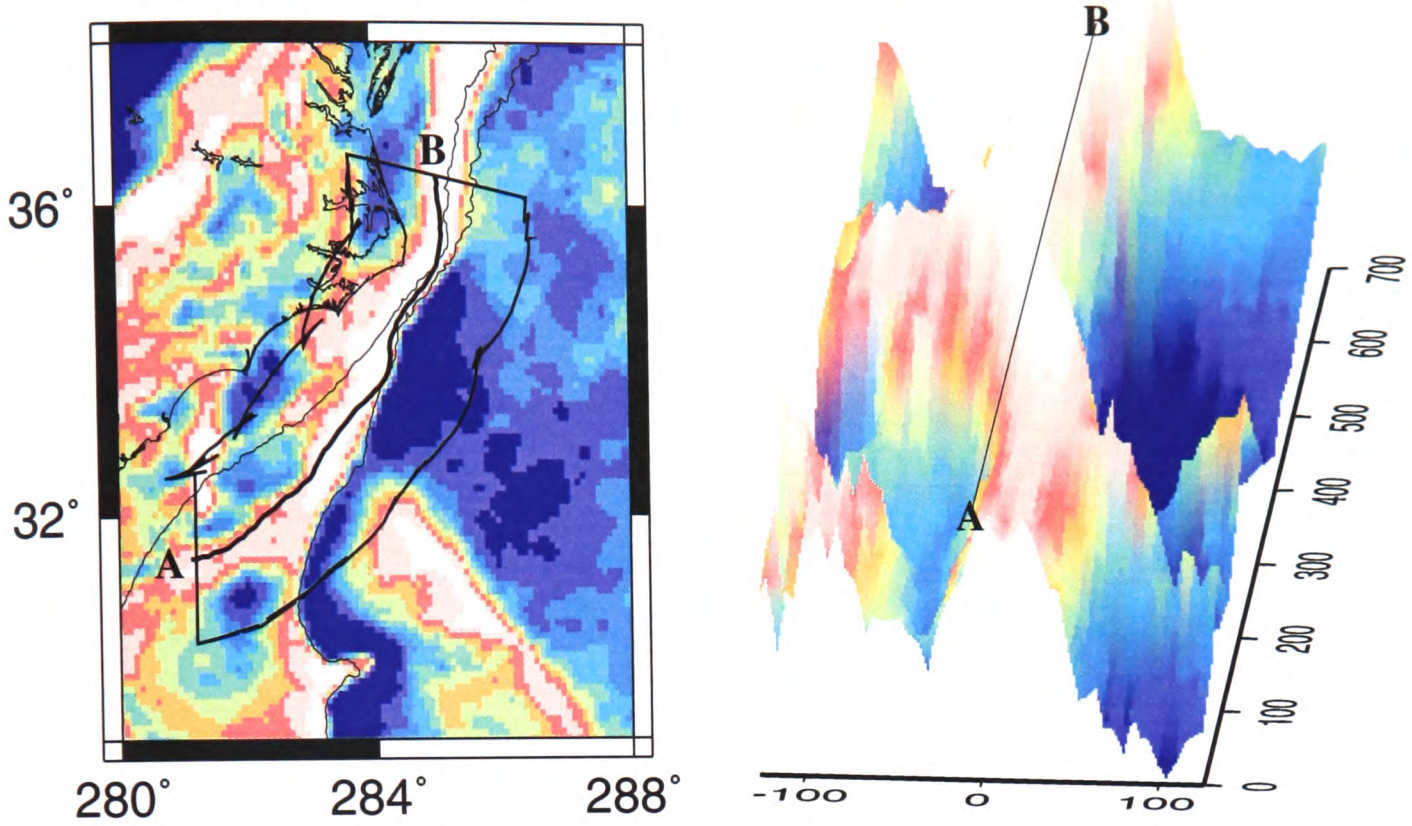
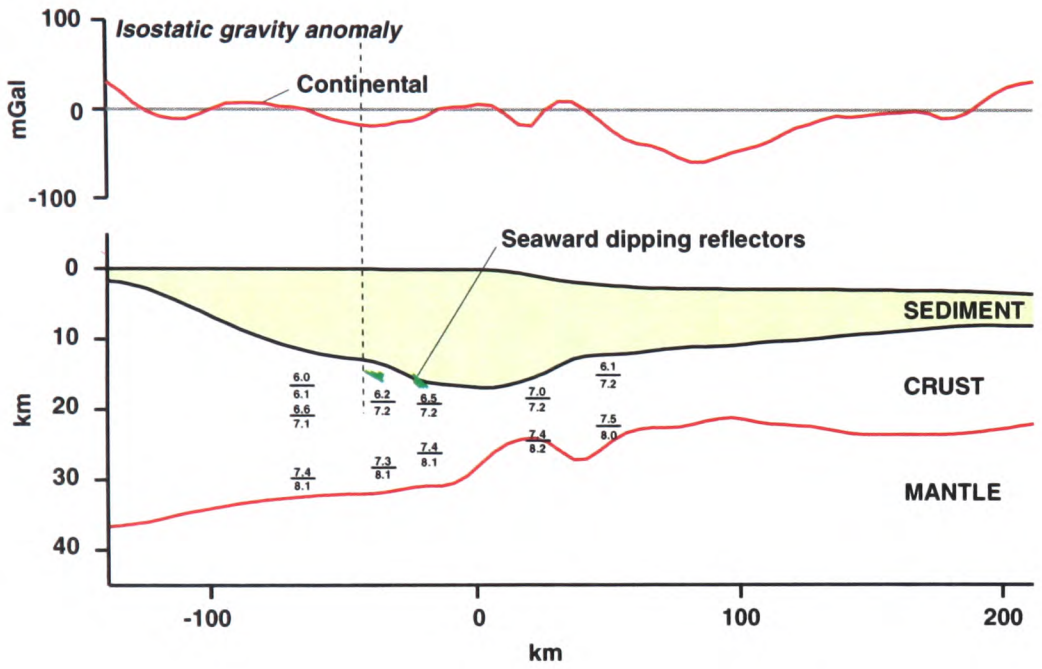
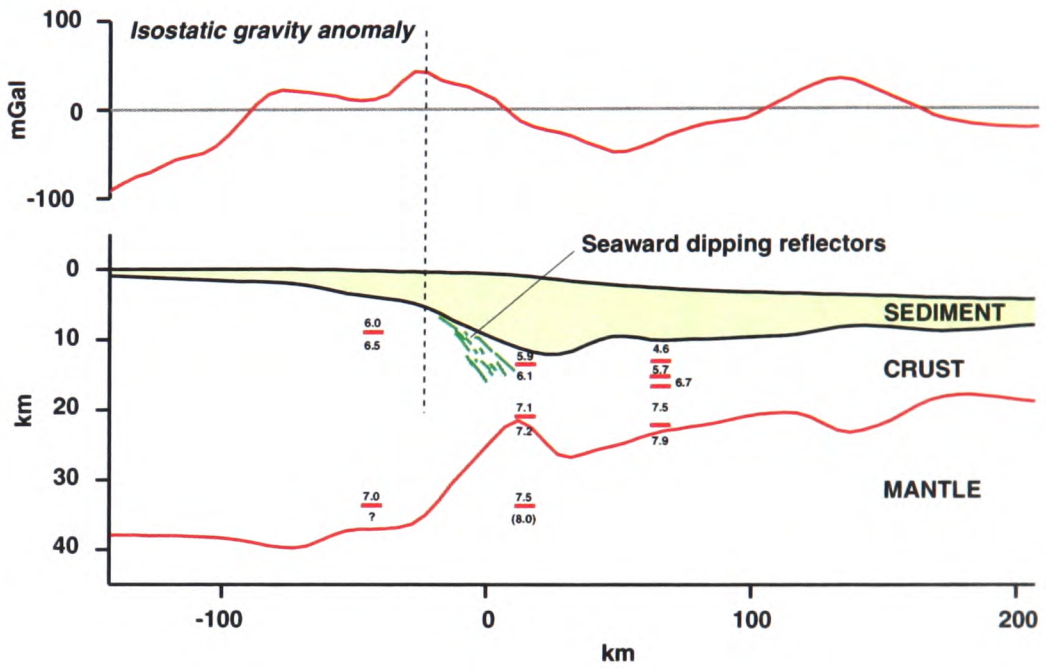


Figure 6.9: Swaths along the Carolina Trough Isostatic Gravity anomaly in map and perspective view. a) Observed gravity anomaly (free-air offshore, Bouguer onshore), b) Carolina Trough Isostatic Gravity Anomaly.

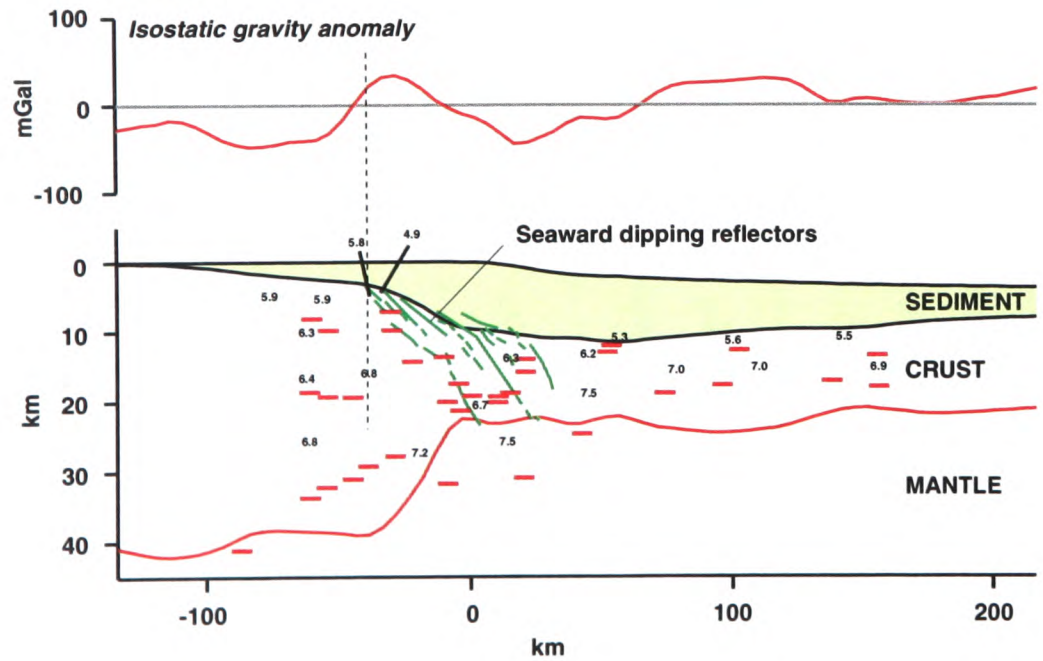
LASE



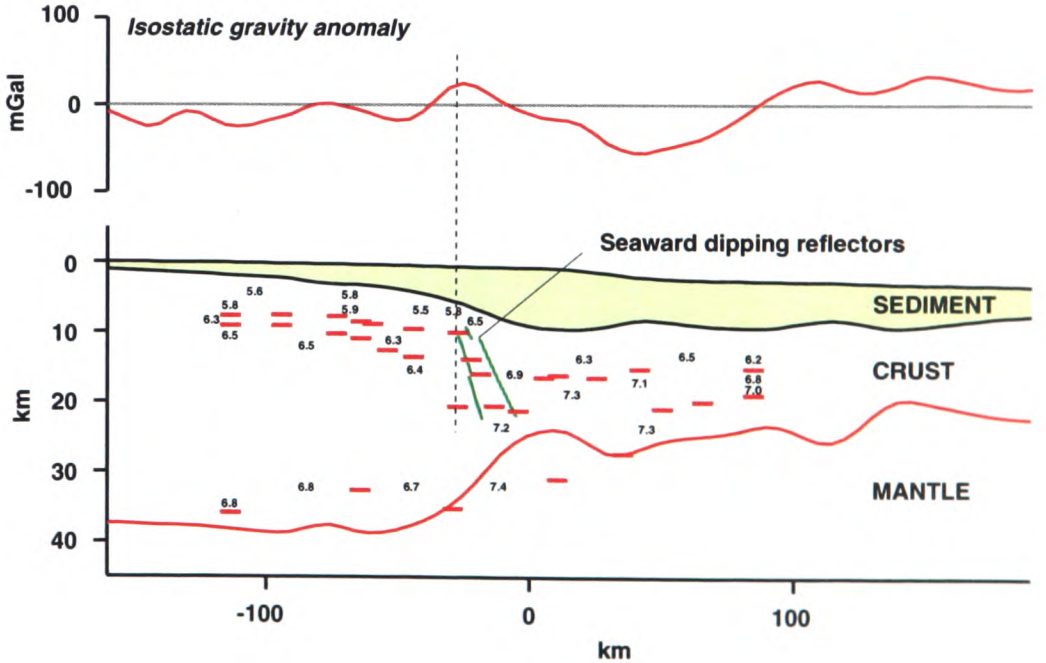
EDGE 801



USGS 32



BA-6



CTIGA to the south.

The relationship between the CTIGA, and the East Coast and Brunswick magnetic anomalies (ECMA and BMA) also points to a volcanic origin. Talwani *et al.* [1995] modelled a single volcanic source for both anomalies (see Chapter 3, Section 3.2), and the CTIGA runs directly between them from the start of the ECMA at the Blake Spur Fracture Zone to their intersection north of Cape Hatteras (Figure 6.11). Whether volcanic or not, the location of the CTIGA suggests that it shares a common source with the magnetic anomalies.

North of 36^oN a series of smaller amplitude flexural IGA peaks may be related to the CTIGA. However, these mimic peaks of the free-air edge effect gravity anomaly (Figure 6.12), and are accompanied only be the ECMA. If they share a common source with the CTIGA then it is discontinuous in this part of the margin.

A large and continuous IGA high from 40^oN northwards (labelled 'A' in Figure 6.8) begins just within the northernmost part of the high quality USGS sediment isopach data, and continues along the shelf break (and hence the peak of the free-air gravity anomaly edge effect high) into a region where the sediment thickness grids are poorly constrained. There is a strong possibility that the lack of good data in this area prevented effective minimisation of the edge effect gravity anomaly.

6.3.2 Along strike segmentation

Behn & Lin [2000] inferred along strike segmentation of the Eastern USA passive continental margin from spectral analysis of a transect of the Airy isostatic edge effect gravity anomaly high[3] (see Chapter 3, Section 5.3, and Figure 3.16). They observed an IGA (normalised) spectral energy peak at $300-500km$ wavelengths that they suggest could relate to segmentation either of margin volcanism or T_e, and a second peak at $100-150km$ wavelength that is comparable to $(100-150km)$ spectral energy peaks in the mid-Atlantic Ridge (MAR) crustal magnetisation and mantle Bouguer anomaly.

A repeat of their approach using the data from this thesis (Figure 6.13a) presents a similar Airy isostatic gravity anomaly with (normalised) spectral energy peaks at $c.470km$

[3]Based on a model in which water and sediment are locally compensated by Airy isostasy at the Moho

Figure 6.10: Flexural isostatic gravity anomalies and observed (deep seismic) and calculated crustal structure. 'Continental' model (red lines) refers to the iterative (spatially varying T_e) analysis; 'oceanic' model (blue lines) refers to a model in which T_e evolves as the depth of the 450^oC oceanic isotherm given by a 1-D cooling plate model.

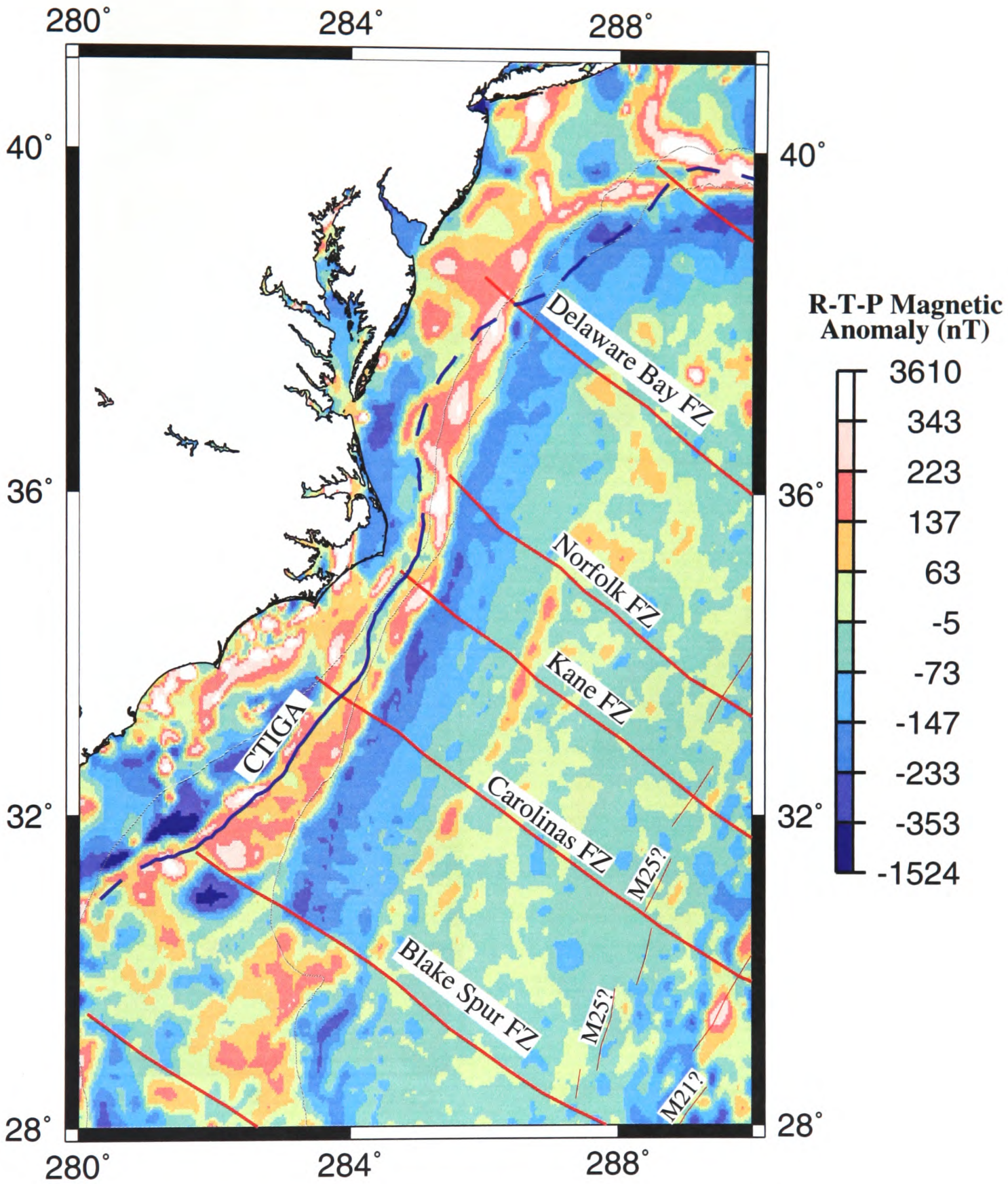


Figure 6.11: Relationship of the Carolina Trough Isostatic Gravity Anomaly (CTIGA) high (solid line) to magnetic anomalies and fracture zones. Dashed line links discontinuous IGA highs to the north and south of the CTIGA.

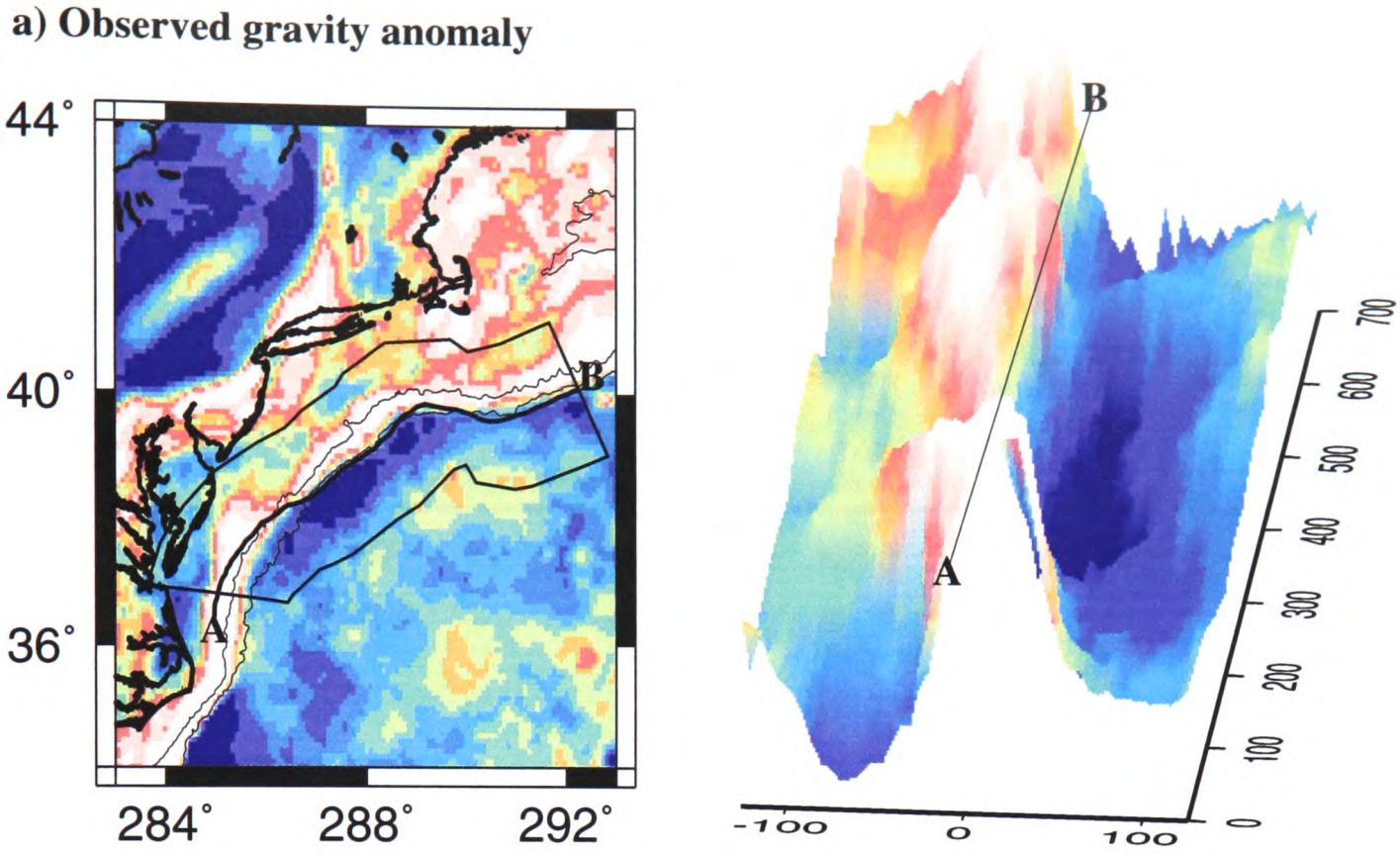


Figure 6.12: Swaths along the discontinuous Baltimore Canyon Trough isostatic gravity anomaly high. Observed gravity anomaly (free-air offshore, Bouguer onshore), b) Flexural isostatic gravity anomaly.

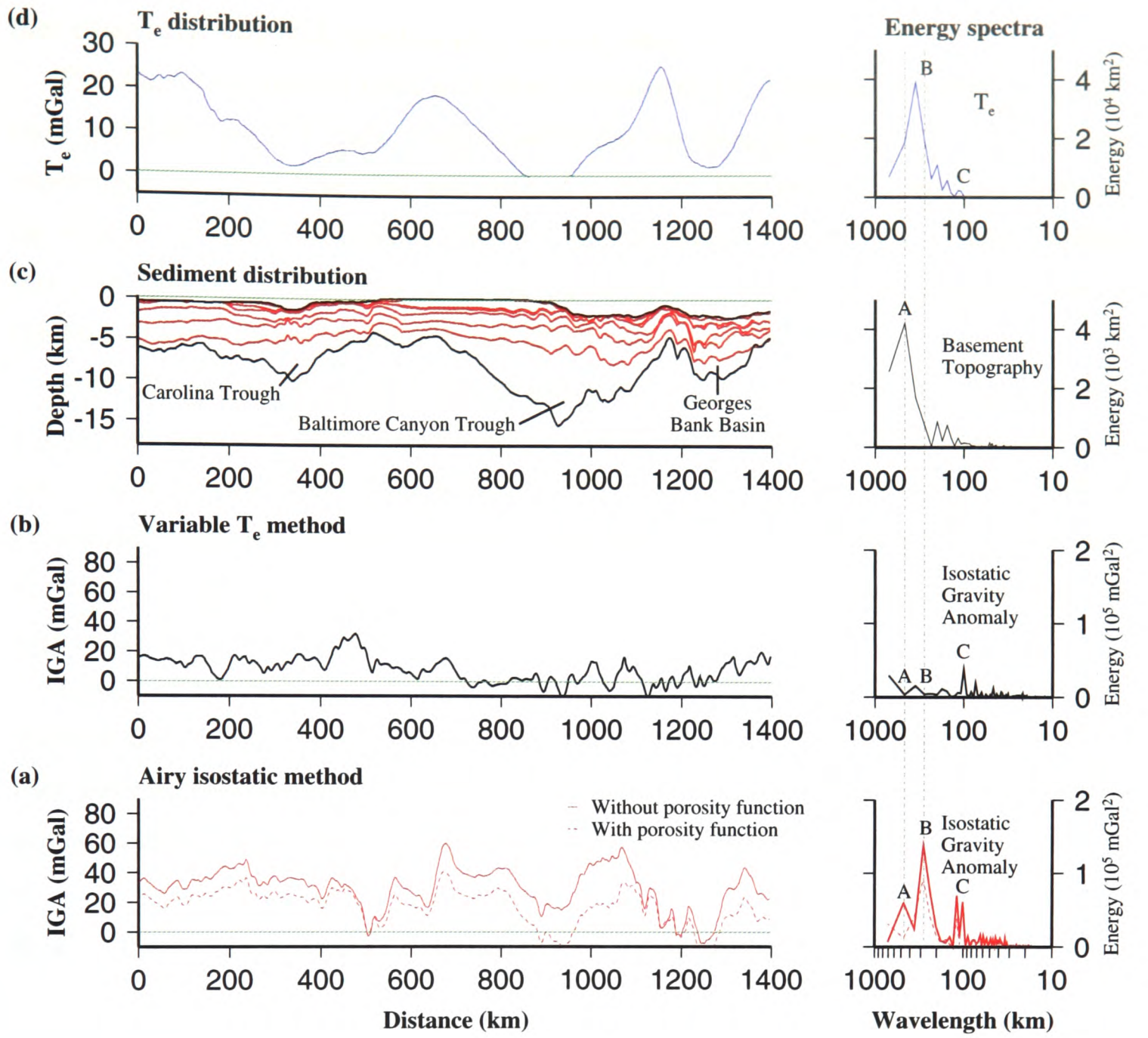


Figure 6.13: Comparison of along-strike segmentation of the (a) Airy isostatic edge effect gravity anomaly high calculated with uniform density sediment (solid line) and a model in which sediment porosity decreases as a function of depth (dashed line, see text), (b) flexural isostatic gravity anomaly high, (c) underlying sediment distribution, and (d) recovered effective elastic thickness distribution, along the Eastern USA passive margin, together with the normalised spectral energy for each profile. 'A', 'B', and 'C', correspond Airy IGA spectral peaks at $480km$, $280km$, and $100-120km$ respectively, and are discussed in the text.

('A'), *c.*$280km$ ('B'), and $100-120km$ ('C') wavelengths. The results are not identical because the datasets used are not the same as those used by Behn & Lin [2000].

The flexural process-oriented approach adopted in this thesis markedly reduces the IGA edge effect high; which contains only 7.3% of the total energy in the observed edge effect high, and 29% of the energy in the Airy IGA high (compare Figure 6.13a with Figure 6.13b). It also effectively eliminates the spectral peak at $300-500km$ wavelengths ('A' and 'B'); evidence that it is segmentation of elastic thickness, and not volcanism,

that causes the Airy IGA spectral peak in this range.

The Airy IGA spectral peak at $100km$ wavelength ('C') retains over half its amplitude in the flexural IGA high. Unfortunately this wavelength corresponds to the $100km$ wavelength bandpass filter that was applied to the T_e distribution in order to maintain the stability of the finite difference flexural approximation. Hence it is unclear whether this IGA spectral peak relates to: short wavelength T_e segmentation; segmentation of the Mid-Atlantic Ridge (as Behn & Lin [2000] suggest); or both.

Spectral analysis of basement depth along the flexural IGA edge effect high reveals a dominant peak at $c.480km$ wavelength (labelled 'A' in Figure 6.13c). Comparison of the spectral energy of the Airy isostatic gravity anomaly with and without inclusion of sediment porosity (dashed and solid lines respectively in Figure 6.13a) shows that the $480km$ wavelength peak in the simplest Airy isostatic model is due to omission of depth-dependent sediment density variations.

Low T_e in the deepest parts of the Carolina Trough, Baltimore Canyon Trough, and Georges Bank Basin supports earlier arguments (cf. Section 6.2.2) that positive feedback between effective elastic thickness and sediment deposition has tended to maintain primary offshore depocenters in regions of long term lithospheric weakness.

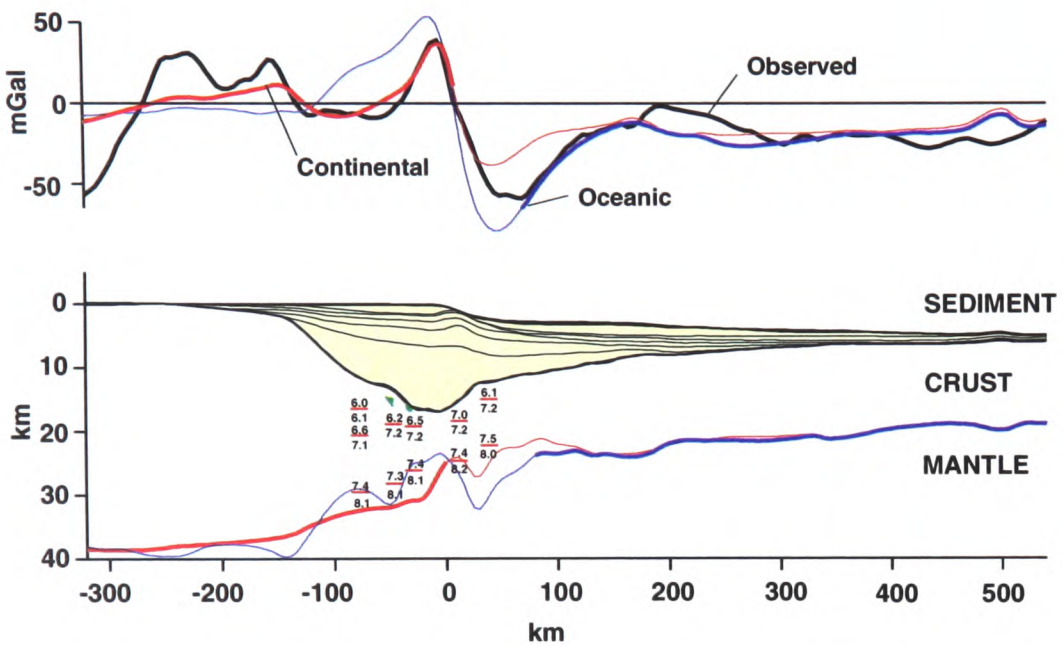
6.4 The oceanic to continental transition

Flexural analysis effectively minimises the Eastern USA isostatic edge effect gravity anomaly. However, along two of the four deep seismic transects of the margin (LASE and BA-6) the seaward free-air edge effect gravity low better represented by an 'oceanic' model (described in Chapter 5, Section 4) in which T_e evolves from a $180Ma$ break-up as the depth of the 450^oC oceanic isotherm in a 1-D cooling plate model (Figure 6.14).

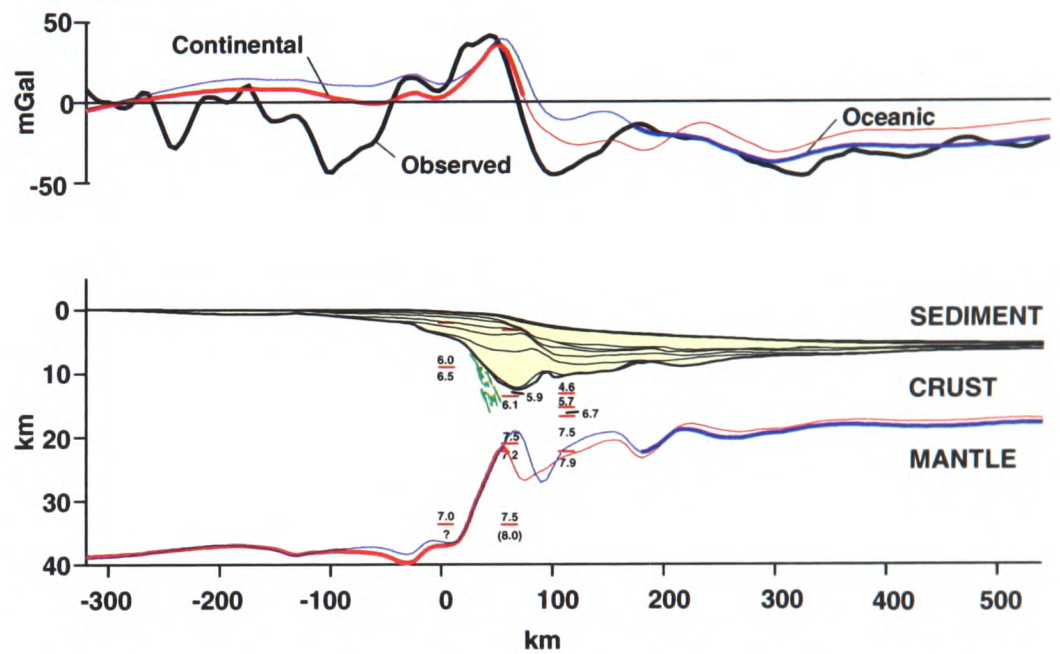
This presents the possibility that gravity anomalies could be used to distinguish between lithospheric types. As Figure 6.15 shows, this approach works in places (profiles 4-8, 15-17, 20-27, 30, and 33-35), but the transition between distinctly oceanic and continental lithospheric behaviour is often broad (e.g. profile 21), and is not always defined on both sides (e.g. profiles 5 and 35). While the separation may reflect the width of a transitional zone toward purely oceanic lithosphere, it may also be a result of discontinuity between the two models. Along the remainder of the margin the OCT remains unconstrained, either because the oceanic and continental gravity anomalies are not sufficiently different, or because of other contributions to the free-air gravity anomaly that neither method recovers.

The use of gravity anomalies and flexural methods to identify the oceanic and conti-

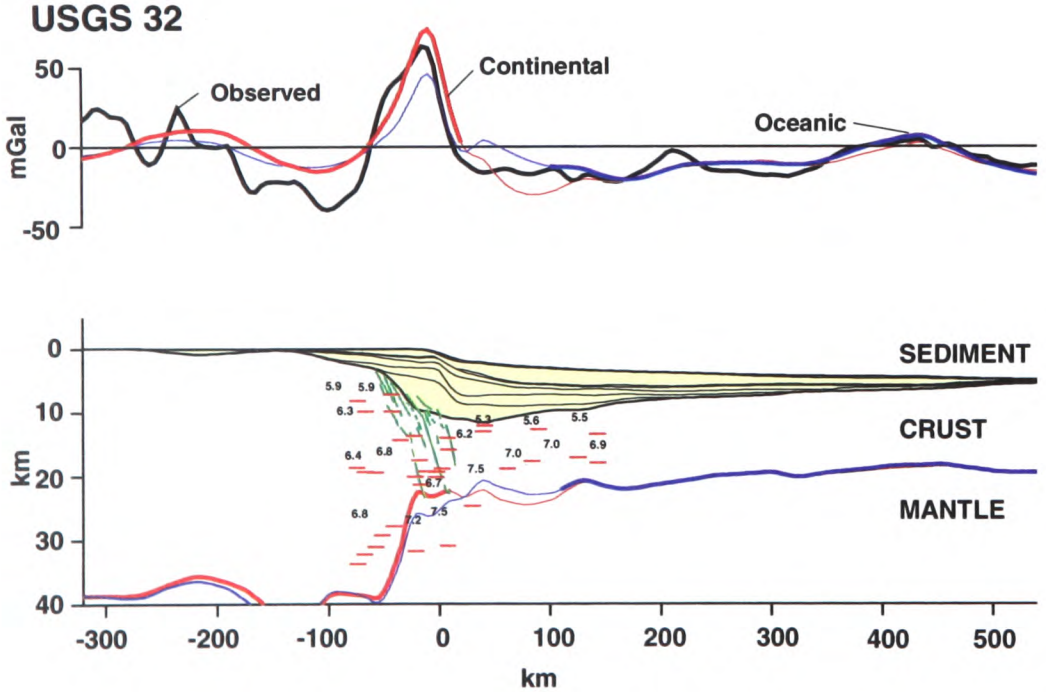
LASE



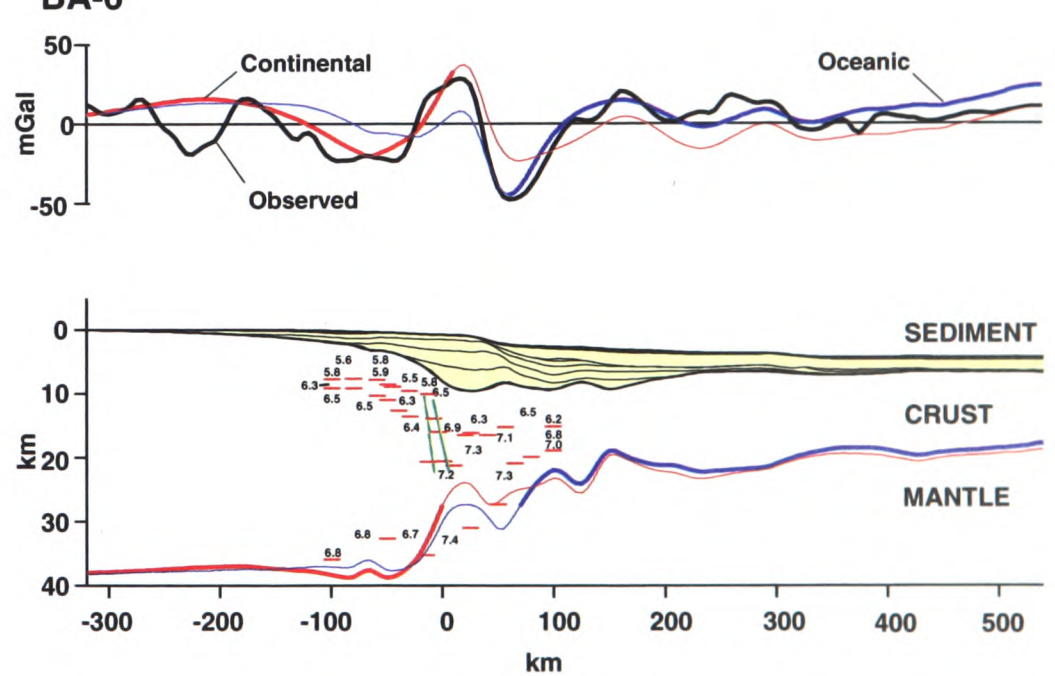
EDGE 801



USGS 32



BA-6



nental lithosphere is somewhat successful, but segments of the OCT remain unmapped. The method of Sawyer [1985b], in which flattening of the total tectonic subsidence (TTS) curve is used to identify the oldest purely oceanic crust, may provide a more robust constraint on the oceanic edge of the OCT. Application of this method to transects of the oceanic TTS from this thesis provides a more continuous outline of the onset of normal seafloor spreading than was found using gravity anomalies (Figure 6.16).

The two methods (based on gravity and TTS respectively) complement each other. The gravity method provides constraint mainly in regions where there is a deep and well confined free-air gravity anomaly low (e.g. central Baltimore Canyon Trough), and the TTS method confines the oceanic edge along the rest of the margin. There is agreement where the two methods overlap.

The shelf edge (and hence the free-air edge effect gravity anomaly high) consistently remains close to the location of the oldest oceanic lithosphere. Only where the Blake Plateau edge has erosionally retreated landward (see Chapter 3, Section 2.1) do the two depart (Figure 6.16, line 4). Hence both the shelf edge and the free-air edge effect gravity anomaly tend to approximate the location of the OCT.

Most of the Atlantic fracture zones (Blake Spur, Kane, Norfolk, Long Island, and Atlantis) correspond either to significant offsets of the OCT, or to changes in its orientation. A section of the low T_e Baltimore Canyon Trough (lines 21 – 23), bounded by the Delaware and Long Island fracture zones, is marked by a rougher TTS surface then its neighbours. It is possible that the adjacent fracture zones began as syn-rift offsets between a 'ductile' lithospheric segment and more 'brittle' lithosphere to either side.

The proximity of the boundary between transitional (or continental) and oceanic crust to the ECMA suggests that it contributes to the magnetic anomaly (Figure 6.17a). However, in the northern part of the margin the OCT is found on the seaward side of the ECMA, and in the southern side it is to the landward side. Clearly if the source of the ECMA is continuous along the margin then it must produce a similar magnetic anomaly whether it contrasts with oceanic or rift stage continental crust. An alternative suggestion is that a source body at basement level extends across the OCT south of Cape Hatteras, producing the BMA low on the continental side and ECMA high on the

---

Figure 6.14: Observed and calculated free-air gravity anomalies; and observed (deep seismic) and calculated crustal structure. 'Continental' model (red lines) refers to the iterative (spatially varying T_e) analysis; 'oceanic' model (blue lines) refers to a model in which T_e evolves as the depth of the $450°C$ oceanic isotherm given by a 1-D cooling plate model.

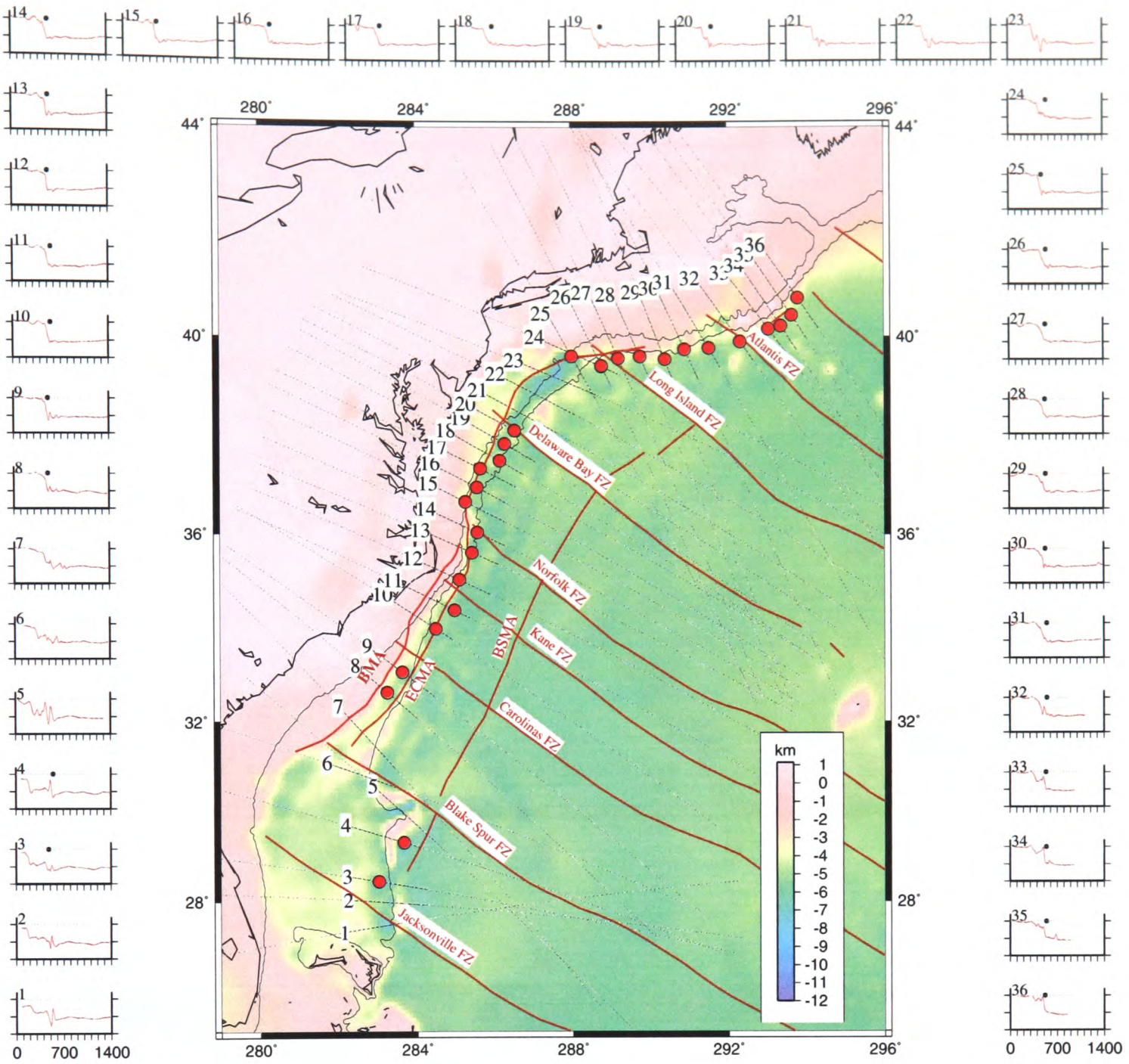


Figure 6.15: Identification of the oceanic to continental transition on the basis of comparison between observed (black lines) and calculated free-air gravity anomalies. 'Continental' model (red lines) refers to the iterative (spatially varying T_e) analysis; 'oceanic' model (blue lines) refers to a model in which T_e evolves as the depth of the 450^oC oceanic isotherm from a 1-D cooling plate model. Limits of identifiable continental and oceanic lithosphere are marked by red and green circles respectively. Note that in many locations either one or both ends of the OCT are not constrained.

oceanic side, but narrows to the north, leaving a single high-low couple associated with the abutment of earliest oceanic crust against the rifted margin.

This interpretation is compatible with models by a number of authors (e.g. Alsop & Talwani [1984]; Holbrook *et al.* [1994a]; Talwani *et al.* [1995], see Chapter 3, Section 5) in which the magnetic anomalies are caused by rifting volcanism. In particular, the magnetic anomalies along deep seismic lines EDGE 801 and USGS 32 have been modelled by Talwani *et al.* [1995] (see Chapter 2, Figure 3.11) such that a widened volcanic body extends across the OCT producing the ECMA high on the oceanic side, *c.*40km from

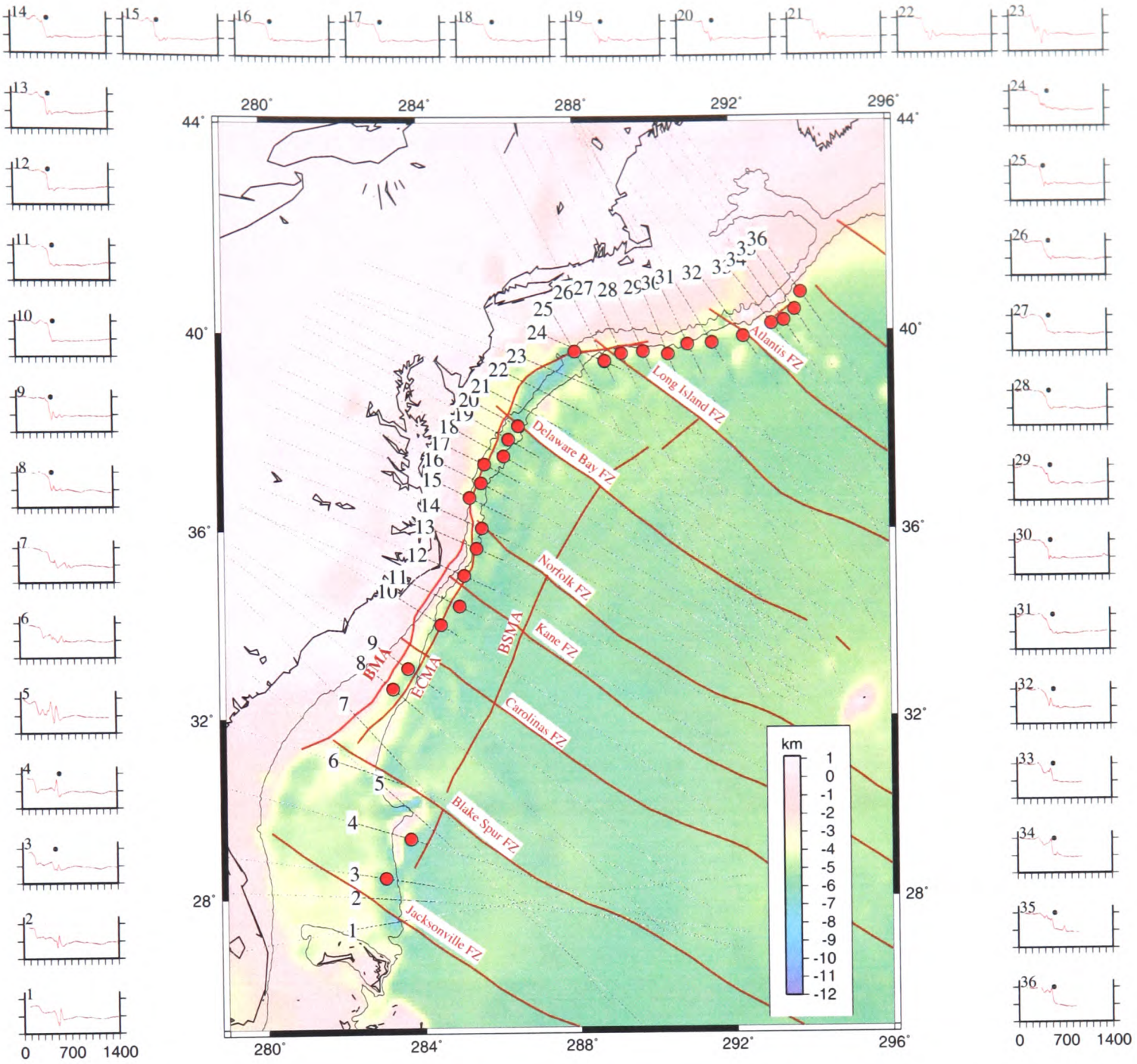
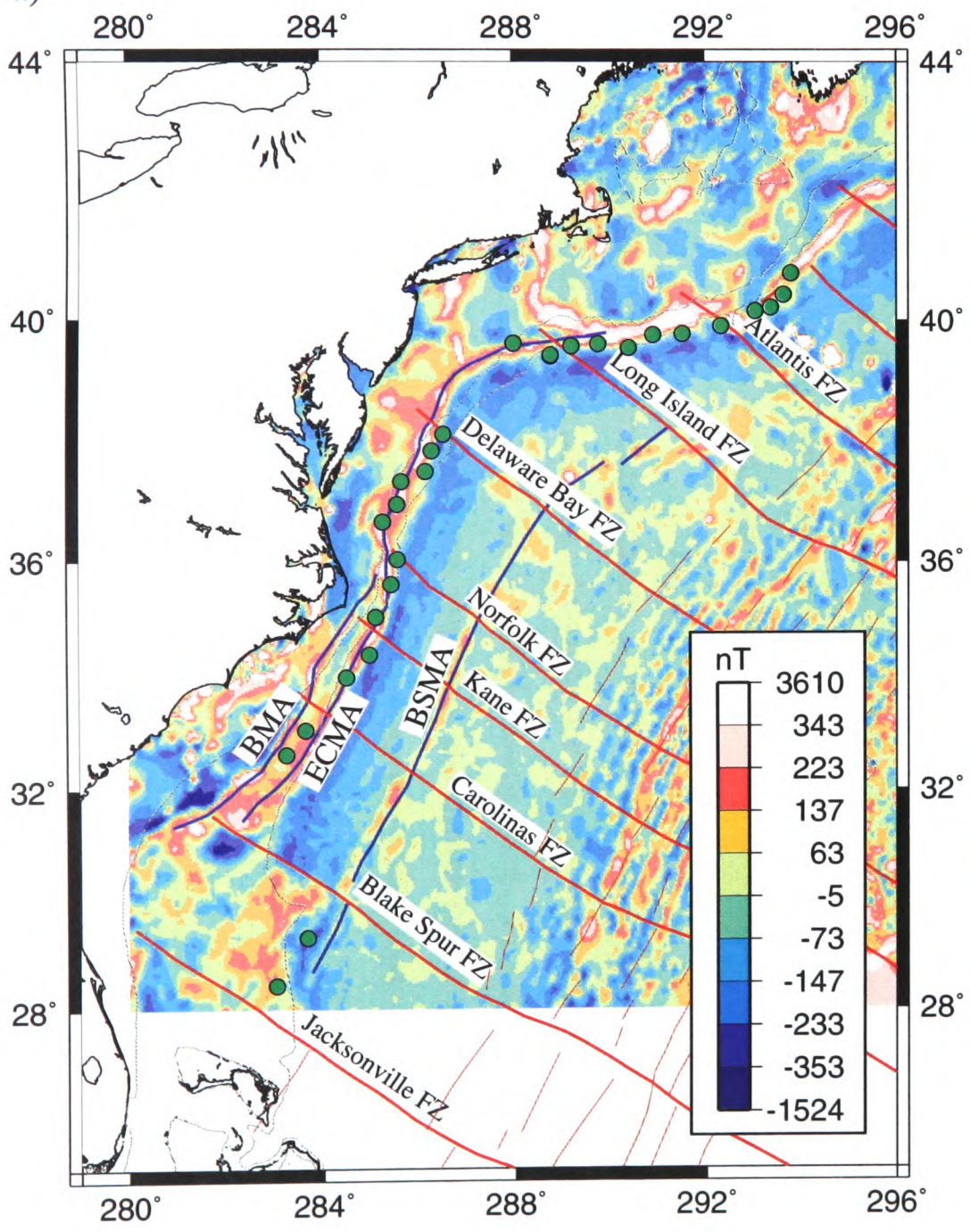


Figure 6.16: Identification of oldest continental lithosphere on the basis of 'oceanic' analysis (in which T_e evolves as the depth to the 450^oC oceanic isotherm given by a 1-D cooling plate model) total tectonic subsidence. Red circles mark the oldest identifiable oceanic lithosphere.

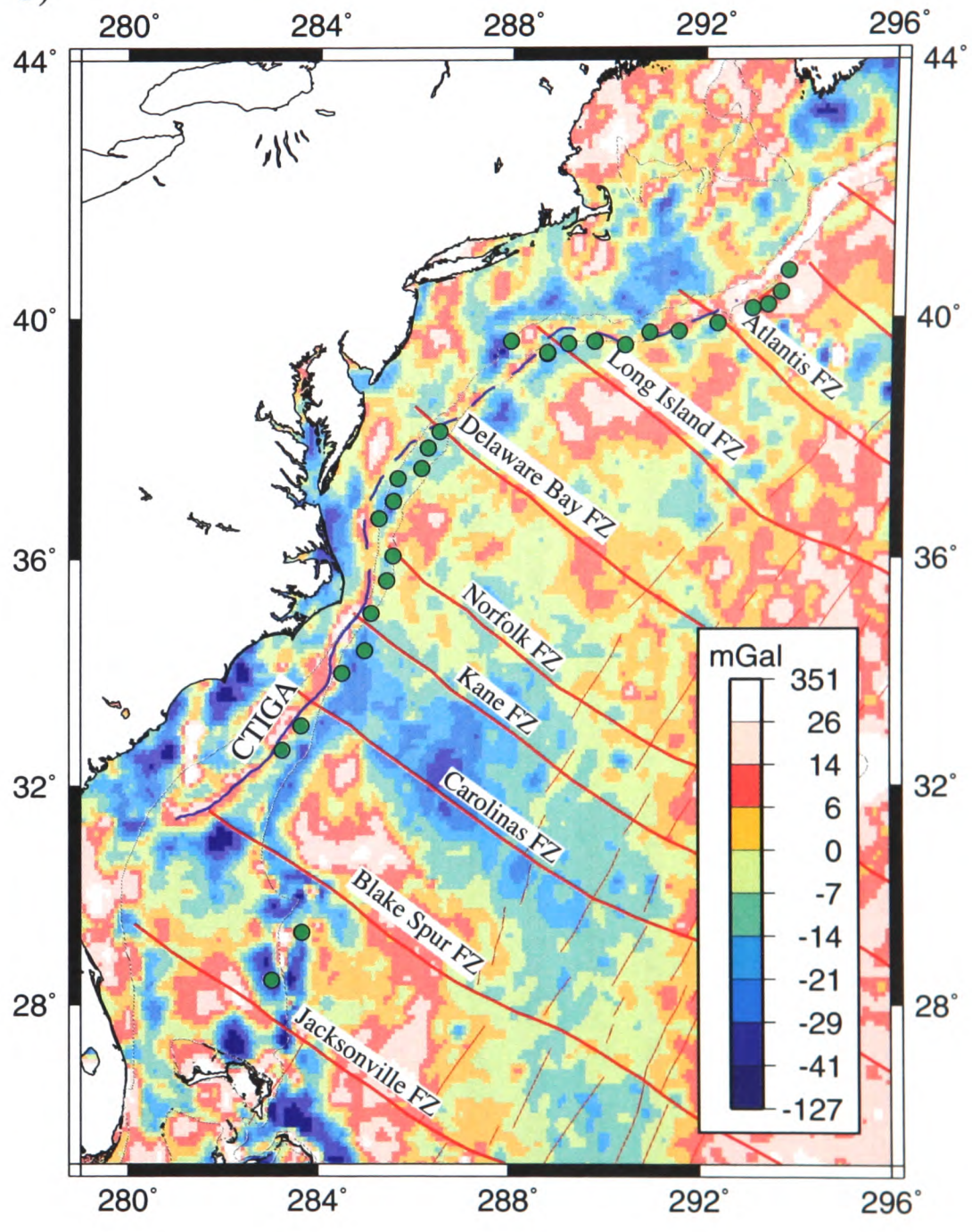
the BMA low produced by the magnetic contrast at the continental end. By contrast, their model for the LASE line involves a much narrower volcanic body that produces a single magnetic anomaly couple, with a direct transition from the magnetic low at the continental end to the magnetic high over the continent-ocean boundary.

If the CTIGA is due to a volcanic wedge extending linearly along the Carolina Trough, then the picks of earliest oceanic lithosphere suggest that extrusive volcanism eminated from the most greatly thinned continental lithosphere, adjacent to the line of break-up (Figure 6.17b).

a)


280°
284°
288°
292°
296°
44°
40°
36°
32°
28°
Atlantis FZ
Long Island FZ
Delaware Bay FZ
Norfolk FZ
Kane FZ
Carolinas FZ
Blake Spur FZ
Jacksonville FZ
BMA
ECMA
BSMA
nT
3610
343
223
137
63
-5
-73
-147
-233
-353
-1524

b)


280°
284°
288°
292°
296°
44°
40°
36°
32°
28°
Atlantis FZ
Long Island FZ
Delaware Bay FZ
Norfolk FZ
Kane FZ
Carolinas FZ
Blake Spur FZ
Jacksonville FZ
CTIGA
mGal
351
26
14
6
0
-7
-14
-21
-29
-41
-127

6.5 Summary

The origins of structural segmentation at the Eastern USA passive continental margin have been considered in the light of a 3-D process-oriented analysis of sediment thickness, gravity anomalies, and effective elastic thickness (T_e).

Although it has been shown that the integrated mechanical strength of the lithosphere has been limited by the degree of thinning during rifting and by curvature induced yielding, these contributions alone do not explain along-strike segmentation of T_e. Similarly, there is a broad correspondence between low T_e and large sediment thicknesses that suggests a thermal contribution to low T_e regions, but does not explain why weakness in the Baltimore Canyon Trough continues landward of the hinge zone.

To explain the alternation of 'strong' platforms and 'weak' embayments along the margin it is necessary to consider structural contributions that pre-date the Atlantic rifting event. The lithosphere that has been the weakest flexurally was also the most 'ductile' during rifting. Thus the broad rift-stage crust of the 'weak' Blake Plateau Basin and Baltimore Canyon Trough contrasts with the narrow Carolina Trough, which is bounded by the extensive 'strong' platform defined by the Cape Fear Arch and Norfolk High.

A source for this inherited along-strike segmentation is the long history of major tectonic events that preceded Atlantic rifting. In the case of the Blake Plateau Basin, the T_e segmentation is compatible with suggestions that the basin basement is a portion of 'ductile' African craton that remained sutured to the North American craton during rifting. There may be a failed rift within the reactivated suture zone along the northwestern edge of the basin.

Recent controversy has surrounded claims that the continental upper mantle is generally weak (cf. Chapter 2, Section 4.2). Allowing for brittle weakness in the top part of the upper crust and a potentially weak ductile lower crust, T_e values in excess of $30km$ approaching the marginal platforms require a significant upper mantle contribution to long term strength. These estimates are compatible with coastal plain estimates of Pazzaglia & Gardner [1994] ($\sim 40km$) and Armstrong & Watts [2001] ($34 - 44km$). However, their relevance to the ongoing debate is limited because extensive magmatism

---

Figure 6.17: Relationship between the reduced-to-pole magnetic anomaly (a), the flexural isostatic gravity anomaly (b), oldest identifiable oceanic crust (see Figure 6.16), and oceanic fracture zones. BMA - Brunswick Magnetic Anomaly; ECMA - East Coast Magnetic Anomaly; BSMA - Blake Spur Magnetic Anomaly; CTIGA - Carolina Trough Isostatic Gravity Anomaly.

during rifting (as beneath the ridge in subsequent seafloor spreading) could have removed hydrous phases responsible for upper mantle weakness elsewhere.

The effectiveness of the process-oriented analysis is demonstrated by a spectral analysis of the flexural IGA high. The high contains only 7% of the energy in the observed free-air edge effect high, and 29% of that in the Airy IGA. A long wavelength ($300 - 500km$) spectral energy peak in the along-strike Airy IGA edge effect high is explained by structural segmentation (represented in the form of spatial variations in T_e) in the same waveband, and hence is absent from the flexural IGA spectrum.

The newly identified 'Carolina Trough Isostatic Gravity Anomaly' (CTIGA) is remarkable for its uniformity along a large (over $700km$) segment of the margin, but also for its absence in the 'weak' regions to the south and north of the Carolina Trough. Its location places it directly over (volcanic?) seismic seaward dipping reflectors from the origin of the East Coast Magnetic Anomaly (ECMA) at the Blake Spur Fracture Zone to its intersection with the Brunswick Magnetic Anomaly (BMA) north of Cape Hatteras. This, together with a large disparity between the seismic and modelled Moho along the BA-6, USGS 32, and EDGE-801 deep seismic lines, suggests that this part of the margin experienced extensive extrusive volcanism and igneous intrusion during rifting, possibly accompanied by magmatic underplating.

Identification of the ocean to continent boundary or transition (OCT) suggests that if volcanism is the source of the CTIGA, ECMA, and BMA, then it was extruded through thinned continental crust close to the final line of break-up. The geometry of magnetic anomalies relative to the OCT is compatible with a magnetic model by Talwani *et al.* [1995] in which a seaward dipping wedge of volcanic material can produce a separate ECMA high and BMA low where it terminates against oceanic and rift-stage continental crust respectively (as in the vicinity of the CTIGA), but only a narrow ECMA high-low couple corresponding to the ocean-continent boundary if the width of the wedge is smaller (as to the north of the CTIGA).

If, as the process oriented analysis suggests, the (volcanic?) source of the CTIGA is confined to the strongest part of the margin, then there is a possible intrinsic relationship between segmentation of lithospheric strength and the distribution of new volcanic material emplaced during rifting. Chapter 7 investigates whether the CTIGA can be explained by a volcanic source, and if so what implications there are for rift segmentation and the use of potential field anomalies as a means of estimating the distribution of volcanic material at passive continental margins.

Chapter 7

Igneous contributions to the Eastern USA continental margin

In Chapter 6 it was suggested that the Carolina Trough Isostatic Gravity anomaly, East Coast Magnetic Anomaly (ECMA), and Brunswick Magnetic Anomaly (BMA), may share a common volcanic source. If so, then the Eastern USA passive continental margin is not only segmented in terms of mechanical thickness, but also in terms of syn-rift volcanism.

In this chapter the possibility of a volcanic origin for the CTIGA is investigated using synthetic models which consider the isostatic effects of extrusive volcanism, igneous intrusion, and magmatic underplating. The use of potential anomalies to infer the distribution of volcanic material along passive margins is reassessed in the light of these models and observations from the Eastern USA margin process-oriented analysis.

7.1 Synthetic models

The synthetic models presented below have been constructed such that they all produce the same total tectonic subsidence (TTS) prior to sedimentation. This allows the gravity contributions of each volcanic load to be isolated from a calculated sum anomaly based on sediment backstripping and Airy isostatic compensation of the TTS. The result is effectively an isostatic gravity anomaly after removal of non-volcanic (thinning and sediment loading) contributions to the free-air gravity anomaly, and is therefore suitable for direct comparison with the Eastern USA CTIGA.

In the synthetic models, uniform densities are assumed for volcanic material (underplated and intrusive $2900 kgm^{-3}$, extrusive $2640 kgm^{-3}$), crust ($2850 kgm^{-3}$), mantle ($3330 kgm^{-3}$), sediment ($2600 kgm^{-3}$), and water ($1030 kgm^{-3}$). The TTS prior to sed-

iment loading is described by a linear gradation from $0km$ to $-5km$ elevation over a $250km$ distance.

7.1.1 Extrusive volcanism

The first set of models, of which an example is shown in Figure 7.1, involve flexural loading of a passive margin by wedges of extrusive volcanic material. The flexural IGA is derived by subtracting the calculated anomaly based on sediment backstripping and isostatic compensation of the total tectonic subsidence (the 'non-volcanic reconstruction') from the 'observed' anomaly that includes the contributions of volcanic loading.

In the example shown the T_e is $10km$ at the time of volcanic emplacement, and the triangular volcanic body is $5km$ thick and $150km$ wide (comparable to seaward dipping reflectors observed in reflection seismic data along the BA-6, USGS 32, and EDGE-801 deep seismic transects, see Figure 6.10). The synthesized flexural IGA consists of a high bounded by lows to either side, with a total amplitude of $\sim 26mGal$. Because of similarities in the loading geometry, the form of the IGA is similar to free-air anomalies observed over flexurally compensated oceanic seamounts.

Volcanic bodies of other widths and thicknesses have been modelled with a range of supporting elastic plate thicknesses. In general, increasing the body width increases the wavelength of the IGA, but reduces its amplitude, and increasing the body thickness or density increases the IGA amplitude but does not greatly affect the wavelength. Increasing T_e invariably increases both the amplitude and the wavelength of the IGA. Lateral changes in the body location alter the 'observed' free-air gravity anomaly, but have little affect on the isostatic gravity anomaly unless the body depth is greatly reduced.

7.1.2 Underplating

A similar set of models, in which volcanic material is accreted to the base of the lithosphere, demonstrate the effects of underplating on rifting and sum gravity anomalies (Figure 7.2).

The example shown assumes $T_e = 10km$ (as before). In keeping with the width of the (volcanic?) high velocity zone observed in deep seismic studies (BA-6, USGS 32, EDGE-801, and LASE, see Chapter 3, Section 2.3, Figure 3.6), the ($380km$ wide, $10km$ thick) volcanic body is larger than that in the example extrusive model. The flexural isostatic gravity anomaly due to the underplate has a considerably smaller amplitude ($\sim 6mGal$) than that due to extrusive volcanism.

The polarity of the underplated IGA is opposite to that due to extrusive volcanism,

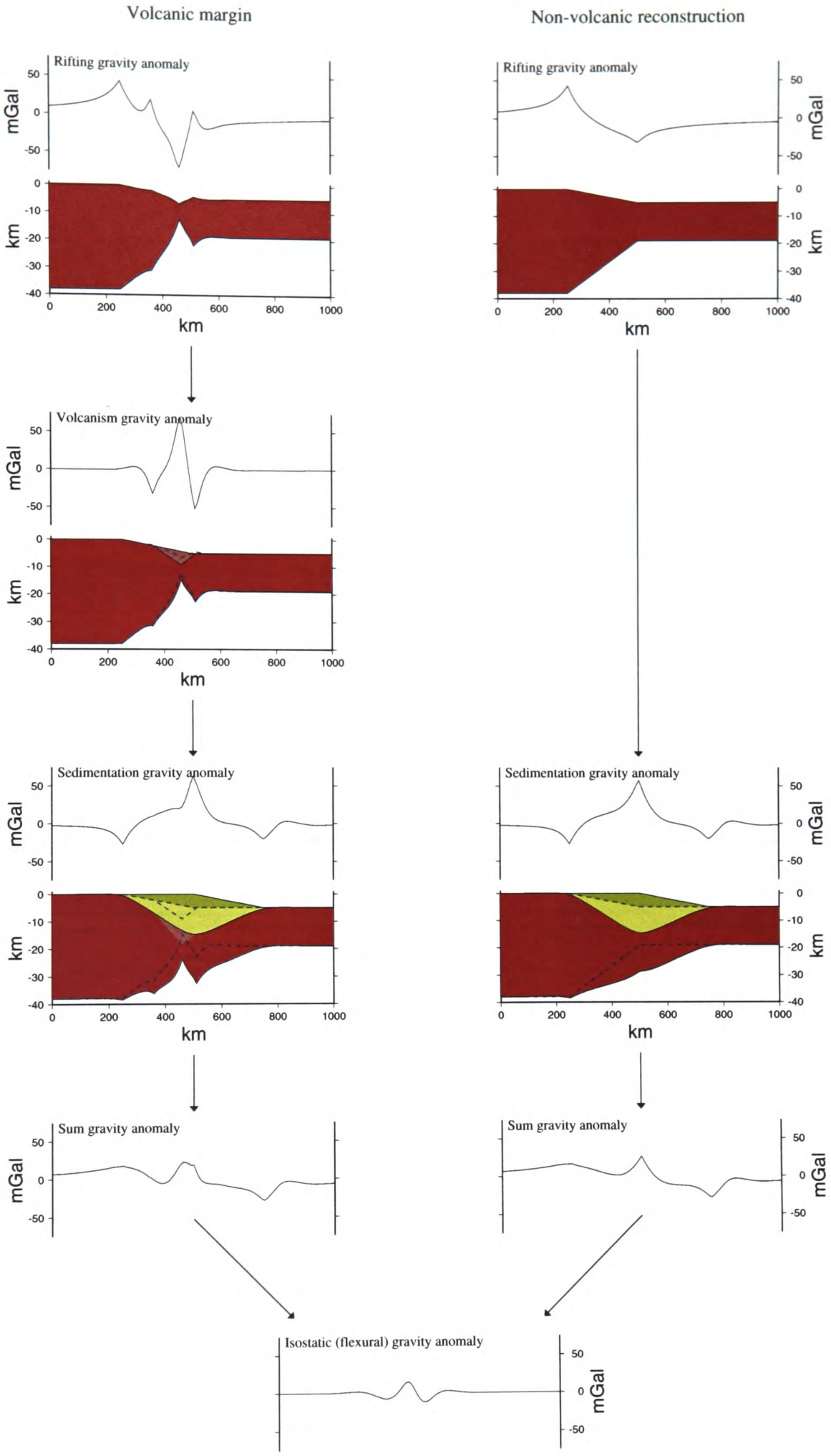


Figure 7.1: Synthetic extrusive volcanism isostatic gravity anomaly. 'Volcanic margin' created by flexural compensation ($T_e = 10km$) of a subaerially emplaced volcanic wedge and sediment load. 'Non-volcanic reconstruction' based on sediment backstripping. IGA given by subtraction of the non-volcanic anomaly from the volcanic anomaly. Dashed lines show margin geometry prior to each process. See text for discussion.

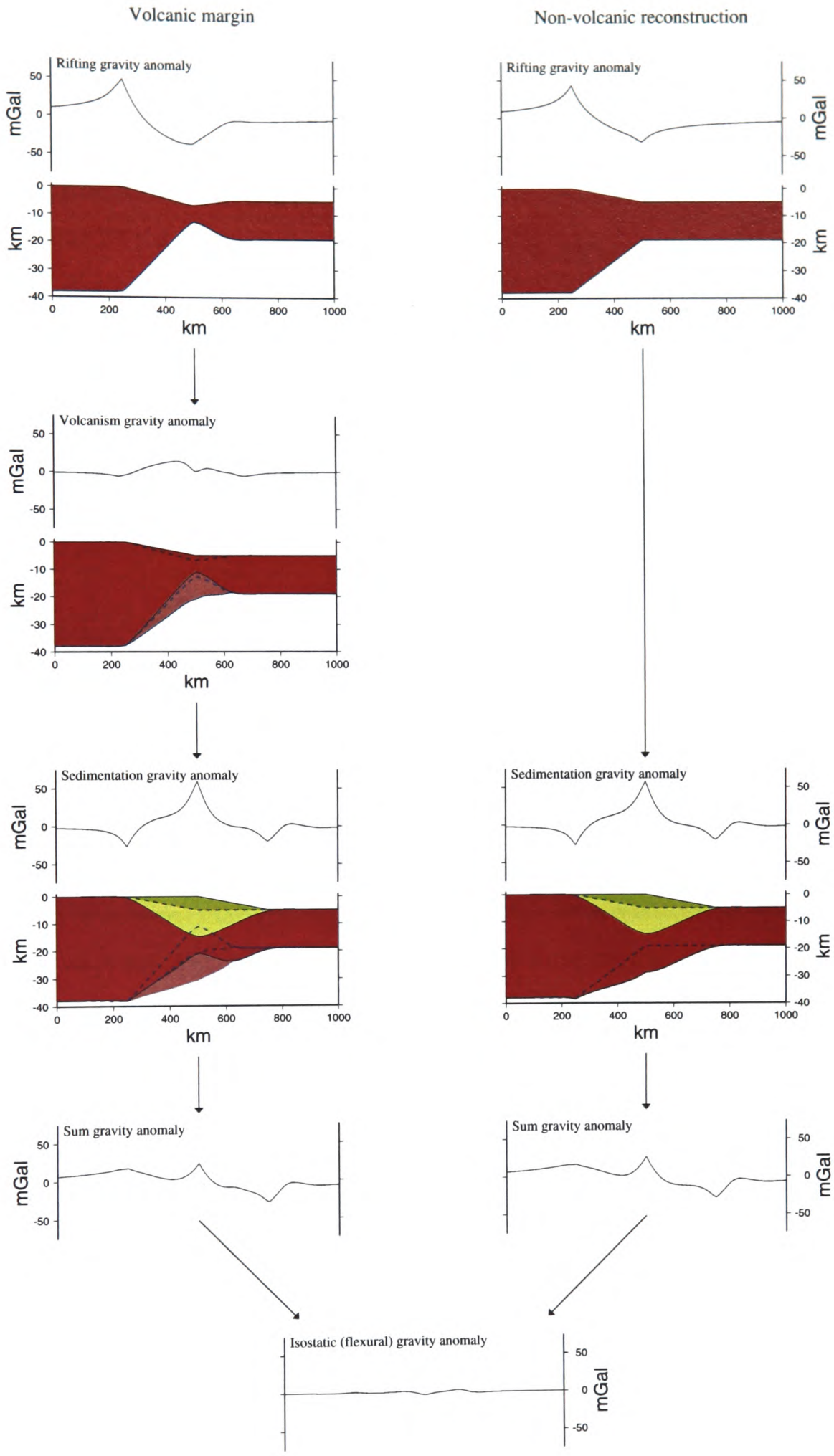


Figure 7.2: Synthetic magmatic underplate isostatic gravity anomaly. 'Volcanic margin' created by flexural compensation of an underplate and sediment load. 'Non-volcanic reconstruction' based on sediment backstripping. IGA given by subtraction of the non-volcanic anomaly from the volcanic anomaly. Dashed lines show margin geometry prior to each process. See text for discussion.

and consists of a low flanked by highs. This is because the underplate is buoyant relative to the mantle it displaces, and hence causes flexural upwarping of the crust above. The upshot is that the negative gravity contributions from replacement of mantle by underplate have a shorter wavelength and larger amplitude than the combined positive contributions due to flexural replacement of crust with underplate at the Moho and of water with crust at the surface.

Both the width and depth of the volcanic body contribute to the amplitude and wavelength of the flexural IGA. Although increasing the thickness of the underplate increases the amplitude of the anomaly, increasing the width has the opposite effect. Finally, because the size of the underplate driven upwarp is controlled by the buoyancy of the underplate relative to the mantle, a lower underplate density results in a larger isostatic anomaly.

7.1.3 Intrusive volcanism

A final suite of synthetic models (Figure 7.3) investigate the effect of extensive igneous intrusion of the rift stage crust, as is apparent in deep seismic surveys crossing the Eastern USA passive margin. Because the intrusive material is emplaced within the full thickness of the crust, the compensation is effectively Pratt-type isostasy (in which isostasy is maintained by lateral variations in crustal density), rather than Airy-type. The thickness of igneous material is determined by a mass-substitution when calculating the thickness of crust that isostatically balances the total tectonic subsidence.

In the example shown the intruded part of the crust grades from 0% of the total crustal thickness at $250km$ into the model to 100% of the crustal thickness at $400km$, it then grades back to 0% across an implicit ocean to continent boundary between $500km$ and $550km$ into the model. The isostatic gravity anomaly has a total amplitude of $7mGal$ and consists of a low over the central body, bounded by a larger high at the continental end and a smaller high at the oceanic end.

The amplitude of the anomaly can be raised by increasing the density of the body, or by steepening the boundaries against 'normal' crust to either side. However, the local isostatic condition ensures that despite the greater volume of igneous crust, the amplitude of the isostatic gravity anomaly remains similar in size to that in the underplate model.

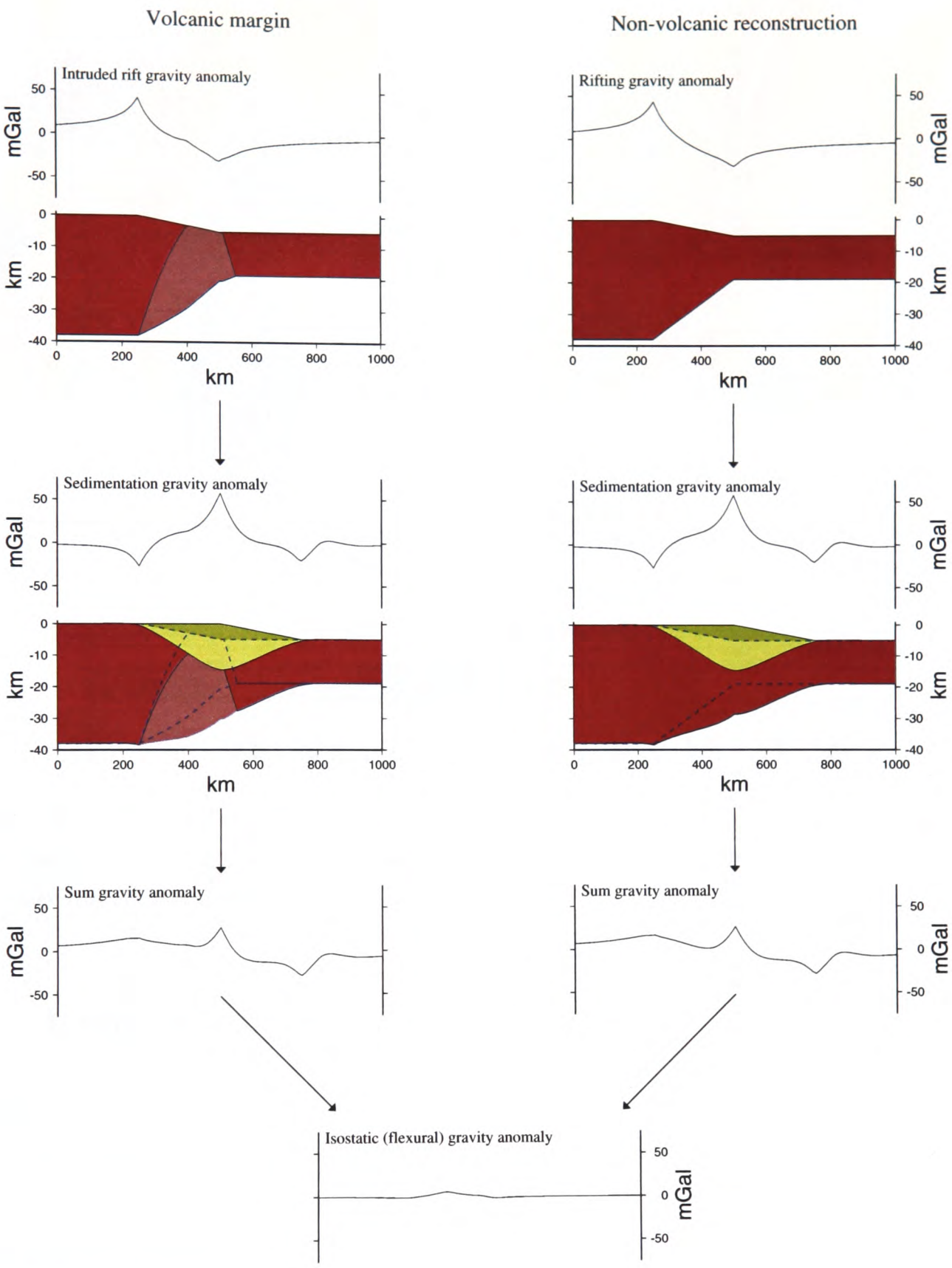


Figure 7.3: Synthetic model of igneous intrusion isostatic gravity anomaly.'Volcanic margin' created using local isostatic compensation of the intruded crust, and flexural compensation ($T_e = 10km$) of a sediment load. 'Non-volcanic reconstruction' based on sediment backstripping. IGA given by subtraction of the non-volcanic anomaly from the volcanic anomaly. Dashed lines show margin geometry prior to each modelled process. See text for discussion.

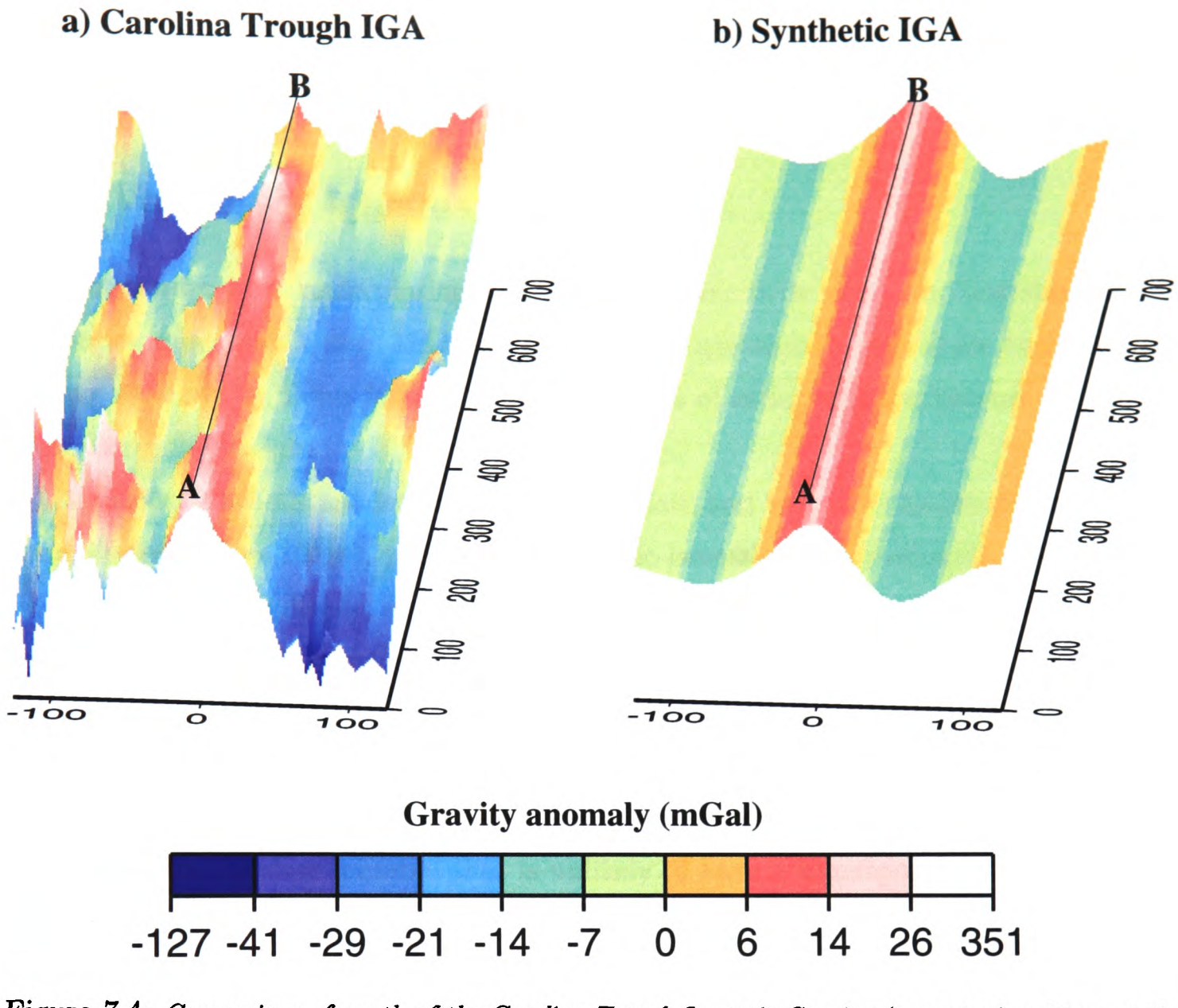


Figure 7.4: Comparison of swath of the Carolina Trough Isostatic Gravity Anomaly (see Figure 6.9) with a synthetic isostatic gravity anomaly due to an extrusive volcanic wedge at basement depth (extended along-strike from model shown in Figure 7.1).

7.2 A volcanic isostatic gravity anomaly

Comparison of the isostatic gravity anomaly modelled for an extrusive volcanic wedge (shown in Figure 7.5) against the Carolina Trough Isostatic Gravity Anomaly (CTIGA) demonstrates a similarity of amplitude and wavelength that is remarkable for such a simple model (Figure 7.4).

It has already been shown (Chapter 6, Section 3.1) that the CTIGA: is coincident with (volcanic?) seaward dipping reflectors; runs between the (volcanic?) East Coast and Brunswick magnetic anomalies; and is located landward of the line of break-up. These lines of evidence, together with existing magnetic models, support an argument that the CTIGA is due to an extrusive volcanic wedge emplaced during rifting.

Equally important is the absence of the CTIGA along the rest of the margin. If this is indicative of lesser rifting volcanism, as comparison of analysis results with the LASE

seismic line suggests, then there are implications for past estimates of the distribution and volume of igneous crust along the margin.

7.3 Volume of igneous crust

The suggestion that underplating and intrusion have little effect on isostatic gravity anomalies along the Eastern USA margin calls into question the use of an Airy isostatic gravity anomaly by Behn & Lin [2000] as a means of estimating the volume of igneous crust along the margin.

A simple synthetic model, in which underplate and extrusive bodies are flexurally compensated ($T_e = 10km$), produces a synthetic isostatic gravity anomaly that is comparable in form, amplitude, and wavelength to the isostatic gravity anomalies studied by Behn & Lin [2000] (Figure 7.5).

The model shows that, while a linear relationship between *extrusive* igneous thickness and the isostatic gravity anomaly is possible, no such relationship is observed for the *total* thickness of igneous material. This is because the total thickness includes a large thickness of underplate material that is unlikely to have a significant effect on the IGA (as has already been demonstrated). Igneous intrusion during rifting could contribute even greater thicknesses of igneous material without greatly altering the isostatic gravity anomaly.

It appears that the relationship between total igneous thickness and the isostatic gravity anomaly observed by Behn & Lin [2000] is no more than a reflection of the distribution of underplated and intrusive material relative to the extrusive material that is the dominant cause of the IGA. This is why it is possible for there to be large thicknesses of igneous crust beneath IGA lows on the synthetic profile (see Figure 7.5a).

It is, then, evident that the use of gravity anomalies to directly constrain the total volume of igneous crust along the Eastern USA passive margin is flawed. At best, the volume of *extrusive* igneous material could be estimated using the apparent linear relationship between extrusive igneous thickness and the isostatic gravity anomaly.

If, as the similarity between observed data from the EDGE 801 and BA 6 seismic lines in Figure 7.5 suggests, it were assumed that extrusive volcanism occurs only at some critical intruded thickness (c.$10 - 15km$), then the volume of igneous crust below could be inferred. Such an approach would use the critical thickness, the width of the rift stage crust, and the presence of an extrusive IGA, but would not be applicable in regions where extrusive volcanism is either absent or too limited to produce a notable IGA signal.

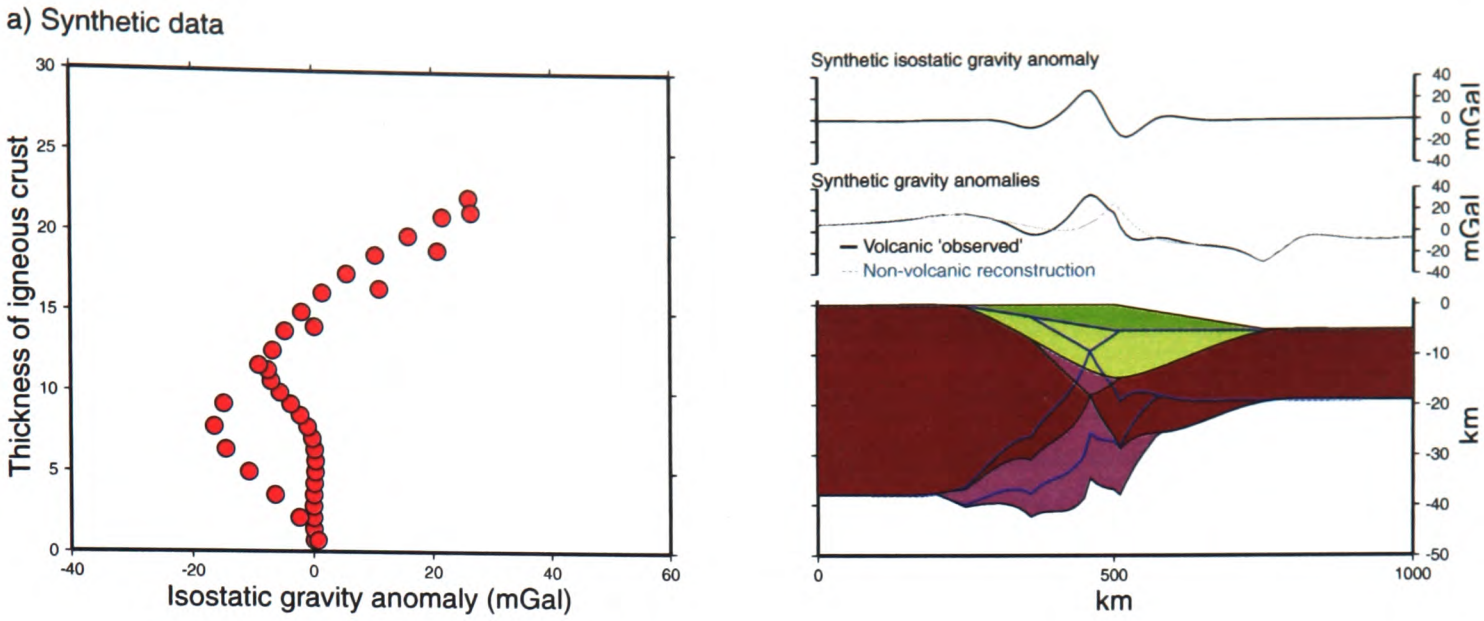


Figure 7.5: Correlation between isostatic gravity anomalies and total thickness of igneous crust. a) Synthetic correlation from model shown in (b); in which igneous extrusion, magmatic underplating, and subsequent sediment loading are flexurally compensated ($T_e = 10km$; densities and method as in Figure 7.1 and Figure 7.1; blue lines are volcanic margin geometry prior to sediment loading). c) Observed correlation from the BA-6 (open squares) and EDGE-801 (solid circles) lines (from Behn & Lin [2000]). d) Comparison of observed and synthetic correlations.

7.4 Comparison with the Southeast Greenland margin

If, as has been suggested, extrusive volcanism gives rise to distinct gravity anomalies, then combined backstripping and gravity modelling techniques could be used to identify such contributions at other margins. On this basis, a process-oriented analysis that includes gravity contributions due to flexurally compensated extrusive volcanism has been applied to a transect of the Southeast Greenland margin.

A study of the 1996 SIGMA 2 seismic transect [Korenaga *et al.*, 2001] allowed sediment and flood basalt geometries and densities to be controlled for a 2D flexural analysis of the margin (Figure 7.6). The method used backstripping of the sediments

and flood basalts to determine the crustal thickness (Densities: basalt=2750kgm^{-3}; sediment=2600kgm^{-3}; crust=2900kgm^{-3}; mantle=3300kgm^{-3}). Calculation of rifting, volcanic, sedimentation, and sum (calculated free-air) gravity anomalies allowed T_e ($22km$) to be constrained against the observed free-air anomaly.

The resulting structure produces a sum gravity anomaly that agrees closely with the free-air anomaly (leaving only a small isostatic gravity anomaly). However, the model Moho is not in accord with the seismic Moho (Figure 7.6e). To deal with this disparity a novel approach is applied in which it is assumed that the minimisation of the isostatic gravity anomaly (and hence the T_e estimate) is real, but that igneous intrusion explains the greater seismic thickness of the crust while making only a small contribution to the isostatic gravity anomaly.

To create the intrusion, the difference between the seismic and model Mohos is used to generate an 'equivalent intruded thickness' (intruded density of 3100kgm^{-3}) with the same (hence equivalent) isostatic balance as the original model, and the same Moho as is observed seismically (Figure 7.7). This intrusion is unloaded (using local isostasy) from the original backstrip, to generate a new total tectonic subsidence and rift Moho (Figure 7.7b). From this, sequential emplacement of all of the backstripped loads leads to rifting, underplate, flood basalt (SDR), sedimentation and sum gravity anomalies (Figure 7.7b,c,d,e,f). The isostatic gravity anomaly remains essentially unchanged from the original method, but the model structure is in much better agreement with the observed seismic structure. In particular, the upper surface of the intrusion conforms well with the 3000kgm^{-3} density contour, and (as dictated by the model) the lower surface conforms with the seismic Moho.

The method is novel because it allows deep seismic data to be explained in terms of a flexural model without biasing the recovery of T_e from process-oriented (SDR and sedimentation) contributions to the free-air gravity anomaly. In the case of the Sigma 2 transect, Korenaga *et al.* [2001] were unable to explain the free-air gravity anomaly using their density distribution, and instead speculated a dense shallow crust body beneath the SDRs for which there was no seismic evidence. The process-oriented model presented here, however, explains both the free-air anomaly and the seismic Moho with only small departures from the observed seismic structure.

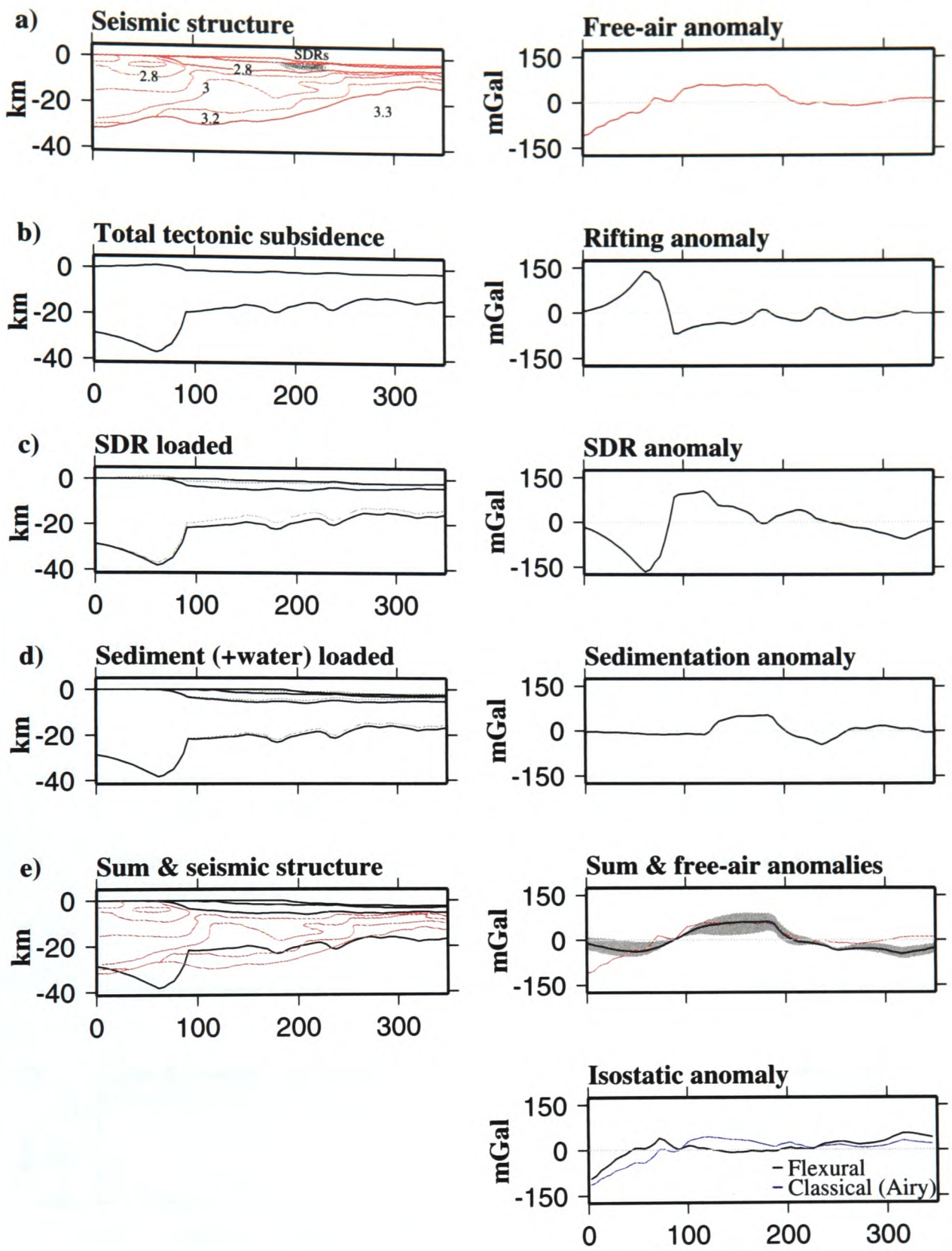


Figure 7.6: Process-oriented analysis of the southeast Greenland margin Sigma 2 deep seismic transect. a) Seismic structure and free-air gravity anomaly (digitised from Korenaga *et al.* [2001]. Contours are seismically determined densities in gcm^{-3}. Seismic reflection seaward dipping reflectors (SDRs) digitised from Korenaga *et al.* [2000]. b-d) Analysis based on flexural backstripping ($T_e = 22km$) of sediments, water, and SDRs. e) Comparison of modelled and observed structure and free-air gravity anomalies (shading shows range of calculated free-air anomalies for $10km \leq T_e \leq 30km$). f) Flexural isostatic gravity anomaly, with Airy isostatic gravity anomaly for comparison purposes. Feint lines show structure prior to each load.

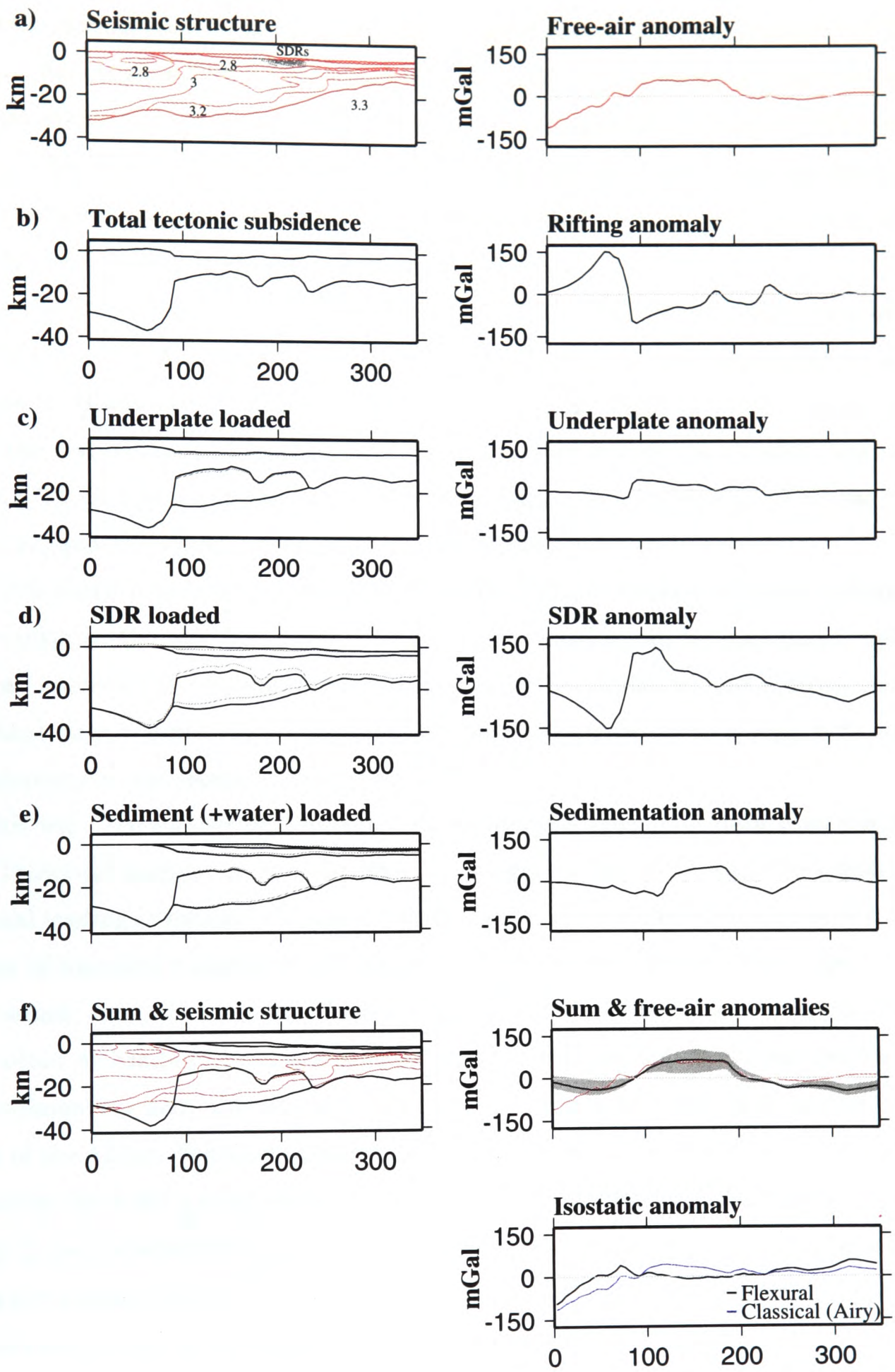


Figure 7.7: Process-oriented analysis of the southeast Greenland margin Sigma 2 deep seismic transect. Description as in Figure 7.6, except for the addition of an Airy-isostatically compensated underplate in b).

7.5 Summary

Synthetic models show that the Carolina Trough Isostatic Gravity Anomaly (CTIGA) high and flanking lows can be explained by a flexurally loaded wedge of extrusive igneous material extending along more than $700km$ of the length of the Eastern USA passive margin. Together with seismic data and existing volcanic models for the East Coast and Brunswick magnetic anomalies (ECMA and BMA), this supports a strong igneous contribution to this part of the margin during rifting.

The lack of a continuous equivalent to the CTIGA north of the intersection between the BMA and ECMA suggests that the ECMA alone is not (as some authors, such as Kelemen & Holbrook [1995], have suggested) a signifier of similarly extensive volcanism along the rest of the margin. Nor does the single deep seismic line (LASE) not crossed by the CTIGA provide evidence of such a strong igneous contribution as do the (BA-6, USGS 32, and EDGE-801) deep seismic lines to the south.

While there is substantial evidence that the CTIGA marks the most volcanic part of the margin, the question of whether the entire margin can be considered 'volcanic' remains unanswered. Simple models of magmatic underplating and igneous intrusion show that large volumes of such material could exist along the entire margin with minimal contributions to the isostatic gravity anomaly.

This has been further demonstrated by an analysis applied to data from the South-east Greenland margin, from which the free-air gravity anomaly could be explained by identical loading of extrusive volcanics, water, and sediment; whether with or not a large volume of intruded material was modelled in the lower part of the rifted crust.

It seems, then, that the contribution of igneous material to a passive margin can only be resolved by combining process-oriented analysis with seismic data that constrains not just sedimentary and extrusive volcanic thicknesses, but also crustal velocities and the depth of the Moho. Without these pieces of information there will be no direct means of evaluating the volume of igneous crust from potential anomalies. The counterpoint to this is that T_e can be reliably constrained on the basis of backstripping of loads emplaced onto the upper surface of the crust, without significant bias from broad regions of anomalous crustal density and/or underplating.

Chapter 8

Conclusions

8.1 Introduction

The primary aim of this study was to use combined 3-D backstripping and gravity modelling techniques to determine the T_e structure of the Eastern USA passive continental margin. The T_e structure could then be used to infer the extent of segmentation of the margin, and to investigate the various contributions of structural inheritance, rifting, and sedimentation to the long term strength of the rifted continental lithosphere.

This chapter summarises the data, methods, and results that contributed to this goal, and suggests areas of further research.

8.2 Data

The methods used in this thesis rely on high quality sediment data for modelling of flexural subsidence, and high quality gravity data for process-oriented gravity modelling. The primary sediment isopach data were supplied directly by the United States Geological Survey (USGS), courtesy of Debbie Hutchinson (USGS, Woods Hole Oceanographic Institute), and the necessary terrestrial and satellite derived gravity anomaly data were already in the public domain.

The USGS 3-D sediment data grids are confined to the boundaries of offshore seismic surveys conducted in 1973 to 1978. Prior to flexural subsidence and gravity anomaly modelling it was therefore necessary to supplement them with data from other sources. To this end, isopach contours from the western North Atlantic and onshore well data from the Continental of Stratigraphic Units of North America project were approximately correlated with units from the USGS dataset. These were then gridded together with additional constraints from oceanic age contours, a global sediment thickness grid, and a defined coastal plain fall line. The result is a set of seven gridded units that trace isopach

thicknesses from the coastal plain to the North Atlantic abyssal plain.

8.3 Methods

For the analysis to be applied to the Eastern USA passive continental margin it was necessary to modify the process-oriented method such that spatial variations in T_e (traditionally obtained by trial and error) could be efficiently derived using an iterative method of adjustment. Foremost in achieving this were the application of a rapid finite difference approximation, and a new approach to calculation of process-oriented gravity anomalies. Without the computational savings that were made, the iterative nature of this study would have rendered it impractical.

The applied process-oriented analysis method consisted of iterative application of:

1. Sediment backstripping using a finite difference approximation of non-uniform elastic plate flexure.

2. Crustal reconstruction with an Airy isostatic assumption.

3. Approximation of process-oriented gravity anomalies by Parker's method.

4. Constraint of T_e through minimisation of the RMS isostatic gravity anomaly.

Its use was supported by Airy isostatic and uniform plate analyses, sensitivity studies, and investigation of the possible role of strength during rifting.

A similar 'oceanic' method of analysis, in which the backstripping T_e distribution was controlled by the 450^oC oceanic isotherm depth, provided a possible means of distinguishing between oceanic and continental lithosphere along the margin.

Following the process-oriented analysis, a suite of 2-D volcanic studies simulated the contributions of rifting volcanism to the isostatic gravity anomaly. These led to reassessment of the distribution of volcanic material along the Eastern USA margin, and to a comparative study of the free-air gravity anomaly across the Southeast Greenland margin. In the latter case it was demonstrated that process-oriented analysis could be allied with isostatically compensated deep seismic structure without compromising the unique constraint of T_e.

8.4 Summary of results

8.4.1 Segmentation of mechanical thickness

The effective elastic thickness of the Eastern USA rifted continental lithosphere has been shown to be limited by the degree of thinning, and by the amount of inelastic yielding caused by flexural curvature of the sediment loaded lithosphere. Both processes act to reduce T_e, but other sedimentation effects (such as insulation) have probably contributed to long term low T_e in the marginal basins.

Rifting and sedimentation alone do not explain the alternation of 'strong' and 'weak' zones (conforming to marginal 'platforms' and 'embayments') along the margin. This long term segmentation of the margin is apparently due to inheritance of pre-existing structural fabric.

As evidenced by the width of the rift-stage basement, the lithosphere that has been the weakest flexurally was also the most ductile during rifting. The broad rift-stage crust of the 'weak' Blake Plateau Basin and Baltimore Canyon Trough contrasts with the narrow Carolina Trough rift-stage crust bounded by the 'strong' Cape Fear Arch and Norfolk High, which together form the most prominent and extensive of the marginal platforms.

The along-strike isostatic gravity anomaly (IGA) high based on the derived T_e distribution contains only 7% of the energy in the free-air edge effect anomaly, and 29% of that in the Airy isostatic gravity anomaly. A long ($300 - 500km$) wavelength spectral energy peak in the Airy IGA high is absent from the flexural IGA. This, together with a peak in the same waveband of the along-strike T_e distribution, suggests that long wavelength variations in the Airy IGA high are due to flexural compensation of the sediment load.

8.4.2 Volcanism

An along strike flexural IGA high following over $700km$ of the margin (dubbed the Carolina Trough Isostatic Gravity Anomaly, CTIGA) has been identified. This anomaly has not been recognised in previous studies based on Airy isostasy. The anomaly extends from the Blake Spur Fracture Zone to the intersection of the Brunswick (BMA) and East Coast (ECMA) magnetic anomalies, suggesting a continuous source along its length.

The CTIGA (observed as a high with flanking lows) is interpreted as a result of extrusive volcanism. Simple elastic plate models show that the anomaly is consistent with a flexurally compensated wedge of volcanic material extruded subaerially during rifting. Its location is in accord with the observation of seismic seaward dipping reflectors along parts of seismic lines BA-6, USGS 32, and EDGE 801, and is compatible with a

model [Talwani *et al.*, 1995] in which the BMA and ECMA (which are located to either side of the CTIGA high) share a common volcanic source. Continuation of the ECMA as a narrower low-high magnetic couple to the north follows a path close to the OCT, suggesting it is sourced either from less extensive volcanism, or from the ocean-continent boundary.

The CTIGA is located seaward of the Carolina Trough hinge zone, which marks the boundary between the narrowest rift stage crust and the most prominent marginal platform (made up of the Cape Fear Arch and Norfolk High). If passive mantle upwelling during rifting caused linear volcanism between the BA-6, USGS 32, and EDGE 801 deep seismic lines [Kelemen & Holbrook, 1995], then comparatively rapid and focussed thinning could explain enhanced volcanism in the Carolina Trough.

Simple elastic plate models have also been used to assess the isostatic gravity anomalies associated with magmatic underplating. These anomalies are smaller in amplitude than those due to extrusive volcanism. In the context of the Eastern USA margin, such anomalies will either be too small to be observed above other contributions to the IGA, or are obscured by the larger amplitude CTIGA. This limits how effectively the IGA can be used to estimate the total volume of igneous crust along the margin, as has recently been attempted by Behn & Lin [2000]. The apparent lack of a large volcanic source for the ECMA from Cape Hatteras northwards suggests that the igneous volume estimates of Kelemen & Holbrook [1995] may not be correct.

To the south of the CTIGA the ECMA ends, and the BMA turns landward across central Florida. The source of this part of the BMA may be a suture between the Iapetan African and American cratons. Reactivation of this suture during rifting could have formed a failed rift suggested by high stretching factors in the western Blake Plateau Basin. However, in the absence of other evidence both the source of the BMA in this area, and the presence of a failed rift, remain speculative.

8.4.3 Oceanic to continental transition

The final line of break up has been identified using both gravity anomalies and total tectonic subsidence. Gravity has the potential to resolve boundaries to the ocean to continent transition because of the fundamentally different flexural responses of oceanic lithosphere and stretched continental lithosphere, but its use is subject to qualitative interpretation of observed and calculated gravity anomalies. Flattening of the TTS has also been used to infer the edge of the earliest oceanic crust, but provides no information on the width (if any) of the transition zone. The results of the two methods are in good agreement, and together constrain the OCT along almost the entire margin.

The earliest 'normal' oceanic crust is generally found close to the reduced-to-pole ECMA high, and just seaward of the Carolina Trough Isostatic Gravity Anomaly high. This adds to the evidence that the CTIGA and Carolina Trough ECMA and BMA are markers of an extensive volcanic wedge that extends across the line of break-up.

8.5 Primary conclusions

Relating to the Eastern USA passive continental margin:

1. Lithospheric strength of extended continental lithosphere is limited by the weakening effects of thinning of the lithosphere during rifting and curvature of the lithosphere induced by flexural sediment loading in the marginal basins. These, together with the thermal effects of sedimentation, explain weaknesses in the most deeply sedimented parts of the margin.

2. The extended continental lithosphere is segmented along-strike in terms of its long-term integrated mechanical strength. This explains the distribution of structural platforms and embayments along the margin, and the narrowing and widening of the rift-stage basement in regions where the lithosphere was 'strong' and 'weak' respectively during rifting. Along-strike segmentation influenced the rifting process and can be observed landward of the hinge zone, suggesting that it was acquired from the long tectonic history that pre-dated Atlantic rifting.

3. The margin lithosphere appears to be segmented in terms of volcanic structure. The 'Carolina Trough Isostatic Gravity Anomaly' (CTIGA) is independent of the free-air edge effect gravity anomaly, and can be explained by a flexurally compensated wedge of extrusive volcanic material emplaced along $700km$ of the margin's length. Its location is compatible with a volcanic source for the Brunswick Magnetic Anomaly and East Coast Magnetic Anomaly in the Carolina Trough. The CTIGA and BMA are not observed north of Cape Hatteras; suggesting that such pervasive volcanism does not continue into the Baltimore Canyon Trough and Georges Bank Basin.

4. Igneous intrusion and/or underplating of the margin lithosphere are unlikely to produce observable contributions to free-air or isostatic gravity anomalies. As the bulk of this material lies beneath the Curie depth, existing estimates of the volume of igneous crust based on the margin gravity and magnetic anomalies may not be correct.

5. The location of the oceanic to continental transition has been estimated through comparison of 'oceanic' and 'continental' calculated gravity anomalies against the observed free-air gravity anomaly, and using the total tectonic subsidence. Its location supports interpretation of the CTIGA as a marker of extrusive volcanism close to the line of break-up.

Relating to process-oriented analysis:

1. 2-D process-oriented gravity anomaly modelling can be extended to 3-D using efficient analysis techniques. The iterative approach applied yields statistically robust estimates of the T_e distribution in a manner that has not been possible using traditional 2-D trial and error methods.

2. Minimisation of the flexural isostatic gravity anomaly over a wide area can reveal features such as the CTIGA, which are otherwise concealed by the gravity contributions of large crustal loads and their flexural compensation.

3. 2-D process-oriented modelling of extrusive volcanism and its flexural compensation shows that volcanism contributes significantly to free-air and isostatic gravity anomalies at some margins (including those of the Eastern USA and southeast Greenland). However, gravity anomalies due to intruded or underplated loads are small due to their comparatively long wavelengths and large depths of burial. Hence it is possible that large thicknesses of intruded or underplated igneous material emplaced during rifting will not be associated with an observable isostatic gravity anomaly.

8.6 Future work

Eastern USA margin This study has demonstrated that the Eastern USA passive margin is segmented in terms of both mechanical structure and volcanism. However, three of the four deep seismic studies of the margin (BA-6, USGS 32, and EDGE-801) cross similar mechanical and volcanic structure in the Carolina Trough and southern Baltimore Canyon trough. The structure of the central Baltimore Canyon Trough is very different; T_e remains low ($< 10km$) from the Raritan Embayment to the central basin, and the CTIGA is absent. There has been a tendency for recent studies to extrapolate Carolina Trough and southern Baltimore Canyon Trough crustal structure along the margin, but it is now clear that these sub-basins are not representative of the margin as a whole. The LASE line lacks the velocity resolution of later surveys, rendering its

volcanic interpretation uncertain. A new deep seismic experiment in the vicinity of the LASE line, and providing comparable resolution to the BA-6 and EDGE-801 lines, would provide a better reference for comparison of structure in the weak/non-volcanic(?) central Baltimore Canyon Trough with that in the strong/volcanic Carolina Trough. Although there is a history of deep seismic experiments crossing the margin shelf-break, there is now an evident need for deep seismic experiments that parallel it. The primary purpose of such experiments would be to investigate along-strike variations in crustal structure and margin volcanism. This could reveal more evidence of the structural variations that control segmentation of T_e along the margin.

Other margins It has been demonstrated that structural segmentation of a passive margin can be readily resolved in terms of spatial variations in T_e, and interpretation of the flexural isostatic gravity anomaly. Such an approach can reveal volcanic features of the free-air gravity anomaly that would otherwise be obscured by the contributions of sediments and their flexural compensation. Compilations of 3-D sediment data with comparable resolution to the one used here are becoming available for other margins (for example for the Gulf of Mexico and Iberia). These should be used to determine the degree that these margins are segmented, and to investigate whether volcanic segmentation is a common feature of passive continental margins. If so, it will need to be considered how this can be explained in terms of existing models for volcanic and non-volcanic rifting.

Appendix A

Finite difference software

```
PROGRAM FD_FLEX3D

C ###################################################################
C Finite difference, variable Te flexure program.
C Paul Wyer. December 1999

C Derivations by Jon Stewart and Paul Wyer

C Needs to be linked to LAPACK subroutines DGBTRF and DGBTRS
C Also requires fourn from Numerical Recipes in Fortran 77,
C       Press et al. 1992. University of Cambridge Press, Camb.
C E.g. to compile Sun: f77 -Lperf -lsunperf fd_flex3d.f fourn.f
C Can be linked directly to LAPACK libraries on other systems.
C ###################################################################

C P is a value representing 2D position i,j
C uxp = UserXpoints
C uyp = UserYpoints
C where P(max) = uxp*uyp

C         Eg. (uxp=4, uyp=3):

C 1(1,1) 2(2,1) 3(3,1) 4(4,1)

C 5(1,2) 6(2,2) 7(3,2) 8(4,2)

C 9(1,3) 10(2,3) 11(3,3) 12(4,3)

C Hence Q(P,n) represents a series of coefficients relating to
C the finite difference solution at position P. There are
C uxp*uyp equations to solve for uxp*uyp flexural responses, and
C each equation has terms relating to points +/- 2*uxp away from P.
C So Q has dimensions (uxp*uyp,uxp*uyp)

C Now, RoGeeH contains load solutions on input to dgbtrs and
C flexure solutions on output. These relate to
```

```
C Q(uxp*uyp,uxp*uyp)*W(uxp*uyp) = RoGeeH(uxp*uyp)

C Q is reduced to a band matrix A using LAPACK band storage.

C ***NOTES***
C Correct band storage information is contained in the routines
C called. The definition in the LAPACK manual is erroneous.

C ***At present the program reads xyzhd in GMT output order
C ***I.e. working from upper-left with X changing most rapidly.
C ***xyz data must have exactly uxp by uyp data points.

C The approximation is memory limited

C uxp <= uyp
C uxp*uxp*uyp <= 8000000 on a 512Mb RAM system
C uxp*uxp*uyp <= 1000000 on 128Mb RAM

C Rigidity derivatives are calculated in the Fourier domain.
C Hence: N is a power of 2, where N >= max(uxp,uyp)
Integer N, UserXpoints, UserYpoints
print*, "#######################################################"
print*, "Finite  difference approx of elastic plate  flexure."
print*, "Marine Geophysics Group, University of Oxford, 1999."
print*, "#######################################################"
print*
print*, "Memory limitations:"
print*, "  512Mb Ram:  xpoints*xpoints*ypoints <= 8000000"
print*, "  128Mb Ram:  xpoints*xpoints*ypoints <= 1000000"
print*

C Really just a shell for the "real" program contained in MAIN

print*, "Number of points in X dimension, uxp"
read*, UserXpoints
print*
print*, "Number of points in Y dimension, uyp"
read*, UserYpoints
print*
print*, "Dimension for rigidity transforms, N"
print*, "N is a power of 2, where: N > uxp, N > uyp"
read*, N
print*

call MAIN(N,UserXpoints,UserYpoints)

END
```

```
C ###############################################################

SUBROUTINE MAIN(N,UserXpoints,UserYpoints)

C ###############################################################

integer N, UserXpoints, UserYpoints
double precision A(4*UserXpoints+2*UserXpoints+1,
     +                    UserXpoints*UserYpoints)
double precision B(UserXpoints*UserYpoints)
double precision DelX(N),DelY
integer IPV(4*UserXpoints+2*UserXpoints+1,
     +                   UserXpoints*UserYpoints)
integer I,J,direx,INF,NRH,P,kl,ku,LDAB,NF(1:2)
integer uxp,uyp,unn
real RoS(UserXpoints,UserYpoints)
real RoGeeH(UserXpoints,UserYpoints)
real H(UserXpoints,UserYpoints)
real XO,YO,DelXdeg,DelYdeg,DelRo,RoM,RoIn,AvLat
real Dx(2*N,N),Dy(2*N,N),Dxy(2*N,N),Dxx(2*N,N),Dyy(2*N,N)
real Te(2*UserXpoints,UserYpoints),FTe(2*N,N),Lon,Lat,Pi2
character*10, outfile
character TRAN
IMPLICIT NONE

C Set parameters and dimensions

RoM = 3330.
RoIn = 1030.
DelRo=RoM-RoIn
Pi2 = 6.28318530718
uxp = UserXpoints
uyp = UserYpoints
unn = UserXpoints*UserYpoints

C print*,uxp,uyp,unn

C Read in all data

call GetLoad (XO,YO,H,RoS,RoGeeH,Te,FTe,DelXdeg,DelYdeg,N,
     +   uxp,uyp)

AvLat = ABS(YO+DelYdeg*UserYpoints/2)
print*,"P Average Latitude is: ", AvLat

print*," Load distribution read"
print*,"W Rigidity distribution read"

C Calculate DelX, DelY values by latitude.
```

```
Lat = YO
DelY = ABS(DelYdeg*111.*1.0E+3)
Do 5 J=1,N
  Lat = Lat+DelYDeg
C   DelX(J) = DelXdeg*111.*1.E+3
C   DelX(J) = DelXdeg*111.*COS(Pi2*AvLat/360)*1.E+3
  DelX(J) = DelXdeg*111.*COS(Pi2*Lat/360)*1.E+3
5 CONTINUE

C Calculate derivatives of D.
C ***Remember that these are in (2*N,N) matrices with first***
C ***series alternating real/complex parts!                  ***

NF(1) = N
NF(2) = N
direx = 1
call FOURN (FTe,NF,2,direx)
print*,"y Fourier transformed Te"
call DERIVATIVES (FTe,Dx,Dy,Dxy,Dxx,Dyy,N)
print*,"e Used Te to derive Fourier rigidity derivatives"

direx=-1
call FOURN (Dx,NF,2,direx)
call FOURN (Dy,NF,2,direx)
call FOURN (Dxy,NF,2,direx)
call FOURN (Dxx,NF,2,direx)
call FOURN (Dyy,NF,2,direx)
print*,"r Inverse transformed derivatives"

C Calculate FD coefficients.

CALL FD_COEFF (A,DelX,DelY,Te,Dx,Dy,Dxy,Dxx,Dyy,DelRo,N,
     +   uxp,uyp)
C Note: Te returns containing rigidity (D) values
print*," Finite difference coefficients derived"

CALL REPACK (RoGeeH,B,N,uxp,uyp)
print*,"1 Repacked data for efficient FD solution"

C Solve the finite difference problem (linear equations in w and q)
C using a banded Ax=b solution...

ku = uxp+uxp
kl = ku
LDAB=2*kl+ku+1

CALL DGBTRF(unn,unn,kl,ku,A,LDAB,IPV,INF)
print*,"9 LU Factorisation complete"
C print*,INF
```

```
C Transpose matrix Q?
TRAN="N"
C Number of RHS columns?
NRH=1
C Double precision U-L factorised array Q comes from DGBTRF

C Pivot indices, IPV, come from DGETRF
C Double precision array B goes in as RoGeeH values, comes out
C as solution matrix.
C INFO = 0 means successful exit.
C INFO = i means i-th argument is illegal.

CALL DGBTRS(TRAN,unn,kl,ku,NRH,A,LDAB,IPV,B,unn,INF)
print*,"9 Flexure solved"
C print*,INF

C CALL DATAOUT(B,N,DelX,DelY,XO,YO,uxp,uyp)

PRINT*,'9'
     2 PRINT*,'NAME OF OUTPUT FILE?'
READ*,OUTFILE

OPEN(UNIT=3,FILE=OUTFILE,STATUS='NEW',ACCESS='SEQUENTIAL',ERR=2)
Lat = YO-DelYDeg
P = 0

Do 15 j=1,uyp
     Lat = Lat+DelYDeg
     Lon = XO-DelXDeg
     Do 16 i=1,uxp
P=P+1
Lon = Lon+DelXDeg
IF (ABS(B(P)).LT.0.1) B(P)=0.0
write(3,*) Lon,Lat,real(-B(P))
16  Continue
15 Continue

print*," Done"
RETURN
END
```

```
C ######################################################################

SUBROUTINE GETLOAD (XOg,YOg,SH,RS,RGHS,Te,FTe,DegX,DegY,N,
     +     uxp,uyp)

C ######################################################################

integer N,uxp,uyp
real SH(uxp,uyp),RS(uxp,uyp),RGHS(uxp,uyp)
real XOg,YOg,X1g,X2g
real null,Te(2*uxp,uyp),FTe(2*N,N),grv
real Av

C Sed file is of the form:

C Lon, Lat, Sed-Thickness, Sed-Density, Plate-Rigidity

5 PRINT*,'NAME OF SEDIMENT FILE?'
PRINT*,'Data should be of the form:'
print*,'  Lon, Lat, Sed-Thickness(m), Sed-Density(kgm-3), Te(km)'
print*,''

C READ*,SEDFILE
C OPEN(UNIT=1,FILE=SEDFILE,STATUS='OLD',ACCESS='SEQUENTIAL',ERR=5)
OPEN(UNIT=1,FILE="load.xy",STATUS='OLD',ACCESS='SEQUENTIAL')

Av = 0.
grv = 9.81

READ(1,*) XOg,YOg,SH(1,1),RS(1,1),Te(1,1)
RS(1,1) = RS(1,1)-1030
RGHS(1,1)= RS(1,1)*SH(1,1)*grv
Te(1,1) = Te(1,1)*1.0E+3
FTe(1,1)= Te(1,1)

Av = Av+Te(1,1)/real(uxp*uyp)

Do 90 I=2,uxp
     R=2*I-1
     READ(1,*) X1g,Y1g,SH(I,1),RS(I,1),Te(R,1)
     RS(I,1) = RS(I,1)-1030
     RGHS(I,1)= RS(I,1)*SH(I,1)*grv
     Te(R,1) = Te(R,1)*1.0E+3
     FTe(R,1)= Te(R,1)
     DegX = X1g-X2g
     X2g = X1g
     Av = Av+Te(R,1)/real(uxp*uyp)
90 CONTINUE

DegY=-DegX
```

```
DO 100 J=2,uyp
  DO 110 I=1,uxp
    R=2*I-1
    READ(1,*) null,null,SH(I,J),RS(I,J),Te(R,J)
    RS(I,J) = RS(I,J)-1030
    RGHS(I,J)= RS(I,J)*SH(I,J)*grv
    Te(R,J) = Te(R,J)*1.0E+3
    Av = Av+Te(R,J)/real(uxp*uyp)
110   CONTINUE
100 CONTINUE

C Subtract average Te from FTe in order to make transform
C cleaner. No need to reverse this later, as FTe is only used
C to find derivatives of Te.
C Fills FTe matrix to N*N (N = integer power of 2)

Do 620 J=1,N
   Do 630 I=1,N
     R = (2*I-1)
     IF((I.LE.uxp).AND.(J.LE.uyp)) THEN
       FTe(R,J)=Te(R,J)-Av
     ELSE IF(J.LE.uyp) THEN
       FTe(R,J)=Te(2*uxp-1,J)-Av
     ELSE IF(I.LE.uxp) THEN
       FTe(R,J)=Te(R,uyp)-Av
     ELSE
       FTe(R,J)=Te(2*uxp-1,uyp)-Av
           ENDIF
630      CONTINUE
620 CONTINUE

RETURN
END
```

```
C ######################################################################

SUBROUTINE DERIVATIVES (FTe,DxDev,DyDev,DxyDev,DxxDev,DyyDev,N)

C ######################################################################

real FTe(2*N,N),DxDev(2*N,N),DyDev(2*N,N)
real DxxDev(2*N,N),DyyDev(2*N,N),DxyDev(2*N,N)
real Pi,Pi2
double precision RealTe,ComplexTe,Fi,Fj,F1,F2
double precision Pi2x,Pi2y,Pi4xy,Pi4xx,Pi4yy
IMPLICIT NONE
integer N,Ni2

Pi=3.141593


Pi2 = Pi*Pi
Ni2 = N*N

Pi2x = 2.*Pi/Ni2
Pi2y = 2.*Pi/Ni2
Pi4xy = -4.*Pi2/Ni2
Pi4xx = -4.*Pi2/Ni2
Pi4yy = -4.*Pi2/Ni2

C Ni2 divisions are to deal with N*N multiplication by the inverse
C transform.
C DeltaX and DeltaY terms are dealt with later in FD_COEFF

C Fi and Fj represent locations in the Fourier array.
C See Numerical Recipes Figure 12.4.1, Section 12.4, p.517

Do 120 F2=1,N,1
  if (F2.LT.N/2) then
   Fj = DBLE(F2) - 1.
  else if (F2.EQ.N/2+1) then
   Fj = 1.
  else
   Fj = DBLE(F2) - 1. - DBLE(N)
  endif

  Do 130 F1=1,2*N-1,2
    RealTe = FTe(F1,F2)
           ComplexTe = FTe(F1+1,F2)
    if (F1.LT.N) then
     Fi = (DBLE(F1)+1.)/2. - 1.
    else if (F1.EQ.N+1) then
     Fi = 1.
    else
```

```
      Fi = (DBLE(F1)+1.0)/2. - 1. - DBLE(N)
     endif

C The solutions below are for Te derivatives, _NOT_ rigidity, D

C real values
C    (Complex D multiplied by complex number)
     DxDev(F1,F2) = (Pi2x*Fi*ComplexTe)
     DyDev(F1,F2) = (Pi2y*Fj*ComplexTe)
C    (Real D multiplied by real number)
     DxyDev(F1,F2) = -(Pi4xy*Fi*Fj*RealTe)
     DxxDev(F1,F2) = (Pi4xx*Fi*Fi*RealTe)
     DyyDev(F1,F2) = (Pi4yy*Fj*Fj*RealTe)
C complex values
C    (Real D multiplied by complex number)
     DxDev(F1+1,F2) = -(Pi2x*Fi*RealTe)
     DyDev(F1+1,F2) = -(Pi2y*Fj*RealTe)
C    (Complex D multiplied by real number)
     DxyDev(F1+1,F2) = -(Pi4xy*Fi*Fj*ComplexTe)
     DxxDev(F1+1,F2) = (Pi4xx*Fi*Fi*ComplexTe)
     DyyDev(F1+1,F2) = (Pi4yy*Fj*Fj*ComplexTe)
130    CONTINUE
120  CONTINUE
     RETURN
     END
```

```
C ######################################################################

SUBROUTINE FD_COEFF (A,DelX,DelY,D,Dx,Dy,Dxy,Dxx,Dyy,DelRo,N,
     +    uxp,uyp)

C ######################################################################

C Takes in derivatives of D and returns the linear equation matrix Q
C For the finite difference solution.
C Data for Q is put straight into banded matrix A to save memory.

double precision DelX(N),DelY,Q2(N*N)
double precision A(4*uxp+2*uxp+1,uxp*uyp)
double precision CA,CAy,CB,CBy,CC,CD,CDy,CE,CF,CFy,dlx,dly
real D(2*uxp,uyp),Dx(2*N,N),Dy(2*N,N),Dxy(2*N,N)
real Dxx(2*N,N),Dyy(2*N,N),N2N
integer X,Y,P,N,qj(13),kl,ku,mi,uxp,uyp
real DelRo

grv = 9.81

C Del functions are the deltaX deltaY parts of the FD solution.

C D functions are rigidity and it's derivatives.
C "C..." functions are the "repeated functions" used to make the
C solutions more efficient.

P=0
RN=DBLE(N)
N2N=real(N*N)

kl = uxp+uxp
ku = kl

pr = 1.-0.25**2

CC Initialize Q
C Do 62 i = 1,N*N
C   Do 63 j = 1,N*N
C    Q2(i,j) = 0.0
C   63   CONTINUE
C   62 CONTINUE

dly=ABS(DelY)
Do 10 Y=1,uyp,1
  dlx=ABS(DelX(Y))
  Do 20 X=1,uxp,1

    R = 2*X-1
    P=P+1
```

```
            Delxx  = 1./(dlx*dlx)
      Delyy  = 1./(dly*dly)
      Delxxx = Delxx/dlx
      Delyyy = Delyy/dly
      Delxxxx= Delxxx/dlx
      Delyyyy= Delyyy/dly
      Delxxyy= 2.*Delxx*Delyy
      Delxy  = (1.-0.25)/(2.*dlx*dly)
      Delxxy = Delxx/dly
      Delxyy = Delyy/dlx

C Note: At this stage D(R,Y) contains Te values
C       DTe=21.E+10*(D(R,Y)*D(R,Y))/(12.0*pr)
C       D2Te= 63.E+10*(D(R,Y)*D(R,Y))/(12.0*pr)
      DTe = 30.E+10*(D(R,Y)*D(R,Y))/(12.0*pr)
      D2Te = 3.*DTe

C Convert D(R,Y) from Te to rigidity.
      D(R,Y) = DTe*D(R,Y)/3.

C Te derivatives below -> multiply by d(D)/d(Te) to get D derivatives...
C ...However, d(D)/d(Te) is different for Dxy than for Dx, Dy, Dxx, ...
C       and Dyy.
C dlx,dly terms relate to their use in FD coefficients.
      Dx(R,Y) = DTe*Dx(R,Y)/(RN*dlx)
      Dy(R,Y) = DTe*Dy(R,Y)/(RN*dly)
      Dxy(R,Y) = D2Te*Dxy(R,Y)/(N2N*dlx*dly)
      Dxx(R,Y) = DTe*Dxx(R,Y)/(N2N*dlx*dlx)
      Dyy(R,Y) = DTe*Dyy(R,Y)/(N2N*dly*dly)

      CA = Delxxx * Dx(R,Y)
      CAy = Delyyy * Dy(R,Y)
      CB = Delxxxx * D(R,Y)
      CBy = Delyyyy * D(R,Y)
      CC = Delxy * Dxy(R,Y)
      CD = Delxxy * Dx(R,Y)
      CDy = Delxyy * Dy(R,Y)
      CE = Delxxyy * D(R,Y)
      CF = Delxx * (Dxx(R,Y)+0.25*Dyy(R,Y))
      CFy= Delyy * (Dyy(R,Y)+0.25*Dxx(R,Y))

C Use repeated functions to get coefficient values.
C Q is a matrix of N*N equations, with a sparse width of N.

XX = X+2
YY = Y+2

         if ((X.GT.2).AND.(XX.LE.uxp).AND.(Y.GT.2).AND.(YY.LE.uyp)) then
```

```
qj(1) = P
qj(2) = P+2
qj(3) = P-2
qj(4) = P+uxp+uxp
qj(5) = P-uxp-uxp
qj(6) = P+uxp+1
qj(7) = P-uxp-1
qj(8) = P-uxp+1
qj(9) = P+uxp-1
qj(10) = P+uxp
qj(11) = P-uxp
qj(12) = P+1
qj(13) = P-1

Q2(P) = -2.*(CF + CFy) + 6.*(CB + CBy) + 4.*CE + DelRo*grv

Q2(P+2) = CA + CB
Q2(P-2) = -CA + CB
Q2(P+uxp+uxp) = CAy + CBy
Q2(P-uxp-uxp) = -CAy + CBy

Q2(P+uxp+1) = CC + CD + CDy + CE
Q2(P-uxp-1) = CC - CD - CDy + CE
Q2(P-uxp+1) = -CC - CD + CDy + CE
Q2(P+uxp-1) = -CC + CD - CDy + CE

Q2(P+uxp) = CFy - 2.*CAy - 4.*CBy - 2.*CD - 2.*CE
Q2(P-uxp) = Q2(P+uxp) + 4.*CAy + 4.*CD
Q2(P+1) = CF - 2.*CA - 4.*CB - 2.*CDy - 2.*CE
Q2(P-1) = Q2(P+1) + 4.*CA + 4.*CDy

Do 732 qset=1,13
  mi = kl+ku+1+P-qj(qset)
  A(mi,qj(qset)) = Q2(qj(qset))
732  CONTINUE

else

A(kl+ku+1,P) = DelRo*grv

       endif

20     CONTINUE
10   CONTINUE

RETURN
END
```

```
C ######################################################################

SUBROUTINE REPACK (RGHS,B,N,uxp,uyp)

C ######################################################################

integer i,uxp,uyp
Double Precision B(uxp*uyp)
Real RGHS(uxp,uyp)
C integer mi, mj

P=0

kl = uxp+uxp
ku = kl

Do 95 j=1,uyp
  Do 96 i=1,uxp
    P=P+1
    B(P)=RGHS(I,J)
96   CONTINUE
95 CONTINUE
RETURN
END
```

Bibliography

ABERS, G. A., & LYON-CAEN, H. 1990. Regional gravity anomalies, depth of the foreland basin and isostatic compensation of the New Guinea Highlands. *Tectonics*, **9**, 1479–1493.

AIRY, G. B. 1855. On the computation of the effect of the attraction of the mountain-masses, as disturbing the apparent astronomical latitude of stations in geodetic surveys. *Phil. Trans. Roy. Soc. Lond.*, **145**, 101–104.

ALBERT, R. A., PHILLIPS, R. J., DOMBARD, A. J., & BROWN, C. D. 2000. A test of the validity of yield strength envelopes with an elastoviscoplastic finite element model. *Geophys. J. Int.*, **140**, 399–409.

ALEXANDROV, A. V., & POTAPOV, V. D. 1990. *Basics of theory of elasticity and plasticity (in Russian).* Vischaya Schkola, Moscow, 400p.

ALLEN, P. A., & ALLEN, J. R. 1990. *Basin analysis: Principles and applications.* Blackwell Science: Oxford, United Kingdom, 451 p.

ALLEN, P. A., CRAMPTON, S. L., & SINCLAIR, H. D. 1991. The inception and early evolution of the North Alpine Foreland Basin, Swizterland. *Basin Res.*, **3**, 143–163.

ALLMENDINGER, R. W., JORDAN, T. E., KAY, S. M., & ISACKS, B. L. 1997. The evolution of the Altiplano–Puna plateau of the Central Andes. *Ann. Rev. Earth Planet. Sci.*, **25**, 139–74.

ALSOP, L. E., & TALWANI, M. 1984. The East Coast Magnetic Anomaly. *Science*, **226**, 1189–1191.

ANDERSON, G. D. 1951. *The dynamics of faulting.* Oliver and Boyd Ltd.: Edinburgh, United Kingdom.

ANDO, C. J., COOK, F. A., OLIVER, J. E., BROWN, L. D., & KAUFMAN, S. 1983. Crustal geometry of the Appalachian orogen from seismic reflection studies. *Pages 83–101 of:* HATCHER, JR., R. D., WILLIAMS, H., & ZEITZ, L. (eds), *Contributions to the tectonics and geophysics of mountain chains.* Geol. Soc. Amer. Memoir 158. Geological Society of America.

ARMSTRONG, G., & WATTS, A. B. 2001. Spatial variations in Te in the southern Appalachians, Eastern United States. *J. Geophys. Res.*, **106**, 22009–22026.

ARTEMJEV, M. E., & KABAN, M. K. 1994. Density inhomogeneities, isostasy and flexural rigidity of the lithosphere in the Transcaspian region. *Tectonophyscis*, **240**, 281–297.

ASADA, T., & SHIMAMURA, H. 1975. A structure of the oceanic lithosphere as revealed by ocean-bottom seismography. *paper presented at the Interdisciplinary Symposia, 16th General Assembly.* Intl. Union of Geod. and Geophys., Grenoble.

ASPDEN, J. A., & LITHERLAND, M. 1992. The geology and Mesozoic collisional history of the Cordillera Real, Ecuador. *Tectonophysics*, **205**, 187–204.

ATHY, L. F. 1930. Density, porosity and compaction of sedimentary rocks. *AAPG Bull.*, **14**, 1–24.

AUDET, D. M. 1995. Modelling of porosity evolution and mechanical compaction of calcareous sediments. *Sedimentology*, **42**, 355–373.

AUDET, D. M., & WATTS, A. B. 1994. Flexure modelling of the northwest African continental margin with an application to the Canary Islands (abstract). *Page 581 of: Eos Trans. AGU*, vol. 75(44), Fall Meet. suppl.

AUSTIN, JR., J. A., & UCHUPI, E. 1982. Continental-oceanic transition off southwest Africa. *AAPG Bull.*, **66**, 1328–1347.

AUSTIN, J. A., STOFFA, P. L., PHILLIPS, J. D., OH, J. Y., SAWYER, D. S., PURDY, G. M., REITER, E., MAKRIS, J. 1990. Crustal structure of the Southeast Georgia embayment Carolina Trough - Preliminary results of a composite seismic image of a continental suture and a volcanic passive margin. *Geology*, **18**, 1023–1027.

BABY, P., GUILLER, B., OLLER, J., HERAIL, G., MONTEMURRO, D., & SPECHT, M. 1993. Structural synthesis of the Bolivian Subandean Zone. *Pages 159–162 of: Extended Abstracts, Second International Symposium Andean Geodynamics.* Oxford, England: ORSTROM.

BACHMANN, G. H., MÜLLER, M., & WEGGEN, K. 1987. Evolution of the Molasse Basin (Germany, Switzerland). *Tectonophysics*, **137**, 77–92.

BAGGULEY, J. G. 1997. *The application of seismic and sequence stratigraphy to the post-rift megasequence offshore Namibia.* Ph.D. thesis, Oxford Brookes University, Oxford, England.

BAHLBURG, H., & FURLONG, K. P. 1996. Lithospheric modeling of the Ordovician foreland basin in the Puna of northwestern Argentina: on the influence of arc loading on foreland basin formation. *Tectonophysics*, **259**, 245–258.

BALKWILL, H. R., RODRIGUEZ, G., PAREDES, F. I., & ALMEIDA, J. P. 1995. Northern part of Oriente basin, Ecuador: Reflection seismic expression of structure. *Pages 559–571*

of: TANKARD, A. J., SUÁREZ S., R., & WELSINK, H. J. (eds), *Petroleum Basins of South America.* AAPG Memoir 62. Tulsa, OK: American Association of Petroleum Geologists.

BALMINO, G. 1993. Orbital geometry and the theory of radial orbit error for altimetry. *Pages 243–315 of:* RUMMEL, R. & SANSÒ, F. (eds), *Satellite Altimetry in Geodesy and Oceanography.* Lecture Notes in Earth Sciences 50. Springer-Verlag.

BANKS, R. J., PARKER, R. L., & HUESTIS, S. P. 1977. Isostatic compensation on a continental scale: local versus regional mechanisms. *Geophys. J. R. Astron. Soc.*, **51**, 431–452.

BANKS, R. J., FRANCIS, S. C., & HIPKIN, R. G. 2001. Effects of loads in the upper crust on estimates of the elastic thickness of the lithosphere. *Geophys. J. Int.*, **145**, 291–299.

BARRELL, J. 1914a. The strength of the Earth's crust, II, Regional distribution of isostatic compensation. *J. Geol.*, **22**, 145–165.

BARRELL, J. 1914b. The strength of the Earth's crust, IV, Heterogeneity and rigidity of the crust as measured by departures from isostasy. *J. Geol.*, **22**, 289–314.

BARRELL, J. 1914c. The strength of the Earth's crust, V, The depth of masses producing gravity anomalies and deflection residuals. *J. Geol.*, **22**, 441–468 & 537–555.

BARRELL, J. 1914d. The strength of the Earth's crust, VI, Relations of isostatic movements to a sphere of weakness; the asthenosphere. *J. Geol.*, **22**, 655–683.

BARRELL, J. 1914e. The strength of the Earth's crust, VIIA, Variation of strength with depth as shown by the nature of departures from isostasy. *J. Geol.*, **22**, 729–741.

BARRELL, J. 1915. The strength of the Earth's crust, VIIB, Variation of strength with depth as shown by the nature of departures from isostasy. *J. Geol.*, **23**, 27–44.

BARTON, P. J., & WOOD, R. J. 1984. Tectonic evolution of the North Sea Basin: Crustal stretching and subsidence. *Earth Planet. Sci. Lett.*, **49**, 987–1022.

BASSI, G. 1991. Factors controlling the style of continental rifting: Insights from numerical modelling. *Earth Planet. Sci. Lett.*, **105**, 430–452

BASSI, G., KEEN, C. E., & POTTER, P. 1993. Contrasting styles of rifting: Models and examples from the Eastern Canadian margin. *Tectonics*, **12**, 639–655.

BATT, G. E., & BRAUN, J. 1997 On the thermomechanical evolution of compressional orogens. *Geophys. J, Int.*, **129**, 364–382.

BEAUMONT, C. 1981. Foreland basins. *Geophys. J. R. Astron. Soc.*, **65**, 291–329.

BEAUMONT, C., KEEN, C. E., & BOUTILIER, R. 1982. On the evolution of rifted continental margins: comparison of models and observations for the Nova Scotian margin. *Geophys. J. R. Astron. Soc.*, **70**, 667–715.

BEAUMONT, C., QUINLAN, G., & HAMILTON, J. 1988. Orogeny and stratigraphy: Numerical models of the Paleozoic in the Eastern Interior of North America. *Tectonics*, **7**, 389–416.

BEAUMONT, C., ELLIS, S., & PFIFFNER, A. 1999. Dynamics of sediment subduction-accretion at convergent margins: short-term modes, long-term deformation, and tectonic implications. *J. Geophys. Res.*, **104**, 17573–17602.

BECHTEL, T. D., FORSYTH, D. W., & SWAIN., C. J. 1987. Mechanisms of isostatic compensation in the vicinity of the East African Rift, Kenya. *Geophys. J. R. Astron. Soc.*, **90**, 445–465.

BECHTEL, T. D., FORSYTH, D. W., SHARPTON, V. L., & GRIEVE, R. A. F. 1990. Variations in the effective elastic thickness of the North American lithosphere. *Nature*, **343**, 636–638.

BECK, S. L., ZANDT, G., MYERS, S. C., WALLACE, T. C., SILVER, P. G., & DRAKE, L. 1996. Crustal thickness variations in the central Andes. *Geology*, **24**, 407–410.

BEHN, M. D., & LIN, J. 2000. Segmentation in gravity and magnetic anomalies along the US East Coast passive margin: Implications for incipient structure of the oceanic lithosphere. *J. Geophys. Res.*,**105**, 25769–25790.

BESSIS, J. 1986. Some remarks on the studies of continental rifting: Application to the Gulf of Lions margin (Western Mediterranean). *Mar. Pet. Geol.*, **3**, 37–63.

BIRD, J. M., & DEWEY, J. F. 1970. Lithospheric plate-continental margin tectonics and the evolution of the Appalachian orogen. *Geol. Soc. Am. Bull.*, **81**, 1031–1060.

BIRD, P. 1978. Initiation of intracontinental subduction in the Himalaya. *J. Geophys. Res.*, **83**, 4975–4987.

BIRD, P. 1991. Lateral extrusion of lower crust from under high topograpy, in the isostatic limit. *J. Geophys. Res.*, **96**, 10275–10286.

BLUNDELL, D., FREEMAN, R., & MUELLER, S. (eds). 1992. *A Continent Revealed - The European Traverse.* Cambridge University Press.

BODINE, J. H., & WATTS, A. B. 1979. On lithospheric flexure seaward of the Bonin and Mariana trenches. *Earth Planet. Sci. Lett.*, **43**, 132–148.

BODINE, J. H., STECKLER, M. S., & WATTS, A. B. 1981. Observations of flexure and the rheology of the oceanic lithopshere. *J. Geophys. Res.*, **86**, 3695–3707.

BOSCOVICH, R. J. 1755. *De Litteraria expeditione per pontificam ditionem ad dimetiendos duos meridiani gradus.* Rome.

BOTT, M. H. P. 1976. Formation of sedimentary basins of graben type by extension of the continental crust. *Tectonophysics*, **36**, 77–86.

BOUGUER, P. 1749. *La Figure de la Terre.* Paris.

BOYD, F. R., GURNEY, J. J., & RICHARDSON, S. H. 1985. Evidence for a 150-200 km thick Archaean lithosphere from diamond inclusion thermobarometry. *Nature*, **315**, 387–389.

BRACE, W. F., & KOHLSTEDT, D. L. 1980. Limits on lithospheric stress imposed by laboratory experiments. *J. Geophys. Res.*, **85**, 6248–6252.

BRADLEY, D. C., & KIDD, W. S. F. 1991. Flexural extension of the upper continental crust in collisional foredeeps. *Geol. Soc. Am. Bull.*, **103**, 1416–1438.

BRAUN, J., & BEAUMONT, C. 1989. A physical explanation of the relation between flank uplifts and the breakup unconformity at rifted continental margins. *Geology*, **17**, 760–764.

BROOKS, M. 1970. Positive Bouguer anomalies in some orogenic belts. *Geol. Mag.*, **111**, 399–400.

BROTCHIE, J. F., & SILVESTER, R. 1969. On crustal flexure. *J. Geophys. Res.*, **74**, 5240–5245.

BROWN, P. M., MILLER, J. A., & SWAIN, F. M. 1972. Structural and stratigraphic framework, and spatial distribution of permeability of the Atlantic Coastal Plain, North Carolina to New York. U. S. Geological Survey, Prof Paper 796.

BROWN, R. W., RUST, D. J., SUMMERFIELD, M. A., GLEADOW, A. J. W., & DE WIT, M. C. J. 1990. An Early Cretaceous phase of accelerated erosion on the south-western margin of Africa: Evidence from apatite fission track analysis and the offshore sedimentary record. *Nucl. Tracks Radiat. Meas.*, **17**, 339–350.

BRUNET, M. F. 1986. The influence of the evolution of the Pyrenees on adjacent basins. *Tectonophysics*, **129**, 343–354.

BUCK, W. R. 1986. Small-scale convection induced by passive margin rifting: The cause of uplift of rift shoulders. *Earth Planet. Sci. Lett.*, **77**, 362–372.

BUCK, W. R. 1991. Modes of continental lithospheric extension. *J. Geophys. Res.*, **96**, 20161–20178.

BUCK, W. R., LAVIER, L. L., POLIAKOV, A. N. B. 1999. How to make a rift wide. *Phil. Trans. R. Soc. Lon.*, **357A**, 671–690.

BULLARD, W. C. 1936. Gravity measurements in East Africa. *Phil. Trans. R. Soc.*, **235**, 445–531.

BURBANK, D. W., BECK, R. A., & MULDER, T. 1996. The Himalayan Foreland Basin. *Pages 149–188 of:* YIN, A., & HARRISON, M. (eds), *The Tectonic Evolution of Asia.* Cambridge University Press.

BURCHFIEL, B. C. 1980. Eastern European Alpine system and the Carpathian orocline as an example of collisional tectonics. *Tectonophysics*, **63**, 31–61.

BURCHFIEL, B. C., LIPMAN, P. W., & ZOBACK, M. L. (eds). 1993. *The Cordilleran orogen: conterminous US.* The Geology of North America, vol. G-3. Boulder, Colo.: Geological Society of America.

BURKE, K., DEWEY, J. F., & KIDD, W. S. F. 1977. World distribution of sutures – the sites of former oceans. *Tectonophysics*, **40**, 69–99.

BUROV, E. B., & CLOETINGH, S. 1997. Erosion and rift dynamics: new thermomechanical aspects of post-rift evolution of extensional basins. *Earth Planet. Sci. Lett.*, **150**, 7–26.

BUROV, E. B., & DIAMENT, M. 1995. The effective elastic thickness (T_e) of continental lithosphere: What does it really mean? *J. Geophys. Res.*, **100**, 3905–3927.

BUROV, E. B., & DIAMENT, M. 1996. Isostasy, equivalent elastic thickness, and inelastic rheology of continents and oceans. *Geology*, **24**, 419–422.

BUROV, E. B., KOGAN, M. G., LYON-CAEN, H., & MOLNAR, P. 1990. Gravity anomalies, the deep structure and dynamic processes beneath the Tien Shan. *Earth Planet. Sci. Lett.*, **96**, 367–383.

BUROV, E. B., HOUDRY, F., DIAMENT, M., & DÉVERCHÉRE, J. 1994. A broken plate beneath the North Baikal rift zone revealed by gravity modelling. *Geophys. Res. Lett.*, **21**, 129–132.

BUROV, E., JAUPART, C., & MARESCHAL, J. C. 1998. Large-scale crustal heterogeneities and lithospheric strength in cratons. *Earth Planet. Sci. Lett.*, **164**, 205–219.

BUROV, E., & POLIAKOV, A. 2001. Erosion and rheology controls on synrift and postrift evolution: Verifying old and new ideas using a fully coupled numerical model. *J. Geophys. Res.*, **106**, 16461–16481.

BYERLEE, J. 1978. Friction of rocks. *Pure Appl. Geophys.*, **116**, 615–626.

CALDWELL, J. G., & TURCOTTE, D. L. 1979. Dependence of the thickness of the elastic oceanic lithosphere on age. *J. Geophys. Res.*, **84**, 7572–7576.

CALDWELL, J. G., HAXBY, W. F., KARIG, D. E., & TURCOTTE, D. L. On the applicability of a universal elastic trench profile. *Earth Planet. Sci. Lett.*, **31**, 239–246.

CALMANT, S., & CAZENAVE, A. 1986. The effective elastic lithosphere under the Cook–Austral and Society islands. *Earth Planet. Sci. Lett.*, **77**, 187–202.

CALVERT, A. J., & POTTS, C. G. 1985. Seismic evidence for hydrothermally altered mantle beneath old crust in the Tydeman fracture zone. *Earth Planet. Sci. Lett.*, **75**, 439–449.

CAPORALI, A. 1995. Gravity anomalies and the flexure of the lithosphere in the Karakoram, Pakistan. *J. Geophys. Res.*, **100**, 15075–15085.

CARTER, N. L., & TSENN, M. C. 1987. Flow properties of continental lithosphere. *Tectonophysics*, **136**, 27–63.

CHANG, H. K., KOWSMANN, R. O., & FIGUEIREIDO, A. M. F. 1992. Tectonics and stratigraphy of the East Brazil Rift system: an overview. *Tectonophysics*, **213**, 97–138.

CHEN, W. P, & MOLNAR, P. 1983. Focal depths of intracontinental and intraplate earthquakes and their implications for the thermal and mechanical properties of the lithosphere. *J. Geophys. Res.*, **88**, 4183–4214.

CHÉRY, J. F., LUCAZEAU, M., DAIGNIÉRES, M., & VILOTTE, J. P. 1992 Large uplift of rift flanks: A genetic link with lithospheric rigidity? *Earth Planet. Sci. Lett.*, **112**, 195–211.

CHIGNE, N., & HERNANDEZ, L. 1990. Main aspects of petroleum exploration in the Apure area of Southwestern Venezuela 1985–1987. *Pages 55–75 of:* BROOKS, J. (ed), *Classic Petroleum Provinces.* Geol. Soc. Lond. Spec. Publ., no. 50. Geol. Soc. Lond.

CHILDS, O. E., & SALVADOR, A. 1985. Correlation of stratigraphic units of North America (COSUNA). *AAPG Bull.*, **69**, 173–189.

CHOPRA, P. N., & PATERSON, M. S. 1984. The role of water in the deformation of dunite. *J. Geophys. Res.*, **89**, 7861–7876.

CHOWNS, T. M., & WILLIAMS, C. T. 1983. Pre-Cretaceous rocks beneath the Georgia Coastal Plain - Regional implications. *Chapter L of:* GOHN, G. S., (ed.), *Studies related to the Charleston, South Carolina, Earthquake of 1886 - Tectonics and seismicity.* U. S. Geological Survey, Prof Paper 1313-L.

CLEMSON, J., CARTWRIGHT, J., & BOOTH, J. 1997. Structural segmentation and the influence of basement structure on the Namibian passive margin. *J. Geol. Soc. London*, **154**, 477–482.

CLOETINGH, S., & BANDA, E. 1992. Mechanical Structure. *Pages 80–91 of:* BLUNDELL, D., FREEMAN, R., & MUELLER, S. (eds), *A continent revealed – The European Geotraverse.* Cambridge Universiy Press.

CLOETINGH, S., & BUROV, E. B. 1996. Thermomechanical structure of European continental lithosphere: constraints from rheological profiles and EET estimates. *Geophys. J. Int.*, **124**, 695–723.

CLOETINGH, S., VAN WEES, J. D., VAN DER BEEK, P. A., & SPADINI, G. 1995. Role of pre-rift rheology in kinematics of extensional basin formation: constraints from thermomechanical models of Mediterranean and intracratonic basins. *Mar. Pet. Geol.*, **12**, 793–807.

CLOETINGH, S. A. P. L., WORTEL, M. J. R., & VLAAR, N. J. 1984. Passive margin evolution, initiation of subduction and the Wilson Cycle. *Tectonophysics*, **109**, 147–163.

COCHRAN, J. R. 1979. An analysis of isostasy in the world's oceans, 2, Midocean ridge crests. *J. Geophys. Res.*, **84**, 4713–4729.

COCHRAN, J. R. 1980. Some remarks on isostasy and the long-term behaviour of the continental lithosphere. *Earth Planet. Sci. Lett.*, **46**, 266–274.

COCHRAN, J. R. 1983. Effect of finite rifting times on the development of sedimentary basins. *Earth Planet. Sci. Lett.*, **66**, 289–302.

COCKS, L. R. M., MCKERROW, W. S., & VAN STAAL, C. R. 1997. The margins of Avalonia. *Geol. Mag.*, **134**, 627–636.

COGAN, J., RIGO, L., GRASSO, M., & LERCHE, I. 1989. Flexural tectonics of southeastern Sicily. *J. Geodyn.*, **11**, 189–241.

COOK, F. A. 1984. Geophysical anomalies along strike of the southern Appalachians. *Tectonics*, **3**, 45–61.

COOK, F. A., & OLIVER, J. E. 1981. The Late Precambrian-Early Palaeozoic continental edge in the Appalachian orogen. *Am. J. Sci.*, **281**, 993–1008.

COOK, F. A., ALBAUGH, D. S., BROWN, L. D., KAUFMAN, S., OLIVER, J. E., & HATCHER, JR., R. D. 1979. Thin-skinned tectonics in the crystalline southern Appalachians; COCORP seismic-reflection profiling of the Blue Ridge and Piedmont. *Geology*, **7**, 563–567.

COOPER, M. A., ALVAREZ, F. T. ADDIS, CORAL, M., GRAHAM, R. H., HAYWARD, A. B., HOWE, S., MARTINEZ, J., NAAR, J., PEÑAS, R., PULHAM, A. J., & TABORDA, A. 1995. Basin Development and tectonic history of the Llanos basin, Eastern Cordillera, and Middle Magdalena Valley, Colombia. *AAPG Bull.*, **79**, 1421–1443.

COUDERT, L., FRAPPA, M., VIGUIER, C., & ARIAS, R. 1995. Tectonic subsidence and crustal flexure in the Neogene Chaco basin of Bolivia. *Tectonophysics*, **243**, 277–292.

COURTNEY, R. C., & BEAUMONT, C. 1983. Thermally-activated creep and flexure of the oceanic lithosphere. *Nature*, **305**, 201–204.

COWARD, M. P. 1981. The junction between Pan-African mobile belts in Namibia: its structural history. *Tectonophysics*, **76**, 59–73.

COX, K. G. 1980. A model for continental flood basalts. *J. Petrol.*, **21**, 629–650.

CRAMPTON, S. L., & ALLEN, P. A. 1995. Recognition of forebulge unconformity associated with early stage foreland basin development: example from the North Alpine foreland basin. *AAPG Bull.*, **79**, 1495–1514.

DALLMEYER, R. D., WRIGHT, J. E., SECOR, D. T., & SNOKE, A. W. 1986. Character of the Alleghanian orogeny of the southern Appalachians; Part 2, Geochronological constraints on the tectonothermal evolution of the eastern Piedmont in South Carolina. *Geol. Soc. Am. Bull.*, **97**, 1329–1344.

DALY, M. C. 1989. Correlations between Nazca/Farallon plate kinematics and forearc basin evolution in Ecuador. *Tectonics*, **8**, 769–790.

DALY, M. C., CHOROWICZ, J., & FAIRHEAD, J. D. 1989. Rift basin evolution in Africa: the influence of reactivated steep basement shear zones. *Pages 309–334 of:* COOPER, M. A., & WILLIAMS, G. D. (eds), *Inversion Tectonics.* Geol. Soc. Lond. Spec. Publ., no. 44. Geol. Soc. Lond.

DALY, R. A. 1940. *Strength and Structure of the Earth.* New York: Prentice Hall, Inc.

DANIELS, D. L., ZIETZ, I., & POPENOE, P. 1983. Distribution of subsurface Lower Mesozoic rocks in the southeastern United States, as interpreted from regional aeromagnetic and gravity maps. *Chapter K of:* GOHN, G. S., (ed.), *Studies related to the Charleston, South Carolina, Earthquake of 1886 - Tectonics and seismicity.* U. S. Geological Survey, Prof Paper 1313-K.

DARWIN, G. H. 1882. On the stresses caused in the interior of the earth by the weight of continents and mountains. *Phil. Trans. Roy. Soc. Lond.*, **172**, 187–230.

DAVIES, J. F. 1979. Thickness and thermal history of continental crust and root zones. *Earth Planet. Sci. Lett.*, **44**, 231–238.

DAVIES, J. H., & VON BLANCKENBURG, F. 1994. Slab breakoff: A model of lithospheric detachment and its test in the magmatism and deformation of collisional orogens. *Earth Planet. Sci. Lett.*, **129**, 85–102.

DAVISON, I. 1997. Wide and narrow margins of the Brazilian South Atlantic. *J. Geol. Soc. London*, **154**, 471–476.

DE BOER, J. Z., MCHONE, J. H., PUFFER, J. H., RAGLAND, P. C., & WHITTINGTON, D. 1988. Mesozoic and Cenozoic magmatism. *Pages 217–241 of:* SHERIDAN, R. E., & GROW, J. A. (eds), *The Atlantic Continental margin U.S.*. The Geology of North America, vol. I2. Boulder, Colo.: Geol. Soc. of Am.

DE MATOS, R. M. D., & BROWN, L. D. 1992. Deep seismic profile of the Amazonian craton (Northern Brazil). *Tectonics*, **11**, 621–633.

DEMETS, C., GORDON, R., ARGUS, D., & STEIN, S. 1990. Current Plate Motions. *Geophys. J. Int.*, **101**, 425–478.

DERCOURT, J., ZONENSHAIN, L. P., RICOU, L.-E., KAZMIN, V. G., LE PICHON, X., KNIPPER, A. L., GRANDJACQUET, C., SBORTSHIKOV, I. M., GEYSSANT, J., LEPVRIER, C., PECHERSKY, D. H., BOULIN, J., SIBUET, J.-C., SAVOSTIN, L. A., SOROKHTIN, O., WESTPHAL, M., BAZHENOV, M. L., LAUER, J. P., & BIJU-DUVAL, B. 1986. Geological evolution of the Tethys belt from the Atlantic to the Pamirs since the Lias. *Tectonophysics*, **123**, 241–315.

DÉVERCHÈRE, J., PETIT, C., GILEVA, N., RADZIMINOVITCH, N., MELNIKOVA, V., & SAN'KOV, V. 2001. Depth distribution of earthquakes in the Baikal rift system and its implications for the rheology of the lithosphere. *Geophys. J. Int.*, **146**, 714–730.

DEWEY, J. F. 1982. Plate Tectonics and the evolution of the British Isles. *J. Geol. Soc. London*, **139**, 371–412.

DEWEY, J. F. 1988. Lithospheric stress, deformation, and tectonic cycles: the disruption of Pangaea and the closure of Tethys. *Pages 23–40 of:* AUDLEY-CHARLES, M. G., & HALLAM, A. (eds), *Gondwana and Tethys.* Geol. Soc. Lond. Spec. Publ., no. 37. Geol. Soc. Lond.

DEWEY, J. F., & BURKE, K. 1974. Hot spots and continental breakup: some implications for continental collision. *Geology*, **2**, 57–60.

DEWEY, J. F., & LAMB, S. H. 1992. Active tectonics of the Andes. *Tectonophysics*, **205**, 79–95.

DEWEY, J. F., HELMAN, M. L., TURCO, E., HUTTON, D. H. W., & KNOTT, S. D. 1989. Kinematics of the Western Mediterranean. *Pages 265–283 of:* COWARD, M. P., DIETRICH, D., & PARK, R. G. (eds), *Alpine Tectonics.* Geol. Soc. Lond. Spec. Publ., no. 45. Geol. Soc. Lond.

DIAMENT, M., & KOGAN, M. G. 1990. Long-wavelength gravity anomalies and the deep thermal structure of the Baikal Rift. *Geophys. Res. Lett.*, **17**, 1977–1980.

DIAMENT, M., SIBUET, J. C., & HADAQUI, A. 1986. Isostasy of the northern Bay of Biscay continental margin. *Geophys. J. R. Astron. Soc.*, **86**, 893–907.

DIECCHIO, R. J. 1993. Stratigraphic interpretation of the Ordovician of the Appalachian basin and implications for Taconian flexural modeling. *Tectonics*, **12**, 1410–1419.

DILLON, W. P., PAULL, C. K., & GILBERT, L. E. 1985. History of the continental margin off Florida; the Blake Plateau basin. *Pages 189–216 of:* POAG, C. W. (Ed), *Geologic evolution of the United States Atlantic Margin.* New York: Van Nostrand Rheinhold.

DILLON, W. P., & POPENOE, P. 1988. The Blake Plateau Basin and Carolina Trough. *Pages 291–328 of:* SHERIDAN, R. E., & GROW, J. A. (eds), *The Atlantic Continental margin U.S.*. The Geology of North America, vol. I2. Boulder, Colo.: Geol. Soc. of Am.

DINGLE, R. V. 1993. Structural and sedimentary development of the continental margin off southwestern Africa. *Communs. geol. surv. Namibia*, 35–42.

DIVINS, D. L., & RABINOWITZ, P. D. 1991. Total sediment thickness map for the South Atlantic Ocean. *Pages 147–148 of:* G. B, UDINTSEV (ed), *International Geological and Geophysical Atlas of the Atlantic and Pacific Oceans (GAPA).* Intergovernmental Oceanographic Comission.

DORMAN, L. M., & LEWIS, B. T. R. 1970. Experimental isostasy 1. Theory of determination of the Earth's isostatic response to a concentrated load. *J. Geophys. Res.*, **75**, 3357–3365.

DORN, J. E. 1954. Some fundamental experiments on high temperature creep. *Journal of the Mechanics and Physics of Solids*, **3**, 85–116.

DRAKE, JR., A. A., SINHA, A. K., LAIRD, J., & GUY, R. E. 1989. The Taconic Orogeny. *Pages 101–177 of:* HATCHER, JR., R. D., THOMAS, W. A., & VIELE, G. W. (eds), *The Appalachian–Ouachita Orogen in the United States.* The Geology of North America, vol. F2. Boulder, Colo.: Geol. Soc. of Am.

DUNBAR, J. A., & SAWYER, D. S. 1989. How preexisting weaknesses control the style of continental breakup. *J. Geophys. Res.*, **94**, 7278–7292.

DUROY, Y., FARAH, A., & LILLIE, R. J. 1989. Subsurface densities and lithospheric flexure of the Himalayan foreland in Pakistan. *Pages 217–236 of:* MALINCONICO, JR., L. L., & LILLIE, R. J. (eds), *Tectonics of the western Himalayas.* Special Paper 232. Geological Society of America.

DUTTON, C. E. 1889. On some of the greater problems of physical geology. *Bull. Philos. Soc. Wash.*, **11**, 51–64.

EBINGER, C. J., & HAYWARD, N. J. 1996. Soft plates and hot spots: views from Afar. *J. Geophys. Res.*, **101**, 21859–21876.

EBINGER, C. J., BECHTEL, T. D., FORSYTH, D. W., & BOWIN, C. O. 1989. Effective elastic plate thickness beneath the East African and Afar Plateaus and dynamic compensation of the uplifts. *J. Geophys. Res.*, **94**, 2883–2901.

EBINGER, C. J., KARNER, G. D., & WEISSEL, J. K. 1991. Mechanical strength of extended continental lithosphere: constraints from the western rift system, Africa. *Tectonics*, **10**, 1239–1256.

EBINGER, C. J., POUDJOM DJOMANI, Y., MBEDE, E., FOSTER, A., & DAWSON, J. B. 1997. Rifting Archaean lithosphere: the Eyasi–Manyara–Natron rifts, East Africa. *J. Geol. Soc. London*, **154**, 947–960.

ELLIS, S., FULLSACK, P., & BEAUMONT C. 1995. Oblique convergence of the crust driven by basal forcing: implications for length-scales of deformation and strain partitioning in orogens. *Geophys. J. Int.*, **120**, 24–44.

EMERY, K. O., UCHUPI, E., PHILLIPS, J. D., BOWIN, C. O., BUNCE, E. T., & KNOTT, S. T. 1970. Continental rise off eastern North America. *AAPG Bull.*, **54**, 44–108

ENGLAND, P. C. 1983. Constraints on extension of continental lithosphere. *J. Geophys. Res.*, **88**, 1145–1152.

ENGLAND, P. C., & HOUSEMAN, G. 1986. Finite strain calculations of continental deformation 2. Comparison with the India-Asia collision zone. *J. Geophys. Res.*, **91**, 3664–3676.

FAIRHEAD, J. D., WATTS, A. B., CHEVALIER, P., EL-HADDEH, B., GREEN, C. M., STUART, G. W., WHALER, K. A., & WINDLE, I. 1988. *African Gravity Project.* Tech. rept. GETECH, Dep. Earth. Sci., Univ. Leeds.

FALVEY, D. A. 1974. The development of continental margins in plate tectonic theory. *Aus. Pet. Exp. Ass. J.*, **14**, 95–106.

FAN, G., WALLACE, T. C., BECK, S. L., & CHASE, C. G. 1996. Gravity anomaly and flexural model: constraints on the structure beneath the Peruvian Andes. *Tectonophysics*, **255**, 99–109.

FEININGER, T., & SEGUIN, M. K. 1983. Simple Bouguer gravity anomaly field and the inferred crustal structure of continental Ecuador. *Geology*, **11**, 40–44.

FILMER, P. E., MCNUTT, M. K., & WOLFE, C. J. 1993. Elastic thickness of the lithosphere in the Marquesas and Society Islands. *J. Geophys. Res.*, **98**, 19565–19577.

FLETCHER, R. C., & HALLET, B. 1983. Unstable extension of the lithosphere: a mechanical model for Basin and Range structure. *J. Geophys. Res.*, **88**, 7457–7466.

FORSYTH, D. W. 1977. The evolution of the upper mantle beneath mid-ocean ridges. *Tectonophysics*, **38**, 89–118.

FORSYTH, D. W. 1985. Subsurface loading and estimates of the flexural rigidity of continental lithosphere. *J. Geophys. Res.*, **90**, 12623–12632.

FOSTER, A., & NIMMO, F. 1996. Comparisons betweem the rift systems of East Africa, Earth and Beta Regio, Venus. *Earth Planet. Sci. Lett.*, **143**, 183–195.

FOSTER, A., EBINGER, C., MBEDE, E., & REX, D. 1997. Tectonic development of the northern Tanzanian sector of the East African Rift system. *J. Geol. Soc. London*, **154**, 689–700.

FOUCHER, J.-P., LE PICHON, X., & SIBUET, J.-C. 1982. The ocean-continent transition in the uniform lithosphere stretching model: role of partial melting in the mantle. *Phil. Trans. Roy. Soc. Lond.*, **A305**, 27–43.

FOWLER, S., & MCKENZIE, D. P. 1989. Gravity studies of the Rockall and Exmouth Plateaus using SEASAT altimetry. *Basin Res.*, **2**, 27–34.

FOWLER, S. R., WHITE, R. S., SPENCE, G. D., & WESTBROOK, G. K. 1989. The Hatton Bank continental margin – II: Deep structure from two-ship expanding spread seismic profiles. *Geophys. J. Int.*, **96**, 295–309.

FUKAO, G.-W., NI, J., & WALLACE, T. 1994. Gravity anomaly across the Peruvian Andes. *J. Geophys. Res.*, **99**, 3867–3890.

GAHLI, A. 1989. *Structural Analysis: A Unified Classical and Matrix Approach.* Third edn. Chapman and Hall, New York.

GALLAGHER, K. 1989. An examination of some uncertainties associated with estimates of sedimentation rates and tectonic subsidence. *Basin Res.*, **2**, 97–114.

GERE, J. M., & TIMOSHENKO, S. P. 1991. *Mechanics of Materials.* Third edn. Chapman and Hall.

GERRARD, I., & SMITH, G. C. 1982. Post-Palaeozoic succession and structure of the Southwestern African continental margin. *Pages 49–74 of:* WATKINS, J. S., & DRAKE, C. L. (eds), *Studies in Continental Margin Geology.* AAPG Memoir 46. Tulsa, OK: American Association of Petroleum Geologists.

GILBERT, G. K. 1874. Progress Report. *U. S. Geog. and Geol. Surv. W. 100th Mer.* United States Geological Survey: Washington D. C., Government Printing office.

GILBERT, G. K. 1889. The strength of the Earth's crust. *Geol. Soc. Am. Bull.*, **1**, 23–27.

GILBERT, G. K. 1890. *Lake Bonneville.* United States Geological Survey: Washington D.C., Government Printing office, 438 p.

GILBERT, L. E., & DILLON, W. P. 1981. Bathymetric map of the Blake Escarpment. United States Geological Survey: Field Studies Map MF-1362.

GLADCZENKO, T. P. 1994. *Crustal structure and composition of selected transient large igneous provinces.* Cand. Scient. Thesis, Univ. of Oslo, Oslo, Norway.

GLADCZENKO, T. P., HINZ, K., ELDHOLM, O., MEYER, H., NEBEN, S., & SKOGSEID, J. 1997. South Atlantic volcanic margins. *J. Geol. Soc. London*, **154**, 465–470.

GLAZNER, A. F., & BARTLEY, J. M. 1985. Evolution of lithospheric strength after thrusting. *Geology*, **13**, 42–45.

GOETZE, C., & EVANS, B. 1979. Stress and temperature in the bending lithosphere as constrained by experimental rock mechanics. *Geophys. J. R. Astron. Soc.*, **59**, 463–478.

GOHN, G. S. 1988. Late Mesozoic and early Cenozoic geology of the Atlantic Coastal Plain: North Carolina to Florida. *Pages 107–130 of:* SHERIDAN, R. E., & GROW, J. A. (eds), *The Atlantic Continental margin U.S.*. The Geology of North America, vol. I2. Boulder, Colo.: Geol. Soc. of Am.

GOODWILLIE, A. M., & WATTS, A. B. 1993. An altimetric and bathymetric study of elastic thickness in the central Pacific Ocean. *Earth Planet. Sci. Lett.*, **118**, 311–326.

GOODWIN, A. M. 1996. *Principles of Precambrian Geology.* Academic Press.

GOTZE, H.-J., LAHMEYER, B., SCHMIDT, S., & STRUNK, S. 1994. The lithospheric structure of the Central Andes (20°S - 26°S) as inferred from the interpretation of regional gravity. *Pages 7–21 of:* REUTTER, K.-J., SCHEUBER, E., & WIGGER, P. J. (eds), *Tectonics of the Southern Central Andes.* New York: Springer-Verlag.

GOVERS, R., & WORTEL, M. J. R. 1999. Some remarks on the relation between vertical motions of the lithosphere during extension and the necking depth parameter inferred from kinematic modeling studies. *J. Geophys. Res.*, **104**, 23245–23253.

GRAVITY ANOMALY MAP COMMITTEE. 1987. Gravity anomaly map of North America (1:5,000,000). Geol. Soc. Am. Continent-Scale Map-002 (5 sheets). Boulder, Colo.: Geol. Soc. of Am.

GREEN, C. M., & FAIRHEAD, J. D. 1991. The South American Gravity Project. *Pages 82–95 of:* TORGE, W., FLETCHER, A. G., & TANNER, J. G. (eds), *Recent Geodetic and Gravimetric Research in Latin America.* New York: Springer-Verlag.

GROTZINGER, J., & ROYDEN, L. 1990. Elastic thickness of the Slave Craton at 1.9 Gyr and implications for the thermal evolution of the continents. *Nature*, **347**, 64–66.

GROW, J. A., MATTICK, R. E., & SCHLEE, J. S. 1979. Multichannel seismic depth sections and interval velocities over outer continental shelf and upper slope between Cape Hatteras and Cape Cod. *Pages 65–83 of:* WATKINS, J. S., MONTADERT, L., & DICKERSON, P. W. (eds), *Geological and geophysical investigations of continental margins.* Am. Assoc. Pet. Geol.,Mem. 29.

GROW, J. A. 1980. Deep structure and evolution of the Baltimore Canyon Trough in the vicinity of the COST No. B-3 well. *Pages 117–132 of:* SCHOLLE, P. (ed), *Geological Studies of the COST No. B-3 Well.* U. S. Geological Survey, Circ. 833.

GROW, J. A. & SHERIDAN, R. E. 1988. U.S. Atlantic Continental Margin; A typical Atlantic-type or passive continental margin. *Pages 1–7 of:* SHERIDAN, R. E., & GROW, J. A. (eds), *The Atlantic Continental margin U.S.*. The Geology of North America, vol. I2. Boulder, Colo.: Geol. Soc. of Am.

GUNN, R. 1937. A quantitative study of mountain building on an unsymmetrical earth. *J. Frank. Inst.*, **224**, 19–53.

GUNN, R. 1943a. A quantitative study of isobaric equilibrium and gravity anomalies in the Hawaiian Islands. *J. Frank. Inst.*, **236**, 373–390.

GUNN, R. 1943b. A quantitative study of the influence of the lithosphere on the anomalies of gravity. *J. Frank. Inst.*, **236**, 47–65.

GUNN, R. 1944. A quantitative study of the lithosphere and gravity anomalies along the Atlantic coast. *J. Frank. Inst.*, **237**, 139–154.

GUNN, R. 1947. Quantitative aspects of juxtaposed ocean deeps, mountain chains and volcanic ranges. *Geophysics*, **12**, 238–255.

GUNN, R. 1949. Isostasy – Extended. *J. Geol.*, **57**, 263–279.

GURNIS, M. 1993. Phanerozoic marine inundation of continents driven by dynamic topography above subducting slabs. *Nature*, **364**, 589–593.

GUTSCHER, M.-A. 1995. Crustal structure and dynamics in the Rhine Graben and the Alpine foreland. *Geophys. J. Int.*, **122**, 617–636.

HADDAD, D., & WATTS, A. B. submitted. Subsidence history, gravity anomalies and flexure of the northeast Australian margin in Papua New Guinea. *submitted to Tectonics.*

HALL, J. 1859. Geology of New York State. *Canadian J.*, **3**, 69.

HANKS, T. C. 1971. The Kuril trench–Kokkaido system: Large shallow earthquakes and simple models of deformation. *Geophys. J. R. Astron. Soc.*, **23**, 173–189.

HAQ, B. U., HARDENBOL, J., & VAIL, P. R. 1987. Chronology of fluctuating sea levels since the Triassic. *Science*, **235**, 1156–1167.

HARLAND, W. B., ARMSTRONG, R. L., COX, A. V., CRAIG, L. E., SMITH, A. G., & SMITH, D. G. 1990. *A Geologic Time Scale 1989.* Cambridge University Press.

HARRY, D. L., & MICKUS, K. L. 1998. Gravity constraints on lithospheric flexure and the structure of the Late Paleozic Ouachita orogen in Arkansas and Oklahoma, south-central North America. *Tectonics*, **17**, 187–202.

HARTE, B., HUNTER, R. H., & KINNY, P. D. 1993. Melt geometry, movement and crystallization in relation to mantle dykes, veins and metasomatism. *Phil. Trans. R. Soc. Lond.*, **A342**, 1–21.

HARTLEY, R. W. 1994. *Isostasy of Africa: Implications for the Thermo-Mechanical Behaviour of the Continental Lithosphere.* Ph.D. thesis, Univ. of Oxford, Oxford, England.

HARTLEY, R. W., WATTS, A. B., & FAIRHEAD, J. D. 1996. Isostasy of Africa. *Earth Planet. Sci. Lett.*, **137**, 1–18.

HATCHER, JR., R. D. 1987. Tectonics of the Southern and Central Appalachian Internides. *Ann. Rev. Earth Planet. Sci.*, **15**, 337–362.

HATCHER, JR., R. D. 1989. Tectonic synthesis of the U.S. Appalachians. *Pages 511–535 of:* HATCHER, JR., R. D., THOMAS, W. A., & VIELE, G. W. (eds), *The Appalachian–Ouachita Orogen in the United States.* The Geology of North America, vol. F2. Boulder, Colo.: Geol. Soc. of Am.

HAXBY, W. F., TURCOTTE, D. L., & BIRD, J. M. 1976. Thermal and mechanical evolution of the Michigan Basin. *Tectonophysics*, **36**, 57–75.

HAY, W. W., & SIBUET, J.-C. (eds). 1984. *Init. Repts. DSDP.* Vol. 75. Washington D.C.: U.S. Government Printing Office.

HAYFORD, J. F., & BOWIE, W. 1912. *The effect of topography and isostatic compensation upon the intensity of gravity.* United States Coast and Geodetic Survey Spec. Publ. 12.

HEISKANEN, W. A., & VENING MEINESZ, F. A. 1958. *The Earth and its gravity field.* McGraw-Hill: New York, Toronto and London. 470p.

HERTZ, H. 1884. On the equilibrium of floating elastic plates. *Wiedemann's Ann.*, **22**, 449.

HETÉNYI, M. 1946. *Beams on Elastic Foundations.* First edn. University of Michigan Press.

HIRTH, G., & KOHLSTEDT, D. L. 1996. Water in the oceanic upper mantle: implications for rheology, melt extraction and the evolution of the lithosphere. *Earth Planet. Sci. Lett.*, **144**, 93–108.

HOBBS, B. E., ORD, A., & TEYSSIER, C. 1986. Earthquakes in the ductile regime? *Pure Appl. Geophys.*, **1986**, 309–336.

HOFFMAN, P. F. 1990. Geological constraints on the origin of the mantle root beneath the Canadian Shield. *Pages 67–76 of:* DEWEY, J. F., GASS, I. G., CURRY, G. B., HARRIS, N. B. W., & ŞENGÖR, A. M. C. (eds), *Allochthonous terranes.* Cambridge University Press.

HOLBROOK, W. S., & KELEMEN, P. B. 1993. Large igneous province on the US Atlantic margin and implications for magmatism during continental breakup. *Nature*, **364**, 433–436.

HOLBROOK, W. S., REITER, E. C., PURDY, G. M., SAWYER, D., STOFFA, P. L., AUSTIN, JR., J. A., OH., & J., MAKRIS, J. 1994a. Deep structure of the U.S. Atlantic continental margin, offshore South Carolina, from coincident ocean-bottom and multichannel seismic data. *J. Geophys. Res.*, **99**, 9155–9178.

HOLBROOK, W. S., PURDY, G. M., SHERIDAN, R. E., GLOVER, III, L., TALWANI, M., EWING, J., & HUTCHINSON, D. 1994b. Seismic structure of the U.S. Mid-Atlantic continental margin. *J. Geophys. Res.*, **99**, 17871–17891.

HOLT, W. E., & STERN, T. A. 1991. Sediment loading on the Western Platform of the New Zealand continent. *Earth Planet. Sci. Lett.*, **107**, 523–538.

HOPPER, J. R., & BUCK, W. R. 1993. The initiation of rifting at constant tectonic force: Role of diffusion creep. *J. Geophys. Res.*, **98**, 16213–16221.

HORTON, B. K., & DECELLES, P. G. 1997. The modern foreland basin system adjacent to the Central Andes. *Geology*, **25**, 895–898.

HORVÁTH, F. 1993. Towards a mechanical model for the formation of the Pannonian basin. *Tectonophysics*, **226**, 333–357.

HOUSEKNECHT, D. W. 1986. Evolution from passive margin to foreland basin: the Atoka Formation of the Arkoma Basin, south-central USA. *Pages 327–345 of:* ALLEN, P. A., & HOMEWOOD, P. (eds), *Foreland Basins.* Spec. Publ. Int. Assoc. Sedimentol., no. 8. Blackwell, Oxford.

HOUSEMAN, G. A., MCKENZIE, D. P., & MOLNAR, P. 1981. Convective instability of a thickened boundary layer and its relevance for the thermal evolution of continental convergent belts. *J. Geophys. Res.*, **86**, 6115–6132.

HUBBARD, R. J., PAPE, J., & ROBERTS, D. G. 1985. Depositional sequence mapping as a technique to establish tectonic and stratigraphic framework and evaluate hydrocarbon potential on a passive continental margin. *Pages 79–91 of:* BERG, O. R., & WOOLVERTON, D. G. (eds), *Seismic Stratigraphy II: An Integrated Approach.* AAPG Memoir 39. Tulsa, OK: American Association of Petroleum Geologists.

HUTCHINSON, D. R., GROW, J. A., KLITGORD, K. D., & SWIFT, B. A. 1982. Deep structure and evolution of the Carolina Trough. *Pages 129–152 of:* WATKINS, J. S., & DRAKE, C. L. (eds), *Studies in Continental Margin Geology.* AAPG Memoir 34. Tulsa, OK: American Association of Petroleum Geologists.

HUTCHINSON, D. R., GROW, J. A., & KLITGORD, K. D. 1983. Crustal structure beneath the southern Appalachians: Nonuniqueness of gravity modeling. *Geology*, **11**, 661–615.

HUTCHINSON, D. R., KLITGORD, K. D., & DETRICK, JR., R. S. 1986. Rift basins of the Long Island platform. *Geol. Soc. Am. Bull.*, **97**, 688–702.

HUTCHINSON, D. R., POAG, C. W., & POPENOE, P. 1995. *Geophysical database of the East Coast of the United States Southern Atlantic Margin: Stratigraphy and velocity from multi-channel seismic profiles.* U. S. Geological Survey, Open File Report 95-27. 176pp.

HUTCHINSON, D. R., POAG, C. W., JOHNSON, A., POPENOE, P., & WRIGHT, C. 1996. *Geophysical database of the East Coast of the United States Southern Atlantic Margin: Stratigraphy and velocity in map grids.* U. S. Geological Survey, Open File Report 96-55. 165pp.

HYNES, A. 1994. Gravity, flexure, and the deep structure of the Grenville Front, eastern Quebec and Labrador. *Can. J. Earth Sci.*, **31**, 1002–1011.

ISACKS, B. L. 1988. Uplift of the central Andean plateau and bending of the Bolivian orocline. *J. Geophys. Res.*, **93**, 3211–3231.

IVERSON, W. P., & SMITHSON, S. B. 1982. Master décollement root zone beneath the southern Appalachians and crustal balance. *Geology*, **10**, 241–245.

IVERSON, W. P., & SMITHSON, S. B. 1983. Reprocessed COCORP southern Appalachian reflection data: Root zone to Coastal Plain. *Geology*, **11**, 422–425.

JACKSON, J. 2002. Strength of the continental lithosphere: Time to abandon the jelly sandwich? *GSA Today*, **12**, 4–10.

JAILLARD, E., SOLER, P., CARLIER, G., & MOURIER, T. 1990. Geodynamic evolution of the northern and central Andes during Early to Middle Mesozoic times: a Tethyan model. *J. Geol. Soc. London*, **147**, 1009–1022.

JAMES, D. E. 1971. Plate-tectonic model for the evolution of the central Andes. *Geol. Soc. Am. Bull.*, **82**, 3325–3346.

JAMIESON, T. F. 1865. On the history of the last geological changes in Scotland. *Quat. J. Geol. Soc.*, **21**, 161–203.

JANSA, J. F. 1981. Mesozoic carbonate platforms and banks of the Eastern North American margin. *Marine Geology*, **44**, 97–117.

JANSA, J. F. 1986. Paleoceanography and evolution of the North Atlantic Ocean Basin during the Jurassic. *Pages 603–616 of:* VOGT, P. R., & TUCHOLKE, B. E. (eds), *The Western North Atlantic region.* The Geology of North America, vol. M. Boulder, Colo.: Geol. Soc. of Am.

JANSSEN, M. E., TORNÉ, M., CLOETINGH, S., & BANDA, E. 1993. Pliocene uplift of the eastern Iberian margin: Inferences from quantitative modelling of the Valencia Trough. *Earth Planet. Sci. Lett.*, **119**, 585–597.

JARVIS, G. T., & MCKENZIE, D. P. 1980. Sedimentary basin formation with finite extension rates. *Earth Planet. Sci. Lett.*, **48**, 42–52.

JIN, Y., MCNUTT, M. K., & ZHU, Y. 1994. Evidence from gravity and topography data for folding of Tibet. *Nature*, **371**, 669–674.

JIN, Y., MCNUTT, M. K., & ZHU, Y. 1996. Mapping the descent of Indian and Eurasian plates beneath the Tibetan Plateau from gravity anomalies. *J. Geophys. Res.*, **101**, 11275–11290.

JORDAN, T. E. 1981. Thrust loads and basin evolution, Cretaceous, Western United States. *AAPG Bull.*, **65**, 2506–2520.

JORDAN, T. H. 1988. Structure and formation of the continental tectosphere. *Pages 11–37 of:* MENZIES, M. A., & COX, K. G. (eds), *Oceanic and Continental Lithosphere: Similarities and Differences.* Oxford, U.K.: Clarendon Press.

JUDGE, A. V., & MCNUTT, M. K. 1991. The relationship between plate curvature and elastic plate thickness: A study of the Peru–Chile Trench. *J. Geophys. Res.*, **96**, 16625–16640.

KANE, K. A., & HAYES, D. E. 1992. Tectonic corridors in the South Atlantic. Evidence for long-lived mid-ocean ridge segmentation. *J. Geophys. Res.*, **97**, 17317–17330.

KARIG, D. E., CALDWELL, J. G., & PARMENTIER, E. M. 1976. Effects of accretion on the geometry of the descending lithosphere. *J. Geophys. Res.*, **81**, 6281–6291.

KARNER, G. D. 1991. Sediment blanketing and the flexural strength of extended continental lithosphere. *Basin Res.*, **3**, 177–185.

KARNER, G. D., & WATTS, A. B. 1982. On isostasy at Atlantic-type continental margins. *J. Geophys. Res.*, **87**, 2923–2948.

KARNER, G. D., & WATTS, A. B. 1983. Gravity anomalies and flexure of the lithosphere at mountain ranges. *J. Geophys. Res.*, **88**, 10449–10477.

KARNER, G. D., STECKLER, M. S., & THORNE, J. A. 1983. Long-term thermo-mechanical properties of the continental lithosphere. *Nature*, **304**, 250–253.

KARNER, G. D., EGAN, S. S., & WEISSEL, J. K. 1992. Modeling the tectonic development of the Tucano and Sergipe-Alagonas rift basins, Brazil. *Tectonophysics*, **215**, 133–160.

KAULA, W. M. 1969. Earth's gravity field: Relation to global tectonics. *Science*, **169**, 982–985.

KEEN, M. J. 1969. Possible edge effect to explain magnetic anomalies off the eastern seaboard of the U.S.. *Nature*, **222**, 72–74.

KEEN, C. E. 1985. The dynamics of rifting: Deformation of the lithosphere by active and passive driving forces. *Geophys. J. R. Astron. Soc.*, **80**, 95–120.

KEEN, C. E., & DEHLER, S. A. 1993. Stretching and subsidence: Rifting of conjugate margins in the North Atlantic region. *Tectonics*, **12**, 1209–1229.

KEEN, C. E., & DEHLER, S. A. 1997. Extensional styles and gravity anomalies at rifted continental margins: Some North Atlantic examples. *Tectonics*, **16**, 744–754.

KEEN, C. E., LONCAREVIC, B. D., REID, I., WOODSIDE, J., HAWORTH, R. T., & WILLIAMS, H. 1990. Tectonic and geophysical overview. *Pages 31–85 of:* KEEN, M. J., & WILLIAMS, G. L. (eds), *Geology of the Continental Margin off Eastern Canada.* The Geology of North America, vol. 2. Ottowa: Geol. Surv. of Can.

KELEMEN, P. B., & HOLBROOK, W. S. 1995. Origin of thick, high-velocity igneous crust along the U.S. East Coast Margin. *J. Geophys. Res.*, **100**, 10077–10094.

KING, T. A. 1998. *Mechanisms of Isostatic Compensation in Areas of Lithospheric Extension: Examples from the Aegean.* Ph.D. thesis, Univ. of Leeds, Leeds, England.

KING, T. A., EBINGER, C., STARK, C., COLLIER, R., & CHAILAS, S. 1996. Isostasy across Greece and the Aegean Sea; are all collapsing orogens weak? (abstract). *Page 703 of: Eos Trans. AGU*, vol. 77(46), Fall Meet. suppl.

KIRBY, S. H. 1983. Rheology of the lithosphere. *Rev. Geophys.*, **21**, 1458–1487.

KIRBY, S. H., & KRONENBERG, A. K. 1987. Rheology of the lithosphere: Selected topics. *Rev. Geophys.*, **25**, 1219–1244.

KLEMPERER, S., & HOBBS, R. (eds). 1992. *The BIRPS atlas: Deep seismic reflection profiles around the British Isles.* Cambridge University Press.

KLITGORD, K. D., & BEHRENDT, J. C. 1979. Basin structure of the U.S. Atlantic continental margin. *Pages 85–112 of:* WATKINS, J. S., MONTADERT, L., & DICKERSON, P. W. (eds), *Geological and geophysical investigations of continental margins.* Am. Assoc. Pet. Geol.,Mem. 39.

KLITGORD, K. D., & GROW, J. A. 1980. Jurassic seismic stratigraphy and basement structure of the western Atlantic magnetic quiet zone. *AAPG Bull.*, **64**, 1658–1680.

KLITGORD, K. D., DILLON, W. P., & POPENOE, P. 1983. Mesozoic tectonics of the southeastern United States Coastal Plain and continental margin. U. S. Geological Survey, Prof Paper 1313-P.

KLITGORD, K. D., POPENOE, P., & SCHOUTEN, H. 1984. Florida: A Jurassic transform plate boundary. *J. Geophys. Res.*, **89**, 7753–7772.

KLITGORD, K. D., HUTCHINSON, D. R., & SCHOUTEN, H. 1988. U.S. Atlantic margin; Structure and tectonic framework. *Pages 19–55 of:* SHERIDAN, R. E., & GROW, J. A. (eds), *The Atlantic Continental margin U.S..* The Geology of North America, vol. I2. Boulder, Colo.: Geol. Soc. of Am.

KLITGORD, K. D., & SCHNEIDER, C. M. 1994. *Geophysical database of the East Coast of the United States Northern Atlantic Margin: Velocity analyses.* U. S. Geological Survey, Open File Report 94-192. 74pp.

KLITGORD, K. D., POAG, C. W., SCHNEIDER, C. M., & NORTH, L. 1994. *Geophysical database of the East Coast of the United States Northern Atlantic Margin: Cross sections and gridded database (Georges Bank Basin, Long Island Platform, and Baltimore Canyon Trough).* U. S. Geological Survey, Open File Report 94-637. 189pp.

KLITGORD, K. D., & SCHOUTEN, H. 1986. Plate kinematics of the Central Atlantic. *Pages 351–378 of:* VOGT, P. R., & TUCHOLKE, B. E. (eds), *The Western North Atlantic region.* The Geology of North America, vol. M. Boulder, Colo.: Geol. Soc. of Am.

KOGAN, M. G., & MCNUTT, M. K. 1987. Isostasy in the USSR, 1, Admittance data. *Pages 301–307 of:* FUCHS, K., & FROIDEVAUX, C. (eds), *The Composition, Structure, and Dynamics of the Lithosphere-Asthenosphere System.* Geodyn. Ser., vol. 16. Washington, D. C.: AGU.

KOMINZ, M. A., & BOND, G. C. 1986. Geophysical modelling of the thermal history of foreland basins. *Nature*, **320**, 252–256.

KOOI, H., CLOETINGH, S., & BURRUS, J. 1992. Lithospheric necking and regional isostasy at extensional basins, 1, Subsidence and gravity modeling with an application to the Gulf of Lions margin (SE France). *J. Geophys. Res.*, **97**, 17553–17571.

KORENAGA, J., HOLBROOK, W. S., KENT, G. M., KELEMEN, P. B., DETRICK, R. S., LARSEN, H.-C., HOPPER, J. R., & DAHL-JENSEN, T. 2000. Crustal structure of the Southeast Greenland margin from joing refraction and reflection seismic tomography. *J. Geophys. Res.*, **105**, 21591–21614.

KORENAGA, J., HOLBROOK, W. S., DETRICK, R. S., & KELEMEN, P. B. 2001. Gravity anomalies and crustal structure at the Southeast Greenland margin. *J. Geophys. Res.*, **106**, 8853–8870.

KORSTGÅRD, J. A., & LERCHE, I. 1992. Flexural plate reprensentation of Danish Central Graben evolution. *J. Geodyn.*, **16**, 181–209.

KORVIN, G. 1984. Shale compaction and statistical physics. *Geophys. J. R. Astron. Soc.*, **78**, 35–50.

KOWSMANN, R., LEYDEN, R., & FRANCISCONI, O. 1977. Marine seismic investigations, Southern Brazil margin. *AAPG Bull.*, **61**, 546–557.

KRUSE, S., & MCNUTT, M. K. 1988. Compensation of Paleozoic orogens: A comparison of the Urals to the Appalachians. *Tectonophysics*, **154**, 1–17.

KUCKES, A. F. 1977. Strength and rigidity of the elastic lunar lithosphere and implications for present-day mantle convection in the moon. *Phys. Earth Planet. Inter.*, **14**, 1–12.

KUNDERT, K. S., & SANGIOVANNI-VINCENTELLI, A. 1988. *Sparse User's Guide,* Version 1.3a. Dep. of Electr. Eng. and Comput. Sci., Univ. of Calif., Berkeley.

KUSZNIR, N. J. 1991. The distribution of stress with depth in the lithosphere - thermorheological and geodynamic constraints. *Phil. Trans. Roy. Soc. Lon.*, **A337**, 95–110.

KUSZNIR, N. J., & EGAN, S. S. 1990. Simple-shear and pure-shear models of extensional sedimentary basin formation: Application to the Jean d'Arc basin, Grand Banks of Newfoundland. *Pages 304–322 of:* TANKARD, A. J. & BLACKWELL, H. R. (eds), *Extensional tectonics of the North Atlantic margins.* AAPG Memoir 46. Tulsa, OK: American Association of Petroleum Geologists.

KUSZNIR, N. J., & KARNER, G. D. 1985. Dependence of the flexural rigidity of continental lithosphere on rheology and temperature. *Nature*, **316**, 138–142.

KUSZNIR, N. J., & PARK, R. G. 1987. The extensional strength of the continental lithosphere: its dependence on geothermal gradient, and crustal composition and gradient. *Pages 35–52 of:* COWARD, M. P., DEWEY, J. F., & HANCOCK, P. L. (eds), *Continental Extensional Tectonics.* Geol. Soc. Lond. Spec. Publ., no. 28. Geol. Soc. Lond.

KUSZNIR, N. J., MARSDEN, G., & EGAN, S. S. 1991. A flexural-cantilever simple-shear/pure-shear model of continental lithosphere extension: Applications to the Jeanne d'Arc Basin, Grand Banks and Viking Graben, North Sea. *Pages 41–60 of:* ROBERTS, A. M., YIELDING, G., & FREEMAN, B. (eds), *The Geometry of Normal Faults.* Geol. Soc. Lond. Spec. Publ., no. 56. Geol. Soc. Lond.

LAMB, S. 2002. Is it all in the crust? *Nature*, **420**, 130–131.

LAMB, S., & HOKE, L. 1997. Origin of the high plateau in the Central Andes, Bolivia, South America. *Tectonics*, **16**, 623–649.

LAMB, S., HOKE, L., KENNAN, L., & DEWEY, J. 1997. Cenozoic evolution of the Central Andes in Bolivia and northern Chile. *Pages 237–264 of:* BURG, J.-P., & FORD, M. (eds), *Orogeny Through Time.* Geol. Soc. Lond. Spec. Publ., no. 121. Geol. Soc. Lond.

LANKREIJER, A., MOCANU, V., & CLOETINGH, S. 1997. Lateral variations in lithospheric strength in the Romanian Carpathians: constraints on basin evolution. *Tectonophysics*, **272**, 269–290.

LASE STUDY GROUP. 1986. The structure of the U.S. East coast passive margin from large aperature seismic experiments (LASE). *Mar. Pet. Geol.*, **3**, 234–242.

LASKE, G., & MASTERS, G. 1997. A global digital map of sediment thickness. *Page F483 of: Eos Trans. AGU*, vol. 78, Fall Meet. suppl.

LAVIER, L. L., & STECKLER, M. S. 1997. The effect of sedimentary cover on the flexural strength of continental lithosphere. *Nature*, **389**, 476–479.

LEEDS, A. R. 1975. Lithosperic thickness in the western Pacific. *Phys. Earth Planet. Lett. Inter.*, **11**, 61–64.

LEFORT, J. P., & VAN DER VOO, R. 1981. A kinematic model for the collision and complete suturing between Gondwanaland and Laurasia in the Carboniferous. J. Geol., **89**, 537–550.

LEMOINE, M., BAS, T., ARNAUD-VANNEAU, A., ARNAUD, H., DULMONT, T., GIDON, M., BOURBON, M., DE GRACIANSKY, P.-C., RUDKIEWICZ, J.-L., MEGARD-GALLI, J., & TRICART, P. 1986. The continental margin of the Mesozoic Tethys in the Western Alps. *Mar. Pet. Geol.*, **3**, 179–199.

LERNER-LAM, A. L., & JORDAN, T. H. 1987. How thick are the continents? *J. Geophys. Res.*, **92**, 14007–14026.

LEWIS, B. T. R., & DORMAN, L. M. 1970. Experimental isostasy 2. An isostatic model for the U.S.A. derived from gravity and topography data. *J. Geophys. Res.*, **175**, 3367–3386.

LEYDEN, R., LUDWIG, W. J., & EWING, M. 1971. Structure of the continental margin off Uruguay and Brazil. *AAPG Bull.*, **55**, 2161–2173.

LIGHT, M. P. R., MASLANYJ, M. P., & BANKS, N. L. 1992. New geophysical evidence for extensional tectonics on the divergent margin offshore Namibia. *Pages 257–270 of:* STOREY, B. C., ALABASTER, T., & PANKHURST, R. J. (eds), *Magmatism and the Causes of Continental Break-up.* Geol. Soc. Lond. Spec. Publ., no. 68. Geol. Soc. Lond.

LIGHT, M. P. R., MASLANYJ, M. P., GREENWOOD, R. J., & BANKS, N. L. 1993. Seismic sequence stratigraphy and tectonics offshore Namibia. *Pages 163–191 of:* WILLIAMS, G. D., & DOBB, A. (eds), *Tectonics and Seismic Sequence Stratigraphy.* Geol. Soc. Lond. Spec. Publ., no. 71. Geol. Soc. Lond.

LIHOU, J. C. 1996. Stratigraphy and sedimentology of the Sardona unit, Glarus Alps: Upper Cretaceous/Middle Eocene deep-marine flysch sediments from the Ultrahelvetic realm. *Eclogae Geol. Helv.*, **89**, 721–752.

LILLIE, R. J. 1984. Tectonic implications of subthrust structures revealed by seismic profiling of the Appalachian–Ouachita orogenic belt. *Tectonics*, **3**, 619–646.

LILLIE, R. J. 1991. Evolution of gravity anomalies across collisional mountain belts: clues to the amount of continental convergence and underthrusting. *Tectonics*, **10**, 672–687.

LILLIE, R. J., BIELIK, M., BABUŠKA, V., & PLOMEROVÁ, J. 1994. Gravity modelling of the lithosphere in the Eastern Alpine–Western Carpathian–Pannonian Basin region. *Tectonophysics*, **231**, 215–235.

LIZARRALDE, D., & HOLBROOK, W. S. 1997. U.S. mid-Atlantic margin structure and early thermal evolution. *Jour. Geophys. Res.*, **102**, 22855–22875.

LOBKOVSKY, L. I., & KERCHMAN, V. I. 1992. A two-level concept of plate tectonics: Application to geodynamics. *Tectonophysics*, **199**, 343–374.

LORENZO, J. M., O'BRIEN, G. W., STEWART, J., & TANDON, K. 1998. Inelastic yielding and forebulge shape across a modern foreland basin: North West Shelf of Australia, Timor Sea. *Geophys. Res. Lett.*, **25**, 1455–1458.

LOUP, B. 1992. Mesozoic subsidence and stretching models of the lithosphere in Switzerland (Jura, Swiss Plateau and Helvetic realm). *Eclogae Geol. Helv.*, **85**, 541–572.

LOWRY, A. R., & SMITH, R. B. 1994. Flexural rigidity of the Basin and Range–Colorado Plateau–Rocky Mountain transition from coherence analysis of gravity and topography. *J. Geophys. Res.*, **99**, 20123–20140.

LOWRY, A. R., & SMITH, R. B. 1995. Strength and rheology of the western U.S. Cordillera. *J. Geophys. Res.*, **100**, 17947–17963.

LYNCH, H. D., & MORGAN, P. 1990. Finite-element models of continental extension. *Tectonophysics*, **174**, 115–135

LYON-CAEN, H., & MOLNAR, P. 1983. Constraints on the structure of the Himalaya from an analysis of gravity anomalies and a flexural model of the lithosphere. *J. Geophys. Res.*, **88**, 8171–8191.

LYON-CAEN, H., & MOLNAR, P. 1984. Gravity anomalies and the structure of Western Tibet and the southern Tarim Basins. *Geophys. Res. Lett.*, **11**, 1251–1254.

LYON-CAEN, H., & MOLNAR, P. 1985. Gravity anomalies, flexure of the Indian plate, and the structure, support and evolution of the Himalaya and Ganga Basin. *Tectonics*, **4**, 513–538.

LYON-CAEN, H., & MOLNAR, P. 1989. Constraints on the deep structure and dynamic processes beneath the Alps and adjacent regions from an analysis of gravity anomalies. *Geophys. J. Int.*, **99**, 19–32.

LYON-CAEN, H., MOLNAR, P., & SUÁREZ, G. 1985. Gravity anomalies and flexure of the Brazilian Shield beneath the Bolivian Andes. *Earth Planet. Sci. Lett.*, **75**, 81–92.

MACARIO, A., MALINVERNO, A., & HAXBY, W. F. 1995. On the robustness of elastic thickness estimates obtained using the coherence method. *J. Geophys. Res.*, **100**, 15163–15172.

MACKWELL, S. J., ZIMMERMAN, M. E., & KOHLSTEDT, D. L. 1998. High temperature deformation of dry diabase with application to tectonics on Venus. *J. Geophys. Res.*, **103**, 975–984.

MAŢENCO, L., ZOETEMEIJER, R., CLOETINGH, S., & DINU, C. 1997. Lateral variations in mechanical properties of the Romanian external Carpathians: inferences of flexure and gravity modelling. *Tectonophysics*, **282**, 147–166.

MAGGI, A., JACKSON, J. A., MCKENZIE, D., & BAKER, C. 2000a. A reassessment of focal depth distributions in southern Iran, the Tien Shan and northern India: Do earthquakes really occur in the continental mantle? *Geophys. J. Int.*, **143**, 629–661.

MAGGI, A., JACKSON, J. A., MCKENZIE, D., & PRIESTLY, K. 2000b. Earthquake focal depths, effective elastic thickness, and the strength of the continental lithosphere. *Geology*, **28**, 495–498.

MAGNAVITA, L. P., DAVISON, I., & KUSZNIR, N. J. 1994. Rifting, erosion, and uplift history of the Recôncavo-Tucano-Jatobá Rift, northeast Brazil. *Tectonics*, **13**, 367–388.

MANDELBROT, B. B. 1967. How long is the coast of Britain? Statistical self-similarity and fractional dimension. *Science*, **156**, 636–638.

MANSPIEZER, W. 1985. Early Mesozoic history of the Atlantic passive margin. *Pages 1–23 of:* POAG, C. W.(Ed), GEOLOGIC EVOLUTION OF THE UNITED STATES ATLANTIC MARGIN. New York: Van Nostrand Rheinhold.

MANSPIEZER, W., & COUSMINER, H. L. 1988. Late Triassic-Early Jurassic synrift basins of the U.S. Atlantic margin. *Pages 197–216 of:* SHERIDAN, R. E., & GROW, J. A. (eds), *The Atlantic Continental margin U.S.*. The Geology of North America, vol. I2. Boulder, Colo.: Geol. Soc. of Am.

MARKL, R. G., BRYAN, G. M., & EWING, J. I. 1970. Structure of the Blake-Bahama outer ridge. *J. Geophys. Res.*, **75**, 4539–4555.

MARKL, R. G., & BRYAN, G. M. 1983. Stratigraphic evolution of the Blake Outer Ridge. *AAPG Bull.*, **67**, 663–683.

MARTIN, H. 1955. Notes on the Dwyka succession and on some pre-Dwyka valleys in South West Africa. *Trans. Geol. Soc. S. Africa.*, **56**, 37–42.

MARZOLI, A., RENNE, P. R., PICCIRILLO, E. M., ERNESTO, M., BELLIENI, G., & DE MIN, A. 1999. Extensive 200 million-year-old continental flood basalts of the central Atlantic magmatic province. *Science*, **284**, 616–618.

MASEK, J. G., ISACKS, B. L., FIELDING, E. J., & BROWAEYS, J. 1994. Rift flank uplift in Tibet: Evidence for a viscous lower crust. *Tectonics*, **13**, 659–667.

MASLANYJ, M. P., LIGHT, M. P. R., GREENWOOD, R. J., & BANKS, N. L. 1992. Extension tectonics offshore Namibia and evidence for passive rifting in the South Atlantic. *Mar. Pet. Geol.*, **9**, 590–601.

MATHALONE, J. M. P., & MONTOYA, R. M. 1995. Petroleum geology of the sub-Andean basins of Peru. *Pages 423–444 of:* TANKARD, A. J., SUÁREZ S., R., & WELSINK, H. J. (eds), *Petroleum Basins of South America.* AAPG Memoir 62. Tulsa, OK: American Association of Petroleum Geologists.

MATTICK, R. E. 1982. Significance of the Mesozoic carbonate bank-reef sequence for the petroleum geology of the Georges Bank basin. *Pages 93–104 of:* SCHOLLE, P. (ed), *Geological Studies of the COST No. B-3 Well.* U. S. Geological Survey, Circ. 833.

McAdoo, D. C., Martin, C. F., & Poulouse, S. 1985. Seasat observations of flexure: Evidence for a strong lithosphere. *Tectonophysics*, **116**, 209–222.

McCormick, D. S., & Grotzinger, J. P. 1992. Evolution and significance of an overfilled alluvial foreland basin: Burnside Formation (1.9Ga), Kilohigok Basin, N.W.T., Canada. *Basin Res.*, **4**, 253–378.

McHone, J. G., & Butler, J. R. 1984. Mesozoic igneous provinces of New England and the opening of the North Atlantic Ocean. *Geol. Soc. Am. Bull.*, **95**, 757–765.

McHone, J. G. 1996. Broad-terrane Jurassic flood basalts across northeastern North America. *Geology*, **24**, 319–322.

McHone, J. G. 2000. Non-plume magmatism and tectonics during the opening of the central Atlantic Ocean. *Tectonophysics*, **316**, 287–296.

McKenzie, D. P. 1978. Some remarks on the development of sedimentary basins. *Earth Planet. Sci. Lett.*, **40**, 25–32.

McKenzie, D. P. 1989. Some remarks on the movement of small melt fractions in the mantle. *Earth Planet. Sci. Lett.*, **95**, 53–72.

McKenzie, D. P. 2003. Estimating T_e in the presence of internal loads. *J. Geophys. Res.*, **108**, 10.1029/2002JB001766.

McKenzie, D. P., & Bowin, C. O. 1976. The relationship between gravity and bathymetry in the Atlantic Ocean. *J. Geophys. Res.*, **81**, 1903–1915.

McKenzie, D. P., & Fairhead, J. D. 1997. Estimates of the effective elastic thickness of the continental lithosphere from Bouguer and free air gravity anomalies. *J. Geophys. Res.*, **102**, 27523–27552.

McKenzie, D., & Jackson, J. 2002. Conditions for flow in the continental crust. *Tectonics*, **21**, doi:10.1029/2002TC001394.

McMillan, I. K. 1990. Foraminiferal biostratigraphy of the Barremian to Miocene rocks of the Kudu 9A-1, 9A-2 and 9A-3 boreholes. *Communs. geol. surv. Namibia*, **6**, 23–29.

McNutt, M. K. 1983. Influence of plate subduction on isostatic compensation in northern California. *Tectonics*, **2**, 399–415.

McNutt, M. K. 1984. Lithospheric flexure and thermal anomalies. *J. Geophys. Res.*, **89**, 11180–11194.

McNutt, M. K. 1990. Flexure reveals great depth. *Nature*, **343**, 596–597.

McNutt, M. K., & Judge, A. V. 1990. The superswell and mantle dynamics beneath the South Pacific. *Science*, **248**, 969–975.

McNutt, M. K., & Kogan, M. G. 1987. Isostasy in the USSR, 2, Interpretation of admittance data. *Pages 309–327 of:* Fuchs, K., & Froidevaux, C. (eds), *The Composition, Structure, and Dynamics of the Lithosphere-Asthenosphere System.* Geodyn. Ser., vol. 16. Washington, D. C.: AGU.

McNutt, M. K., & Parker, R. L. 1978. Isostasy of Australia and the evoloution of the compensation mechanism. *Science*, **199**, 773–775.

McNutt, M. K., Diament, M., & Kogan, M. G. 1988. Variations of elastic plate thickness at continental thrust belts. *J. Geophys. Res.*, **93**, 8825–8838.

McNutt, M. K., Sichoix, L., & Bonneville, A. 1996. Modal depths from shipboard bathymetry: There IS a South Pacific Superswell. *Geophys. Res. Lett.*, **23**, 3397–3400.

Mégard, F. 1984. The Andean orogenic period and its major structures in central and northern Peru. *J. Geol. Soc. London*, **141**, 893–900.

Milici, R. C., & de Witt, Jr., W. 1988. The Appalachian Basin. *Pages 427–469 of:* Sloss, L. L. (ed), *Sedimentary Cover-North American Craton.* The Geology of North America, vol. D2. Boulder, Colo.: Geol. Soc. of Am.

Miller, R., Carstens, H., & Wolden, T. 1994. Namibia's hyrodcarbon potential being opened for further exploration. *Oil and Gas Journal*, **92**, 123–128.

Milner, S. C., Le Roex, A. P., & O'Connor, J. M. 1995. Age of Mesozoic igneous rocks in northwestern Namibia and their relationship to continental breakup. *J. Geol. Soc. London*, **152**, 97–104.

Mohriak, W. U., Hobbs, R., & Dewey, J. F. 1990. Basin-forming processes and the deep structure of the Campos Basin, offshore Brazil. *Mar. Pet. Geol.*, **7**, 94–122.

Molnar, P., & Lyon-Caen, H. 1988. Some simple physical aspects of the support, structure, and evolution of mountain belts. Special Paper 218, 179–207. Geological Society of America.

Mon, R., & Salfity, J. A. 1995. Tectonic evolution of the Andes of northern Argentina. *Pages 260–283 of:* Tankard, A. J., Suárez S., R., & Welsink, H. J. (eds), *Petroleum Basins of South America.* AAPG Memoir 62. Tulsa, OK: American Association of Petroleum Geologists.

Mooney, W. D., Laske, G., & Masters, T. G. 1998. CRUST 5.1: A global crustal model at 5° x 5°. *J. Geophys. Res.*, **103**, 727–747.

MORGAN, J. W. 1983. Hot spot tracks and the early rifting of the Atlantic. *Tectonophysics*, **94**, 123–139.

MOUNTAIN, G. S., & TUCHOLKE, B. E. 1985. Mesozoic and Cenozoic geology of the U.S. Atlantic continental slope and rise. *Pages 293–341 of:* POAG, C. W.(Ed), GEOLOGIC EVOLUTION OF THE UNITED STATES ATLANTIC MARGIN. New York: Van Nostrand Rheinhold.

MUELLER, S., & PHILLIPS, R. J. 1995. On the reliability of lithospheric constraints derived from models of outer-rise flexure. *Geophys. J. Int.*, **123**, 887–902.

MUGNIER, J. L., & VIALON, P. 1986. Deformation and displacement of the Jura cover on its basement. *J. Struct. Geol.*, 373–387.

MÜLLER, R. D., ROEST, W. R., ROYER, J.-Y., GAHAGAN, L. M., & SCLATER, J. G. 1997. Digital isochrons of the world's ocean floor. *J. Geophys. Res.*, **102**, 3211–3214.

MUNK, W. H., & CARTWRIGHT, D. E. 1966. Tidal spectroscopy and prediction. *Phil. Trans. Roy. Soc. Lond.*, **A259**, 533–581.

MURPHY, J. B., & NANCE, R. D. 1991. Supercontinent model for the contrasting character of Late Proterozoic orogenic belts. *Geology*, **19**, 469–474.

NELSON, K. D., ARNOW, J. A., MCBRIDE, J. H., WILLEMIN, J. H., HUANG, J., ZHENG, L., OLIVER, J. E., BROWN, L. D., & KAUFMAN, S. 1985. New COCORP profiling in the southeastern United States. Part I: Late Paleozoic suture and Mesozoic rift basin. *Geology*, **13**, 714–718.

NEREM, R. S., JEKELI, C., & KAULA, W. M. 1995. Gravity field determination and characteristics: Retrospective and prospective. *J. Geophys. Res.*, **100**, 15053–15074.

sc Newman, R., & White, N. 1997. Rheology of the continental lithosphere inferred from sedimentary basins. *Nature*, **385**, 621–624.

NUNN, J. A., CZERNIAK, M., & PILGER, R. H. 1987. Constraints on the structure of the Brooks Range and Colville Basin, northern Alaska, from flexure and gravity analysis. *Tectonics*, **6**, 603–617.

NYBLADE, A. A., & POLLACK, H. N. 1993. A global analysis of heat flow from Precambrian terrains: implications for the thermal structure of Archean and Proterozoic lithosphere. *J. Geophys. Res.*, **98**, 12207–12218.

NYBLADE, A. A., & ROBINSON, S. W. 1994. The African superswell. *Geophys. Res. Lett.*, **21**, 765–768.

OH, J., PHILLIPS, J. D., AUSTIN, JR., J. A., & STOFFA, P. L. 1991. Deep-penetration seismic reflection images across the United States continental margin. *Pages 225–240 of:* MEISSNER, R., BROWN, L, DÜRRBAUM, H.-J., FRANKE, W., FUCHS, K., & SEIFERT, F. (eds), *Continental lithosphere: Deep seismic reflections.* Geodyn. Ser., vol. 22. Washington, D. C.: AGU.

OH, J., AUSTIN, JR., J. A., PHILLIPS, J. D., COFFIN, F. M., & STOFFA, P. L. 1995. Seaward dipping reflectors offshore the southeastern United States: Seismic evidence for extensive volcanism accompanying sequential formation of the Carolina trough and Blake Plateau basin. *Geology,* **23**, 9–12.

OJEDA, G. Y., & WHITMAN, D. 2002. Effect of windowing on lithosphere elastic thickness estimates obtained via the coherence method: Results from northern South America. *J. Geophys. Res.*, **11**, ???–???.

OLLIER, C. D. 1995. Tectonics and landscape evolution in Southeast Australia. *Geomorphology,* **12**, 37–44.

OLSEN, P. E. 1997. Stratigraphic record of the early Mesozoic breakup of Pangea in the Laurasia-Gondwana rift system. *Annu. Rev. Earth Planet. Sci.*, **25**, 337–401.

OWENS, J. P., & GOHN, G. S. 1985. Depositional history of the Cretaceous Series in the U.S. Atlantic Coastal Plain: Stratigraphy, paleoenvironments, and tectonic controls of sedimentation. *Pages 25–86 of:* POAG, C.W. (ed), *Geological Evolution of the United States Atlantic Margin.* New York: Van Nostrand Rheinhold.

PARDO-CASAS, F., & MOLNAR, P. 1987. Relative motion of the Nazca (Farallon) and South America plates since Late Cretaceous time. *Tectonics,* **6**, 233–248.

PARKER, R. L. 1972. The rapid calculation of potential anomalies. *Geophys. J. R. Astron. Soc.*, **31**, 447–455.

PARMENTIER, E. M. 1987. Dynamic topography in rift zones: Implications for lithospheric heating. *Phil. Trans. R. Soc. Lon.*, **321** 23–25.

PARSONS, B., & MCKENZIE, D. P. 1978. Mantle convection and the thermal structure of the plates. *J. Geophys. Res.*, **83**, 4485–4496.

PARSONS, B., & SCLATER, J. 1977. An analysis of the variation of ocean floor bathymetry and heat flow with age. *J. Geophys. Res.*, **82**, 803–827.

PATTON, T. L., & O'CONNOR, S. J. 1988. Cretaceous flexural history of northern Oman Mountain foredeep, United Arab Emirates. *AAPG Bull.*, **72**, 797–809.

PAULL, C. K., & DILLON, W. P. 1980. Structure, stratigraphy, and geological history of Florida-Hatteras Shelf and inner Blake Plateau. *AAPG Bull.*, **64**, 339–358.

PAZZAGLIA, F. J., & GARDNER, T. W. 1994. Late Cenozoic flexural deformation of the middle United-States Atlantic passive margin. *J. Geophys. Res.*, **99**, 12143–12157

PEGLER, G., DAS, S., & WOODHOUSE, J. H. 1995. A seismological study of the eastern New Guinea and the western Solomon Sea regions and its tectonic implications. *Geophys. J. Int.*, **122**, 961–981.

PEREZ-GUSSINYE, M., LOWRY, A. R., WATTS, A. B., & VELICOGNA, I. 2003. On the recovery of effective elastic thickness using spectral methods: examples from synthetic data and from the Fennoscandian Shield. *Submitted to J. Geophys. Res. Oct 2003.*

PETIT, C., & EBINGER, C. 2000. Flexure and mechanical behavior of cratonic lithosphere: Gravity models of the East African and Baikal rifts. *J. Geophys. Res.*, **105**, 19151–19162.

PFIFFNER, O. A. 1986. Evolution of the North Alpine Foreland Basin in the central Alps. *Pages 219–228 of:* ALLEN, P. A., & HOMEWOOD, P. (eds), *Foreland Basins.* Spec. Publ. Int. Assoc. Sedimentol., no. 8. Blackwell, Oxford.

PFIFFNER, O. A. 1992. Alpine Orogeny. *Pages 180–190 of:* BLUNDELL, D., FREEMAN, R., & MUELLER, S. (eds), *A continent revealed – The European Geotraverse.* Cambridge Universiy Press.

PFIFFNER, O. A., ERARD, P.-F., & STÄUBLE, M. 1997. Two cross sections through the Swiss Molasse Basin. *Pages 64–72 of:* PFIFFNER, O. A., LEHNER, P., HEITZMAN, P., MUELLER, ST., & STECK, A. (eds), *Deep Structure of the Swiss Alps: Results from NRP 20.* Basel: Birkhäuser.

PILKINGTON, M. 1990. Lithospheric flexure and gravity anomalies at Proterozoic plate boundaries in the Canadian Shield. *Tectonophysics*, **176**, 277–290.

PINET, C., JAUPART, C., MARESCHAL, J.-C., GARIEPY, C., BIENFAIT, G., & LAPOINTE, R. 1991. Heat flow and structure of the lithosphere in the eastern Canadian Shield. *J. Geophys. Res.*, **96**, 19941–19963.

PITMAN, W. C. 1978. The relationship between eustasy and stratigraphic sequences at passive margins. *Geol. Soc. Am. Bull.*, **89**, 1389–1403.

PLAFKER, G., & BERG, H. C. (eds). 1994. *The Geology of Alaska.* The Geology of North America, vol. G-1. Boulder, Colo.: Geological Society of America.

PLUMB, K. A. 1979. The tectonic evolution of Australia. *Earth-Science Reviews*, **14**, 205–249.

POAG, W. C., & VALENTINE, P. C. 1988. Mesozoic and Cenozoic stratigraphy of the United States Atlantic continental shelf and slope. *Pages 67–85 of:* SHERIDAN, R. E., & GROW, J. A. (eds), *The Atlantic Continental margin U.S.*. The Geology of North America, vol. I2. Boulder, Colo.: Geol. Soc. of Am.

POLLACK, H. N. 1986. Cratonization and thermal evolution of the mantle. *Earth Planet. Sci. Lett.*, **80**, 175–182.

POLLACK, H. N., HURTER, S. J., & JOHNSON, J. R. 1993. Heat flow from the earth's interior: Analysis of the global data set. *Rev. Geophys.*, **31**, 267–280.

POPENOE, P., & ZIETZ, I. 1977. The nature of the geophysical basement beneath the Coastal Plain of South Carolina and northeastern Georgia. *Pages 119–137 of:* RANKIN, W., (ed.), *Studies related to the Charleston, South Carolina, Earthquake of 1886 - a preliminary report.* U. S. Geological Survey, Prof Paper 1028.

POUDJOM DJOMANI, Y. H., NNANGE, J. M., DIAMENT, M., EBINGER, C. J., & FAIRHEAD, J. D. 1995. Effective elastic thickness and crustal thickness variations in west central Africa inferred from gravity data. *J. Geophys. Res.*, **100**, 22047–22070.

POULIMENOS, G., & DOUTSOS, T. 1997. Flexural uplift of rift flanks in central Greece. *Tectonics*, **16**, 912–923.

PRATT, J. H. 1855. On the attraction of the Himalaya Mountains, and of the elevated regions beyond them upon a plumb-line in India. *Phil. Trans. Roy. Soc. Lond.*, **145**, 53–101.

PRATT, J. H. 1859. On the deflection of the plumb-line in India caused by the attraction of the Himalaya mountains and the elevated regions beyond; and its modification by the compensating effect of a deficiency of matter below the mountain mass. *Phil. Trans. Roy. Soc. Lond.*, **149**, 745–778.

PRATT, T. L., ÇORUH, C., COSTAIN, J. K., & GLOVER, III, L. 1988. A geophysical study of the Earth's crust in central Virginia: Implications for Appalachian crustal structure. *J. Geophys. Res.*, **93**, 6649–6667.

PRESS, W. H., FLANNERY, B. P., TEUKOSLSKY, S. A., & VETTERLING, W. T. 1992. *Numerical Recipes in C.* Second edn. Cambridge Univ. Press, New York.

PRICE, M., & SUPPE, J. 1994. Mean age of rifting and volcanism on Venus deduced from impact crater densities. *Nature*, **372**, 756–759.

PRICE, R. A. 1973. Large-scale gravitational flow of supracrustal rocks, Southern Canadian Rockies. *Pages 491–502 of:* DE JONG, K. A., & SCHOLTEN, R. A. (eds), *Gravity and Tectonics.* New York: John Wiley.

QUINLAN, G. M., & BEAUMONT, C. 1984. Appalachian thrusting, lithospheric flexure, and the Palaeozoic stratigraphy of the eastern interior of North America. *Can. J. Earth Sci.*, **21**, 973–996.

RABINOWITZ, P. D., & LABRECQUE, J. 1979. The Mesozoic South Atlantic ocean and evolution of its continental margin. *J. Geophys. Res.*, **85**, 5973–6002.

RAGLAND, P. C. 1991. Mesozoic igneous rocks. *Pages 95–118 of:* PUFFER, J. H., & RAGLAND, P. C. (eds), *The geology of the Carolinas.* University of Tennessee Press, Knoxville.

RAMPINO, M. R., & STOTHERS, R. B. 1988. Flood basalt volcanism during the past 250 million years. *Science*, **241**, 663–668.

RAMSAY, J. G. 1981. Tectonics of the Helvetic Nappes. *Pages 293–310 of:* MCCLAY, K. R., & PRICE, N. J. (eds), *Thrust and Nappe Tectonics.* Geol. Soc. Lond. Spec. Publ., no. 9. Geol. Soc. Lond.

RANALLI, G. 1997. Rheology of the lithosphere in space and time. *Pages 19–37 of:* BURG, J. P., & FORD, M. (eds), *Orogeny through time.* Geol. Soc. Lond. Spec. Publ., no. 121. Geol. Soc. Lond.

RAPP, R. H., WANG, Y. M., & PAVLIS, N. K. 1991. *The Ohio State 1991 geopotential and sea surface topography harmonic coefficient models.* Tech. rept. 410. Dep. of Geod. Sci. and Surv., Ohio State Univ., Columbus.

RAVAUT, P., AL YAHYA'EY, A., BAYER, R., & LESQUER, A. 1993. Résponse isostatique de la plate-forme arabique au chargement ophiolitique en Oman. *Compte Rendue de l'Academie Science Paris*, **317**, 463–470.

RIBE, N. M. 1982. Interpretation of frequency response functions for oceanic gravity and bathymetry. *Geophys. J. R. Astron. Soc.*, **70**, 273–294.

RODGERS, J. 1970. *The Tectonics of the Appalachians.* New York: Wiley-Interscience.

ROEDER, D. 1988. Andean-age structure of Eastern Cordillera (province of La Paz). *Tectonics*, **7**, 23–39.

ROWLEY, D. B., & SAHAGIAN, D. 1986. Depth dependent stretching: A different approach. *Geology*, **14**, 32–35.

ROYDEN, L., & KEEN, C. E. 1980. Rifting processes and thermal evolution of the continental margin of eastern Canada determined from subsidence curves. *Earth Planet. Sci. Lett.*, **51**, 343–361.

ROYDEN, L. H. 1988a. Flexural behaviour of the continental lithosphere in Italy: Constraints imposed by gravity and deflection data. *J. Geophys. Res.*, **93**, 7747–7766.

ROYDEN, L. H. 1988b. Late Cenozoic tectonics of the Pannonian basin system. *Pages 27–48 of:* ROYDEN, L. H., & HORVÁTH, F. (eds), *The Pannonian Basin: A Study in Basin Evolution.* AAPG Memoir 45. Tulsa, OK: American Association of Petroleum Geologists.

ROYDEN, L. H. 1993. The tectonic expression of slab pull at continental convergent boundaries. *Tectonics*, **12**, 303–325.

ROYDEN, L. H., & HORVÁTH, F. (eds). 1988. *The Pannonian Basin: A Study in Basin Evolution.* AAPG Memoir 45. Tulsa, OK: American Association of Petroleum Geologists.

ROYDEN, L. H., & KARNER, G. D. 1984. Flexure of the lithosphere beneath the Apennine and Carpathian foredeep: Evidence for an insufficient topographic load. *AAPG Bull.*, **68**, 704–712.

RUPPEL, C. 1995. Extensional processes in continental lithosphere. *J. Geophys. Res.*, **100**, 24187–24215.

RUPPEL, C., & MCNUTT, M. K. 1990. Regional compensation of the Greater Caucasus mountains based on an analysis of Bouguer gravity data. *Earth Planet. Sci. Lett.*, **98**, 360–379.

RUPPEL, C., KOGAN, M. G., & MCNUTT, M. K. 1993. Implications of new gravity data for Baikal rift zone structure. *Geophys. Res. Lett.*, **20**, 1635–1638.

RUST, D. J., & SUMMERFIELD, M. A. 1990. Isopach and borehole data as indicators of rifted margin evolution in southwestern Africa. *Mar. Pet. Geol.*, **7**, 277–287.

RUTTER, E. H., & BRODIE, K. H. 1991. Lithosphere rheology - a note of caution. *J. Struct. Geol.*, **13**, 363–367.

SALVADOR, M., & KELLOG, J. N. 1991. Gravity field, crustal structure and effective elastic thickness of the northern Andes (abstract). *Page 91 of: Eos Trans. AGU*, vol. 71, Spring Meet. suppl. American Geophysical Union.

SAMSON, S. D. 1995. Is the Carolina Terrane part of Avalon? *Pages 253–264 of:* HIBBARD, J. P., VAN STAAL, C. R., & CAWOOD, P. A. (eds), *Current perspectives in the Appalachian–Caledonian Orogen.* Geological Association of Canada Special Paper 41. Geological Association of Canada. Toronto, ON, Canada.

SANDWELL, D. T., & SMITH, W. H. F. 1997. Marine gravity anomaly from Geosat and ERS 1 satellite altimetry. *J. Geophys. Res.*, **102**, 10039–10054.

SAWYER, D. S. 1985a. Brittle failure in the upper mantle during extension of continental lithosphere. *J. Geophys. Res.*, **90**, 3021–3025.

SAWYER, D. S. 1985b. Total tectonic subsidence: A parameter for distingushing crust type at the U.S. Atlantic continental margin. *J. Geophys. Res.*, **90**, 7751–7769.

SAWYER, D. S., SWIFT, B. A., SCLATER, J. G., & TOKSZ, M. N. 1982a. Extensional model for the subsidence of the northern United States Atlantic continental margin. *Geology*, **10**, 134–140.

SAWYER, D. S., TOKSZ, M. N., SCLATER, J. G., & SWIFT, B. A. 1982b. Thermal evolution of the Baltimore Canyon Trough and Georges Bank Basin. *Pages 743–762 of:* WATKINS, J. S. & DRAKE, S. L. (eds), *Studies in Continental Margin Geology.* Am. Assoc. Pet. Geol.,Mem. 34.

SCHEGG, R., LEU, W., CORNFORD, C., & ALLEN, P. A. 1997. New coalification profiles in the Swiss Molasse Basin (Western Switzerland): Implications for the thermal and geodynamic evolution of the Alpine foreland. *Eclogae Geol. Helv.*, **90**, 79–96.

SCHLEE, J. S., & FRITSCH, J. 1983. Seismic stratigraphy of the Georges Bank basin complex, offshore New England. *Pages 223–251 of:* WATKINS, J. S., & DRAKE, C. L. (eds) *Studies in continental margin geology.* AAPG Memoir 34. Tulsa, OK: American Association of Petroleum Geologists.

SCHLEE, J. S., & JANSA, L. F. 1981. The paleoenvironment and development of the eastern North American continental margin. *Pages 71–80 of: Geology of continental margins; International Geological Congress, 26th Paris, July 7-17, 1980, Colloque C3.* Oceanologica Acta, no SP, supplement to v4.

SCHLEE, J. S., & KLITGORD, K. D. 1986. Structure of the North Atlantic continental margin. *J. Geologic Education*, **34**, 72–89.

SCHLEE, J. S., & KLITGORD, K. D. 1988. Georges Bank Basin: A regional synthesis. *Pages 243–268 of:* SHERIDAN, R. E., & GROW, J. A. (eds), *The Atlantic Continental margin U.S..* The Geology of North America, vol. I2. Boulder, Colo.: Geol. Soc. of Am.

SCHLEE, J. S., MANSPIEZER, W., & RIGGS, S. R. 1988. Paleoenvironments: Offshore Atlantic U.S. margin. *Pages 365–385 of:* SHERIDAN, R. E., & GROW, J. A. (eds), *The Atlantic Continental margin U.S..* The Geology of North America, vol. I2. Boulder, Colo.: Geol. Soc. of Am.

SCHOLLE, P. A. (ed). 1977. *Geological studies on the COST No. B-2 Well, U.S. Mid-Atlantic Outer Continental Shelf Area.* U. S. Geological Survey, Circ. 750. 71p.

SCHOLLE, P. A. (ed). 1980. *Geological studies on the COST No. B-3 Well, U.S. Mid-Atlantic Outer Continental Slope Area.* U. S. Geological Survey, Circ. 833. 132p.

SEMPERE, T. 1995. Phanerozoic evolution of Bolivia and adjacent areas. *Pages 207–230 of:* TANKARD, A. J., SUÁREZ S., R., & WELSINK, H. J. (eds), *Petroleum Basins of South America.* AAPG Memoir 62. Tulsa, OK: American Association of Petroleum Geologists.

ŞENGÖR, A. M. C., & NATAL'IN, B. A. 1996. Paleotectonics of Asia: fragments of a synthesis. *Pages 486–640 of:* YIN, A., & HARRISON, M. (eds), *The Tectonic Evolution of Asia.* Cambridge University Press.

SENO, T., & YAMANAKA, Y. 1996. Double seismic zones, compressional deep trench-outer rise events, and superplumes. *Pages 347–355 of:* BEBOUT, G. E., SCHOLL, D. W., KIRBY, S. H., & PLATT, J. P. (eds), *Subduction: Top to bottom.* Geophysical Monograph, vol. 96. Washington, DC: American Geophysical Union.

SHACKLETON, R. M. 1986. Precambrian collision tectonics in Africa. *Pages 329–349 of:* COWARD, M. P., & RIES, A. C. (eds), *Collision Tectonics.* Geol. Soc. Lond. Spec. Publ., no. 19. Geol. Soc. Lond.

SHEFFELS, B., & MCNUTT, M. K. 1986. The role of subsurface loads and regional compensation in the isostatic balance of the Transverse Ranges, California. *J. Geophys. Res.*, **91**, 6419–6431.

SHERIDAN, R. E., GROW, J. A., BEHRENDT, J. C., & BAYER, K. C. 1979. Seismic refraction study of the continental edge off the eastern United States. *Tectonophysics*, **59**, 1–26.

SHERIDAN, R. E., MUSSER, D. L., GLOVER, III, L., TALWANI, M., EWING, J. I., HOLBROOK, W. S., PURDY, G. M., HAWMAN, R., & SMITHSON, S. 1993. Deep seismic reflection data of EDGE U.S. mid-Atlantic continental-margin experiment: Implications for Appalachian sutures and Mesozoic rifting and magmatic underplating. *Geology*, **21**, 563–567.

SIBSON, R. H. 1977. Fault rocks and fault mechanisms. *J. Geol. Soc. London*, **133**, 191–213.

SIBSON, R. H. 1982. Fault zone models, heat flow and the depth distribution of earthquakes in the continental crust of the United States. *Bull. Seismol. Soc. Am.*, **72**, 151–163.

SIESSER, W. G. 1980. Late Miocene origin of Benguela upwelling system off northern Namibia. *Science*, **208**, 283–285.

SIMPSON, R. W., JACHENS, R. C., BLAKELY, R. J., & SALTUS., R. W. 1986. A new isostatic residual gravity map of the conterminous United States with a discussion on the significance of isostatic residual anomalies. *J. Geophys. Res.*, **91**, 8348–8372.

SINCLAIR, H. D. 1996. Plan-view curvature of foreland basins and its implications for the palaeostrength of the lithosphere underlying the western Alps. *Basin Res.*, **8**, 173–182.

SINCLAIR, H. D. 1997. Flysch to molasse transition in peripheral foreland basins: The role of the passive margin versus slab breakoff. *Geology*, **25**, 1123–1126.

SINCLAIR, H. D., & ALLEN, P. A. 1992. Vertical versus horizontal motions in the Alpine orogenic wedge: Stratigraphic response in the foreland basin. *Basin Res.*, **4**, 215–232.

SINCLAIR, H. D., COAKLEY, B. J., ALLEN, P. A., & WATTS, A. B. 1991. Simulation of foreland basin stratigraphy using a diffusion model of mountain belt uplift and erosion: An example from the central Alps, Switzerland. *Tectonics*, **10**, 599–620.

SKOGSEID, J. 1994. Dimensions of the Late Cretaceous–Paleocene Northeast Atlantic rift derived from Cenozoic subsidence. *Tectonophysics*, **240**, 225–247.

SLEEP, N. H., & SNELL, N. S. 1976. Thermal contraction and flexure of mid-continent and Atlantic continental basins. *Geophys. J. R. Astr. Soc.*, **45**, 125–154.

SLOSS, L. L., & SCHERER, W. 1975. Geometry of sedimentary basins: Applications to the Devonian of North America and Europe. *Pages 71–88 of:* WHITTEN, E. H. T. (ed), *Quantitative studies in the geological sciences.* Geol. Soc. Amer. Memoir 142 Geological Society of America.

SMITH, W. H. F., & SANDWELL, D. T. 1997. Global seafloor topography from satellite altimetry and ship depth soundings. *Science*, **277**, 1957–1962.

SMITH, W. H. F., & WESSEL, P. 1990. Gridding with continuous curvature splines in tension. *Geophysics*, **55**, 293–305.

SMREKAR, S. E. 1994. Evidence for active hotspots on Venus from analysis of Magellan gravity data. *Icarus*, **112**, 2–26.

SNYDER, D. B., & BARAZANGI, M. 1986. Deep crustal structure and flexure of the Arabian plate beneath the Zagros collisional mountain belt as inferred from gravity observations. *Tectonics*, **5**, 361–373.

SONDER, L. J., & ENGLAND, P. C. 1989. Effects of a temperature-dependent rheology on large-scale continental extension. *Geophys. Res. Lett.*, **94**, 7603–7619.

SPADINI, G., CLOETINGH, S., & BERTOTTI, G. 1995. Thermo-mechanical modeling of the Tyrrhenian Sea: Lithospheric necking and kinematics of rifting. *Tectonics*, **14**, 629–644.

STARK, C. P., & STEWART, J. 1997. Mapping lithospheric strength and loading using wavelet transform admittance and coherence (abstract). *Page 35 of: Eos Trans. AGU*, vol. 78(46), Fall Meet. suppl.

STECKLER, M. S. 1985. Uplift and extension of the Gulf of Suez: Indications of induced mantle convection. *Nature*, **317**, 135–139.

STECKLER, M. S., & TEN BRINK, U. S. 1986. Lithospheric strength variation as a control on new plate boundaries: examples from the Gulf of Suez. *Earth Planet. Sci. Lett.*, **79**, 120–132.

STECKLER, M. S., & WATTS, A. B. 1978. Subsidence of the Atlantic-type continental margin off New York. *Earth Planet. Sci. Lett.*, **41**, 1–13.

STEGENA, L., GÉCZY, B., & HORVÁTH, F. 1975. Late Cenozoic evolution of the Pannonian basin. *Tectonophysics*, **26**, 71–90.

STEIN, C. A., & STEIN, S. 1992. A model for the global variation in oceanic depth and heat flow with lithospheric age. *Nature*, **359**, 123–129.

STEINMANN, G. 1929. *Geologie von Peru.* Heidelberg: Karl Winter.

STEPHENSON, R. A., NAKIBOGLU, S. M., & KELLY, M. A. 1989. Effects of asthenospheric melting, regional thermoisostasy, and sediment loadgin on the thermomechanical subsidence of extensional sedimentary basins. *Pages 17–27 of:* PRICE, R. A. (ed), *Origin and evolution of sedimentary basins and their energy and mineral resouces.* AGU Geophys. Monog. Ser. 48. Washington, DC: American Geophysical Union.

STERN, T. A., & TEN BRINK, U. S. 1989. Flexural uplift of the Transantarctic Mountains. *J. Geophys. Res.*, **94**, 10315–10330.

STEWART, J., & WATTS, A. B. 1997. Spatial variations of flexural rigidity at mountain ranges. *J. Geophys. Res.*, **102**, 5327–5352.

STEWART, J., WATTS, A. B., & BAGGULEY, J. G. 2000. 3-D subsidence analsyis and gravity modelling of the continental margin offshore Namibia. *Geophys. J. Int.*, **141**, 724–746.

STEWART, J. 1998. *Gravity anomalies and lithospheric flexure: Implications for the thermal and mechanical evolution of the continental lithosphere.* Ph.D. thesis, University of Oxford, Oxford, England.

STOCKMAL, G. S., BEAUMONT, C., & BOUTILIER, R. 1986. Geodynamic models of convergent margin tectonics: Transition from rifted margin to overthrust belt and consequences for foreland basin development. *AAPG Bull.*, **70**, 181–190.

SU, W. J., WOODWARD, R. L., & DZIEWONSKI, A. M. 1994. Degree-12 model of shear velocity heterogeneity in the mantle. *J. Geophys. Res.*, **99**, 6945–6980.

SUTTER, J. F. 1985. Progress on geochronology of Mesozoic diabases and basalts. *Pages 110–114 of:* ROBINSON G. P., & FROELICH, A. J. (eds), *Proceedings of the second U.S. Geological Survey on the Early Mesozoic basins of the eastern United States.* U. S. Geological Survey, Circ. 946.

SĂNDULESCU, M. 1988. Cenozoic tectonic history of the Carpathians. *Pages 17–25 of:* ROYDEN, L. H., & HORVÁTH, F. (eds), *The Pannonian Basin: A Study in Basin Evolution.* AAPG Memoir 45. Tulsa, OK: American Association of Petroleum Geologists.

TAKESHITA, T., & WENK, H. R. 1988. Plastic anisotropy and geometrical hardening in quartzites. *Tectonophysics*, **149**, 345–361.

TALWANI, M., WORZEL, J. L., & LANDISMAN, M. 1959. Rapid computations for two dimensional bodies with application to the Mendocino submarine fracture zone. *Jour. Geophys. Res.*, **64**, 49–59.

TALWANI, M., EWING, J., SHERIDAN, R. E., HOLBROOK, W. S., & GLOVER, III, L. 1995. The EDGE experiment and the U.S. East Coast magnetic anomaly. *Pages 155–181 of:* BANDA, E., TORNÉ, M., & TALWANI, M. (eds), *Rifted Ocean-Continent Boundaries.* Kluwer Academic Publishers.

TANG, J., & LERCHE, I. 1992. Tertiary flexural evolution of the Beaufort–Mackenzie Basin, Canada. *Mar. Pet. Geol.*, **9**, 245–255.

TANG, J., LERCHE, I., & COGAN, J. 1992. An inverse method for calculating basement geometries in foreland basins. *J. Geodyn.*, **15**, 85–106.

TANKARD, A. J. 1986. On the depositional response to thrusting and lithospheric flexure: examples from the Appalachian and Rocky Mountain basins. *Pages 369–392 of:* P. A. ALLEN AND P. HOMEWOOD (ed), *Foreland Basins. Spec. Publ. Int. Assoc. Sedimentol., 8.* Blackwell.

TANNER, J. G. 1967. An automated method of gravity interpretation. *Geophys. J. R. Astron. Soc.*, **13**, 339–347.

TASSARA, A., & YAÑEZ, G. 1996. Thermomechanical segmentation of the Andes (15°S - 50°S): A flexural analysis approach. *Pages 115–118 of: Extended Abstracts, Third International Symposium Andean Geodynamics.* St. Malo, France: Paris, ORSTROM.

TAYLOR, P. T., & RAVAT, D. 1995. An interpretation of the Magsat anomalies of central Europe. *J. Appl. Geophys.*, **34**, 83–91.

TAYLOR, S. R. 1989. Geophysical framework of the Appalachians and adjacent Grenville Province. *Pages 317–348 of:* PAKISER, L. C., & MOONEY, W. D. (eds), *Geophysical Framework of the Continental United States.* Geol. Soc. Amer. Memoir 172. Geological Society of America.

THEUNISSEN, K., KLERKX, J., MELNIKOV, A., & MRUMA, A. 1996. Mechanisms of inheritance of rift faulting in the western branch of the East African Rift, Tanzania. *Tectonics*, **15**, 776–790.

THOMAS, W. A. 1977. Evolution of the Appalachian–Ouachita salients and recesses from reentrants and promontories in the continental margin. *Am. J. Sci.*, **277**, 1233–1278.

THOMAS, W. A. 1991. The Appalachian–Ouachita rifted margin of southeastern North America. *Geol. Soc. Am. Bull.*, **103**, 415–431.

THOMPSON, A. B. 1992. Water in the Earth's upper mantle. *Nature*, **358**, 295–302.

THORNE, J., & WATTS, A. B. 1989. A quantitative analysis of North Sea subsidence. *AAPG Bull.*, **73**, 88–116.

THURBER, C. H., & TOKSÖZ, M. N. 1978. Martian lithospheric thickness from elastic flexure theory. *Geophys. Res. Lett.*, **5**, 977–980.

TIMOSHENKO, S. P., & WOINOWSKY-KRIEGER, S. 1959. *Theory of Plates and Shells.* Second edn. New York: McGraw-Hill.

TODD, B. J., & KEEN, C. E. 1989. Temperature effects and their geological consequences at transform margins. *Can. J. Earth Sci.*, **26**, 2591–2603.

TOMEK, C., & HALL, J. 1993. Subducted continental margin imaged in the Carpathians of Czechoslovakia. *Geology*, **21**, 535–538.

TOTH, J., KUSZNIR, N. J., & FLINT, S. S. 1996. A flexural isostatic model of lithosphere shortening and foreland basin formation: Application to the Eastern Cordillera and Subandean belt of NW Argentina. *Tectonics*, **15**, 213–223.

TREHU, A. M., BALLARD, A., DORMAN, L. M., GETTRUST, J. F., KLITGORD, K. D., & SCHREINER, A. 1989. Structure of the lower crust beneath the Carolina Trough, U.S. Atlantic continental margin. *J. Geophys. Res.*, **94**, 10585–10600.

TREHU, A. M., KLITGORD, K. D., SAWYER, D. S., & BUFFLER, R. T. 1987. Regional investigations of the crust and upper mantle, Atlantic and Gulf of Mexico continental margins. *Pages 349–382 of:* PAKISER, L., & MOONEY, W. D. (eds), *Geophysical framework of the continental United States.* Geol. Soc. Amer. Memoir 172. Geological Society of America.

TURCOTTE, D. L. 1992. *Fractals and Chaos in Geology and Geophysics.* Cambridge University Press.

TURCOTTE, D. L., & SCHUBERT, G. 1982. *Geodynamics: Applications of Continuum Physics to Geological Problems.* John Wiley and Sons.

TURCOTTE, D. L., MCADOO, D. C., & CALDWELL, J. G. 1978. An elastically-perfectly plastic analysis of the bending of the lithosphere at a trench. *Tectonophysics*, **47**, 193–205.

UCHUPI, E., PHILLIPS, J. D., & PRADA K. E. 1970. Origin and structure of the New England Seamount Chain. *Deep Sea Res.*, **17**, 483–494.

ULIANA, M. A., BIDDLE, K. T., & CERIDAN, J. 1989. Mesozoic extension and the formation of the Argentine sedimentary basin. *Pages 599–614 of:* TANKARD, A. J., & BALKWILL, H. R. (eds), *Extensional Tectonics and Stratigraphy of the North Atlantic Margins.* AAPG Memoir 46. Tulsa, OK: American Association of Petroleum Geologists.

UPCOTT, N. M., MUKASA, R. K., EBINGER, C. J., & KARNER, G. D. 1996. Along-axis segmentation and isostasy in the Western Rift, East Africa. *J. Geophys. Res.*, **101**, 3247–3268.

VAIL, P. R., MITCHUM, JR., R. M., TODD, R. G., WIDMIER, J. M, THOMPSON, III., S, SANGREE, J. B., BUBB, J. N., & HATLEILID, W. G. 1977. Seismic stratigraphy and global changes of sea level. *Pages 49–212 of:* PAYTON, C. E. (ed), *Seismic Stratigraphy - Applications to Hydrocarbon Exploration.* Am. Assoc. Pet. Geol.,Mem. 26.

VAN BALEN, R. T., VAN DER BEEK, P. A., & CLOETINGH, S. A. P. L. 1995. The effect of rift shoulder erosion on stratal patterns at passive margins: Implications for sequence stratigraphy. *Earth Planet. Sci. Lett.*, **134**, 527–544.

VAN DER BEEK, P. 1997. Flank uplift and topography at the Central Baikal Rift (SE Siberia): A test of kinematic models for continental extension. *Tectonics*, **16**, 122–136.

VAN DER BEEK, P., CLOETINGH, S., & ANDRIESSEN, P. 1994. Mechanisms of extensional basin formation and vertical motions at rift flanks: Constraints from tectonic modelling and fission-track thermochronology. *Earth Planet. Sci. Lett.*, **121**, 417–433.

VAN DER BEEK, P. A., & CLOETINGH, S. 1992. Lithospheric flexure and the tectonic evolution of the Betic Cordilleras (SE Spain). *Tectonophysics*, **203**, 325–344.

VAN DER HILST, R. D., WIDIYANTORO, S., & ENGDAHL, E. R. 1997. Evidence for deep mantle circulation from global tomography. *Nature*, **386**, 578–584.

VAN HEIJST, H. J. 1997. *New Constraints on the Seismic Structure of the Earth from Surface Wave Overtone Phase Velocity Measurements.* Ph.D. thesis, Univ. of Oxford, Oxford, England.

VAN WEES, J. D., & CLOETINGH, S. 1994. A finite-difference technique to incorporate spatial variations in rigidity and planar faults into 3-D models for lithospheric flexure. *Geophys. J. Int.*, **117**, 179–195.

VAN WEES, J. D., & CLOETINGH, S. 1996. 3D flexure and intraplate compression in the North Sea Basin. *Tectonophysics*, **266**, 343–359.

VAUCHEZ, A., BARRUOL, G., & TOMMASI, A. 1997. Why do continents break up parallel to ancient orogenic belts? *Terra Nova*, **9**, 62–66.

VENING MEINESZ, F. A. 1931. Une nouvelle méthode pour la réduction isostatique régionale de l'intensité de la pesanteur. *Bull. géod.*, **29**, 35–51.

VENING MEINESZ, F. A. 1950. Les Grabens Africans resultant de compression ou de tension dans la crôute terrestre? *Inst. R. Kolonial Belge Bull.*, **21**, 529–552.

VERHOEF, J., & JACKSON, H. R. 1991. Admittance signatures of rifted and transform margins: examples from eastern Canada. *Geophys. J. Int.*, **105**, 229–239.

VIDOTTI, R. M. 1997. *Lithospheric Structure Beneath the Paraná and Parnaíba Basins, Brazil from Regional Gravity Analyses.* Ph.D. thesis, Univ. of Leeds, Leeds, England.

VINE, F. J., & MATTHEWS, D. H. 1963. Magnetic anomalies over oceanic ridges. *Nature*, **199**, 947–949.

VINK, G. E., MORGAN, J. W., & ZHAO, W. L. 1984. Preferential rifting of continents; a source of displaced terranes. *J. Geophys. Res.*, **89**, 10072–10076.

VOGT, P. R. 1973. Early events in the opening of the North Atlantic. *Pages 693–712 of:* TARLING, D. H., & RUNCORN, S. K. (eds), *Implications of continental drift to the Earth Sciences, v2.* London Academic Press.

VON HERZEN, R. P., CORDERY, M. J., DETRICK, R. S., & CHANGLE, F. 1989. Heat flow and the thermal origin of hot spot swells: The Hawaiian Swell revisited. *J. Geophys. Res.*, **94**, 13783–13799.

WALCOTT, R. I. 1970. Flexural rigidity, thickness and viscosity of the lithosphere. *J. Geophys. Res.*, **75**, 3941–3954.

WALCOTT, R. I. 1972. Gravity, flexure and the growth of sedimentary basins at the continental edge. *Geol. Soc. Am. Bull.*, **83**, 1845–1848.

WARD, L. W., & STRICKLAND, G. L. 1985. Outline of Tertiary stratigraphy and depositional history of the U.S. Atlantic coastal plain. *Pages 87–123 of:* POAG, C.W. (ed), *Geological Evolution of the United States Atlantic Margin.* New York: Van Nostrand Rheinhold.

WASCHBUSCH, P. J., & ROYDEN, L. H. 1992. Spatial and temporal evolution of foredeep basins: Lateral strength variations and inelastic yielding in continental lithosphere. *Basin Res.*, **4**, 179–196.

WATTS, A. B. 1978. An analysis of isostasy in the world's oceans, 1, Hawaiian–Emperor seamount chain. *J. Geophys. Res.*, **83**, 5989–6004.

WATTS, A. B. 1988. Gravity anomalies, crustal structure and flexure of the lithosphere at the Baltimore Canyon Trough. *Earth Planet. Sci. Lett.*, **89**, 221–238.

WATTS, A. B. 1992. The effective elastic thickness of the lithosphere and the evolution of foreland basins. *Basin Res.*, **4**, 169–178.

WATTS, A. B. 2001. *Isostasy and flexure of the lithosphere.* Cambridge University Press: Cambridge, United Kingdom, 458 p.

WATTS, A. B., & BUROV, E. B. 2003. Lithospheric strength and its relationship to the elastic and seismogenic layer thickness. *Earth Planet. Sci. Lett.*, **213**, 113–131.

WATTS, A. B., & COCHRAN, J. R. 1974. Gravity anomalies and flexure of the lithosphere along the Hawaiian–Emperor seamount chain. *Geophys. J. R. Astron. Soc.*, **38**, 119–141.

WATTS, A. B., & FAIRHEAD, J. D. 1997. Gravity anomalies and magmatism along the western continental margin of the British Isles. *J. Geol. Soc. London*, **154**, 523–529.

WATTS, A. B., & MARR, C. 1995. Gravity anomalies and the thermal and mechanical structure of rifted continental margins. *Pages 65–94 of:* BANDA, E., TORNÉ, M., & TALWANI, M. (eds), *Rifted Ocean-Continent Boundaries.* Kluwer Academic Publishers.

WATTS, A. B., & RYAN, W. B. F. 1976. Flexure of the lithosphere and continental margin basins. *Tectonophysics*, **36**, 25–44.

WATTS, A. B., & STECKLER, M. S. 1979. Subsidence and eustasy at the continental margin of eastern North America. *Pages 218–234 of: Deep Drilling Results in the Atlantic Ocean: Continental Margins and Palaeoenvironments.* Maurice Ewing Series, vol. 3. American Geophysical Union.

WATTS, A. B., & STEWART, J. 1998. Gravity anomalies and the segmentation of the continental margin offshore West Africa. *Earth Planet. Sci. Lett.*, **156**, 239–252.

WATTS, A. B., & TALWANI, M. 1974. Gravity anomalies seaward of deep-sea trenches and their tectonic implications. *Geophys. J. R. Astron. Soc.*, **36**, 57–102.

WATTS, A. B., & THORNE, J. A. 1984. Tectonics, global changes in sea-level and their relationship to stratigraphic sequences at the U.S. Atlantic continental margin. *Mar. Pet. Geol.*, **4**, 319–339.

WATTS, A. B., & TORNÉ, M. 1992. Subsidence history, crustal structure and thermal evolution of the Valencia Trough: A young extensional basin in the western Mediterranean. *J. Geophys. Res.*, **97**, 20021–20041.

WATTS, A. B., & ZHONG, S. 2000. Observations of flexure and rheology of oceanic lithosphere. *Geophys. J. Int.*, **142**, 855–875.

WATTS, A. B., BODINE, J. H., & STECKLER, M. S. 1980. Observations of flexure and the state of stress in the oceanic lithosphere. *J. Geophys. Res.*, **85**, 6369–6376.

WATTS, A. B., KARNER, G. D., & STECKLER, M. S. 1982. Lithospheric flexure and the evolution of sedimentary basins. *Pages 249–281 of:* KENT, P., BOTT, M. H. P., MCKENZIE, D. P., & WILLIAMS, C. A. (eds), *The Evolution of Sedimentary Basins.* Phil. Trans. Roy. Soc. Lond.

WATTS, A. B., TEN BRINK, U. S., BUHL, P., & BROCHER, T. M. 1985. A multichannel seismic study of lithospheric flexure across the Hawaiian–Emperor seamount chain. *Nature*, **315**, 105–111.

WATTS, A. B., LAMB, S. H., FAIRHEAD, J. D., & DEWEY, J. F. 1995. Lithospheric flexure and bending of the Central Andes. *Earth Planet. Sci. Lett.*, **134**, 9–21.

WEISSEL, J. K., & KARNER, G. D. 1989. Flexural uplift of rift flanks due to mechanical unloading of the lithosphere during extension. *J. Geophys. Res.*, **94**, 13919–13950.

WERNICKE, B. 1985. Uniform-sense normal simple shear of the continental lithosphere. *Can. J. Earth Sci.*, **22**, 108–125.

WESSEL, P. 1992. Thermal stresses and the bimodal distribution of elastic thickness estimates of the oceanic lithosphere. *J. Geophys. Res.*, **97**, 14177–14193.

WESSEL, P. 1993. A reexamination of the flexural deformation beneath the Hawaiian islands. *J. Geophys. Res.*, **98**, 12177–12190.

WESSEL, P., & HAXBY, W. F. 1990. Thermal stresses, differential subsidence, and flexure at oceanic fracture zones. *J. Geophys. Res.*, **95**, 375–391.

WESSEL, P., & SMITH, W. H. F. 1995. New version of the Generic Mapping Tools released. *Eos Trans. AGU*, **76**, 329.

WHITE, N. 1993. Recovery of strain rate variation from inversion of subsidence data. *Nature*, **366**, 449–452.

WHITE, N. 1994. An inverse method for determining lithospheric strain rate variation on geological timescales. *Earth Planet. Sci. Lett.*, **122**, 351–371.

WHITE, N., & MCKENZIE, D. P. 1988. Formation of the 'Steers Head' geometry of sedimentary basins by differential stretching of the crust and mantle. *Geology*, **16**, 250–253.

WHITE, R. S. 1992. Crustal structure and magmatism of North Atlantic continental margins. *J. Geol. Soc. London*, **149**, 841–854.

WHITE, R. S., MCKENZIE, D. P., & O'NIONS, R. K. 1992. Oceanic crustal thickness from seismic measurements and rare earth element inversions. *J. Geophys. Res.*, **97**, 19683–19715.

WHITE, S. H., BURROWS, S. E., CARRERAS, J., SHAW, N. D., & HUMPHRIES, F. J. 1980. On mylonites in ductile shear zones. *J. Struct. Geol.*, **2**, 175–187.

WHITMAN, D. 1994. Moho geometry beneath the eastern margin of the Andes, northwest Argentina, and its implications to the effective elastic thickness of the Andean foreland. *J. Geophys. Res.*, **99**, 15277–15289.

WICKHAM, J. S., ROEDER, D., & BRIGGS, G. 1976. Plate tectonics models for the Ouachita foldbelt. *Geology*, **4**, 173–176.

WILLET, S. D., CHAPMAN, D. S., & NEUGEBAUER, H. J. 1985. A thermo–mechanical model of continental lithosphere. *Nature*, **314**, 520–523.

WILLIAMS, H., & HATCHER, JR., R. D. 1982. Suspect terranes and accretionary history of the Appalachian orogen. *Geology*, **10**, 530–536.

WILLIAMS, H., & HATCHER, JR., R. D. 1983. Appalachian suspect terranes. *Pages 33–53 of:* Hatcher, Jr., R. D., & Zietz, I. (eds), *Contributions to the tectonics and geophysics of mountain chains.* Geol. Soc. Amer. Memoir 158. Geological Society of America.

WILLIAMS, H., HOFFMAN, P. F., LEWRY, J. F., MONGER, J. H. W., & RIVERS, T. 1991. Anatomy of North America: thematic geologic portrayals of the continent. *Tectonophysics*, 117–134.

WILSON, J. T. 1965. A new class of faults and their bearing on continental drift. *Nature*, **207**, 343–348.

WILSON, J. T. 1966. Did the Atlantic close and then re-open? *Nature*, **211**, 676–681.

WOOLER, D. A., SMITH, A. G., & WHITE, N. 1992. Measuring lithospheric stretching on Tethyan passive margins. *J. Geol. Soc. London*, **149**, 517–532.

WORZEL, J. L. 1965. Deep structure of coastal margins and mid-oceanic ridges. *Pages 335–361 of:* WHITTARD, W. F., & BRADSHAW, R. (eds), *Submarine Geology and Geophysics.* London: Butterworths, for Colston Research Society.

WORZEL, J. L. 1968. Advances in marine geophysical research of continental margins. *Can. J. Earth Sci.*, **5**, 963–983.

WU, P. 1991. Flexure of lithosphere beneath the Alberta Foreland Basin: Evidence of an eastward stiffening continental lithosphere. *Geophys. Res. Lett.*, **18**, 451–454.

YOSHII, T. 1975. Regionality of group velocities of Rayleigh waves in the Pacific and the thickening of the plate. *Earth Planet. Sci. Lett.*, **25**, 302–312.

YOUNG, C. J. 1992. *Tectonic Evolution of the Southern African Passive Margins.* Ph.D. thesis, Univ of Leeds, Leeds, England.

ZIEGLER, P. A. 1982. Faulting and graben formation in western and central Europe. *Phil. Trans. Roy. Soc. Lond.*, **A305**, 113–143.

ZOBACK, M. D., & TOWNEND, J. 2001. Implications of hydrostatic pore pressures and high crustal strength for the deformation of intraplate lithosphere. *Tectonophysics*, **336**, 19–30.

ZOETEMEIJER, R., DESEGAULX, P., CLOETINGH, S., ROURE, F., & MORETTI, I. 1990. Lithospheric dynamics and tectonic-stratigraphic evolution of the Ebro Basin. *J. Geophys. Res.*, **95**, 2701–2711.

ZUBER, M. T. 1994. Plate tectonics: Folding a jelly sandwich. *Nature*, **371**, 650–651.

ZUBER, M. T., & PARMENTIER, E. M. 1986. Lithospheric necking: A dynamic model for rift morphology. *Earth Planet. Sci. Lett.*, 373–383.

ZUBER, M. T., PARMENTIER, E. M., & FLETCHER, R. C. 1986. Extension of continental lithosphere; a model for two scales of Basin and Range deformation. *J. Geophys. Res.*, **91**, 4826–4838.

ZUBER, M. T., BECHTEL, T. D., & FORSYTH, D. W. 1989. Effective elastic thickness of the lithosphere and mechanisms of isostatic compensation in Australia. *J. Geophys. Res.*, **94**, 9353–9367.